

REPORT DOCUMENTATION PAGE

Form Approved OMB No. 0704-0188

Public reporting burden for this collection of information is estimated to average 1 hour per response, including the time for reviewing instructions, searching existing data sources, gathering and maintaining the data needed, and completing and reviewing the collection of information. Send comments regarding this burden estimate or any other aspect of this collection of information, including suggestions for reducing this burden to Washington Headquarters Services, Directorate for Information Operations and Reports, 1215 Jefferson Davis Highway, Suite 1204, Arlington, VA 22202-4302, and to the Office of Management and Budget, Paperwork Reduction Project (0704-0188), Washington, DC 20503.

1. AGENCY USE ONLY (Leave blank)		2. REPORT DATE 27 May 1997	3. REPORT TYPE AND DATES COVERED Conference Proceedings
4. TITLE AND SUBTITLE Proceedings of the 1st International Gamma-Ray Laser Workshop (GARALAS '95)		5. FUNDING NUMBERS F6170895W0400	
6. AUTHOR(S) Conference Committee			
7. PERFORMING ORGANIZATION NAME(S) AND ADDRESS(ES) Institute of Atomic Physics -IFTAR P.O. box MG-6 Bucharest, Magurele 76900 Romania		8. PERFORMING ORGANIZATION REPORT NUMBER N/A	
9. SPONSORING/MONITORING AGENCY NAME(S) AND ADDRESS(ES) EOARD PSC 802 BOX 14 FPO 09499-0200		10. SPONSORING/MONITORING AGENCY REPORT NUMBER CSP 95-1044	
11. SUPPLEMENTARY NOTES			
12a. DISTRIBUTION/AVAILABILITY STATEMENT Approved for public release; distribution is unlimited.		12b. DISTRIBUTION CODE A	
13. ABSTRACT (Maximum 200 words) The Final Proceedings for First International Gamma-Ray Laser Workshop, 19 August 1995 - 23 August 1995 The Topics covered include: Pump sources and mechanisms, spectroscopy, superfluorescence, lasing without inversion, energetics, materials.			
14. SUBJECT TERMS		15. NUMBER OF PAGES 496	
		16. PRICE CODE N/A	
17. SECURITY CLASSIFICATION OF REPORT UNCLASSIFIED	18. SECURITY CLASSIFICATION OF THIS PAGE UNCLASSIFIED	19. SECURITY CLASSIFICATION OF ABSTRACT UNCLASSIFIED	20. LIMITATION OF ABSTRACT UL

NSN 7540-01-280-5500

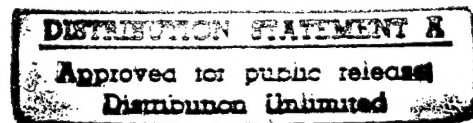
Standard Form 298 (Rev. 2-89)
Prescribed by ANSI Std. Z39-18
298-102

VOLUME 107
1997

HYPERFINE INTERACTIONS

JOURNAL DEVOTED TO RESEARCH IN
THE BORDER REGIONS OF SOLID STATE,
ATOMIC AND NUCLEAR PHYSICS

Editors:
G. Langouche – H. de Waard



 BALTZER
SCIENCE
PUBLISHERS

19970702 056

BALTZER SCIENCE PUBLISHERS BV, AMSTERDAM, THE NETHERLANDS

© J.C. Baltzer AG, Science Publishers, 1997

All rights reserved. No part of this publication may be reproduced, stored in a retrieval system or transmitted in any form or by any means, electronic, mechanical, photocopying, recording or otherwise, without the prior permission of the publisher.

HYPREFINE INTERACTIONS, JOURNAL EDITION: ISSN 0304 3834

HYPERFINE INTERACTIONS

ASSOCIATE EDITORIAL BOARD

- N. Benczer-Koller**
Department of Physics
Rutgers University
New Brunswick, NJ 08903
USA
- E. Bodenstedt**
Institut für Strahlen- und Kernphysik
der Universität Bonn
Nussallee 14–16
D-5300 Bonn 1
Germany
- J.H. Brewer**
Department of Physics
University of British Columbia
Vancouver, B.C.
V6T 2A6 Canada
- D. Chaplin**
University College
The University of New South Wales
Australian Defence Force Academy
Campbell, ACT
Australia 2600
- H.G. Devare**
Tata Institute of Fundamental Research
Bombay 400 005
India
- E. Gerdau**
II. Institut für Experimentelle Physik
Universität Hamburg
D-2000 Hamburg 50
Germany
- V.I. Goldanskii**
Institute of Chemical Physics
2–6 Vorobjevskoe Shausse
Moscow V-334
Russia 117334
- G. Goldring**
Department of Physics
The Weizmann Institute of Science
Rehovot
Israel
- P. Gütlich**
Institut für Anorganische und Analytische Chemie
Johannes Gutenberg Universität
D-6500 Mainz
Germany
- R.H. Herber**
Department of Chemistry
Wright and Rieman Laboratories
P.O. Box 939
Piscataway, NJ 08854
USA
- H.-J. Kluge**
Institut für Physik
Universität Mainz
Postfach 3980
D-6500 Mainz
Germany
- K.S. Krane**
Department of Physics
Oregon State University
Corvallis, OR 97331-6507
USA
- T. Minamisono**
Department of Physics
Osaka University
Toyonaka 560
Japan
- D.E. Murnick**
Department of Physics
Rutgers University
Newark, NJ 07102
USA
- K. Nagamine**
Meson Science Laboratory
The University of Tokyo
7-3-1 Hongo, Bunkyo-ku
Tokyo 113
Japan
- C. Petitjean**
Paul Scherrer Institut
CH-5234 Villigen
Switzerland
- L.I. Ponomarev**
I.V. Kurchatov Institute
Ploschad Kurchatova
Moscow 123182
Russia
- G. Schatz**
Institut für Physik
Universität Konstanz
D-7750 Konstanz
Germany
- J.S. Soares**
Lab. de Fisica
Universidade de Lisboa
Lisbon 1200
Portugal
- G.D. Sprouse**
Department of Physics
State University of New York at Stony Brook
Stony Brook, NY 11794
USA
- J.C. Stevens**
Mössbauer Effect Data Center
University of North Carolina
Ashville, NC 28814
USA
- N.J. Stone**
Clarendon Laboratory
University of Oxford
1 Keble Road
Oxford OX1 2NP
Great Britain
- T. Yamazaki**
Department of Physics
Faculty of Science
University of Tokyo
Bunkyo-ku
Tokyo
Japan
- F.-C. Yang**
Department of Nuclear Science
Fudan University
Shanghai
People's Republic of China

1997

GAMMA-RAY LASERS

Proceedings of the
1st International Gamma-Ray Laser Workshop
(GARALAS'95)

Predeal, Romania
19–23 August 1995



Editors:
C.B. Collins – L.A. Rivlin

BALTZER SCIENCE PUBLISHERS BV, AMSTERDAM, THE NETHERLANDS

© J.C. Baltzer AG, Science Publishers, 1997

All rights reserved. No part of this publication may be reproduced, stored in a retrieval system or transmitted in any form or by any means, electronic, mechanical, photocopying, recording or otherwise, without the prior permission of the publisher.

HYPFINE INTERACTIONS, JOURNAL EDITION: ISSN 0304 3834

GAMMA-RAY LASERS (GARALAS'95)

Proceedings of the 1st International Gamma-Ray Laser Workshop (GARALAS'95)
(Predeal, Romania, 19–23 August 1995)

Foreword

The development of a gamma-ray laser has stood as a formidable challenge to science and scientists for more than thirty years. In that time visible lasers have become commonplace in everyday life, appearing in science, surgery, supermarket and, through the compact disc, sound. No less remarkable has been the march toward ever increasing photon energies, now reaching soft X-rays. Still, the ultimate goal of the coherent production of gamma-rays remains unfulfilled, despite the recognition of its promise so early after the invention of the ruby laser. The strongly interdisciplinary nature of the problem requires a fusion of concepts from traditionally unrelated fields like quantum electronics and nuclear physics and this has provided both the challenge and the attraction. From this intriguing combination it is understandable that for many the gamma-ray laser has become more than just a topic of research, but instead of life-long goal.

In this context, the present defines a unique point in time which may prove to be a milestone in gamma-ray laser research. Recently introduced concepts and experimental results are extremely encouraging and these developments have arrived at a moment of great opportunities. Now, it has become possible to convene a meeting of truly international scope by which to assemble the leading scientists and to crystallize their community in to a recognizable field, perhaps as some have suggested into an "invisible laboratory". This First International Gamma-Ray Laser Workshop GARALAS'95 is intended to provide a fertile environment for the exchange and critical review of ideas and results. Although some concepts may be controversial, we are reminded of the importance of open discussion in a collegial atmosphere: "It is better to debate a question without settling it than to settle a question without debating it" [Joseph Joubert].

As Co-Chairs we have been charged with organizing the Program of the Workshop so as to encompass the widest possible range of topics, both experimental and theoretical, and to include the leading scientists from around the world. It has been a great pleasure to accept this challenge and we thank the members of the International Organizing Committee, Profs. C.B. Collins, R. Coussemant, G.R. Hoy, Yu.Ts. Oganessian, L.A. Rivlin, A. Sandulescu and V.I. Zoran, for this opportunity. We hope to have discharged our responsibilities successfully and look forward to the future with great anticipation.

James J. Carroll

University of Texas at Dallas/ Youngstown

State University

Anatoly A. Zadernovsky

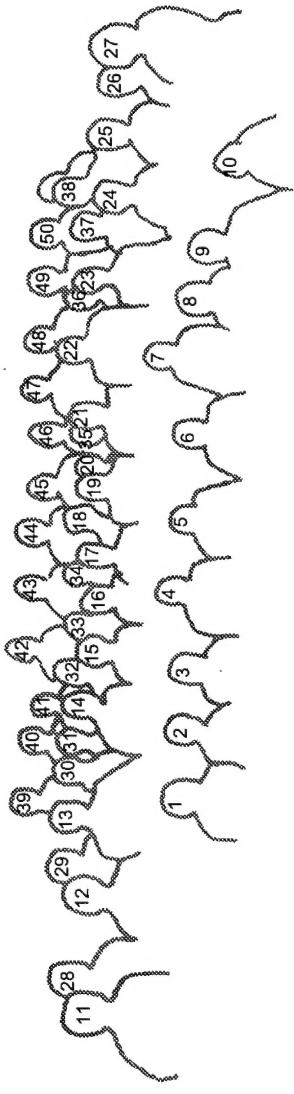
Moscow Institute of Radioengineering

Electronics and Automation

Program Co-Chairs

GARALAS'95





-
1. H. Roberts
 2. V.I. Kirichthouck
 3. I. Bibicu
 4. V.I. Zoran
 5. R. Coussemant
 6. I.I. Popescu
 7. J.J. Carroll
 8. V.V. Samartsev
 9. R.N. Shakhmurotov
 10. O. Constantinescu
 11. N.A. Enaki
 12. V.I. Vysotskii
 13. G.A. Skorobogatov
 14. A. Calboreanu
 15. A.V. Davydov
 16. A. Petrakiev
 17. T. Arisawa
 18. E. Stefanescu
 19. S.A. Karamian
 20. A.A. Zadernovsky
 21. A. Sandulescu
 22. C.B. Collins
 23. O. Kocharovskaya
 24. E. Craciun
 25. D. Craciun
 26. M. Constantinescu
 27. V. Ghita
 28. J.D. Silk
 29. J. McIver
 30. G.R. Hoy
 31. M. Hallada
 32. N. Mandache
 33. C. Popescu
 34. M. Ganciu
 35. L.A. Rivlin
 36. G. Neyens
 37. S.V. Karyagin
 38. M. Petrascu
 39. F.J. Agee
 40. D.L. Penache
 41. C. Penache
 42. C.A. Ur
 43. T.M. Zajac
 44. A.P. Tonchev
 45. G. Simon
 46. V.S. Djamko
 47. S.A. Moiseev
 48. I.V. Sokolyuk
 49. E.K. Sadykov
 50. I. Panaitescu

Preface

The movement of charged particles in confined volumes leads to the emission of electromagnetic radiation. Electrons in antennas emit radio waves and micro-waves; electrons moving in molecules and atoms radiate photons of infrared, light or X-rays; and charges moving in nuclei emit gamma-rays. At small scales the motions of charges are quantized and such electromagnetic radiation is emitted during transitions between the discrete levels of energy storage that are allowed in the confined volumes. However, in some cases because of selection rules, this quantized energy storage can last for relatively long times, on the order of milliseconds for "metastable" atoms and years for "isomeric" nuclei. The case of isomeric nuclei represents the greatest concentration of electromagnetic energy that is possible without a nuclear reaction. Storage densities reach MJ/mg for durations of a third of a century.

The same rules of electromagnetic radiation apply to all systems, so, in principle, excited states of nuclei and even isomers could be induced to emit their stored energy in a concentrated flash of short wavelengths. There is some coherence in all stimulated emission and the ultimate goal of research in this direction has been to develop enough coherence to realize a gamma-ray laser, the term which common usage has affixed as a name to the entire field. However, success in even the earliest stages of induced gamma emission (IGE) would have great technical significance.

A particularly interdisciplinary problem induced gamma emission (IGE) depends upon concepts which must be fused from traditionally diverse fields such as quantum electronics, nuclear physics, and materials science. Both strength and weakness at the same time, such richness in diversity had made it difficult to crystallize a truly recognizable field. However, recent advances in research have had aspects of breakthroughs and the time had clearly arrived to provide the structure for the responsible investigation and development of induced gamma emission (IGE) under proper international auspices. The NATO-Advanced Research Workshop GARALAS'95 was the first meeting of researchers from such diverse backgrounds and communities to span the entire scope of issues needed for an examination of the feasibility of a gamma-ray laser and other IGE devices.

The First International Gamma-Ray Laser Workshop, GARALAS'95, was organized under the auspices of an international advisory board:

Prof. Carl B. Collins, director, Center for Quantum Electronics, Univ. of Texas at Dallas, TX, USA;

Preface

Prof. Romain Coussement, Inst. voor Kern- en Stralingsfysika, Univ. of Leuven, Leuven, Belgium;

Prof. Gilbert R. Hoy, Phys. Dept., Old Dominion Univ., Norfolk, VA, USA;

Prof. Yuri Ts. Oganessian, director, Flerov Lab. of Nuclear Reactions, JINR, Dubna, Russia;

Prof. Lev A. Rivlin, Moscow Inst. of Radioengineering, Electronics and Automation, Moscow, Russia;

Prof. Aurel Sandulescu, vice-president, Romanian Academy, Bucharest, Romania;

Dr. Valeriu T. Zoran, director, Inst. of Phys. and Nuclear Engineering, Bucharest, Romania;

with Dr. Collins and Dr. Zoran serving as workshop directors. The scientific program was organized by the program co-chairs, Prof. James J. Carroll, Dept. of Phys., Youngstown State Univ., Youngstown OH, USA, and Dr. Anatoly A. Zadernovsky, Moscow Inst. of Radioengineering, Electronics and Automation, Moscow, Russia.

The Workshop GARALAS'95 was centrally located in an attractive region of Romania in order to build upon a strong scientific infrastructure while balancing travel costs and accessibility. Objectives were to promote the exchange of ideas and results while obtaining critical review of our work within the normal and pleasant framework of invited and contributed talks.

Hosted by a Romanian advisory board chaired by Dr. T. Necsoiu, director, Institute of Atomic Physics of Romania, the committee of Dr. D. Barb, Acad. I.I. Popescu, Dr. M. Petrascu, and Acad. V. Vlad assisted by the scientific secretaries, D.L. Penache and C.A. Ur, situated GARALAS'95 at the Timis conference center in the Carpathian Alps of Romania. Near the town of Predeal, it was located in a wooded area at a modest altitude and provided a beautiful venue for the 46 registered participants. As originally announced, the workshop was held from August 19 to 23, 1995. Sunday, 20th was the "conference trip" which provided the opportunity for participants to get acquainted or reacquainted while enjoying some of the unique scenery in the neighborhood, including the castle of count Vlad Tepes (Dracula). The excursion finished with a trip to the Carpathian overlook Fundata (which means "end of the world") and a grill in the hidden valley village of Moieciu. Technical sessions were full and began on monday morning and finished wednesday evening, the 23rd.

Substantial progress was reported at GARALAS'95 in all of the critical issues. Particular experiments with the isomer ^{180}Ta had shown that intense flashes of X-rays can trigger IGE from isomers without nuclear reactions – and without particle emissions or lingering radioactivities. Cross sections do not occur, and exceeded theoretical estimates by six orders of magnitude. Systematic studies of the experimental data predicted that similar cross sections would be found for the isomers of

Preface

^{178}Hf , storing the greatest known amounts of electromagnetic energy. There was significant controversy over the energy needed for the trigger photon to release the storage in ^{178}Hf with predictions ranging from 13 to 300 keV.

Theoretical results suggested that the development of some coherence during superradiant IGE could permit the manipulation of the phasing (directionality) of outputs without optics or mirrors. Gain-without-inversion (GWI) techniques were described that could give control of coherence well below threshold for conventional lasing and AVL/S (atomic vapor laser *isomer* separation) methods could provide for the concentration of isomeric nuclei to solid densities for use in future experiments and prototype devices. Controversial but impressive experimental results indicated that collective interactions of excited nuclei had already led to the self-stimulation of gamma-ray output and the coherent fractions of output from assemblies of nuclei such as ^{125}Te were reported to exceed 1%. Such exciting results had not been generally appreciated before the workshop because of their interdisciplinary nature and clearly proved the importance of continued research on these topics. The frontiers of our vision were extended greatly by advanced proposals for stimulated annihilation radiation, gamma emission from deeply cooled beams, and for even the entirely new field of quantum nucleonics, the analog of quantum electronics.

There were profound consequences of the technical accomplishments of this First International Gamma-Ray Laser Workshop, GARALAS'95. Particular concern was focused by one US participant, Dr. H. Roberts, whose report is included in this volume when he advised: "... achieving stimulated gamma release without a fission process, is a worthy goal. Such an accomplishment would *likely be comparable to the initial nuclear breakthrough over 50 years ago.*" This realization had the effect of firming the impression that the time had arrived to provide the structure for the responsible investigation and development of induced gamma emission (IGE) under proper international auspices. Accordingly, the GARALAS'95 Community elected to reorganize into a permanent commission, ICIGE, the International Commission on Induced Gamma Emission. It is an open organization whose constitution was adopted after the workshop on September 8, 1995. The commission has an advisory board, a secretariat (contact person, C.B. Collins), an administrative center in Bucharest, Romania, as well as editorial offices in Youngstown, USA and Moscow, Russia.

The First International Gamma-Ray Laser Workshop, GARALAS'95, was completely successful in crystallizing a community of colleagues in this new interdisciplinary field of IGE, but also went beyond the accomplishments of the technical program to build a structure to encourage further responsible interaction. The pervasive conclusion was that the way seems clear for rapid and significant future progress.

The guest editors would like to take the opportunity to express the great appreciation of the GARALAS community to the sponsors of the First International Gamma-Ray Laser Workshop organized as a NATO Advanced Research Workshop (ARW):

Preface

NATO Scientific and Environmental Division;
US Air Force European Office of Aerospace Research and Development
(EOARD);
University of Leuven, Institute for Nuclear and Radiation Physics;
SRS Technologies, Inc. (USA);
University of Texas at Dallas, Center for Quantum Electronics;
Romanian Academy;
The ELIAS Foundation of Bucharest, Romania;
The Ministry of Research and Technology of Romania;
The Institute of Atomic Physics, Bucharest, Romania;
The Institute of Physics and Nuclear Engineering, Bucharest, Romania;
The Institute of Optoelectronics, Bucharest, Romania.

Their support and encouragement were responsible for the successes of
GARALAS'95.

Carl B. Collins
Dallas, Texas, USA

Lev A. Rivlin
Moscow, Russia

Contents

Foreword

Preface

1. Foundations

Progress in the pumping of a gamma-ray laser <i>C.B. Collins and J.J. Carroll</i>	3
<i>K</i> -mixing in nuclear reactions <i>Yu.Ts. Oganessian and S.A. Karamian</i>	43
Gamma-ray lasing by free nuclei and by matter–antimatter beams <i>L.A. Rivlin</i>	57
Radiation machines for gamma-ray laser research <i>F.J. Agee</i>	69
The inelastic channel in time-domain Mössbauer spectroscopy <i>W.C. McDermott III and G.R. Hoy</i>	81
The importance of stimulated gamma release from isomers <i>H. Roberts</i>	91

2. Candidate Preparation and Characterization

Separation of an isotope as a precursor of a gamma-ray laser medium <i>T. Arisawa, M. Miyabe, A. Sugiyama, K. Yamazaki, A. Ohzu, Y. Suzuki, K. Akaoka, I. Wakaida and Y. Maruyama</i>	101
Production, chemical and isotopic separation of the $^{178m^2}\text{Hf}$ high-spin isomer <i>Yu.Ts. Oganessian, M. Hussonnois, Ch. Briançon, S.A. Karamian, Z. Szeglowski, D. Ledu, R. Meunier, M. Constantinescu, J.B. Kim and O. Constantinescu</i>	129
Evidence for <i>K</i> mixing in ^{178}Hf <i>C.B. Collins, J.J. Carroll, Yu.Ts. Oganessian and S.A. Karamian</i>	141
Limits on spurious contributions to integrated cross sections for photoexcitation and de-excitation of isomers <i>J.J. Carroll and C.B. Collins</i>	149
Excitation of the high-spin ^{180}Hf isomer and de-excitation of the ^{180}Ta isomer in (γ, γ') reactions <i>A.G. Belov, Yu.P. Gangrsky, A.P. Tonchev and P. Zuzaan</i>	167

Contents

A mechanism for excitation of metastable levels by (γ, γ') reactions <i>V.S. Dzjamko, I.V. Sokolyuk and T.M. Zajac</i>	175
3. Inversionless Amplification	
Lasing without inversion: problems and prospects <i>O. Kocharovskaya</i>	187
Emission of gamma rays by electron–nuclear double transitions <i>S. Olariu, J.J. Carroll, C.B. Collins and I.I. Popescu</i>	197
Lasing without inversion due to cooling subsystem <i>R.N. Shakhmuratov</i>	205
Sub-threshold inversionless quasi-stationary gamma amplification on the basis of Mössbauer ^{57}Fe nuclei and spin-crossover systems in non-conductive complex compounds with ^{57}Co <i>V.I. Vysotskii, V.V. Vysotskii, R.N. Kuz'min and V.P. Bugrov</i>	213
4. Mössbauer Effects	
Gamma-ray tuning by stimulated emission of recoil phonons <i>A.A. Zadernovsky</i>	219
Experiments on the gravity effect on the ^{109}Ag gamma resonance <i>V.G. Alpatov, Yu.D. Bayukov, A.V. Davydov, Yu.N. Isaev, G.R. Kartashov, M.M. Korotkov, V.E. Rad'ko, A.A. Sadovsky and V.M. Samoylov</i>	231
Recoil-free resonant gamma-ray absorption in ^{57}Fe nuclei in the presence of a strong microwave field <i>M. Petrascu, D. Barb, I. Bibicu and D. Tarina</i>	247
Mössbauer transition dynamics in conditions of strong excitation of nuclear spins <i>E.K. Sadykov, A.G. Isavnin and A.I. Skvortsov</i>	257
The problem of gamma-laser and controlling of Mössbauer nuclei decay (theory and practice) <i>V.I. Vysotskii, V.P. Bugrov, A.A. Kornilova, R.N. Kuz'min and S.I. Reiman</i>	277
Inhomogeneous and homogeneous broadening effects on nuclear resonance experiments <i>B. Balko, I.W. Kay, J. Nicoll, J.D. Silk and G. Herling</i>	283
Models for homogeneous line broadening in long-lived nuclear states <i>J. Odeurs and R. Coussement</i>	299
Quantum interferences at nuclear level crossing <i>R. Coussement and G. Neyens</i>	307
5. Collective Phenomena	
Quantum optics with nuclear gamma radiation <i>G. Neyens, R. Coussement and J. Odeurs</i>	319

Contents

Two-photon cooperative emission in the presence of a thermal electromagnetic field <i>N.A. Enaki and D. Mihalache</i>	333
Theory of single-photon echo (SP-echo) and the possibility of its experimental study in the gamma-region <i>S.A. Moiseev</i>	345
Dicke superradiance in a biphenyl crystal doped with pyrene molecules and the possibility of this phenomenon in the gamma range <i>V.V. Samartsev</i>	359
Superfluorescence in the presence of inhomogeneous broadening and relaxation <i>B. Balko, I.W. Kay, J.D. Silk, R. Vuduc and J.W. Neuberger</i>	369
Time-domain, nuclear-resonant, forward scattering: the classical approach <i>G.R. Hoy</i>	381
Collective polynuclear superradiance rather than stimulated emission of Mössbauer radiation from $^{125m^2}\text{Te}$ and $^{123m^2}\text{Te}$ <i>G.A. Skorobogatov and B.E. Dzevitskii</i>	401
6. Pump Sources	
X-ray generation in inverse capillary discharges for pumping <i>V.I. Zoran, M. Ganciu, A.M. Pointu, C.B. Collins and I.-I. Popescu</i>	415
Stimulation of beta-decay by laser radiation <i>V.M. Buimistrov</i>	431
7. Innovative Approaches	
Possibilities for gamma-ray stimulated emission experiments <i>P. Kamenov and A. Petrakiev</i>	441
8. The Gamma-Ray Solid Laser	
Gamma-ray solid laser: the heat problem and means of solution <i>S.V. Karyagin</i>	449
Gamma-ray solid laser: realization of pumping <i>S.V. Karyagin</i>	465
Gamma-ray solid laser: ion-optical system for fast high-quality focusing of powerful non-paraxial ion beams of large format enriched with excited nuclei <i>A.A. Sysoev, I.V. Shchekina and S.V. Karyagin</i>	481
Author index	493

Section 1

Foundations

Progress in the pumping of a gamma-ray laser

C.B. Collins

*University of Texas at Dallas, Center for Quantum Electronics, PO Box 830688,
Richardson, TX 75083-0688, USA*

and

J.J. Carroll

*Youngstown State University, Department of Physics and Astronomy,
Youngstown, OH 44555, USA*

A gamma-ray laser would stimulate coherent emission of radiation at wavelengths below 1 Å from excited states of nuclei. However, the difficulties in realizing such a device were considered insurmountable when the first cycle of study ended in 1981. Since then, research on the feasibility of a gamma-ray laser has taken on a completely new character. A nuclear analog of the ruby laser has been proposed and many of the component steps for pumping the nuclei have been demonstrated experimentally. A quantitative model based upon the new data and the concepts of this decade shows the gamma-ray laser to be feasible if some real isotope has its properties sufficiently close to the ideals. The greatest positive impact has come from the discovery of giant resonances for pumping nuclei with photons that greatly reduce the levels of input power needed. Most recently, attention has been focused upon efforts to demonstrate prelasing levels of fluorescence from simulation nuclides and actual gamma-ray laser candidates. Problems being addressed are the acquisition of macroscopic samples of the best nuclei for testing and the demonstration of appropriate instrumentation.

1. Introduction

Many advanced technologies would benefit from non-nuclear sources of high energy density. The importance would be greatest if concentrated energies could be stored for long times and then released at controlled rates on time scales of nanoseconds to microseconds. For power released as electromagnetic waves, the archetypical system would probably be the laser, although many applications such as lithography need only the flash of “light” and not its coherence. In any event, gamma rays would represent the ultimate form for such “light”.

Gamma rays are subject to the same basic laws governing the absorption and emission of electromagnetic radiation as prevail at longer wavelengths. However, since the energies per photon are so much greater, there seem to be singular advantages in gamma-ray analogs of atomic and molecular sources for the production of

intense pulses of "light". Such perceptions have driven the 33 year quest for the ultimate pulsed-power device, *the gamma-ray laser*. In fact, the advantages accrue more from the higher densities for the storage of energy than from the shorter wavelengths available upon release. A flash of induced emission at gamma-ray wavelengths would be of great technological importance in its own right, while at the same time demonstrating the means for pumping a gamma-ray laser.

Any grouping of electrically charged particles can radiate electromagnetic waves with the characteristic size of the charge distribution generally determining the type of photons most efficiently emitted. Antennas emit radio waves, waveguide structures emit microwaves, electrons oscillating against the positive nuclei in atoms emit optical light and X-rays, and protons and neutrons moving in nuclei emit gamma rays. Once emitted, gamma rays are no different from X-rays which often have the same energies. Since the oscillating charges in the nucleus emit their energy as short-wavelength electromagnetic waves *this process is not a nuclear reaction*. None of the interior particles are emitted to cause a nuclear reaction and the nucleus finishes as the stable (non-radioactive) ground state of the same isotope of the same element.

The nucleus is the smallest part of an atom which in turn is the smallest structural unit of physical matter. Thus, quantum mechanics teaches that the motions of the charged particles found within the nucleus will represent the highest velocities of circulation possible in a sample of any material. This fundamental precept means that the very highest densities of (non-nuclear) energy storage will be found in the motions of those charges. Just as in the case of atoms, the movement of charges in a nucleus can absorb photons of electromagnetic waves, which in this case are X-rays, and make a transition to an excited state of higher energy. Because of the high energy densities and great velocities, the charges usually reradiate such energies in times too short to be measured ($< 10^{-18}$ s.) However, in rare cases selection rules sufficiently inhibit the coupling of the particle motion to the electromagnetic field for the energies to be stored for tens and even thousands of years in those special nuclei. Such long-lived (meta-stable), high-energy states of excitation are termed isomeric levels and the materials are simply known as isomers. Such isomers are natural sources of high energy densities.

Our research on the gamma-ray laser identified 29 outstanding isomers which store exceptionally high densities of energy. Four examples are cited in table 1; to appreciate the energy densities presented there it should be noted that a μg of material is comparable to the amount of ink used to print a period at the end of a sentence. It can be seen that the energy storage of the best of the isomers, $^{178}\text{Hf}^{\text{m}2}$ is more than a gigajoule per gram. Since one of its key transitions for the output of electromagnetic radiation has a lifetime of 70 ns after triggering, the power density available from that material is $(1.3 \times 10^9 \text{ J g}^{-1}/7 \times 10^{-8} \text{ s})$, or about *0.05 exawatt per gram*.

Since isomers derive their long shelf lives from their poor coupling to electromagnetic waves, it was traditionally thought to be impossible to trigger the release

Table 1

Summary of important properties [35] of four of the 29 most promising candidate isomers for a gamma-ray laser

Isomer	Energy density (J/ μ g)	Shelf halflife $T_{1/2}$	Trigger photon (MeV)
$^{177}\text{Hf}^m$	1500	51 min	~ 0
$^{178}\text{Hf}^{m2}$	1300	31 yr	< 0.5
$^{179}\text{Hf}^m$	600	25 d	~ 1.5
$^{180}\text{Ta}^m$	40	$> 10^{15}$ yr	~ 2.8

of the stored energy. However, a recent and major breakthrough in research on the feasibility of a gamma-ray laser showed the existence of a giant pumping resonance at an energy near 2.5 MeV in nuclei with masses around 180. In effect, this resonance provided a "gateway" state through which the selection rules making an isomer long-lived could be violated. If an isomeric level initially stored an energy of 2.0 MeV, only 0.5 MeV would be needed to reach a gateway at 2.5 MeV. The absorption of an X-ray photon of that energy would excite the system to such a level which would be very strongly coupled to the electromagnetic fields. The sum of the stored energy and that of the trigger X-ray photon would then be promptly emitted, or dumped, as gamma rays.

The concept for dumping the energy from controlled fractions of isomeric populations has been demonstrated in a series of experiments with the fourth of the materials listed in table 1. This was first accomplished at the Center for Quantum Electronics at the University of Texas at Dallas (UTD) and was subsequently confirmed in separate experiments at the Institut für Kernphysik, Technische Hochschule Darmstadt. The systematics for the occurrence of the giant pumping resonances has been proven in a series of UTD experiments which located them in nuclei in the region of masses between 167 and 195.

The triggered release of stored energy into electromagnetic waves works and works well. The pervasive problem has been that of the 29 promising materials, only two have yet been available for study. The production of this type of ultrahigh energy density materials is still in its infancy, although remarkable progress has already been made. For example, more than 10^{16} nuclei of the best of the materials, $^{178}\text{Hf}^{m2}$ are already available. Although not yet mass-separated and carrier-free, this is an amount from which it should be possible to obtain a target containing more than 10^{15} nuclei with essentially 100% inversion for future experiments.

It would be the very best of all possibilities to be able to immediately realize the release of high energy densities into a coherent radiation field. However, simply the induced emission of gamma rays from an isomeric sample at such powers would be of considerable technological significance. That goal is close at hand. Once attained, the development of increasing levels of coherence can be approached as a next logical objective. The triggering of the gamma radiation has been the object of our research as a first step in the pumping of a gamma-ray laser.

2. Technical background

2.1. HISTORY

Research on the development of a gamma-ray laser has followed a cyclical pattern over the past 33 years with a marked abundance of concepts and approaches. Because of the complex branching of approaches it is often difficult to follow the development of a particular idea in order to properly recognize the brilliance of the early work. However, the origins are perfectly clear. The original proposal for a gamma-ray laser was made by the distinguished Russian Professor Lev Rivlin in 1961 [1]. It went largely unnoticed at the time and the first cycle of research on this topic developed a strong momentum two years later as a result of independent early publications from the US [2,3] and Russia [4,5].

In the first cycle of study which lasted from 1963–1980, considerable attention was given to the problem of suddenly assembling a critical density of prepumped nuclei to reach the threshold for stimulated emission. At the end of this period it was generally accepted that such brute force approaches, usually requiring *in situ* pumping and involving only a single (output) photon, were essentially hopeless. In an encyclopedic review, Baldwin and coauthors [6] concluded the general impossibility of a gamma-ray laser based upon all techniques for pumping known in 1980. That review effectively documented the failure of the traditional approaches to a gamma-ray laser, those relying on the use of intense particle fluxes for input energy. However, toward the end of the first cycle of research the precursors of a new interdisciplinary concept began to appear [7–13]. Based upon nuclear analogs of quantum electronics, these “optical” approaches developed rapidly and launched a renaissance in the field. The basic theory [14–16] of upconversion at the nuclear level was in place by 1982 for the two possible variants, coherent and incoherent upconversion. The use of either multiphoton processes or multiple electromagnetic transitions to release the energy stored in isomers avoided many of the difficulties encountered with more traditional pumping schemes.

Since 1980, research on the feasibility of a gamma-ray laser has taken on a completely new character. In the first half decade a series of experiments verified that the concepts of quantum electronics could be applied at the nuclear level [17–21]. By 1986 one blueprint for a gamma-ray laser [16] had been established and a substantial effort was initiated toward the demonstration of its feasibility. This article reviews the major advances of the most recent decade along that line. Those advances have significantly increased the likelihood of the feasibility of a gamma-ray laser while demonstrating the means for the induced emission of gamma radiation. Excellent concepts for the development of coherence in the levels being pumped, together with even more advanced approaches to lasing, are discussed by the proponents of those ideas elsewhere in this issue.

2.2. CONCEPTS

At first approach it would seem that the prospects for all ultrashort-wavelength lasers would be vitiated by a very fundamental factor [6]. The basic ν^3 dependence of electron transition probabilities upon frequency, ν so limits the storage of pump energies in atoms and molecules that even now some of the largest pulsed-power machines are able to excite only millijoules of laser output and then only at soft X-ray energies. In contrast there are four unique advantages of a gamma-ray laser that would accrue from its operation upon electromagnetic transitions of nuclei:

1. The constant linking ν^3 with lifetime is more favorable by orders-of-magnitude because of the accessibility of a variety of transition moments. The effects pumped by an input pulse can be integrated up to larger values for longer times.
2. Nuclear meta-stables store keV and even MeV for years. With upconversion schemes most of the energy is input *ex situ*, long before the time of use and triggering requirements are small.
3. Nuclear transitions need not experience thermal broadening and natural linewidths are routinely obtained. Without broadening, electromagnetic cross sections are large and values for 1 Å transitions typically exceed the cross section for the stimulation of Nd in YAG.
4. Working meta-stables can be concentrated to solid densities.

The essential concept driving the renaissance in gamma-ray laser research was the “optical” pumping of nuclei [7–16]. In this context optical meant X-rays, but the fundamentals were the same. Useful, resonant absorption of pump power would occur over short distances in a thin low-Z medium to produce high concentrations of excited nuclei while wasted wavelengths would only be degraded to heat in much larger volumes. This was the basic concept for avoiding the severe material damage which would have destroyed the Mössbauer effect that would have resulted from the particle-pumping schemes of the first cycle of research emphasized before 1980. In the blueprint of 1982 for upconversions [16], one of several possible types of resonant photopumping was envisioned to transfer the stored population of an isomer to a “gateway” state at the head of a cascade leading to the upper laser level. Of the cases considered, this nuclear analog of the ruby laser embodied the simplest concepts for a gamma-ray laser. Not surprisingly, the greatest rate of achievement in the last decade in the pumping of high-energy density media has been realized in that direction.

For ruby, the identification and exploitation of a bandwidth funnel were the critical keys in the development of the first laser. There was a broad absorption band linked through efficient cascading to the narrow laser level. Our theory [16] called

for a nuclear analog of this structure which was unknown in 1986 when intensive experiments were started. Now, that theory has been confirmed.

2.3. THEORETICAL MODEL

The sequence for triggering the release of the energy stored in an isomeric state [16,22] is shown in fig. 1. The population in the initial level is transferred to a broad pump band, or “gateway” state, which bridges the selection rules that would otherwise limit the coupling of the isomer to the electromagnetic fields. The normal decay from the gateway is accompanied by the emission of immediate fluorescence and leads to the principal laser level from which the sustained output of power will be emitted. Population can be accumulated in that level by continuing to run the pump cycle for a time comparable to the lifetime of the output state.

Pumping processes like that of fig. 1 have been known for over 50 years [23,24] although relatively few results have been published in that time. Practical difficulties with the calibration and availability of sources of irradiation had limited the

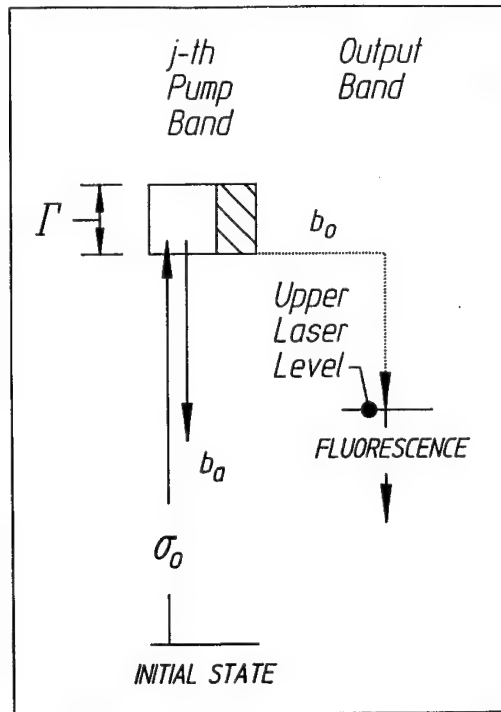


Fig. 1. Schematic representation of the pumping of a fluorescence level through a pump band, or gateway state, of natural width Γ . The initial level from which the population is excited with an absorption cross section σ_0 can be either a ground state or an isomer. The branching ratios b_a and b_o give the probabilities that the gateway will decay directly back to the initial state, and directly or by cascade to the fluorescence level, respectively. Only a single gateway is shown but there could be more; the index j is used to identify individual pump bands.

degree of reproducibility achieved in work prior to about 1987, as discussed in the next section. The processes are classified as inelastic scattering, or (γ, γ') , reactions in the literature of nuclear physics where the γ and γ' represent the incident and scattered photons, respectively. In terms of the target nucleus X the notation is $X(\gamma, \gamma')X^*$ in which X^* represents the same nucleus in its final state of excitation. If the final state is an isomer, the * is replaced by m.

For a sample that is optically thin at the pump wavelength, a computation of the number of nuclei pumped by a (γ, γ') reaction into a given excited state should be straightforward [16,22,25]. Most intense X-ray sources emit continua, either because bremsstrahlung is initially produced or because spectral lines are degraded by Compton scattering in the immediate environment. Then the irradiation of a sample containing N_i target nuclei in the initial state results in a time-integrated yield of final-state nuclei, N_f according to the general relation

$$N_f = N_i \Phi_0 \int_0^{E_0} \sigma(E) F(E, E_0) dE, \quad (1)$$

where the photoexcitation reaction is described by the energy-dependent cross section, $\sigma(E)$. The photon continuum is represented by an endpoint, E_0 and the time-integrated spectral intensity, ϕ which is written as the product of the total X-ray flux incident on the sample, Φ_0 in photons cm^{-2} , and a function $F(E, E_0)$ that gives the distribution of intensities within the continuum. The distribution is normalized so that

$$\int_0^{E_0} F(E, E_0) dE = 1. \quad (2)$$

All (γ, γ') reactions occurring at energies below the threshold for particle evaporation resonantly excite discrete levels [25,26]; for the population of isomers the relevant levels are pump bands like that depicted in fig. 1. Only one gateway appears there, but there could be more. Each gateway, identified by the index j , would be excited at a different energy, E_j but all would branch to some extent into the same fluorescent final state f. Although the width of the j th level is broad on a nuclear scale, it is narrow in comparison to the scale of energies E over which $F(E, E_0)$ varies. Thus, the final-state yield can be written from eq. (1) as

$$A_f(E_0) \equiv \frac{N_f}{N_i \Phi_0} = \sum_j (\sigma \Gamma)_{fj} F(E_j, E_0), \quad (3)$$

where the activation, $A_f(E_0)$ has been introduced. This quantity is the fractional yield of the final state f, normalized per unit photon flux in the irradiating continuum. The summation in eq. (3) extends over all gateways whose excitation energies are less than the endpoint. In this expression $(\sigma \Gamma)_{fj}$ is the integrated cross section for the production of the final-state population, N_f as a result of excitation through the gateway at E_j , so that

$$(\sigma\Gamma)_{fj} = \int_{E_j-\Delta}^{E_j+\Delta} \sigma(E) dE, \quad (4)$$

where Δ is an energy small compared to the spacing between gateways but large in comparison to their widths. For each gateway the integration is performed over a Lorentzian line shape which for a purely radiative transition has the natural width, $\Gamma = (\hbar \ln 2)/T_{1/2}$, with $T_{1/2}$ being its halflife. It is straightforward to show that

$$(\sigma\Gamma)_{fj} = (\pi b_a b_o \Gamma \sigma_0/2)_{fj}, \quad (5)$$

in which the branching ratios b_a and b_o specify the probabilities that a population pumped by absorption into the j th gateway will decay back into the initial state or, by cascade, to the output level, respectively. The quantity $\sigma_0/2$ is the peak of the Breit–Wigner cross section [25,27] for the absorption transition,

$$\sigma_0 = \frac{\lambda^2}{2\pi} \frac{2I_j + 1}{2I_g + 1} \frac{1}{\alpha_p + 1}. \quad (6)$$

where λ is the wavelength of the X-ray at the resonant pump energy E_j , the angular momenta of the gateway and ground states are I_j and I_g , respectively, and α_p is the total internal conversion coefficient for the pump step shown in fig. 1.

Whether or not the initial state being pumped is the ground state or a long-lived isomeric level, the principal figure of merit is the integrated cross section. This quantity reflects the efficacy for the transfer of population to a fluorescence level, and therefore its availability to an output transition. Thus, it is the nuclear equivalent of the fluorescence efficiency, so important in the early development of atomic and molecular lasers.

3. Critical experiments

3.1. FOUNDATIONS

3.1.1. Model verification

The most tractable (γ, γ') reactions for study are those for the photoexcitation of stable isotopes from their ground states up to isomeric levels. In many cases the product is sufficiently long-lived to be readily examined after termination of the input irradiation, although lessons can be learned that can be applied to excitation of the shorter-lived levels more useful in a laser. The prototype for basic study has been the reaction $^{111}\text{Cd}(\gamma, \gamma')^{111}\text{Cd}^m$ exciting the 48.6 min level at 396 keV. Three of the classical measurements of integrated cross section were conducted in 1979, 1982, and 1986 as reported in refs. [28–30], respectively. Probable errors were quoted as varying only from 7 to 14%, and yet no two of the measurements were

even within a factor of 2 from each other. This discrepancy led to serious contentions over the way in which the expected fluorescence yields were calculated [29]. Because of the pervasive disagreements in the literature about nuclear photopumping, one of the first priorities in the most recent cycle of research was placed upon quantitative validation of the model.

Many of the early conflicting measurements were performed with the use of radioisotopes for the irradiation of samples. From the perspective of laser physics, those would appear to be the most unreliable sources of energetic photons for (γ, γ') reaction studies. Although assumed to emit line spectra, in actual usage they produced intensities which were dominated by continua resulting from photons which had sustained multiple Compton scattering by collimators and shielding in the irradiation environment. Such multiple scatterings are difficult to calculate and are still impossible to measure in practical laboratory configurations without further perturbing the spectra. In contrast, the spectral intensities of bremsstrahlung are routinely calculated with high accuracy from measured accelerator currents and target geometries by well established, modern computer codes [31,32] such as are commonly used in radiological treatment planning [33].

In our experimental work of the last five years the bremsstrahlung from six accelerators in different experimental environments was used to verify the fluorescence model of eqs. (1)–(6) and to cross-check the accelerator intensities. The devices involved in this effort were the e-beam machines DNA/PITHON at Physics International and DNA/Aurora at the US Army Research Laboratory, a 4 MeV and a 6 MeV medical linac at the University of Texas Health Sciences Center, the superconducting injector to the storage ring at Darmstadt (S-DALINAC) and our own 4 MeV linac, the Texas-X. Spectral intensities from bremsstrahlung targets irradiated by these accelerators were calculated with the EGS4 coupled electron/photon transport code [31] for the linacs and with the TIGER code [32] for the e-beam devices. The codes were adapted for each individual configuration and closely monitored values of electron currents were used as inputs to the calculations. In this way both $F(E, E_0)$ and Φ_0 were obtained. In some instances Φ_0 was separately verified by in-line dosimetry using thermoluminescent dosimeters (TLDs) or ionization chambers.

Of the many potential nuclides which might be used to confirm the formulations of eqs. (1)–(6), the early literature [34] supported the calculation of integrated cross sections for very few. Table 2 includes those which were known with sufficient accuracy to serve as standards. In the convenient units of $10^{-29} \text{ cm}^2 \text{ keV}$, values of integrated cross section ranging from the order of unity to a few tens characterize bandwidth funnels that are sufficient for demonstrations of nuclear fluorescence from reasonable amounts of material at readily accessible levels of input.

In the calibration experiments, samples with typical masses of grams were exposed to the bremsstrahlung from the six accelerators for times ranging from seconds to hours for the continuously operating machines and to single flashes from the pulsed devices. The activations, A_f of eq. (3) were determined by counting the

Table 2

Summary of nuclides, and excitation energies, E_j , and integrated cross sections for their gateway states, that are sufficiently well-known from the literature to permit their use as calibration standards. Some integrated cross sections were calculated by eqs. (5) and (6) using constituent parameters found in the literature [34,35], while other values were directly obtained in the referenced experiments

Isomer	$T_{1/2}$	E_{fluor} (keV)	E_j (MeV)	$(\sigma\Gamma)_{fi}$ ($10^{-29} \text{ cm}^2 \text{ keV}$)
<i>Levels useful below 1.4 MeV[36,39,42]</i>				
$^{77}\text{Se}^m$	17.45 s	162	0.250	0.20
			0.480	0.87
			0.818	0.7
			1.005	30
$^{79}\text{Br}^m$	4.9 s	207	0.761	5.9
$^{87}\text{Sr}^m$	2.8 h	388	1.2	8.5
$^{115}\text{In}^m$	4.5 h	336	1.078	18.7
<i>Levels useful below 4 MeV[39,47,48,81]</i>				
$^{79}\text{Br}^m$	4.9 s	207	1.8	65
$^{87}\text{Sr}^m$	2.8 h	388	1.9	16
			2.7	430
$^{115}\text{In}^m$	4.5 h	336	1.4	64
			1.6	10.1
			2.8	540
			3.3	760
$^{137}\text{Ba}^m$	2.6 m	662	3.2	220

photons spontaneously emitted from the samples after transferring them from an accelerator chamber to a quieter environment. Usual corrections were made for the isotopic abundance, for the loss of activity during irradiation and transit, for the counting geometry, for the self-absorption of the fluorescence, and for the tabulated efficiencies [35] for the emission of signature photons from the populations, N_f . The self-absorption factor required a calculation of photon transport within the target materials which was verified in some cases by confirming that the same sample masses in different geometries with different correction factors gave the same final populations.

Measured results were in close agreement [36] with the predictions of eq. (3) using the values of $(\sigma\Gamma)_{fi}$ given in table 2. A typical example for the reaction $^{87}\text{Sr}(\gamma, \gamma')^{87}\text{Sr}^m$ is shown in fig. 2b in which the plot of activation against bremsstrahlung endpoint gives its “excitation function” [37]. Particularly valuable were the data [38] obtained with the S-DALINAC because of its ability to continuously vary the endpoint. A change of E_0 , as well as altering Φ_0 , modulates the spectral distribution function, $F(E_j, E_0)$ at all of the important energies for resonant excitation, E_j . The largest effect occurs when E_0 is increased from a value just below a gateway to one exceeding it so that $F(E_j, E_0)$ varies from zero to some finite value as depicted in fig. 2a.

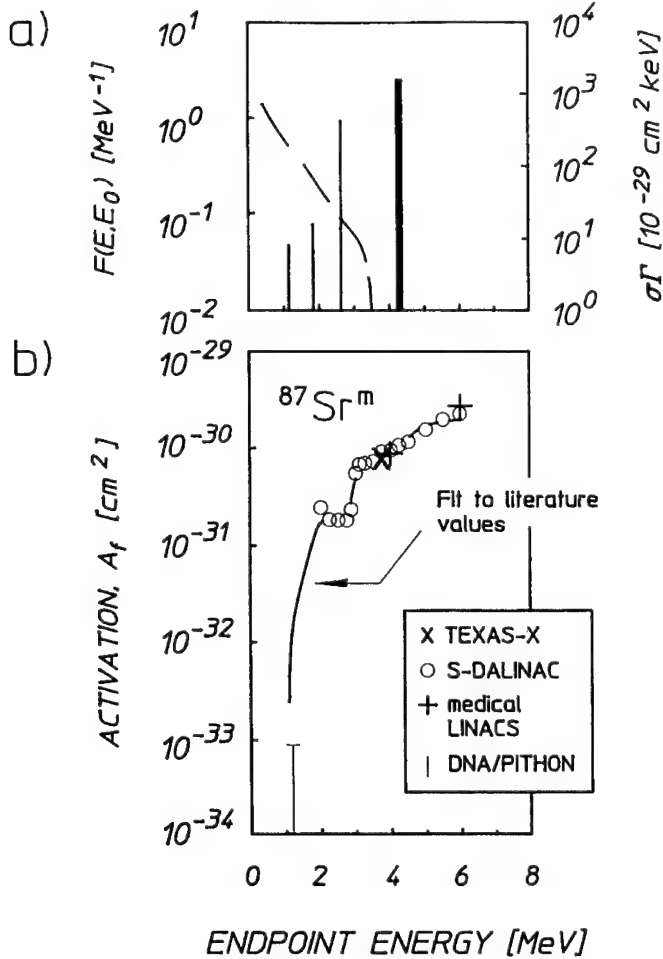


Fig. 2. (a) Calculated spectral distribution function, $F(E, E_0)$ for a typical bremsstrahlung continuum (dashed line) with an endpoint of $E_0 = 3.5$ MeV plotted with the left-hand axis. Gateway excitation energies and integrated cross sections available from the earlier literature [39] are shown by the thin vertical bars and are plotted with the right-hand axis. The thick vertical bar indicates a gateway found in the recent experiments of ref. [38]. All gateway parameters are listed in table 2. (b) Measured activations, $A_f(E_0)$ obtained using five different accelerators [37,38,51] for the reaction $^{87}\text{Sr}(\gamma, \gamma')^{87}\text{Sr}^m$ plotted with symbols as functions of bremsstrahlung endpoint. The solid curve plots the expected excitation function computed with the model of eqs. (1)–(6).

Early work [39,40] on (γ, γ') reactions had shown that excitation functions displayed very pronounced “activation edges” at the resonant excitation energies, E_j of gateways. Such activation edges are clearly seen in the data of fig. 2b. There is excellent agreement between measurements obtained with the different accelerators, and between the experimental data and the model calculations made using the literature values [38,39] of table 2. It is useful to note that the units of A_f are those of

area because they are a type of average cross section quite different from the σ_0 of eq. (6) that describes an individual transition. The small ordinate values are due to the normalization of eq. (3) which effectively averages the large σ_0 at the resonant energy E_j over the broad bandwidth of the entire irradiating continuum, within which most $E \neq E_j$.

3.1.2. Pump calibration

The high level of agreement between the measurements and the model established a confidence level sufficient to support the use of (γ, γ') reactions which populate isomers as a means of selectively sampling the spectra of single X-ray pulses like those from e-beam devices. This technique of X-ray activation of nuclei (XAN) directly measures absolute intensities at discrete energies corresponding to the E_j of gateways accessible to the bremsstrahlung [36,41–44]. An example of an XAN calibration is shown in fig. 3 for the spectrum from a single shot at an endpoint of 1.4 MeV from DNA/PITHON [42]. No scaling was involved and absolute intensities were obtained using eq. (3), integrated cross sections from table 2, measured masses of the samples, the distances, and the activations produced. Having cali-

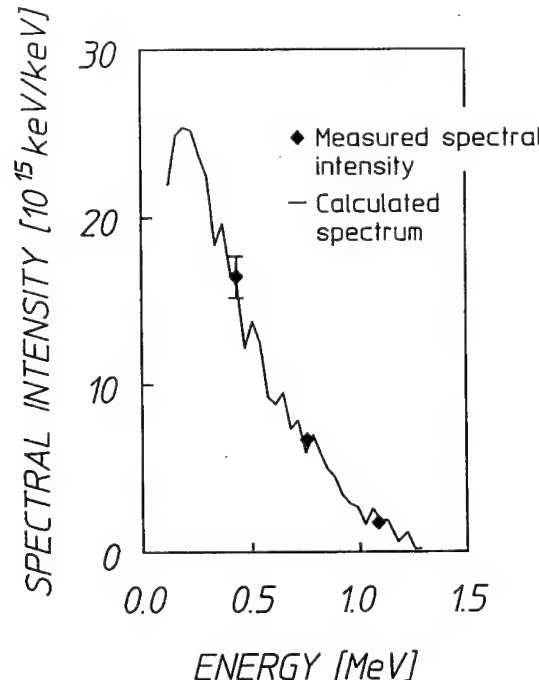


Fig. 3. Spectral intensity expressed in units of total photon energy per unit bandwidth for 1.4 MeV bremsstrahlung from DNA/PITHON measured [42] using the XAN technique (symbols) with the gateway parameters of table 2, compared with a spectrum computed (curve) with the TIGER code [32]. Uncertainties of the measured points are comparable to the size of the symbols except where otherwise indicated.

brated the spectral sources used in these experiments, the persisting uncertainties in the optical pumping of $^{115}\text{In}^m$ and $^{111}\text{Cd}^m$ were resolved [45,46] as being primarily due to the use of radioisotopes as sources of irradiation [26].

Following the further improvements in the nuclear data base listed in table 2, it has been possible to extend the XAN procedure to span the range to 4 MeV [47,48]. Fig. 4. shows an example of direct measurements [47] of the spectral intensity from a 4 MeV linac using the nuclear standards from table 2 in comparison with the calculated bremsstrahlung output.

These calibration studies served to confirm both the traditional model of nuclear activation summarized in eqs. (1)–(6) and to validate the computer codes for calculating bremsstrahlung intensities based on measured accelerator parameters. Now, there can be no reasonable doubt of procedures for quantitatively measuring integrated cross sections if an experiment is carefully performed with a bremsstrahlung source of pump radiation. Examples of data from such successful measurements are shown in figs. 5 and 6.

3.1.3. Limits on spurious contributions

Sources of possible spurious contaminations of the measurements were carefully considered as reviewed elsewhere [49]. Overall, spurious contributions to the measured activations due to natural background and incidental (e,e'), (γ,n), (n,γ) and

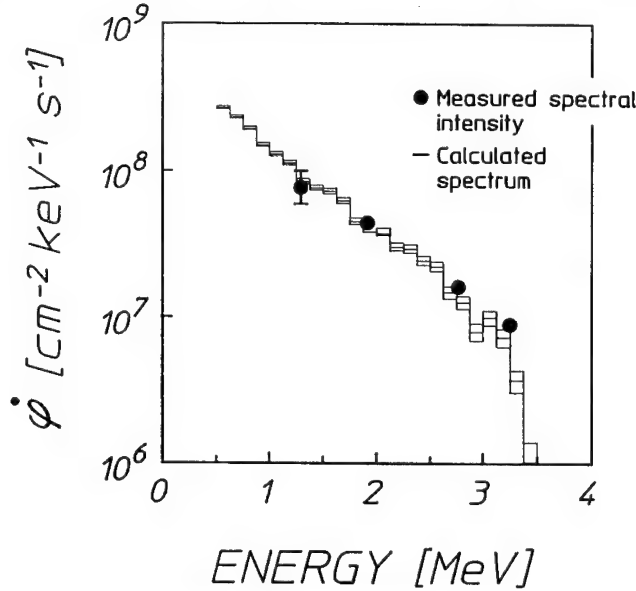


Fig. 4. Instantaneous spectral intensity, ϕ , for 4 MeV bremsstrahlung from the Texas-X measured [47] using the XAN technique (symbols) with the gateway parameters of table 2, compared with a spectrum computed (lines) with the EGS4 code [31]. Statistical errors associated with the calculations are indicated by the bars on the histograms. Uncertainties of the measured points are comparable to the size of the symbols except where otherwise indicated.

(n,n') reactions were found to be negligible on the basis of both theory and direct measurements.

3.2. GIANT PUMPING RESONANCES

3.2.1. Discovery

Expressed as partial widths, $b_a b_0 \Gamma$, the integrated cross sections for the excitation of $^{77}\text{Se}^m$, $^{79}\text{Br}^m$, and $^{115}\text{In}^m$ seen in table 2 correspond to 39, 5, and 94 μeV , respectively. While among the largest values reported prior to our studies, these results still left an aura of credibility to the traditional impressions that partial widths for exciting isomers would be limited to about 1 μeV .

Tempering expectations that integrated cross sections of even the magnitudes of table 2 might be expected for the pumping of actual isomeric candidates for a

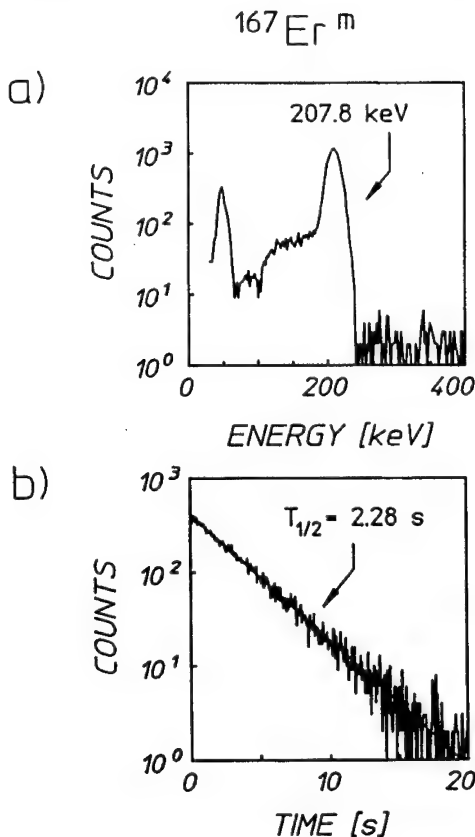


Fig. 5. Fluorescence data [51] from the decay of $^{167}\text{Er}^m$ following its excitation with 6 MeV bremsstrahlung from a medical linac for an irradiation of 25 s. The pulse-height (energy) spectrum of (a) and the multichannel-scalar (decay) spectrum of (b) were obtained using a NaI(Tl) spectrometer. The measurements of fluorescence energy and lifetime were in excellent agreement with the literature values [35].

gamma-ray laser was a concern for the conservation of various projections of the angular momenta of the nuclei. Many of the interesting candidate isomers belong to the class of nuclei deformed from the normally spherical shape. For those nuclides there is an additional quantum number of dominant importance, K , which is the projection of individual nucleonic angular momenta upon the axis of elongation. To this is added the collective rotation of the nucleus to obtain the total angular momentum J . The resulting system of energy levels resembles that of a diatomic molecule for which

$$E_n(K, J) = E_n(K) + B_n J(J + 1), \quad (7)$$

where $J \geq K \geq 0$ and J takes the values $|K|, |K| + 1, |K| + 2, \dots$. In this expression B_n is a rotational constant that is inversely proportional to the nuclear moment of

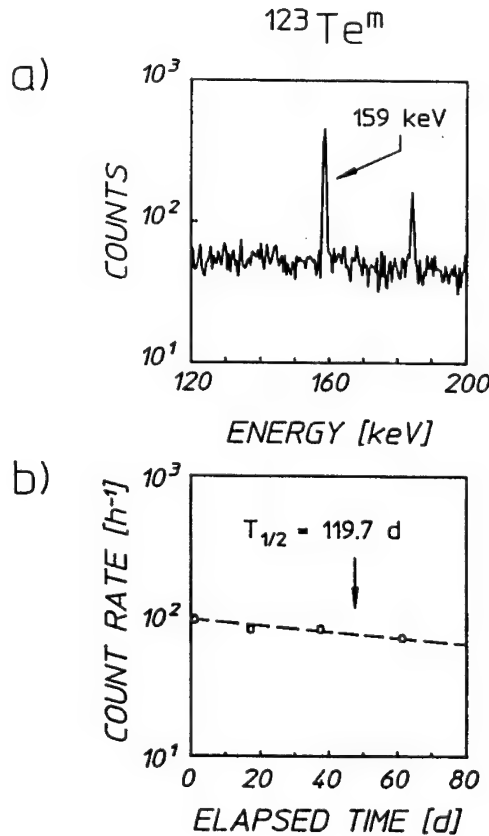


Fig. 6. Fluorescence data [51] from the decay of $^{123}\text{Te}^m$ following its excitation with 6 MeV bremsstrahlung from a medical linac for an irradiation of 2 h. The pulse-height (energy) spectrum of (a) and the counting-rate (decay) spectrum of (b) were obtained using a HPGe spectrometer. Counting periods used to obtain the measurements of (b) were 10 h. The measurements of fluorescence energy and lifetime were in excellent agreement with the literature values [35].

inertia, and $E_n(K)$ is the lowest value for any level in the resulting “band” of energies identified by other quantum numbers n . That level is termed the “bandhead”. The selection rules for electromagnetic transitions then require both $|\Delta J| \leq M$ and $|\Delta K| \leq M$, where M is the multipolarity of the transition. In most cases an isomeric state has a large lifetime because it lies in a band whose value of K differs considerably from those of lower levels to which it would otherwise be radiatively connected. As a consequence, bandwidth funneling processes such as shown in fig. 1 that start from isomeric levels must span substantial changes in K and component transitions have been expected to have large, and hence unlikely, multipolarities.

From this perspective the candidate isomer, $^{180}\text{Ta}^m$ was the most initially unattractive as it had the largest difference in K between isomer and ground state, $8\hbar$. However, because a macroscopic sample was readily available, $^{180}\text{Ta}^m$ became the first isomeric material to be optically pumped to a fluorescent level. This particular nuclide carries a dual distinction. It is the rarest stable isotope occurring in nature [35] and it is the only naturally occurring isomer. The ground state of ^{180}Ta is 1^+ with a halflife of 8.1 h while the tantalum nucleus of mass 180 occurring with 0.012% natural abundance is actually the 9^- isomer, $^{180}\text{Ta}^m$. It has an adopted excitation energy of 75.3 keV and a halflife in excess of 1.2×10^{15} years.

In an experiment conducted in 1987, 1.2 mg of $^{180}\text{Ta}^m$ was exposed to bremsstrahlung and a large fluorescence yield was obtained [50]. This was the first time a (γ, γ') reaction had been excited from an isomeric target as needed for a gamma-ray laser and was the first evidence of the existence of giant pumping resonances. Simply the observation of fluorescence from a milligram-sized target proved that an unexpectedly large reaction channel had opened. Usually grams of material had been required in this type of experiment [51].

The energy-level diagram of ^{180}Ta and its daughters [34] is shown in fig. 7, together with a schematic representation of the individual steps in the excitation and detection of the $^{180}\text{Ta}^m(\gamma, \gamma')^{180}\text{Ta}$ reaction. As can be seen in the figure, the principal means for the detection of the ^{180}Ta ground state lies in observing the K_{α} lines of its daughter ^{180}Hf , produced by electron capture decay. The efficiency for the emission of K_{α} photons relative to the number of ^{180}Ta decays is about 57% [35]. The target used in these experiments was enriched to contain 1.2 mg of ^{180}Ta diluted in 24.7 mg of ^{181}Ta . Deposited as a dusting of oxide near the center of the surface of a 5 cm disk of Al and overcoated with a 0.25 mm layer of Kapton, this sample was believed to be free from self absorption of the X-rays from the daughter Hf. Such a construction minimized corrections to the raw data and since self-absorption was neglected, the final results could only underestimate the activation had there been some unexpected absorption.

The sample was exposed to bremsstrahlung from the 6 MeV medical linac whose output dose rate had been calibrated with an accuracy of $\pm 3\%$. This was the machine that presented the worst-case neutron flux which could have contributed another 6% error. However, as described below, the measurements were subsequently confirmed in absolute comparisons with data taken at the S-DALINAC.

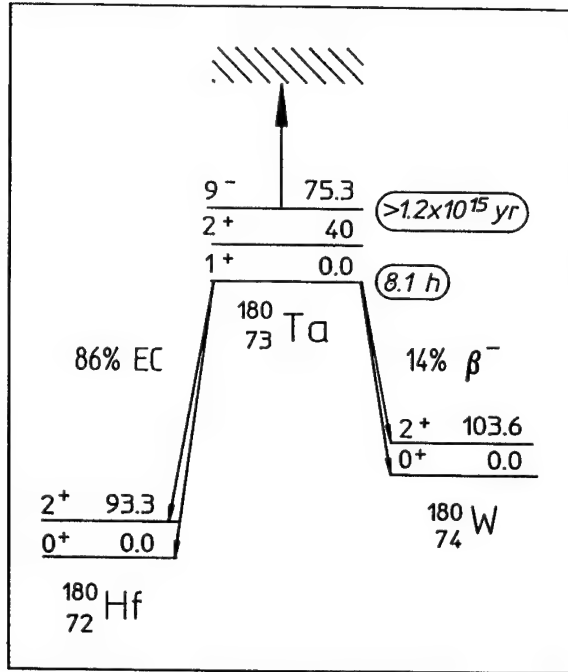


Fig. 7. Schematic energy-level diagram [34,50] of ^{180}Ta and its daughters. Energies are given in keV and the halflives of the tantalum ground state and the isomer are shown. The upward arrow indicates the pump transition to the gateway represented by the hatched level. The cascade from the gateway is unknown but leads to the ground state which transmutes to the two daughters by electron capture and beta decay. The primary signatures of the decay of the ground state are K lines from ^{180}Hf characterized by the lifetime of the parent, $^{180}\text{Ta}^g$.

After the irradiation, the sample was counted with an n-type, HPGe spectrometer. Conventional techniques were used to calibrate the counting system with isotopic standards. Fig. 8 shows the spectra from the enriched target before and after a 4 h, 6 MeV irradiation, while fig. 9 shows the dependence upon time of the counting rate observed in the Hf(K_α) peaks after the exposure. Data points are plotted at the particular times at which the instantaneous counting rate equals the average counting rate measured over the finite time intervals shown. The figure shows the close agreement between the measured decay and the literature value for the ground-state halflife of 8.1 h. Analyses [38,50] of the data indicated that the partial width for the dumping of $^{180}\text{Ta}^m$ was around 0.5 eV.

To determine the transition energy, E_j from the $^{180}\text{Ta}^m$ isomer to the gateway level, a series of irradiations [38] was made at the S-DALINAC facility using fourteen different endpoints in the range from 2.0 to 6.0 MeV. The existence of an activation edge was clearly seen in the data shown in fig. 10b. The fitting of such data to the expression of eq. (3) by adjusting trial values of $(\sigma I)_j$ provided the integrated cross sections for the dumping of $^{180}\text{Ta}^m$ isomeric populations into freely radiating

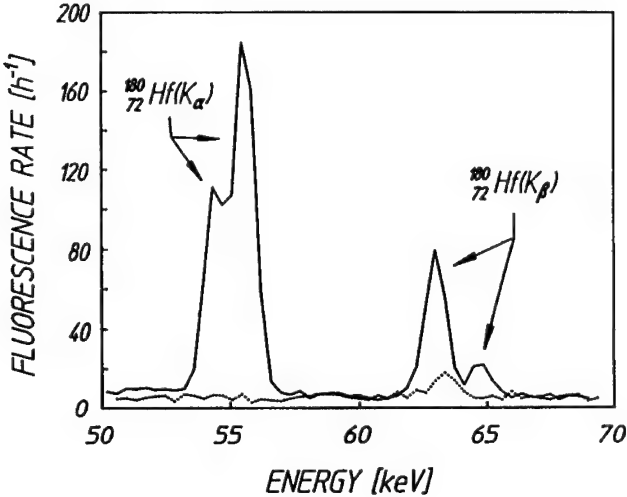


Fig. 8. Pulse-height spectra [50] showing fluorescence counting rates from an enriched sample of $^{180}\text{Ta}^m$ before (dotted) and after (solid) irradiation with the 6 MeV medical linac. The measurements were made with a HPGe spectrometer. The prominent K lines from daughter ^{180}Hf nuclei produced by decay of ^{180}Ta ground states indicate the dumping of significant numbers of ^{180}Ta isomers in this mg-sized sample.

states. Reported values [38] are summarized in table 3 and shown schematically in fig. 10a. The lowest-lying giant pumping resonance was found at an excitation energy near 2.8 MeV.

The integrated cross sections in table 3 are enormous values exceeding anything previously reported for transfer through a bandwidth funnel by two orders of magnitude. In fact they are 10 000 times larger than the values usually measured for (γ, γ') reactions in nuclei.

3.2.2. Systematics

A survey of 19 isotopes [51] conducted with the four U.S. accelerators over a fairly coarse mesh of bremsstrahlung endpoints confirmed the existence of giant resonances for the photoexcitation of isomers in the region of masses near 180. A summary of the results is shown in fig. 11. Activation edges observed in excitation functions measured [52] using the S-DALINAC continued to support the identifications of integrated cross sections for pumping and dumping of isomers in the mass-180 region that were on the order of 10 000 times greater than usual values. Another study [53] with the S-DALINAC showed that the giant pumping resonances reappeared at lower masses near 120. The close similarity seen in fig. 11 for integrated cross sections and excitation energies for gateways between nuclei with such dissimilar single-particle structures seems to support the identification of the giant pumping resonances with some type of property of the nuclear core. Whatever the mechanisms, the experimental fact remains that interband transfer

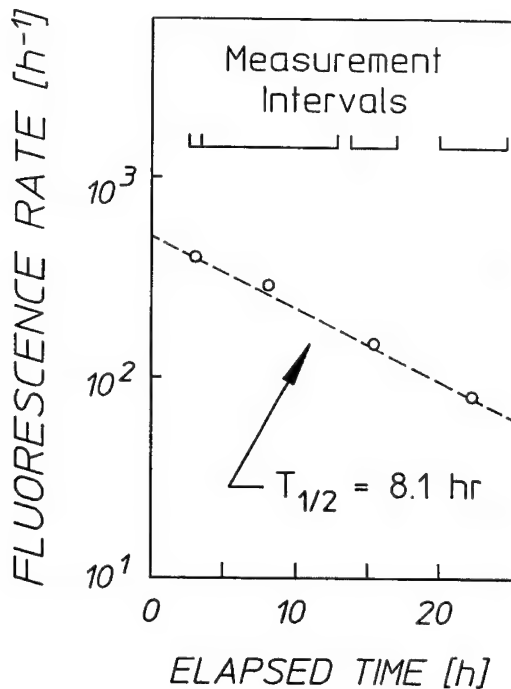


Fig. 9. Decay spectrum [50] plotting counting rates measured for the Hf K_a lines seen in fig. 8 as a function of time elapsed from the end of the irradiation. The measurements were made over the intervals shown and uncertainties in the observations were comparable to the size of the plotted symbols. The measured decay rate was in excellent agreement with the literature value [35].

processes connecting isomers to freely radiating levels can almost commonly be pumped through enormous partial widths reaching 0.5 eV, even when the transfer of angular momentum must be as great as $\Delta K = 8$. It seems this is the nuclear analog of the giant resonance for pumping ruby at the atomic level.

3.2.3. Structure

As encouraging as were the studies showing the frequency with which giant pumping resonances occurred throughout the table of nuclides, a major concern remained. To lower pump requirements for a laser it is necessary that the $(\sigma\Gamma)$ be large, but this alone is not sufficient. In the ideal case [54] the integrated cross section would be elevated by a strong width multiplying a cross section for absorption having the maximum value possible from eq. (6). In that case the ratio of pump power per unit volume absorbed resonantly to excite nuclei to the fraction absorbed nonresonantly and degraded to heat would be the largest possible. This is an important factor in thermal survival.

The density of excited states is very high in the nuclei favored in fig. 11, and is especially so in ¹⁸⁰Ta because it is one of the few stable odd-odd nuclei. It could have been the case that the remarkable magnitude found for $(\sigma\Gamma)$ in the dumping of

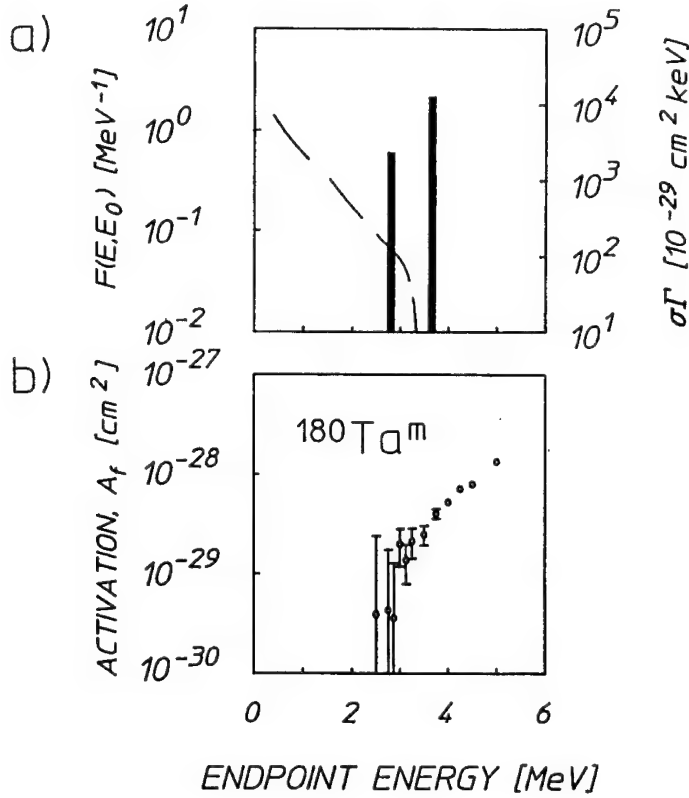


Fig. 10. (a) Calculated spectral distribution function, $F(E, E_0)$ for a typical bremsstrahlung continuum (dashed line) with an endpoint of $E_0 = 3.5$ MeV plotted with the left-hand axis. Gateway excitation energies and integrated cross sections measured in the experiments of ref. [38] are shown by the thick vertical bars and are plotted with the right-hand axis. (b) Measured activations, $A_f(E_0)$ obtained with the S-DALINAC [38] for the reaction $^{180}\text{Ta}^m(\gamma, \gamma')^{180}\text{Ta}$ plotted with symbols as functions of bremsstrahlung endpoint. The activation edge at 2.8 ± 0.1 MeV indicated the excitation energy of the lowest gateway; its magnitude was sufficient to characterize it as a giant pumping resonance.

the population of $^{180}\text{Ta}^m$ was the result of a great number of adjacent gateways with $(\sigma\Gamma)_{fj}$ of unremarkable size, but adding in eq. (3) to give a surprising total yield. While such a result would have still been exciting, it would have been much less helpful in rejecting the waste pump power degraded to heat. To show that this was not the case required that scattering measurements be performed.

From fig. 1 it can be seen that photoexcitation events which do not lead to the population of the state f should be detected by the re-emission, or elastic scattering, of the incident photon initially absorbed by the gateway. In analogy with the $(\sigma\Gamma)_{fj}$ of eq. (5), the integrated cross section for scattering can be written,

$$(\sigma\Gamma)_{0j} = (\pi b_a^2 \Gamma \sigma_0 / 2)_{0j}. \quad (8)$$

A large value of $(\sigma\Gamma)_{0j}$ would insure that enough photons could be scattered for

Table 3

Recently measured values [38] of integrated cross sections and excitation energies for gateways in the reaction $^{180}\text{Ta}^m(\gamma, \gamma')^{180}\text{Ta}$

E_j (MeV)	$(\sigma\Gamma)_{fj}$ (10^{-29} cm 2 keV)
2.8 ± 0.1	$12\,000 \pm 2000$
3.6 ± 0.1	$35\,000 \pm 5000$

spectroscopic analysis to determine at what energies the corresponding transitions were excited. In the event $b_a < 1$, some fraction of the gateway-state population would also decay to the isomer to contribute to $(\sigma\Gamma)_{fj}$ and the energies for excitation of some of the giant pumping resonances could be accurately determined.

The design of an experiment to compliment activation measurements by identifying scattering from the pumping resonances requires a nuclide with several favorable properties. It must have an isomer with a reasonable lifetime of seconds to hours and be available in gram quantities with isotopic purity. Beyond such practical concerns would be the desire to have the nuclear structure well characterized for energies below those at which giant pumping resonances would be expected. With

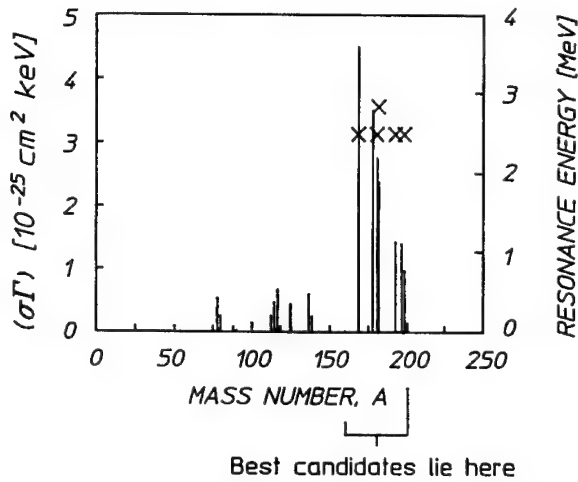


Fig. 11. Integrated cross sections and excitation energies, plotted with the left-hand and right-hand axes, respectively, for gateways measured in the experiments of refs. [38,51,52,78] which pump or dump populations of isomers. Integrated cross sections are given as the equivalent, single-gateway value at a reference energy of 2.125 MeV. The groupings of pumping strengths seen in the figure correspond to mass islands between magic numbers for neutrons and protons. The best candidates for a gamma-ray laser lie within the mass-180 island which contains the largest values of integrated cross section corresponding to giant pumping resonances. Within each island, the integrated cross sections and gateway excitation energies vary only slowly with changing mass number A , despite differing single-particle structures among neighboring nuclides.

these constraints it was relatively straightforward to identify ^{115}In as an optimal vehicle for a first test.

A modern experimental arrangement especially designed for nuclear resonance fluorescence (NRF) experiments has been recently described [55]. The spectrum of the intense bremsstrahlung produced by the S-DALINAC accelerator was calibrated in real time from readily resolved reference transitions observed in the scattered radiation from Al and B wafers which sandwiched the In target. In order to cover an energy range $E_j \simeq 1.5\text{--}4.5$ MeV, measurements were performed at end-points of 3.1, 4.6 and 5.2 MeV. The variation of E_0 also provided the means to distinguish ground-state (elastic) transitions from decays to excited states. Detailed scattering spectra are shown in the literature [56].

The integrated cross sections obtained from the excitation of the final state, $^{115}\text{In}^m$ and the photon scattering are shown in fig. 12a. The excitation energies corresponding to the large $(\sigma\Gamma)_{fj}$ values of gateways are shown in the upper part of fig. 12a. The widths of the histograms represent the experimental uncertainty in those energies. The striking result is that except for a few moderate levels around 3.0 and 3.7 MeV, all strongly scattering (γ, γ') transitions were found within the energy regions corresponding to the gateways. Thus, those transitions (or a subset thereof) must have been responsible for the isomer population. No other (γ, γ') states were resolved in the lower part of fig. 12a up to $E_j = 5$ MeV. This confirmed that all important pump bands in this range had been identified.

Further insight was attained from a theoretical analysis within the unified model

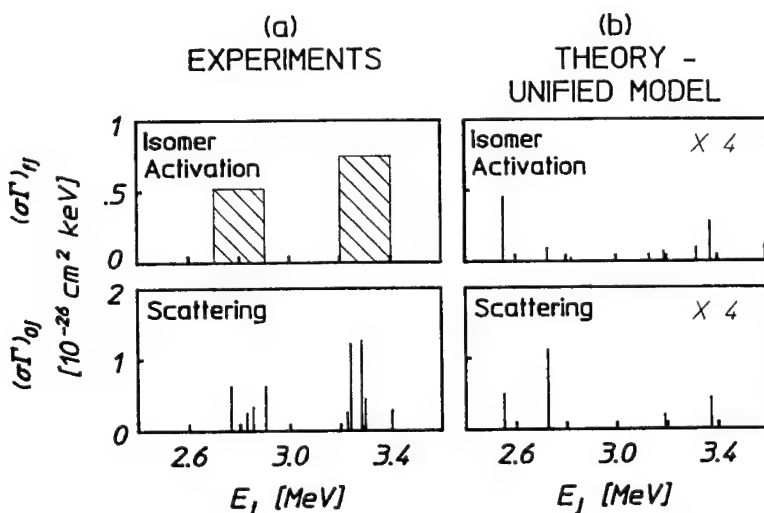


Fig. 12. Comparison of integrated cross sections [56] for ^{115}In plotted as functions of gateway excitation energy, E_j , obtained from (a) experimental measurements, and (b) unified-model calculations. The upper panels show values of $(\sigma\Gamma)_{fj}$ of eq. (5) for the photoexcitation reaction $^{115}\text{In}(\gamma, \gamma')^{115}\text{In}^m$, while the lower panels show values of $(\sigma\Gamma)_0j$ of eq. (8) for elastic photon scattering, $^{115}\text{In}(\gamma, \gamma)^{115}\text{In}$.

[55] which is well suited to nuclei like ^{115}In near shell closure. The configuration space was built by proton 1h-states (relative to the semi-magic ^{116}Sn nucleus) and 1p–2h states across the major shell (relative to ^{114}Cd) coupled to collective phonons (up to three quadrupole and two octupole) in the underlying cores. A residual interaction was then used to mix the two subspaces. The comparison to experiment was accomplished by first computing all possible upward E1, M1, or E2 transitions in such a system. Then for states with a large partial width for transitions to the ground state, the full decay cascade was taken into account to determine model values for $(\sigma\Gamma)_{0j}$ and $(\sigma\Gamma)_{fj}$. In accordance with the experimental results, strong gateways were found only in a limited energy region above $E_j = 2.5$ MeV; typical $(\sigma\Gamma)_{fj}$ values at lower energies were reduced by a factor of about 10–100. The total number of important states was small, in agreement with the measurements.

Fig. 12b presents the theoretical results which show a rough division of transition strengths into two groups which might be related to the experimental $(\sigma\Gamma)_{fj}$ data. Although a one-to-one correspondence seemed beyond the limits of the approach, simply summing the model $(\sigma\Gamma)_{fj}$ within each group compared favorably to the experimental values. The overall agreement seemed quite encouraging and indicated that no major part of the relevant configuration space was missed. A detailed analysis of the main decay branches revealed a clear picture of the important amplitudes in the gateway wavefunctions. All theoretical pump bands had $J^\pi = 7/2^+$ and the coupling to the ground state was dominated in all cases by single-particle $1g_{9/2} \rightarrow 1g_{7/2}$ spin-flip transitions. The first steps in the decays to the isomer in the model calculations proceeded mainly via E1 or E2 transitions.

The critical point to be made from this study, and supported by similar results [57] for the reaction $^{89}\text{Y}(\gamma, \gamma')^{89}\text{Y}^m$, is that nuclear structure theory, scattering measurements and photoactivation experiments all confirmed that giant pumping resonances corresponded to a small number of discrete gateways. Absorption cross sections approached those ideals of eq. (6) needed to separate the wasted deposition of heat from the useful excitation of nuclei in a sample pumped with intense X-rays.

3.2.4. Significance

The significance of these favorable developments to laser feasibility may be appreciated with the help of analogs from the atomic scale. In atoms there is a familiar increase in the density of levels available for excitation as transition energies approach the limit for photoionization. The number of such Rydberg states is generally on the order of n^3 , where n is the principal quantum. Thus it is difficult to pump significant energy into a selected level with a continuum source of modest spectral width. The general difficulty in scaling X-ray lasers is a clear illustration of this problem and it seems that only the rigor imposed by selection rules allows the few cases demonstrated to work at all.

In nuclei the situation could have been even worse because the likelihood is much greater for there to be levels that from the atomic perspective would be considered

analogous to multiply excited states. The nuclear level density is more difficult to specify quantitatively, but an approximation of $\exp(\sqrt{n})$ is reasonably indicative as excitation energies approach that needed to remove the first particle in a photonuclear reaction. Since selection rules were shown to be bridged by the striking efficiency with which $\Delta K = 8$ could be lost in ^{180}Ta , there was a clear hazard that highly excited nuclear levels could not be selectively excited as needed for a gamma-ray laser. Sum rules limit the strength per unit bandwidth available at a particular transition energy and there was the possibility that the sum would be smoothly distributed over the great number of levels in any interval of high excitation. Then the deposition of pump energy into nuclear excitation would have been diluted into a much larger volume by the small cross sections available to any component transition. Such a distribution of gateway strength was not found, constituting a second breakthrough of comparable importance to that achieved by dumping the population of $^{180}\text{Ta}^m$.

The giant pumping resonances found in ^{115}In show that the transition strength is concentrated into relatively few discrete lines. The nuclear structure model identified this particular case as an example of fragmented spin-flip transition strength, but the point critical to laser feasibility is the limited degree of the fragmentation. Relatively few transitions to gateway states collected all of that type of transition strength available over the range of energies from 2–5 MeV. The mechanism for this fragmentation was less clear, having arisen from detailed unified-model calculations.

Additional support for the existence of K -mixing levels in nuclides near $A = 180$ has come from recent studies that found unexpected enhancements [58–61] to low-multipolarity transitions near 2.5 MeV which were relatively unhindered by large ΔK . However, the most striking result was measured [62] for the spontaneous de-excitation of the 3.7 μs isomer $^{174}\text{Hf}^m$. There the decay of the isomer was found to occur primarily by a transition through a state at 2685 keV in which sufficient K mixing occurred for $\Delta K = 14$ to be lost between the isomer and the ground-state bands. As shown in fig. 13, this energy is remarkably close to that of the giant pumping resonance at 2800 ± 100 keV for ^{180}Ta , and other large gateways (fig. 11) for neighboring nuclei in the mass-180 island. An interesting speculation introduced as early as 1991 [63], and later amplified in 1993 [64] may explain the existence of strong, low-multipolarity transitions similar to the giant pumping resonances in nuclei near mass 180. At certain energies of excitation, collective oscillations of the core nucleons may break the symmetry upon which rests the identification of angular-momentum projections of the pure single-particle states. Within this energy range single-particle states of differing K would be strongly mixed and the possibility for transferring larger amounts of ΔK with greater partial widths might be enhanced. The energetics for giant pumping resonances for nuclei with quite dissimilar single-particle structures supports the identification of those gateways with K -mixing levels arising from a core property. In such a case, the integrated cross sections and excitation energies would be expected to vary slowly

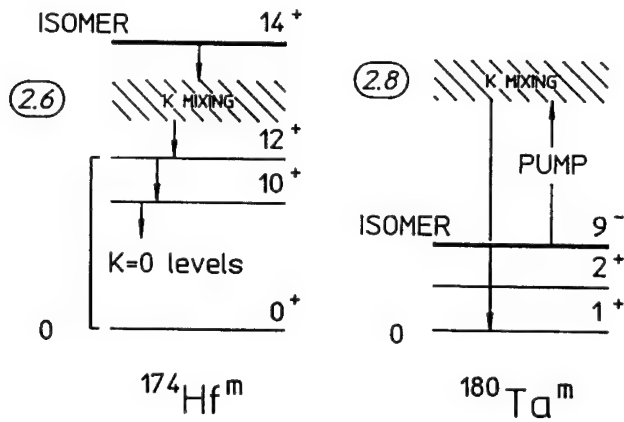


Fig. 13. Energetics for the spontaneous decay of the $3.7 \mu\text{s}$ isomer $^{174}\text{Hf}^m$ through a K-mixing level at 2.6 MeV which provided $\Delta K = 14$, compared with that for the dumping of populations of $^{180}\text{Ta}^m$ through a giant pumping resonance at $2.8 \pm 0.1 \text{ MeV}$ which provided $\Delta K = 8$. Both intermediate levels are expected to be admixtures of single-particle states having differing values of the K quantum number.

among neighboring nuclei. This behavior [52] is seen in fig. 14 that plots the quantity S which is proportional to $(\sigma\Gamma)$ against nuclear deformation, a core property. Elevated interest in K -mixing processes at low energies has motivated other studies which have suggested the related concept of tunnelling through a triaxial barrier as the underlying mechanism [65,66].

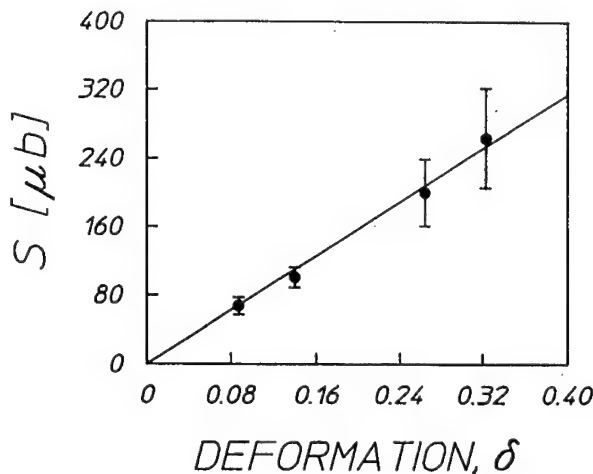


Fig. 14. Isomer excitation probabilities, S , plotted as a function of ground-state deformation, δ showing a slow variation consistent with a core property for the giant pumping resonances [52]. The quantity $S \equiv (\sigma\Gamma)_{ij}/E_j$, defined assuming a dipole character for the absorption step, is summed over the energy region $2-4.5 \text{ MeV}$ and is proportional to the reduced transition probability.

4. Thermal economy of a gamma-ray laser

Our model of a gamma-ray laser for the 1990's is not fundamentally different from the nuclear analog of the ruby laser described in 1982 [16], envisioned as a thin film of diluent doped with isomeric nuclei and pumped with a flash of X-rays in a slab geometry. The question of feasibility still rests on the degree to which the properties of some real nuclide approach those of the ideals being modeled. What has changed over the past half decade is that the discovery of giant pumping resonances has enabled some of the original constraints to be relaxed. The result is that the feasibility of a gamma-ray laser has been enhanced by orders of magnitude over that originally estimated in 1982. Thus, as summarized here, it has been useful [54] to recompute the model in terms of the new data obtained during the past five years.

Since the better candidate isomers for a gamma-ray laser have never been fabricated in macroscopic amounts, precise knowledge of the properties of the best nuclide is not available. Moreover, since feasibility is such a complex function of the nuclear parameters, the assumptions introduced into any model will critically affect the estimates of feasibility in strongly nonlinear ways. For the computation reported here the following parameters were assumed:

1. A single pump band exists which is a giant pumping resonance with a partial width of $b_a b_o \Gamma = 1 \text{ eV}$.
2. The pump transition is centered on an energy $E_j = 30 \text{ keV}$.
3. The initial state is assumed to be isomeric with an excitation energy so high that the previous statement (2) is possible.
4. The output transition is around 100 keV.
5. The active nuclei are diluted in a thin film of diamond or Be.
6. The Borrmann effect contributes a factor of 10 enhancement to the ratio of cross sections for resonant to nonresonant absorption.

The most sensitive assumptions are those of statements 2 and 3 about the width and excitation energy of the giant pumping resonance. The range of excitation energies over which isomers can be found is very large and it has already been shown experimentally that isomers can be dumped into freely radiating states, even through $\Delta K = 8$ or $\Delta K = 14$. The only doubt here is a statistical one; whether or not a giant pump resonance can be found within 30 keV of an isomer.

Following our development of 1982 [16], under small signal conditions the mid-range requirement of 10^{-4} is obtained for the pumped fraction,

$$\frac{N_f}{N_i} \geq \frac{\sigma_{NR}}{\sigma_R} \approx 10^{-4}, \quad (9)$$

where σ_R and σ_{NR} are the cross sections for useful, resonant nuclear absorption and nonresonant photoelectric absorption, respectively. The value of 10^{-4} includes

a Borrmann enhancement to a value of $\sigma_{\text{NR}}/\sigma_{\text{R}} \approx 10^{-3}$ from ref. [6]. Eq. (9) sets the pump intensity needed for threshold, and with it the amount of waste heat to dissipate.

The essential concept in the management of the thermal economy is that the mean free path (MFP) for a photon resonant with the nuclear pump transition is much shorter than the MFP for nonresonant, photoelectric absorption to produce heat. Also, the MFP for a photoelectron produced in the nonresonant channel is greater in the diluent than the MFP for the photons pumping the nuclear resonance. This means that a thin film of diamond can be doped or implanted with active nuclei to provide useful absorption of incident photons in the bandwidth of the giant pumping resonance while the majority of the nonresonant photons will pass through the film into a substrate which can be cooled by ablation or cryogenics. Moreover, primary photoelectrons produced by the small fraction of nonresonant events occurring in the film can escape before their energy is degraded to heat.

The quantitative expression of this strategy is obtained by substituting eq. (3) into eq. (9) and assuming a single giant resonance dominates so that the sum is unnecessary. Solving for the spectral intensity, $\phi_j = \Phi_0 F(E_j, E_0)$ for 30 keV pump photons, the spectral fluence, $F_j \equiv E_j \phi_j$ at threshold is found to be

$$F_j = 177 \text{ mJ cm}^{-2}\text{eV}^{-1}. \quad (10)$$

This gives the energy flux per unit bandwidth within the gateway resonance which must be incident upon the film.

For the likely cases of rare earth or platinide elements, the 30 keV pump energy lies below the K edge and about 15 keV above the L edge. As a result, primary photoelectrons produced by nonresonant absorption in the active medium should have energies on the order of 15 keV and ranges of 6.0 and 3.0 μm in Be and C, respectively [67]. Thus, only about 10 and 20% of the primaries, respectively, should be stopped in a 0.67 μm thick host film of Be or diamond. This thickness corresponds to the MFP for resonant absorption at a concentration of 10% doping. The fraction of the incident pump energy degraded into heat in the laser film because of nonresonant absorption becomes

$$f(\text{Be}) = 4.8 \times 10^{-4}, \quad (11\text{a})$$

or

$$f(\text{C}) = 2.4 \times 10^{-4}. \quad (11\text{b})$$

Considering that edge filters or ablation layers could reduce the bandwidth of the pump radiation to 3 keV before reaching the doped layer of active medium, the incident fluence lying outside the bandwidth for resonant absorption would be 3000 times greater than the value of eq. (10). However, only the fractions of eqs. (11a) and (11b) are capable of being degraded into heat in the sensitive layer. The resulting energy balance can be summarized at threshold by the first two lines of table 4.

Dividing those fluences by the 0.67 μm thickness gives the energy loading of the

Table 4

Summary of the thermal economy at threshold for a gamma-ray laser nuclide doped into a film of 0.67 μm thickness of the low-Z materials shown

Quantity	Material	
	Be	C(diamond)
Resonant input fluence	177 mJ cm^{-2}	177 mJ cm^{-2}
Fluence degraded to heat	127 mJ cm^{-2}	255 mJ cm^{-2}
Resonant energy density	2.6 kJ cm^{-3}	2.6 kJ cm^{-3}
Thermal loading	1.9 kJ cm^{-3}	3.8 kJ cm^{-3}

laser film shown in table 4. These values are quite significantly below the levels of heating required to degrade the recoil-free fractions in the case of Be or diamond lattices. Baldwin [6] has summarized the involved dependence of the recoil-free fraction of gamma transitions upon recoil energy, lattice parameters, and temperature. He showed that even at a temperature T equal to the Debye temperature, Θ_D , the recoil-free fraction is not significantly degraded (by more than a factor of 2) for a transition even so energetic as to give a classical recoil energy of $0.14\Theta_D$. Since diamond is characterized by $\Theta_D = 2230 \text{ K}$, this means a transition of 100 keV is little affected by a temperature increase up to $T = \Theta_D$. It is a textbook computation [68] to estimate that the energy content of the phonons for a material with $\Theta_D = 2230 \text{ K}$ at a temperature of $T = \Theta_D$ is about 11 kJ cm^{-3} . Comparing this with the estimated thermal loading of 3.8 kJ cm^{-3} gives a “safety factor” of almost three. A comparable margin is obtained for a Be lattice.

To summarize, it is convenient to recast the threshold fluence of eq. (10) into more tangible terms. The spectral fluence of $177 \text{ mJ cm}^{-2} \text{ eV}^{-1}$ corresponds to 530 J cm^{-2} if the bandwidth of the pump X-rays is arranged to be 3 keV, a practical separation which might be filtered between K edges. Even if pumped instantaneously so that no waste heat were transported away, the thermal loading would reach only one third of the limit for retaining the Mössbauer effect in a diamond lattice. If derived from an X-ray line of 30 eV width, the threshold fluence would be only 5.3 J cm^{-2} . In that case the thermal loading would reach only 1/300 of the critical limit.

Even beyond this point much can be done to reduce heating further. All calculations so far considered the generation of the waste heat to be instantaneous. The time for the transit of a phonon across the 0.67 μm thickness of the inverting layer is on the order of only 100 ps so that the transport of significant amounts of heat into a diamond heat sink is possible on a nanosecond time scale. Yet most of the fluorescent levels of interest for inversion [16] have lifetimes of tens of nanoseconds to tens of microseconds. This is many times the period for the transport of phonons out of the film so that orders of magnitude can be realized in reducing the thermal loading further below the limits specified so far. However, all these techniques require pre-

cise knowledge about the energy levels and absorption edges of the materials involved. Until the properties of the best candidate for a gamma-ray laser are known, the exact specifications of the solution to the disposal of the waste heat cannot be generally articulated. The examples summarized here show that there are many orders of magnitude in the safety margin between likely amounts of heating and the much larger amounts which can be tolerated in stiff lattices such as Be and diamond.

5. Candidate isomer for a gamma-ray laser

5.1. CANDIDATES AND SIMULATIONS

An exact ranking of the 29 candidate isomers for a gamma-ray laser depends upon a complex weighing of combinations of nuclear parameters, many of which are poorly known. However, the potential importance of several nuclides is magnified by some very pragmatic considerations. These issues are typified by comparisons of the four examples presented in table 1.

From the perspective of shelf life and availability, $^{180}\text{Ta}^m$ is far superior. It is a naturally occurring material composing 0.012% of all tantalum and can be prepared simply by separating natural Ta by atomic mass. Samples of milligram weight exist and one such specimen was used in the breakthrough experiment that proved X-rays can dump the energy stored in isomeric populations. In contrast, the entire world inventory of $^{178}\text{Hf}^{m2}$ was reported in 1992 to be about 10^{15} nuclei [69] although recently this amount has been increased to about 5×10^{16} .

However, from the perspective of triggering $^{180}\text{Ta}^m$ appears to be much less practical. Although the energy storage is still impressively high, the isomeric level lies quite low in energy when compared to the value for the excitation of the K -breaking gateway at 2.8 MeV. For $^{178}\text{Hf}^{m2}$ the energy of the isomer at 2.45 MeV is the highest known that still lies below the likely gateway energy between 2.5 and 3.0 MeV [70]. The isomer $^{174}\text{Hf}^m$ is even higher at 3.312 MeV, but the availability [61] of a spontaneous transition down to the K -mixing level at 2.685 MeV reduces its shelf halflife to only 3.7 μs . Ideally for ease of triggering, an isomer would store as much energy as possible without exceeding that of the K -breaking level for that nuclide. As long as the transition energy needed for triggering is positive, the isomer cannot dump spontaneously as happens with $^{174}\text{Hf}^m$. The lifetime of the initial population will then be long and problems of storage will be minimized. Guided to $^{178}\text{Hf}^{m2}$ by energetics, a reasonable next concern from the pragmatic viewpoint is for the duration of the trigger pulse.

Even in the best scenarios the requirement for the energy in a trigger pulse is large. The problem is compounded if the fluorescence lifetime of the level into which the isomeric population is to be dumped is too short. Large pulsed-power devices typically deliver their outputs over durations of nanoseconds to a few

microseconds, so it would be desirable to utilize a laser candidate with strong fluorescence lines of comparable lifetimes. In this case as well, the $^{178}\text{Hf}^{\text{m}2}$ is favorable since it has transitions with lifetimes of both tens of ns and tens of μs , as will be seen in the following section.

The experiments needed to confirm our pragmatic scoring of the better of the 29 candidates for a gamma-ray laser have been postponed by the difficulties in obtaining samples. Thus, it has seemed fruitful to identify simulation nuclei which could serve as vehicles with which to develop systems and instrumentations for future triggering studies. To be useful a simulation nuclide needs to have a strong output fluorescence transition that can be reached by cascade from a K -breaking resonance pumped from the ground state by intense X-ray pulses. Moreover, the levels radiating such transitions should have lifetimes of tens of ns to tens of μs . Meeting these criteria were the four convenient simulation nuclides listed in table 5 whose excitation we have recently studied [71].

Excitation of those nuclides was provided by our 4 MeV Texas-X linac which produces 150 mA pulses of electrons of 4 μs duration at a repetition rate of 250 Hz. These are routinely converted to bremsstrahlung with a cooled Pt converter. The difficulty in this type of experiment which must be performed *in situ* lies in Compton scattering of the bremsstrahlung from the samples and a milligram-sized target support which produces background noise that tends to obscure gamma fluorescence. Our present system has used electronic gating to reduce the sensitivity of the detector during the pump pulses. A combination of issues limits the recovery of the data acquisition system by a minimum product of fluorescence energy and delay time which currently is 150 keV \times 2 μs . Shown in fig. 15 are data [71] from delayed fluorescence at 482 keV from the 18 μs level of ^{181}Ta after a recovery time of 7.22 μs from the end of the X-ray pulse. The literature value of the fluorescence-state lifetime agrees well with the measured decay. The energetics of the process are summarized in the diagram of fig. 16. Similar results are shown in fig. 17 for the nuclide ^{176}Hf for which the relevant energy levels are summarized in fig. 18.

Table 5

Summary of properties [35,74] of nuclides useful in simulating the pumping of the better of the 29 candidates for a gamma-ray laser

Nuclide	Abundance (%)	Output transitions (keV)	Fluorescence lifetime (μs)
^{81}Br	49.31	260 276	37.6
^{176}Hf	5.206	736 1043	9.6, 9.9
^{181}Ta	99.988	346 482	18
^{201}Hg	13.1	521	92

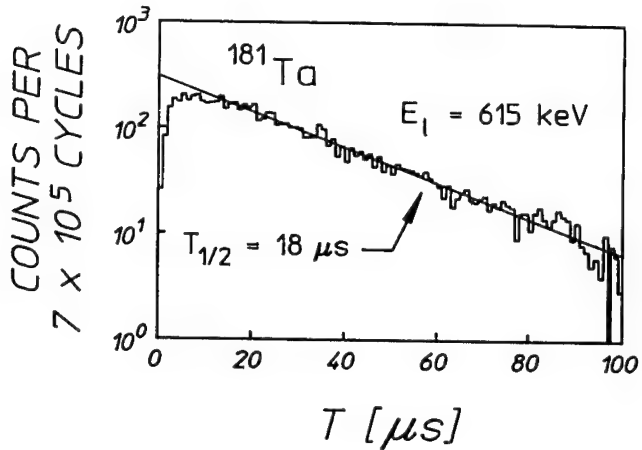


Fig. 15. Fluorescence detected at 482 keV from the decay of the 615 keV isomer of ^{181}Ta . The data were obtained [71] using a gated detector system and corresponded to nearly 10^6 acquisition cycles taken over 45 min. The solid line shows a fit to the data which agrees well with the literature value [34] for the lifetime of the 615 keV level.

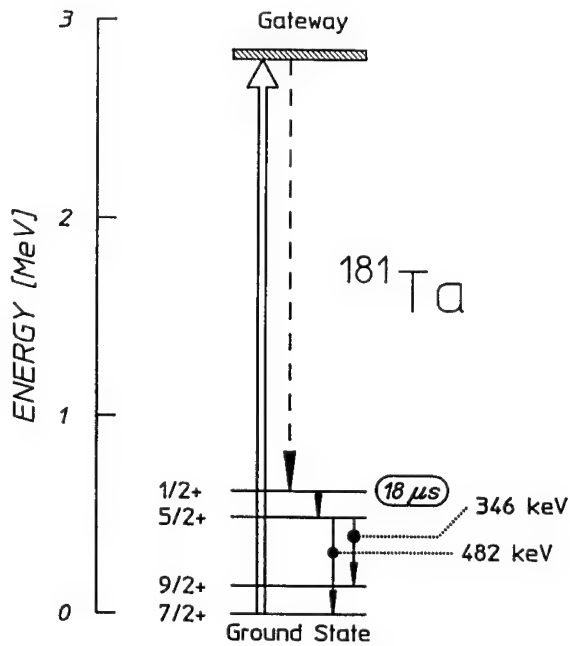


Fig. 16. Schematic diagram showing the energy levels [74] important for the excitation of the 615 keV, 18 μs state in ^{181}Ta . The large upward arrow indicates the absorption transition to a gateway located [71] near 2.8 MeV which populates that laser-like level by a branch of its decay cascade (shown by the dashed arrow). Transitions providing photons used to detect the fluorescence are indicated with their energies.

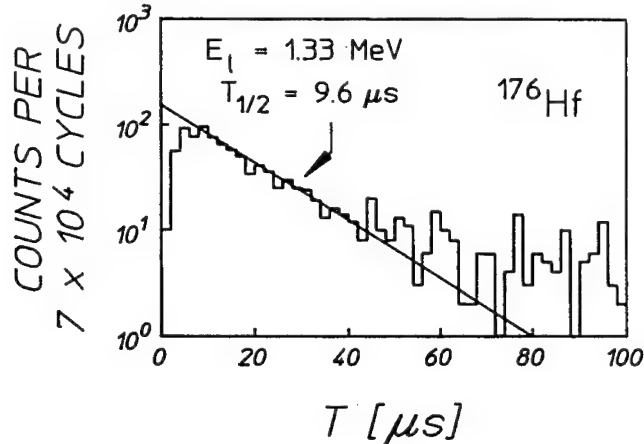


Fig. 17. Fluorescence detected from the decay of the 1333 keV isomer of ^{176}Hf . The data were obtained [71] using a gated detector system and corresponded to nearly 10^5 acquisition cycles taken over 5 min. The solid line shows a fit to the data which agrees well with the literature value [34] for the lifetime of the 1333 keV level.

Analyses of the fluorescence data using eqs. (1)–(4) yielded new values for the integrated cross sections for pumping of short-lived μs fluorescence. Fig. 19 shows these results included in the summary plot of fig. 11. It is encouraging to observe that the systematics for the pumping of these simulated laser levels closely follows the trends already established for the excitation of longer-lived levels which were easier to study. As yet the complementary data on the excitation energies needed to reach the pumping gateways have not been measured in these simulations, but they might reasonably be expected to also continue the established systematics.

5.2. FIRST-RANKED CANDIDATE

The first priority candidate for a gamma-ray laser is the 31-year isomer of ^{178}Hf , superior to the next possibilities by orders of magnitude. The energy-level diagram [72–74] for ^{178}Hf is shown in fig. 20 with prominent fluorescent transitions indicated. The fundamental question is whether the giant pumping resonance will be found at the level shown in the figure that is predicted by systematics. In case of a weak success in which K -breaking is tending to fail we would expect pumping to preferentially populate the band to the right of the figure. This would lead to fluorescence at 437 keV with 35% efficiency from the bandhead having a 68 μs lifetime, well within current experimental capabilities demonstrated by the simulations.

In the event of a strong success in which K -breaking is complete, we would expect to preferentially populate the left-side band which leads to fluorescence at 922 keV with 65% efficiency and 1247 keV with 30% efficiency from the bandhead having a 78 ns lifetime. Demonstrations of dumping the stored energy from the isomer

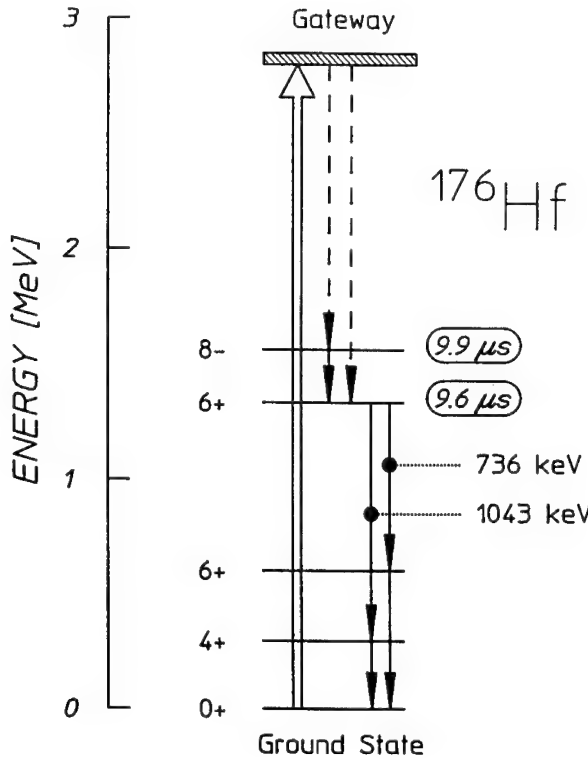


Fig. 18. Schematic diagram showing the energy levels [74] important for the excitation of the 1333 keV, 9.6 μ s state in ^{176}Hf . The large upward arrow indicates the absorption transition to a gateway located [71] near 2.8 MeV which populates that laser-like level by a branch of its decay cascade (shown by the dashed arrow). Transitions providing photons used to detect the fluorescence are indicated with their energies.

would then require the use of an accelerator with shorter pulses such as the APEX-I device in our facility. This e-beam machine produces 30 kA of electrons in pulses of 30 ns duration at energies variable from 0.7–1.2 MeV. Although a single-shot device, it served well in our first investigations of gamma fluorescence [36,42]. Moreover, there is a great advantage in the use of this type of device since it can be configured to use bremsstrahlung having 0.7–0.8 MeV endpoints to pump the left-side band that will give signal fluorescence at 1.25 MeV. It should be straightforward to set discrimination levels in the detection electronics to reject the scattered pump radiation which consists of photons at much lower energies.

The expected number of fluorescent photons can be calculated with two assumptions about the overall integrated cross section for pumping to fluorescence,

$$(\sigma\Gamma)_{\text{sys}} = 5 \times 10^{-25} \text{ cm}^2 \text{keV}, \quad (12a)$$

and

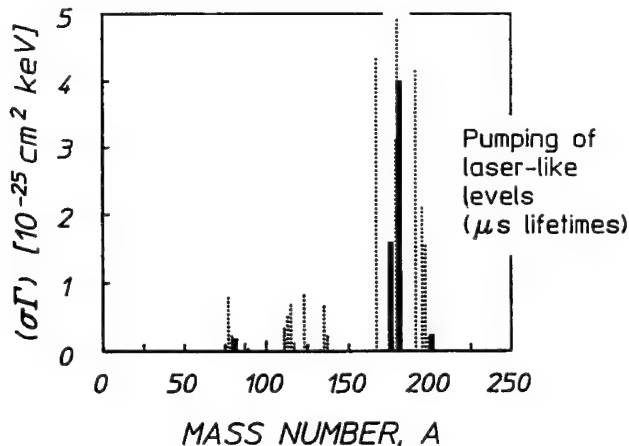


Fig. 19. Integrated cross sections for populating laser-like levels in the simulation nuclei superimposed on those of fig. 11 for the pumping and dumping of long-lived isomers. Again, the groupings correspond to mass islands between magic numbers and the best candidates are identified as neighbors of ^{180}Ta .

$$(\sigma\Gamma)_{\text{best}} = 2.5 \times 10^{-23} \text{ cm}^2 \text{ keV}, \quad (12b)$$

where the first value is consistent with the measurements of fig. 19 and the second is scaled for the dependence on pump energy given by eq. (6). The range of excitation energies spanned by the measurements of figs. 11 and 19 is insufficient to determine any further correlation between $(\sigma\Gamma)$ and the energy needed for triggering. For a target of 10^{15} nuclei, the Texas-X linac would produce 8×10^5 or 4×10^7 fluorescence photons per hour for the cross sections of eqs. (12a) and (12b), respectively. In that case there is an ample safety margin for the arrangement of realistic geometries for the collection and detection of the fluorescence.

6. Conclusions

The current cycle of research into the feasibility of a gamma-ray laser started in 1982 with the emergence of a strongly interdisciplinary approach. Generally characterized by the study of nuclear analogs of concepts of quantum electronics already proven at the atomic and molecular levels, major advances have been realized in this period. Documented throughout this volume, they provide a richness of options for developing output coherence once excited nuclear states can be coupled to the radiation field.

Reviewed here have been our own work concerned with pumping (or triggering) enough nuclei into states which can be coupled when desired. Supported by strong collaborations with colleagues at the Technische Hochschule Darmstadt, the Flerov Laboratory for Nuclear Reactions at Dubna, and the CSNSM and IPN

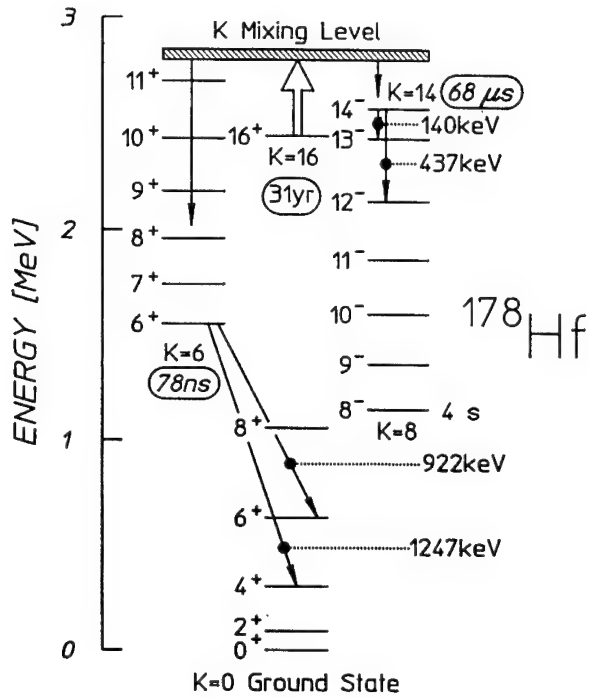


Fig. 20. Schematic energy-level diagram [72–74] of ^{178}Hf . The spontaneous decay of the 31 year isomer proceeds through an yrast band which does not excite transitions in the left-hand $K = 6$ band or the $K = 14$ band. The 68 μs bandhead decays by a cascade through the right-hand $K = 8$ band. The position of the K -mixing giant pumping resonance inferred from systematics is shown by the wide shaded band near 2.8 MeV and the large upward arrow indicates the pump transition from the 31 year isomer. Transitions providing fluorescence photons useful for the detection of the pumping reaction are identified along with their energies.

Laboratories at the Orsay Campus, major breakthroughs have been achieved that drastically improve the prospects for success. Primary has been the discovery of K -breaking levels in some nuclei at reasonably accessible energies. Unknown before 1988 [50], such levels have significance also in astrophysics [75], and were independently found in the decay of exotic nuclei [61] in 1990.

Transitions to the K -breaking levels provide giant pumping resonances which are analogous to the bandwidth funnels that made the ruby laser possible. Since they can be accessed either from ground states or from isomeric levels, K -breaking levels make *ex situ* pumping of a gamma-ray laser a reasonable proposition. Precursive nuclides can be pumped into isomeric states either by reactors or by accelerators outside of the more fragile structures in which they would be used. Studies of systematics have shown the pervasive occurrence of K -breaking levels across islands of mass that contain the 29 candidate isomers originally preferred for a gamma-ray laser. In principle, many of these isomers could be produced *ex situ* so that the requirements for triggering the conversion to freely radiating states

would represent relatively modest demands for the remainder of the *in situ* pumping to the K -breaking level. While computations of the thermal economy of the *in situ* step depend upon high exponents of the unknown properties of the particular isomer and its host medium, reasonable targets are not necessarily destroyed by the waste pump power. Safety margins of orders of magnitude built into the estimates of thermal loading anticipate the emergence of parameter values less favorable than those modeled.

Most recently, an extension of the systematics studies has shown that the favorable occurrence of giant resonances for pumping nuclear fluorescence extends to the excitation of laser-like transitions having lifetimes on the order of μs . Also, the basic structural concept of doping the working nuclides into a thin diamond film at a target concentration of 10% has been demonstrated [76] and examples of Mössbauer nuclei implanted into diamond are already commercially available.

From the larger perspective it seems reasonable to conclude that the first breakthrough in determining the feasibility of a gamma-ray laser has been followed by a second. The proof that isomeric populations can be dumped by pumping them with intense pulses of X-rays has been followed by the demonstration that the strengths for doing so are fragmented into relatively few discrete transitions of great intensity. These are precisely the necessary conditions for the concentration of useful pump power into the selective excitation of nuclear populations while dissipating power degraded to heat in much larger volumes. In the test case of ^{115}In , most amenable to computation, the pump step was found to be a spin-flip transition whose strength was only slightly fragmented into weaker components despite the higher state densities between 2 and 5 MeV. Complete agreement was demonstrated between our pumping measurements, independent scattering studies and theory in 1991 [56]. The particular structure of the K -breaking levels in the higher mass range of most importance has been proposed for the case of ^{174}Hf [61]. We have tried to develop algorithms for rationalizing transition strengths in neighboring nuclides from scaling studies like that of ref. [52], but the matter of accurate interpolation among the measurements remains a complex question.

While the paucity of actual samples has inhibited the final demonstration of feasibility, estimates of likely yields from such experiments have shown that strong levels of fluorescence from laser-like levels of the 31 year isomer $^{178}\text{Hf}^{\text{m}2}$ should be observable when the material becomes available. On the basis of shelf life and energy storage it seems a clear choice for the best candidate isomer for induced gamma-ray emission [70], a key triggering step in a gamma-ray laser. These conclusions would seem to provide a strong motivation for the production of this first ranked candidate for use in a gamma-ray laser. Another interesting proposal is suggested for two steps of *ex situ* pumping. The estimates of the likely yields from a microweighting sample with the Texas-X suggest that a macroscopic sample could be converted by $^{178}\text{Hf}^{\text{m}2}(\gamma, n)^{177}\text{Hf}^{\text{m}2}$ with a more robust source to produce a significant amount of the 51 min $^{177}\text{Hf}^{\text{m}2}$. As described in a companion article [70], systematics indicate that the transition energy from that latter isomer to the K -mixing

level is extremely small. This nuclide might then serve in schemes in which very low-energy photons are used to mix properties of an isomeric level with those of some member of a freely radiating yrast band which is nearly resonant in energy. However, detailed experiments have recently shown [77] that K mixing in particle reactions is sufficiently strong to inhibit the production of significant numbers of high-spin daughters from high-spin targets. This precludes an efficient (γ, n) conversion of $^{178}\text{Hf}^{\text{m}2}$ into $^{177}\text{Hf}^{\text{m}2}$, but nevertheless supports the appearance of K mixing in nuclides near $A = 180$.

The strongest conclusion to communicate here is that the persistent tenets of theoretical dogma which have historically [6] inhibited the development of a gamma-ray laser have been eliminated by experimental studies of the past five years. There is no need to melt the host lattice in order to pump a nuclear system to the laser threshold. There are no a priori obstacles to the realization of a gamma-ray laser. A gamma-ray laser seems feasible if the right combination of energy levels occurs in some real material. The overriding question to resolve is whether or not one of the better of the candidate nuclides has its isomeric level within a few tens or even hundreds of keV of one of the giant resonances for dumping angular momenta as seems to be the case with the priority candidate for a gamma-ray laser, $^{178}\text{Hf}^{\text{m}2}$.

References

- [1] L.A. Rivlin, USSR Patent #621265 (Appl. Jan. 10, 1961).
- [2] G.C. Baldwin, J.P. Neissel, J.P. Terhune and L. Tonks, Proc. IEEE 51 (1963) 1247.
- [3] V. Vali and W. Vali, Proc. IEEE 51 (1963) 182.
- [4] L.A. Rivlin, Vopr. Radioelectron. 6 (1963) 43.
- [5] B.V. Chirikov, Sov. Phys. JETP 17 (1963) 1355.
- [6] G.C. Baldwin, J.C. Solem and V.I. Goldanskii, Rev. Mod. Phys. 53 (1981) 678.
- [7] V.S. Letokhov, Sov. J. Quant. Electron. 3 (1974) 360.
- [8] B. Arad, S. Eliezer and Y. Paiss, Phys. Lett. 74A (1979) 395.
- [9] C.B. Collins, S. Olariu M. Petrascu and I. Popescu, Phys. Rev. Lett. 42 (1979) 1397.
- [10] C.B. Collins, S. Olariu, M. Petrascu and I. Popescu, Phys. Rev. C 20 (1979) 1942.
- [11] S. Olariu, I. Popescu and C.B. Collins, Phys. Rev. C 23 (1981) 50.
- [12] S. Olariu, I. Popescu and C.B. Collins, Phys. Rev. C 23 (1981) 1007.
- [13] C.B. Collins, in: *Proc. Int. Conf. on Lasers '80*, ed. C.B. Collins (STS Press, McLean, VA, 1981) p. 524–531.
- [14] C.B. Collins, in: *Laser Technique for Extreme Ultraviolet Spectroscopy*, eds. T.J. McIlrath and R.R. Freeman, AIP Conf. Proc. no. 90 (New York, 1982) p. 454–464.
- [15] C.B. Collins, in: *Proc. Int. Conf. on Lasers '81*, ed. C.B. Collins (STS Press, McLean, VA, 1982) p. 291–295.
- [16] C.B. Collins, F.W. Lee, D.M. Shemwell, B.D. DePaola, S. Olariu and I. Popescu, J. Appl. Phys. 53 (1982) 4645.
- [17] B.D. DePaola and C.B. Collins, J. Opt. Soc. Am. 1 (1984) 812.
- [18] C.B. Collins and B.D. DePaola, in: *Laser Techniques in the Extreme Ultraviolet*, eds. S.E. Harris and T.B. Lucatorto, AIP Conf. Proc. no. 119 (New York, 1984) p. 45–53.
- [19] C.B. Collins and B.D. DePaola, Optics Lett. 10 (1985) 25.

- [20] B.D. DePaola, S.S. Wagal and C.B. Collins, *J. Opt. Soc. Am. B* 2 (1985) 541.
- [21] B.D. DePaola and C.B. Collins, *J. Opt. Soc. Am. B* 1 (1984) 812.
- [22] C.B. Collins, in: *Handbook of Laser Science and Technology* (CRC Press, Boca Raton, 1991) p. 561–567.
- [23] B. Pontecorvo and A. Lazard, *C.R. Acad. Sci.* 208 (1939) 99.
- [24] G.B. Collins, B. Waldman, E.M. Stubblefield, and M. Goldhaber, *Phys. Rev.* 55 (1939) 507.
- [25] F.R. Metzger, *Prog. Nucl. Phys.* 7 (1959) 54.
- [26] P. von Neumann-Cosel, A. Richter, J. Carroll and C.B. Collins, *Phys. Rev. C* 44 (1991) 554.
- [27] G. Breit and E. Wigner, *Phys. Rev.* 49 (1936) 519.
- [28] Y. Watanabe and T. Mukoyama, *Bull. Inst. Chem. Res. Kyoto Univ.* 57 (1979) 72.
- [29] M. Krcmar, A. Ljubicic, K. Pisk, B. Logan and M. Vrtar, *Phys. Rev. C* 25 (1982) 2097.
- [30] I. Bikit, J. Slivka, I.V. Anicin, L. Marinkov, A. Ruydic and W.D. Hamilton, *Phys. Rev. C* 35 (1987) 1943.
- [31] W.R. Nelson, H. Hirayama and D.W.O. Rogers, Stanford Linear Accelerator Center Report no. SLAC 265 (1985) unpublished.
- [32] J.A. Halbleib and T.A. Mehlhorn, *ITS: The Integrated TIGER Series of Coupled Electron/Photon Monte Carlo Transport Codes*, Sandia National Laboratories Report SAND84-0573 (1984) unpublished.
- [33] R. Mohan, C. Chui and L. Lidofsky, *Med. Phys.* 12 (1985) 595.
- [34] *Evaluated Nuclear Structure Data File* (Brookhaven National Laboratory, Upton, New York, 1986).
- [35] E. Browne and R.B. Firestone, *Table of Radioactive Isotopes* (Wiley, New York, 1986) p. 180.
- [36] J.A. Anderson and C.B. Collins, *Rev. Sci. Instrum.* 58 (1987) 2157.
- [37] J.J. Carroll and C.B. Collins, in *Proc. Int. Conf. Lasers and Appl. (LASERS '93)* (1994) p. 171–178.
- [38] C.B. Collins, J.J. Carroll, T.W. Sinor et al., *Phys. Rev. C* 42 (1990) R1813.
- [39] E.C. Booth and Brownson, *Nucl. Phys.* A98 (1967) 529.
- [40] E. Guth, *Phys. Rev.* 59 (1941) 325.
- [41] Y. Paiss, C.D. Eberhard and C.B. Collins, *J. de Phys.* 48 (1987) 131.
- [42] J.A. Anderson and C.B. Collins, *Rev. Sci. Instrum.* 59 (1988) 414.
- [43] J.A. Anderson, J.M. Carroll, K.N. Taylor et al., *Nucl. Instrum. Meth. B* 40/41 (1989) 1189.
- [44] J.A. Anderson, C.D. Eberhard, K.N. Taylor, J.M. Carroll, J.J. Carroll, M.J. Byrd and C.B. Collins, *IEEE Trans. Nucl. Sci.* 36 (1989) 241.
- [45] C.B. Collins, J.A. Anderson, Y. Paiss, C.D. Eberhard, R.J. Peterson and W.L. Hodge, *Phys. Rev. C* 38 (1988) 1852.
- [46] J.A. Anderson, M.J. Byrd and C.B. Collins, *Phys. Rev. C* 38 (1988) 2833.
- [47] J.J. Carroll, D.G. Richmond, T.W. Sinor, K.N. Taylor, C. Hong, J.D. Standifird and C.B. Collins, *Rev. Sci. Instrum.* 64 (1993) 2298.
- [48] P. von Neumann-Cosel, N. Huxel, A. Richter, C. Spieler, J.J. Carroll and C.B. Collins, *Nucl. Instrum. Meth. A* 338 (1994) 425.
- [49] J.J. Carroll and C.B. Collins, these proceedings (1st Int. Gamma-Ray Laser Worksh., 1995), *Hyp. Int.* 107 (1997) 149.
- [50] C.B. Collins, C.D. Eberhard, J.W. Glesener and J.A. Anderson, *Phys. Rev. C* 37 (1988) 2267.
- [51] J.J. Carroll, M.J. Byrd, D.G. Richmond et al., *Phys. Rev. C* 43 (1991) 1238.
- [52] C.B. Collins, J.J. Carroll, K.N. Taylor, D.G. Richmond, T.W. Sinor, M. Huber, P. von Neumann-Cosel, A. Richter and W. Ziegler, *Phys. Rev. C* 46 (1992) 952.
- [53] J.J. Carroll, T.W. Sinor, D.G. Richmond et al., *Phys. Rev. C* 43 (1991) 879.
- [54] C.B. Collins, J.J. Carroll, K.N. Taylor, T.W. Sinor, C. Hong, J.D. Standifird and D.G. Richmond, *Laser Interaction and Related Plasma Phenomenon*, eds. G.H. Miley and H. Hora, 10 (Plenum, NY, 1992) 151.

- [55] W. Ziegler, C. Rangacharyulu, A. Richter and C. Spieler, Phys. Rev. Lett. 65 (1990) 2515.
- [56] P. von Neumann-Cosel, A. Richter, C. Spieler, W. Ziegler, J.J. Carroll, T.W. Sinor, D.G. Richmond, K.N. Taylor, C.B. Collins and K. Heyde, Phys. Lett. B 266 (1991) 9.
- [57] M. Huber, P. von Neumann-Cosel, A. Richter et al., Nucl. Phys. A559 (1993) 253.
- [58] H. Friedrichs, B. Schlitt, J. Margraf et al., Phys. Rev. C 45 (1992) 892.
- [59] H. Friedrichs, S. Lindenstruth, B. Schlitt et al., Nucl. Phys., A553 (1993) 553.
- [60] H. Xie, Ch. Ender, J. Gerl et al., Phys. Rev. C 48 (1993) 2517.
- [61] P.M. Walker, G.D. Dracoulis, A.P. Byrne, T. Kibèdi and A.E. Stuchbery, Phys. Rev. C 49 (1994) 1718.
- [62] P.M. Walker, F. Sletten, N.L. Gjorup et al., Phys. Rev. Lett. 65 (1990) 416.
- [63] C.B. Collins, J.J. Carroll, T.W. Sinor and K.N. Taylor, *Ultrashort- Wavelength Lasers*, SPIE 1551 (1991) 166.
- [64] C.B. Collins, J.J. Carroll, K.N. Taylor, T.W. Sinor, C. Hong, J.D. Standifird and D.G. Richmond, Laser Part. Beams 11 (1993) 43.
- [65] G. Sletten, N.L. Gjorup, S. Juutinen et al., Nucl. Phys. A520 (1990) 325.
- [66] B. Crowell, P. Chowdhury, S.J. Freeman et al., Phys. Rev. Lett. 72 (1994) 1164.
- [67] G. Knopf and W. Pau, in: *Alpha, Beta and Gamma-Ray Spectroscopy*, ed. K. Siegbahn (North Holland, Amsterdam, 1965) p. 1–25.
- [68] C. Kittel, *Introduction to Solid State Physics*, 6th ed. (Wiley, New York, 1986) p. 106.
- [69] Yu.Ts. Oganessian, S.A. Karamian, Y.P. Gangrski et al., J. Phys. G: Nucl. Part. Phys. 18 (1992) 393.
- [70] C.B. Collins, J.J. Carroll, Yu.Ts. Oganessian and S.A. Karamian, these proceedings (1st Int. Gamma-Ray Laser Worksh., 1995), Hyp. Int. 107 (1997) 141.
- [71] C. Hong, K.N. Taylor, J.J. Carroll, T.W. Sinor and C.B. Collins, Rev. Sci. Instrum. (1995) submitted.
- [72] T.L. Khoo and G. Lovhoiden, Phys. Lett. 67B (1977) 271.
- [73] R.K. Sheline, D.G. Burke, M.M. Minor and P.C. Sood, Phys. Rev. C 48 (1993) 911.
- [74] *National Nuclear Data Center Online Evaluated Nuclear Structure Data File (ENSDF)*, (Brookhaven National Laboratory, 1994).
- [75] J.J. Carroll, J.A. Anderson, J.W. Glesener, C.D. Eberhard and C.B. Collins, Astrophys. J. 344 (1989) 454.
- [76] T.W. Sinor, J.D. Standifird, F. Davanloo, K.N. Taylor, C. Hong, J.J. Carroll and C.B. Collins, Appl. Phys. Lett. 64 (1994) 1221.
- [77] Yu.Ts. Oganessian and S.A. Karamian, these proceedings (1st Int. Gamma-Ray Laser Worksh., 1995), Hyp. Int. 107 (1997) 43.
- [78] J.J. Carroll, C.B. Collins, K. Heyde et al., Phys. Rev. C 48 (1993) 2238.

K-mixing in nuclear reactions

Yu.Ts. Oganessian ^a and S.A. Karamian ^{a,b}

^a FLNR JINR, 141980 Dubna, Russia

^b Ludwig-Maximilians Univ., D-85748 Garching, Germany

Isomer-to-ground-state ratios are measured for the group of photon- and α -induced nuclear reactions. The photonuclear reactions on high-spin isomeric targets – $^{178}\text{Hf}^{\text{m}2}$ (16^+) and $^{180}\text{Ta}^{\text{m}}$ (9^-) – were detected successfully. Results are analysed from the point of view of the K -selectivity manifestation for the level population. The yields comparison with the regular values confirms strong K -mixing at high excitations.

1. Introduction

Isomer-to-ground-state ratios, $Y_{\text{m}}/Y_{\text{g}}$, of the reaction yields (cross-sections) should be sensitive to the K -hindrance factor if it influences the final levels population. Structure hindrances are well known in radioactive decays when levels below 3 MeV are populated. In nuclear reactions the structure selectivity was not detected clearly. The statistical model description is successful in many cases and thus confirms the smearing out of the structure peculiarities at excitations of about neutron binding energy. The presence of some special K -mixed levels which serve as intermediate states for the K -forbidden transitions was suggested in some cases, for instance in refs. [1,2]. At the same time one can find in the literature some indications of the K -selectivity in nuclear reactions [3–5].

The feeding of the levels in the (n,γ) reaction was studied in ref. [3]. In the $(n,2n)$ reaction the authors [4] have observed a three times higher cross-section for the production of the $^{179}\text{Hf}^{\text{m}2}$ isomer compared to that of $^{178}\text{Hf}^{\text{m}2}$ despite that the spins of initial and final states of the reactions influence oppositely. One can search for an explanation in terms of the K -selectivity. Also $\sigma_{\text{m}}/\sigma_{\text{g}}$ values measured in (α,n) reactions cannot be reproduced [5] in the statistical model calculations within the regular choice of the moment of inertia value, $J \approx 0.8J_{\text{rig,rot}}$. One can suppose an additional decrease of σ_{m} values due to some K -hindrance factor. Thus the problem of K -selectivity in nuclear reactions should be studied in more detail both in theoretical and experimental approaches.

New interesting possibilities arise in the reaction with high-spin isomers. The $\sigma_{\text{m}}/\sigma_{\text{g}}$ values were measured earlier in many nuclear reactions on low-spin g.s. targets; however, the treatment of the measured isomeric yields is complicated due to restrictions both by the ΔJ and ΔK changes. High-spin targets are preferential because the spin limitations are not very drastic in this case and the presence of

some hindrance factor by the K quantum number can be detected easier than with ground-state targets.

One can formulate the problem of studying the isomer-to-ground-state ratios for many reactions including the reactions on high-spin targets, and after systematization and analysis to make a conclusion about K -selectivity in nuclear reactions. The photon-induced reactions are of special interest because of the developed theoretical descriptions as well as importance for some applications, for instance, for the γ -ray laser problem. The probability of levels population in nuclear reactions plays a key role for the efficient pumping of the laser transition. Studies in this field supply the basic physical information for the future γ -laser project.

2. Photonuclear reaction yield ratios

The excitation functions of photon-induced nuclear reactions are regulated by a giant dipole resonance (GDR) in the photon absorption cross-section σ_{GDR} and by the competition between different channels of the excited nucleus decay. The standard behaviour of the excitation functions is illustrated in fig. 1.

Photonuclear reactions are studied regularly using the electron-beam-induced bremsstrahlung radiation of continuous spectrum. Produced in the (γ, x) reactions the number of atoms, N_x , is expressed, as known, by the equation:

$$N_x(E_e) = N_{\text{tar.}} N_e S^{-1} \int_0^{E_e} \frac{d^3 W}{dE d\Omega de} \Delta\Omega \sigma_{\text{GDR}}(E) P_x(E) dE, \quad (1)$$

where $N_{\text{tar.}}$ is the number of target atoms, N_e is the number of electrons which reach the bremsstrahlung converter, $d^3 W/dE d\Omega de$ is the spectral distribution of the bremsstrahlung radiation normalized to one electron and to the unit of solid angle, P_x is the absolute probability of the particle (x) emission from the excited nucleus, E_e is the end-point of the spectrum and S is the cross-area of the sample which covers the solid angle $\Delta\Omega$. The functional $N_x(E_e)$ contains the excitation function of

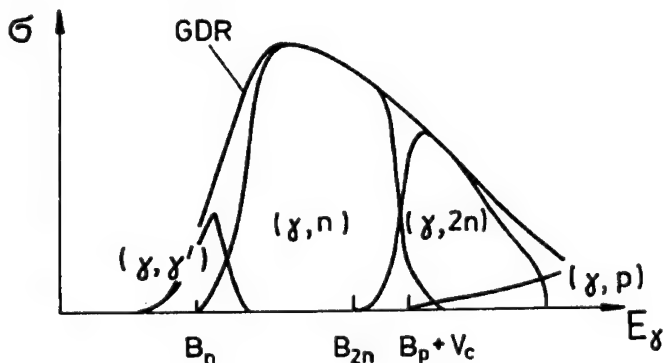


Fig. 1. Excitation functions of photonuclear reactions (illustration).

the reaction integrated with the weight function of the bremsstrahlung spectrum. Following eq. (1) one can introduce naturally the yield of the reaction product:

$$Y_x = \frac{N_x}{N_{\text{tar.}} \cdot N_e} . \quad (2)$$

In such a definition the yield contains only the measured values and thus it is most convenient when production intensities are compared, in particular, for deducing the isomer-to-ground-state ratio, Y_m/Y_g . An absolute value Y_x is dependent certainly on the irradiation geometry and the electron-gamma conversion efficiency. When the standard conditions of the irradiation are conserved the yields ratio characterizes the ratio of the spectrum-weighted cross-sections, and can be used for the physical conclusions.

Experiments for studying photonuclear reactions were carried out in the standard geometry shown in fig. 2. The electron beam of the Dubna MT-25 microtron with energy varying in the range $E_e = 16-24$ MeV and an intensity of $15 \mu\text{A}$ was used for the production of the γ -radiation on the tungsten converter of 2.5 mm thickness. The stack of activated samples was placed just behind the converter to enhance the absolute activities. After irradiation the activated samples were studied by the γ -spectrometry method using the Ge-detector. The radioactive products were defined quantitatively after the measurement of γ -spectra taking into account the individual isotopes decay properties compiled in the Nucl. Data Sheets, the Ge-detector efficiency and the time factors of accumulation and decay.

The targets of ^{nat}Hf and ^{nat}Ta were exposed and the induced γ -activity was measured. Many radioactive products were detected. Relative yields of reactions are presented in table 1 for $E_e = 23.5$ MeV. They are normalized to the yield of abundant reaction $^{181}\text{Ta}(\gamma, n)^{180}\text{Ta}^g$. One can see that some reactions have yield values of 10^5-10^6 times below that of the most probable reaction – (γ, n) . However, they

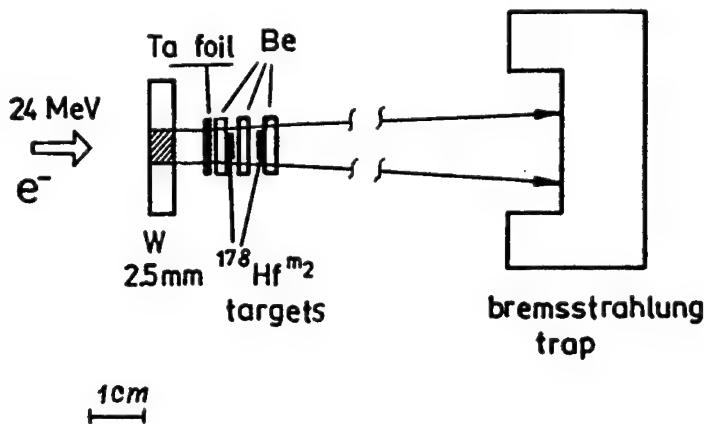


Fig. 2. Schematic layout of activated samples on the e-beam of the Dubna microtron in experiments on bremsstrahlung-induced reaction studies.

Table 1

Bremsstrahlung-induced reaction yields measured at $E_e = 23.5$ MeV with ^{nat}Ta , ^{nat}Hf , and $^{178}Hf^{m2}$ targets

Reaction	J_t	J_g	J_m	Y (rel. un.)	Y_m/Y_g^a
$^{181}Ta(\gamma,n)^{180}Ta^g$	7/2	1	9	1	—
$^{181}Ta(\gamma,p)^{180}Hf^m$	7/2	0	8	5.6×10^{-5}	0.04
$^{181}Ta(\gamma,\alpha)^{177}Lu^8$	7/2	7/2	23/2	6.8×10^{-6}	—
$^{180}Ta^m(\gamma,2n)^{178}Ta^m$	9	1	7	0.06	
$^{180}Ta^m(\gamma,2n)^{178}Ta^g$	9	1	7	0.02	3.0
$^{180}Ta^m(\gamma,p)^{179}Hf^{m2}$	9	9/2	25/2	1.3×10^{-4}	0.09
$^{180}Hf(\gamma,\gamma')^{180}Hf^m$	0	0	8	0.8×10^{-4}	0.0029
$^{180}Hf(\gamma,p)^{179}Lu$	0	7/2	—	1.6×10^{-3}	—
$^{179}Hf(\gamma,\gamma')^{179}Hf^{m2}$	9/2	9/2	25/2	3.9×10^{-5}	0.0014
$^{179}Hf(\gamma,p)^{178}Lu^m$	9/2	1	9	3.9×10^{-4}	
$^{179}Hf(\gamma,p)^{178}Lu^g$	9/2	1	9	5.2×10^{-4}	0.75
$^{178}Hf(\gamma,p)^{177}Lu^m$	0	7/2	23/2	$\leq 0.8 \times 10^{-6}$	
$^{178}Hf(\gamma,p)^{177}Lu^g$	0	7/2	23/2	1.8×10^{-3}	≤ 0.005
$^{178}Hf^{m2}(\gamma,n)^{177}Hf^{m2}$	16	7/2	37/2	0.12	0.12
$^{177}Hf(\gamma,2n)^{175}Hf$	7/2	5/2	—	1.2	—
$^{176}Hf(\gamma,n)^{175}Hf$	0	5/2	—	—	
$^{174}Hf(\gamma,n)^{173}Hf$	0	1/2	—	0.95	—
$^{174}Hf(\gamma,2n)^{172}Hf$	0	0	—	5.5×10^{-2}	—

^a Random errors of the Y_m/Y_g values are typically about $\pm(15\text{--}20)\%$.

were detected and this characterizes the sensitivity of our measurements. The last one is important for the case of experiments with exotic $^{180}Ta^m$ and $^{178}Hf^{m2}$ targets which are described below.

The energy dependence of the yields was measured too, the results are demonstrated in fig. 3. For some isotopes with a low yield the measurements could be done only at the highest energy, $E_e = 23.5$ MeV.

For the $^{178}Lu^{m,g}$ and $^{178}Ta^{m,g}$ products the yields were defined both for the ground and isomeric states. So, the isomer-to-ground-state ratio, Y_m/Y_g , was deduced immediately. For the other products, $^{177}Lu^{m2}$, $^{179}Hf^{m2}$ and $^{180}Hf^m$, the ground states are stable and could not be detected. The g.s. yields were assumed to be the same as for the neighbouring nuclides formed in the reactions of the same type.

The energy dependencies of the Y_m/Y_g values measured for four nuclides are shown in fig. 4. One can see that the Y_m/Y_g ratio is not very sensitive to the bremsstrahlung end-point energy in the range of 16–24 MeV. That is understandable because the increasing of the electron energy produces the gain in the absolute intensity of the photons, however it doesn't increase significantly the excitation energy of the compound nucleus which is limited, as shown in fig. 1, by the competition of other reaction channels. The compound nucleus spin is also not influenced due to the dipole capture dominance. Finally, the evident energy dependence of the

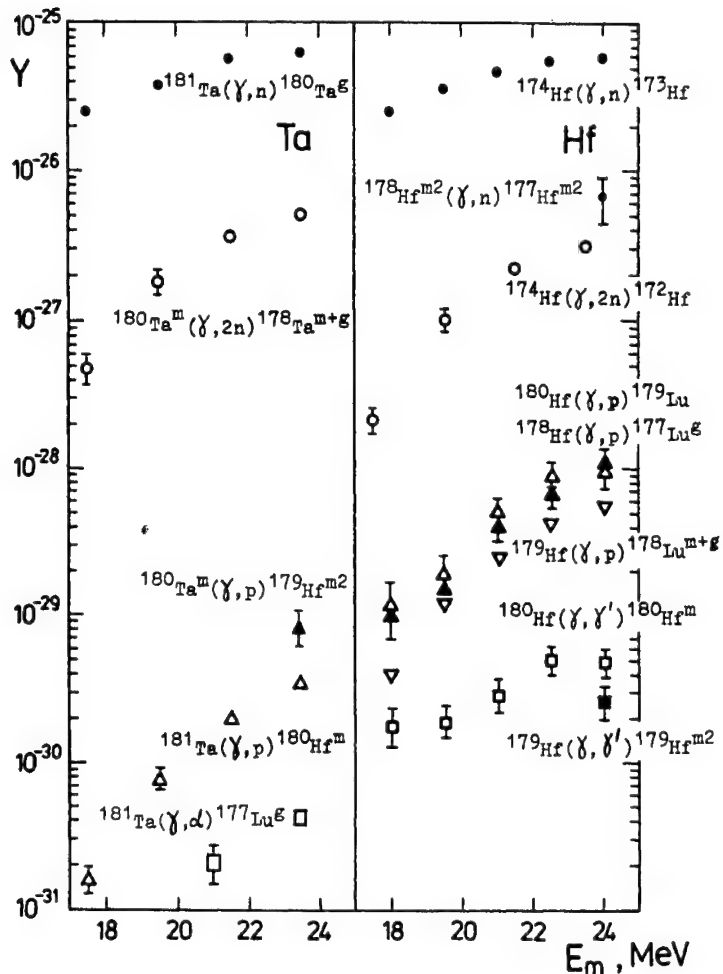


Fig. 3. Yields of the photonuclear reactions on the Hf and Ta targets as a function of the bremsstrahlung end-point energy.

Y_m/Y_g was detected only for the $^{181}\text{Ta}(\gamma, \text{p})^{189}\text{Hf}^m$ reaction. The emission of more energetic protons leads to the increase of the evaporation residue spin which is reflected in the growth of the 8^+ isomeric yield.

Reactions with $^{180}\text{Ta}^m$ and $^{178}\text{Hf}^m2$ targets are of special physical interest. At the same time there are special experimental difficulties to observe them since a tiny quantity of the target material is available. Thus, separate experiments were carried out to detect the reactions: $^{180}\text{Ta}^m(\gamma, 2\text{n})^{178}\text{Ta}^{g,m}$, $^{180}\text{Ta}^m(\gamma, \text{p})^{179}\text{Hf}^m2$ and $^{178}\text{Hf}^m2(\gamma, \text{n})^{177}\text{Hf}^m2$.

Reactions with $^{180}\text{Ta}^m$ were observed using the ^{nat}Ta targets. The natural abundance of the ^{180}Ta ($J^\pi = 9^-$) nuclide is as low as 1.2×10^{-4} . Reaction products of the $^{180}\text{Ta}^m$ should be detected in the presence of the 10^4 times more intensive back-

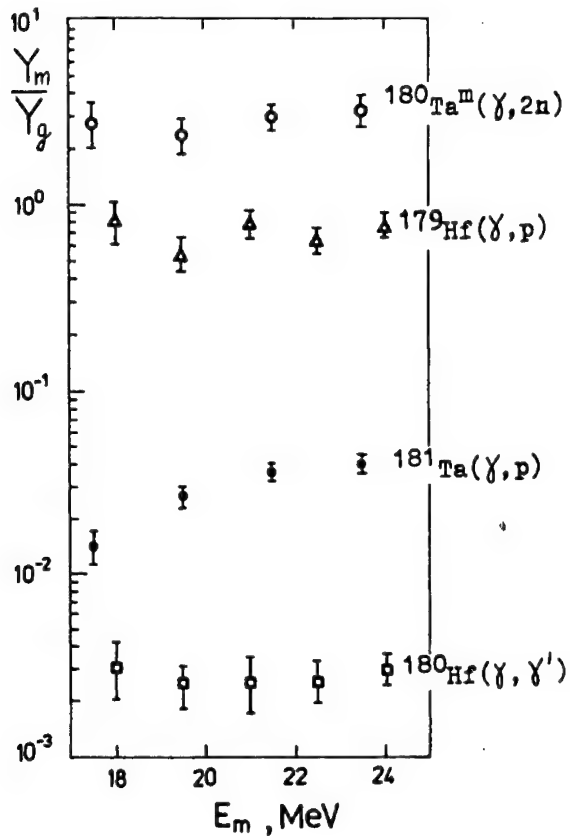


Fig. 4. Energy dependence of the isomer-to-ground-state ratios in the bremsstrahlung-induced reactions.

ground of the ^{181}Ta products. Fortunately, in the irradiation of ^{181}Ta only a few γ -radioactive nuclides are created. The most probable reaction $^{181}\text{Ta}(\gamma, n)$ leads to the isotope $^{180}\text{Ta}^g$, 8.15 h lived. Its soft γ -radiation ($E_\gamma = 93.3$ and 103.6 keV) could be absorbed easily by a 1 mm Pb absorber.

The detected and background activities in experiments with the $^{180}\text{Ta}^m$ are characterized in table 2. For the observation of each individual radioactive nuclide ($^{178}\text{Ta}^g$, $^{178}\text{Ta}^m$ or $^{179}\text{Hf}^{m2}$) the irradiation conditions were optimized specially taking into account the lifetime, decay γ -line energies and reaction yield. The $(\gamma, 2n)$ reaction is probable enough, and we have succeeded to observe [6] the lines of the $^{178}\text{Ta}^{g,m}$ with good statistics on the level of the intensity of the $^{180}\text{Hf}^m$ (5.5 h) isomer produced in the (γ, p) reaction on the abundant ^{181}Ta isotope.

The $^{179}\text{Hf}^{m2}$ absolute activity produced in the $^{180}\text{Ta}^m(\gamma, p)$ reaction was by several orders of magnitude lower, and we used a 1 g ^{nat}Ta target to enhance the sensi-

Table 2

Conditions for the observation of photonuclear reactions on isomeric, 9^- , $^{180}\text{Ta}^m$ nucleus

Reaction	E_e (MeV)	Observed γ -lines, E_γ (keV)	Background activities	Reaction with abundant ^{181}Ta nuclide, and its threshold (MeV)
$^{180}\text{Ta}^m(\gamma, 2n)$	17–22	$^{178}\text{Ta}^m, 7^-$ (2.4 h) 325.6 426.4 $^{178}\text{Ta}^9, 1^+$ (9.3 min) 1340.9 1350.6	$^{180}\text{Ta}^g$ (8.15 h) $^{180}\text{Hf}^m$ (5.5 h) ^{64}Cu (12 h)	$(\gamma, 3n)$ 22.1
$^{180}\text{Ta}^m(\gamma, p)$	23.5	$^{179}\text{Hf}^{m2}, 25/2^-$ 362.6 453.7	^{182}Ta (115 d)	(γ, pn) 24.5

tivity of the experiment. In this case the background ^{182}Ta activity was accumulated in the target after long enough exposures due to the neutron flux created in the converter. Finally, we have observed most intensive lines of the $^{179}\text{Hf}^{m2}$ as tiny peaks on the Compton background of the ^{182}Ta spectrum. It was possible to deduce the yield of the $^{179}\text{Hf}^{m2}$ and to estimate the isomer-to-ground-state ratio referring to the standard (γ, p) reaction yield measured in the other cases. The Y_m/Y_g values are given in table 1.

The $^{178}\text{Hf}^{m2}$ 16^+ isomer, being long-lived (31 y) yrast-trap, described as a four-quasiparticle deformation-aligned $K = 16$ state is a really exotic nuclear object. It was accumulated in a quantity of 2×10^{15} atoms in intensive irradiations of the highly enriched ^{176}Yb target by the 36 MeV α -particle beam on the cyclotron at Dubna [7]. The $^{178}\text{Hf}^{m2}$ nuclei were produced in the $^{176}\text{Yb}(\alpha, 2n)$ reaction with an isomer-to-ground-state ratio of about 4%. In addition to the $^{178}\text{Hf}^g$, other stable Hf isotopes were also produced in the reactions and they are finally contained in the chemically isolated Hf fraction. Special $^{178}\text{Hf}^{m2}$ targets were prepared on the Be substrates for the bremsstrahlung irradiations. Beryllium demonstrates the lowest level of the bremsstrahlung-induced activation among other possible materials.

To observe the $^{178}\text{Hf}^{m2}(\gamma, n)^{177}\text{Hf}^{m2}$ reaction the induced activity of the 51 min lived five-quasiparticle $37/2^-$ isomer of ^{177}Hf was searched in the spectra measured after intensive bremsstrahlung exposures at $E_e = 23.5$ MeV. The scheme of the irradiation is shown in fig. 2. The stack of two $^{178}\text{Hf}^{m2}$ targets (10^{14} atoms in total) on Be backings with the Be catcher between them was exposed. The $^{177}\text{Hf}^{m2}$ nuclei were emitted from the thin target layers due to the recoil momentum produced by the neutron emission and collected by the catcher. A collection efficiency was calcu-

lated based on experimental results [8]. Application of the catcher technique was necessary to decrease significantly the background counting rate in the Ge-detector when very weak activity of $^{177}\text{Hf}^{\text{m}2}$ is measured. The maximum energy of its γ -lines, $E_\gamma = 638.2 \text{ keV}$ exceeds that one for $^{178}\text{Hf}^{\text{m}2} - 574.2 \text{ keV}$. However, in the detection of the $^{178}\text{Hf}^{\text{m}2}$ spectra the counting rate at energies of $> 574.2 \text{ keV}$ was not low due to the adding of the cascade of γ -quanta in the detector. For instance an intensive sum-peak of 639.8 keV was observed due to the adding of the $213.4 + 426.4 \text{ keV}$ quanta in the cascade. This sum-energy line, which disturbs the measurements of the $^{177}\text{Hf}^{\text{m}2}$ activity, was suppressed by a 7 mm Pb absorber. Some continuous-spectrum counting rate still remains there because of the Compton signals adding.

The application of the catcher in irradiation and the thick enough Pb absorber in the measurements decreases the efficiency, however it permits us to improve the effect-background ratio to the level which is appropriate for the detection of the induced $^{177}\text{Hf}^{\text{m}2}$ activity. Nevertheless, the background spectra should be subtracted from the $^{178}\text{Hf}^{\text{m}2}$ activation spectra. The four species of the background spectra were measured with high statistics:

1. Background of the detector shielded by the lead housing.
2. The spectrum due to the $^{178}\text{Hf}^{\text{m}2}$ activity. (The catcher touches the $^{178}\text{Hf}^{\text{m}2}$ layers in the irradiation and a small part of the $^{178}\text{Hf}^{\text{m}2}$ is transferred.)
3. The activity induced on the admixtures in the Be foil.
4. The activity induced on Hf stable isotopes presented in the target.

The role of the latter background was negligible, the other three species produce a comparable background counting rate. The irradiations of the $^{178}\text{Hf}^{\text{m}2}$ on the microtron at the maximum energy and intensity were repeated eight times. The spectra after the background subtraction were stored together. Finally, the peak at the right energy position, 638.2 keV, was observed, its area was about 70 ± 26 counts. This peak is attributed to the $^{177}\text{Hf}^{\text{m}2}$ produced in the $^{178}\text{Hf}^{\text{m}2}(\gamma, n)$ reaction. Its intensity was transformed to the number of $^{177}\text{Hf}^{\text{m}2}$ atoms produced during the irradiation. The yield value was deduced and compared to the calibration reaction $^{181}\text{Ta}(\gamma, n)^{180}\text{Ta}^g$ yield measured under identical conditions:

$$\frac{Y(^{177}\text{Hf}^{\text{m}2})}{Y(^{180}\text{Ta}^g)} = 0.12^{+0.05}_{-0.04}.$$

This ratio reflects the isomer-to-ground-state ratio of the $^{178}\text{Hf}^{\text{m}2}(\gamma, n)$ reaction. Only 12% of the total reaction yield reaches the $37/2^-, m_2$ state in ^{177}Hf . The experiments with isomeric targets are described in more detail elsewhere [9].

The isomer-to-ground-state ratios have thus been determined for three photon-induced reactions on isomeric targets as well as for the group of reactions on the g.s. low-spin targets.

3. Reactions with ${}^4\text{He}$ ions

The excitation functions for the production of the ${}^{177}\text{Lu}^m$, ${}^{178}\text{Hf}^{m2}$, ${}^{179}\text{Hf}^{m2}$ and ${}^{178}\text{Ta}^m$ isomers in α -induced reactions were measured on the cyclotron beam. The stack of targets and degrader foils was exposed and the cross-section of the isomer formation is measured by the induced γ -activity. Individual γ -lines of the isomer decay were detected and their intensities were transformed into the cross-section. The excitation functions and isomer-to-ground-state ratios are demonstrated in fig. 5 for ${}^{177}\text{Lu}^m$ ($23/2^-$), ${}^{179}\text{Hf}^{m2}$ ($25/2^-$) and ${}^{178}\text{Hf}^{m2}$ (16^+) isomers produced in the $(\alpha, p2n)$, (α, n) and $(\alpha, 2n)$ reactions respectively.

The σ_m/σ_g values for ${}^{177}\text{Lu}^m$ is influenced by a rather high threshold of the $(\alpha, p2n)$ reaction which leads to a lower spin of the evaporation residue than that for the other products. The trend for decreasing the σ_m/σ_g values at the highest energies is due to the contribution of the pre-equilibrium emission mechanism. The reaction ${}^{176}\text{Hf}(\alpha, pn){}^{178}\text{Ta}^m$ was studied earlier [10], the results will be used in the below systematics of the isomer-to-ground-state ratios.

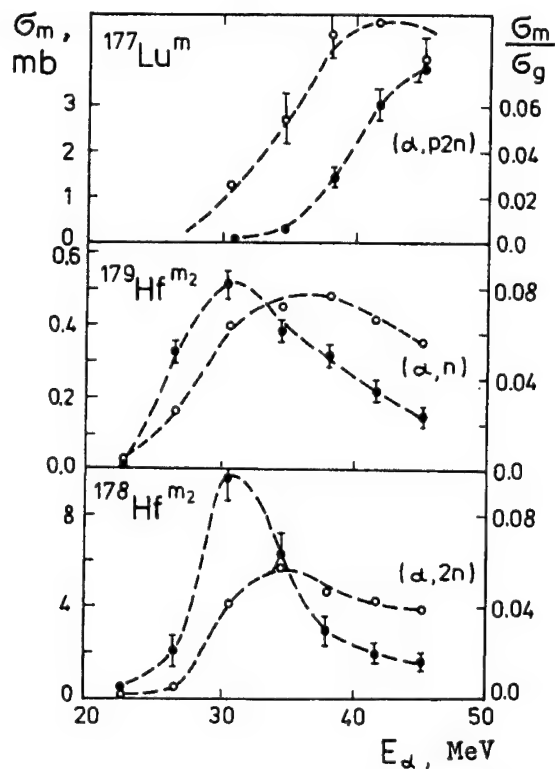


Fig. 5. Cross-sections (●) and σ_m/σ_g (○) values measured for the Lu and Hf isomers in the bombardment of the ${}^{176}\text{Yb}$ target by the ${}^4\text{He}$ -ion beam as a function of ion energy. Dashed line is a guide over experimental points.

The data available in the literature [4,5,11,12] are also attracted. For all cases we have calculated a maximum angular momentum, I_{\max} , released in the reaction because the I_{\max} values either are not presented in original publications or they are underestimated [11] significantly. The unified way for the I_{\max} calculation should be used. We have used the standard semiclassical formulations. Reactions with 14 MeV neutrons [4] and protons [11] are combined together with the group of α -induced reactions. In paper [4], σ_m/σ_g values were not deduced, it could be done easily since the total cross-sections for the (n,2n) reactions are known with a good accuracy.

The reaction: $^{176}\text{Lu}(\alpha,2n)^{178}\text{Ta}$, studied in ref. [12], is of special interest since the target nucleus has a spin 7, and it is thus one of the examples when the reaction of a high-spin (isomeric) nucleus is studied. To deduce the isomer-to-ground-state ratio the intensities [12] of the most abundant transitions in the prompt γ cascades leading to a high-spin state and to a low-spin state of the final nucleus were compared and correction on the electron conversion was introduced. The resulting high-to-low spin ratio was included in the systematics described below.

The σ_m/σ_g behaviour has a tendency to saturation with projectile-energy growth or even demonstrates a maximum (fig. 5). Therefore, we have selected the σ_m/σ_g values taken at the highest energy or the maximum value in case the maximum has been reached.

4. Systematics of the σ_m/σ_g values and discussion

The data available for the systematization for the case of fast neutrons, protons and α -particles are commented above. Cross-sections for another group of reactions – reactions with thermal neutrons – are compiled in ref. [13]. The $^{178}\text{Hf}^{m2}(n,\gamma)^{179}\text{Hf}^{m2}$ reaction was studied in ref. [14], the cross-section for the m^2 state in the ^{179}Hf was measured successfully, however the ground state was not detected, and we can estimate only a lower limit for the σ_m/σ_g value. For the photon-induced reactions we consider the data presented in table 1 as well as the literature results of refs. [15–17]. Thus the three sets of the σ_m/σ_g values for the three groups of the reactions are available for the systematization.

Let us motivate the necessity of such systematics. Being plotted it allows us to check whether a special nuclear structure of an isomeric state (used as a target) plays an important role in the population of the high-spin isomer in the reaction product. In other words, some light can be thrown on the selectivity of the level population in the de-excitation cascades. In particular, the role of the K quantum number at high excitation energies can be clarified.

One cannot expect the combination of all results together within a general systematics, since the spin distributions in the reactions with thermal neutrons, photons and α -particles are very different. So, the groups are considered separately. In all cases the reactions on deformed nuclei from Nd to Re are selected to avoid an

additional scattering of the σ_m/σ_g values due to the shell-structure effects in the level density.

The central problem is to find an appropriate parameter for the σ_m/σ_g systematization. Assume that the product nucleus has only two final states: a low-spin g.s. and a high-spin i.s. In the statistical model the low probability for the population of an i.s. is explained by the angular momentum deficit. We therefore try to establish a systematics of the σ_m/σ_g values by plotting them versus the spin difference of the input and output channels of the reaction:

$$\Delta J = J_t + J_b + I_{\max} - J_{i.s.}, \quad (3)$$

where J_t and J_b are the spins of the initial target and projectile, I_{\max} is a maximum orbital momentum of the projectile and $J_{i.s.}$ is the spin of the i.s. populated.

The reaction yield, which does not end up in an isomeric state, feeds the g.s. because of the absence of other long-lived states. The g.s. spin therefore does not influence the σ_m/σ_g ratio in such an approximation. Only, when the i.s. and g.s. have nearly equal spins this approach may fail and such reactions are excluded from consideration.

The systematics is shown in fig. 6. One can see that the points are scattered around straight lines, demonstrating the exponential growth of the isomeric yield

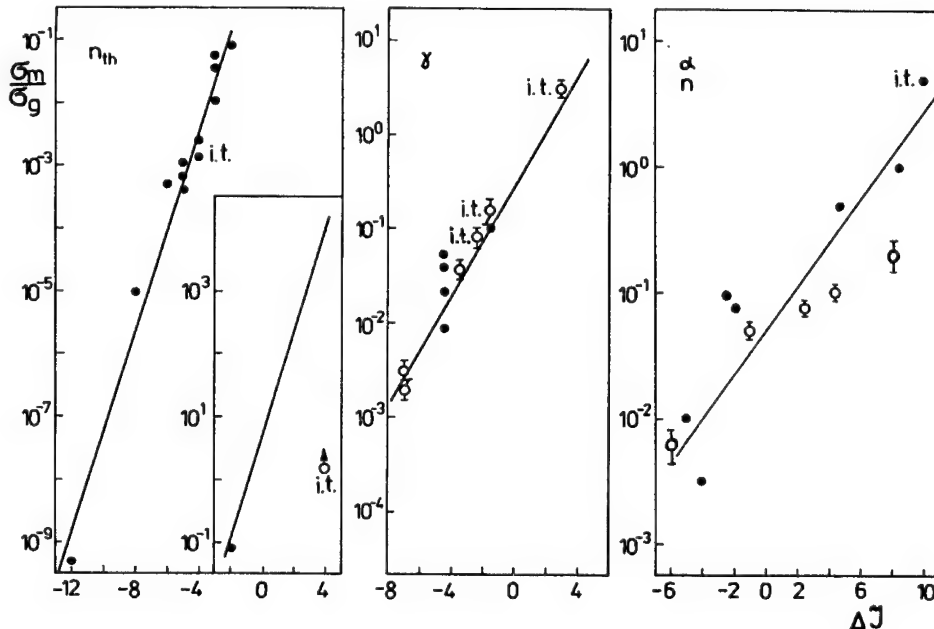


Fig. 6. Isomer-to-ground-state ratios systematics versus spin deficit in reactions induced by (a) thermal neutrons, (b) photons and (c) α -particles. Results of the present measurements are shown by open circles and the literature data [4,5,11–14,15–17] by full ones. The “i.t.” index indicates high-spin targets.

with decreasing spin deficit. As expected, the slope of these guide lines is different for different groups of the reactions. After α -particle absorption the compound nucleus has a wide angular momentum distribution from 0 to I_{\max} while thermal neutron capture leads to a spin variation of $\pm 1/2$. That influences the slope of the lines in fig. 6.

The scattering of the points can be explained by the experimental data errors as well as by the factors which were not taken into account in the systematization by the simple parameter. If the K -selectivity exists, then a low ΔK value in any reaction should manifest itself in the position of the corresponding point noticeably higher in respect to the other points in fig. 6.

Points for the reactions on high-spin (isomeric) targets are marked by the index "i.t.". One can not say that they lay significantly above the systematics lines. Their mismatch with the other points does not exceed the random scattering of the points, and the excess factor was estimated to be below 1.5–2.0. Even a high enough value of $Y_m/Y_g = 3$ for the $^{180}\text{Ta}^m(\gamma, 2n)^{178}\text{Ta}$ reaction could be explained by the positive ΔJ value in this reaction. One can conclude that a strong selectivity for the population of "target-like" single particle states in the product nucleus does not manifest itself.

Thus, the systematics confirms rather a presence of the total K -mixing in excited products of the reactions. It should be reminded that the final states of the reactions are populated normally in the cascades of electromagnetic transitions after particle emission. Therefore the conclusion about the total K -mixing corresponds to the states near and below the neutron binding energy.

How can one explain the K -mixing presence? The K quantum number is, as known, an asymptotic quantum number which is introduced in the case of the axial symmetry of the nuclear shape. The latter one is not conservative with excitation energy. The shape coexistence, shape isomers and superdeformed bands are known. In fig. 7 the potential energy of a nucleus is shown schematically as a function of the γ -deformation parameter. The prolate and oblate minima, both axially symmetric

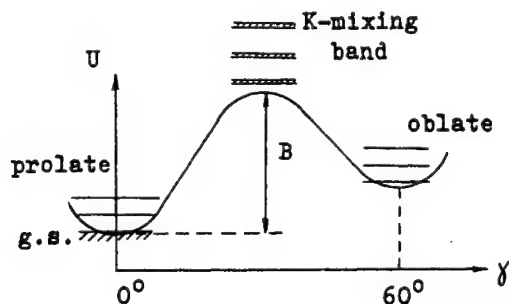


Fig. 7. Nuclear potential versus γ -deformation and collective bands of different shape symmetry (schematic view).

are separated by some barrier. When the excitation energy exceeds this barrier, the band of triaxial shape states arises and it can be mixed with the bands of pure axial symmetry. The triaxial wave functions cannot be characterized by any K quantum number. Their admixture to the other states breaks the K quantum number selection rules.

5. Conclusion

The isomer-to-ground-state ratios for photon-, neutron- and α -particle-induced reactions are systematized. The total K -mixing for the evaporation residue states is deduced. It means that the population of any single particle configuration in the reaction is allowed if the spin and excitation energy are sufficient. The γ -ray laser pumping processes thus are not restricted by an additional hindrance due to the K quantum number selection rule.

Acknowledgement

One of the authors (S.A.K.) thanks the Ludwig-Maximilians Universität München for a guest professorship and the organizing committee of the Gamma-Ray Laser Workshop for the financial support of his participation.

References

- [1] C.B. Collins, J.J. Carroll, T.W. Sinor, M.J. Byrd, D.G. Richmond, K.N. Taylor, M. Huber, P. V. Neumann-Cossel, A. Richter, C. Spieler and W. Zigler, Phys. Rev. C42 (1990) 1813.
- [2] P.M. Walker, G. Sletten and N.L. Gjorup, Phys. Rev. Lett. 65 (1990) 416.
- [3] J. Rekstad, T.S. Tveter and M. Guttormsen, Phys. Rev. Lett. 65 (1990) 2122.
- [4] Yu Weixiang, Lu Hanlin and Zhao Wenrong, Chin. J. Nucl. Phys. 14(4) (1992) 326.
- [5] A.F. Tulinov, O.V. Fotina, T.V. Chuvilskaya, L.Ya. Shavtvalov and A.A. Shirokova, Bull. Russ. Acad. Sci., Phys. issue, 57 (1993) 135.
- [6] S.A. Karamian, Acta Phys. Pol. 26 (1995) 375.
- [7] Yu.Ts. Oganessian and S.A. Karamian, Review Talk on Int. Conf. Nuclear Shapes and Nuclear Structure, Antibes, France, June 1994; Preprint JINR, E15-94-408 (Dubna, 1994).
- [8] V.A. Von Lint, R.A. Schmitt and C.S. Suffredini, Phys. Rev. 121 (1991) 1457.
- [9] S.A. Karamian, J. de Boer, Yu.Ts. Oganessian et al., Z. Phys. A 356 (1996) 23.
- [10] G. Gorski, S.A. Karamian, Yu.Ts. Oganessian and S.L. Bogomolov, J. Radioanal. Nucl. Chem., Articles, 170(2) (1993) 353.
- [11] V.Yu. Denisov, V.A. Zheltonozhski and S.V. Reshit'ko, Russ. J. Nucl. Phys. 56 (1993) 99.
- [12] F. Dubbers, L. Funke, P. Kemnitz and K.D. Shilling, Nucl. Phys. A 315 (1979) 317.
- [13] S.F. Mughabghab, *Neutron Cross Sections, vol. I, part B* (Academic Press, 1984).
- [14] Yu.Ts. Oganessian, S.A. Karamian, V.M. Nazarov and Z. Szeglowski, JINR Rapid Commun. 3 (54) (1992) 72, Dubna.

- [15] V.M. Mazur, V.A. Zheltonozhski and Z.M. Bigan, Russ. J. Nucl. Phys. 58 (1995) 970.
- [16] I.N. Vishnevski, Z.M. Bigan, V.A. Zhetlonozhski and V.M. Mazur, *Nucl. Spectroscopy and Nucl. Structure, Proc. 39th conf., St.-Petersburg* (1989) p. 317; *ibid, 38th conf.* (1988) p. 323.
- [17] N.P. Balabanov, A.G. Belov, Yu.P. Gangsksy, F.G. Kondev, A. Tonchev et al., *Nucl. Spectroscopy and Nucl. Structure, Proc 44th Conf., St.-Petersburg* (1994) p. 203.

Gamma-ray lasing by free nuclei and by matter–antimatter beams

Lev A. Rivlin

*Moscow State Institute of Radio Engineering, Electronics, and Automation MIREA,
78 Vernadsky Ave., Moscow, 117454, Russia
E-mail: rla@superlum.msk.ru*

I discuss the possibilities to induce the gamma-ray emission departing from attempts to use the Mössbauer effect. Three separate approaches are considered: (A) Stimulated radiative transitions in deeply cooled nuclear beams with hidden inversion; (B) external two-photon ignition of nuclear lasing accompanied by gamma-ray giant pulse emission; and (C) burst-like radiative annihilation of relativistic beams of electrons and positrons or parapositronium atoms ignited by an external beam of soft photons.

1. Introduction

Why is the problem of gamma-ray lasing so attractive and important [1–3]? To my mind, the reason is that solving this problem will

- extend the basic principle of induced boson emission, successfully applied in the optical laser physics, to a new class of quantum oscillators, namely, nuclei and antiparticles;
- open up opportunities for using in modern science and technology a new energy range of coherent photons, namely, keV and even MeV;
- introduce into practice a new type of nuclear reactions, namely, the chain reaction of induced radiative transitions.

I believe that progress in this field will give birth to a new branch of science and technology – *quantum nucleonics* – that should extrapolate quantum electronics and nonlinear optics into new range of high photon energies and new quantum amplifying media.

Gamma-ray lasing is a very diverse interdisciplinary problem involving many independent keystone tasks, for instance,

- (a) Development of the methods for preparing the amplifying media: pumping shortlived isomers, educating longlived metastable nuclei, embedding them into

the solid matrix, cooling the nuclear ensembles, originating the matter–antimatter particle beams, arranging the truly inversionless amplifying states, making use of K-mixing in nuclei and Stokes and anti-Stokes transitions, constructing the efficient pumping sources, etc;

- (b) Development of the efficient gain process providing the overcoming of the threshold: choosing the proper nuclear level structure, surmounting the various kinds of inhomogeneous line-broadening, minimizing the photon losses, arranging the feasible feedback, making use of superfluorescence and various cooperative effects, etc;
- (c) Stating the criteria for choosing the candidate from the variety of isomers based on results of points (a) and (b), development of computer searching program and nomination of the “lucky” nuclei.

In the present analysis I will pay attention to some aspects of the gain-process development.

Beginning with the very first Russian and American proposals, which were put forward more than three decades ago [4–6], the main concepts of stimulating the gamma-ray emission were based on making use of Mössbauer transitions in nuclei embedded in a solid matrix [1–3]. The only, but very important merit of this approach is the possibility of minimizing the spontaneous linewidth down to the natural radiative value. Unfortunately this opportunity must be paid by numerous well known complications inherent for the solid state usage that are not surmounted until today [1–3].

Therefore it is of interest to explore in parallel to the well tramped Mössbauer’s path various alternative ways departing from the necessity for a solid matrix. Here three separate approaches will be discussed:

- A.** Stimulated radiative transitions in populations of deeply cooled isomeric nuclei without total inversion (or with so-called hidden inversion) [7–10];
- B.** External two-photon ignition of nuclear gamma-ray lasing accompanied by the emission of a giant pulse of photons [10,11];
- C.** Burst-like radiative annihilation of relativistic beams of electrons and positrons or parapositronium atoms ignited by an external beam of soft photons.

The analysis presented here possesses mainly a qualitative character and is more a task statement giving directions for further investigations than that it is a final solution to the whole problem. All the versions discussed make use of free particles. So one of the main purpose is the overcoming of the inhomogeneous Doppler line-broadening that causes the pernicious influence on the photon-gain coefficient.

2. Stimulated emission from a monokineticized nuclear beam without total inversion

2.1. SPECTRALLY LOCAL INVERSION AND THE THRESHOLD CONDITION IN FREE NUCLEI POPULATIONS

The nuclear recoil accompanying any hard-photon radiative process causes the splitting of emission and absorption lines. So, if the temperature T of free nuclei is low enough,

$$kT < E^2/2Mc^2 \ln(n_1/n_2), \quad (1)$$

it is possible to obtain a local inversion over part of the spectral line without a total excess of the concentration of excited nuclei n_2 over that of unexcited ones n_1 (neglecting state degeneracy) [8]. Here M is the mass of nucleus, E the transition energy, k the Boltzmann constant, and c the speed of light. It should be remarked that optical lasers with spectrally local (or hidden) inversion of different origin have long been in use (for instance, semiconductor diode lasers). As follows from eq. (1) a deep inversion can be easily achieved when $T < 1$ K. Say, for $Mc^2 = 100$ GeV and $E = 10$ keV spectrally local inversion at the center of emission line is achieved at $T = 0.5$ K, if $n_2/n_1 = 10^{-7}$, that is by several orders of magnitude lower than the concentration required for total inversion.

Much more deep cooling down to the submicrokelvin range is needed to overcome the threshold

$$kT < 2\pi M[c^3\hbar^3 n_2 \Delta\omega_\gamma / E^3 \kappa n]^2, \quad (2)$$

in other words, to ensure the excess of gain over the photon losses of any kinds (n is the total concentration of nuclei, κ the total cross section of the photoeffect and the Compton scattering, $\Delta\omega_\gamma < \Delta\omega_D$ the natural radiative linewidth, $\Delta\omega_D$ the Doppler linewidth) [8]. In fact, there is no need to implement truly thermodynamic cooling of the nuclei to lower the negative influence of thermal motion on the photon gain. Ensuring of high monokineticity of nuclei with respect to the translational degree of freedom coinciding with the expected direction of the gamma-ray flux by any feasible method is a quite adequate solution.

2.2. PREPARING THE MONOKINETIZED AND DENSE NUCLEAR BEAM

To achieve the monokineticized nuclear beam may mean the use of various known methods of laser-light pressure that can provide an effective temperature in the nanokelvin range [12], but it is needed to be improved in order to rise the particle concentration.

Another combined method involves an electrical acceleration of ions accompanied by optical laser selection of their velocities [13,14]. The laser light plays here

the role of Maxwell's demon determining the particle velocity, whereas the electric field executes the task set by the demon.

But the pure electric methods probably are the simplest ones. When ions are accelerated by an electric field the longitudinal velocity spread drops drastically due to the quadratic dependence of the kinetic energy on the velocity [7,8]. The new longitudinal temperature after acceleration over the voltage U is equal to

$$kT = (kT_0)^2 \ln 2/4eU, \quad (3)$$

where T_0 is the initial temperature, and e the ion charge [8]. For instance, the acceleration by $U = 100$ kV reduces the temperature from $T_0 = 80$ K down to $T = 1$ μ K. There are some limitations in this cooling process caused by the ion-beam space charge, the Nyquist noises, the second-order Doppler effect, the intermolecular forces, etc. [8–10].

Unfortunately the possibility of solving the task of the beam-density enhancement arising in parallel to the cooling problem is not evident today. The known useful methods of electron optics and laser-assisted compression might be complemented by the ballistic focusing of neutral particles [8,9]. This method includes the electron optics for setting the proper initial conditions to the parent negative ions and the optical laser for electron photodetachment to neutralize them. Then the population of neutral atoms with almost unperturbed initial conditions moves unhindered by Coulomb repulsion along the trajectories coming together. Estimates show an expected density enhancement of 1000.

2.3. MAXIMUM TOTAL GAIN OVER THE OPTIMUM BEAM LENGTH

Spontaneous decay of the metastable isomers with the lifetime $\tau < (\Delta\omega_\gamma)^{-1}$ limits the optimum beam length,

$$L = u\tau \ln(n_2/n_{\text{th}}), \quad (4)$$

where u is the translational velocity of the beam, and n_{th} the threshold concentration of n_2 that follows from eq. (2) by converting them to an equality [8,9].

The total gain over this length reaches its maximum [8,9]

$$G_{\max} \approx \exp \left[n\kappa u\tau \left(\frac{n_2}{n_{\text{th}}} - \ln \frac{n_2}{n_{\text{th}}} - 1 \right) \right]. \quad (5)$$

So the whole scenario will require the following sequence of operations: forming a beam of metastable isomers and rapid supplying them from the hot pumping zone; deep beam cooling and compression; and realization of stimulated gamma-ray emission in prepared cold and dense beam.

A numerical example for a hypothetical isomer with a charge of 20, $E = 2.5$ keV, $\tau = 1$ μ s: monokineticization by acceleration up to the particle energy $eU = 100$ keV reduces the temperature from $T_0 = 4$ K down to $T = 2.5$ nK; positive gain over the beam length $L = 180$ cm arises when the current density of the

parent ion beam exceeds 1 A/cm² taking into account a density enhancement of 1500 [8,9].

3. External ignition of gamma-ray giant-pulse emission

3.1. ELIMINATION OF THE NEGATIVE INFLUENCE OF RANDOM PARTICLE MOTION ON THE GAIN MAKING USE OF A TWO-PHOTON STIMULATED PROCESS

This approach is also based on the elimination of the pernicious influence of random motion of free particles, but does not demand any cooling to involve into stimulated emission all the particles with randomly distributed individual velocities. It uses all the experience gained in two-photon sub-Doppler optical spectroscopy. Excited states suitable for such experiments are those for which two-photon transitions are competitive with one-photon decay channels [11].

Let us consider the stimulation of radiative two-quanta transitions in free nuclei by two counterpropagating external photon beams. It can be seen from the laws of energy and momentum conservation that the total energy of both photons emitted in opposite directions is given by the equation

$$h(\omega_1 + \omega_2) = E + h\delta\omega \frac{u}{c} - \frac{(h\delta\omega)^2}{2Mc^2}, \quad (6)$$

where ω_1 and ω_2 are the photon frequencies, $\delta\omega = \omega_1 - \omega_2$ the frequency detuning, u the longitudinal random velocity of the nucleus. The latter term is due to recoil. Supposing the homogeneous line-width $\Delta\omega_0$ to be extremely small ($\Delta\omega_0 = 0$), one can see that the motion of the nucleus with arbitrary random velocity does not violate the resonance condition between radiation and nuclear transition only if $\delta\omega = 0$. Thus all the nuclei with different random velocities are included in the process of stimulated emission into the central mode with $\delta\omega = 0$ and $\omega_1 = \omega_2$. If we take into account the finite homogeneous line-width $\Delta\omega_0$, the total number $N_0 = c/\Delta u \gg 1$ of pairs of such modes situated in the allowed detuning interval $\delta\omega_A = \Delta\omega_0(c/\Delta u)$ is inversely proportional to the width of velocity distribution function Δu .

Therefore the spectral distribution of two-photon emission stimulated by two external photon beams propagating in opposite directions features a narrow peak, which corresponds to an increased rate of emission fed by all the nuclei independently of their random velocities [11].

3.2. TWO-QUANTA AMPLIFICATION OF COUNTERPROPAGATING PHOTON BEAMS

The stationary two-quanta amplification of two counterpropagating photon beams with densities I and I^* and spectral width $\Delta\omega_0$ within the interval $\delta\omega_A$ is governed by simple equations:

$$\begin{aligned}\frac{dI}{dz} &= \beta(n_2 - n_1)II^*, \\ -\frac{dI^*}{dz} &= \beta(n_2 - n_1)II^*,\end{aligned}\tag{7}$$

where $\beta = \text{const}$ [cm⁴s]. The terms corresponding to spontaneous and spontaneous-stimulated emission and to photon losses are omitted in the case when the product II^* is high enough [11].

Eqs. (7) lead to

$$\frac{dI}{dz} = \beta(n_2 - n_1)I(C - I),\tag{8}$$

where the concentration difference is equal to

$$n_2 - n_1 = \frac{n_0}{1 + I(C - I)/I_s^2},\tag{9}$$

and

$$C = I + I^* = I_{\text{out}} + I_{\text{ign}}^* = I_{\text{out}}^* + I_{\text{ign}} = \text{const}.\tag{10}$$

Here I_{ign} and I_{ign}^* are the input densities of external igniting beams, I_{out} and I_{out}^* the output beam densities, n_0 the initial concentration difference when $I = I^* = 0$, I_s the saturation beam density that depends on the used pumping scheme.

The result of integration of eq. (8) is the transcendent equation for the net output $I_n = I_{\text{out}} - I_{\text{ign}} = I_{\text{out}}^* - I_{\text{ign}}^*$,

$$\left[\frac{I_n}{I_s} + \frac{I_{\text{ign}}}{I_s} \left(1 + \frac{1}{\mu} \right) \right]^{-1} \ln \left[\left(\frac{I_n}{I_{\text{ign}}} + 1 \right) \left(\frac{I_n}{I_{\text{ign}}} \mu + 1 \right) \right] + \frac{I_n}{I_s} = \beta n_0 I_s L,\tag{11}$$

where $\mu = I_{\text{ign}}/I_{\text{ign}}^*$.

Its solution, presented in fig. 1, shows the ambiguity of the dependence of the normalized net output I_n/I_s on the product $\beta n_0 I_s L$: the curves posses an S-like form. So one can expect the avalanche-like jumping behaviour of the output intensity accompanied by devastating the excited states and the emission of a giant gamma-ray pulse if the initial concentration difference n_0 reaches some critical value.

Of course, the jump process itself is beyond description by the stationary solution (eq. (11)). But the enormous value of the jump manifests almost full transformation of the energy of inverted states into coherent gamma-radiation. The nonlinearly deepens and the output jump grows if the ignition asymmetry increases ($\mu \gg 1$).

3.3. NONLINEAR MIRRORLESS DYNAMIC FEEDBACK DUE TO STIMULATED TWO-PHOTON EMISSION

Such kind of burst generation of coherent gamma-photons is due to the special type of dynamic distributed feedback arising the two-photon emission induced by

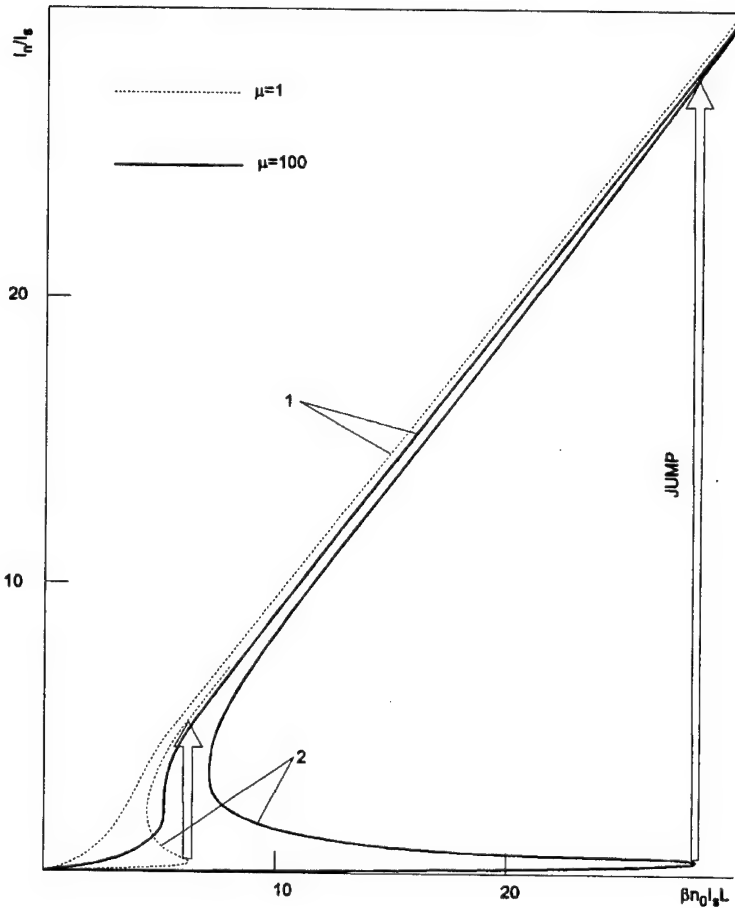


Fig. 1. Normalized net output I_n/I_s versus the product $\beta n_0 I_s L$ (curves 1: $(I_{\text{ign}}/I_s)^2 = 0.5$; curves 2: $(I_{\text{ign}}/I_s)^2 = 0.01$).

two counterpropagating beams. Setting up of this nonlinear dynamic feedback with the coupling coefficient

$$\rho = \frac{1}{I} \frac{dI^*}{dz} = \beta(n_2 - n_1)I^* \quad (12)$$

proceeds in each event of two-photon stimulated emission because all the new photons hit perfectly the wanted modes of opposite directions. One can also pay attention to the presence of a standing wave (the first feedback symptom) in this process. Such dynamic feedback cropping up in the two-photon induced emission without any mirrors is important because the creation of reflecting structures for the gamma-ray range is a very complicated task [11].

3.4. SOME REMARKS ON THE GAIN AND VARIOUS KIND OF LINE BROADENING

The gain constant β of two-photon emission strongly depends on the level scheme of the nucleus due to the resonance denominator $(1-2E_i/E)^2$, where E_i is the energy of the interjacent level between the lasing levels.

If the detuning in the denominator is too small, the stimulated two-photon transition degenerates into two independent single-photon transitions in series. Therefore the detuning must sufficiently exceed the Doppler width [11]

$$(1 - 2E_i/E)^2 \gg 2(kT/Mc^2) \ln 2. \quad (13)$$

To eliminate the time-of-flight line-broadening and the collision broadening one must demand the fulfillment of the following inequalities for the reactor dimensions l and the total concentration of nuclei n :

$$l \gg \frac{c}{\Delta\omega_0} \sqrt{3kT/Mc^2}, \quad (14)$$

$$n \ll (\Delta\omega_0/c\sigma) \sqrt{Mc^2/3kT} \quad (15)$$

(σ being the collision cross section) [11].

The second-order Doppler broadening must be much smaller than the homogeneous line width $\Delta\omega_0$:

$$2\omega(kT/Mc^2) \ll \Delta\omega_0. \quad (16)$$

Actually the Doppler broadening may be caused by random velocities gained by the nuclei during the pumping (besides the influence of the thermal motion). For instance, the noncoherent X-ray pumping with the photon frequency ω_p causes additional effective "temperature" [11]

$$kT_{\text{eff}} \approx (h\omega_p)^2/Mc^2 < kT. \quad (17)$$

3.5. EXTERNAL TWO-PHOTON IGNITION OF THE NUCLEAR EMISSION OF GIANT GAMMA-RAY PULSES

Thus external ignition of the two-quanta stimulated radiative process by the counterpropagating photon beams triggers the common emission of the giant pulse into the wanted mode by all the nuclei with different random velocities due to the arising of intrinsic dynamic nonlinear distributed feedback without any reflecting structures. The resulting efficiency of the emission process on the whole may vary widely depending on the competition of the positive effect of eliminating the Doppler line-broadening and the negative influence of turning to the second-order transition.

It should be pointed out that unfortunately all the gamma-ray sources known

today are not up to the mark in the respect of the needed value of the igniting beam brightness even in the case of a hypothetical “lucky” nucleus that, of course, might not exist at all. Therefore this method may be useful only to emit the giant burst of gamma-quanta of big peak amplitude by the final stage of some amplifying chain, for instance, in series with an X-ray or gamma-ray laser, relativistic undulator or free-electron laser and so on.

4. Igniting the burst-like annihilation by external soft photons

4.1. TRIGGERING OF STIMULATED ANNIHILATION OF RELATIVISTIC ELECTRONS AND POSITRONS OR PARAPositRONIUM ATOMS

Antimatter is the perfect source of states with negative temperature [15]. One-photon radiative annihilation of free particles is completely forbidden, a fact which is an important contributory factor for applying the two-photon ignition method described above to emit the giant pulse of annihilation radiation. However in contrast with the previous nuclear case the elimination of particle-motion effects on the efficiency of stimulated annihilation is not attainable in practice because of the complete disappearance of both emitting particles.

The smallness of the particle masses, m , leads to another positive point: it is possible to lower the requirements on the igniting photon source by making use of the relativistic motion of small-mass particles to transform the photon frequency, beam divergence and beam density [16]. In fact, the resonance condition for the stimulating of one step of a two-photon transition by soft photons can be carried out by the Doppler effect, if electrons and positrons or parapositronium atoms [17] move along coincident trajectories with energy per particle of $mc^2\gamma$, where γ satisfies

$$\gamma + (\gamma^2 - 1)^{1/2} = mc^2/h\omega_{\text{ign}}^*, \quad (18)$$

and one of two counterpropagating beams of igniting photons with the frequency ω_{ign} is directed opposite to the moving particles. For instance, the particle energy should be equal to $mc^2\gamma \sim 260$ MeV ($\gamma \sim 500$) when $h\omega_{\text{ign}}^* = 0.5$ keV.

Simultaneously the beam density of photons acting in the igniting process in the coordinate system travelling with the particles increases $mc^2/h\omega_{\text{ign}}^* \approx 1000$ times. Besides this almost all the radiation from the isotropic igniting source is collected into the wave-vector cone with the solid angle

$$\Delta\Omega \approx \gamma^{-2} \quad (19)$$

around the longitudinal axis of the same travelling coordinate system, that is for the same example into $\Delta\Omega \sim 4 \times 10^{-6}$ sr. This means, for instance, that the high-temperature laser plasma with X-ray brightness 10^{26} photons/cm²s sr in the fre-

quency band $\Delta\omega/\omega = 10^{-4}$ [18] builds up in the particle coordinate system ($\gamma \sim 500$) the narrow beam of brightness equal to 10^{35} photons/cm²s sr.

Of course, only one step of the two-photon annihilation transition deals with all these positive factors. To stimulate the second step the photon energy of the counterpropagating external igniting beam must reach the enormous value equal to

$$\hbar\omega_{\text{ign}} = mc^2[\gamma + (\gamma^2 - 1)^{1/2}] = \hbar\omega_{\text{ign}}^*[\gamma + (\gamma^2 - 1)^{1/2}]^2 \quad (20)$$

(in the discussed case $\omega_{\text{ign}}/\omega_{\text{ign}}^* = 10^6$ and $\hbar\omega_{\text{ign}} \sim 0.5$ GeV). But, fortunately, in fact there might be no need in the second external igniting source because the exactly fitting photon beam arises in the moving electron–positron medium due to spontaneous-stimulated radiative annihilation caused by the first igniting beam [16]. In such a radiative transition the external field induces only one step, whereas the second photon is emitted spontaneously. But these spontaneous photons are emitted into a narrow frequency band around the mc^2/h and a narrow wave-vector cone around the longitudinal axis opposite to the first igniting beam according to the laws of energy and momentum conservation [16]. They play the role of the second counterpropagating igniting beam. Of course, its intensity is much smaller than that of the first one. This increases the ignition asymmetry and consequently deepens the nonlinearity of the whole process, but does not eliminate the possibility of the giant-pulse emission.

4.2. UNILATERAL EMISSION OF A GeV-PHOTON GIANT PULSE

The frequencies of emitted annihilation photons coincide, of course, with the igniting ones. So

$$\omega_{\text{out}} = \omega_{\text{ign}} = [\gamma + (\gamma^2 - 1)^{1/2}]^2 \omega_{\text{out}}^* \gg \omega_{\text{out}}^* = \omega_{\text{ign}}^*, \quad (21)$$

and, consequently, the net energy output,

$$P = \hbar\omega_{\text{out}} I_n = [\gamma + (\gamma^2 - 1)^{1/2}]^2 P^*, \quad (22)$$

is strongly asymmetric in spite of the equality of the net photon output $I = I^*$. This means that almost the whole energy of the gamma-ray giant pulse is emitted unilaterally in the direction of relativistic particle motion.

Acknowledgement

The research described in this publication was made possible in part by grant no. JF1100 from the International Science Foundation and the Russian Government.

References

- [1] G.C. Baldwin, J.C. Solem and V.I. Gol'danskii, Rev. Mod. Phys. 53 (1981) 687.
- [2] V.I. Goldanskii, R.N. Kuzmin and V.A. Namiot, Top. Curr. Phys. 25 (1981) 49.
- [3] G.C. Baldwin, Phys. Rep. 87 (1982) 1.
- [4] L.A. Rivlin, Author's Certificate no. 621 265, appl. Jan. 10, 1961; publ. June 25, 1979, Byull. Izobret no. 23 (1979) 220 (in Russian).
- [5] V. Vali and W. Vali, Proc. IEEE 51 (1963) 182.
- [6] G.C. Baldwin, J.P. Neissel, J.P. Terhune and L. Tonks, Proc. IEEE 51 (1963) 1247.
- [7] L. Cohen, J. Quant. Spectr. Radiat. Transfer 40 (1988) 735.
- [8] L.A. Rivlin, Sov. J. Quant. Electron. 22 (1992) 471.
- [9] L.A. Rivlin, *Induced Gamma-Ray Emission and Related Topics*, presented on 11th Int. Worksh. Laser Interaction and Related Plasma Phenomena, Monterey, CA, USA, 1993.
- [10] L.A. Rivlin, Int. J. Laser Phys. 5 (1995) 297.
- [11] L.A. Rivlin, *Nuclear Two-Quanta Gamma-Ray Lasing by Strong-Field Ignition*, presented on 12th Int. Conf. Laser Interaction and Related Plasma Phenomena, Osaka, Japan, 1995.
- [12] P. Meystre, *Toward Nonlinear Atom Optics*, presented on OSA Annual Meeting, Toronto, Canada, 1993.
- [13] L.A. Rivlin, Sov. J. Quant. Electron. 20 (1990) 564.
- [14] L.A. Rivlin, Sov. J. Quant. Electron. 21 (1991) 593.
- [15] L.A. Rivlin, Sov. J. Quant. Electron. 4 (1975) 1151.
- [16] L.A. Rivlin, Sov. J. Quant. Electron. 8 (1978) 1412.
- [17] L.A. Rivlin, Sov. J. Quant. Electron. 9 (1979) 353.
- [18] R.C. Elton, *X-Ray Lasers* (Academic Press, Boston, 1990) ch. 7.

Radiation machines for gamma-ray laser research

Forrest J. Agee

*Phillips Laboratory, Attn. (PL/WSR), 3550 Aberdeen Ave.,
Kirtland AFB, NM 87117, USA*

In the basic research efforts to define the optimum isomers for making a gamma-ray laser, a variety of radiation sources have been used to find the nuclear gateways that make the idea possible. The radiation sources have several roles to play in the gamma-ray laser process, including pumping isomers to excited states with long lifetimes and in subsequently pumping these to short-lived states that quickly decay. This paper reviews the technology of the radiation sources and the desirable characteristics relative to pumping and triggering in gamma-ray laser research.

1. Background

Researchers who studied the isomeric states of nuclei thirty years ago were led to both relatively precise values for activation energy of nuclides and to relatively small cross sections for them. The 3 MeV electron Van de Graaff machine used in the work had excellent precision (10 keV), which enabled making measurements of the cross section thresholds to an accuracy of 20 to 30 keV. The Van de Graaff used platinum targets backed by water to produce the bremsstrahlung with a beam current of 150 μ A. The precision of charging voltage and repeatability of Van de Graaffs make them extremely useful for such work. However, the voltage limitation of the machine available to them also limited them to the relatively small cross sections accessible below 3 MeV [1]. Therefore these earlier data gave little support for the feasibility of gamma-ray lasers due to the small cross sections measured. The resolution, however, was quite good for the studies of nuclei such as $^{87}\text{Sr}^m$, and accordingly, three gateways to nuclear activation were isolated at 1.22, 1.88, and 2.66 MeV. The integrated cross sections were determined to be 8.4, 16, and 380 to within 50% for each gateway measured in units of 10^{-29} cm^2keV . The early work, which could access end-point energies to 3 MeV, lacked the range of end-point energies that were available to subsequent researchers, who were able to use low- and high-energy bremsstrahlung flash X-ray machines and medical linear accelerators with end-point energies up to almost four times the energy available earlier. The results of the expanded search have been exciting in terms of the additional gateways that have been found at higher energy.

2. Work on the gamma-ray laser

At the time that gamma-ray laser research began in earnest in the 1980s, the precision that had been available in the earlier work was no longer available in North America, as Van de Graaff technology was no longer in vogue following the demise of Ion Physics as a manufacturer of these machines. So a different approach had to be developed. The strategy used in subsequent work in the United States was to find a variety of machines that provided a range of energies (at least 0.5 to 8 MeV) for use in developing an understanding of the isomeric possibilities in nuclei and the structure of states that could be used to make a gamma-ray laser. To this end, researchers at the University of Texas at Dallas (UTD) identified a number of

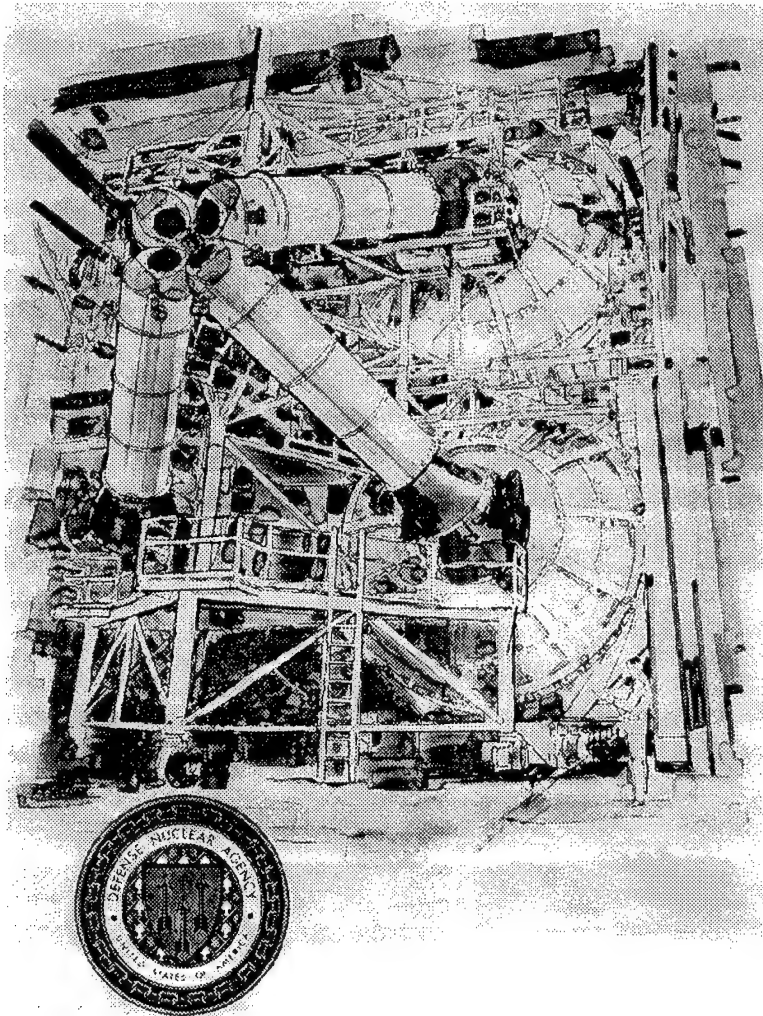


Fig. 1. The AURORA flash X-ray machine.

machines used for various research and medical purposes that gave access to energies from 0.5 to 12 MeV, and also constructed several machines at UTD to support the effort. The relativistic electron beam machines used in the later work included two flash X-ray machines [2–4], several medical linacs in Texas, and a research linac at Darmstadt, Germany [5].

The Flash X-ray machines such as the AURORA (fig. 1) were designed to be used in either the bremsstrahlung or electron beam modes for a variety of research and development purposes. The Pithon machine (fig. 2) at Physics International in San Leandro, Calif., USA, was designed to produce extremely high dose rates with a voltage range from 0.5 to 1.5 MeV that could be adjusted by varying the charging voltage. The flash X-ray machine is arranged with a Marx generator that charges a low-impedance water line that is switched to generate a high current delivered to a diode with a tantalum target. The result is a very intense source of bremsstrahlung, optimized to produce pulses 50–60 ns wide. It can generate up to 100 krad(Si) at a dose rate up to 2×10^{12} rad(Si)/s at the maximum charge of 1.5 MV (fig. 3). The left column is the appropriate one for small sample exposures such as those required for gamma-ray laser research. The relative spectral intensity of the Pithon when charged to an end-point energy of 1.5 MeV is shown at the left side of fig. 4 [4].

The high-energy range between 6 and 11 MeV was also available in the form of a giant flash X-ray machine, the AURORA machine at Adelphi, Md., USA (fig. 5). The AURORA machine was five stories high, had four Marx generators that could

Pithon

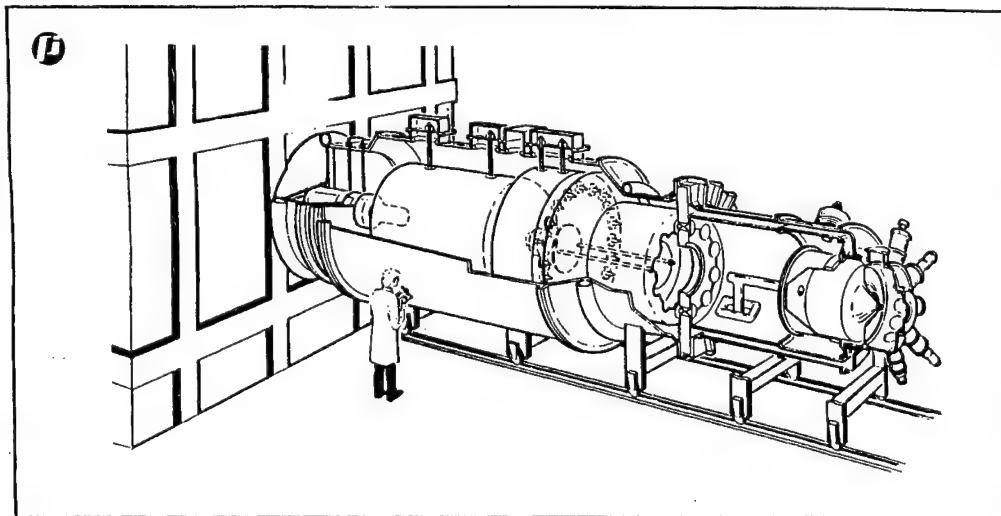


Fig. 2. The Pithon machine at Physics International in San Leandro, California.

Pithon

BREMSSTRAHLUNG CHARACTERISTICS

Area (cm ²) (D _{min} /D _{max} > 0.5)		100	1,000	10,000
Area-Weighted Mean Dose	B _{1.0}	30	6	0.6
	B _{1.5}	100	20	2
kRad (Si)	B _{1.0}	6 × 10 ¹¹	1 × 10 ¹¹	1 × 10 ¹⁰
	B _{1.5}	2 × 10 ¹²	3 × 10 ¹¹	3 × 10 ¹⁰
Area-Weighted Mean Dose Rate	B _{1.0}	0.8	0.2	0.02
	B _{1.5}	3	0.7	0.07
Fluence	B _{1.0}	40	9	0.9
	B _{1.5}	120	30	3
Maximum Dose*	B _{1.0}	7 × 10 ¹¹	2 × 10 ¹¹	2 × 10 ¹⁰
	B _{1.5}	2 × 10 ¹²	5 × 10 ¹¹	5 × 10 ¹⁰
Maximum Dose Rate*	B _{1.0}			
	B _{1.5}			
Rad (Si)/s				

*Over significantly smaller area than shown. Isodose curves available upon request from facility manager.

- X-ray Pulse FWHM: 50-60 ns
- Rise time: 25 ns

SXR

Spectrum ⁽¹⁾	Nominal Yield (Unshielded) (kJ)	Fluence at 5 cm (Unshielded) cal/cm ²	Fluence ⁽²⁾ Over 20 mm ² (mcal/cm ²)	Fluence ⁽²⁾ Over 1000 cm ² (mcal/cm ²)
Kr (1.6 - 2.5 keV)	15	11	200	2.5
Ar (3.0 - 4.5 keV)	7	5	600	1.2

⁽¹⁾ See spectra in introduction.

⁽²⁾ Behind survivable, hermetic debris shield (see introduction).

Fig. 3. Characteristics of the Pithon machine.

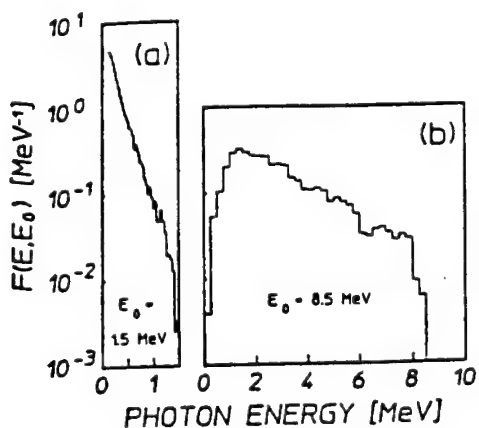


Fig. 4. Relative spectral intensities $F(E, E_0)$ of the bremsstrahlung typically produced by nuclear simulators used to irradiate samples in these experiments. The curves are normalized so that their areas are unity. The devices employed were (a) DNA/PITHON, with an end point of $E_0 = 1.5$ MeV; (b) DNA/Aurora, with an end point of $E_0 = 8.5$ MeV.

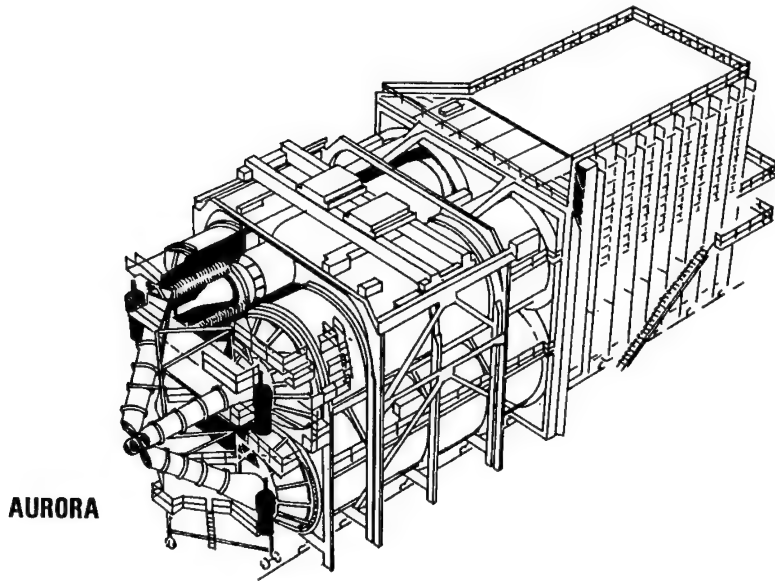
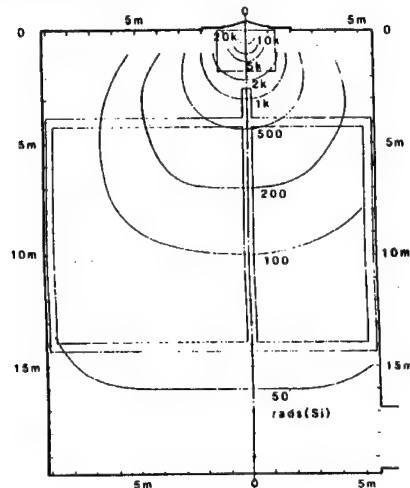


Fig. 5. The AURORA machine at Adelphi, Maryland.

be charged to as much as 12 MV [2]. They were arranged to pulse charge four oil-filled blumleins that were switched simultaneously to generate up to 300 000 A in each pulse-forming line. When switched, the four current pulses arrived at four diodes simultaneously with a resulting radiation pulse at high voltage of 45 krad(SI) with a pulse width of 120 ns and a corresponding dose rate of 3×10^{11} rad(Si)/s (fig. 6). The AURORA spectrum is shown on the right-hand side of fig. 4 for an end-point energy of 8.5 MeV [4]. The spectrum and that for Pithon were generated using the Integrated Tiger Series (ITS) of computer code [6] and were normalized by the total dose and the end-point energy. The spectrum of both flash X-ray machines could be varied by changing the charge voltage provided that the range was kept in the range at which the pulse lines would work. Since the AURORA design uses magnetic self-insulation to transport the current pulses from the blumleins to the radiation diodes, the voltage had to be high enough (greater than 6 MeV) to accomplish this. The resulting radiation pattern is uniform over about 0.1 m^3 , which was convenient for irradiating isomeric samples. A potential advantage for studying isomers with very short half-lives is that the deposition of radiation from flash X-ray machines occurs in such a short time. This maximizes the activation, which could have advantages over other methods for which a comparable dose occurs over periods of time comparable to or greater than the half-life of the isomer. However, for practical purposes, this consideration was unimportant, since the half-lives of isomers of interest typically were of the order of seconds and longer. Consequently, a figure of merit of flux sufficiency is that the source should

Aurora

BREMSSTRAHLUNG ISODOSE

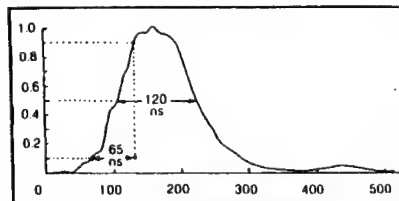


BREMSSTRAHLUNG CHARACTERISTICS

Area (cm^2) ($D_{\text{min}}/D_{\text{max}} > 0.5$)		1,000	3,000	10,000	70,000*
Area-Weighted Mean Dose kRad (Si)	$B_{7.0}$	42	36	6.8	0.8
Area-Weighted Mean Dose Rate kRad (Si)/s	$B_{7.0}$	3.0×10^{11}	2.6×10^{11}	4.8×10^{10}	5.6×10^9
Maximum Dose* kRad (Si)	$B_{7.0}$	45	45	8	1
Maximum Dose Rate* Rad (Si)/s	$B_{7.0}$	3.2×10^{11}	3.2×10^{11}	6.1×10^{10}	7.0×10^9

*Over significantly smaller area than shown. The 70,000 cm^2 area is a rectangle 3.5 m wide \times 2.0 m high.

X-RAY PULSE (TYPICAL)



- FWHM: 120 ns
- Rise Time: 65 ns

Fig. 6. Characteristics of the AURORA machine.

be able to provide a flux of about 10^{13} photons/ cm^2 in the exposure in a time short compared to the lifetime of the isomer to be studied [7].

Another consideration in using variable end-point machines like the flash X-ray machines is that the bremsstrahlung dose and dose rate vary as the cube of the voltage, so that the corresponding dose and dose rate for lower end-point energies was correspondingly less than that shown for maximum charge (11 MV for Aurora and 1.5 MV for Python) in figs. 3 and 6. Also, the AURORA machine is capable of somewhat higher charge voltage now (12 MV), due to the installation of new Marx generators, as well as now having added flexibility in pulse shape and number of pulses and an ability to produce a higher dose and dose rate for small samples [3]. The latter capability was not used in the experiments at AURORA due to a desire to accommodate some fast sample retrieval apparatus and a desire to use the uniform illumination over the samples that was available in the normal mode of opera-

tion using all four tubes. The rate of exposures at the flash X-ray machines was about one shot per hour at the maximum, and typically, the experiments proceeded at a slower pace than that. The flux of photons corresponding to the spectra of shots shown in fig. 4 was 4×10^{14} at Pithon and 5×10^{13} at AURORA [5].

The energy region between 1.5 and 6 MeV was covered by a number of linear accelerators. These included the 4 MeV and 6 MeV linacs at the University of Texas Health Sciences Center and the superconducting injector to the storage ring (S-DALINAC) at the Institut für Kernphysik, Technische Hochschule Darmstadt, Germany, and a 4 MeV linac (Texas-X) at the Center for Quantum Electronics at the University of Texas at Dallas (fig. 7). The medical linacs provided single energy end-points for use in exploring this region. Of these machines however, one was uniquely useful, the S-DALINAC at Darmstadt, because of its ability to continuously vary the end-point energy. This accelerator could be tuned to end-point energies $E_0 = 2\text{--}5$ MeV, and a tantalum converter was used to generate the bremsstrahlung [8]. Overall, the Pithon and AURORA machines made it possible to identify a connection with earlier work and to identify that there were gateways of much interest below 6 MeV and above 1.5 MeV. The other machines made it possible to narrow down the range in which the gateways were located.

The machines discussed above were most useful in developing the understanding of the nuclear states that could be accessed by pumping. The goal would be to find long-lived isomers that could store energy for years, and also look for states that could later be pumped with moderate- or low-energy X-rays to a short-lived state (microseconds or nanoseconds lifetime) from which the isomer would transition to the ground state. The pump source for this final transition would logically be a short-pulse X-ray machine with a pulse length in the range of tens of ns to tens of μs .

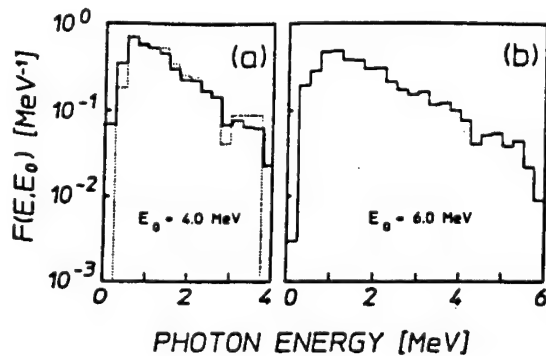


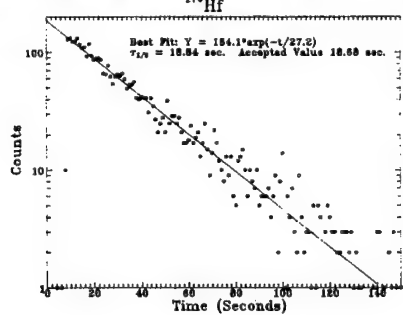
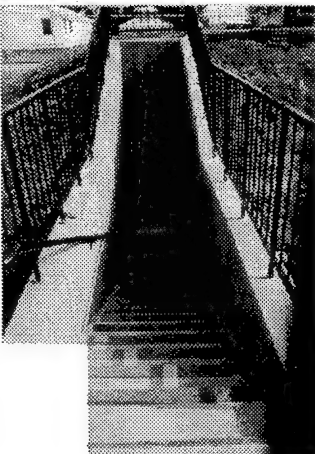
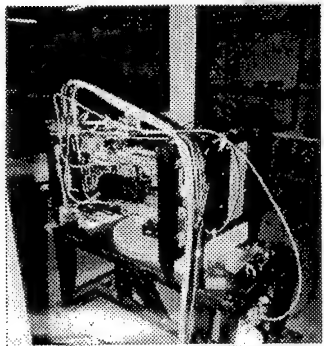
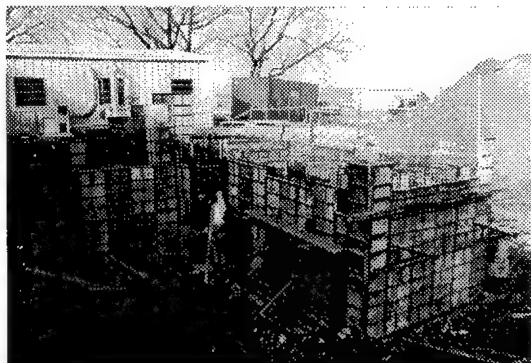
Fig. 7. Relative spectral intensities $F(E, E_0)$ of the bremsstrahlung produced by the medical lines used to irradiate samples in these experiments. The curves are normalized so that their areas are unity. The solid lines indicate empirical fits to the calculated spectra as discussed in the text. The devices employed were as follows: (a) Varian Clinac 4/100, with a nominal end point of 4 MeV. The dotted curve shows the spectrum obtained from ref. [21] that contains a computational artifact at about 3 MeV. (b) Varian Clinac 1800, operated in the nominal 6 MeV end-point mode.

The Texas-X linac (fig. 8) was designed to test this approach to the final pumping scheme. It was designed to produce high current and high photon flux in pulses a few μ s duration. The machine parameters were designed to produce 4 MV electrons with a pulse length of 2.78 μ s and a pulse repetition frequency of 360 Hz. The resulting duty factor was 1/1000 and the time-integrated current was 150 μ A. The machine was arranged to be located in a buried concrete structure with the beam 1.4 m from the floor and oriented along the long axis (7.3 m) of the room. The other dimensions were 2.6 m high and 2.3 m wide. The electrons were extracted through a

FACILITIES

*During 1991-1992
the University of
Texas at Dallas
constructed a radia-
tion facility
dedicated to the
pumping of nuclear
materials.*

*A 4 MeV High
Intensity Linac
was procured
and emplaced.*



*Early data proved
intensity. Example
shows activation
from a single 30 s
burst.*

Fig. 8. Texas-X Linear accelerator facility at the university of Texas at Dallas.

Cu and Be window with a water-cooled tantalum converter [9]. This machine verified that short-lifetime isomers could be populated in the same way as the long-lived ones.

For the final pumping stage, the optimum machine would appear to be one that produced high fluxes in the ns to hundreds of ns range. Such a machine was constructed at the University of Texas at Dallas, the APEX-1. It produced electron beams with 30 kA in 30 ns long pulses at energies that could be varied from 0.7 to 1.2 MeV [10]. There are, of course many possibilities for this flash X-ray source to trigger the release of the isomeric stored energy, as well as those for pumping the metastable states for long-term storage and research purposes. One such configuration that has merit is the stacked blumlein pulser developed at the University of Texas at Dallas. This concept has been advanced in various forms that provide a flexible array of choices in terms of operating voltage, pulse width, and repetition rate. These pulsers feature a single switching element that commutes a voltage multiplying stack of blumleins that are arranged to add their voltages in series at the diode load. The voltage multiplication approaches the number of blumleins in series. The repetition rate is limited by the capability of the switch, often a thyratron, typically capable of 100 Hz. The resulting radiation source is suitable for moderate

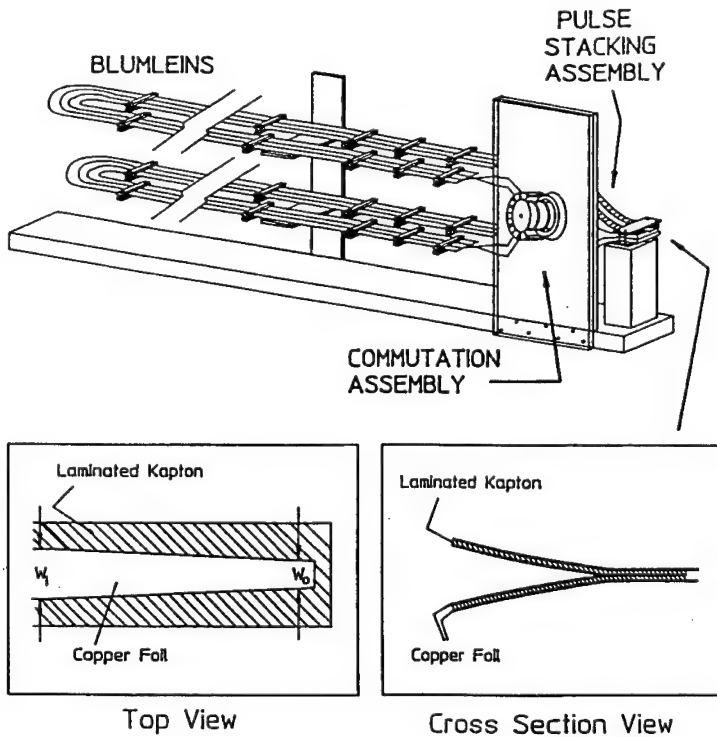


Fig. 9. Stacked blumlein pulser featuring two lines arranged for 600 ns pulses.

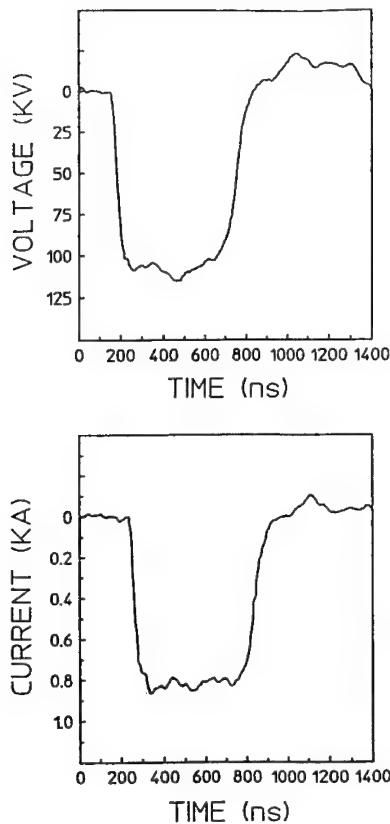


Fig. 10. Voltage and current pulses for stacked blumlein pulser with two lines.

repetition rate pulsers of relatively compact size and variable voltage depending upon the number of lines (as many as a dozen or more) and charge voltage. Figs. 9 and 10 show a two-blumlein pulser optimized for 100 kV and 600 ns pulses. The duration of the pulses is determined by the length of the blumleins, and can be varied from one to hundreds of ns [11,12].

3. Summary

The machines that have contributed to the progress to date on gamma-ray laser research have been of many types, and the characteristics have made possible the systematic studies of potential nuclides achieved that now point the way to exciting experiments to come that may provide the optimum isomer. They also give some insights into the kinds of machines that would prove useful in the future construction of radiation sources using the isomers, both to store the energy in them and to trigger a simultaneous release of the stored energy.

References

- [1] E.C. Booth and J. Brownson, Nucl. Phys. A98 (1967) 529.
- [2] K.R. Prestwich, J.R. Lee, T.W.L. Sanford, F.J. Agee, G.B. Frazier and A.R. Miller, in: *Proc. 1987 IEEE Particle Accelerator Conf.*, Vol. 2 (1987) 892.
- [3] F.J. Agee, Nucl. Instrum. Meth. B56/57 (1991) 1063.
- [4] F.J. Agee, in: *1986 IEEE Nuclear and Space Radiation Effects Conference: Radiation Effects Testing Short Course*, (July 1986), Providence, RI, USA, ed. V.A.J. Van Lint (IEEE/NPSS Radiation Effects Committee, Providence, RI, 1986) Session II, pp. 1–37.
- [5] J.J. Carroll, M.J. Byrd, G.G. Richmond et al., Phys. Rev. 43 (1991) 1238.
- [6] J.A. Halbleib and T.A. Melhorn, Sandia National Laboratories Report SAND 84-0573 (1984).
- [7] J.J. Carroll, private communication (1995).
- [8] P. von Neumann-Cosel, A. Richter, C. Spieler, W. Ziegler, J.J. Carroll, T.W. Sinor, D.G. Richmond, K.N. Taylor, C.B. Collins and K. Heyde, Phys. Lett. B 266 (1991) 9.
- [9] J.J. Carroll, D.G. Richmond, T.W. Sinor, K.N. Taylor, C. Hong, J.D. Standifird, C.B. Collins, N. Huxel, P. von Neuman-Cosel and A. Richter, Rev. Sci. Instrum. 64 (8) (1993) 2298.
- [10] C.B. Collins and J.J. Carroll, Laser Phys. 5 (2) (1995) 209.
- [11] J.D. Bhawalkar, D.L. Borovina, F. Davanloo, C.B. Collins, F.J. Agee and L.E. Kingsley, in: *Proc. Int. Conf. on Lasers '93*, eds. V.J. Corcoran and T.A. Goldman, (STS Press, McLean, VA, 1994) pp. 712–717.
- [12] J.D. Bhawalkar, F. Davanloo, C.B. Collins, F.J. Agee and L.E. Kingsley, in: *Digest of Technical Papers, 9th IEEE Int. Pulsed Power Conf.*, eds. K.R. Prestwich and W.J. Baker (1993) pp. 857–860.

The inelastic channel in time-domain Mössbauer spectroscopy

W.C. McDermott III and Gilbert R. Hoy

Physics Department, Old Dominion University, Norfolk, VA 23529-0458, USA

Time-domain Mössbauer spectroscopy has been interpreted by Hamermesh using a classical optical model. One of the most interesting aspects of the experiments is the observation of a “speed-up” effect. This speed-up effect can be observed by measuring the gamma radiation coming from the source after transmission through a nuclear-resonant “filter”, i.e., the elastic channel, using the delayed-coincidence time-to-amplitude conversion method. This time-domain speed-up effect occurs in the coherent forward scattering of the nuclear-resonant gamma radiation. Time-domain nuclear-resonant forward scattering results observing the inelastic channel, i.e., the X-ray following internal conversion, using a radioactive source have not been obtained previously. Such results are presented for the radioactive-source case using both ^{57}Fe and ^{73}Ge . These two isotopes were chosen because of the differences in the values of the internal conversion coefficients α , i.e., α is 8 and 1310, respectively, for the two cases. In each case experimental data, using both the elastic channel and the inelastic channel, are given. Commercial sources and absorbers of iron-in-rhodium foils were used for the ^{57}Fe experiments. For the ^{73}Ge experiments, we prepared our own sources by electroplating ^{73}As onto Ge single crystals. The Ge absorber was the enriched ^{73}Ge single crystal originally prepared by Pfeiffer. Fits to the experimental elastic-channel data are given using the classical optical model. Our preliminary experimental results using the inelastic channel are inconclusive.

1. Introduction

Time-domain Mössbauer spectroscopy (TDMS), originally called “time filtering”, was first interpreted by Hamermesh [1] using a classical optical model in the early 1960’s. A typical experimental setup for the ^{57}Fe case is shown in fig. 1. Although interesting results [2–8] were obtained, interest in this field subsided. Now, with the advent of synchrotron-radiation sources being used to pump low-lying nuclear levels, time-domain Mössbauer spectroscopy has seen a rebirth in popularity. The electron bunch characteristics of most synchrotron radiation facilities are quite conducive to these types of experiments. Typically, these experiments are done using a fast detector which can recover quickly from the initial pulse of the synchrotron, thereby allowing a measurement of any delayed photons emanating from the absorber. The resulting time-domain synchrotron radiation spectrum exhibits the speed-up effect [9] as predicted by the classical optical model. Since

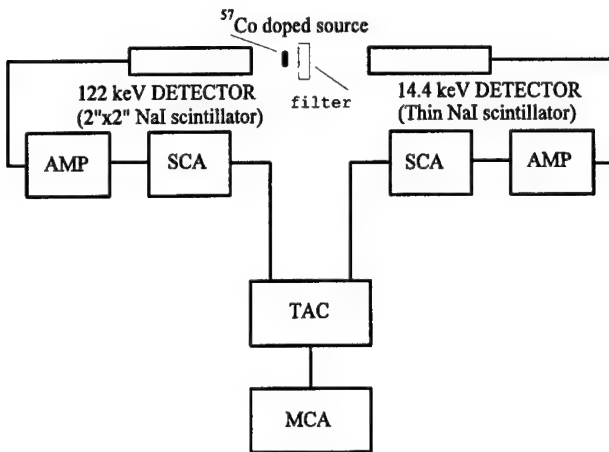


Fig. 1. A typical TDMS experimental setup for ^{57}Fe experiments.

these experiments require fast detectors, such as an organic plastic scintillator with a fast photomultiplier tube or PIN diode detectors, there is little energy discrimination in the timing system. As a result, in an ^{57}Fe experiment, the detector will not only detect the 14.4 keV photons, but it will also detect any photons that are a result of the internal-conversion process. This situation prompts an investigation into whether there will be any speed-up information contained in a TDMS experiment using the X-ray, from the internal-conversion electron processes that take place in the filter, instead of the 14.4 keV gamma ray.

2. Conceptual considerations

In TDMS a classical optical model is used to describe the speed-up effect for the elastic-channel event, i.e., the gamma ray. This model considers the resonant radiation to be traveling through a dispersive medium. As the radiation propagates, each Fourier component gets absorbed and phase shifted differently. Upon emergence, the spectral linewidth is effectively broadened by the medium and hence, from the time-energy uncertainty principle, exhibits a “speed-up” in the lifetime.

In addition, as the gamma ray propagates through the medium and is absorbed by a nucleus the de-excitation favors the internal-conversion process for a number of cases, e.g., ^{57}Fe and ^{73}Ge . If one were to look at the time characteristics of this inelastic channel using the resulting X-rays, would a similar speed-up effect be observed?

3. Experimental setup

There were two isotopes used in these experiments; namely ^{57}Fe and ^{73}Ge . These two isotopes decay through a gamma-gamma cascade, however the internal-conversion coefficient for the first excited states is markedly different. Each of these isotope's parent nuclei decay by electron capture to the second excited state. These second excited states decay to the first excited states by emission of a 53 keV gamma ray for ^{73}Ge and a 122 keV gamma ray for ^{57}Fe . The first excited state energy for ^{73}Ge is 13.26 keV and for ^{57}Fe is 14.4 keV. The internal-conversion coefficient for the ^{73}Ge case is 1310 while for ^{57}Fe it is 8. The natural lifetimes for ^{73}Ge and ^{57}Fe are 4.26 μs and 141 ns, respectively. For the ^{57}Fe experiments the source and absorber were purchased through a commercial vendor. For the Ge experiments the source was prepared in our laboratory. This was done by electroplating ^{73}As onto a Ge single crystal. The crystal was then placed into a tube furnace and heated to 800°C for approximately 72 h. The absorber for the Ge experiments was the same ^{73}Ge -enriched absorber as used by Pfeiffer [10] in his work on the Mössbauer effect in ^{73}Ge .

The experimental setup uses a standard delayed-coincidence, time-to-amplitude converter (TAC) spectroscopy system (see fig. 1). Two detectors were used to detect the gamma-gamma cascade from the decaying isotope. One detector is set, by means of a single-channel analyzer (SCA), to observe the decay from the second excited state to the first excited state. When this photon is detected, this signifies the first excited state has been formed. This signal from the SCA is used as the start pulse for the TAC. The second detector is set to observe the decay from the first excited state to the ground state which provides the stop signal for the TAC. The output from the TAC is a unipolar pulse whose height is proportional to the time difference between the start and the stop pulses. Originally, for our ^{57}Fe experiments, both detectors were NaI(Tl). For the ^{73}Ge experiment, because the 13.26 keV gamma ray is so close to the 10.98 keV K_{β} X-ray, one of the NaI detectors was replaced by a Ge solid-state detector. In another ^{57}Fe experiment, the detectors were also switched to this same Ge solid-state detector and NaI detector system. This was necessary because radiation was able to Compton scatter from one detector to the other, satisfying the energy windows set by the SCA on each leg of the coincidence setup, and as a result, produced an unwanted prominent "prompt" peak in the timing spectrum.

4. Experimental data

TDMS runs for the elastic-channel decay in both ^{73}Ge and ^{57}Fe are given in fig. 2 and fig. 3, respectively. Both of these spectra have been fit using the classical optical theory. This model (which includes parameters for the resonant-medium thickness and a source-absorber detuning factor) is convoluted with a Gaussian

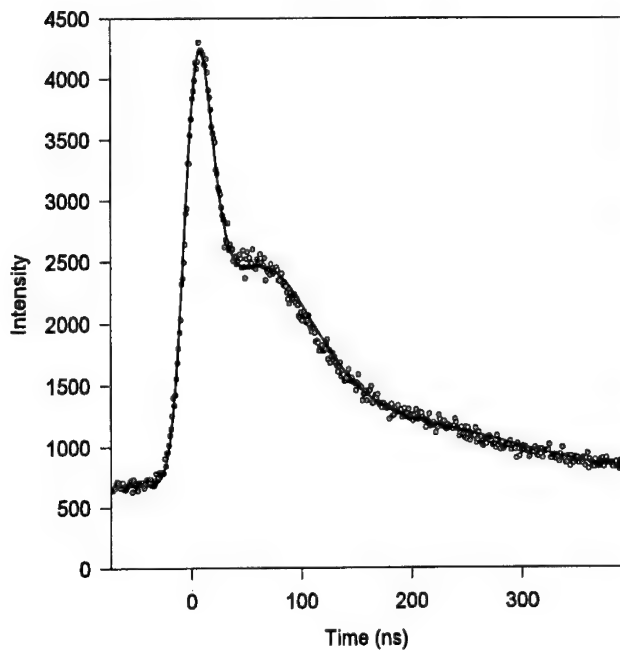


Fig. 2. TDMS results using the ^{57}Fe 14.4 keV gamma ray.

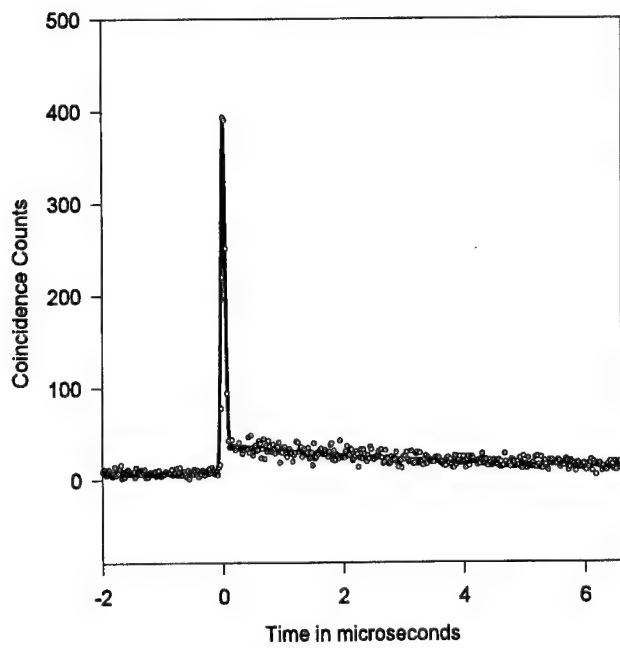


Fig. 3. TDMS results using the ^{73}Ge 13.26 keV gamma ray.

Table 1

Parameter	^{73}Ge	^{57}Fe
Lifetime τ	3.9 μs	141 ns
Resonant-medium thickness	0.5	22
Detuning factor $\Delta\omega$	$> 100\Gamma$	1.4Γ

function to account for the timing resolution of the spectroscopy system. In addition, a Gaussian-shaped prompt and a flat background were included. The parameters determined for the two experiments are given in table 1. As is demonstrated, theory and experiment, as far as the ^{57}Fe case is concerned, are in reasonable agreement. Unfortunately, the time-to-amplitude converter used in the ^{73}Ge lifetime measurements was known to be non-linear which resulted in the lifetime discrepancy. The detuning factor for the ^{73}Ge case had to be taken to be large due to what appears to be an isomer shift between the source and "filter".

Next we considered the inelastic channel. The results for a ^{57}Fe experiment are shown in fig. 4 and the results for a ^{73}Ge experiment are shown in fig. 5. Clearly there is an uninteresting prompt component in both spectra. However, the exponential portion of the Fe spectrum does not agree with the natural lifetime curve. On the other hand, no such deviation is observed in the Ge lifetime curve.

In order to better understand the time structure of these results, an experiment was performed in which the energy window for the stop signal of the TAC was set

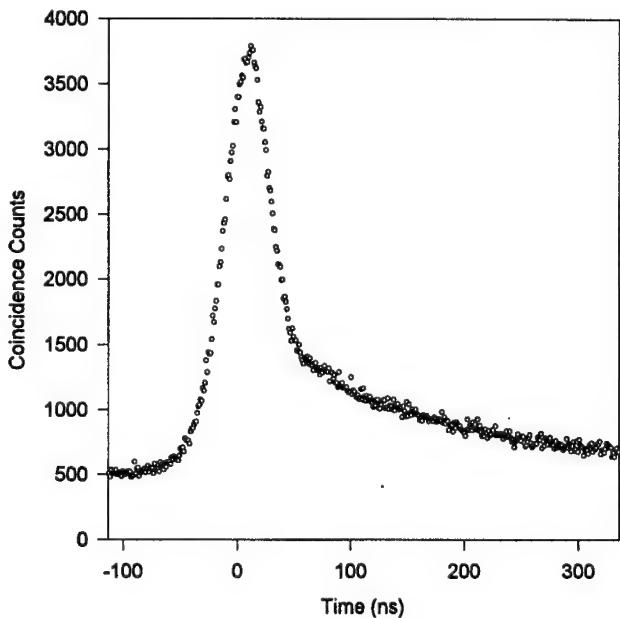


Fig. 4. TDMS results using the ^{57}Fe X-ray.

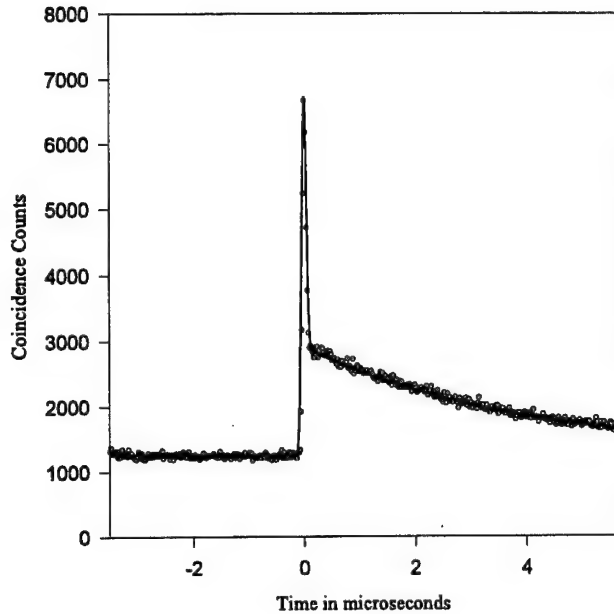


Fig. 5. TDMS results using the ^{73}Ge X-ray.

on the Compton background portion of the ^{57}Fe pulse-height spectrum. The position of the energy window was centered at 8 keV and had a width such that there was no overlap with the iron X-ray peak. The results of the experiment are shown in fig. 6. This result reveals that there is a time filtering characteristic to the Compton background. We interpret this result to be due to resonantly-filtered 14.4 keV gamma rays being Compton scattered into the energy window of the SCA.

5. Discussion

As seen in fig. 3, TDMS results using the 13.26 keV gamma ray in the ^{73}Ge case are difficult to obtain. This is of course due to the large value of the internal-conversion coefficient. Figs. 7 and 8 give some indication of the difficulties. The data collection time for fig. 3 was 40 days. Using the X-ray, some of which result from the internal-conversion process, results were more easily obtained. Further research is needed to test our ^{73}As sources against the enriched ^{73}Ge absorber using standard Mössbauer absorption spectroscopy to ensure that the local environments of the source nuclei are favorable for observing the Mössbauer effect.

The situation is quite different for the ^{57}Fe case. Using the 14.4 keV gamma ray, TDMS results are relatively easy to obtain. Such a spectrum is shown in fig. 2. However, if one looks carefully at the fit using the classical optical model, as shown in fig. 9, it is fairly clear that the theoretical shape is not quite correct. These small

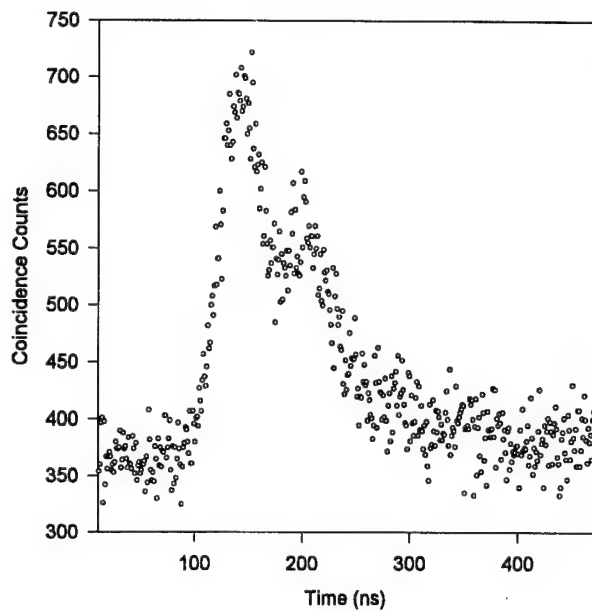


Fig. 6. TDMS results using the Compton scattered radiation in the iron case.

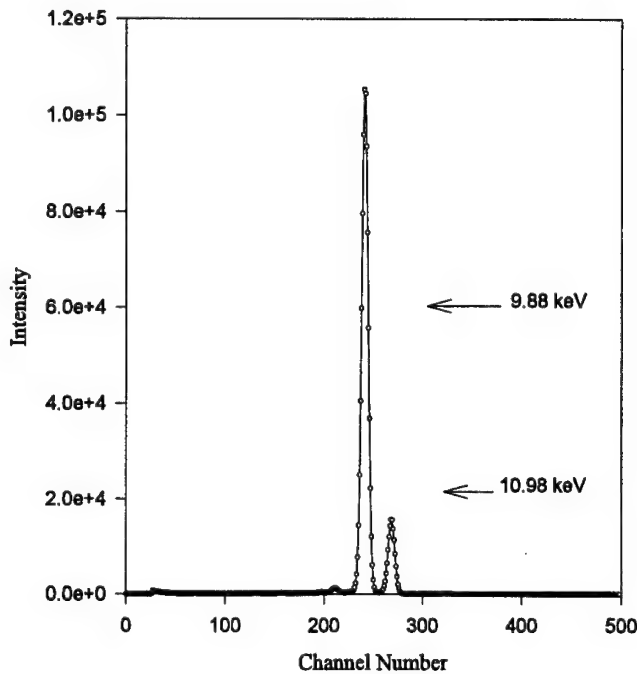


Fig. 7. Pulse-height spectrum showing the Ge X-ray peaks.

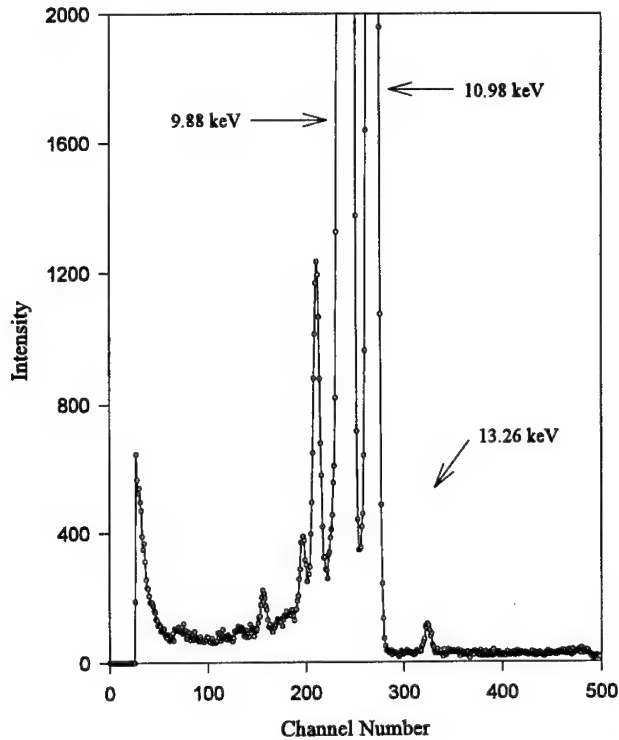


Fig. 8. Expanded view of ^{73}Ge pulse-height spectrum showing the 13.26 keV gamma ray.

deviations have been seen by other investigators, but have not been emphasized in reporting results.

A quantum-mechanical one-dimensional model [11] for nuclear-resonant forward scattering is under development. In this quantum-mechanical model the recoil-free emission and absorption processes correspond to the classical optical model. However, clearly there are other processes that are occurring, e.g., recoil and inelastic events in the absorber. These other processes are handled in a natural way in the quantum-mechanical approach. In contrast, it is not clear, in the classical optical model, how one should treat such processes. The general shape of TDMS theoretical spectra, using the quantum-mechanical model incorporating the recoil events in the absorber, appears promising. This model also predicts a non-exponential time characteristic for the inelastic channel. If one looks carefully at the results shown in fig. 4 in the area just to the right of the "prompt" peak, there is an indication of a deviation from a simple exponential behavior. However, as suggested by the results given in fig. 6, Compton scattering of the 14.4 keV gamma radiation does show time filtering or speed-up effects. This Compton background extends into the region of the X-ray peak itself, therefore one would expect a time-filtering contribution from the elastic channel even in this case. These preliminary

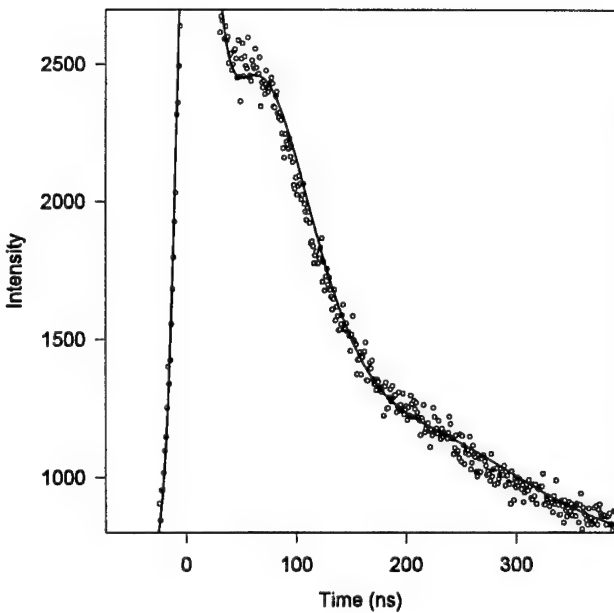


Fig. 9. An expanded view of the results shown in fig. 2. Note that the shape of the theoretical curve does not follow the shape given by the data very well.

results indicate that special care must be taken in order to properly interpret time-domain Mössbauer spectroscopy.

References

- [1] F.J. Lynch, R.E. Holland and M. Hamermesh, Phys. Rev. 120 (1960) 513.
- [2] C.S. Wu, Y.K. Lee, N. Benczer-Koller and P. Simms, Phys. Rev. Lett. 5 (1960) 432.
- [3] S.M. Harris, Phys. Rev. 124 (1961) 1178.
- [4] W. Neuwirth, Z. Physik 197 (1966) 473.
- [5] W. Triftshäuser and P.P. Craig, Phys. Rev. Lett. 16 (1966) 1161.
- [6] W. Triftshäuser and P.P. Craig, Phys. Rev. 162 (1967) 274.
- [7] D.W. Hamill and G.R. Hoy, Phys. Rev. Lett. 21 (1968) 724.
- [8] G.R. Hoy and P.P. Wintersteiner, Phys. Rev. Lett. 28 (1972) 877.
- [9] See, for example, U. van Bürck and G.V. Smirnov, Hyp. Int. 19 (1994) 313.
- [10] L. Pfeiffer, R.S. Raghavan, C.P. Lichtenwanger and A.G. Cullis, Phys. Rev. B 12 (1975) 4793.
- [11] G.R. Hoy, unpublished results.

The importance of stimulated gamma release from isomers

H. Roberts

SRS Technologies, 500 Discovery Dr., Huntsville, AL 35806, USA

The potential applications of the gamma-ray laser are discussed to illustrate the potential benefit of the development of this field of nuclear science, as well as the risks and responsibilities associated with isomer development beyond their current status as nuclear curiosities. The similarities and differences between the development of a gamma-ray laser based on nuclear isomers and the initial development of nuclear science and engineering are compared.

1. Introduction

Nuclear isomerism has been known for over 70 years but was of little significance outside its implications for nuclear structure. With the advent of the microwave and optical lasers came renewed interest in isomers as a medium for high-energy lasing. It is sometimes observed in the field of optical lasers that *any* medium can be made to lase if one can pump it hard enough. This approach was initially considered for isomers as well. However, using a nuclear device to pump an isomer “hard enough” seems impolitic. Such direct neutron pumping through Mössbauer techniques was heavily pursued in the seventies but mostly abandoned by 1980 [1]. Even precision Mössbauer tuning held little prospect of overcoming the high flux requirements and thermal problems associated with direct down-pumping on the isomer state. Today the role of the Einstein coefficients for Mössbauer approaches is not fully resolved for isomeric hyperfine transitions. Other papers in these proceedings address these topics [2–4]. The emphasis on achieving stimulated release now focuses on finessing the problem by one of a few means. The majority of this conference concerns upconversion and bandhead funneling through K-mixing states to achieve lasing inversions and energy extraction. Typical of this are refs. [5–7]. Alternative approaches being considered today include NEET (or TEEN) nuclear–atomic state interactions [8] and non-fissile shape isomerism. [9]

To support these approaches the international efforts discussed at this conference are focused upon development of theoretical models, computational analyses for large n systems, decay mechanisms, state measurements, coupling schemes, state “dressing” schemes, cross-section measurements, stimulation sources, tailored isomer production and isolation processing, to mention a few. The result of

this large body of international research is a frequently repeated plea that we need to “do the experiment” or even some frustration with “why hasn’t it already been done?” The fact is that the underlying political and economic forces that drive and support this type of research have greatly diminished worldwide in the last five years. The funding sources necessary “to do the experiment” are not excited about cross-section studies. Those doing the research shared at this conference understand implicitly that pursuit of stimulated gamma emission, without a fission process, is a worthy goal. But we have not well communicated the significance of the possibility to those who fund the research. This paper is intended to address some of these possibilities and the wider economic/political implications of the research.

2. Far-term possibilities

Let us consider the far-term possibilities of achieving stimulated gamma emission at sub-fissile energies. While the near-term holds promise of achieving incoherent isomer pumping, papers here also address the prospects for directed coherent beams. The nuclear state energy densities are six orders of magnitude greater than for any current lasing medium. This leads directly to some interesting possibilities. For example, lasers now serve as the backbone of communication systems. Consider the million-fold increase in available *bandwidth* of a coherent laser operating at 1 MeV. The worldwide bandwidth consumed in all communication satellites combined could be encompassed with a single isomeric carrier. As another far-term possibility, consider that a high-energy coherent isomer laser could allow direct probes of astronomical bodies outside the solar system that current chemical/electron-based lasers cannot access.

There is some precedent for such incredible possibilities opened by entry into the high-energy state of the nucleus. Fifty one years ago the world would have considered the possibility of releasing an equivalent 20 000 tons of energy from 0.02 tons of metal to be similar fancy. One year later mass/energy equivalence became reality in a particularly grim demonstration. It is not unreasonable to draw comparisons between the research that led to that demonstration and the ongoing research today relative to the gamma-ray laser.

These comparisons will show that technically we stand today on much firmer ground to support progress toward the goal. An extensive scientific infrastructure and conceptual framework is firmly in place for the development of a gamma-ray laser, if nature is nice and the properties of particular materials are determined to be suitable. A comparably suitable infrastructure did not exist in the earlier period. But technical issues will likely be overshadowed by political and economic issues.

The significance of development of a gamma-ray laser could be just as awesome in effect as the initial nuclear experiment, if not in scientific scope. The power of the fissile nucleus cannot be transported directly. Either it must be used in place

(reactors) or delivered by conventional means (ships, planes, projectiles). The energy output from stimulated isomer emission, if incoherent, will likely be similarly limited. However, coherent stimulation of isomers may allow penetrating nuclear scale energies to be delivered on the wings of the EM field at the speed of light. This is both the appeal and the terror of the prospect. Is this a valid concern? We will examine by way of comparison some of these impolite issues. It is not reasonable, desirable nor wise to attempt to restrict such basic science. But we should at the least have some idea of where the science is headed.

To develop the first fissile reactions required the development of a new branch of science – nuclear physics. Today that science is so well developed that it is somewhat difficult to generate interest in “low energy” nuclear reactions. (Unfortunately the development of high-energy physics has reached cosmological proportion mostly beyond the reach of earth-bound accelerators, leading to such theses as David Lundley’s *The End of Physics*. Hopefully he is wrong. [10]) The initial nuclear scientists were developing a new *source* of energy. The scope of the development of a gamma-ray laser is not nearly so expansive. The gamma-ray laser is developing a new regime for energy management of emission from low nuclear states. Fortunately, a validated, detailed formalism for the nucleus already exists as a basis to examine the concepts such as presented at this conference. We do not have to invent a new field of science to develop a gamma-ray laser. Not only does a formalism exist to treat large-*N* systems, but computational methods and facilities are readily available in terms of technology. It is not clear whether these tools are being fully applied by those institutions that have the capability to perform such modeling. The scientific infrastructure is in place to develop the laser. We may not even have to develop a new field of engineering if the concepts such as a nuclear analog to the ruby laser [11] can be extended to the gamma-ray laser. What we do need are materials. It is here that the comparison is most instructive.

In the past the necessary fissile materials were provided by nature awaiting mining in bulk quantities for subsequent enrichment processing. Of course this enrichment process quickly refocused on artificial means of producing the more efficient isotopes from nuclear reactions of enriched uranium materials. Several kilograms of material were needed to reach a critical mass. In contrast, a gamma-ray laser is not a critical-mass device. Much smaller masses of isomer materials can be effective in achieving pumped inversion. This is fortunate since no naturally abundant source for isomers exist, with one poor exception. As anyone working with isomers can readily appreciate, having even a microgram of a material that doesn’t naturally exist is a formidable hurdle. That these materials have to be made artificially in accelerators or reactors may be the most significant limitation that allows the gamma-ray laser to be used in ways that are reasonably limited in scope without becoming a global force of mass destruction.

The scale of effort required in the prior scientific generation to bring nuclear technology to fruition was also driven largely by materials. While today we see the development proceeding from large national and academic accelerator facilities; at

that time, nuclear physics was practiced in small chemistry labs. However, the scarcity of enriched materials required development of massive dedicated facilities. These facilities in turn supported large staffs who gained unique experience in the processing and handling of radioactive and toxic materials in all phases. Hot chemistry became routine procedure. Furthermore, while natural sources of useful isomers do not exist, the stockpiles of spent nuclear fuels may prove to be a rich source for the isomers we seek. It is not obvious that this line of research is being pursued. This nuclear legacy is all in place to build upon to develop and extract isomers for use in gamma-ray lasers. The academies are heavily populated with specialty chairs, staffs and eager post-docs well trained in high-energy physics. This is a luxury not available prior to 50 years ago. New separation technologies, such as provided by conventional lasers, are available today that allow much more efficient and cost-effective material preparation. The state of conventional materials has also progressed dramatically to allow innovative use of materials such as diamond films and carbon macromolecules for isomer host materials. The point here is that while the materials problem is large, there exists an equally large infrastructure well suited for solving the materials problem. Furthermore, having over 50 years of experience in related materials ensures that much more cost-effective methods are available now than were then. For this reason using the prior efforts as a basis for estimating costs for development of the gamma-ray laser materials would not be valid. We have proceeded so far down the learning curve for the production of artificial nuclear materials that such cost comparisons would have little meaning, unless significantly adjusted to account for the progress in the engineering of isotopic materials.

Possibly the most significant aspect of comparison for the previous and current research is that the former was carried out under times of extreme international duress in a highly competitive and isolated process. In contrast, GARALAS '95 embodies the best of the internation spirit of scientific cooperation. This may prove to be the decisive factor if achievement of a gamma-ray laser proves successful.

3. Potential applications

Potential applications for such a technology illustrate the importance of development of this technology. The following examples all assume that energy extraction is successfully demonstrated with low pump energies (< 100's keV) and reasonable photon flux requirements (i.e. not a nuclear explosive pump).

3.1. HIGH-ENERGY LASERS

High-energy lasers would allow significant extensions to the state-of-the-art in conventional laser spectral coverage. Probes into low-lying nuclear states could become more precise and allow evaluation of *n*th order effects such as might paral-

lel non-linear optical phenomena in atomic states. Condensed matter physics would have an entirely new means of studying the state and phase change phenomena. A gamma-based microscope could potentially reveal the atomic quantum structure directly, much as X-rays reveal crystalline structure. The potential applications are limited only by one's vision. These are only a few of the possibilities.

3.2. COMMUNICATIONS

The enormous bandwidth available using a gamma photon wavelength would be significant and warrant the development of this technology on its own merits. Such a bandwidth, for example, could be necessary to fully implement the capability of the next generation of optically based massively parallel computers. These will require rapid transport of data between neural nodes to imprint the processing patterns from one processing center to another. A new less populated generation of gamma satellite communications could replace the rapidly growing crowd of comm sats competing for orbit and position. Not only could fewer satellites be used to offer equivalent bandwidth, but coherent beams would allow much closer positioning of the satellite platforms.

3.3. INDUSTRIAL GAMMA SOURCES

Simply having the ability to control intense gamma radiation sources opens up many industrial applications and extends existing applications. Gamma imaging of deep structural elements greatly enhances the regime of non-destructive testing. Intense switchable gamma sources could lead to development of high-flux ionization sources useful in material processing industry.

3.4. FOOD PRODUCTION

The well known lethal interaction of gamma radiation on biological systems could be useful in developing improved sterilization methods. Bacteria, viruses, biological molds, fungi and possibly toxins can be neutralized with megarad doses of low-energy gamma radiation. Current sources require prohibitive exposure times. An intense gamma source could lead to not only safer processing facilities and packaging, but also purer foods. Foods that have had all the bacteria killed can also be stored for much longer periods and at room temperatures.

3.5. MEDICAL IRRADIATION

Isomers already play a role in medical radiation. ^{99}Tc is a medical isomer routinely used as a short-duration source. Additional isomers suitable for medical applications will surely spin off from a development program pursuing the gamma-ray laser. However, stimulated emission is directly applicable. Microdoses of isomer

could be implanted for long duration, intense short bursts for pathogenic treatment of cancers. An isomer-based external radiation source would be much safer than traditional sources such as ^{60}Co because it can be turned off rather than merely shielded. A directional coherent source would have enormous benefits in terms of not only facility safety but reduced patient exposure and ancillary activation as well.

3.6. POWER AND ENERGY APPLICATIONS

The isomer is in essence a nuclear battery for storage of energy. It can be charged and recharged. Success in developing stimulated emission allows for delivery of its stored energy on demand at controlled rates. All of these characteristics are inherently different from conventional lasers in which the prime pump energy is input simultaneously with the stimulated emission. The energy in an isomer lasing system is stored independently from the stimulation pump energy. This allows the possibility of using isomers for remote prime power applications such as for deep space flight or long-duration remote instrumentation. The incipient decay provides thermal energy and when required high energy densities could be extracted for shorter duration needs. The possibility of using isomers as the prime energy source for space propulsion systems is also under consideration.

Clearly such power applications would require larger masses of isomer than the other applications already mentioned. There is an interesting parallel here to the former generation of emerging nuclear technology. Initially the tailings of unrelated mining operations were a prime source already known for easily accessible uranium materials. Likewise, the spent fuels from nuclear reactors are potentially a ready source for raw isomers already in the excited state. It remains to be seen what the total available yield of such materials could be, pending identification of the isomer forms desired.

3.7. ENVIRONMENTAL CLEANUP

It would indeed be ironic if this phase of nuclear development would provide the technology to make reprocessing of spent fuels economically attractive. The extraction of activated isomers for lasing applications could be that stimulus. However, not all isomers in spent fuels are likely to be suitable for laser applications. In spite of this, these isomers may lend themselves to being pumped down to lower states. Even if the process were inefficient the isomeric pumping could lead to altering the overall radioactive output to a more benign state.

Another possible application of a stimulated gamma emission is the neutralization of biological contamination on either localized or widespread scale. Current means of decontaminating biological disasters, such as saturation with formaldehyde, also leave the facility terminally uninhabitable. It must be destroyed after decontamination. An incoherent gamma emission from stimulated isomers would

produce an isotropic output that falls off rapidly (r^{-2}) with distance. A contaminated facility could be sterilized without sustaining permanent damage itself.

3.8. DEFENSE APPLICATIONS

This may be the area of greatest interest. Virtually all the aforementioned applications can find counterparts in military ventures. However isomer lasing should not be confused with the military potential of existing fissile nuclear materials. Low-energy isomers cannot fission. At best this technology can produce either a localized but very intense isotropic incoherent gamma burst or a directed coherent pulse of gamma irradiation. In either case the technology is not a likely candidate as an offensive weapon of mass destruction (WMD). However, it is a strong candidate as a potential *counter* to such WMDs. Intense gamma radiation interacts with explosive, chemical and biological materials via particularly damaging mechanisms. This possibility levies a strong responsibility on those countries able to pursue the production of isomer materials to ensure that this technology is adequately controlled once development proceeds to the point of these applications.

4. Concluding thoughts

As with any such technology of comparable potential, there comes the responsibility to understand the risks as well as benefits. We have tried to illuminate not only the potential benefits but also some of these risks. We must consider the nature of this technology, the potential limits imposed by the availability of materials, and the role the research community can play in meaningful dialog with the political and economic community at large as this technology comes to fruition.

References

- [1] G.C. Baldwin, J.C. Solem and V.I. Gol'danskii, Rev. Mod. Phys. 53 (1981) 687.
- [2] B. Balko et al., these proceedings (1st Int. Gamma-Ray Laser Worksh., 1995), Hyp. Int. 107 (1997) 283, 369.
- [3] E.K. Sadykov et al., these proceedings (1st Int. Gamma-Ray Laser Worksh., 1995), Hyp. Int. 107 (1997) 257.
- [4] V.P. Aleshin and V.I. Kirischuk, these proceedings.
- [5] L.A. Rivlin, these proceedings (1st Int. Gamma-Ray Laser Worksh., 1995), Hyp. Int. 107 (1997) 57.
- [6] C.B. Collins and J.J. Carroll, these proceedings (1st Int. Gamma-Ray Laser Worksh., 1995), Hyp. Int. 107 (1997) 3.
- [7] A.V. Andreev, these proceedings.
- [8] Y.-K. Ho, Z.-S. Yuan and Z.-Y. Pan, these proceedings.
- [9] P. Bonche, S.J. Krieger, P. Quentin and M.S. Weiss, Nuc. Phys. A 500 (1989) 308.
- [10] D. Lundley, *The End of Physics* (Basic Books, HarperCollins Publ., 1993).
- [11] C.B. Collins, J.J. Carroll, K.N. Taylor, T.W. Sinor, C. Hong, J. Standifird and D.G. Richmond, Laser Interact. Relat. Plasma Phenom. 10 (1993) 151.

Section 2

Candidate Preparation and Characterization

Separation of an isotope as a precursor of a gamma-ray laser medium

Takashi Arisawa, Masabumi Miyabe^a, Akira Sugiyama^a, Kazunobu Yamazaki^a, Akira Ohzu^a, Yoji Suzuki^a, Katsuaki Akaoka^a, Ikuo Wakaida^a, Yoichiro Maruyama^a

*Department of Advanced Photon Research Program, Japan Atomic Energy Research Institute,
Uchisaiwaicho 2-2-2, Chiyodaku, 100 Tokyo, Japan*

^a*Separation Engineering Laboratory, Department of Fuels and Chemistry Researches, Japan Atomic Energy Research Institute, Uchisaiwaicho 2-2-2, Chiyodaku, 100 Tokyo, Japan*

The nuclear isomer $^{178}\text{Hf}^m$, expected to be the most promising candidate for the gamma-ray medium, is rather difficult to produce in large quantities. There are a few ways to create this isomer, such as the irradiation of ^{179}Hf with high-energy neutrons through the $(n,2n)$ reaction, the irradiation of ^{176}Yb with high-energy α particles through the $(\alpha,2n)$ reaction, the irradiation of ^{181}Ta with protons through the $(p,2p2n)$ reaction. In some of these reaction schemes the isotopically pure target works better than the natural one from the viewpoint of spectroscopic purity, handling of radioactive materials and productivity. However, isotope separation of heavy elements for producing a precursor as a target material is difficult in terms of cost/effectiveness. The atomic vapor laser isotope separation (AVLIS) method is expected as the most efficient way compared with the normal electromagnetic separation method.

1. Introduction

The development of an ultra-short wavelength laser has long been expected. Gamma rays have been obtained from ordinary radio isotopes, but the beam quality is bad in terms of coherence and intensity. Basic studies on gamma-ray lasers have been achieved for a long time, and there are several ways to find possibilities, which are categorized in several different ways like an inverse Compton scattering and nuclear excitation. The former one is the concept in which high-energy electrons interact with high-density photons contained in a super-cavity to emit high-energy photons. The advantage of this method lies in the possibility to have a tunable gamma ray, whereas the requirements for the monochromaticity and the beam emittance of electron beams are quite tight. The latter method could be achieved either by neutron excitation or by photon excitation. The route using neutrons is not very much recommended because of the poor monochromaticity of neutron energy. Up-conversion-type nuclear excitation of a nuclear isomer with high-energy photons could be very much promising [1,2].

In this case the specified isotope is required for the target materials as a precursor, which could be more efficiently obtained by the AVLIS method than by an electromagnetic one, because the latter requires whole isotopes as ions and ion extraction capability is limited by the ion density generated in the ion source which is higher than AVLIS method, because AVLIS works only with the ion of the minor component.

A nuclear isomer is produced by the irradiation of an isotopic precursor produced by the reaction of elements with neutrons or accelerated particles. The isotopes used can be effectively separated by the laser isotope separation method.

2. Production of a nuclear isomer [3,4]

2.1. COMPARISON OF NATURAL AND ISOTOPE-TAILORED TARGETS

In order to show that precursors made of a specific isotope are recommendable to produce isomers, let us take a Hf target as an example.

When hafnium metal with a natural assay is irradiated with high-energy neutrons, the five isotopes shown in fig. 1 are involved in this nuclear reaction.

In case (a), the ^{174}Hf isotope is converted to ^{173}Hf through the $(n,2n)$ reaction, in which ^{173}Hf decays with a half-life of 23.6 h to the stable isotope ^{173}Yb via ^{173}Lu , whose half-life is 1.37 years.

In case (b), the ^{176}Hf isotope is converted to ^{175}Hf through the $(n,2n)$ reaction, which decays to the stable isotope ^{175}Lu with a half-life of 70 days. In case (c), the ^{178}Hf isotope is converted to ^{175}Yb through the reaction (n,α) , which decays to the stable isotope ^{175}Lu with a half-life of 4.19 days. In case (d₁), the ^{180}Hf isotope is converted to ^{177}Yb through the (n,α) reaction, $^{179}\text{Hf}^{\text{m}2}$ through the $(n,2n)$ reaction

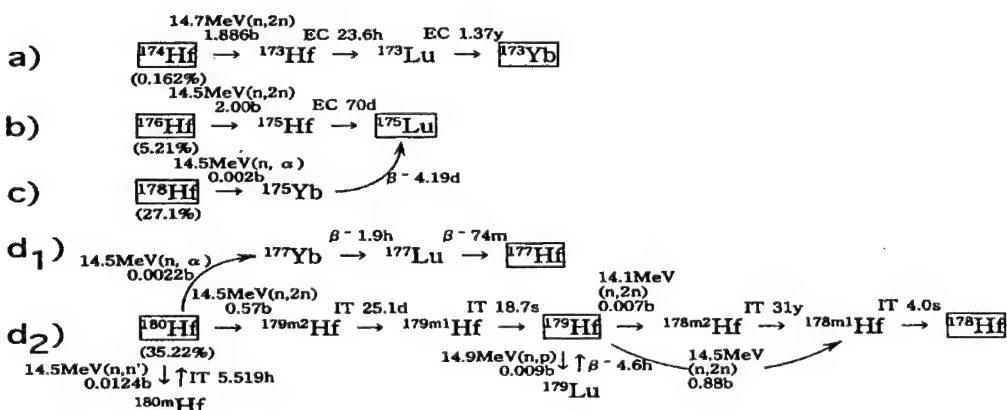


Fig. 1. High-energy neutron reaction for natural hafnium.

and $^{180}\text{Hf}^m$ through the (n,n') reaction. Out of these three different reactions a portion of 97.5% produces $^{179}\text{Hf}^{m2}$. And ^{177}Yb is changed to the stable isotope ^{177}Hf via ^{177}Yb with a half-life of 1.9 h or via ^{177}Lu with a half-life of 74 min. The meta-stable species $^{179}\text{Hf}^{m2}$ is converted also to ^{178}Hf by a number of radiative decays after a high-energy neutron is absorbed. In case (d₂), ^{179}Hf is converted either to $^{178}\text{Hf}^{m2}$ ($T_{1/2} = 31$ y) through the $(n,2n)$ reaction or to $^{178}\text{Hf}^{m1}$ ($T_{1/2} = 4.0$ s) through the $(n,2n)$ reaction or to ^{179}Lu ($T_{1/2} = 4.6$ h) through the (n,p) reaction. Out of these three types of reactions, a portion of 98.2% directly forms $^{178}\text{Hf}^{m1}$ and 0.78% forms $^{178}\text{Hf}^{m2}$, which decays to $^{178}\text{Hf}^{m1}$ through the IT transition. As a result, $^{178}\text{Hf}^{m1}$ decays to the stable isotope ^{178}Hf . The isotope ^{179}Lu again returns to ^{179}Hf .

In conclusion the reaction cross section for reaction (a) is 270 times as large as that for $^{179}\text{Hf}(n,2n)^{178}\text{Hf}^{m2}$, although the abundance ratio of ^{174}Hf is smaller than that of ^{179}Hf by two orders, which results in a 3.2 times larger production of ^{173}Lu than of $^{178}\text{Hf}^{m2}$. As this radioactive lutetium isotope has a fairly long lifetime, a difficult handling situation would be encountered. Reaction (b) produces also byproducts in an amount 100 times as large as the specified target material. this byproduct might also cause difficulty in handling, because the decay time is as long as 70 days. Reaction (d) produces ^{176}Yb , ^{177}Yb and ^{177}Lu , but each reaction cross section does not exceed the reaction cross section for $^{178}\text{Hf}^{m2}$. And what is better, the half-life for each byproduct is 4.19 d, 1.9 h and 74 min, respectively, which will not cause a significant problem, if sufficient cooling time is prepared. The reaction system for hafnium metal with a natural assay is shown in fig. 2.

Therefore, the way using ^{179}Hf as a target material is far better than using the material with a natural assay from the viewpoint of safe handling (see table 1).

2.2. PRODUCTION OF A NUCLEAR ISOMER FROM AN ISOTOPIC PRECURSOR

The hafnium isomer is said to be the most promising medium for a gamma-ray laser. There are several different ways to produce the $^{178}\text{Hf}^{m2}$ isomer, as shown in table 2, one of which is a method using the ^{176}Yb isomer with the help of the $(\alpha,2n)$ reaction by $^4\text{He}^+$ ion bombardment. Another scheme is the activation of the ^{177}Hf or ^{179}Hf isotope with neutrons. Still another way is the one to use Ta isotopes in which the ^{181}Ta isotope reacts with a proton beam with the help of nuclear spallation. The reaction $^{180}\text{Ta}(d,\alpha)^{178}\text{Hf}^{m2}$ might possibly be high because its reaction enthalpy is small.

A large synchrotron radiation facility named SPring8 is now under construction by JAERI/RIKEN and will be due in 1997. This 8 GeV electron storage ring will emit tunable X-ray radiation from several hundred eV up to several hundreds of keV which can be used for the spectroscopy of some nuclear isomers. Tunable X-ray wavelengths are realized by either an undulator, a wiggler or a bending magnet together with a monochromator. Some of the ports are equipped with the beam lines in which several types of polarization are generated. Spectroscopic studies are

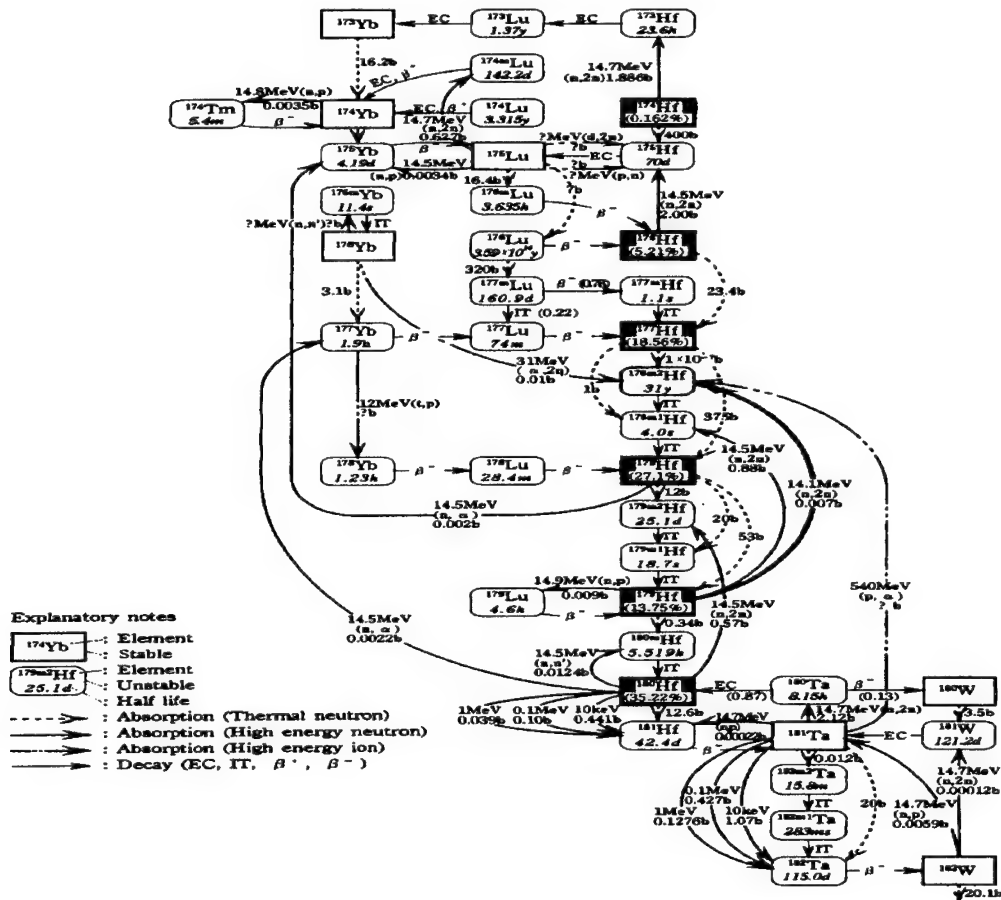


Fig. 2. Decay trees for Hf isotopes with particle irradiation.

Table 1
Comparison of enriched material with natural material for the neutron reaction

Target	Enriched (^{179}Hf)	Natural material
Nuclear species after irradiation	$^{178}\text{Hf}^{\text{m}2}$, $^{178}\text{Hf}^{\text{m}1}$, ^{178}Hf , ^{179}Hf , ^{179}Lu (short lifetime)	$^{178}\text{Hf}^{\text{m}2}$, ^{176}Hf , ^{177}Hf , $^{178}\text{Hf}^{\text{m}1}$, ^{178}Hf , $^{179}\text{Hf}^{\text{m}2}$ (10 month cooling required), $^{179}\text{Hf}^{\text{m}1}$, ^{179}Hf , ^{179}Lu (short lifetime), $^{180}\text{Hf}^{\text{m}}$ (short lifetime), ^{180}Hf , ^{174}Hf , ^{173}Hf , ^{173}Lu , ^{173}Yb , ^{175}Hf , ^{175}Yb , ^{175}Lu , ^{177}Yb , ^{177}Lu
Target material	small beam size	large beam size
Separation	isotope (isomer) separation	isotope and isomer separation
Radioactivity	moderate	high

Table 2
Production of $^{178}\text{Hf}^{\text{m}2}$

Reaction type	$^{176}\text{Yb}(\alpha, 2n)$ $^{178}\text{Hf}^{\text{m}2}$	$^{177}\text{Hf}(\text{n}, \gamma)$ $^{178}\text{Hf}^{\text{m}2}$	$^{179}\text{Hf}(\text{n}, 2n)$ $^{178}\text{Hf}^{\text{m}2}$	$^{180}\text{Ta}(\text{d}, \alpha)$ $^{178}\text{Hf}^{\text{m}2}$	$^{181}\text{Ta}(\text{p}, 2\text{p}2\text{n})$ $^{178}\text{Hf}^{\text{m}2}$
Cross section (mb)	10	10^{-4}	7	higher value expected at low particle energy	30–70 (nuclear spallation)
Byproducts	^{178}Hf (150 mb)	$^{178}\text{Hf}^{\text{m}1}$ (1.1b), ^{178}Hf (366b) (shortlife)	$^{178}\text{Hf}^{\text{m}1}$ (0.88 b), ^{178}Lu (9 mb) (shortlife)	^{178}Hf	^{172}Hf , ^{175}Hf , ^{178}Hf , etc.
Natural assay (%)	12.7	18.66	13.75	0.012	99.98
Beam source	$^{4}\text{He}^{+}$ ion (31 MeV)	Neutron (thermal)	Neutron (14 MeV)	—	P (800 MeV) 500–600 μA
Typical beam source flux (particles/cm ² s)	(4 μg obtained at JINR-Dubna)	2×10^{14}	(Reactor) < 14 MeV (RI) < 14 MeV $T(d,n)^4\text{He}$ is better	—	(40 μg obtained at LAMPF)
Radioactivity (Bq/ $^{178}\text{Hf}^{\text{m}2}$ μg)	5.85×10^3	5.85×10^3	5.85×10^3	—	6.3×10^9
Advantages	1. Results at JINR 2. <i>Isomer separation avoidable</i>	1. Utilization of nuclear reactor 2. Large amount can be irradiated	1. Small number of byproducts 2. <i>Isomer separation avoidable</i>	1. Chemical separation available after irradiation 2. <i>Isomer separation avoidable</i>	1. Higher production rate
Disadvantages	1. Huge accelerator required 2. <i>Isotope separation required</i>	1. Huge byproducts 2. Small cross section 3. Neutron absorber 4. <i>Isotope separation required</i>	1. <i>Isotope and isomer separation required</i> 2. Huge accelerator required	1. <i>Isotope separation required</i> 2. Huge accelerator required 3. <i>Extremely high separation required due to nuclear activity due to nuclear spallation method</i>	1. High energy proton accelerator required 2. <i>Isotope and isomer separation required</i> 3. <i>Extremely high separation required due to nuclear spallation method</i>

to be made in the experimental station shown in fig. 3, which will be due in a few years.

2.2.1. Production through the $^{176}\text{Yb}(\alpha, 2n)^{178}\text{Hf}^{m2}$ reaction

An accelerated $^4\text{He}^+$ ion is bombarded onto a target of ^{176}Yb to produce the Hf isomer. An assay of 12.7% in natural ytterbium is reacted with 10 mb reaction cross section at the energy of 31 MeV. The additional reaction is $^{176}\text{Yb}(\alpha, 2n)^{178}\text{Hf}$ with 150 mb reaction cross section at 31 MeV. A production rate of 0.015 $\mu\text{g}/\text{day}$ was achieved at JINR (Dubna) with a 100 μA beam intensity. About one fifth of that capacity would be produced by the AVF(azimuthally varying field)-type cyclotron of JAERI (Takasaki, Japan) with 100 μA at 10–180 MeV acceleration energy.

2.2.2. Production through the $^{177}\text{Hf}(n, \gamma)^{178}\text{Hf}^{m2}$ reaction

Thermal neutrons constantly generated inside the nuclear reactor could be used for producing the Hf isomer through the $^{177}\text{Hf}(n, \gamma)^{178}\text{Hf}^{m2}$ reaction. The isotope ^{177}Hf with a natural assay of 18.606% is reacted with 0.1 μb reaction cross section which brings a large amount of byproducts such as $^{178}\text{Hf}^{m1}$ (reaction cross section: 1.1 b), ^{178}Hf (366 b). This method can advantageously make use of the affluent neutrons in reactors with a typical flux of 10^{14} – 10^{15} n/cm^2 . But byproducts with high radioactivity are generated and the reactivity in the nuclear reaction itself is possibly degraded by the insertion of the large amount of Hf materials which is a distinguished neutron absorber.

2.2.3. Production through the $^{179}\text{Hf}(n, 2n)^{178}\text{Hf}^{m2}$ reaction

High-energy neutrons can be used for this reaction. The hafnium isotope, ^{179}Hf , with a natural abundance of 13.75% is irradiated by neutrons to produce a hafnium isomer by the reaction $^{179}\text{Hf}(n, 2n)^{178}\text{Hf}^{m2}$ with 7 mb reaction cross section at 14 MeV. Byproducts are produced through the $^{179}\text{Hf}(n, 2n)^{178}\text{Hf}^{m1}$ reaction with a cross section of 0.88 b at 14.5 MeV and $^{179}\text{Hf}(n, p)^{179}\text{Lu}$ with 9 mb at 14 MeV. Although the number of byproducts is small, long-term irradiation is required to produce a significant quality of the Hf isomer. Several methods to obtain high-energy neutrons are considered to fulfill this process.

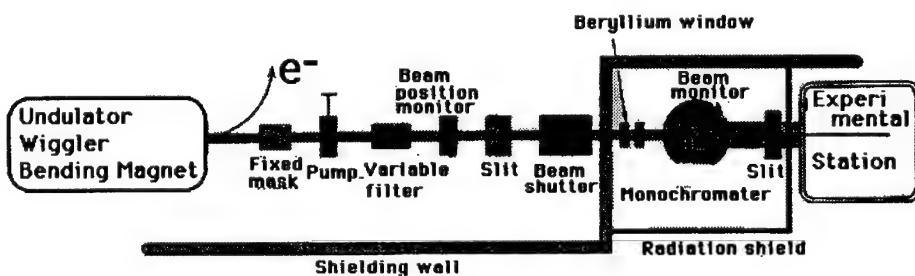


Fig. 3. X-ray spectroscopy using synchrotron radiation (SPring8).

As conventional nuclear reactors have neutrons with a wide spectrum in the low-energy region (normally less than 2 MeV), they are not useful for this purpose. Neutrons can be generated from a reaction with radio isotopes such as ^{226}Ra -Be, ^{227}Ac -Be, ^{244}Cm -Be, ^{24}Na -D₂O, which are not effective, because even the highest energy cannot exceed 5 MeV. At present the high-energy neutron reaction of $^{179}\text{Hf}(n,2n)^{178}\text{Hf}^{m2}$ could be used in the FNS (fusion neutronics source) facility, JAERI, as shown in fig. 4. The well-known T(d,n)⁴He reaction to produce 14 MeV can be employed for this purpose.

High-energy neutrons in this facility are produced by the reaction between deuterium and tritium. Deuterium is ionized in a duo-plasmatron and a rotating tritium target is irradiated with this ion beam. The resultant neutron beam flux is 4×10^{12} n/s for a 0° beamline and 3×10^{11} n/s for an 80° beam line. In the most typical example, 1 mol of pure ^{179}Hf can be converted to 4 µg of Hf isomer after one year irradiation with the 4×10^{12} n/s neutron generation rate.

2.2.4. Production through the $^{180}\text{Ta}(d,\alpha)^{178}\text{Hf}^{m2}$ reaction

Accelerated protons are used for the reaction with the target material, tantalum isotope, to produce the Hf isomer through the $^{180}\text{Ta}(d,\alpha)^{178}\text{Hf}^{m2}$ reaction with an unknown reaction cross section. As the natural abundance of ^{180}Ta isotope is rare, i.e. 0.012%, isotope separation is required before the irradiation. A very high current proton accelerator will be used to achieve this method.

2.2.5. Production through the $^{181}\text{Ta}(p,2p2n)^{178}\text{Hf}^{m2}$ reaction

The reaction product has a very high activity due to the production method which is based on the nuclear spallation method, though the reaction rate is rather high. Isomer separation is required after irradiation of the target in order to reduce radioactivity which is otherwise extremely high. For the same reason isomer separation is sometimes required after irradiation.

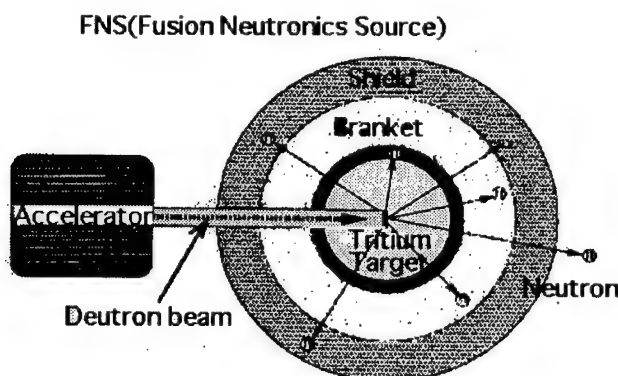


Fig. 4. Concept of the FNS facility.

3. Atomic vapor laser isotope/isomer separation method [8,9]

Among many kinds of isotope separation like the gaseous diffusion method, the centrifugal method, chemical exchange etc., AVLIS (atomic vapor laser isotope separation) is the most efficient method for separating isotopes of heavy elements. As the AVLIS method is based on the resonant multiple photo-ionization process, atoms can easily be ionized with a low photon flux, which is related to the high utilization efficiency of photons, and the atomic spectrum is narrow enough so that the photons with tunable wavelengths are easily absorbed by the specific isotope without being absorbed by non-specified isotopes. Therefore this method could achieve separation at a high separation factor by one single operation, could be economical and could be used to enrich isotopes for a precursor as target materials as well as to enrich isomers for the gamma-ray laser development.

The whole separation process is divided into four major subprocesses for convenience, i.e. the evaporation process for generating an atomic beam, the photo-ionization process for ionizing isotopes selectively by the resonant multi-step photo-ionization method, the ion extracting process for recovering isotopic ions from laser-induced plasma, and the light propagation process for propagating laser beams in the optically thick atomic medium with the interaction between photons and specific elements. Fig. 5 shows the conceptual drawing of the AVLIS process based on the three-step photo-ionization method, in which four subprocesses are indicated.

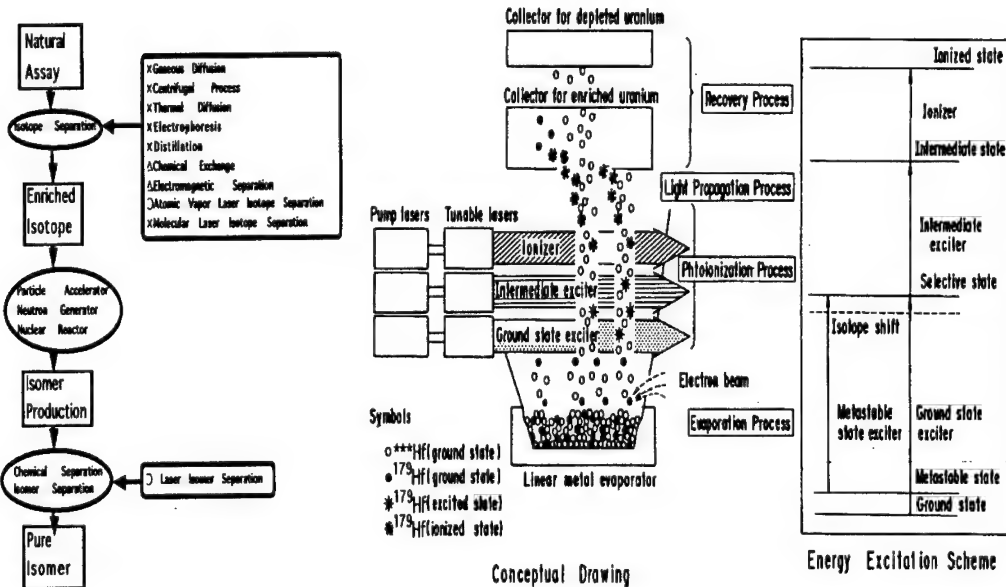


Fig. 5. Isotope/isomer separation and concept of the AVLIS process.

Well-tuned tunable laser beams with three different colors illuminate the isotopic medium at the same time after combining each color. The specified isotopic atom at the ground state is excited to the selective excitation level by discriminating the isotope shift. The excited atom is then further excited to the ionized state through the two-step transition, i.e. intermediate excitation and ionization. In the case that a large portion of atoms are thermally populated in their lower metastable states due to the high temperature evaporation which might be encountered in the hafnium case, some of those states could be processed by adding another tunable laser beam to excite them to the commonly populated selective excitation level from the ground state, unless the metastable population is well relaxed.

The photo-ionization process includes all the above processes. The ion extraction process consists of the collection of depleted metal and the extraction of product ions. The light propagation process deals with the interaction of long travelling laser beams and a near resonant medium to increase the production rate. Fig. 6 shows the process evaluation scheme to optimize the subprocesses to construct the whole integrated process system.

Under the development program of the evaporation process, data are taken on the velocity of atoms in the vapor, the internal energy of atoms, spatial distribution of the vapor, vapor density and evaporation efficiency. For the photo-ionization process, spectroscopic data are taken on the energy levels, photo-absorption cross section, excited state lifetime, quantum number, isotope shift and hyperfine structure, which are used for optimizing the combination of wavelength, photon flux and detuning.

For the ion extraction process, data are taken on the characteristics of the

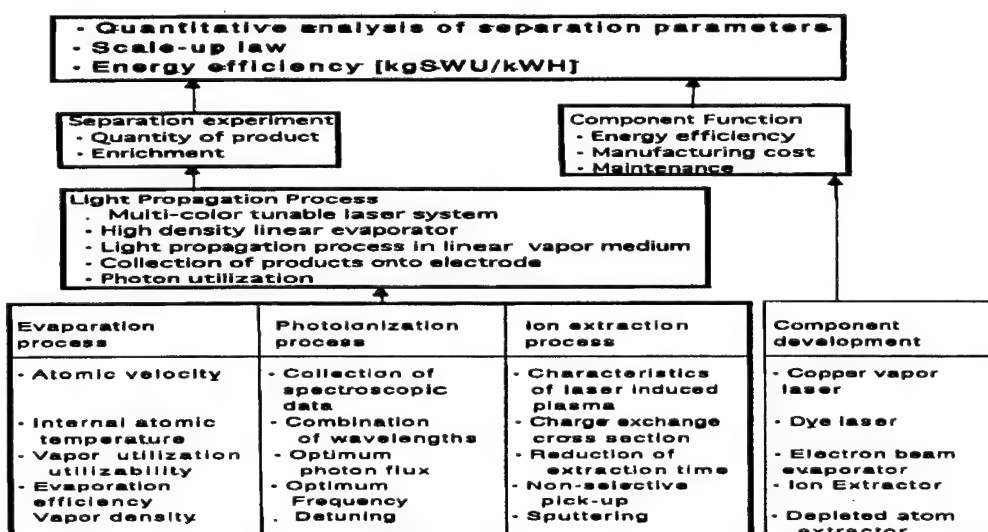


Fig. 6. Development of a separation process.

laser-induced plasma, charge exchange cross section, scattering rate and sputtering rate to obtain a short extraction time period and low enrichment loss. For the light propagation process, a high-density linear evaporator, four-color tunable laser system are constructed to collect product ions onto the electrode and to evaluate the photon utilization. From these data the energy efficiency and scale-up law for separative work are determined. Parameters required for multi-step photo-ionization scheme construction are excitation levels, ionization levels, photoabsorption cross sections in each transition, radiative lifetimes, J -values etc., see fig. 7. Especially photo-ionization levels are important among other things to obtain a high rate of ion extraction from the atomic level systems considered.

Isotope shifts and hyperfine structures are also important together with the multi-step photo-ionization parameters. Heavy elements normally have many isotopes, some of which are odd in the nuclear spin quantum number, inducing hyperfine structures in the electron structure. The position and the spread of this hyperfine structure are important to the isotopic selectivity. Taking the uranium atom as an example in fig. 8, some of the transitions show the hyperfine structure narrower than the isotope shift, but not in other cases.

Based on these collected parameters the most effective combination of level transitions is selected. In this selection process the integrated scheme cross section, which is the resultant cross section for every transition included, is examined, see fig. 9. Even if one of the transitions in the multiple photo-ionization scheme is large enough while other transitions are less probable, this combination of transitions

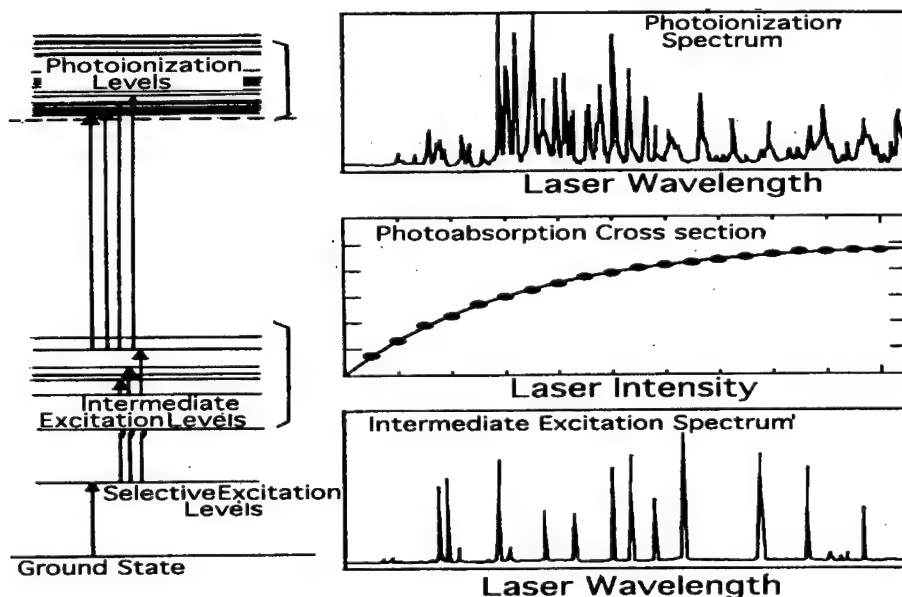


Fig. 7. Construction of a multi-step photo-ionization scheme.

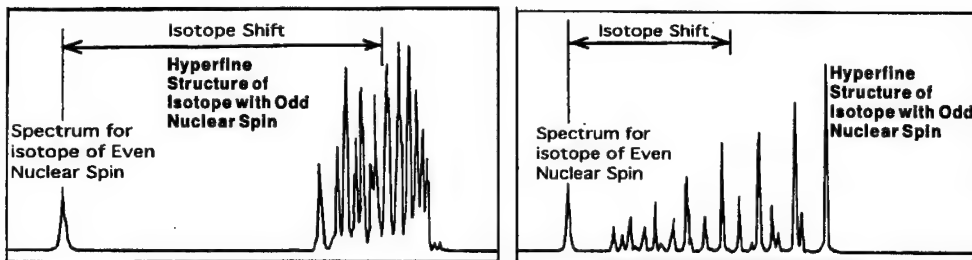


Fig. 8. Typical isotope shifts and hyperfine structures. (Left: hyperfine structure less than the isotope shift; right: hyperfine structure larger than the isotope shift.)

might not be useful. A rough estimate is made using the cross section data, and finally priority is shown by simulating the photodynamic characteristic of the system.

After getting the first-order priority, the final determination of the multiple photo-ionization scheme is made by taking into account the selectivity of enrichment, see fig. 10. In the case of ^{176}Yb the photo-ionization of non-specified isotopes whose absorption spectrum is positioned in the vicinity of the target isotope spectrum should be eliminated as much as possible to get a high isotopic selectivity. In the case of ^{179}Hf , which has a hyperfine structure, the interaction between the laser line structure and the complicated hyperfine structure should be taken care of together with the spectrum mixing with other isotopes.

3.1. ISOTOPE SEPARATION APPLIED TO THE SPECIFIC ELEMENTS

Let us take the isotope separation of Yb and Hf as examples for the precursor of isomer production.

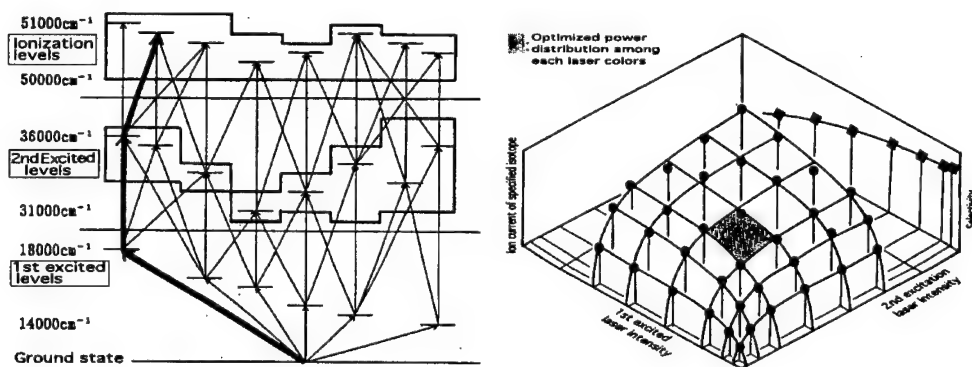


Fig. 9. Three-step photo-ionization schemes and optimized laser power.

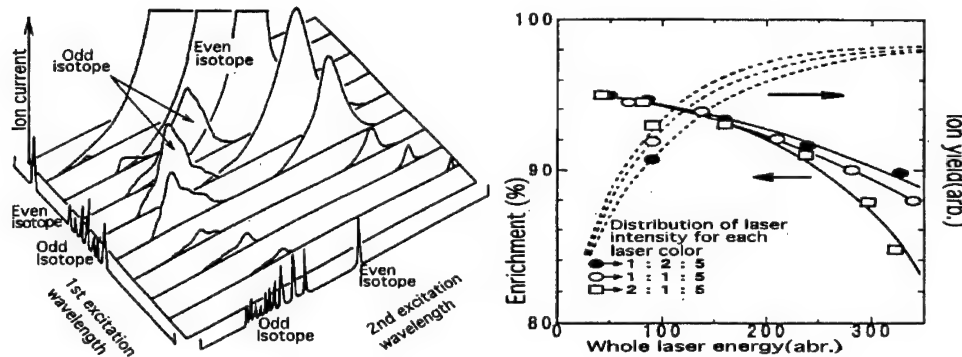


Fig. 10. Selective photo-ionization conditions.

3.1.1. Yb separation scheme

Ytterbium isotope separation of ^{168}Yb has been achieved for producing a precursor for ^{169}Yb which is useful for the non-destructive test of a thin piping system. The element Yb is located in the upper position of the lanthanides whose ground state electron state is $6s5p(^1\text{S}_0)$ with the f-shell closed. The electron structure is similar to an alkaline earth element, which is rather simple in the lower-lying energy levels. Unlike the elements such as Gd or U which are the normal targets of the atomic vapor laser isotope separation method, Yb has a very small number of candidate states in constructing a multiple photo-ionization scheme. For example the populated levels during the high-temperature evaporation are nothing but the ground state. And the three-step photo-ionization schemes available for a dye laser system pumped by a high repetition rate green laser such as a copper vapor laser are limited to 17992 cm^{-1} as the first excited state, 32694 , 34350 and 35197 cm^{-1} as the second excited states, see fig. 11.

Auto-ionization states which are useful for efficient photo-ionization are rarely found in this Yb case. So far, several auto-ionizing states are observed, but have very weak transitions which are shown as a typical Fano-profile with the q parameters 0.5 for 51435 cm^{-1} and -1.2 for the 50567.4 cm^{-1} transition. Therefore the adequate photo-ionization is achieved by the higher Rydberg transitions which are composed of $^1\text{P}_1$, $^3\text{P}_1$ and $^3\text{P}_2$ sequences in the case of the excitations from 35197 cm^{-1} and 32694 cm^{-1} , see fig. 12.

Lifetimes of excited states are measured based on the delayed coincidence method. Most of these data are already reported in several papers.

Transition cross sections are measured by several different ways. The saturation method is applied to the transitions from 35197 cm^{-1} to Rydberg states, $6s^135p^1(^3\text{P}_2)$, $6s^137p^1(^1\text{P}_1)$. These transitions have relatively large cross sections, but the photo-ionization transition from 32694 cm^{-1} to 50567 cm^{-1} rarely occurs compared with the transition between 32694 cm^{-1} and $37p(^3\text{P}_2)$, which results in a small cross section of $1 \times 10^{-17}\text{ cm}^2$. The dependence of photo-ionization cross sec-

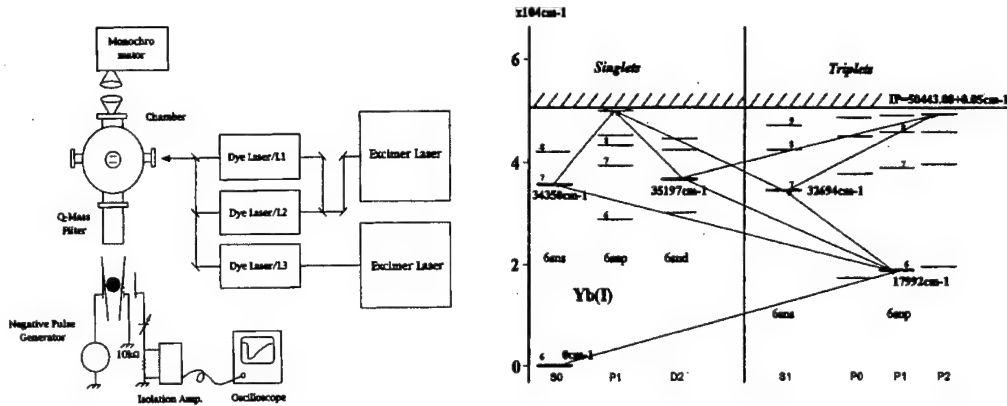


Fig. 11. Experimental set-up and isotope separation schemes.

tion on the Rydberg number is shown in fig. 13 in the low number region. Relatively large cross sections are shown in the transition to the $n^* = 12$ (or $n = 15$) state.

The branching method is also useful to measure the cross section. Taking a transition from 17992 cm^{-1} to 32694 cm^{-1} as an example, a branching ration of 0.223 was obtained, from which the oscillator strength was calculated as 0.281. The atom excited to the first excited state 17992 cm^{-1} can be photo-ionized to the auto-ionization levels through the 34350 cm^{-1} or 35197 cm^{-1} level. Even in the largest case for the latter transition the cross section is as small as $5 \times 10^{-18} \text{ cm}^2$.

Isotope shifts of the second excited state, 35197 cm^{-1} and the Rydberg state were measured in terms of the mass number difference between 176 and 172 using TOF by analyzing the photo-ions produced by the Rydberg transition. The isotope shift for the second transition $17992 - 35197 \text{ cm}^{-1}$ is shown in fig. 14. As a result the iso-

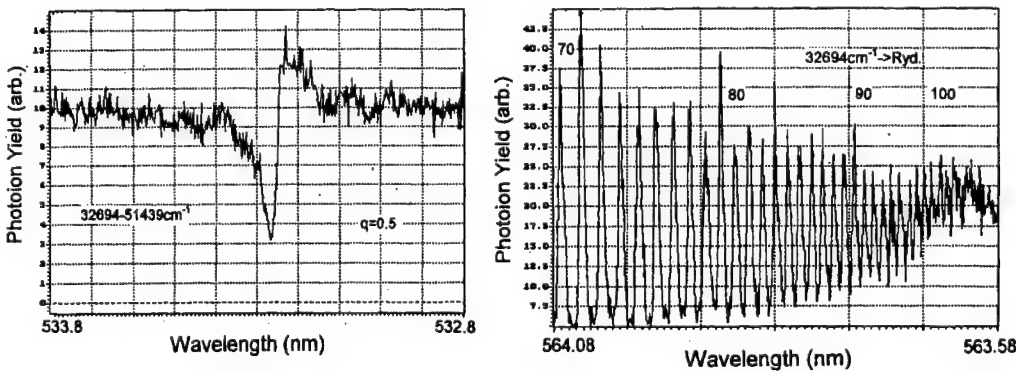


Fig. 12. Auto-ionization (left) and high Rydberg ionization (right).

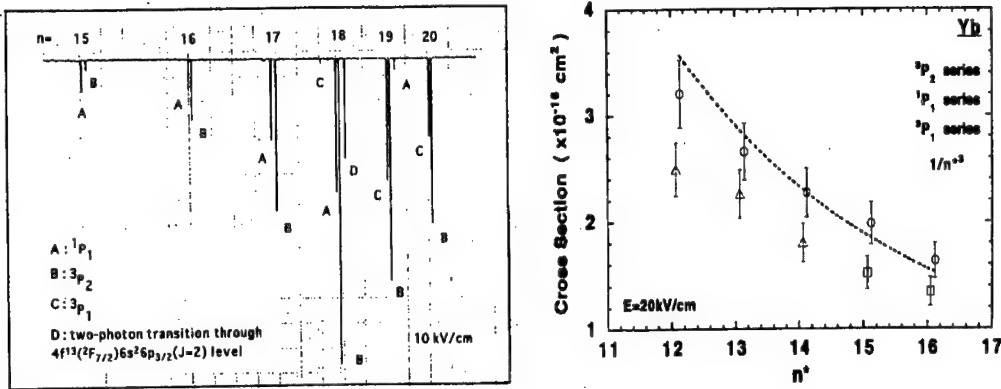


Fig. 13. High Rydberg ionization and cross section.

topo shifts were obtained as 4.2 GHz for 35197 cm^{-1} , and 120 MHz for the $n = 60$ Rydberg state.

Photo-ionization dynamics is generally described by quantum-mechanical equations. However when the ion extraction rate is fast or when the laser linewidth and absorption spectrum width are wide, coherent interaction is not much dominant. In such cases the multi-step equation system is roughly converted to the rate equation model without noticeable error. After systematic calculation with some assumption, the effective transition rate is obtained where σ_m is the cross section for the m th excited level, optimum photon flux ratio and the equivalent integrated scheme cross section σ_{opt} as follows:

$$\sigma_{\text{opt}} = \left(\sum_{m=1}^n \sqrt{\frac{m}{\sigma_m}} \right)^{-2}.$$

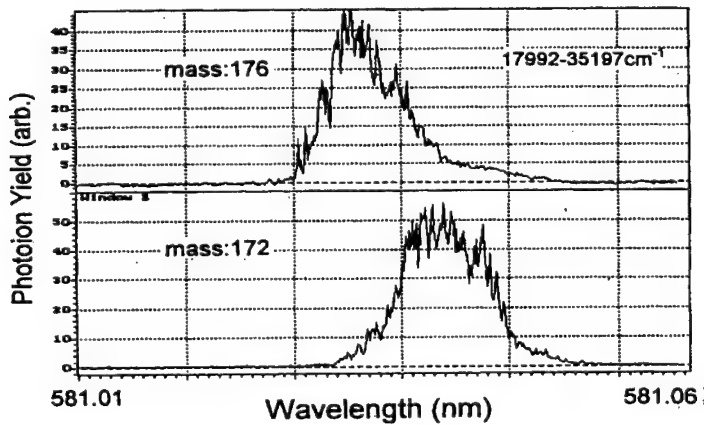


Fig. 14. Selective photo-ionization of Yb.

These parameters are used for comparing photo-ionization efficiency with each other.

To photo-ionize ^{176}Yb effectively based on multiple photo-ionization, three adjacent isotopes to be considered are ^{174}Yb , ^{171}Yb and ^{173}Yb , which have isotope shifts of 954.2, -1117.3 and -1432.6 MHz, respectively, against the ^{176}Yb isotope for the first transition. These numbers are sufficiently large compared to typical laser linewidth, which results in good selectivity during the transition from the ground state to the first excitation state. The situation would be very much changed if ^{168}Yb is selected as a specified target isotopes. Two of the candidates for the second excited states, which are 34350 cm^{-1} and 32694 cm^{-1} with isotope shifts of 370 MHz for ^{174}Yb and 850 MHz for ^{172}Yb , respectively, have relatively small isotope shifts.

On the contrary, another candidate, 35197 cm^{-1} , has a relatively large isotope shift except to one isotope ^{173}Yb whose isotope shift is 316 MHz, which is close to the ^{176}Yb spectrum. If the selectivity of ^{176}Yb against the ^{173}Yb isotope is kept high during the first transition, this scheme would have good enrichment after all. Therefore, if the first excitation process can discriminate ^{174}Yb isotopes, any other upper transitions could be used unless the transition cross section is small. But, if the selectivity between ^{174}Yb and ^{176}Yb is low, 35197 cm^{-1} will be selected as a second excitation level to increase selectivity.

The integrated scheme photo-ionization cross sections for the transition from the ground state to the 17P Rydberg state are $8.4 \times 10^{-16}\text{ cm}^2$ via 35197 cm^{-1} , $7.1 \times 10^{-16}\text{ cm}^2$ via 34350 cm^{-1} and $3.3 \times 10^{-16}\text{ cm}^2$ via 32694 cm^{-1} , respectively. The two-photon scheme through 35197 cm^{-1} is relatively large with a cross section of $1.3 \times 10^{-17}\text{ cm}^2$, which is possibly used for the ionization. This scheme might increase the photo-ionization rate, because it can constantly remove ions from the photo-ionization system even during laser illumination, whereas the transition to the Rydberg state with electrostatic ionization has no such process.

From the viewpoint of jittering of laser pulses, an excited lifetime of 16.5 ns for 32694 cm^{-1} is shorter than that of 1100 ns for 35197 cm^{-1} . Special care should be taken for the polarization combination of each laser beam, because Yb has a low J number. Taking the level 34350 cm^{-1} and 32694 cm^{-1} as examples for the first and second excitation, horizontal polarization is solely utilized for the former case and only the vertical one is useful for the latter case, while the transition to the level 35197 cm^{-1} has no losses for any type of polarization.

Based on the consideration described above and a precise analysis using a comparison with the experimental results, the least photon flux is obtained for a saturated ionization degree keeping the selectivity extremely high. In a rough estimation, the highest integrated scheme cross section is obtained for case c in fig. 15 with the laser energy distribution ratio 1 : 10 : 7. A three-color tunable laser system pumped by a copper vapor laser system composed of four 200 W units would be able to produce 100 g of ^{176}Yb isotope in a year.

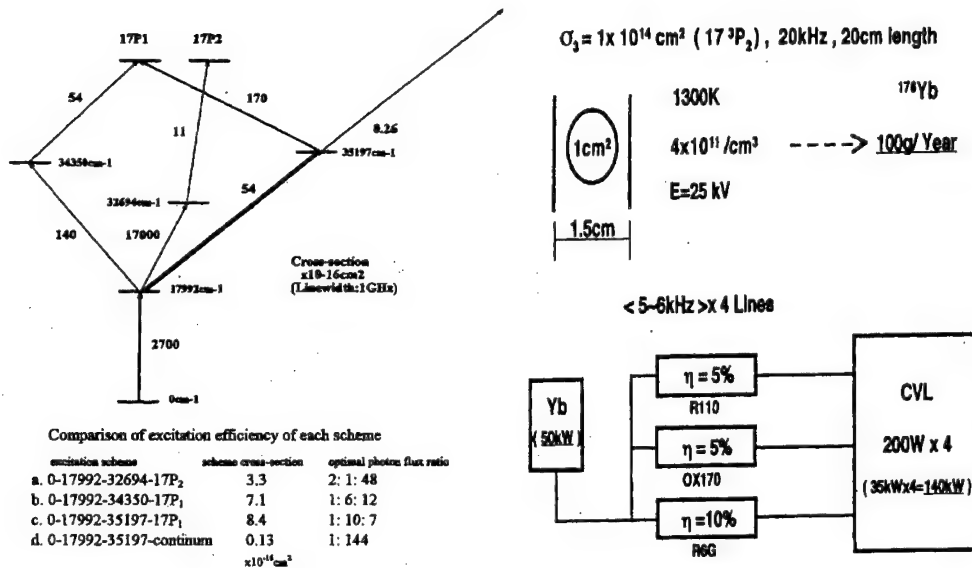


Fig. 15. Integrated scheme cross sections and small-scale production.

3.1.2. Hf separation scheme

As we haven't had sufficient spectroscopic data on Hf so far, we'd like to consider the isotope separation of ^{179}Hf by making use of the data from the reference paper, see fig. 16. The ionization of the hafnium atom is 55047.9 cm^{-1} and is a little bit higher than the uranium atom to which three-step photo-ionization is applied with visible wavelengths. In the case of the Hf atom three-step photo-ionization is available in two ways, one of which is a route using visible wavelengths, and the other of which is the one to use mixed wavelengths of UV and visible. In the visible route a rather short wavelength is not practical, because the most available tunable laser for the AVLIS method is driven by a high repetition rate laser such as a copper vapor laser, with which it is difficult to emit at a shorter region of the visible wavelength. The mixed wavelengths could be applied more efficiently by use of the second harmonics of a visible laser coupled with the transitions with large gf value.

The isotope shift and isomer shift are small while the hyperfine structure is fairly large because of a large nuclear spin of $I = \frac{9}{2}$ for ^{179}Hf and $I = 16$ for the nuclear isomer $^{178}\text{Hf}^{\text{m}2}$. Isotope shifts do not exceed 100 mK even with 4 masses included. In the case of isotope separation of ^{179}Hf , at both side of this isotope ^{178}Hf and ^{180}Hf exist, which would result in poor selectivity in the single transition. This situation can be improved with the help of the polarization transition method available for Zr or Gd in which the J number is decreased with the excitation level raised in the way $J = 2 \rightarrow 1 \rightarrow 1 \rightarrow 0$ in each step.

In the case of isomer separation of $^{178}\text{Hf}^{\text{m}2}$ with the nuclear spin $I = 16$, judging from the isomer shift of -134.6 MHz between ^{178}Hf and $^{178}\text{Hf}^{\text{m}2}$ for the transition from 8983.75 cm^{-1} to 26463.93 cm^{-1} and the hyperfine distribution of 12 GHz, high selectivity is not expected [18]. Spectroscopic separation between ^{179}Hf and $^{178}\text{Hf}^{\text{m}2}$ cannot be realized with the polarization scheme. As isomer the shift gener-

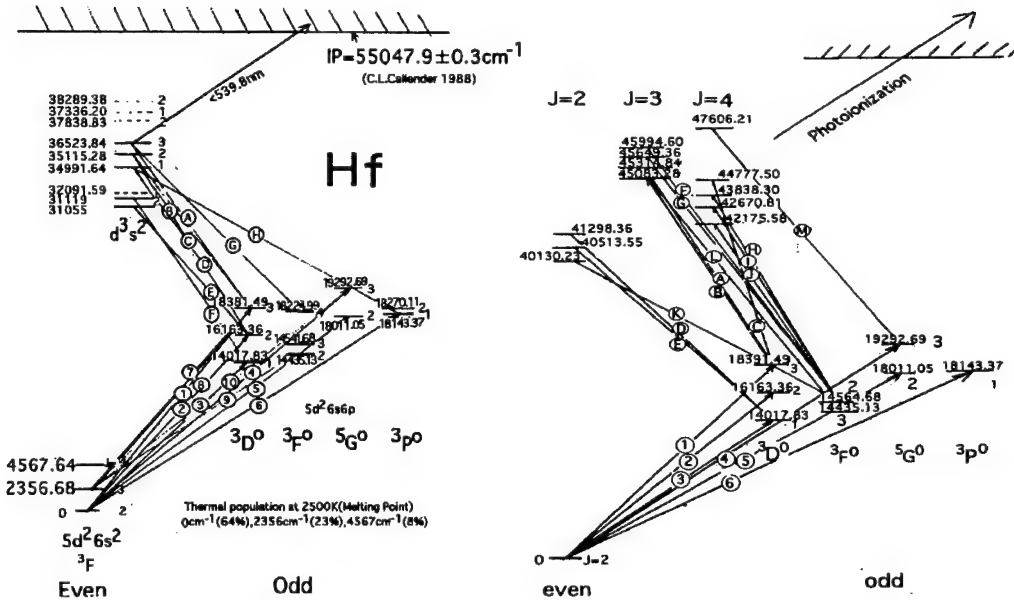


Fig. 16. Photo-ionization schemes for Hf(I) [17] (Left: visible system; right: UV mixed system.)

ally appears in the lower mass side, coexistence of isotopes with low masses is recommended to be avoided.

As hafnium is a refractory metal with a high melting point, an electron beam gun evaporator is required in order to heat it up to 3000 K or higher, aiming at the adequate vapor density, see fig. 17. In this case the lowest metastable state 2356 cm^{-1} could be thermally occupied, see table 3. But taking into consideration the adiabatic expansion which occurs after the high-pressure evaporation, such a populated state would easily be depopulated by the collision during the expansion. From the viewpoint of other thermal properties like thermal conductivity and surface tension, it does not seem so difficult to vaporize hafnium metal in high density.

Although data on the energy levels in the higher excitation region, the hyperfine structure and isotope shifts are not well established for hafnium atoms, the isotopic separation scheme based on three-color-three-step photo-ionization can be shown below.

4. Large-scale production scheme

Many key parameters are included in the characterization of the AVLIS process. We have proposed several optimizing methods for each subprocess like evaporation, photo-ionization, ion extraction and light propagation, which are not men-

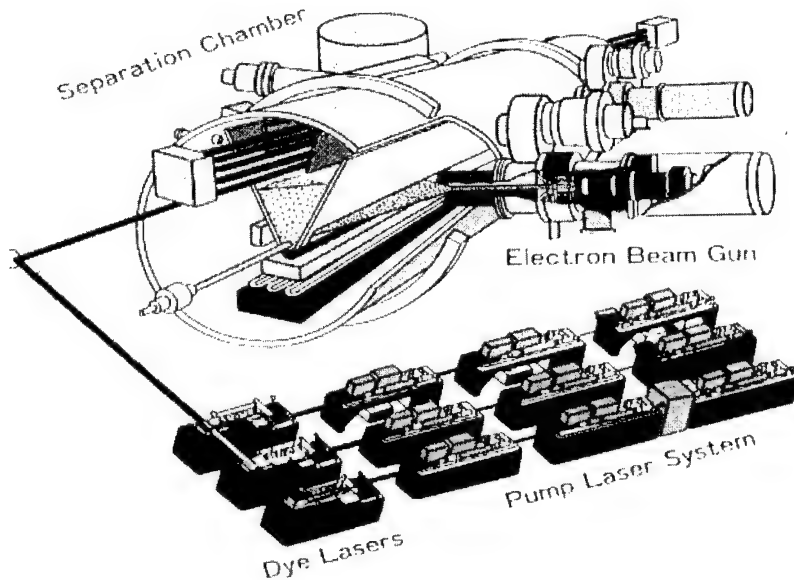


Fig. 17. Conceptual drawing of the separating system.

tioned in this paper. After optimization in each subprocess many parameters regarding operational conditions are fixed based on the simulation for the construction of the most appropriate separation process. Then the enrichment experiment is achieved by extracting a small amount of product, from which total separative power is obtained. When we look at the distribution of the product along the 1 m of the linear electrode, we find that around the central part of the electrode the production rate is highest due to the high adhesion rate of scattered atoms.

4.1. EVAPORATOR

In generating atomic vapor, the following points are also considered: narrow Doppler width, generation of a high-density atomic beam, high directivity of atomic beam, well-cooled internal energy states, high energy efficiency, non-selective ionization of atoms by collision with electrons, behavior of electrons on the surface of liquid metal, etc.

When heated metal in the crucible is melted, liquid metal starts moving, which enhances heat losses and instability in the evaporation. This surface flow is induced due to the surface tension difference caused by a temperature gradient, which is modeled by parameters such as surface tension, surface dent due to the vapor pressure, portion of the vapor not recondensed on the liquid surface, Clausius–Clapeyron's constant, etc. Internal flow is induced in the crucible after the above surface movement and is described by the Navier–Stokes equation which gives the

Table 3

Two lower levels for multi-step photo-ionization of Hf (upper: visible system; lower: UV mixing wavelengths system)

Symbol	Lower states (cm ⁻¹)	Upper states (cm ⁻¹)	Wavelength (nm)	gf	Isotope shifts (180–176)	Ref.
1	0	18381	543.874	0.048	12.6	[13]
2	0	16163	618.513	0.082	19.3	[15]
3	0	14017	713.181	0.052	13	[13]
4	0	19292	518.186	0.032	-59.0	[12]
5	0	18011	555.060	0.028	-61.6	[12]
6	0	18143	551.012	0.019	13	[13]
7	2356	18381	623.858	0.087	13	[13]
8	2356	16163	724.087	0.011		
9	2356	18011	638.623	0.011	-65.8	[12]
10	2356	19292	590.294	-	-61.5	[14]
A	18381	36523	551.045	0.033		
B	18381	35115	597.428	0.14		
C	16163	35115	527.504	0.069	16.5	[13]
D	16163	34991	530.968	0.058		
E	16163	31055	671.348	0.039	-109.0	[12]
F	14017	31119	584.586		-116.6	[13]
G	18224	36523	546.331		-64.3	[13]
H	18143	34991	593.369	0.11		
Symbol	Lower states (cm ⁻¹)	Upper states (cm ⁻¹)	Wavelength (nm)	gf	Isotope shifts (180–176)	Ref.
1–10	same as above					
A	18381.49	45364.84	370.492	1.2		[15]
B	18381.49	45083.28	374.399	0.70		[15]
C	18381.49	44777.50	378.737	0.39		[15]
D	14017.83	41298.36	366.460	0.30		[15]
E	14017.83	40513.55	377.312	0.20		[15]
F	14541.68	45994.60	317.843	0.46		[15]
G	14541.68	45649.36	321.372	0.87		[15]
H	14541.68	43838.30	341.234	0.44		[15]
I	14541.68	42670.81	355.400	0.86		[15]
J	14541.68	42175.58	361.768	0.56		[15]
K	14541.68	40130.23	390.190	0.13		[15]
L	14435.13	45083.28	326.190	0.39		[15]
M	1929.69	47606.21	353.087	2.2		[15]

mass and heat transfer in the crucible driven by the surface movement of the liquid metal which is called Malangoni flow.

After the precise measurement of the heat losses due to the above liquid metal movement in a crucible, we showed that the heat losses increase rapidly in the large Malangoni number region. This heat loss could be sometimes reduced by using special kind of alloys.

Distribution of temperature, velocity and stream function of liquid metal in a cylindrical crucible are also measured, which shows that the surface flow driven by the surface tension gives a strong spread of high-temperature liquid towards the crucible.

Even if lasers with a precise narrow linewidth exist which can resolve the isotope shift properly, selective excitation is not realized, unless the target atomic beam has reasonably narrow Doppler width. As the separative power is proportional to the atomic density, it is important to know the maximum allowable density.

The directivity of the atomic beam is also important to introduce most atoms into the photoreaction region effectively. Experimentally obtained angular distribution of the atomic beam is normally fitted to a cosine curve similar to Knudsen-cell-type effusion in equilibrium with the ambient temperature, that is, vapor flux distribution per solid angle is given by the modified cosine law.

Fig. 18 shows the spatial distribution of the vapor produced by the pure uranium metal in the linear crucible. Uniform distribution is obtained over 1 m in the axial direction and good directivity is realized in the transverse distribution.

The velocity of an atom with mass m equilibrated at temperature T is written as the mathematical mean velocity $[8kT/\pi m]^{1/2}$, if a Maxwell-Boltzman distribution is assumed. However when an electron beam is used for heating hafnium metal this velocity is different from the above value, because the energy transfers from the electrons to the atoms which results in the internal energy change by adiabatic expansion. And this is also different from the maximum attainable velocity $[2\gamma kT_s/(1)m]^{1/2}$ which is realized when an atom with specific heat ratio γ is effused through a nozzle at infinite Mach number. The velocity is related to the internal

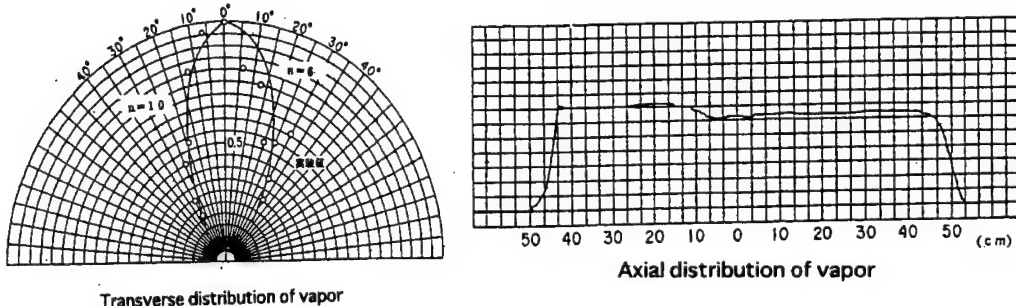


Fig. 18. Spatial distribution of the atomic beam.

energy and the population at the ground state as well as the lower metastable states. It is increased when the atomic internal energy is adiabatically cooled down. After the expansion internal energy is redistributed to the atoms in the atomic beam.

The internal temperature decreases with the increase of the evaporation rate, and atoms can be cooled down more than 1500 K when feed metal is evaporated in the vacuum chamber by electron beam bombardment at a very high temperature, which thermally excites atoms from the ground state to several lower metastable states. Highly populated lower metastable states are not appropriate for the efficient photoexcitation, because the laser beams illuminate atoms mainly in the ground state. The atomic vapor thus generated is cooled down by around 1000 K due to the adiabatic expansion, which increases the population of the ground state in the photoreaction zone. In the case that some lower metastable states are considerably populated even after cooling, some of the metastable states are used as target levels. In the hafnium isotope separation the ground state as well as the lowest metastable might be used to enhance the atom utilization efficiency. With the four-wavelength-three-step photo-ionization scheme, feed atoms are ionized from both states. Heating the metal with a high-power electron beam may cause also thermal ionization and collisional ionization which dilutes the enriched photo-ions at the photo-reaction zone (fig. 19).

In the case of ytterbium (MP 824 K), the atomic beam is generated from the crucible heated up to 1300 K. The resistive heating method is used for the vaporization of ytterbium instead of the electron beam gun heating for hafnium metal.

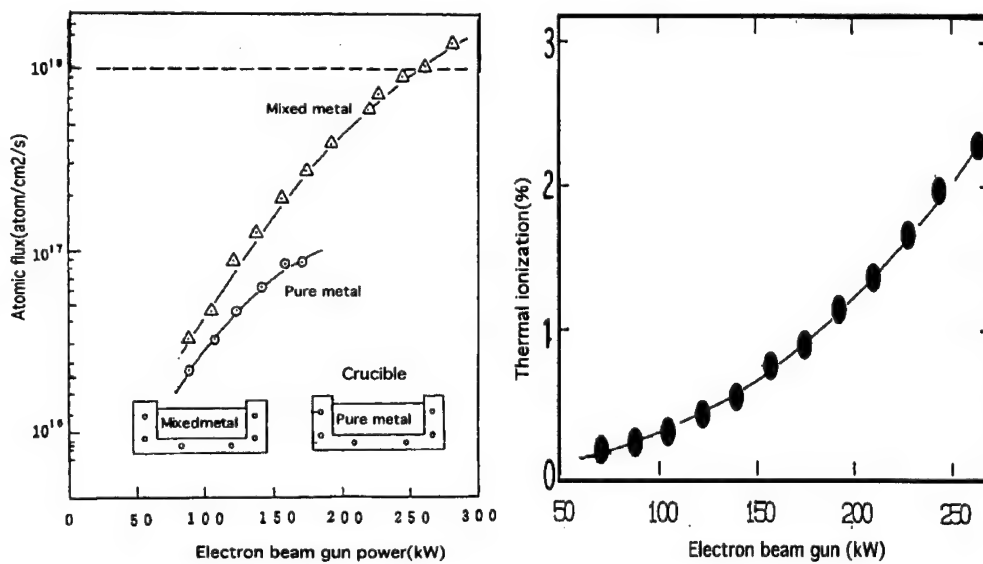


Fig. 19. High-intensity evaporation system.

4.2. LASER SYSTEM [10,11]

When lasers are used in the visible region, tunable photons with an energy of 2 eV from dye laser systems are to be used for three-step photo-ionization, because the most advanced ionization limit corresponds to around 6 eV. When ultraviolet light is used, one photon corresponds to around 3 eV, so that the two-step photo-ionization scheme will be adopted for most heavy elements with an ionization energy of 6 to 7 eV. The AVLIS method requires these photons at a high average flux, because one mol of material can be processed by the cumulative photon energy of the order of MJ which is possibly obtained only by an efficient tunable laser source. This kind of tunable laser should have a narrow linewidth, high pulse energy, high stability, high repetition rate, low beam divergence, high energy efficiency, and capability to be manufactured at low cost. To accomplish the resonant multi-step photo-ionization, lasers with the following specification are hence necessary corresponding to the spectroscopic data. Linewidth of 0.1–1 GHz comparable to the isotope shift. Pulse energy around 0.5–1 J. Wavelength stability better than 50 MHz. Repetition rate over 20 kHz to cover the whole atomic beam moving at high speed. Beam divergence with a near diffraction limit to propagate over one hundred meter. Overall energy efficiency of 0.5%. Pulse width around 100 ns shorter than excited state lifetime. Average power of several tens of kW in the tunable wavelength. Total energy efficiency over 1%. Lifetime not shorter than 3000 h. To satisfy the above requirements, we have constructed several light sources as follows, depending on the experimental conditions.

a) Pumping light sources

High average power lasers with high reliability and high efficiency are required to pump dye lasers, some of which could be excimer lasers or diode pumped solid state lasers (fig. 20).

- Copper vapor laser MOPA system with injection lock + dye laser system for high average power source.
- Excimer laser with injection lock + dye laser system for high peak power source.
- Diode pumped Nd : YAG laser with second harmonics generation + dye laser system for compact laser source with high energy efficiency as shown in fig. 20.
- Nd : YAG laser with second harmonics generation + Ti : sapphire laser system for stable and compact laser source with wide tunable wavelength range. We describe below three different pumping sources and two different tunable light sources.

b) Tunable light sources

Tunable lasers for AVLIS application require high average power, high reliabil-

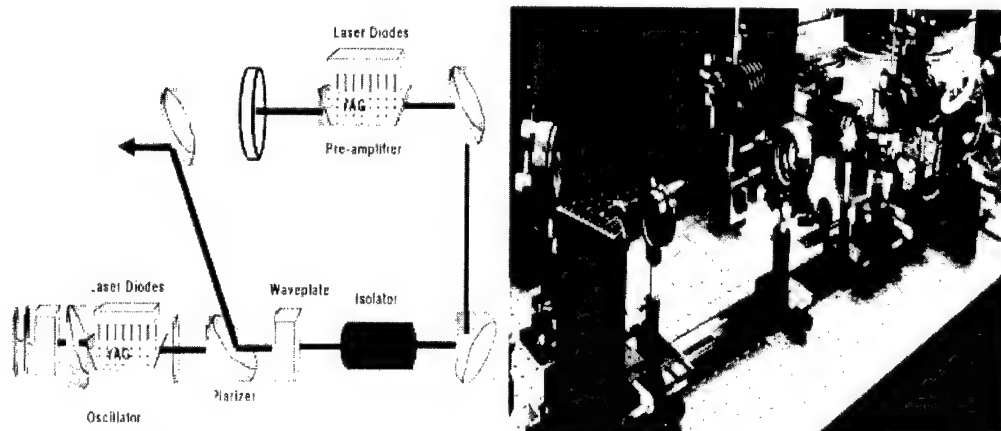


Fig. 20. LD pumped solid state green laser for pump source.

ity and high stability. One of the candidates is a Ti : sapphire laser, but it needs a good pumping source and non-linear crystal for converting wavelength from a fundamental wavelength to the visible one at high efficiency. A direct application of a diode laser as a tunable source might be promising in the future, if wavelength range coverage, average power and price are satisfied. From this point of view, the CVL pumped dye laser will play a major role in the field of a high-power tunable source for the time being.

4.3. LARGE VOLUME PHOTO-IONIZER

In the application of the AVLIS process to the enrichment plant, tunable laser beams interact with the specified atomic isotope in the long path of medium aiming at the enhancement of the reaction volume up to the order of a m^3 which is the product of cross-sectional area and path length of the laser beam.

This long propagation also enhances the photon utilization efficiency. During the propagation in the reaction medium the wavefronts of the laser beams are degraded by the nonlinear effect, see fig. 21. Taking into consideration the atomic beam velocity and the laser beam width, the thermal blooming phenomenon does not occur because of the short pulse width, but the self-(de)focusing is observed due to the local change of the diffraction index. These phenomena are caused not only by the resonant photoreaction of the specified isotope but also by the near resonant interaction with non-specified isotopes. After the self-focusing and self-trapping phenomena, the laser beam might make a filamentation or decrease the upper state population by superradiance. These phenomena induce big changes in the spatial distribution of laser beam intensity and frequency which brings out inefficiency in the separation process. We measured the change of a laser beam radius in a small

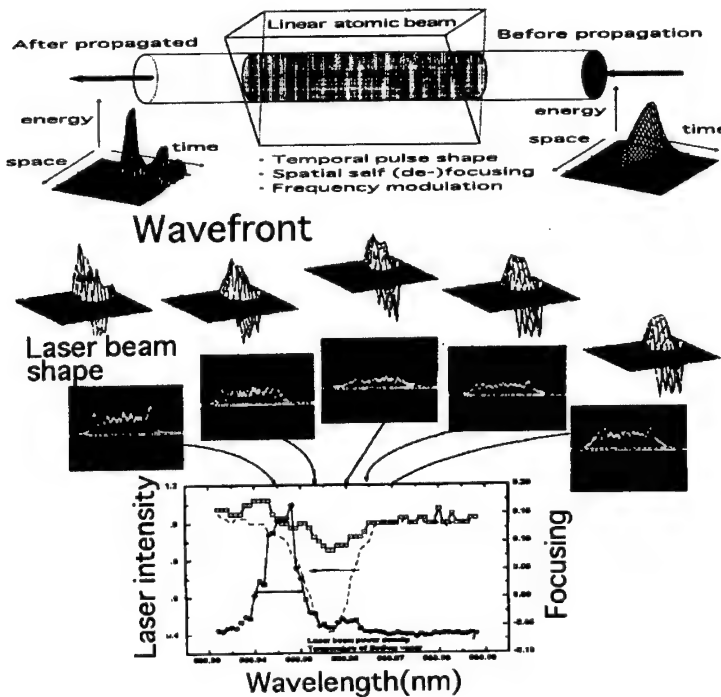


Fig. 21. Example of wavefront distortion for long pass reaction.

detuning region of the tunable laser frequency for the two-level system in the medium with the long propagation distance.

A measurement was made concerning the effect of light propagation on the temporal, frequency and spatial region using heat pipes. After the experiment we started to measure the light propagation effect through the long atomic vapor of uranium atoms as a function of detuning. Simulation of spatial distribution of laser energy propagating through the near resonant isotopic medium was analyzed based on the density matrix equation of motion combined with Maxwell's propagation equation. Distinguished deformation is observed.

Wavefront distortion depends strongly on the dispersion in the target medium. In the shorter wavelength region relative to the central absorption spectrum, a propagating laser beam tends to distort its wavefront so that the laser beam is self-focused. This could happen in large volume production, because the absorption spectrum of minor isotope is very close to that of the non-specified isotopes, which will affect the dispersion relationship. Many types of distortion occur, and among them focusing distortion is the most influential to the reaction.

4.4. ION EXTRACTOR

Plasma induced by laser beam illumination using the multiple photo-ionization

process is measured by electro-static probes, in which the electron current captured by the probe is expressed by $I_e = I_{es} \exp\{-e(V_s - V_p)/kT_e\}$ under the electron saturation condition, where I_{es} is the electron saturation current, V_s the plasma potential, V_p the electrode potential.

The electron temperature is obtained from the above formula, which shows that it is considerably low. Such low electron temperature is originated from the multi-step photo-ionization scheme, which makes use of auto-ionizing states located slightly above the ionization limit. An atom excited to the auto-ionizing level rapidly releases an electron. The amount of released energy is redistributed to the ion and electron. Kinetic energy transferred to the electron is as low as 0.1 eV. Therefore the electro-static field is rejected from the plasma region due to the short Debye length, which is defined by $V = (e/r) \exp(-r/\lambda_D)$, where λ_D is Debye's length or sheath thickness.

Generally speaking, the density of ions extracted with the static electric field from the relatively active plasma with an electron temperature of around 10 eV should be lower than 10^{12} ions/cm³, if effective extraction is expected. Space charge limited current is written by the Langmuir-Child formula $J = \frac{4}{9}e[2e/m]^{1/2}V^{3/2}/d^2$, where V is the voltage applied to the electrode and d the distance between anode and cathode. On the other hand temperature limited current is expressed by $J = n_i e[kT_e/m]^{1/2}$. Therefore the ion extraction rate depends on the thermal movement proportional to the square root of T_e . Based on these experimental data we take the following measures to extract ions effectively from laser induced plasma at a low electron temperature. The highest allowable extraction speed is realized by applying voltage as high as possible to collect as much ions from the moving plasma at the similar speed with the neutral atom. Some of the result are shown in fig. 22 where the linear separator is used to produce the isotopic heavy element. A higher speed is realized by increasing electron temperature. Avoidance of sputtering from

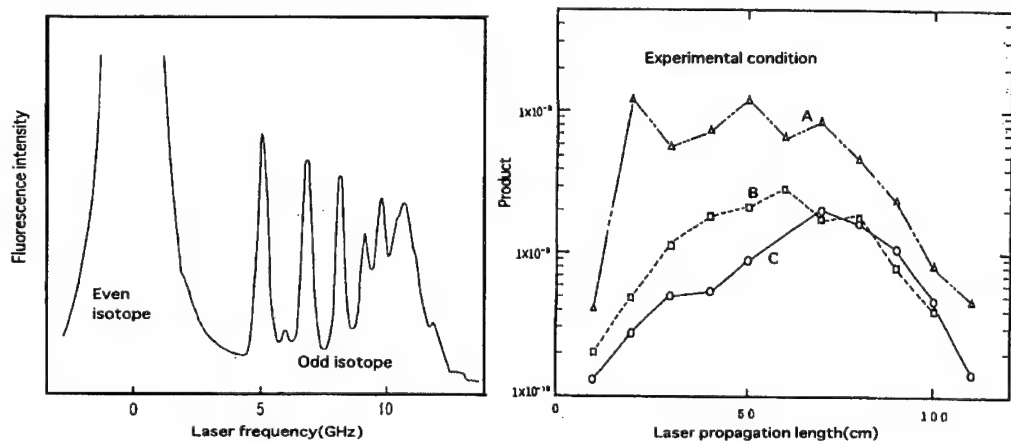


Fig. 22. Reaction for the linear reactor.

the once collected ions on the electrode due to the high momentum of ions, an interaction period as short as possible to reduce the chance for charge exchange and ionization collision are also important. From these points of view, plasma heating can be considered to enhance the electron temperature, but care must be taken not to heat up electrons as high as the ionization limit.

As the AVLIS process is usually applied to the separation of a trace amount of isotopic components, the degree of ionization is low, even if 100% ionization of the specified isotope is achieved, that is, the ions coexist with a huge amount of neutral atoms.

For this reason during the extraction of isotopically pure ions from the laser induced plasma, charge exchange easily occurs by the collision between ions. The charge exchange cross section is obtained as a function of collisional energy for the reaction system like $^{***}\text{Yb} + ^{176}\text{Yb}^+ \rightarrow ^{***}\text{Yb}^+ + ^{176}\text{Yb}$, where $^{***}\text{Yb}$ denotes the isotopes other than ^{176}Yb . Scattering of neutral atoms in the atomic beam is also important. We measure the adhesion of the neutral atoms as a function of atomic density. As a result of the experiment the adhesion rate of neutral atoms from the atomic beam onto the electrode is turned out to be mainly caused by the two-body scattering process. Special care should be taken in order to avoid charge exchange and scattering from the neutral atoms as shown in fig. 23.

5. Conclusion

The separator is a target cell for tunable laser beams in which a long linear atomic beam is generated so that the laser beam could interact as much as atoms to increase

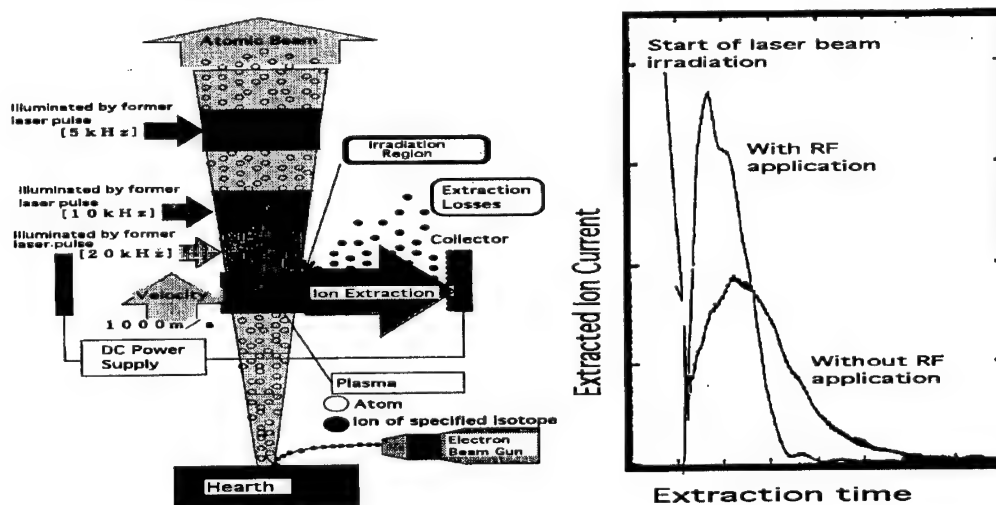


Fig. 23. Enhancement of the ion extraction rate.

the reaction volume. For most atoms with a high melting point, electron beam guns with either a transverse type cathode or a Pierce-type cathode can be used. The linear cathode type has no scanning mechanism, whereas the Pierce type has a scanning mechanism to get uniformly distributed atomic density along the linear photo reactor. We constructed a one meter long linear evaporator with scanning electron beam gun which is operated by two Pierce-type electron beam guns. Care must be taken so that the laser beam colors could cover all the atoms spread in the frequency field by inducing the AC Stark effect to broaden the spectrum, by chirping the laser frequency or by operating lasers with multiple longitudinal modes.

After optimization in each subprocess mentioned above, many parameters regarding operational conditions are fixed, based on the simulation for the construction of the most appropriate separation process. Then the enrichment experiment is achieved by extracting a small amount of the product, from which the total separative power is obtained. When we look at the distribution of the product along the long linear electrode, we find that around the central part of the electrode the production rate is highest due to the high adhesion rate of scattered atoms.

The distribution of the recovered products along the linear electrode was obtained. In the collection of ions from the moving plasma with the linear electrode, neutral atoms tend to scatter with each other, which make neutral atoms to attach to the electrodes and dilute enriched product as shown in fig. 24, where ^{aaa}M is the specified isotope and $^{***}M$ are the isotopes other than the specified isotope.

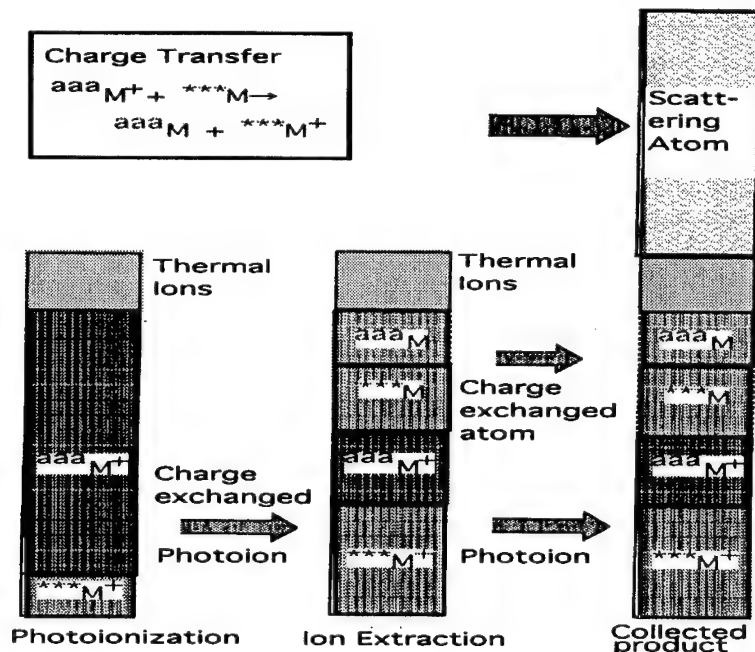


Fig. 24. Optimization of separator conditions.

In the case of Yb or Hf isotope separation very high enrichment is required, while in uranium enrichment the enhancement of isotopic concentration is only 4% from 0.72%. Therefore selectivity losses encountered especially in the ion extraction process must be extremely decreased. Pick-up of neutral atoms and charge exchange should be carefully reduced by introducing a new electrode design, RF-type extraction system, and so on.

References

- [1] C.B. Collins, C.D. Eberhard, J.W. Glesener and J.A. Anderson, Phys. Rev. C37 (1988) 2267.
- [2] J.J. Carroll, M.J. Byrd, D.G. Richmond, T.W. Sinor, K.N. Taylor, W.L. Hodge, Y. Paiss, C.D. Eberhard, J.A. Anderson, C.B. Collins, E.C. Scarbrough, P.P. Antich, F.J. Agee, D. Davis, G.A. Huttline, K.G. Kerris, M.S. Litz and D.A. Whittaker, Phys. Rev. C43 (1991) 1238.
- [3] Yu.Ts. Oganessian et al., J. Phys. G, Nucl. Part. Phys. 18 (1992) 393–399.
- [4] J.B. Wilhermy et al., *Proc. 4th Int. Conf. on Nuclei far from Stability (Helsingør)* (1981) p. 684.
- [5] C.P.J. Barty, C.L. Gordon III and B.E. Lemoff, Opt. Lett. 19 (1994) 1442.
- [6] M.D. Perry and G. Mourou, Science 264 (1994) 917.
- [7] D.L. Matthews, Phys. Rev. Lett. 54 (1985) 110.
- [8] T. Arisawa, Y. Maruyama, Y. Suzuki, M. Kato, I. Wakaida, K. Akaoka, M. Miyabe, A. Ohzu and A. Sugiyama, Optoelectron. Dev. Technol. 8 (1993) 203.
- [9] Y. Maruyama, Y. Suzuki, T. Arisawa and K. Shiba, Appl. Phys. B44 (1987) 163.
- [10] Y. Maruyama, M. Kato, A. Sugiyama and T. Arisawa, Opt. Commun. 81 (1991) 67.
- [11] M. Hermann, *CLEO'95 CtuM4*.
- [12] A.G. Golovin and I.F. Kramer, Opt. Spectrosc. 23 (1966) 195.
- [13] J. Cajko, Z. Phys. 234 (1970) 443.
- [14] A. Anastassov, Yu.P. Gangrsky, K.P. Marinova, B.N. Markov, B.K. Kul'djanov and S.G. Zemlyanoi, Hyp. Int. 74 (1992) 31.
- [15] J. Schecker, A. Berger, J. Das, S. Dutta, G. Gwinner, C.H. Holbrow, T. Kuhl, T. Lauritsen, G.D. Sprouse and F. Xu, Phys. Rev. A46 (1992) 3740.
- [16] C.H. Corliss, W.R. Bozman, *Experimental transition probabilities for spectral lines of seventy elements*, NBS Monograph 53 (Washington, 1962).
- [17] C.L. Callender, P.A. Hackett, D.M. Rayner, J. Opt. Soc. Am. B5 (1988) 1341.
- [18] N. Boos et al., Phys. Rev. Lett. 72 (1994) 2689.

Production, chemical and isotopic separation of the $^{178m^2}\text{Hf}$ high-spin isomer

Yu.Ts. Oganessian ^a, M. Hussonnois ^b, Ch. Briançon ^c, S.A. Karamian ^a,
Z. Szeglowski ^a, D. Ledu ^c, R. Meunier ^c, M. Constantinescu ^d, J.B. Kim ^b and
O. Constantinescu ^d

^a Joint Institute for Nuclear Research, Dubna, Russia

^b Institut Physique Nucléaire, Orsay, France

^c CSNSM, Orsay, France

^d Institute of Atomic Physics, Bucharest, Romania

The $^{178m^2}\text{Hf}$ with its long-lived ($T_{1/2} = 31$ y), high-spin $I^\pi = 16^+$, isomeric state, is a challenge for new and exotic nuclear physics studies. The $^{178m^2}\text{Hf}$ isomer has been produced in microweighting quantities using the $^{176}\text{Yb}(\alpha, 2n)$ nuclear reaction, by irradiation with a high-intensity beam using the U-200 cyclotron in Dubna. Radiochemistry and mass separation methods have been developed, with the aim to separate and purify the produced Hf material. Thin targets of isomeric hafnium-178 on carbon backings have been prepared and used in experiments with neutron, proton and deuteron beams.

1. Introduction

During the last few years, investigations on nuclear reactions with radioactive nuclei have developed intensively. One way was to use radioactive beams of “exotic” nuclei such as ^8He , ^9Li , ^{11}Li , ^{14}Be and others. Another method uses radioactive target techniques, which often exhibit advantages connected with the possibility of using traditional methods and earlier built experimental set-ups. In this case, the isotope life-time yields some limitations.

Some years ago, the idea of using the long-lived hafnium $^{178m^2}\text{Hf}$ isomer as a high-spin nuclear target has been suggested. This isomer has a high $I = 16^+$ spin, a relatively long half-life of 31 years and a relatively low excitation energy of 2.45 MeV. The long half-life and very high spin make $^{178m^2}\text{Hf}$ a unique nuclear probe, which enables high-spin phenomena studies in a new approach.

Five years ago, a research program has been started, as a result of the JINR-Dubna, CSNSM and IPN Orsay cooperation, under coordination of Professor Yu.Ts. Oganessian (JINR-Dubna), Dr. Ch. Briançon (CSNSM-Orsay) and Dr. M. Hussonnois (IPN-Orsay). Now, it has become a wide program, involving 16 institutes from six countries: JINR-Dubna, CSNSM-Orsay, IPN-Orsay, CENBG-Bordeaux, GSI in Darmstadt, LMU and TU Munich, Jagellonian University Cracow, Sussex University, Laboratoire A. Cotton-Orsay, Kurchatov Institute-

Moscow, CEA-France (Bruyeres-le-Chatel), Princeton University, CEBAF-Newport (Virginia), Vanderbilt University and Texas University. The aim of the program is the $^{178m^2}\text{Hf}$ isomer production and utilization in different physical experiments.

The first step towards it was the $^{178m^2}\text{Hf}$ isomer production in microweighting quantities.

2. $^{178m^2}\text{Hf}$ production

For the $^{178m^2}\text{Hf}$ isomer production the following conditions should to be satisfied:

- the use of a production reaction able to assure an optimum with respect to the absolute yield of accumulated nuclei and also to the ratio between the isomeric and ground state values;
- intensive long irradiation in order to accumulate a microweighting isomer quantity.

Several different reactions have been used in the past with the aim to produce $^{178m^2}\text{Hf}$ for spectroscopic studies. The used reactions, the irradiation conditions and σ_m/σ_g isomeric ratio are given in table 1.

The most convenient $^{178m^2}\text{Hf}$ production is by means of the $^{176}\text{Yb}(\alpha, 2n)$ reaction. Several irradiations of enriched ^{176}Yb targets (95.7%) have been performed in Alma-Ata and Dubna in order to determine the excitation functions and study the optimal conditions for the ^{178}Hf isomeric nuclei production. The isomeric formation cross section was determined by γ -activity (fig. 1) [1].

As expected, the isomeric excitation function is shifted about 5 MeV to the right compared to the calculated excitation function for the ^{178}Hf nucleus in the ground

Table 1
 $^{178m^2}\text{Hf}$ Isomer production

Reaction	Projectile energy (MeV)	σ_{m^2}/σ_g	Ref.
$^{177}\text{Hf}(n,\gamma)^{178m^2}\text{Hf}$	thermal	10^{-9}	R.G. Helmer, C.W. Reich (1968)
$^{181}\text{Ta}(\gamma, p2n)^{178m^2}\text{Hf}$	< 85	low	F.W.N. de Boer (1976)
$^{181}\text{Ta}(\alpha, \alpha p2n)^{178m^2}\text{Hf}$	120	—	J. van Klinken (1980)
$^{181}\text{Ta}(p, \alpha)^{178m^2}\text{Hf}$	92.5	10^{-3}	W. Kutchera et al. (1980)
$^{176}\text{Yb}(\alpha, 2n)^{178m^2}\text{Hf}$	26	0.01	T. Khoo et al. (1977)
$^{176}\text{Yb}(\alpha, 2n)^{178m^2}\text{Hf}$	27	0.005	A. Kluger
$^{176}\text{Yb}(\alpha, 2n)^{178m^2}\text{Hf}$	32	0.05	Dubna, Alma-Ata
$^{176}\text{Yb}(\alpha, 2n)^{178m^2}\text{Hf}$	40	0.08	Dubna, Alma-Ata

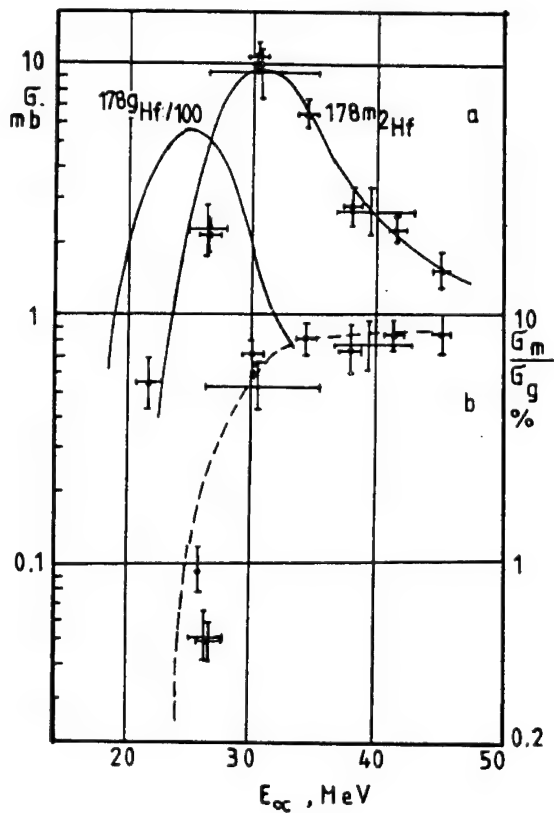


Fig. 1. Cross section of ^{178}Hf ground-state (calculated) and $^{178m^2}\text{Hf}$ production at an isomeric-to-ground-state ratio as a function of the α beam energy.

state. The isomeric ratio grows with the ^4He ions energy and reaches saturation at a value of 0.07–0.08. The optimum energetic interval lies from 28 to 36 MeV, where the absolute cross section of the isomer formation is maximal and the isomeric ratio (0.05) is not yet low. For $^{178m^2}\text{Hf}$ isomer production in a quantity of hundreds of nanograms the Flerov Laboratory of Nuclear Reactions cyclotron U-200 has been modified for intensive α -particle beam mode operation. The plasma-type ion source, the cyclotron center ion optics, the biological shielding against the cyclotron radiation and the elements of the beam extraction system using a stripper have been subjected to modifications. As a result, one could obtain up to 150 μA of $^4\text{He}^{2+}$ ions on the target with a 36 MeV energy. This corresponds to approximately 6 kW of thermic power which raises a serious problem of heat removal from the target. A water-cooled tilted target has been chosen.

The effective beam time needed in order to produce $\sim 5 \times 10^{14} \text{ }^{178m^2}\text{Hf}$ atoms using a 100 μA current of 36 MeV He ions amounts to 500 h.

Irradiation of these targets not only produces Hf isotopes but also RE radioiso-

topes and induces Al and impurities activation. After irradiation, the ^{176}Yb oxide target is scratched out from the backing and chemical separation must isolate Hf isotopes from the Yb and Al bulk and from many other radionuclides.

3. Chemical separation and purification

For the separation of hafnium isotopes (formed in $^{176}\text{Yb}_2\text{O}_3$ (96%) targets) from the bulk of reaction products, we have adopted a chemical scheme based on selective chromatographic extraction of Hf from HNO_3 solutions on columns filled with tri-n-octylphosphine oxide (TOPO) (fig. 2). Thus, after eight months cooling time the irradiated target, usually 300–400 mg of $^{176}\text{Yb}_2\text{O}_3$ has been dissolved in a mixture of 12M HNO_3 , 11.5M HCl and 11M HClO_4 after heating to 180°C in an autoclave for 12 h. This procedure is necessary because irradiated rare-earth oxides are very hard to dissolve. The solution has been dried and the residue has been dissolved in 6M HNO_3 . The resulting solution has been passed through a column ($l = 60 \text{ mm}$, $\phi = 3 \text{ mm}$) filled with 20% TOPO sorbed on a copolymer of divinylbenzene and styrene (Wofatite EP-60, 100–200 μm). In these conditions Hf is adsorbed in the column. After adsorption, the column has been washed with 6M HNO_3 in order to ensure hafnium isolation from rare earth and from many other elements and impurities produced in the backing irradiation process. The hafnium fraction elution was performed with 0.2M HF. In this separation process we have been able to obtain an 80–90% efficiency.

Inasmuch as the described method cannot provide a complete purification of hafnium from Fe, Sc and other metals, another chemical scheme was developed in order to obtain a high degree of purification (fig. 3). Thus, the hafnium fraction eluted from the TOPO column, in 0.2M HF, is passed through a column filled with the anion exchanger Dowex 1x8, conditioned with 0.2M HF, 5M HF and 0.5M acetic acid solutions. Thus, the Fe, Ni, Co, Cu and Sc traces have been eluted. Finally, hafnium was eluted in a small volume using a (1 : 1) 1M CH_3COOH and 2M HCl mixture. The hafnium fraction γ -spectra before and after the described procedure are shown in fig. 4. A complete purification from all undesirable γ -activities is evident.

A number of six irradiations were performed, until now, at the U-200 cyclotron in Dubna, using $^{176}\text{Y}_2\text{O}_3$ (96%) enriched as target (see table 2). The first three runs had a testing character while the produced quantity was low. Because the target initial material – the commercial ^{176}Yb isotope – has a 96% enrichment, reactions on light Yb isotopes lead to accumulation of the rather long-lived γ -activities of light hafnium isotopes, such as ^{175}Hf ($T = 70 \text{ d}$), and ^{172}Hf ($T = 683 \text{ d}$). The presence of some impurities (Fe, Ti, Cu, Zn, Zr, etc.) in the target or in the backing material can also generate strong γ -activities. Their presence is undesirable when the substance is used for nuclear spectroscopic measurements. There are two possibilities to avoid disturbing isotopes: one is to minimize the amount of other Hf iso-

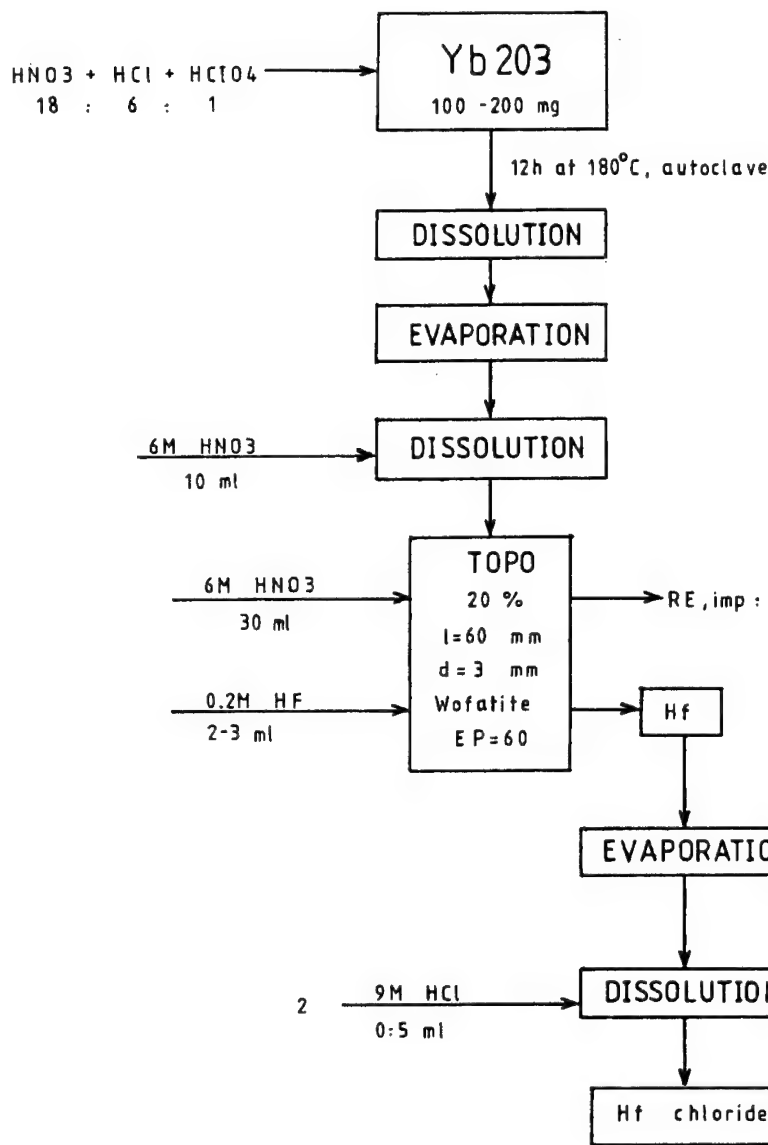


Fig. 2. Scheme for the chemical separation of the Hf fraction from an irradiated Yb target.

topes in the target by performing a ^{176}Yb (96%) superenrichment and the other one is to use mass-separation of the produced Hf for a most radical purification against other Hf isotopes.

The task of $^{178m^2}\text{Hf}$ target preparation for different physical experiments has made the use of both possibilities necessary.

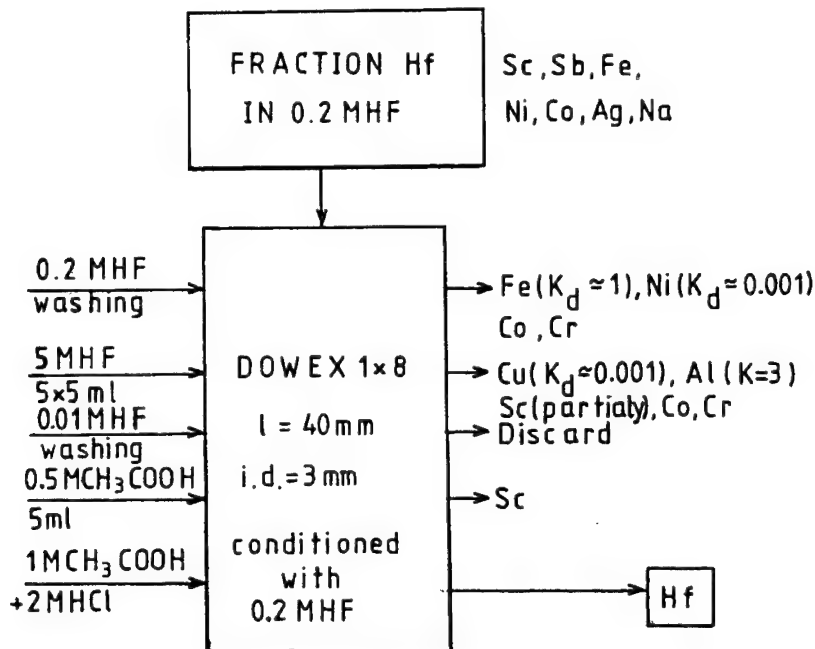


Fig. 3. Scheme for the purification of the Hf fraction.

4. ^{176}Yb superenrichment

^{176}Yb (96%) superenrichment has been accomplished at the PARIS mass-separator of CSNSM-Orsay, using 300–400 mg $^{176}\text{Yb}_2\text{O}_3$ (96%) loads, which had to be separated. The ^{176}Yb isotope was collected into a small graphite box, from which it was periodically recovered, by following an appropriate scheme (fig. 5). In order to eliminate the carbon, the mixture has been calcinated and ^{176}Yb has been purified by precipitation as oxalates which was finally transformed into oxide by means of a new calcination. In about 20 successive mass-separations effectuated during a three month period, followed by adequate chemistry and recuperation, we have succeeded to obtain 910 mg of superenriched ^{176}Yb , starting from 7 g of $^{176}\text{Yb}_2\text{O}_3$ (96%). The yield of superenriched ^{176}Yb raised to about 13%. Neutron activation analysis effectuated in Orsay, as well as in Dubna has shown that only about 1/1000 of the initially present ^{174}Yb remains in the superenriched final sample. Thus, we are able to evaluate the ^{176}Yb after superenrichment at 99.998%. Starting from this superenriched isotope, four irradiations have been carried out, until now, at the Dubna cyclotron U-200 (table 2), in the above-mentioned conditions. After irradiation, the ^{175}Hf and ^{172}Hf production has been found to be substantially suppressed (a decrease by four orders of magnitude). The superenriched ^{176}Yb exposed to the ^4He ion beam was repeatedly regenerated and purified after Hf fraction elution for secondary utilization on subsequent runs. The ^{177m}Lu ($T = 160$ d) activity,

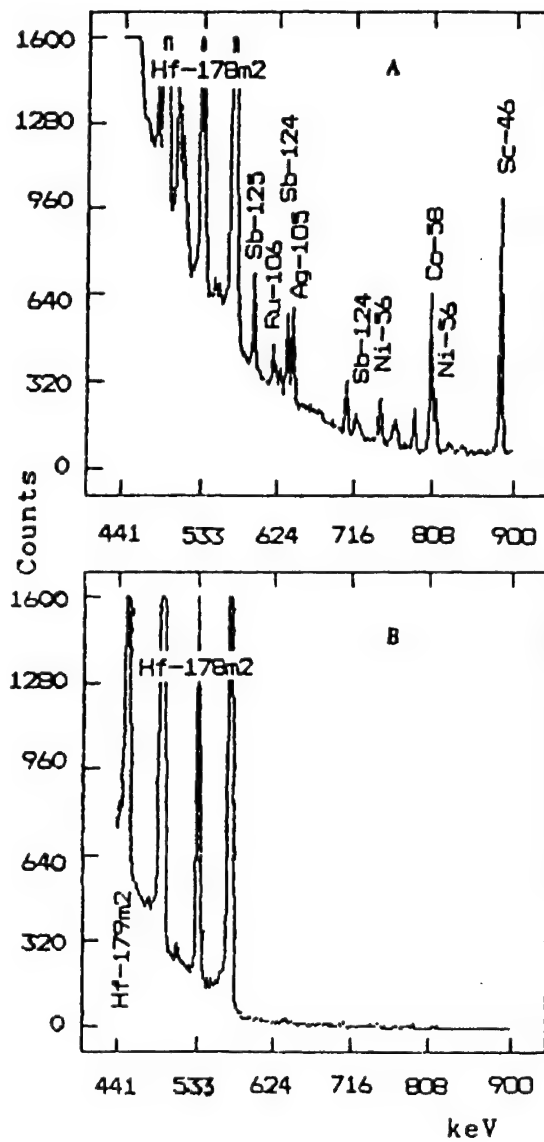


Fig. 4. Fragments of hafnium γ -spectra. (A) Before and (B) after the chemical purification.

induced by the ${}^4\text{He}$ beam, served for chemical yield control during these operations.

After each separation, the unseparated ${}^{176}\text{Yb}$, remaining in the different mass-separator parts (ion-source, electrode, walls, etc.), has been regenerated from the mixture containing different separator metallic constituents (Cu, Fe, Cr, Ni, Mo, etc.), by means of chemical separation using an adequate scheme. The scheme is based on two subsequently precipitations: the first one with NH_4OH concentrate in

Table 2
 ^{178}Hf isomer accumulation runs at the U-200 Dubna cyclotron

Target no.	^{176}Yb enrichment (%)	Date of the run	He integral no. of ions	$^{178m^2}\text{Hf}$ produced atoms
1	93	1989	2.6×10^{19}	1.4×10^{13} Alma-Ata
2	96	jun. 1990	1.5×10^{18}	0.4×10^{13} Alma-Ata
3	96	jul. 1990	6.2×10^{18}	1.6×10^{13}
4	96	nov. 1990	1.3×10^{20}	1.2×10^{14}
5	96	dec. 1990	2.1×10^{20}	1.6×10^{14}
6	96	dec. 1991	0.6×10^{20}	0.6×10^{14}
7	99.998	dec. 1991	4.5×10^{20}	3.5×10^{14}
8	96	dec. 1992	0.7×10^{20}	0.8×10^{14}
9	99.998	febr. 1993	3.4×10^{20}	4.8×10^{14}
10	99.998	nov. 1993	2.4×10^{20}	3.4×10^{14}
11	99.998	nov. 1994	3.2×10^{20}	4.6×10^{14}

hydroxide form, when Cu and Ni are eliminated, and the second one with saturated oxalic acid solution which ensures the elimination of Cr, Fe, and other impurities. After these chemical separations 5 g of the initial 7 g product, have been recovered.

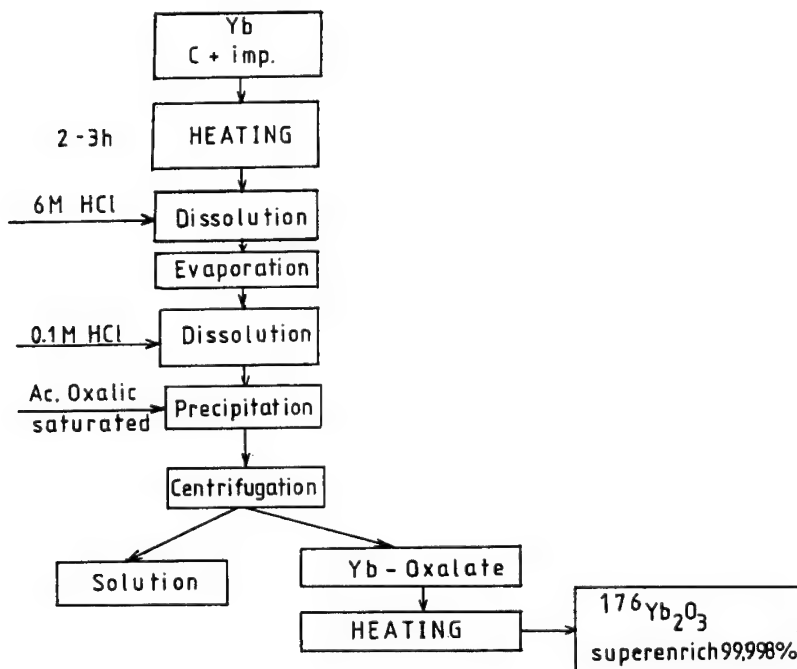


Fig. 5. Recuperation scheme of ^{176}Yb isotopically superenriched at the PARIS mass-separator.

5. Isotopic separation of ^{178}Hf and $^{178m^2}\text{Hf}$ high-spin isomer

The isotopic separation of ^{178}Hf and its high-spin $^{178m^2}\text{Hf}$ isomer, from chemically separated samples, has also been accomplished in Orsay, with the PARIS mass-separator.

After preliminary tests of Hf isotopic separation, using initial 200 µg quantities of natural hafnium labelled with the ^{175}Hf ($T = 70$ d) and ^{181}Hf ($T = 42.4$ d) radioactive isotopes, we have obtained separation yields which we could optimize from 5% up to 15%. As the ^{178}Hf quantities to be separated lie in the µg range, from tests performed it resulted that isotopic separation should be better controlled by addition of a small ^{176}Hf quantity. To avoid modification of the initial $^{178m^2}\text{Hf}/^{178}\text{Hf}$ isomeric ratio we have chosen to prepare (by means of the mass-separator) superenriched ^{176}Hf containing less than 10^{-4} g/g ^{178}Hf .

In order to minimize the ^{176}Hf quantity present in the separation fraction, a separation with 25 µg of added ^{176}Hf was performed, and a yield of 15% has also been obtained.

Five separations of ^{178}Hf together with the $^{178m^2}\text{Hf}$ isomer have been carried out, with initial $^{178m^2}\text{Hf}$ quantities ranging from 10^{13} to 10^{14} atoms and adding 25 µg of superenriched ^{176}Hf . The mixtures were evaporated as chloride on quartz wool, placed inside a carbon tube introduced into the ion source furnace. Using CCl_4 as chlorination agent and transport gas, after a slow heating process, the gaseous hafnium chloride was introduced in the arc chamber where it has been decomposed, ionized and finally separated. We have succeeded in obtaining very good separation yields, rated between 22 and 25%, with a good reproducibility. An example of the results obtained after isotopic separation is given in fig. 6, which presents the γ -spectra of a sample before and after separation. The disappearance of the characteristic γ -lines of ^{175}Hf , ^{172}Hf and its daughter ^{172}Lu is evident. The ground and isomeric states of the ^{178}Hf mass-separated ions have either been delivered for laser collinear spectroscopy [2] or implanted into a single Hf crystal ($\phi = 5$ mm) and Fe foils for nuclear orientation experiments, as well as being simply collected in a Cu catcher for electron conversion measurements.

6. Target preparation

The creation of isomeric hafnium targets for different physical experiments could be considered as successfull if we succeeded in producing a thin, homogeneous hafnium layer on a thin carbon backing, stable to the influence of charged particle beams under conditions of high-efficiency hafnium material foil deposition (since $^{178m^2}\text{Hf}$ is available only in small quantities).

In order to achieve this, we have chosen the electrospraying method of hafnium nitrates from methanolic solutions or Hf acetates from glacial acetic acid. The preparation of methanolic and acetic solutions from the Hf isotopes oxides has pro-

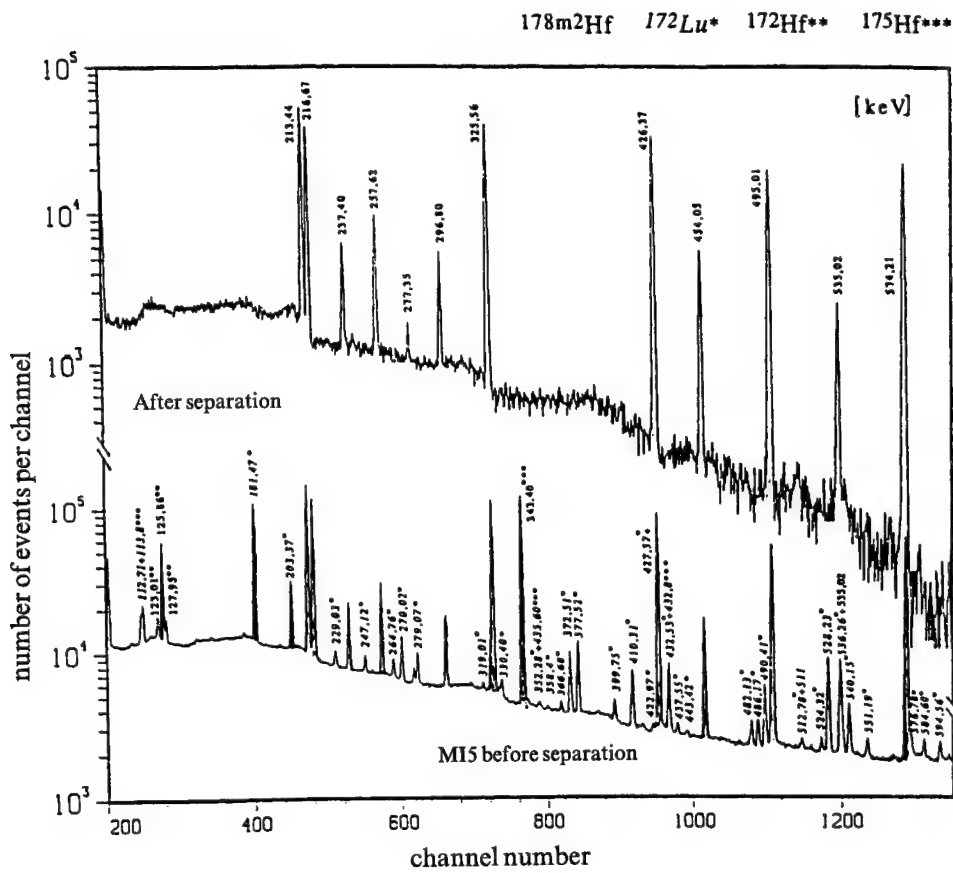


Fig. 6. γ -spectra of the $^{178m^2}\text{Hf}$ isomer before and after isotope mass separation.

ven to be difficult, due to the specific properties of hafnium salts in solution. It has been necessary to establish the preparation conditions in which solutions are stable at room temperature for long periods of time.

Electrospraying of methanolic and acetic acid solutions has been performed with a glass capillary [3] or with a teflon device [4] for a 5.1–6.0 kV potential and a 10–20 μA current. The solution concentration depended on the desired target thickness and layed in the range of 10–200 $\mu\text{g}/\text{ml}$. Various test targets made of stable enriched hafnium isotopes have been manufactured. About 100 targets have been prepared, with diameters rating between 3 and 15 mm and thicknesses from 5 μg to 1.5 mg/ cm^2 , on carbon foils (prepared at the GSI Darmstadt) of 10–40 $\mu\text{g}/\text{cm}^2$ thickness [5]. The target had a good carbon foil adhesion and a good physico-chemical and thermal stability (up to 300°C).

We prepared a first target of this isomer, with a 5 mm diameter on carbon foil ($30 \mu\text{g}/\text{cm}^2$), containing $2.1 \times 10^{14} \text{ }^{178m^2}\text{Hf}$ atoms. The target has been used for inelastic scattering studies of protons (p,p') and deuterons (d,d') performed in

Münich and Orsay [6]. Two different targets have been prepared on carbon foils ($35\text{ }\mu\text{g/cm}^2$), one of them containing 1.46×10^{14} isomer atoms with a 3–4 mm diameter while the other one contained 1.1×10^{14} atoms with a 5–6 mm diameter. Both targets have been used for Coulomb excitation experiments with accelerated ^{208}Pb ions, performed in Darmstadt.

Two isomer targets have been prepared by evaporation on Al foils (99.999% purity and 5 μm thickness) with a 6 mm diameter, containing 0.7×10^{14} and 1.6×10^{14} $^{178m^2}\text{Hf}$ atoms, respectively. These targets have been used in experiments concerning high-spin neutron resonance searches performed with the FAKEL linear electron-accelerator at the Kurchatov Institute in Moscow.

According to the hafnium program coordinators resolution, we have prepared a number of three targets, recently this year, by means of 40 kV $^{178}\text{Hf} + ^{178m^2}\text{Hf}$ implantation into carbon foils ($45\text{ }\mu\text{g/cm}^2$), at the PARIS mass-separator. By operating a series of focal plane modifications we have succeeded in small spot depositions ($2 \times 3\text{ mm}$) of about 2×10^{13} isomer atoms on each target. The obtained targets major advantage consists in the containment of solely the $^{178}\text{Hf} + ^{178m^2}\text{Hf}$ fraction, avoiding undesirable reactions of other hafnium isotopes which would alterate the measurements. One of these targets has been used for deuteron inelastic scattering studies performed at the München Tandem.

References

- [1] Yu.Ts. Oganessian, S.A. Karamian, Y.P. Gangrski, B. Gorski, B.N. Makarov, Z. Szeglowski, Ch. Briançon, D. Ledu, R. Meunier, M. Hussonnois, O. Constantinescu and M.I. Subbotin, *J. Phys. G: Nucl. Part. Phys.* 18 (1992) 393.
- [2] N. Boss et al., *Phys. Rev. Lett.* 72 (1994) 2689.
- [3] M. Hussonnois, L. Brillard and O. Constantinescu, *Nucl. Instrum. Meth.* 224 (1984) 335.
- [4] Z. Szeglowski and Yu.S. Korotkin, *Prib. Tekh. Eksp.* 1 (1991) 206.
- [5] M. Hussonnois, O. Constantinescu, Z. Szeglowski, J.B. Kim and M. Constantinescu, *Heavy Ion Physics*, Scientific Report (1991–1992) 107.
- [6] H.J. Wollersheim et al., *Heavy Ion Physics* (1993) 382.

Evidence for K mixing in ^{178}Hf

C.B. Collins

*The University of Texas at Dallas, Center for Quantum Electronics, PO Box 830688,
Richardson, TX 75083-0688, USA*

J.J. Carroll

*Department of Physics and Astronomy, Youngstown State University, Youngstown,
OH 44555, USA*

Yu.Ts. Oganessian and S.A. Karamian

*Joint Institute for Nuclear Research, Flerov Laboratory of Nuclear Reactions,
Dubna, PO Box 79, 101000 Moscow, Russia*

Systematics for the appearance of K -mixing levels for the pumping or spontaneous decay of multi-quasiparticle isomers in Hf isotopes are detailed in this letter. The possible location of such a level in the nuclide ^{178}Hf is discussed and an experiment is proposed to investigate its existence.

Multi-quasiparticle states in the isotopes of Hf appear as high-spin isomers that are distinguished by the combination of MeV excitation energies and long lifetimes [1]. As is typical for mid-shell isotopes, Hf nuclei have marked prolate deformations that provide a body axis upon which the total angular momentum, J can be quantized in units of $K\hbar$. Thus multi-quasiparticle states serve as the heads of rotational bands corresponding to large values of projection quantum number, K .

The Hf isomers also have angular momenta which are quite different from those of other intrinsic nuclear states. Since strong electromagnetic transitions are generally characterized by low orders of multipolarity, L and selection rules require $|\Delta J| \leq L$, the apparent necessity for large changes in angular momentum would seem to be the cause of the long isomeric lifetimes. However, large ΔJ transitions need not be required. The excitation energies of multi-quasiparticle states are so great that levels with similar angular momenta can be found, built upon the low-spin ground state from as many as 6–8 quanta of rotation, while still remaining below the energy of the isomers. Thus the selection rule upon ΔJ alone cannot be the cause of the isomerism.

The long lifetimes of multi-quasiparticle states of Hf result from the analogous selection rule upon K , generally accepted to be $|\Delta K| \leq L$ for transitions between states in different rotational bands. This is the restriction which severely hinders

electromagnetic decay of the isomers to yrast levels of similar J , but dissimilar K . While providing storage of great energy densities, the selection rule on K would also seem to vitiate otherwise attractive proposals to use concentrations of high-spin isomers for superelastic particle beam applications, (γ, γ') frequency upconversion, and the nuclear analog to the ruby laser. It is very difficult *a priori* to conceive of a trigger process or reaction which would transfer so much ΔK as would be needed to de-excite populations of high-spin isomers to freely radiating states in an efficient, controlled manner.

The key to transitions between high-spin isomers of Hf and yrast states may lie in the existence of mediating levels having mixed values of K . Those "K-mixing" levels would be described by superpositions of eigenfunctions for several different projection quanta corresponding to comparable values of J and could be reached by transitions of low multipolarity both from isomers and from members of bands built upon much lower values of K . A discussion of what type of perturbation could provide the interaction energy necessary for such a fortunate K mixing is left for later.

The first evidence for the de-excitation, or "dumping", of a multi-quasiparticle isomer through a K -mixing level seems to have been reported in 1987 and published in 1988 [2]. Populations of the 10^{15} year, two-quasiparticle isomer $^{180}\text{Ta}^m$ were dumped to the ground state in the reaction $^{180}\text{Ta}^m(\gamma, \gamma')^{180}\text{Ta}$, despite a total change of $\Delta K = 8$. Identified [3] in 1990 as proceeding directly through a previously unobserved state at 2.8 MeV, the reaction was found to be excited with a surprisingly large integrated cross section of $1.2 \times 10^{-25} \text{ cm}^2 \text{ keV}$. Independently, the same year the de-excitation of the $3.7 \mu\text{s}$, four-quasiparticle isomer $^{174}\text{Hf}^m$ was reported [4] to occur as a result of *spontaneous emission* through a K -mixing level lying below the meta-stable state at 2.685 MeV and providing $\Delta K = 14$. The similarity of the excitation energies of the mediating levels in ^{180}Ta and ^{174}Hf , on the order of a pairing interaction, suggested an examination of the systematics of other (γ, γ') reactions that spanned large ΔK . While those reactions might have proceeded through complex cascades, they could have also benefitted from more direct transitions through K -mixing states.

Fig. 1 summarizes the results reported earlier for a systematic investigation [5,6] of integrated cross sections and excitation energies measured for (γ, γ') processes mediating large changes of ΔK . The only known reactions starting on multi-quasiparticle levels seem to be those of $^{174}\text{Hf}^m$ and $^{180}\text{Ta}^m$, so the others shown are for the excitation of one- or two-quasiparticle isomers from ground-state targets. Nevertheless, the trend is compelling and suggests the pervasive existence of a K -mixing level between 2.5 and 2.8 MeV in many mid-shell nuclides below $p = 82$. Moreover, the values of integrated cross section for (γ, γ') reactions occurring through such levels seem to peak in this region, notwithstanding the large ΔK between initial and final states. Such magnitudes would suggest strong transitions of low multipolarity, requiring the change in K to occur in the mediating state.

The persuasive nature of the data plotted in fig. 1 encourages the tentative con-

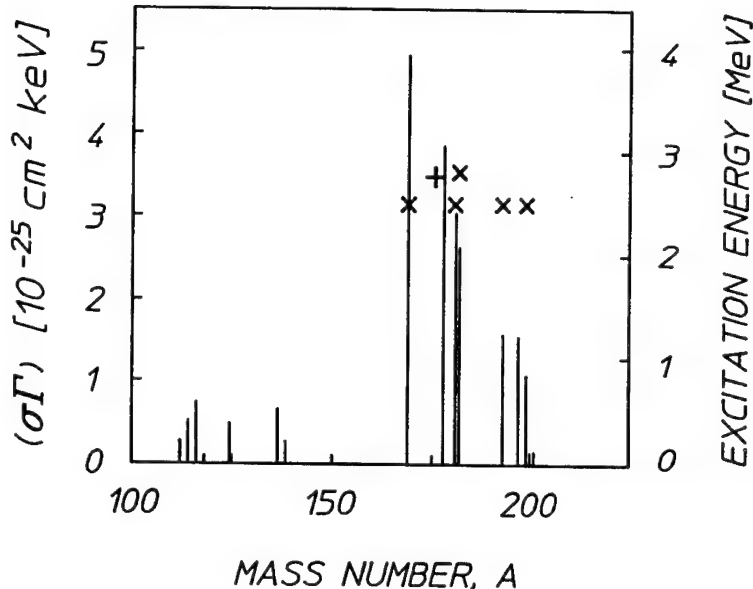


Fig. 1. Summary of systematic studies [5,6] of the excitation and de-excitation of quasiparticle isomers in (γ, γ') reactions. Measured integrated cross sections are plotted by the left-hand axis and the excitation energies for possible K -mixing levels are plotted by the right-hand axis. The \times symbols indicate mediating states excited from the ground state or isomer with bremsstrahlung and the $+$ represents the level through which spontaneous decay of $^{174}\text{Hf}^m$ occurs [4]. Values of integrated cross section peak mid-shell in the mass island below $p = 82$.

clusion that a similar K -mixing level can be expected in the ^{178}Hf system. This would be particularly important for the 31 yr, four-quasiparticle isomer $^{178}\text{Hf}^{m2}$ since such an intermediate state could connect it to yrast states, providing the means for realizing an induced release of the stored energies. Unfortunately, few studies have been conducted for reactions involving $^{178}\text{Hf}^{m2}$ due to great difficulties in obtaining appropriate targets. The present objective is to attempt to estimate the parameters that would describe such a reaction, $^{178}\text{Hf}^{m2}(\gamma, \gamma')^{178}\text{Hf}$ from the data which has recently become available [7].

Fig. 2 shows an expanded view of the data of fig. 1 for the mass island immediately below $p = 82$. Measured excitation energies of apparent K -mixing levels mediating those reactions are plotted as \times and $+$ symbols by the right-hand ordinate and fall between 2.5 and 2.8 MeV, defining an interval ΔE_K within which such levels may be reasonably expected. The circles give the energies of the four- and five-quasiparticle isomers $^{174}\text{Hf}^m$, $^{175}\text{Hf}^m$, $^{176}\text{Hf}^{m3}$, $^{177}\text{Hf}^{m2}$ and $^{178}\text{Hf}^{m2}$, which trend to lower values with increasing mass numbers. Relevant parameters for those isomers are shown in table 1. The important detail in fig. 2 is the position of those isomers relative to the possible excitation energies of K -mixing levels. At present no direct observations of (γ, γ') reactions are available for those isotopes and thus

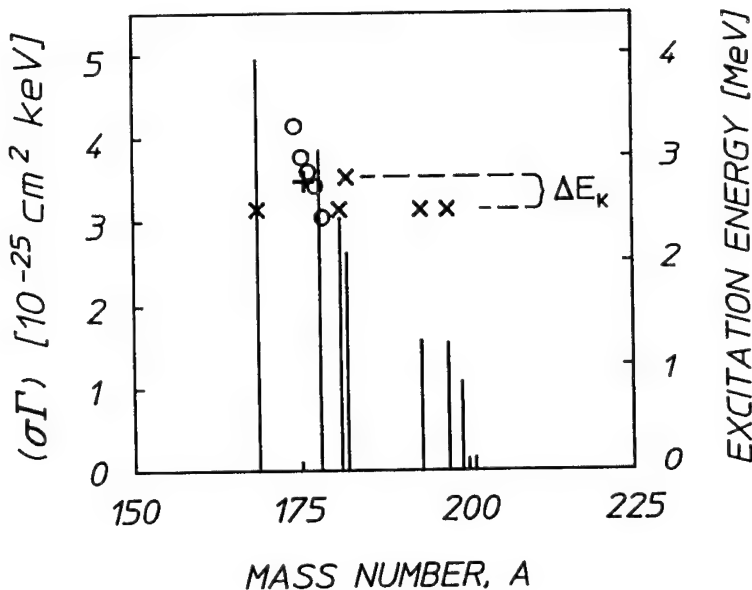


Fig. 2. Expanded view of the data of fig. 1 for the mass island below $p = 82$. Also indicated by the circles are the excitation energies of four- and five-quasiparticle Hf isomers lying between 2 and 3 MeV and having halflives longer than 1 μs . The interval ΔE_K shows the range of energy within which all possible K -mixing levels are expected to lie.

the discussion is based on ΔE_K which bounds the likely energies of mediating states.

For $^{174}\text{Hf}^m$ and $^{175}\text{Hf}^m$ the isomers lie well above the upper bound of ΔE_K and it can be reasonably expected from fig. 2 that those multi-quasiparticle states would be relatively short-lived due to the availability of K -mixing states which could mediate spontaneous decay. As mentioned before, this is indeed the case for $^{174}\text{Hf}^m$ with a halflife of 3.7 μs . Similarly, $^{175}\text{Hf}^m$ has a 1.21 μs halflife. In the case of $^{176}\text{Hf}^{m3}$, the isomer lies at 2.866 MeV, slightly above the upper bound of ΔE_K . Thus, it could be

Table 1

Summary of relevant adopted properties [1] for three-, four-, and five-quasiparticle Hf isomers having excitation energies between 2 and 4 MeV and lifetimes longer than 1 μs . Parentheses indicate suggested values

Isomer	$J^\pi = K^\pi$	Number of quasiparticles [1,9]	Excitation energy (MeV)	Halflife
$^{174}\text{Hf}^m$	14^+	4	3.312	3.7 μs
$^{175}\text{Hf}^m$	$35/2$	5	3.016	1.21 μs
$^{176}\text{Hf}^{m3}$	14^-	4	2.866	401 μs
$^{177}\text{Hf}^{m2}$	$37/2^-$	5	2.740	51.4 min
$^{178}\text{Hf}^{m2}$	16^+	4	2.446	31 yr

expected to have a short lifetime somewhat lengthened by a small transition energy to a K -mixing level. This is supported by a measured halflife of 401 μs . The isomer $^{177}\text{Hf}^{\text{m}2}$ lies just below the upper bound of ΔE_K , possibly at a lower energy than any mediating state. In that event a long lifetime would be suggested since spontaneous decay could not occur, but this could also be the result if a K -mixing level were located little below the isomer. The measured halflife of 51 min agrees well with either possibility. Of most importance to the present discussion, the isomer $^{178}\text{Hf}^{\text{m}2}$ appears to lie below the likely position of a mediating state. This points to a long lifetime and indeed the measured value is 31 yr. Clearly the known halflives of these multi-quasiparticle Hf isomers agree well with the speculation that K -mixing levels are prevalent and lie between 2.5 and 2.8 MeV.

The strong dependence of isomer lifetime on the possible excitation energy of a mediating state is shown directly in fig. 3. Again, ΔE_K indicates the interval within which all measured values for possible K -mixing levels lie. This interval can be further constrained by comparing the data to lifetimes derived from single-particle widths. Since low multipolarities would be indicated for transitions between the

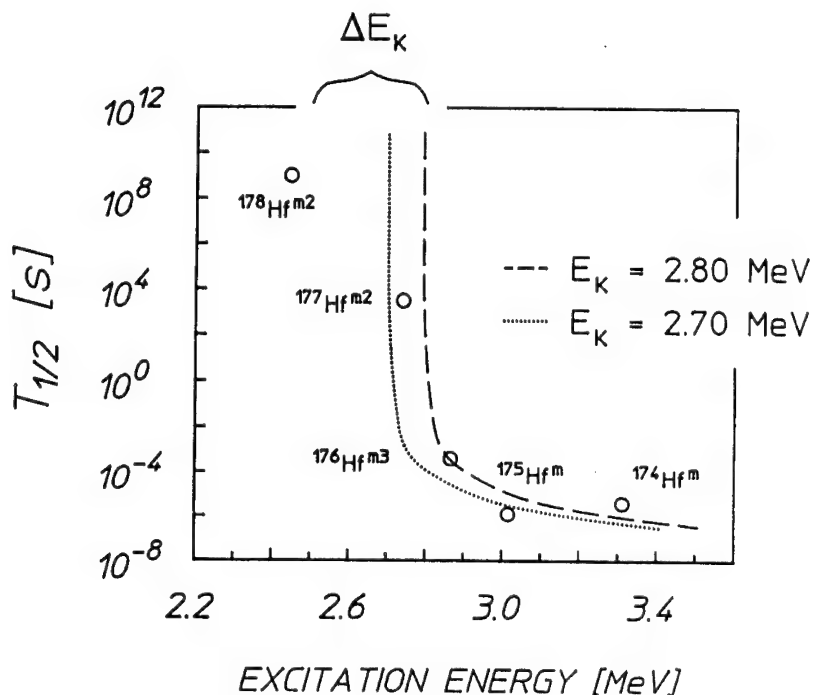
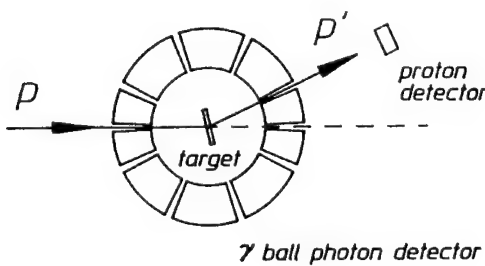


Fig. 3. Plot of halflife as a function of excitation energy for the four- and five-quasiparticle Hf isomers of fig. 2. The interval ΔE_K is shown within which all K -mixing levels are expected to lie based on previous measurements. The curves represent halflives calculated based on the assumption of the availability of dipole transitions for the de-excitation of the isomers for different choices for the energy of the mediating state and further bound the possible positions of such a level.

isomers and states of mixed K , dipole radiation is considered here. Derived using the typical $1/(E_i - E_K)^3$ dependence for dipole transition widths where E_i is the isomer energy and E_K is the energy of the mediating level, the curves in fig. 3 show halflives in good agreement with the measured values. It is doubtful that a K -mixing state could lie much below the isomer $^{177}\text{Hf}^{\text{m}2}$ without affecting its 51 min lifetime. Thus, the value $E_K = 2.7$ MeV used to generate the curve passing just below that isomer represents a lower bound on the likely energy of an intermediate state of mixed K . Likewise, $E_K = 2.8$ MeV provides an upper bound for that energy since larger values produce curves which do not reproduce the lifetimes of the isomers $^{174}\text{Hf}^{\text{m}}$, $^{175}\text{Hf}^{\text{m}}$ and $^{176}\text{Hf}^{\text{m}3}$. The excellent agreement seen between halflives predicted for dipole transitions and those measured provides further evidence for a K -mixing level in $^{178}\text{Hf}^{\text{m}2}$ lying no more than about 300 keV above the isomer.

The presence of such a K -mixing level could in principle be identified in a (γ, γ') reaction study similar to those conducted previously [2,3,6], but might be most easily detected in the proposed experiment shown schematically in fig. 4a. A beam of protons of energy E_0 would be incident on $^{178}\text{Hf}^{\text{m}2}$ nuclei in a sample located within a 4π granular detector array, or “ γ ball”. This arrangement would provide for inelastic scattering of protons in $(p, p'\gamma)$ reactions where the γ refers to photons emitted in the decay of the excited nucleus. Many scattering events would merely excite low-lying members of the ground-state or isomeric rotational bands with a low multiplicity n of accompanying γ -rays. However, the excitation of a K -mixing

a) EXPERIMENTAL ARRANGEMENT



b) EXCITATION FUNCTION

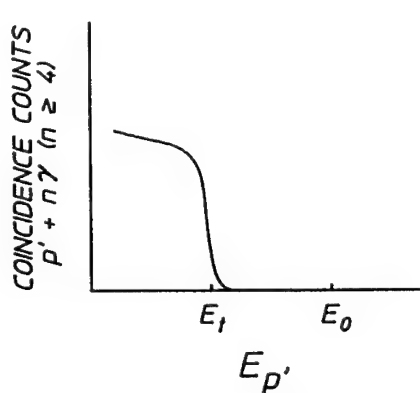


Fig. 4. (a) Schematic depicting a proposed experiment to confirm the existence of a K -mixing state in $^{178}\text{Hf}^{\text{m}2}$. Protons of energy E_0 would be incident on a sample containing $^{178}\text{Hf}^{\text{m}2}$ placed within a 4π granular “ γ ball” detector. The energy of protons scattered in $(p, p'\gamma)$ reactions would be measured by the external detector while the γ ball would record photons resulting from decay of the nucleus. (b) Excitation function expected from a K -mixing level by detecting scattered protons in coincidence with a high multiplicity of γ -rays. The threshold at $E_t = E_0 - E_K$ locates the excitation energy of the mediating level.

state from the isomer would result in a transfer of the isomer to the yrast band with an accompanying large multiplicity of detected photons ($n \geq 4$), since the γ -cascade multiplicity, M_γ is expected to be more than 6–7. Due to the detection efficiency, $n < M_\gamma$. Thus the important aspect in the observation of a K -mixing level would be the measurement of the spectrum of inelastically scattered protons in coincidence with a high multiplicity of photons detected by the γ ball. By selecting only events satisfying this criterion it would be possible to confirm the existence of the K -mixing level in an excitation function like that depicted in fig. 4b. The location of the mediating level would be clearly marked by a threshold at an energy $E_t = E_0 - E_K$.

This article makes no attempt to estimate the probability for the actual existence of a K -mixing state. However, systematics strongly suggest that such a level may exist in $^{178}\text{Hf}^{\text{m}2}$, and at a sufficiently low excitation energy to be of great importance to proposals for the use of this isomer in superelastic particle-beam studies, gamma-ray upconversion and the nuclear analog to the ruby laser. At this point further study is needed for a definitive resolution.

Acknowledgement

Some of the authors gratefully acknowledge the support of this work by BMDO through NRL.

References

- [1] National Nuclear Data Center Online Evaluated Nuclear Structure Data File (ENSDF) (Brookhaven National Laboratory, 1994).
- [2] C.B. Collins, C.D. Eberhard, J.W. Glesener and J.A. Anderson Phys. Rev. C37 (1988) 2267.
- [3] C.B. Collins, J.J. Carroll, T.W. Sinor et al., Phys. Rev. C42 (1990) 1813.
- [4] P.M. Walker, F. Sletten, N.L. Gjorup et al., Phys. Rev. Lett. 65 (1990) 416.
- [5] C.B. Collins and J.J. Carroll, these proceedings (1st Int. Gamma-Ray Laser Worksh., 1995), Hyp. Int. 107 (1997) 3.
- [6] J.J. Carroll, M.J. Byrd, D.G. Richmond et al., Phys. Rev. C43 (1991) 1238.
- [7] Yu.Ts. Oganessian, S.A. Karamian, Y.P. Gangrski et al., in: Proc. Int. Conf. Nuclear Physics in Our Times (1992).
- [8] Yu.Ts. Oganessian, S.A. Karamian, Y.P. Gangrski et al., J. Phys. G: Nucl. Part. Phys. 18 (1992) 393.
- [9] M.E. Bunker and C.W. Reich, Rev. Mod. Phys. 43 (1971) 348.

Limits on spurious contributions to integrated cross sections for photoexcitation and de-excitation of isomers

J.J. Carroll

*Youngstown State University, Department of Physics and Astronomy,
Youngstown, Ohio 44555, USA*

C.B. Collins

*Center for Quantum Electronics, University of Texas at Dallas, PO Box 830688,
Richardson, Texas 75083-0688, USA*

The large values of integrated cross sections for the excitation and de-excitation of nuclear isomers in (γ, γ') reactions provide strong encouragement for the feasibility of an optically pumped gamma-ray laser. For this reason, sources of possible spurious contamination of the measurements were carefully considered. This paper reviews an analysis of possible sources as well as experimental limits on contamination of the isomeric yields. The question of spurious contributions from (n, γ) or (n, n') reactions was examined by estimating the level of thermal, epithermal and fast neutron fluxes based on possible source material in the accelerator environments. Such possibilities were severely reduced by the range of photon energies employed in the studies of 1.5–6 MeV. The expected fluxes were below levels necessary to produce significant isomeric yields in this energy range. Next, experiments were conducted in accordance with standard neutron activation-foil techniques to directly measure any fluxes of neutrons in the accelerator environments. Measurements for fast neutron fluxes were completely negative under even the most likely conditions with a 6 MeV medical linac. Measurable fluxes of thermal and epithermal neutrons were obtained. However, in typical cases the amount of isomeric activation due to “slow” neutrons was 1% of the total activation and 6% in the worst case based on measured fluxes and known values of cross sections.

1. Introduction

In 1982 a blueprint [1] for an optically pumped gamma-ray laser was introduced in which photons would be used to excite a population inversion in nuclei implanted into a thin low- Z host material. This approach would enhance the ratio of useful energy absorbed resonantly by the active nuclei to that absorbed non-resonantly in the host and leading to excess heat. A fundamental question remained the identity of the best-suited isotope, at the most ideal employing upconversion to increase quantum efficiency. Pursuing this question experimental studies of the excitation of nuclear isomers using intense fluxes of X-rays proved to be extremely positive [2]. Even more so were studies in which the one naturally occurring isomer existing

at 100% inversion, $^{180}\text{Ta}^m$ was excited to a higher-lying level which freely radiated by a cascade to the ground state [3,4]. That experiment demonstrated that isomeric populations could be “dumped” to freely radiating states and that in principle upconversion was possible in nuclei. In addition, the integrated cross section characterizing the (γ, γ') reactions dumping that isomer were on the order of 10^4 larger than typical values observed prior to 1988, and more than 10^{19} larger than naive estimates based on single-particle widths. The magnitude of this integrated cross section, and those of many neighboring isotopes having isomers pumped from their ground states, led to the designation “giant pumping resonances” [2].

The discovery of giant pumping resonances provided unexpected encouragement for the feasibility of an optical-pumping gamma-ray laser. Those resonances corresponded to intermediate states, or gateways, which produce isomers through an indirect, two-step process. A gateway first absorbs a photon in a low-multipolarity transition from the ground state and then decays with some appreciable branching ratio to the isomer, as depicted in fig. 1. In the case of $^{180}\text{Ta}^m$, the initial state is

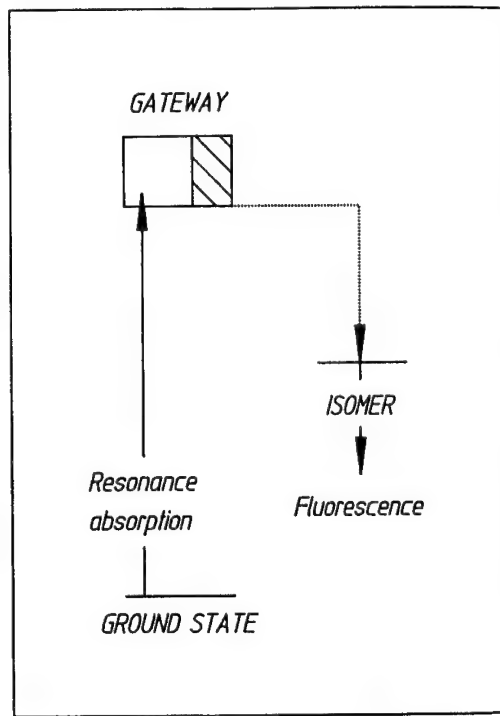


Fig. 1. Schematic representation of the population of an isomer in a (γ, γ') reaction. The process involves two steps, the first being resonant absorption of an incident photon in a transition from the ground state to an intermediate state, or gateway state. The gateway then decays, with a branch cascading to the isomer from which fluorescence may be observed. Only a single gateway is shown but generally isomeric nuclei possess more than one at energies given as E_j . The total probability for production of the isomer through a specific gateway is given by the integrated cross section, $(\sigma\Gamma)_j$.

the isomer and the final level is the ground state. Extensive measurements were conducted over several years using six accelerators in different environments and producing bremsstrahlung having various endpoints. Those accelerators included the Texas-X and S-DALINAC research linacs, 4 and 6 MeV medical linacs with fixed endpoints, and two e-beam devices, DNA/PITHON and DNA/Aurora. Systematics were developed [2] from those results that showed the appearance of giant pumping resonances to be common for nuclei near $A = 180$. Fig. 2 gives these systematics in a form that allows a comparison of the efficiencies of photoexcitation of seventeen nuclides from bremsstrahlung having an endpoint of 6 MeV. In general, the isotopes possess several gateways with different associated integrated cross sections for isomeric excitation. Therefore, to achieve a direct comparison it was necessary for each nuclide to sum the products of integrated cross section and bremsstrahlung spectral intensity at the gateway energy for all intermediate states lying below 6 MeV. The reason for this choice of endpoint will be discussed in the following sections. The summed value was then normalized to the spectral intensity at 2.125 MeV to give the equivalent integrated cross section of a single hypothetical gateway.

The common appearance of giant pumping resonances near $A = 180$ was unexpected because isomers of those nuclides generally arise from a selection rule on the projection quantum, K , of the total angular momentum J . The projection quantum becomes defined for deformed nuclei which have a major axis of symmetry. Each intrinsic single-particle state then acts as the head of a rotational band of levels all having the same value of K . Therefore, electromagnetic transitions which span relatively small ΔJ might be restricted to high multipolarities by a large inter-band ΔK , leading to a long-lived metastable level (a "K isomer"). For this same reason pumping resonances for excitation or de-excitation of isomers by (γ, γ') reactions

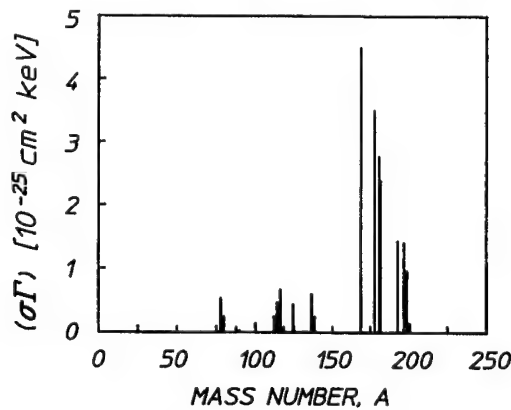


Fig. 2. Comparison of integrated cross sections for gateways of seventeen nuclei studied in ref. [8]. The values of $(\sigma\Gamma)_j$ were summed for E_j below 6 MeV and the sum normalized to 2.125 MeV to give the equivalent integrated cross section of a single, hypothetical gateway. Individual values of $(\sigma\Gamma)_j$ were obtained from measured isomeric yields and were attributed entirely to photons.

were expected to have quite small integrated cross sections. The appearance of giant values attributed to photoexcitation was startling. Therefore, the possibility of spurious contamination of the experimental results due to a variety of sources was considered in four separate studies [4–7] published in 1990–1993 and reviewed here.

2. Contamination sources

Many possible sources of contamination were evaluated, most of which could be summarily excluded as being unimportant. Those could have included contributions to the isomeric yield from natural background or excitation of the samples by (e, e') , (γ, n) , (n, γ) or (n, n') reactions. In the case of a natural background, positive identification of the fluorescence signatures and the amounts of isomeric yields was accomplished by obtaining both energy (pulse-height) and decay (multichannel scalar) spectra. Typical examples [8] are shown in figs. 3 and 4 for the isomers of $^{167}\text{Er}^m$ and $^{123}\text{Te}^m$. As can be seen in those figures, excellent agreement was obtained between the measured halflives and the literature values [9] of 2.28 s and 123 days, respectively. Fluorescence signatures were clearly identified and were well separated from any strong background lines when either NaI(Tl) or HPGe detectors were used.

Inelastic electron scattering, or (e, e') reactions can excite isomeric populations in a manner that at low momentum transfer is quite similar to that of (γ, γ') reactions [10]. However, it has been experimentally shown [11] that the cross sections for electro-excitation of isomers are on the order of 10^2 smaller than for photoexcitation at the same energy. The numbers of electrons available for (e, e') reactions after penetrating the high- Z bremsstrahlung converters are also orders-of-magnitude less than the numbers of X-rays produced. An example of a typical converter is the 3 mm thick tantalum target used in irradiations with the Texas-X [5], within which the range of 4 MeV electrons was only 1.7 mm. Spurious contributions to the measured activations due to (e, e') reactions were therefore negligible. Likewise, contamination from (γ, n) reactions could be excluded since photons within the bremsstrahlung had insufficient energy [12] to reach the thresholds for those processes in the sample materials. The only exceptions were the very highest energy irradiations with DNA/Aurora, but those are not relevant to the present discussion regarding giant pumping resonances lying below 6 MeV.

The question of spurious contributions from neutrons by (n, γ) or (n, n') reactions received more thorough consideration. General theory is found in ref. [13]. All of the accelerators used, other than DNA/PITHON with endpoints less than 1.4 MeV, were capable of evaporating neutrons from some materials in the accelerator environments via (γ, n) reactions. The threshold energy, E_t for such a reaction may be estimated from the mass excesses for a free neutron, δn , the parent nuclide, $\delta(A, Z)$, and the daughter, $\delta(A - 1, Z)$ according to

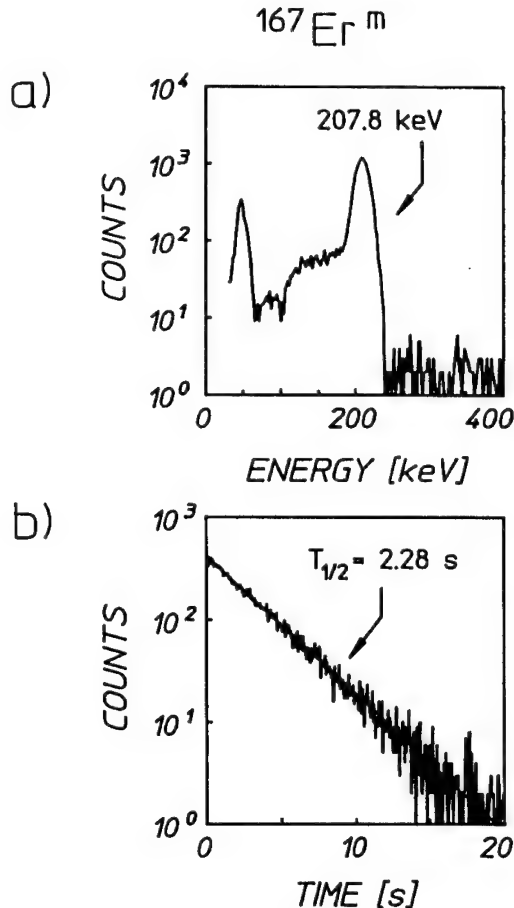


Fig. 3. Fluorescence data [8] from the decay of $^{167}\text{Er}^m$ following its excitation with 6 MeV bremsstrahlung from a medical linac for an irradiation of 25 s. The pulse-height (energy) spectrum of (a) and the multichannel-scalar (decay) spectrum of (b) were obtained using a NaI(Tl) spectrometer. The measurements of fluorescence energy and lifetime were in excellent agreement with the literature values [9].

$$E_t = \delta n + \delta(A - 1, Z) - \delta(A, Z). \quad (1)$$

The energy, E_n of neutrons emitted in a (γ, n) reaction due to monoenergetic photons is given approximately by [14]

$$E_n \approx \frac{M(E_\gamma - E_t)}{m_n + M} + \frac{E_\gamma \sqrt{2m_n M(m_n + M)(E_\gamma - E_t)}}{(m_n + M)^2} \cos \theta, \quad (2)$$

which includes the effect of recoil of the parent nucleus. The $m_n = 938 \text{ MeV}$ and M are the rest masses of the neutron and parent nucleus, respectively, E_γ is the

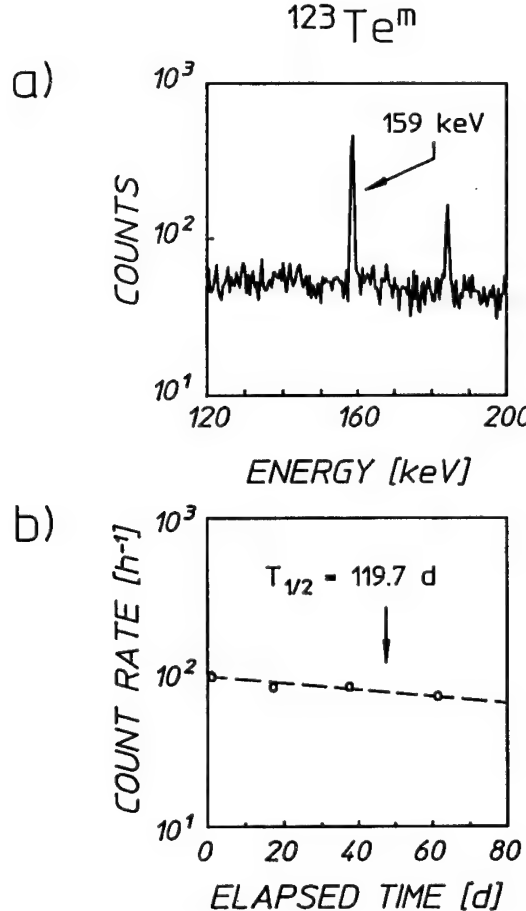


Fig. 4. Fluorescence data [8] from the decay of $^{123}\text{Te}^m$ following its excitation with 6 MeV bremsstrahlung from a medical linac for an irradiation of 2 h. The pulse-height (energy) spectrum of (a) and the counting-rate (decay) spectrum of (b) were obtained using a HPGe spectrometer. Counting periods used to obtain the measurements of (b) were 10 h. The measurements of fluorescence energy and lifetime were in excellent agreement with the literature values [9].

photon energy and θ is the angle of neutron emission relative to the incident photon direction. The second term contributes less than 10% to eq. (2) and is neglected in the following discussion.

The spectral density, $d\phi_n/dE_n$ of neutrons of energy E_n produced by photons of energy E_γ is related to the energy-dependent (γ, n) cross section, $\sigma_{(\gamma,n)}(E_\gamma)$ according to

$$\frac{d\phi_n}{dE_n}(E_n) = N_T \sigma_{(\gamma,n)}(E_\gamma) \frac{d\phi_\gamma}{dE_\gamma}(E_\gamma), \quad (3)$$

where N_T is the number of target parent nuclei and $d\phi_\gamma/dE_\gamma$ is the photon spectral

density in $\text{cm}^{-2}\text{s}^{-1}$. In considering the effect of these neutrons on the production of isomers, the probable impact parameter for inelastic neutron scattering can be readily bounded from the typical values of (n, n') cross sections [15] which near 1 MeV rarely exceed 1b. Thus it can be concluded that only s-wave, p-wave, and perhaps d-wave scattering are probable. In the cases of most isomers, the angular momentum and its projections between initial and final states differ by more than two units, so excitation by fast neutrons cannot result in direct excitation of metastables from their ground states. Therefore, fast neutrons present no natural advantages and simply excite the same gateways important for photoexcitation, but through a non-resonant threshold process. For this reason, it is necessary to calculate the total number of neutrons per second, $N_n(E_j)$ above a gateway energy, E_j as produced from a source material by a photon continuum. This is accomplished by

$$N_n(E_j) = N_t \int_{E_{\gamma 0}}^{E_{\max}} \sigma(E_\gamma) \frac{d\phi_\gamma}{dE_\gamma}(E_\gamma) dE_\gamma, \quad (4)$$

where eq. (2) gives $E_{\gamma 0} = E_t + (1 + m_n/M)E_j$ and $E_{\max} = E_t + (1 + m_n/M)E_0$, with E_0 being the bremsstrahlung endpoint.

We now restrict the discussion to bremsstrahlung having $E_0 \leq 6$ MeV, below which giant pumping resonances have been shown to lie [2]. This limits the number of materials from which neutrons can be evaporated, as shown in table 1. Several of those materials are rare and not present in the accelerator environments. Deuterium occurs within cooling water in some linacs and as bound water in concrete chamber walls. Beryllium is present in some linac heads as an exit window through which electrons pass into air before striking the high-Z converter. The carbon and oxygen isotopes can occur in the atmosphere and again in the concrete, but their photoneutron thresholds are above 4 MeV with cross sections less than 1 mb [16,17]. Due to a beryllium exit window, cooling water and a smaller accelerator chamber providing higher photon intensities to the concrete walls, the 6 MeV medical linac (CLINAC 1800 operated in the 6 MeV mode) was expected to produce the

Table 1

Naturally occurring isotopes having photoneutron thresholds less than 6 MeV. Maximum neutron energies, $E_{n,\max}$ produced by 6 MeV photons were calculated with eq. (2), and neutron binding energies, B_n were obtained from ref. [24].

Isotope	Natural abundance (%)	B_n (MeV)	$E_{n,\max}$ (MeV)
² H	0.015	2.224	1.886
⁶ Li	7.5	5.662	0.281
⁹ Be	100	1.665	3.849
¹³ C	1.1	4.946	0.971
¹⁷ O	0.038	4.142	1.747
¹⁴⁵ Nd	8.3	5.760	0.238
¹⁴⁹ Sm	13.8	5.846	0.153
²³⁵ U	0.72	5.307	0.690

greatest number of neutrons. Actually, calculations based on a 0.025 cm thick Be window compared with the small amounts of cooling water indicate that ${}^9\text{Be}$ at 100% abundance would dominate photoneutron production [15]. The same level of photoneutron production would require more than 3 l of normal water exposed to X-rays in the linac head. Similarly, calculations demonstrated that the amounts of ${}^2\text{H}$, ${}^{13}\text{C}$ and ${}^{17}\text{O}$ in the atmosphere and concrete were insufficient to produce neutron fluxes greater than $1 \text{ cm}^{-2}\text{s}^{-1}$.

Under the assumption that neutrons were emitted isotropically [18] from the Be exit window, it is straightforward to determine the total flux of those particles, $\phi_n(E_j)$ having energies greater than that of a gateway at E_j at the position where samples were tested for photoexcitation. One obtains

$$\phi_n(E_j) = \frac{N_n(E_j)}{4\pi r^2}, \quad (5)$$

where r is the distance from beryllium exit window to sample position, typically 65 cm. Eq. (5) overestimates the neutron flux, shown in fig. 5, because it neglects any attenuation or scattering of neutrons by the intervening bremsstrahlung converter. It is important to note that the total neutron flux at all energies is on the order of $10^3 \text{ cm}^{-2}\text{s}^{-1}$, about 7 orders-of-magnitude less than the corresponding total photon flux [15] of $3.42 \times 10^{10} \text{ cm}^{-2}\text{s}^{-1}$ at the same position.

Using the calculated neutron flux and gateway energies and integrated cross sec-

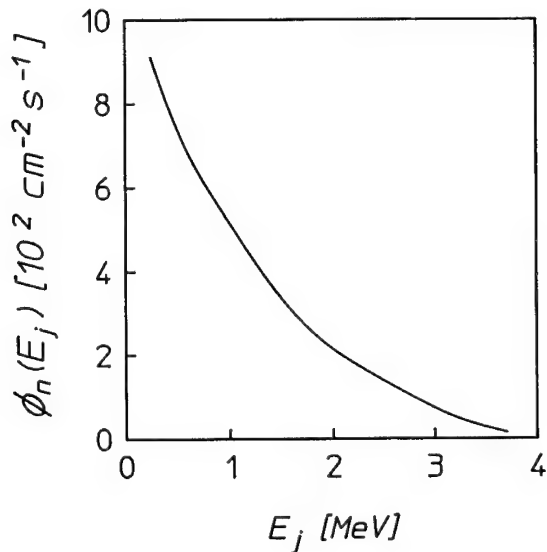


Fig. 5. Total flux of neutrons, $\phi_n(E_j)$ having energies greater than E_j calculated for the irradiation environment having the most possible neutron sources, the CLINAC 1800 6 MeV medical linac. The flux corresponds to a position of 65 cm from the bremsstrahlung converter, the location at which isomeric samples were irradiated in the photoexcitation study of ref. [8].

tions available for many isomers studied with the CLINAC 1800, it was possible to compare the expected isomeric yield due to neutrons and the measured yield. The results are shown in table 2. In the worst case, the calculated flux produced 5.4% of the yield for $^{79}\text{Br}^m$ and in typical instances much less than 1%.

3. Measurements

Notwithstanding the lack of a credible rationale for concern about the possible contamination of yields by (n, n') reactions, measurements were made to determine the fast neutron flux at the position of the irradiated targets. Thermal and epithermal neutron fluxes were also measured.

3.1. FAST NEUTRONS

The measurement of fluxes of neutrons as small as that estimated in the previous section is difficult in the presence of the intense bremsstrahlung used in most (γ, γ') studies. Neutron detectors based on $^{10}\text{Be}(n, \alpha)$ or $^3\text{He}(n, p)$ reactions provide some

Table 2

Comparison of measured activations [2,8], A_γ , attributed to (γ, γ') reactions with those due to the generous estimate of the flux of fast neutrons by (n, n') reactions, $A_{(n, n')}$. The neutron activations were determined from the flux from fig. 5 and measured cross sections available from the literature. The most limiting value of cross section known was used and its type indicated: el – elastic; i – inelastic for isotope; fi – inelastic in isotope, averaged over a fission spectrum; ie – inelastic in element. The fraction of the total activation due to the estimate of fast neutrons is given by $f_{(n, n')}$.

Isomer	A_γ (10^{-20} s $^{-1}$)	σ_{lim} (b)	Type [ref.]	$A_{(n, n')}$ (10^{-20} s $^{-1}$)	$f_{(n, n')}$ (%)
^{77}Se	43.7	0.73	fi [25]	0.066	0.15
^{79}Br	14.2	7.5	el [26]	0.77	5.4
^{87}Sr	5.6	0.11	fi [25]	0.010	0.18
^{89}Y	1.48	0.2	i [27]	0.015	1.0
^{111}Cd	18.5	0.23	fi [25]	0.020	0.11
^{113}In	26.8	0.047	i [28]	0.54	2.0
^{115}In	5.16	0.38	i [29]	0.0045	0.088
^{123}Te	45.4	6	el [26]	0.050	1.1
^{135}Ba	36.5	7.3	el [26]	0.18	0.48
^{137}Ba	11.9	0.66	i [30]	0.061	0.51
^{167}Er	242	9	el [26]	0.80	0.33
^{179}Hf	174	0.4	i [31]	0.035	0.02
^{180}Ta	136	1.8	ie [32]	0.082	0.06
^{191}Ir	81.3	10.3	el [26]	0.33	0.40
^{195}Pt	117	0.68	ie [32]	0.059	0.05
^{197}Au	55.3	1.3	i [32]	0.077	0.14
^{199}Hg	10.4	0.14	i [33]	0.013	0.12

discrimination against photons, but at a level insufficient for this work. Boron detectors, more robust than helium proportional counters, can operate in the presence of X-ray fluxes providing as much as 1 krad h⁻¹. However, this is far below typical irradiation levels for isomeric activation studies at dose rates of greater than 300 rad min⁻¹. In addition, ¹⁰B and ³He detectors are sensitive to thermal rather than fast neutrons, and so a low-Z moderator such as carbon or hydrogen must be employed to insure thermalization of incident neutron fluxes. Of course, in an intense photon bath those moderators may produce additional neutrons, perturbing the measurement.

A common approach to obtaining accurate determinations of fast neutron fluxes employs activation foils. The most sensitive materials [19,20] rely on (n, n') or (n,f) reactions and the yield of their daughters indicates the numbers of incident neutrons having energies greater than specific thresholds. However, for those nuclides (γ, γ') reactions may also produce significant yields, as well as (γ, f) reactions at higher photon energies. Foils can be selected which have less sensitivity to neutrons because of reduced interaction cross sections, but whose daughters cannot be produced by photon reactions to contaminate the results. Using several of those neutron activation foils, measurements were made to determine the numbers of fast neutrons from the CLINAC 1800.

Activation foils serve as threshold detectors and have been commonly employed as a standard means of neutron flux measurements. The techniques are well documented [13] and consist of exposing a set of thin foils to the neutron flux in question, after which they are removed to a gamma spectrometer for the determination of reaction yields from daughter fluorescence. Typically the principle reactions are (n, n'), (n,p), (n,2n) and (n,np) and materials may be chosen to best match the thresholds for those processes in given isotopes with irradiation parameters like the maximum expected neutron energy. For any specific reaction, the number of daughter nuclei produced per second during an exposure, N_d is given by

$$N_d = N_T \int_{E_t}^{\infty} \sigma_r(E) \frac{d\phi_n}{dE}(E) dE, \quad (6)$$

where N_T is the number of target nuclei which sample the neutron flux, $\sigma_r(E)$ is the reaction cross section, E_t is the threshold energy for the reaction, and $d\phi_n(E)/dE$ is the spectral density of fast neutrons of energy E . In practice, eq. (6) is reduced to

$$N_d = N_T \sigma_{\text{eff}} \int_{E_t}^{\infty} \frac{d\phi_n}{dE}(E) dE, \quad (7)$$

where σ_{eff} is the effective reaction cross section [13]. The neutron spectrum is determined by measuring the yields of different reactions having various thresholds. Known values of effective cross sections are used and the spectrum is deconvolved from a set of activation results. Numerical procedures are usually used to accom-

plish this unfolding [21]. In the present work the total flux of fast neutrons rather than their spectrum was of primary concern.

An experiment was conducted in which foils containing elemental Ti and Ni were irradiated with the CLINAC 1800 6 MeV linac. Those materials were chosen for several reasons to match experimental conditions. First, no naturally occurring isotopes of these elements possess isomers, so (γ, γ') reactions could not produce long-lived fluorescence which might interfere with neutron-produced signatures. Next, the endpoint of the linac made (γ, n) and $(n, 2n)$ reactions energetically inaccessible. Finally, the thresholds for (n, p) reactions were well-suited for examining this energy range. Table 3 summarizes the relevant parameters for the reactions used in this study.

The Ti and Ni foils were in the form of disks having radii of 2.54 and 0.65 cm and thicknesses of 0.005 and 0.025 cm, respectively. Two identical disks of each element were employed, with one disk bare and the other encased in a cadmium cover to suppress possible activation due to thermal neutrons. All four disks were placed at a distance of 65 cm from the bremsstrahlung converter in such a way as to not shield each other, and were irradiated simultaneously. Following a one-hour exposure, the foils were removed to a HPGe spectrometer to determine the daughter yields from pulse-height analyses.

In typical spectroscopic measurements, N_d would be obtained from the counts observed in full-energy peaks of daughter signatures after correcting for the durations of transport and counting, transparency of the samples to emission of fluorescence, gamma-ray intensity and detection efficiency. However, spectra evidenced no peaks observable above the level of natural background in the well-shielded detector so a direct deconvolution could not be made. Instead, an upper bound for the total flux of fast neutrons was determined by calculating the maximum signal which could have been hidden in statistical fluctuations of the background. For this a level of 2σ was used as computed over the expected FWHM for the signature-line position and the detector resolution. An upper bound on the total flux of fast neutrons was therefore obtained, as shown in table 4. Also shown there are values of σ_{eff} and E_t .

Table 3

Parameters for accessible reactions for naturally abundant isotopes present in elemental Ti and Ni foils in natural abundance used to measure the flux of fast neutrons [9].

Reaction	Parent abundance (%)	Daughter halflife (d)	Signature photon energy (keV)
$^{46}\text{Ti}(n, p)^{46}\text{Sc}$	8.0	83.83	889.25 1120.51
$^{47}\text{Ti}(n, p)^{47}\text{Sc}$	7.3	3.34	159.38
$^{58}\text{Ni}(n, p)^{58}\text{Co}$	68.077	70.92	810.79

Table 4

Upper bounds calculated from null measurements obtained with Ti and Ni activation foils, with and without cadmium covers. Literature values of parameters employed in eq. (7) are also given [26].

Foil	Daughter	σ_{eff} (mb)	E_t (MeV)	$\phi_n (10^4 \text{ cm}^{-2}\text{s}^{-1})$	
				without Cd	with Cd
Ti	^{46}Sc	2.75	3.0	6.8	57.5
	^{47}Sc	21.4	2.2	5.9	21.5
Ni	^{58}Co	109	2.8	2.8	1.7

The least upper bound on the flux of fast neutrons was obtained to be $1.7 \times 10^4 \text{ cm}^{-2}\text{s}^{-1}$ above 2.8 MeV from the null measurement of the (n,p) reaction on ^{58}Ni in a cadmium cover. This value is a factor of 16 larger than that corresponding to fig. 5 and by scaling accordingly it is possible to estimate the total fast neutron flux to be less than $1.4 \times 10^5 \text{ cm}^{-2}\text{s}^{-1}$. This limit is two orders-of-magnitude larger than the values calculated in the previous section, but still too small to indicate that there were large unrecognized neutron sources. Even in the worse case, this amount of fast neutrons can produce only a relatively small contribution to the production of isomers through (n,n') reactions which might contaminate yields attributed to photoexcitation. For the nuclide ^{115}In , the fractional isomeric yield produced by exposure to the CLINAC 1800 was $5.16 \times 10^{-19} \text{ s}^{-1}$. The literature value for the inelastic scattering cross section is 380 mb for which the upper bound on the flux of fast neutrons gives no more than 12% of the measured activation of the isomer. Of course, the fast neutron flux may well have been much smaller than this upper bound.

The possibility of fast-neutron contributions was further examined by covering samples used in the (γ, γ') studies with a planchette containing heavy water, D_2O to artificially enhance the prevalence of photodissociation neutrons. No increase was observed in isomeric yields.

3.2. THERMAL AND EPITHERMAL NEUTRONS

Fluxes of thermal and epithermal neutrons were measured by a standard activation procedure. Again thin foils were exposed, but those materials were chosen to have large cross sections for neutron capture in the thermal and resonance regions instead of being sensitive to fast neutrons through (n,n') reactions. Foils were exposed in pairs, with one bare and the other being enclosed as before in a cadmium cover. Cadmium possesses a large thermal neutron capture cross section so that a cover having a thickness of 0.076 cm effectively shields enclosed materials from thermal fluxes. The yields from (n, γ) reactions in the bare and shielded foils therefore differ, making it possible to obtain both thermal and epithermal neutron

fluxes. However, this method requires more than taking a simple difference between the yields and a number of correction factors must be included due to the Cd cover.

The approach used here is given by the ASTM standard [22] and references contained therein. The flux of thermal neutrons, ϕ_{th} is related to the "saturated" activities of the bare foil, A_s and the shielded foil, $A_{s,Cd}$ according to

$$\phi_{th} = \frac{1}{g\sigma_0 G_{th}} \left[A_s - A_{s,Cd} F_{Cd} \left(1 + \frac{g\sigma_0 f_1}{G_{res} I_0} + \frac{\sigma_0 w'}{G_{res} I_0} \right) \right], \quad (8)$$

where σ_0 is the cross section for thermal neutron capture and I_0 is the resonance integral. The saturated activities are obtained from the measurements by

$$A_s = \frac{N_{e,s}}{N_T T} \quad \text{and} \quad A_{s,Cd} = \frac{N_{e,s,Cd}}{N_T T}. \quad (9)$$

In this equation, $N_{e,s}$ and $N_{e,s,Cd}$ are the measured yields of daughter nuclei produced by (n, γ) reactions, N_T is the number of target nuclei of the neutron capture parent, and T is the irradiation time. The epithermal neutron flux is found from

$$\phi_{epi} = \frac{A_{s,Cd} F_{Cd}}{I_0}. \quad (10)$$

The factors appearing in eqs. (8) and (10) represent corrections which take into account deviations from the ideal of the capture cross section of cadmium. In general a determination of the total fluxes of thermal and epithermal neutrons requires a detailed a priori knowledge of their spectral distributions. In most instances this information is not available, but the problem is simplified when a detector material exhibits a cross section that varies inversely with incident neutron velocity, v . This would mean that the reaction rates are simply proportional to the total flux of neutrons regardless of the spectral shape. In practice this ideal situation does not occur, but small deviations as in the case of cadmium can be accounted for by introducing the factor g which is tabulated in the literature [22]. The quantities f_1 and w' are used to correct for the amount of activation of shielded samples due to "epithermal" neutrons with energies between their nominal lower bound of 0.13 eV at room temperature, and the cutoff energy of the cadmium cross section at about 0.5 eV. This is accounted for by f_1 assuming an ideal $1/v$ capture cross section while w' corrects for the small deviation from that form. The factors G_{th} and G_{res} are introduced to include self-shielding effects in thick foils. Finally, the additional parameter F_{Cd} is used when the sample foil material is indium [23]. Indium is well-suited for thermal and epithermal neutron measurements due to large capture cross sections for the relatively abundant isotope ^{115}In and a convenient lifetime, 54.15 min of its $^{116}\text{In}^m(n, \gamma)$ daughter. However, the principal capture resonance for ^{115}In is centered at 1.44 eV and its low-energy tail overlaps significantly with the cadmium cutoff at 0.5 eV. As a consequence, the observed yield in shielded samples is reduced from the value which would otherwise occur from epithermal neutron capture. The

factor F_{Cd} scales the shielded activity to compensate for this effect. Despite the number of correction factors included in eqs. (8) and (10), the method is standardized and well-documented with values for those parameters in the literature [22,23].

An experiment was performed to investigate the thermal and epithermal neutron fluxes produced in the environment of the CLINAC 1800. Due to constraints imposed by concomitant goals, the activation foils were irradiated at a distance of 100 cm from the bremsstrahlung converter rather than the 65 cm used previously. Two 0.0254 cm thick indium disks with diameters of 5.08 cm were simultaneously irradiated for 40 min, with one foil bare and the other shielded by a 0.076 cm thick cadmium cover. The cover was formed from two 6.35 cm diameter disks which were stamped in order to create a recessed cavity slightly larger than the dimensions of the indium foils. This insured complete enclosure of the shielded indium sample. Following the irradiation, the foils were transferred to a NaI(Tl) spectrometer to detect signature gamma fluorescence from $^{116}\text{In}^m$.

The saturated activities were determined from the counts in full-energy peaks observed in pulse-height spectra employing the usual corrections for fluorescence lifetime, etc. These were found to be $A_s = (4.6 \pm 0.03) \times 10^{-21} \text{ s}^{-1}$ and $A_{s,Cd} = (1.97 \pm 0.02) \times 10^{-21} \text{ s}^{-1}$. Literature values for f_1 , g , w' , G_{th} and G_{res} were found in ref. [22], and with self-shielding factors differing significantly from 1 because the indium samples were not "thin". For the production of $^{116}\text{In}^m$, the capture cross section and resonance integral are $\sigma_0 = 161 \text{ b}$ and $I_0 = 2593 \text{ b}$. Since the samples presented an areal density of 177 mg cm^{-2} , their thicknesses were larger than the mean-free-path for thermal neutrons. The factor F_{Cd} was estimated [23] from the thickness of the cadmium filter. Using eqs. (8) and (10), the thermal and epithermal neutron fluxes were then calculated to be

$$\phi_{th} = 12 \text{ cm}^{-2}\text{s}^{-1} \quad \text{and} \quad \phi_{epi} = 6 \text{ cm}^{-2}\text{s}^{-1}. \quad (11)$$

The thermal and epithermal neutron fluxes of eq. (11) may be used to estimate the magnitude of contamination of isomeric production otherwise attributed to (γ, γ') reactions. This requires not only taking into account the positions at which samples were exposed, but also careful consideration of the irradiation geometry in which the neutron fluxes were measured. For that study, the CLINAC 1800 was configured to produce bremsstrahlung in a horizontal direction such that the X-rays reached a concrete wall at a distance of 4 m. In the photoexcitation experiments conducted with this device, a vertical configuration was employed with the bremsstrahlung reaching the concrete floor at 2.29 m. An estimated scaling factor was therefore necessary to account for the possibility that the neutrons originated in water within the concrete rather than in the Be. In this unlikely case the neutron fluxes would have been greater for the photoexcitation experiments than for the activation measurement. In the event that the primary source of neutrons was instead the linac head assembly, this upward scaling would be unnecessary

although providing a generous upper bound on the neutron contamination of isomeric yields.

For either configuration, the emission of neutrons from concrete is a secondary event in which their production is proportional to the inverse of the distance from bremsstrahlung converter to wall or floor. Then the neutron flux incident on isomeric targets would vary inversely with the distance from wall or floor to the sample position. This is similar to the traditional radar problem and using the known dimensions it is straightforward to find that the vertical configuration presents the possibility of thermal and epithermal neutron fluxes about a factor of 10 greater than those given in eq. (11).

Table 5 summarizes isomeric nuclides studied with the CLINAC 1800 as part of the large experimental series using different accelerators. In several instances, no parent is naturally occurring from which the isomer could be produced by (*n*, γ) reactions. Capture cross section and resonance integral values for parent isotopes were used to determine the amounts of fractional isomeric yield due to thermal or epithermal neutrons. Those values are given for comparison with the total meas-

Table 5

Total fractional isomeric yields attributed to photons, A_γ [2,8] as compared with upper bounds on the activations, A_{th} and A_{epi} resulting from the measured fluxes of thermal and epithermal neutrons. The latter values included the estimated scale factor to account for the possibility of enhanced neutron production in the vertical CLINAC 1800 configuration. Capture cross sections and resonance integrals for production of the isomers are given where available [34], and when only total values to isomer and ground state are known this is designated by *. Upper bounds on the contributions from all thermal and epithermal neutrons are given by values of f_n .

Isomer	(<i>n</i> , γ) Parent and abundance (%)	A_γ (10^{-20} s^{-1})	σ_{th} (b)	A_{th} (10^{-20} s^{-1})	σ_{epi} (b)	A_{epi} (10^{-20} s^{-1})	f_n (%)
⁷⁷ Se	⁷⁶ Se 9.00	43.7	21	0.25	17	0.1	0.8
⁷⁹ Br	None	14.2		0		0	0
⁸⁷ Sr	⁸⁶ Sr 9.86	5.6	0.84	0.01	5	0.03	0.7
⁸⁹ Y	None	1.48		0		0	0
¹¹¹ Cd	¹¹⁰ Cd 12.49	18.5	0.10	0.001	2	0.012	0.066
¹¹³ In	None	26.8		0		0	0
¹¹⁵ In	None	5.16		0		0	0
¹²³ Te	¹²² Te 2.60	45.4	3 *	0.036	80 *	0.48	1.08
¹³⁵ Ba	¹³⁴ Ba 2.42	36.5	0.16	0.0019	20 *	0.12	0.305
¹³⁷ Ba	¹³⁶ Ba 7.85	11.9	0.01	0.00012	1.6 *	0.0096	0.081
¹⁶⁷ Er	¹⁶⁶ Er 33.60	242	15.0	0.18	100 *	0.6	0.27
¹⁷⁹ Hf	¹⁷⁸ Hf 27.30	174	50.0	0.6	1900 *	11	6.3
¹⁸⁰ Ta	None	136		0		0	0
¹⁹¹ Ir	None	81.3		0		0	0
¹⁹⁵ Pt	¹⁹⁴ Pt 32.90	117	0.10	0.0012	4 *	0.024	0.021
¹⁹⁷ Au	None	55.3		0		0	0
¹⁹⁹ Hg	10.02	10.4	1.92	0.00024	70 *	0.42	4.002

ured activation, A_γ . Also indicated are the limits, expressed in percents, of the neutron contamination of the photoexcitation measurements. In no case is contribution from thermal and epithermal neutrons greater than 6.3% of the isomeric yield, and usual values are less than 1%. This level of contamination is shown graphically in fig. 6.

4. Conclusions

The theoretical expectations of negligible fluxes of thermal, epithermal and fast neutrons were confirmed by direct experimental measurements using standard techniques. Although the spectral distribution of neutrons was not determined in this work, the total neutron fluxes produced at most only relatively small contributions to the total yield of isomers. The contamination of (γ, γ') reaction yields by (n, n') reactions was assuredly undetectable in comparison to possible contributions from (n, γ) reactions which could have been as large as 1% in typical cases and 6% in the worst case where the CLINAC 1800 operated in 6 MeV mode was used. This is because the head of this linac contains Be and cooling water which serve as neutron sources, but in relatively small amounts. In contrast, the Texas-X was designed to have no cooling water and little beryllium exposed to X-rays in the linac head, while the 4 MeV medical linac had only cooling water. The S-DALINAC, DNA/PITHON and DNA/Aurora used in the majority of experiments had neither cooling water nor beryllium exposed to X-rays. These results were consistent with the successes in reproducing the absolute measurements of calibration (γ, γ') reac-

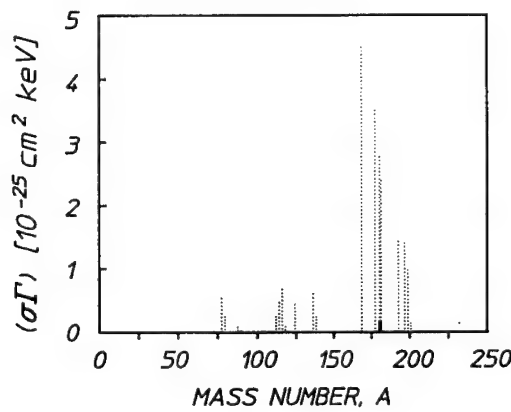


Fig. 6. Integrated cross sections taken from fig. 2 and which were attributed to photons in the study of ref. [8] are given as dotted lines. The heavy line indicates the part of the integrated cross section for excitation of $^{179}\text{Hf}^m$ which should have been attributed to neutrons rather than photons (6.3%). The remaining 93.7% of the integrated cross section was indeed due solely to photons through (γ, γ') reactions. No solid lines are shown for the other isotopes as their neutron contributions were smaller than the graphical resolution.

tions known from the literature [5,6] with so many different accelerators having such a variety of windows, cooling geometries, and physical enclosures.

References

- [1] C.B. Collins, F.W. Lee, D.M. Shemwell and B.D. DePaola, *J. Appl. Phys.* 53 (1982) 4645.
- [2] C.B. Collins and J.J. Carroll, these proceedings (1st Int. Gamma-Ray Laser Worksh., 1995), *Hyp. Int.* 107 (1997) 3, and references therein.
- [3] C.B. Collins, C.D. Eberhard, J.W. Glesener and J.A. Anderson, *Phys. Rev. C* 37 (1988) 2267.
- [4] C.B. Collins, J.J. Carroll, T.W. Sinor, M.J. Byrd, D.G. Richmond, K.N. Taylor, M. Huber, N. Huxel, P. von Neumann-Cosel, A. Richter, C. Spieler and W. Ziegler, *Phys. Rev. C* 42 (1990) 1813.
- [5] J.J. Carroll, D.G. Richmond, T.W. Sinor, K.N. Taylor, C. Hong, J.D. Standifird, C.B. Collins, N. Huxel, P. von Neumann-Cosel and A. Richter, *Rev. Sci. Instrum.* 64 (1993) 2298.
- [6] P. von Neumann-Cosel, N. Huxel, A. Richter, C. Spieler, J.J. Carroll and C.B. Collins, *Nucl. Instrum. Meth. A* 338 (1994) 425.
- [7] J.J. Carroll, T.W. Sinor, D.G. Richmond, K.N. Taylor, C.B. Collins, M. Huber, H. Huxel, P. von Neumann-Cosel, A. Richter, C. Spieler and W. Ziegler, *Phys. Rev. C* 43 (1991) 897.
- [8] J.J. Carroll, M.J. Byrd, D.G. Richmond, T.W. Sinor, K.N. Taylor, W.L. Hodge, Y. Paiss, C.D. Eberhard, J.A. Anderson, C.B. Collins, E.C. Scarbrough, P.P. Antich, F.J. Agee, D. Davis, G.A. Huttlin, K.G. Kerris, M.S. Litz and D.A. Whittaker, *Phys. Rev. C* 43 (1991) 1238.
- [9] E. Browne and R.B. Firestone, *Table of Radioactive Isotopes* (Wiley, New York, 1986).
- [10] J.M. Eisenberg and W. Greiner, eds., *Nuclear Theory, Vol. 2: Excitation Mechanisms of the Nucleus, Electromagnetic and Weak Interactions*, parts I, II (North Holland, Amsterdam, 1970).
- [11] E.C. Booth and J. Brownson, *Nucl. Phys. A* 98 (1967) 529.
- [12] *Evaluated Nuclear Structure Data File* (Brookhaven National Laboratory, Upton, New York, 1986).
- [13] K.H. Beckurts and K. Wirtz, *Neutron Physics*, transl. by L. Dresner (Springer, New York, 1964).
- [14] G.F. Knoll, *Radiation Detection and Measurement*, 1st ed. (Wiley, New York, 1979).
- [15] J.A. Anderson, C.D. Eberhard, J.J. Carroll, M.J. Byrd and C.B. Collins, in: *Center for Quantum Electronics Annual Report – Fy 1988* (unpublished), and references therein.
- [16] K. Fukuda, *Nucl. Phys. A* 156 (1970) 10.
- [17] J.W. Jury, B.L. Berman, D.D. Faul, P. Meyer and J.G. Woodworth, *Phys. Rev. C* 21 (1980) 503.
- [18] T. Lauritsen and F. Ajzenberg-Selove, *Nucl. Phys.* 78 (1966) 1.
- [19] Activation Foil Manual (distributed by Reactor Experiments, Inc., 1965), and references therein.
- [20] *ASTM Standard Method for Determining Neutron Flux, Fluence, and Spectra by Radioactivation Techniques*, Publication E 261-77 (American Society for Testing and Materials, Philadelphia, 1987), and references therein.
- [21] *Foil Activation Data Unfolding Code (FATDUD)*, RSIC Computer Code Collection (Radiation Shielding Information Center, Oak Ridge National Laboratory).
- [22] *ASTM Standard Method for Determining Thermal Neutron Reaction and Fluence Rates by Radioactivation Techniques*, Publication E262-86 (American Society for Testing and Materials, Philadelphia, 1987), and references therein.
- [23] C.W. Tittle, *Nucleonics* 8 (1951) 6.

- [24] J.A. Harvey and D.J. Hughes, in: *American Institute of Physics Handbook*, ed. D.E. Gray (McGraw-Hill, New York, 1963).
- [25] A. Calamand, in: *Handbook on Nuclear Activation Cross Sections*, IAEA Techn. Rep. Ser. 156 (IAEA, Vienna, 1974) pp. 273–324.
- [26] D.I. Garber and R.R. Kenney, eds., *Neutron Cross Sections, Vol. II. Curves* Brookhaven Nat. Lab. Publ. BNL 325 (National Neutron Cross Section Center, Brookhaven National Laboratory, 1976).
- [27] E. Ramström, Nucl. Phys. A 315 (1979) 143.
- [28] H.A. Grench and H.O. Menlove, Phys. Rev. 165 (1968) 165.
- [29] H.C. Martin, B.C. Diven and R.F. Taschek, Phys. Rev. 93 (1954) 199.
- [30] C.P. Swan and F.R. Metzger, Phys. Rev. 100 (1955) 1329.
- [31] G.L. Sherwood, A.B. Smith and J.F. Whalen, Nucl. Sci. Eng. 39 (1970) 67.
- [32] J.B. Guernsey and A. Wattenberg, Phys. Rev. 101 (1956) 1516.
- [33] K. Sakurai and I. Kondo, Nucl. Instrum. Meth. 187 (1981) 649.
- [34] F.W. Walker, J.R. Parrington and F. Feiner, eds., *Chart of the Nuclides*, 14th ed. (General Electric Company, San Jose, CA, 1989).

Excitation of the high-spin ^{180}Hf isomer and de-excitation of the ^{180}Ta isomer in (γ, γ') reactions

A.G. Belov, Yu.P. Gangrsky, A.P. Tonchev and P. Zuzaan

Joint Institute for Nuclear Research, Dubna, Russia

The reaction mechanism of excitation and de-excitation of the high-spin isomers ^{180}Hf ($J = 8^-$) and ^{180}Ta ($J = 9^-$) in inelastic gamma-quanta scattering was investigated. An anomalously large integral cross section and isomeric ratio for ^{180}Ta in comparison to ^{180}Hf were obtained. Level properties influencing these relations are discussed.

1. Introduction

Photonuclear reactions (PNR) at low and mean γ -quanta energies are an important source of information on the atomic nuclei structure. One of the γ -quanta research directions consists of the measurement of the nuclear production probabilities for different quantum states. These investigations will be the most effective if the studied states are in isomeric relation with sufficiently large half-lives in order to separate the irradiation processes and measurements in time.

The main interest in the (γ, γ') reaction investigations is connected to the following facts. First, since there are no Coulomb barrier and binding energy for the γ -quanta, one can obtain excited nuclei both in regions located above and below the nuclear threshold. Second, the momentum transferred to the nucleus by γ -quanta does not vary with the energy increase (it is $1\hbar$ for dipolar absorption and $2\hbar$ for quadrupolar absorption).

This characteristic property of the high-spin population is responsible for the fact that the Isomeric Ratio (IR) is very sensitive to the level density parameter and radiative transition possibility. In deformed nuclei the reason of isomerism and γ -quanta prohibition may consist not only in the large differences between the spins of the isomeric and ground state but also in the differences between their projections on the symmetry axis (K quantum numbers).

The aim of the present paper is to investigate both the reaction mechanism leading to excitation and de-excitation of high-spin isomers in the inelastic γ -scattering and the properties of the levels implied in these processes. As objects of investigation, the ^{180}Hf and ^{180}Ta nuclei have been chosen. These nuclei have identical mass numbers and the same spin difference between the ground and isomeric states ($\Delta I = 8$). At the same time, their level structure is quite different (viz., the ^{180}Hf

nucleus is odd-even while ^{180}Ta is odd-odd exhibiting a great number of high-spin low-lying states.

2. Level properties of ^{180}Hf and ^{180}Ta

The level and radioactive decay schemes for ^{180}Hf and ^{180}Ta are presented in fig. 1 [1]. The ^{180}Hf nucleus presents an isomeric level with $I^\pi = 8^-$ and the isomerism is due to the K quantum number hindrance (K is the spin projection on the nuclear symmetry axis) for γ -transitions on the states of the $K = 0$ ground state rotational band. The isomeric state is a two-quasiparticle one, arising from the decoupling of two protons and has the p[504] p[514] configuration. The ^{180}Hf isomeric state decays through a weak beta-decay branch (0.3%) to ^{180}Ta isomeric state ($I^\pi = 9^-$) with the p[514] n[624] configuration. Due to the large difference between the spins of the isomeric and ground states ($\Delta I = 8$) and to the absence of levels located below the isomeric state, with close spin values, the ^{180}Ta nucleus ($T_{1/2} > 10^{15}$ y) is practically stable in its isomeric state. It is present in the natural Ta-isotope mixture in very small amounts (0.012% or 4×10^{17} atoms in 1 g of Ta).

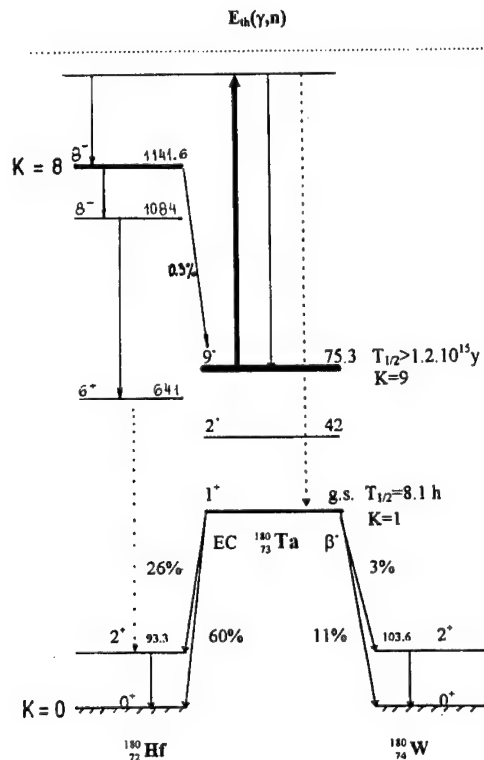


Fig. 1. Decay scheme of ^{180}Hf and ^{180}Ta .

This opens unique possibilities to carry out different experiments using targets consisting of high-spin nuclei, for instance a natural Ta target or a ^{180}Ta enriched one. One of these experiments investigates the de-excitation of the ^{180}Ta isomer using γ -quanta inelastic scattering. Our paper presents the results of the experiment. During this process the isomer captures a γ quantum and subsequently de-excites to the ground state by means of a γ -cascade, while bypassing the isomeric state. This state ($I^\pi = 1^+$), as in fig. 1, decays to ^{180}Hf (K-capture) and to ^{180}W (β -decay) with a half-life convenient to measure (8.1 h).

It is quite probable that such a genetic relation in the $A = 180$ mass number decay chain of Hf-Ta-W plays an important role in nucleosynthesis. In the strong fields of neutron and γ -radiation, which existed, this relation must have expressed itself not only between the ground states but also between the isomeric states of the quoted nuclei. Connected to it, the cross section measurements for the ^{180}Hf isomer excitation and for the ^{180}Ta isomer de-excitation are also interesting for astrophysics. These cross-section measurements will allow to obtain new information necessary for calculating the abundance of these isotopes in nature and will also help in drawing conclusions about the conditions in which nucleosynthesis has taken place (matter density, temperature).

3. Experiment and data analysis

The yields of the investigated isotopes in the ground (^{180}Ta) and isomeric (^{180}Hf) states, were measured using the MT-25 microtron extracted beam at the Flerov Laboratory for Nuclear Reactions, JINR. The microtron description and its main characteristics are presented in ref. [2]. Electron energy variation has been effectuated in two days: over a wide range – orbit-to-orbit transition, in an energy range up to 1.8 MeV – with magnetic field variation. The cooled device made of a 2 mm thickness tungsten disk, behind which a 30 mm aluminium electron absorber was placed, served as a bremsstrahlung target. The tungsten target serves as a catcher for the electrons passing through it during each irradiation and they were measured by using an electrical charge integrator. Electron energy has been determined by measuring the microtron magnetic field using the nuclear magnetic resonance, then measuring the accelerating electrical field frequency. Instability of electron energy during the experiment did not exceed 50 keV.

The Ta (metallic disk 100 μm thick) and Hf (enriched isotopes 99.3%) samples were irradiated with incident energy below the neutron binding energy. The photo-excitation of In served as a monitor reaction (its cross section is very well known [3–6]). The experimental data on the yield ratios for two gamma energies are presented in table 1.

The residual activity of the irradiated samples has been measured with a 60 cm^3 volume and 3 keV resolution (for the 1332 keV ^{60}Co line) Ge(Li) detector. The detector efficiency was determined by a set of OSGI standard samples.

Table 1

The yields of the $^{180\text{m}}\text{Hf}$ isomer and ^{180}Ta ground state related to the yield of the $^{115\text{m}}\text{In}$ isomer

E_0 (MeV)	$Y(^{180\text{m}}\text{Hf})/Y(^{115\text{m}}\text{In}) \times 10^{-4}$	$Y(^{180}\text{Ta})/Y(^{115\text{m}}\text{In})$	$\sigma_{\text{int}}(^{115\text{m}}\text{In})$ (mb keV) [6]
6.0	0.02(1)	< 1	1200
6.5	0.07(2)	5.0(1.5)	2100
7.0	0.17(4)	5.0(1.2)	3200
7.5	0.35(6)	42(8)	4400
8.0	0.36(6)	1600(100)	5700

Usually, in the experiments performed, the accelerated electrons current was 20 μA , the irradiation time was 5 h and a sufficiently long measurement time was employed – in order to collect the necessary count statistics (as a rule, it consists of some thousands of pulses in the measured γ -line peak), see fig. 2.

4. Discussion

The investigation of the (γ, γ') reaction in the low-energy range ($E_\gamma < 6$ MeV) has shown that the main role in photo-absorption, and the subsequent isomers population, is played by a relatively small number of activation states with large partial Γ_i width [8,9]. For some nuclei, including ^{180}Ta , the integral excitation cross section for these states was found to be very large [10,11]. The large cross-section

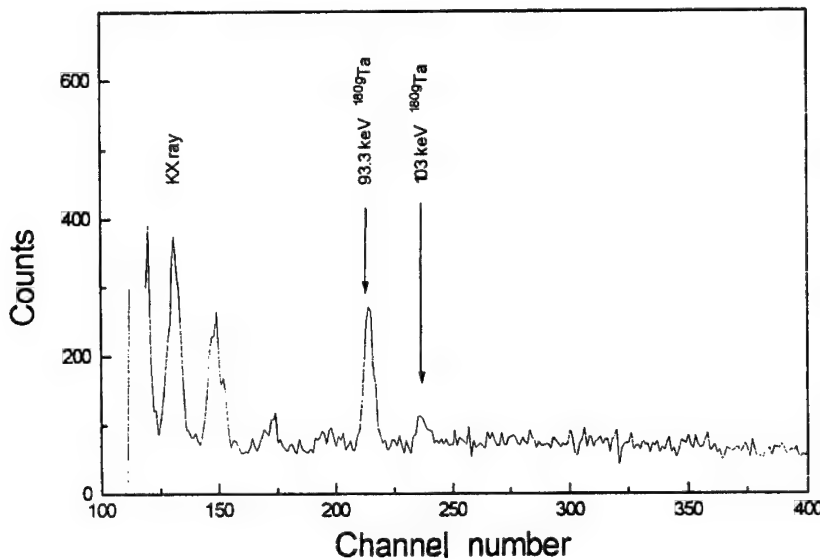


Fig. 2. A γ -spectrum of $^{\text{nat}}\text{Ta}$ produced after irradiation with $E = 7$ MeV electrons.

values may be connected with the following factors: large number of activation state, their widths and the transition probability to the isomer state (the isomeric ratio). The properties of these states are scarcely investigated, making it difficult to judge the importance of any of the above-mentioned factors.

A more definite conclusion can be drawn on the basis of cross-section measurements, for photo-excitation of isomers in the neutron binding energy region. For these energies, the level properties (density, total and partial widths) are derived from neutron resonance studies. The results we presented have been obtained for this energy region.

The fast rise of the isomeric yields with the γ -quanta energy increase and the remarkable overrun above the $E_\gamma < 6$ MeV values, obtained in refs. [10,11], show that the main contribution to the integral isomer excitation cross section comes from the most superior laying states, due to their high density. In this case, the isomeric yield ratio correspond to the ratio of the integral cross sections. Hence on the basis of the measured isomeric yield ratios and the known σ_{int} value for the $^{115}\text{In}(\gamma, \gamma')^{115\text{m}}\text{In}$ reaction (table 1), we can obtain the integral cross section values for the ^{180}Hf isomer excitation and the ^{180}Ta -isomer de-excitation. The values obtained for σ_{int} are shown in table 2. One can see the very large (greater by a 10^4 factor) difference in the reaction cross sections for ^{180}Hf and ^{180}Ta , independent of the fact that the spin difference between the isomeric and ground states is the same ($\Delta I = 8$).

The known state parameters of the ^{115}In , ^{180}Hf and ^{180}Ta nuclei, obtained from neutron resonance systematics [12,13], allow to estimate the total photo-absorption cross sections which consequently enables the determination of the isomeric ratio. In the neutron binding energy region, the cross section for photo-absorption, averaged over a large number of levels, can be expressed as:

$$\sigma = \frac{(2I_i + 1)}{(2I_0 + 1)} \frac{\lambda^2 \Gamma}{8\pi D}, \quad (1)$$

where D is the average distance between levels. Assuming that the investigated nuclei have close values of $\Gamma_i \sim 10^{-2}$ eV and that the D value is taken for one and

Table 2
Integrated cross sections and isomeric ratios for photo-excitation of $^{180\text{m}}\text{Hf}$ and ^{180}Ta

E_0 (MeV)	$^{180\text{m}}\text{Hf}$		^{180}Ta	
	σ_{int} (mb keV)	$(\sigma_m/\sigma_0) \times 10^{-5}$	σ_{int} (mb MeV)	σ_m/σ_0
6.0	0.002(1)	0.010(5)	< 2	
6.5	0.015(5)	0.07(2)	8(3)	0.20(7)
7.0	0.055(9)	0.18(3)	12(4)	0.25(8)
7.5	0.15(3)	0.30(6)		
8.0	0.20(4)	0.32(6)		

the same excitation energy, taking into account the D changes for the spin transitions of excited levels in each nucleus and using relation (1) we can estimate the photo-absorption cross section of the investigated nuclei. These cross sections correspond to the known systematic [15]. The ratio between the cross sections for isomeric excitation (or de-excitation) and the absorption cross sections, obtained using the above-mentioned procedure, integrated over the same energy range, can be considered as isomeric ratios (presented in table 2). Similar to the cross sections case, isomeric ratios differ strongly for ^{180}Hf and ^{180}Ta . The isomeric ratio for the ^{180}Ta de-excitation is practically the same as in the case of isomers excitation when the spin change is not large ($\Delta I = 3-4$). The large integral cross section for $^{180\text{m}}\text{Ta}$ de-excitation makes it an important candidate for the γ -laser.

The observed difference may be the result of the different mechanisms for ^{180}Hf isomer excitation and $^{180\text{m}}\text{Ta}$ isomer de-excitation. Fig. 3 represents the allowed paths of the (γ, γ') reaction for the two nuclei. It is probable that from the excited ^{180}Ta levels with 8^+ , 9^+ and 10^+ spins after the γ -capture, M1 and E2 transitions take place to levels (with close spin values) built on the ^{180}Ta ground state ($I^\pi = 1^+$). The K quantum number hindrance, for these nuclei, may be significantly weakened due to the high level density in the odd-odd nucleus and to the different K values levels mixing. A similar weakening of the K hindrance has been observed, for instance, for transitions between the high-spin levels of the ^{174}Hf nucleus [14]. Such a de-excitation path of the isomer can explain the high isomeric ratio value obtained for the $^{180\text{m}}\text{Ta}(\gamma, \gamma')^{180}\text{Ta}$ reaction, because of the rotational band levels decay is practically effectuated solely to the ground state.

In case of the ^{180}Hf nucleus, this mode of isomer populating is impossible, as from the excited level with $I^\pi = 1^-$ after the γ -capture, the isomer is reached by a

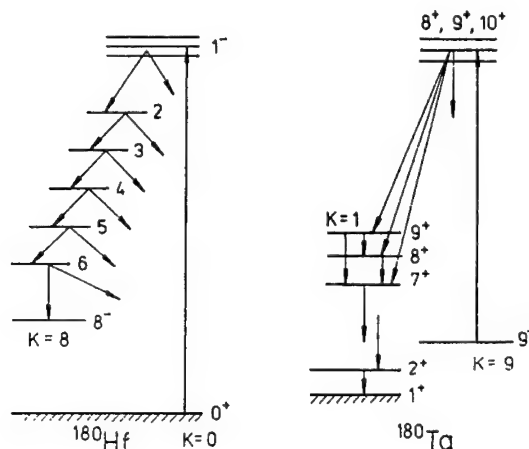


Fig. 3. Excitation scheme of $^{180\text{m}}\text{Hf}$ and de-excitation scheme of $^{180\text{m}}\text{Ta}$ at inelastic scattering of γ quanta.

long γ -cascade competing, at each step, with other decay branches. Such a path of isomer excitation is connected to the small isomeric ratio. The observed isomeric ratio in the $^{180}\text{Hf}(\gamma, \gamma')^{180\text{m}}\text{Hf}$ reaction corresponds to the one calculated on the basis of statistical model using the EMPIRE program [16].

In summary, the above-mentioned experiments demonstrate the large influence of the studied nuclei level structure on the isomer excitation probability (i.e. of the rotational bands existence), rotational transition probabilities, and of the hindrance according to different quantum numbers.

Acknowledgement

Finally, the authors would like to express their gratitude to Profs. Yu.Ts. Oganessian, Yu.E. Pennionzhkevich and N. Balabanov for their interest in the present paper and for useful discussions.

References

- [1] E. Browne, Atomic Data Sheets 71 (1994) 81.
- [2] A.G. Belov, *Workshop on the Application of Microtrons in Nuclear Physics*, Plovdiv, D15-93-80 (1992) 12.
- [3] C.B. Collins, J.A. Anderson, Y. Paiss et al., Phys. Rev. C38 (1988) 1852.
- [4] O.V. Bogdankevich, L.E. Lazareva and F.A. Nicolaev, Zh. Eksp. Teor. Fiz. 31 (1957) 405.
- [5] P. Von Neumann-Cosel, A. Richter, C. Spieler et al., Phys. Lett. B266 (1991) 9.
- [6] W.Y. Warhue and T.G. Williamson, Appl. Radiat. Isot. 37 (1986) 155.
- [7] N.P. Balabanov, A.G. Belov, Yu.P. Gangrsky et al., JINR, E15-93-370 (Dubna, 1993).
- [8] J.J. Carrol, M.J. Byrd, D.G. Richmond et al., Phys. Rev. C43 (1991) 1238.
- [9] J.A. Anderson, M.J. Byrd and C.B. Collins, Phys. Rev. C38 (1988) 2833.
- [10] C.B. Collins, C.D. Eberhard, J.W. Glesener et al., Phys. Rev. C37 (1988) 2267.
- [11] C.B. Collins, J.J. Carrol, T.W. Sinor et al., Phys. Rev. C42 (1990) 1813.
- [12] A.S. Iljinov, M.V. Mebel and N. Bianchi, Nucl. Phys. A543 (1992) 517.
- [13] Yu.V. Sokolov, *Level Density of Atomic Nuclei* (Energoatomizdat, Moscow, 1990).
- [14] G. Sletten, N.J. Gjorup, S. Juutinen et al., Nucl. Phys. A520 (1990) 325.
- [15] M. Herman, A. Marcinkowski, S. Stakiewicz, Comput. Phys. Commun. 33 (1984) 373.
- [16] P.M. Endt and P.A. Smith (eds.), *Nuclear Reactions*, vol. 2 (North-Holland, Amsterdam, 1962).

A mechanism for excitation of metastable levels by (γ, γ') reactions

V.S. Dzjamko, I.V. Sokolyuk and T.M. Zajac

*Uzhgorod State University, Department of Nuclear Physics, 294000, Voloshina st.,
32/142, Uzhgorod, Ukraine*

The analysis of the cross-section of ^{77}Se and ^{87}Sr isomeric states excitation in the (γ, γ') reaction, was carried out using neutron pick-up and stripping reaction results. It allows the shell configurations of the transitions to the activation states to be determined. To check thus obtained conclusions the energies of $J^\pi = 1^-$ excited states for ^{90}Zr and ^{138}Ba were calculated, which are in good agreement with the resonance structure at the γ -quanta elastic scattering in the 5 to 10 MeV energy range.

1. Introduction

Now, interest in the study on excitation of isomeric nuclei in the reaction of γ -quanta inelastically scattering by atomic nuclei has been resumed, mostly by studying the nuclei isomeric states excitation mechanism, which is to a certain degree related to the problem of γ -lasers [1].

The present report is aimed at attracting attention to the possibility of an atomic nucleus to be described by one-nucleon transitions, using the information from the one-nucleon transfer reactions.

We begin with the main regularities, which have been revealed by experimental studies of metastable states excitation in the reaction of γ -quanta inelastically scattering by atomic nuclei within the energy range below 25 MeV.

The study of nuclei isomeric states excitation at the reaction of γ -quanta inelastically scattering by nuclei has been carried out already for about 55 years since the pioneer papers [2,3], and a vast amount of experimental data has been accumulated. A review [4], containing more than 110 references, is devoted mainly to the investigation of the nuclei isomeric states excitation at a γ -quanta energy below 3 MeV. The $A(\gamma, \gamma')A^m$ reaction in the energy range of 4 to 20 MeV was studied in refs. [5–12]. New results of the nuclei isomeric states excitation at the $A(\gamma, \gamma')A^m$ reaction at an energy of 1.5 to 7 MeV in refs. [13–20] and the $A(\gamma, \gamma')A^m$ reaction absolute cross-sections at energies of 4 to 14 MeV [21–27] have been obtained recently. A number of papers [28–31] is devoted to studies of short-lifetime isomeric states excitation at the $A(\gamma, \gamma')A^m$ reaction in the range of energies from 3 to 6 MeV.

In nuclear reactions induced by photons with the energies below 30 MeV, the

main role can be played only by E1, E2 and M1 transitions, while the isomeric transitions mostly belong to the E3, M4, M5 type, evidently implying the low probability of the nucleus isomeric state excitation by γ -quanta (the problem of the nuclei isomeric states direct excitation by the Mössbauer effect is discussed in ref. [32]). Therefore, nucleus isomeric state excitation occurs as follows. A level (usually called the activation level, energetically higher than the metastable one) is excited, for which the probability of the transition to the metastable level is comparable with that of the transition to the ground state. Thus the de-excitation of the activation level results in the isomeric state excitation.

The experimental studies of γ -quanta inelastic scattering by nuclei which have been carried out, can be classified into several groups:

- determination of the principal possibility of the isomers to be activated;
- determination of activation level energies, widths and the activation cross-sections;
- plotting the $A(\gamma, \gamma')A^m$ absolute reaction cross-section versus the γ -quanta energy;
- plotting the $A(\gamma, \gamma')A^m$ reaction integrated cross-section versus the γ -quanta energy;
- applications of the γ -quanta inelastic scattering in γ -activation analysis of materials and γ -radiation monitoring.

It should be noted that the data, obtained from the experiments on the γ -quanta inelastic scattering by nuclei, combined with the results obtained by other techniques for nuclei excitation (e.g. one-nucleon transfer reactions), can give important information on the nucleus energy level structure and the transition multipolarity.

The studies of the nuclei metastable states excitation in (γ, γ') reaction have revealed the metastable states to be populated via the separate activation levels of the nucleus [29–31,33–38], the metastable state excitation cross-sections within the energy range of 3 to 7 MeV being two to three orders of magnitude higher than those below 2.5 MeV. Besides, in ref. [27] the isomeric cross-section ratio in the (γ, γ') reaction (i.e. the ratio of the metastable state excitation cross section in the (γ, γ') reaction to the total photoabsorption cross-section) was noticed to be sensitive to the metastable state shell structure.

The present paper is aimed to perform an analysis of the data on ^{77}Se and ^{87}Sr nuclei metastable states excitation in the energy range below 3 MeV along with the results concerning the single-nucleon transfer reactions for the discussed nuclei.

The problem of the second maximum in $A(\gamma, \gamma')A^m$ reaction cross-sections for ^{89}Y , ^{103}Rh , ^{107}Ag , ^{197}Au , revealed in refs. [6–9] at energies near 20–22 MeV, at present still remains open. The nature of the maximum was discussed in refs. [39,40] in

the framework of the shell model of nuclei and is supposed to be related to the iso-bar-analog resonances, in particular, with 2p–2h excitations.

As noted above, the metastable states in the (γ, γ') reaction are populated via the higher energy excited levels of the nucleus, therefore, the issue on the metastable state population mechanism is reduced to the nuclear levels excitation mechanism.

At the interaction of γ -quanta with atomic nuclei the nuclear level excitation occurs either due to photoabsorption (i.e. via the giant dipole resonance states), or at the γ -quanta inelastic scattering.

Within the discussed range of the excitation energies below 3 MeV there is a discrete spectrum of excited nuclear levels. In this case the γ -quanta inelastic scattering is the main channel of the nucleus excitation.

In the approximation of one resonance level the probability P of exciting an isomeric level is determined by

$$P = \Phi(E_r)\sigma_r, \quad (1)$$

where

$$\sigma_r = g(\lambda^2/4\pi)\Gamma_0\Gamma_{\text{iso}}/\Gamma.$$

The parameters g , Γ_0 , Γ_{iso} , and Γ are, respectively, the statistical weight, the ground state transition width of the resonance level, the partial width for the decay to the isomeric level, and the total width of the resonance level. λ is the wavelength of the γ -quanta which excite the resonance level at the energy E_r . $\Phi(E_r)$ is the flux of photons per unit energy interval.

The analysis of the experimental studies of metastable states excitation in the range of isolated levels, i.e. via the activation states, is based on eq. (1).

At present there are some indications [41–43] of the presence of nonresonant processes at the nuclei metastable states excitation by isotopic sources of γ -quanta. The same issue was discussed in ref. [44].

In this view ref. [45] should be mentioned. Evidently it seems to be a single paper where the mechanism of the nuclear levels non-resonant excitation is proposed. This mechanism is similar to the Compton effect, only instead of the γ -quantum scattering the nucleus excitation occurs. In ref. [45] such a process is called the nucleus Compton excitation.

2. Analysis of isomers excitation data

The analysis of photonucleon reactions, performed in refs. [46–48], indicated a correlation of partial photoproton cross-sections of the population of finite nuclei lower excited states with the pick-up reactions data. In refs. [49,50] a correlation of $(e, e'p)$ and (d, τ) reactions for closed-shell nuclei was also indicated. The correlation of fpg-shell nuclei isomeric states excitation cross-sections in (γ, n) reaction is also

indicated in ref. [51]. Such a correlation probably enables to make the choice in favour of the one-nucleon mechanism of the γ -quanta interaction with the atomic nucleus, at least for the near-magic nuclei. Recently in ref. [52] a positive correlation between the excitation of ^{15}N and ^{39}K nuclei hole states, excited in (γ, γ') and (d, τ) reactions was found. This part of the report will be devoted to the analysis of (γ, γ') reactions with the excitation of ^{77m}Se and ^{87m}Sr nuclei and the data from the (p, d) reactions for ^{78}Se and ^{88}Sr nuclei.

These nuclei are chosen due to the necessary information for them being available from the one-nucleon transfer reaction [53–58] and (γ, γ') reactions [35,36].

Using the spin-dependent sum rule [59] for the spectroscopic factors from the one-nucleon transfer reaction for ^{78}Se and ^{88}Sr nuclei, one can conclude the $1\text{f}2\text{p}1\text{g}$ shell in ^{88}Sr nucleus to be completely filled with neutrons and $2\text{p}_{1/2}$, $2\text{p}_{3/2}$ and $1\text{f}_{5/2}$ subshells in the ^{78}Se nucleus to be completely filled with neutrons, and the $1\text{g}_{9/2}$ subshell to contain only four neutrons.

In table 1 the ^{77}Se and ^{87}Sr nuclei levels with excitation energy below 1.7 MeV for ^{77}Se and below 2.7 MeV for ^{87}Sr are listed.

Only the levels, via which the metastable states can be populated, are included, i.e. those pretending for the activation levels. For the levels, observed in pick-up reactions, the spectroscopic factors C^2S^- are listed. For comparison, the activation level energies, detected in the (γ, γ') reaction in refs. [35,36], are also enumerated.

It is seen that for ^{77}Se nucleus in the (γ, γ') reaction mainly the same levels are observed, as those observed in (p, d) reactions, except the 950 keV level, observed in the (d, p) reaction [54].

As noted above, the $2\text{p}_{1/2}$, $2\text{p}_{3/2}$ and $1\text{f}_{5/2}$ subshells in the ^{78}Se nucleus are completely filled, and the $1\text{g}_{9/2}$ subshell contains four neutrons, which means that the ^{77}Se levels, observed in the (p, d) reaction, are the holes in the corresponding subshells. The ^{77}Se nucleus subshell ground state is the hole state of the $2\text{p}_{1/2}$ subshell. In this case in order to excite the level with energy 250 keV and spin $J^\pi = 5/2^-$, being the $1\text{f}_{5/2}^{-1}$ hole state (as observed in the (p, d) reaction), one should transfer a neutron from the filled $1\text{f}_{5/2}$ subshell to the unfilled $2\text{p}_{1/2}$ subshell, i.e. the $1\text{f}_{5/2} - 2\text{p}_{1/2}$ transition should be realized.

A similar pattern is observed for the rest of the activation levels. The configurations of the transitions, occurring at the activation levels excitation for ^{77}Se , are listed in table 1. The activation level with an energy of 950 keV should, probably, be assigned to the $2\text{p}_{1/2}-3\text{s}_{1/2}$ transition. The transition type for the activation level with an energy of 1600 ± 10 keV, corresponding most likely to the 1623 keV level from the (p, d) reaction [53], cannot be determined, since its structure is undetermined. In the case of the ^{87}Sr nucleus four activation levels with energies below 1220, 1220, 1880 and 2660 keV have been experimentally observed. We assign the activation level with the energy below 1220 keV to the level with an energy of 873 keV. Since the ^{87}Sr isomer was excited by γ -quanta from the isotopic source ^{46m}Sc [4], emitting γ -quanta with the energies of 890 and 1170 keV. The activation level with the energy 1220 keV may correspond to the level with the energy 1228 or

Table 1

E (keV) [58]	J^π	P [58]	nlj	C^2S^- (p, d) [53]	E_a (keV) [36]	Transition configuration	Type
^{77}Se							
0	1/2 ⁻		2p _{3/2} ⁻¹	0.35			
168	7/2 ⁺						
175	9/2 ⁺		1g _{9/2} ⁻¹	2.54			
239	3/2 ⁻						
250	5/2 ⁻	0.32	1f _{5/2} ⁻¹	2.38	250±10	1f _{5/2} →2p _{1/2}	E2
300	5/2 ⁺	—	2d _{5/2} ⁻¹	0.09			
439	5/2 ⁻	0.012	1f _{5/2} ⁻¹	0.37	440±10	1f _{5/2} →2p _{1/2}	E2
521	3/2 ⁻	0.004	2p _{3/2} ⁻¹	0.98	520±10	2p _{3/2} →2p _{1/2}	M1
581	7/2 ⁻	0.034					
680	5/2 ⁺	0.9	2d _{5/2} ⁻¹	0.097			
818	1/2 ⁻	< 10 ⁻⁴	2p _{1/2} ⁻¹				
824	3/2 ⁻	0.08	2p _{3/2} ⁻¹	0.26	825±10	2p _{3/2} →2p _{1/2}	M1
950	1/2 ⁺		3s _{1/2} ⁻¹	0.36 [54]	932±10	2p _{1/2} →3s _{1/2}	E1
1005	3/2 ⁻	0.12	2p _{3/2} ⁻¹	0.15	1000±10	2p _{3/2} →2p _{1/2}	M1
1186	5/2 ⁻	—	1f _{5/2} ⁻¹	0.25	1190±10	1f _{5/2} →2p _{1/2}	E2
1231	5/2 ⁻	0.03	1f _{5/2} ⁻¹	0.54			
1623	(p,d)		—	—	1600±10		
^{87}Sr							
0	9/2 ⁺	[55]	1g _{9/2} ⁻¹	5.4 [56]	[35]		
388	1/2 ⁻		2p _{1/2} ⁻¹	2.42			
873	3/2 ⁻	1	2p _{3/2} ⁻¹	3.91	< 1220	2p _{3/2} →1g _{9/2}	E3
1228	5/2 ⁺	0.11		0.43			
1254	5/2 ⁻	1	1f _{5/2} ⁻¹	4.19	1220	1f _{5/2} →1g _{9/2}	M2
1770	5/2	0.04					
1920	7/2 ⁺			1880			
2116	5/2 ⁻	1					
2169	1/2 ⁺	1					
2414	5/2 ⁻	0.82	1f _{5/2} ⁻¹	0.715			
2660	5/2 ⁻	1	1f _{5/2} ⁻¹	0.57	2660	1f _{5/2} →1g _{9/2}	M2

1254 keV, usually the former being chosen as the activation level. The activation level with an energy of 1880 keV most likely corresponds to the level with an energy of 1920 keV and spin 7/2⁺, which agrees with the fracture at the ^{87}Sr isomer efficiency curve depending on the electron energy in ref. [35]. The level with an energy of 1920 keV is observed in the (p,d) reaction [56], being a multiplet $2^+ \oplus 1g_{1/2}^{-1}$. The activation level with the energy 2660 keV corresponds to the level with the energy 2660 keV, being the hole state in the 1f_{5/2} subshell. The ground state of the ^{87}Sr nucleus is the hole state of the 1g_{9/2} subshell. By using the same procedure, as the above one for the ^{77}Se nucleus, the transition configurations for the excitation of the activation levels with energies below 1220 and 2660 keV could be determined

and are listed in table 1. The level with an energy of 1880 keV falls out of this scheme. The accuracy of the 1220 keV activation level energy measurement is not sufficient for one of the ^{87}Sr levels – 1228 or 1254 keV is to be identified unambiguously.

Thus, the above speculations enable us to conclude the activation level in the range of the excitation energies below 2.7 MeV to be formed due to the one-nucleon transition in the framework of one upper unfilled nuclear shell, for the nuclei in question this being the 1f2p1g shell. These transitions will be referred to as those of type A.

Besides the transitions between the subshells of the same upper nuclear shell being filled to the neighbouring free nuclear shell (the energetic superimposition of whose subshells can be determined from the stripping reactions), are possible. We refer to these transitions as type B. In our case of ^{77}Se , ^{87}Sr nuclei these will be the transitions from the 1f2p1g shell to the 3s2d1g1h shell. Such transitions will result in the formation of a hole state at one of the subshells of the 1f2p1g shell, corresponding to the hole state in an $A - 1$ nucleus, being revealed in the pick-up reaction for the A nucleus, while at one of the subshells of the 3s2d1g1h shell a particle state is formed, corresponding to the particle state of an $A + 1$ nucleus, being revealed in the stripping reaction for the A nucleus. The energy of such a particle-hole state (1p–1h state) can be determined from refs. [60,61] by means of the expression

$$E_{ph} = \varepsilon_p + \varepsilon_h + E_A^c - E_{A+1}^c, \quad (2)$$

where ε_p is the particle state energy determined in the stripping reaction for the A nucleus; ε_h is the hole state energy, determined in the pick-up reaction for the A nucleus; E_A^c , E_{A+1}^c are the binding energies of one nucleon (neutron) in the A or $A+1$ nucleus, respectively.

Using eq. (2), we have estimated E_{ph} energies for the states being formed due to E1 transitions for ^{90}Zr and ^{138}Ba nuclei, since for these nuclei the cross-sections of γ -quanta elastic scattering are available [62,63], while the particle ε_p and ε_h hole state energies are taken from refs. [57,64–66]. In the estimations only the levels possessing the highest spectroscopic factor in the one-neutron transfer reactions, were taken into account. The estimated energies E_{ph} and the energies E_r , corresponding to the observed maxima in the elastic scattering cross-section, are listed in table 2. They are seen to correlate, which means that the observed structure can be explained by the neutron transitions of type B. The transition configurations for the corresponding energies E_{ph} are also listed in table 2.

Thus, in the model of one-nucleon transitions between the subshells along with the one-nucleon transfer reactions data, the resonance structure in the cross-section of γ -quanta elastic scattering by ^{90}Zr and ^{138}Ba nuclei can be explained.

It should be noted that the obtained integrated cross-sections for ^{123m}Te and ^{135m}Ba isomers excitation are higher than those for ^{125m}Te and ^{137m}Ba isomers,

Table 2

Transition configuration	ϵ_h (MeV)	ϵ_p (MeV)	E_{ph} (MeV)	E_r (MeV)	Transition configuration	ϵ_h (MeV)	ϵ_p (MeV)	E_{ph} (MeV)	E_r (MeV)		
^{90}Zr $E_A^c - E_{A+1}^c = 4.8$ MeV					^{138}Ba $E_A^c - E_{A+1}^c = 3.86$ MeV						
2p _{3/2} ⁻¹	2d _{3/2}	1.09	2.04	7.9	8.25	2d _{3/2} ⁻¹	3p _{1/2}	0.0	1.09	4.95	4.8
1f _{5/2} ⁻¹	2d _{3/2}	1.45	2.04	8.3	8.5	2d _{5/2} ⁻¹	2f _{7/2}	1.29	0.0	5.15	5.1
1f _{5/2} ⁻¹	1g _{7/2}	1.45	2.20	8.45	8.75	2d _{3/2} ⁻¹	2f _{5/2}	0.0	1.42	5.28	5.3
1f _{5/2} ⁻¹	2d _{3/2}	2.1	2.04	9.0	9.0	2d _{5/2} ⁻¹	2f _{7/2}	2.0	0.0	5.86	5.8
1f _{5/2} ⁻¹	2d _{3/2}	2.1	2.2	9.1	9.2	1g _{7/2} ⁻¹	1f _{7/2}	2.23	0.0	6.09	6.2
1f _{5/2} ⁻¹	2d _{3/2}	1.45	3.08	9.3	9.35	1g _{7/2} ⁻¹	1f _{7/2}	2.54	0.0	6.4	6.4
1f _{5/2} ⁻¹	1g _{7/2}	1.45	3.47	9.7	9.5	1g _{7/2} ⁻¹	1f _{7/2}	2.99	0.0	6.85	6.8
1f _{5/2} ⁻¹	2d _{3/2}	2.1	3.08	10.0	10.0	1g _{7/2} ⁻¹	1h _{9/2}	2.23	1.28	7.4	7.4
1f _{5/2} ⁻¹	2d _{3/2}	2.1	3.47	10.4	10.4	1g _{7/2} ⁻¹	1h _{9/2}	3.0	1.28	8.1	8.1
				1g _{7/2} ⁻¹	1h _{9/2}	3.0	1.6	8.45	8.4		

respectively, the integrated cross-section value for the isomer excitation decreasing with the mass number of these nuclei.

The analysis of the one-nucleon transfer reactions shows the metastable states of $^{123,125}\text{Te}$, $^{135,137}\text{Ba}$ nuclei to be formed by the $1\text{h}_{11/2}$ subshell. Besides, in these nuclei the $1\text{h}_{11/2}$ subshell is filled with neutrons with the increase of the mass number A . The difference between ^{123}Te and ^{125}Te or ^{135}Ba and ^{137}Ba nuclei consists in the $1\text{h}_{11/2}$ subshell for ^{123}Te and ^{135}Ba being more filled than for ^{123}Te and ^{135}Ba , respectively. Therefore, the population of the $1\text{h}_{11/2}$ subshell by the one nucleon transition via the higher subshell is more probable for ^{123}Te and ^{135}Ba nuclei. This results in the probability of ^{123}Te and ^{135}Ba metastable states population being higher than for ^{125}Te and ^{137}Ba . The difference by one or two orders of magnitude in the integrated cross-sections [16–20] of metastable states excitation within the energy ranges below 3 and above 5 MeV can be explained by the fact that in the first range the isomers are excited via the activation levels being formed due to the type A transitions, while in the second range due to those of type B.

3. Conclusions

The above analysis of the (γ, γ') reaction with the excitation of ^{77}Se and ^{87}Sr nuclei isomeric states within the γ -quanta energy range below 3 MeV along with the one-nucleon transfer reactions data enabled to conclude the activation states, via which the nuclei metastable states are populated, to be excited due to the one-nucleon transitions from the filled subshells to the unfilled one within the same nuclear shell.

Based on this conclusion, we have estimated the energies of ^{90}Zr and ^{138}Ba nuclei 1p–1h states, excited due to the one-nucleon transitions from their upper unfilled subshell to the neighbouring empty shell. The thus obtained 1p–1h state energies

correspond to the resonance structure in the cross-section of γ -quanta elastically scattering by these nuclei.

Within the one-nuclear transitions assumption the nature of the difference in the integrated cross-sections of ^{123}Te and ^{125}Te , ^{135}Ba and ^{137}Ba isomers excitation can be explained.

Thus, the approximation of the one-nucleon transitions between the nuclear sub-shells along with the data from the one-nucleon transfer reactions, proves to be efficient for the analysis of the experiments on the metastable nuclear states excitation in the reaction of γ -quanta inelastic scattering in order to elucidate the mechanism of such reactions.

References

- [1] C.B. Collins et al., J. Appl. Phys. 53 (1982) 4645.
- [2] B. Pontecorvo and A. Lazard, C.R. Acad. Sci. 208 (1939) 99.
- [3] G.B. Collins et al., Phys. Rev. 55 (1939) 507.
- [4] A. Veres, *Magizomerek Gamma-Aktivációja és Alkalmazásuk. Atomenerg. és Magkutatás Újabb Eredm. Kot. 3* (Budapest, 1984).
- [5] A.G.W. Cameron and L. Katz, Phys. Rev. 84 (1951) 608.
- [6] L. Meyer-Sehutzmeister and V.L. Telegi, Phys. Rev. 104 (1956) 185.
- [7] E. Silva and J. Goldemberg, Phys. Rev. 110 (1958) 1102.
- [8] O.B. Bogdankevich, L.E. Lazareva and A.M. Moiseev, JETF 39 (1960) 1224.
- [9] O.B. Bogdankevich, L.E. Lazareva, B.S. Dolbilkin and F.A. Nikolayev, JETF 45 (1963) 882.
- [10] O.B. Bogdankevich, L.E. Lazareva and F.A. Nikolayev, JETF 31 (1956) 405.
- [11] J. Goldemberg and L. Katz, Phys. Rev. 90 (1952) 307.
- [12] J.M. Burkhardt, E.J. Winhold and T.H. Dupree, Phys. Rev. 100 (1955) 199.
- [13] J.A. Anderson, M.J. Byrd and C.B. Collins, Phys. Rev. C 38 (1988) 2838.
- [14] C.B. Collins et al., Phys. Rev. C 37 (1988) 2267.
- [15] C.B. Collins et al. Phys. Rev. C 38 (1988) 1852.
- [16] J.A. Anderson et al., Nucl. Instr. Meth. B40/41 (1989) 452.
- [17] P. von Neuman-Cozel et al., Phys. Lett. B. 266 (1991) 9.
- [18] J.J. Carroll et al., Phys. Rev. C 43 (1991) 1238.
- [19] J.J. Carroll et al., Phys. Rev. C 43 (1991) 897.
- [20] C.B. Collins et al., Phys. Rev. C 46 (1992) 952.
- [21] Z.M. Bigan, V.M. Mazur and I.V. Sokolyuk, Preprint KINR-84-13 (Kiev, KINR, 1984).
- [22] Z.M. Bigan, V.M. Mazur and I.V. Sokolyuk, Preprint KINR-86-2 (Kiev, KINR, 1986).
- [23] Z.M. Bigan, V.M. Mazur and I.V. Sokolyuk, Preprint KINR-86-22 (Kiev, KINR, 1986).
- [24] Z.M. Bigan, V.M. Mazur and I.V. Sokolyuk, Preprint KINR-88-13 (Kiev, KINR, 1988).
- [25] Z.M. Bigan, L.E. Lazareva, V.M. Mazur and I.V. Sokolyuk, Yad. Fiz. 49 (1989) 913.
- [26] V.M. Mazur, I.V. Sokolyuk and Z.M. Bigan et al., Yad. Fiz. 56 (1993) 20.
- [27] I.V. Sokolyuk, Ph.D. Thesis (Kiev, 1989).
- [28] A.P. Dubenskiy, V.P. Dubenskiy and E.A. Boykova, Izv. AN SSSR. Ser. Fiz. 51 (1987) 40.
- [29] A.P. Dubenskiy et al., Izv. AN SSSR. Ser. Fiz. 54 (1990) 1833.
- [30] V. Ponomarev et al., J. Phys. G 16 (1990) 1727.
- [31] A.P. Dubenskiy, V.P. Dubenskiy and E.A. Boykova, Izv. AN SSSR. Ser. Fiz. 57 (1993) 90.
- [32] A.G. Beda, G.E. Bizina and A.V. Davidov, Probl. Yadern. Fiz. Elemt. Chast. (Nauka, Moscow, 1975) p. 209.

- [33] M.L. Wiedenbeck, Phys. Rev. 67 (1945) 92.
- [34] M.L. Wiedenbeck, Phys. Rev. 68 (1945) 1.
- [35] C.E. Booth and J. Brownson, Nucl. Phys. A 98 (1967) 529.
- [36] M. Boivin, Y. Cauchois and Y. Heno, Nucl. Phys. A 137 (1969) 520.
- [37] M. Boivin, Y. Cauchois and Y. Heno, Nucl. Phys. A 176 (1971) 626.
- [38] W.T.K. Johnson, B.T. Chertok and C.E. Dick, Phys. Rev. Lett. 25 (1970) 5991.
- [39] V.V. Balashov, JETP 43 (1962) 2199.
- [40] V.V. Balashov, Proc. Int. Conf. on Low and Intermediate Energy Electromagnetic Interactions, Dubna, 1967 (Moscow) 307.
- [41] A. Ljubicic, K. Pisk and B.A. Logan, Phys. Rev. C 23 (1981) 2238.
- [42] M. Krcmar et al., Phys. Rev. C 25 (1982) 2079.
- [43] M. Krcmar, A. Ljubicic, B.A. Logan and M. Bistrovic, Phys. Rev. C 33 (1986) 293.
- [44] K. Yoshihara et al., Phys. Rev. C 33 (1986) 728.
- [45] I.S. Batkin, Yad. Fiz. 29 (1979) 903.
- [46] J.E.M. Thomson and M.N. Thompson, Nucl. Phys. A 285 (1977) 84.
- [47] J.E.M. Thomson, M.N. Thompson and R.J. Stewart, Nucl. Phys. A 290 (1977) 14.
- [48] R.L. Gulbranson et al., Phys. Rev. C 27 (1983) 470.
- [49] L. Lapikas, Nucl. Phys. A. 434 (1985) 85C.
- [50] P.K.A. de Witt Huberts, Nucl. Phys. A 446 (1985) 301C.
- [51] Z.M. Bigan, V.M. Mazur and I.V. Sokolyuk, Ukr. Fiz. J. 35 (1990) 509.
- [52] R. Moreh and W.C. Sellyey, Phys. Lett. B 185 (1987) 11C.
- [53] L.O. Barbopoulos et al., Nucl. Phys. A 331 (1979) 502.
- [54] L.A. Montestruque, Nucl. Phys. A 305 (1978) 29.
- [55] Ch. Winter et al., Nucl. Phys. A 460 (1986) 501.
- [56] H.P. Block et al., Nucl. Phys. A. 287 (1977) 156.
- [57] H. Taketani, M. Adashi, M. Ogawa and K. Ashibe, Nucl. Phys. A 204 (1973) 385.
- [58] C.M. Lederer and V.S. Shirley, Table of Isotopes (New York, 1978).
- [59] C.F. Clement and S.M. Perez, Nucl. Phys. A 213 (1973) 510.
- [60] A. Lepretre et al., Nucl. Phys. A 175 (1971) 609.
- [61] H. Beil et al., Nucl. Phys. A 172 (1971) 426.
- [62] R. Alarson, R.M. Laszewski, A.M. Nathan and S.D. Hoblit, Phys. Rev. C 36 (1987) 954.
- [63] R.M. Laszewski, Phys. Rev. C 34 (1986) 1114.
- [64] H.P. Block, L. Hulstman, E.J. Kaptein and J. Block, Nucl. Phys. A 273 (1976) 142.
- [65] R.K. Jolly and K. Kashy, Phys. Rev. C 4 (1978) 1398.
- [66] S.S. Ipson, W. Booth and J.G.B. Haigh, Nucl. Phys. A 206 (1973) 114.

Section 3

Inversionless Amplification

Lasing without inversion: problems and prospects

Olga Kocharovskaya

*Institute of Applied Physics, Russian Academy of Science, 46 Ulyanov Street,
603600 Nizhny Novgorod, Russia*

We review the recent progress both in the theory and in experiments on lasing without inversion and discuss the potential application of this phenomenon for the generation of coherent gamma radiation.

1. Introduction

The concept of amplification without inversion (AWI) based on atomic interference in three-level atoms attracted much attention for the past five years [1]. Many different schemes have been suggested theoretically and some of them have already been realized experimentally in the optical range.

The most obvious and appealing potential application of such inversionless schemes would be to get an advantage in the high-frequency domain where fast spontaneous relaxation makes the realization of population inversion difficult.

In this paper we survey both theoretical and experimental results in this domain in view of this specific potential application.

According to the title, this paper consists of two parts, namely, progress and problems. In section 2 we briefly discuss the basic schemes for inversionless amplification concentrating mainly on those schemes which have been realized experimentally. We show that in spite of a large variety of these schemes there is only one simple physical idea beyond all of them. This idea is to suppress the resonant absorption via atomic interference in three-level atoms. At the same time it is possible to distinguish two different mechanisms of inversionless amplification, implying and correspondingly non-implying population inversion in some atomic state basis which can be obtained via unitary transformation of the original energy states basis. In section 3 we discuss the open problems emphasizing some principal thermodynamic restrictions inherent to the process of inversionless amplification and analyzing both advantages and disadvantages of different inversionless schemes in gamma-ray range. Finally, we summarize the major results of both parts pointing out the prospects for the further development of this rapidly extending domain of investigations and indicating the most attractive nearest goals.

2. Progress

2.1. SUPPRESSION OF THE ABSORPTION VIA ATOMIC INTERFERENCE

There are two typical and quite sensible reactions on the idea of inversionless amplification. The first one is: this is impossible and the second one: this is trivial.

Indeed if one bares in mind a closed two-level atomic system, the amplification condition implies a population inversion in order for the transitions from the upper level to prevail the opposite ones. However as soon as one takes into account some additional internal or external degrees of the freedom such as external coherent fields, additional atomic levels, etc., it becomes rather easy to recall many situations where amplification occurs without population inversion. Perhaps, two of the most bright examples of such systems are: a two-level atom driven by the strong field (where amplification of the probe weak field appears in the vicinity of one of the two Rabi sidebands) and Raman laser (which operates without any population inversion). However in both of these cases we are dealing rather with a transformation of the energy from one coherent field into another one. The energy is not taken from the medium. Moreover an upper atomic level may even be completely empty. These and many other suggestions had been widely discussed earlier. The reviews can be found in refs. [1,2].

An idea for inversionless amplification which attracted much attention recently was quite different from the above-mentioned ideas. Namely this idea was to suppress absorption at the resonant transitions via atomic interference. In order to achieve atomic interference one needs, first, to provide two different channels for absorption. Hence, all of these schemes involve a splitting of either the lower or the upper operating level. Second, one needs also to prepare a coherent superposition state of the corresponding sublevels in order to make these channels interfering. A non-equilibrium which is required by the second law of thermodynamics is inserted into such systems not only via a redistribution of the populations (i.e. diagonal elements of the density matrix) but also via an excitation of the coherencies (i.e. off-diagonal elements of the density matrix). It is worth to emphasize that an excitation of the low-frequency (LF) coherence between sublevels in a three-level system has nothing to do with an excitation of the optical polarization, i.e. oscillating dipole moment (as it would be in a two-level system). It serves exclusively for suppression of the resonant absorption. At the same time the energy for amplification is supposed to be taken from the medium via depletion of the upper operating level. Hence incoherent pumping is required in order to populate this upper level but the requirement for this pumping is essentially released due to suppression of the resonant absorption.

This idea of inversionless amplification has been suggested independently and almost simultaneously in three papers [3–5] which stimulated a continuous flow of work in this direction (see for reviews ref. [1]). Many different concrete schemes

based on this idea were proposed. We concentrate below on those schemes which have been realized experimentally.

2.2. INVERSIONLESS SCHEMES REALIZED EXPERIMENTALLY

2.2.1. Simple Λ scheme (fig. 1)

The possibility of inversionless amplification in this scheme as well as its simple physical interpretation were suggested in ref. [3]. As is well known there is such a coherent superposition state of lower sublevels in this scheme that the transition probability to the upper level vanishes at any moment as a result of interference between the two channels 1–3 and 2–3 [6]. This state is called the trapped or non-absorbing state. Therefore, if one has managed to prepare all atoms at lower levels in such a trapped state, any small amount of atoms at the upper level should be sufficient for amplification since there should be transitions from the upper state to the state which is orthogonal to the trapped one. Apparently, such inversionless amplification implies some hidden inversion, namely, with respect to the empty untrapped state. In general, population inversion is required between the upper state and lower populated among the eigenstates of the density submatrix corresponding to the lower sublevels [1, 7]. The physical meaning of the eigenstates of the density submatrix is quite transparent. It is the basis where, by definition, atomic coherence (and hence atomic interference) is absent. Therefore it does not look surprising that an amplification condition in this basis takes a traditional form of population inversion.

The easiest way to realize this scheme is in a nonstationary regime. In this case it is sufficient to excite LF coherence initially, for example by an ultrashort pulse the spectrum of which overlaps the LF splitting. Then it will oscillate with an eigenfrequency and relax. The result of the other probe ultrashort pulse transformation will depend on the values of both the population of the upper level and the LF coherence at the moment when this probe pulse arrives. It was shown [3] that, depending on these initial parameters, both amplification without inversion and inversion without amplification are possible. The first convincing experiment confirming these predictions and demonstrating nonstationary gain without inversion was fulfilled in Sm vapor by the group of Lange at the University of Munster [8]. A

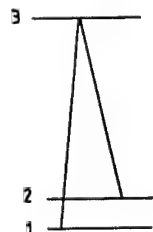
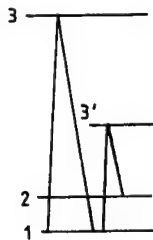


Fig. 1. Simple Λ scheme.

Fig. 2. Double Λ scheme.

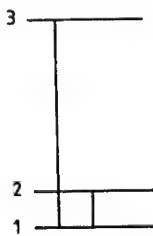
nonstationary gain without inversion has been observed also in three other experiments [9–11], although the first of them remains a subject of the discussions.

2.2.2. Double Λ scheme (fig. 2)

The next interesting question is whether it is possible to realize amplification without inversion in a steady-state regime. One possibility to achieve this is to turn to the double Λ scheme where a bichromatic external field serves for excitation of the LF coherence and as a result a bichromatic probe field may be amplified without inversion at any of the resonant transitions. Since the mechanism of amplification, as in the simple Λ scheme, is based on coherent trapping, a hidden inversion in the basis of the eigenstates of the density matrix is required. This requirement implies, in turn, a real population inversion between the upper level and auxiliary atomic state $3'$. The double Λ scheme was suggested in ref. [12] and has been realized recently experimentally by the group of Lange [13].

2.2.3. h scheme (fig. 3)

This scheme involves driving by the external LF field and probing at the adjacent high-frequency (HF) transition. Strong driving provides both dynamic Stark splitting of the lower operating level and excitation of the coherence between these sublevels. Interference of two absorption channels $1'-3$ and $2'-3$ leads to the suppression of the resonant absorption for a probe field and hence provides amplification even when a population of upper level both in the steady-state regime and initially (in the absence of coherent driving) does not exceed the population of any

Fig. 3. h scheme.

of the two lower sublevels 1 and 2 like in a simple Λ scheme. However an important distinction of this scheme from those discussed above is the absence of the population inversion in the basis of states where atomic interference vanishes. This scheme has been suggested in ref. [14]. A similar scheme but with a down-conversion from pumping to amplifying field has been realized recently in Rb vapor by the group of Hollberg and Scully [15] at the National Institute of Standards, Colorado. Not only gain but also LWI was achieved in this experiment.

2.2.4. P scheme (fig. 4)

This scheme may be viewed as an upside-down Λ scheme. With respect to the problem of inversionless amplification, this scheme was first analyzed by Harris [16] in the case of zero relaxation rate between levels 2 and 1. In this particular case amplification is possible without steady-state inversion [16] but implies "initial" inversion in the absence of the coherent driving. It was shown first in ref. [17] that in general at a finite relaxation rate between levels 2 and 1 amplification is possible even without an "initial" population inversion. It is worth to emphasize also that even the sum of populations of upper sublevels in steady state may be smaller than the population of the lower level. This means that population inversion is absent in any atomic states basis which can be obtained via unitary transformation of the energy states basis since any unitary transformation (including those which diagonalized density matrix or Hamiltonian) conserves a trace of the density matrix. Let us note also that the realization of this scheme requires fast relaxation at the HF transition as compared with a LF transition [17]. This condition is usually difficult to meet due to the ω^3 dependence of the spontaneous decay rate. Nevertheless this scheme has been recently realized in Na vapor by the group of E. Fry and M. Scully at Laser Texas Laboratory in Houston. Both gain and LWI have been demonstrated.

3. Problems

There are still many open problems in the domain of LWI. We discuss below schemes involving no coherent pumping and inversionless schemes in nuclei.

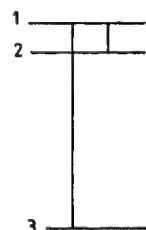


Fig. 4. P scheme.

3.1. SCHEMES INVOLVING NO COHERENT PUMPING

We concentrated above on the schemes involving coherent pumping. Another approach developed by S. Harris is centered on the schemes involving no coherent pumping [4]. These schemes contain an upper level doublet (fig. 5) the coherence of which is induced via a decay process to the common level or continuum of states, for instance, via autoionization, Auger or radiative decay. In the last case a cancellation of the absorption can be understood via interference of two two-photon transitions: 3–2–4 and 3–1–4. Such schemes certainly look very attractive for applications and have been widely studied recently [1]. At the same time, most of the work has been restricted so far by the analysis of the phenomenological models where incoherent pumping was accounted by means of some relaxation rates which are supposed to be independent of the common decay of the upper sublevels. However, it is not the case in general. As is well known, incoherent pumping can essentially destroy an atomic coherence especially when this coherence is itself produced via the decay processes. In particular, in case of the closed three-level system where both decay of the upper sublevels and incoherent pumping are provided by an interaction with a field reservoir, the impossibility of LWI was strictly proved on the basis of self-consistent master equations [7]. The self-consistent quantum treatment of some other specific mechanisms of incoherent pumping in these schemes remains an appealing open problem in this area.

It is worth to note also that such schemes were not studied yet experimentally. In particular, it is not easy to find atoms which suit the scheme with a common radiative decay. Indeed, an interference of the radiative decays implies closely situated sublevels. However the corresponding spacing determined by the electrostatic interaction exceeds usually the decay rate determined by the interaction with the vacuum fluctuations. Hence it was suggested to “compose” atoms whose sublevels “a priori” decay to the same level by means of resonant driving of the upper doublet. Until dynamic Stark splitting is not too large, i.e., the corresponding Rabi frequency does not exceed the upper level radiative decay, both ac-Stark sublevels will indeed decay to the same level and, hence, the interference described above will appear. It is interesting to note that it leads again to the P scheme described in the last section, although on the basis of a very different approach. As has been pointed

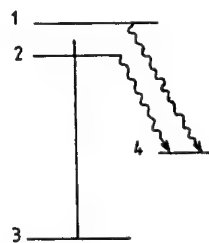


Fig. 5. Scheme with a common decay of upper sublevels.

out already, no hidden inversion is required in general for amplification in this scheme.

Hence one can distinguish, in principle, two mechanisms of LWI: implying and non-implying hidden inversion in an atomic system, respectively. However since both these mechanisms provide amplification in the absence of a real population inversion between the energy atomic levels they are equally interesting for realization of a gamma-ray laser.

3.2. INVERSIONLESS SCHEMES IN THE NUCLEAR RANGE

For a realization of the inversionless schemes described above in the gamma-ray range one needs first to find an appropriate structure of the nuclear levels. As is well known, most nuclei possess a magnetic momentum and hence both Zeeman (under the action of a magnetic field) and hyperfine sublevels often appear in the nuclear structure [18,19]. Moreover, the appearance of the coherent effects under the resonant excitation of these sublevels was demonstrated. In particular, an anti-Stokes scattering was observed of a gamma-radiation by the hyperfine structure of the resonant 14.4 keV gamma-ray transition in ^{57}Fe [20].

The choice of a suitable scheme depends on the ratios of the longitudinal t_1 and transverse t_2 relaxation times at the LF transition to the longitudinal relaxation time at the operating gamma-transitions, t_1/T_1 , t_2/T_1 . These ratios may be varied in the very wide limits depending on the frequency and multiplicity of the operating transition, temperature and structure of the sample, etc. [19–21]. Taking into account that usually $10^{-4} \text{ s} < t_1 < 10^4 \text{ s}$ while $10^{-4} \text{ s} < t_2 < t_1$ we come to the following conclusion. In the case of the long-lived isomer upper level $T_1 \gg t_1 > 10^{-4} \text{ s}$ the double Λ scheme does not work and one needs to turn to the P scheme. On the contrary, in the case of the short-lived isomer $T_1 \ll t_2 < 10^{-4} \text{ s}$ the preference has to be given to the double Λ scheme.

A realization of the double Λ scheme implies a careful selection of the adjacent transition for the purpose of the coherent pumping. One can use for it, for example, some nuclear transitions which may lay in the X-range domain [22], with a pumping by X-ray lasers. It would certainly be the most convenient and reliable way to use modern powerful lasers for coherent pumping, but there is usually a very unfortunate gap in the nuclear structure corresponding to the optical range [19]. Still there is a possibility to use an optical pumping bearing in mind, the existence of the mixed nuclear-electron transitions.

As far as incoherent pumping is concerned, one can use, for example, X-ray bremsstrahlung radiation providing the population of the upper operating level from the long-lived isomer via a broad absorption band linked efficiently with the short-lived operating level. As was experimentally demonstrated recently, the efficiency of such pumping in some materials can essentially exceed the traditional estimates [23].

Using atomic interference allows to reduce the requirement for incoherent

pumping. However, weakness of the nuclear transitions results in the requirement of quite powerful coherent pumping in order to provide this atomic interference. Still a combination of coherent and incoherent pumping provides the additional possibility for variations.

4. Conclusions

We reviewed the major theoretical and experimental results on LWI in atomic systems with splitted operating levels. LWI in such systems is due to the suppression of the absorption from the lower operating levels, which is a consequence of the destructive atomic interference between different paths leading to the absorption. This interference occurs under excitation of the coherence between sublevels.

So far most of the studies concentrated on the optical range. At the first stage of the investigations the major purpose was to prove the feasibility of LWI based on quantum coherence and interference effects. The experiments were conducted in a transient regime at the electron transitions with the Zeeman or hyperfine sublevels of the lower operating state using optical coherent pumping for excitation of the coherent superposition state of these sublevels. Most of the experiments were fulfilled in the vapors of the metals (Na, Sm, Cd) and one experiment was done in Ne.

The next step should be a demonstration of the usefulness of this concept for real applications. In this respect the most challenging and appealing purpose is, certainly, the creation of a gamma-ray laser. The traditional ways of pumping for many years have been failing to provide a population inversion at the operating transitions in this range. Hence, the new opportunity to realize a graser without the need for a population inversion on the basis of the coherent and interference effects deserves the most careful study.

Acknowledgement

This work was supported by the Russian Foundation for Basic Research (no. 96-02-19214a), INTAS/RFBR (no. 95-IN-RU 656) and EC Commission DG III-ESPRIT Project CTIAC 21042.

References

- [1] O. Kocharovskaya, Phys. Rep. 219 (1992) 175;
M.O. Scully, Phys. Rep. 219 (1992) 191;
P. Mandel, Contemp. Phys. 34 (1994) 235;
O. Kocharovskaya, Laser Phys. 5 (1995) 284.
- [2] V.I. Vysotky and R.N. Kusmin, *Gamma-ray lasers* (Moscow Univ. Press, Moscow, 1989) (in Russian).

-
- [3] O. Kocharovskaya and Ya.I. Khanin, Pis'ma Zh. Eksp. Teor. Fiz. 48 (1988) 581 [Sov. JETP Lett. 48 (1988) 630].
 - [4] S.E. Harris, Phys. Rev. Lett. 62 (1989) 1033.
 - [5] M.O. Scully, S.-Y. Zhu and A Gavridiles, Phys. Rev. Lett. 62 (1989) 2813.
 - [6] G. Alzetta et al., Nuovo Cimento, B 36 (1976) 5;
E. Arimondo and G. Orriols, Nuovo Cimento Lett. 17 (1976) 333;
H.M. Gray et al., Opt. Lett. 3 (1978) 218.
 - [7] O. Kocharovskaya and P. Mandel, Quant. Opt. 6 (1994) 217.
 - [8] A. Nottelman, C. Peers and W. Lange, Phys. Rev. Lett. 70 (1993) 1783.
 - [9] J.Y. Gao, Opt. Commun. 93 (1992) 323.
 - [10] E.S. Fry et al., Phys. Rev. Lett. 70 (1993) 3235.
 - [11] W.E. Van der Veer, A. Donzelmann and H.B. Linden van den Heuvell, Phys. Rev. Lett. 73 (1993) 3243.
 - [12] O. Kocharovskaya and P. Mandel, Phys. Rev. A 42 (1990) 523.
 - [13] C. Peters and W. Lange, Adv. Phys. (1995) (to be published).
 - [14] O. Kocharovskaya and P. Mandel, Opt. Commun. 84 (1990) 15.
 - [15] A. Zibrov et al., Phys. Rev. Lett. 75 (1995) 1499.
 - [16] A. Imamoglu, J.E. Field and S.E. Harris, Phys. Rev. Lett. 66 (1995) 1154.
 - [17] O. Kocharovskaya, P. Mandel and Y.V. Radeonychev, Phys. Rev. A 45 (1992) 1997.
 - [18] H. Frauenfelder, E.M. Henley, *Subatomic Physics* (Prentice-Hall, Englewood Cliffs, NJ, 1974).
C.B. Collins et al., J. Appl. Phys. 53 (1982) 4645.
 - [19] A.G. Lundin and E.I. Fedin, *NMR-Spectroscopy* (Moscow, Nauka, 1986) (in Russian).
 - [20] B.D. DePaola and C.B. Collins, J. Opt. Soc. Am. 1 (1984) 812;
C.B. Collins and B.D. DePaola, J. Opt. Soc. Am. 10 (1985) 25.
 - [21] Yu.P. Gangrsky and B.I. Markov, *Nuclei in Laser Beams* (Znaniya, Moscow, 1984) (in Russian).
 - [22] Yu.M. Shirokov and N.P. Yudin, *Nuclear Physics* (Nauka, Moscow, 1980) (in Russian).
 - [23] C.B. Collins et al., Phys. Rev. C 46 (1992) 952;
J.J. Carroll et al., Phys. Rev. C 43 (1991) 1238.

Emission of gamma rays by electron–nuclear double transitions

S. Olariu

*Institute of Physics and Nuclear Engineering, 76900 Magurele, CP MG-6,
Bucharest, Romania*

J.J. Carroll

*Department of Physics and Astronomy, Youngstown State University,
Youngstown, OH 44555, USA*

C.B. Collins

*Center for Quantum Electronics, University of Texas at Dallas, P.O. Box 830688,
Richardson, TX 75083-0688, USA*

and

I.I. Popescu

*Institute of Physics and Technology of Radiation Devices, 76900 Magurele,
CP MG-7, Bucharest, Romania*

In this paper we discuss the relevance of electron–nuclear double transitions for the problem of the amplification of gamma rays. We consider the electron–nuclear coupled system of ^{151}Eu in a CaF_2 lattice, in the presence of a strong static magnetic field. We analyze the possibility of pumping this electron–nuclear coupled system from the ground atomic electron Zeeman level to a higher electron level with the aid of a microwave magnetic field, while the nucleus is simultaneously undergoing a gamma-ray transition to the nuclear ground state. It is shown that an overall inversion condition can be satisfied even in the absence of inversion of the nuclear populations, provided that the ratio of the electron populations in the excited and ground electron Zeeman states has a sufficiently small value.

Nuclear quantum electronics is an interdisciplinary area between nuclear physics and quantum electronics, studying the effects of applied optical, microwave or radio-frequency fields on the emission of gamma rays by the atomic nuclei. The effects of the applied electromagnetic fields comprise at present changes in the spectral and angular distribution of the gamma rays. The goal of the research in nuclear quantum electronics is to achieve induced gamma-ray emission and amplification of gamma rays. At present, this appears to be a distant goal.

A gamma-ray laser pulse would consist of a relatively small number of gamma-ray photons, perhaps 10^{10} photons, but the duration of this pulse would be small, about 1 ns, the pulse would be concentrated on a small area of about 10^{-5} cm^2 , and would have a relatively small spectral width of about 10^{10} s^{-1} . Thus a gamma-ray laser would be a scientific tool characterized by its very high *brilliance*. The amount of energy carried by a gamma-ray laser pulse would be small, on the order of $10 \mu\text{J}$.

In the absence of efficient mirrors at gamma-ray wavelengths, a gamma-ray laser would be a single-pass device. If we represent the active medium as a cylinder of radius a and length L , there will be an uncertainty in the direction of propagation of the pulse of about λ/a , where λ is the gamma-ray wavelength. This uncertainty in the direction of propagation results over a length L in an uncertainty of the transverse position of $L\lambda/a$, which should not exceed a fraction of, say, $\frac{1}{3}$ of the radius a . These diffraction effects then impose a lower limit on the radius a , given by

$$a \geq (3\lambda L)^{1/2}, \quad (1)$$

for $L = 1 \text{ cm}$ and $\lambda = 1 \text{ \AA}$, $a \geq 1.7 \mu\text{m}$.

Let us now turn our attention to the balance between the creation of gamma-ray photons by stimulated emission in the active sample and the absorption of these photons by the sample. Since the half-thickness $d_{1/2}$ for the absorption of photons does not in general exceed a few centimeters even in the MeV range, we can say that the gamma-ray amplification takes place provided that

$$\sigma n_e d_{1/2} > 1, \quad (2)$$

where σ is the cross section for stimulated emission, and n_e the number of excited nuclei per volume. This means that the fraction of excited nuclei n_e/n_0 , where n_0 is the number of nuclei per volume contributing to absorption, has to be

$$\frac{n_e}{n_0} > \frac{1}{\sigma d_{1/2} n_0} = \frac{A u}{\sigma d_{1/2} \rho}, \quad (3)$$

where A and ρ are respectively the atomic number and the density of absorbing nuclei, and $u = 1.67 \times 10^{-27} \text{ kg}$, the atomic mass unit. If we take the cross section for stimulated emission as the Breit–Wigner form

$$\sigma = \frac{4\pi\hbar^2 c^2}{E_\gamma^2}, \quad (4)$$

then the condition (3) becomes

$$\frac{n_e}{n_0} > \frac{A u E_\gamma^2}{4\pi\hbar^2 c^2 \rho d_{1/2}}. \quad (5)$$

The half-thickness for the photon absorption increases approximately quadrati-

cally with energy up to about 200 keV, then $d_{1/2}$ increases much more slowly. This means that the n_e/n_0 threshold for gamma-ray amplification, determined from condition (2), is the same up to energies of about $E_\gamma = 200$ keV, then this threshold increases approximately quadratically with the energy E_γ . For $E_\gamma = 100$ keV, the concentration threshold is

$$\frac{n_e}{n_0} \geq 4 \times 10^{-6} A, \quad (6)$$

where, as mentioned previously, A is the atomic number of the absorbing nuclei. For $A = 100$, the condition (6) is $n_e/n_0 > 4 \times 10^{-4}$, so that the threshold for the concentration n_e of excited state nuclei would be about $n_e \geq 2 \times 10^{19} \text{ cm}^{-3}$. An excited-state concentration of 2×10^{19} nuclei/cm³ is large and very difficult to achieve for excited states with a half-life of about 1 ns. However, the number of excited-state nuclei in a cylindrical sample $L = 1$ cm long and with a radius $a = 1.7 \mu\text{m}$ is 1.8×10^{12} nuclei, and does not appear to be exceedingly large. This suggests that, while a gamma-ray laser is a distant goal, there are many related problems which may constitute the object of sound and valuable research.

An example of this kind is the possibility to obtain an amplification of gamma rays without inversion of the *nuclear* populations by using what has been called *electron–nuclear double transitions*, or ENDTs [1]. The problems of inversionless amplification and electromagnetically induced transparency at the atomic scale have received recently much attention, [2–8] and Coussement et al. [9] have proposed to use quantum interference at nuclear Zeeman level crossings as a way to produce a non-reciprocity between the resonant emission and absorption of gamma rays in a crystal, with applications to the development of a gamma-ray laser. The related problem of the double gamma resonance in paramagnetic substances has been discussed by Sadykov [10].

We have studied theoretically the electron–nuclear coupled system of $^{151}\text{Eu}^{2+}$ in a CaF_2 lattice, in the presence of a strong static magnetic field and under the action of a microwave magnetic field. The energy levels of the $^{151}\text{Eu}^{2+}$ in CaF_2 which are relevant to the present discussion are shown in fig. 1. In fig. 1, M is the projection of the electron angular momentum along the z -direction of the static magnetic field, m_l is the projection along the z -axis of the angular momentum of the ground state of the ^{151}Eu nucleus, and m_u is the projection along z -axis of the angular momentum of the 21.54 keV state of the ^{151}Eu nucleus. The ^{151}Eu nucleus is supposed to be initially in the 21.54 keV excited state, and the atomic electrons in the ground state. We consider the possibility of pumping the electron–nuclear coupled system from the ground atomic electron Zeeman level $M = -\frac{7}{2}$ to a higher electron level $M = -\frac{5}{2}$ with the aid of a resonant microwave field, while the nucleus is undergoing a gamma-ray transition to the nuclear ground state. It can be shown [1] that the ratio of the probability of the electron–nuclear double transition $M = -\frac{7}{2}, m_u \rightarrow M = -\frac{5}{2}, m_l$ to that for the single-photon gamma-ray transition $M = -\frac{7}{2}, m_u \rightarrow M = -\frac{7}{2}, m_l$ is given by

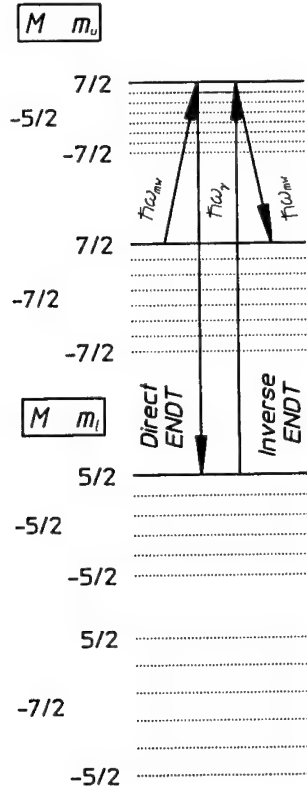


Fig. 1. Energy levels of $^{151}\text{Eu}^{2+}$ in CaF_2 , and direct and inverse electron–nuclear double transitions between these states.

$$R = \frac{7g^2\mu_B^2 H_{\text{mw}}^2}{4\hbar^2 \Gamma^2}, \quad (7)$$

and is independent of m_u and m_l , where $g = 1.9926$ is the electronic gyromagnetic ratio, $\mu_B = 9.274 \times 10^{-24} \text{ JT}^{-1}$ is the Bohr magneton, $\Gamma = \ln 2/T_{1/2}$ is the width of the 21.54 keV nuclear state, the half-life of this excited state being $T_{1/2} = 9.4$ ns, and H_{mw} is the amplitude of the microwave magnetic field, oriented along the x -axis.

If the intensity of the applied static magnetic field is $H = 5$ T, then at a temperature $T = 1$ K for the CaF_2 crystal the Boltzmann factor which determines the ratio of the electron populations in the $M = -\frac{5}{2}$ and $M = -\frac{7}{2}$ states is $\exp[-(E_{-5/2} - E_{-7/2})/kT] = 1.04 \times 10^{-3}$, i.e. the electron population is almost entirely in the $M = -\frac{7}{2}$ state. For $H = 5$ T, the resonance microwave frequency is $\omega_{\text{mw}}^{(\text{R})}/2\pi = 142$ GHz. For an applied microwave magnetic field having this frequency and an amplitude $H_{\text{mw}} = 10^{-4}$ T, the electron–nuclear double transition will result in a gamma-ray line whose position is shown in fig. 2 by the heavy line,

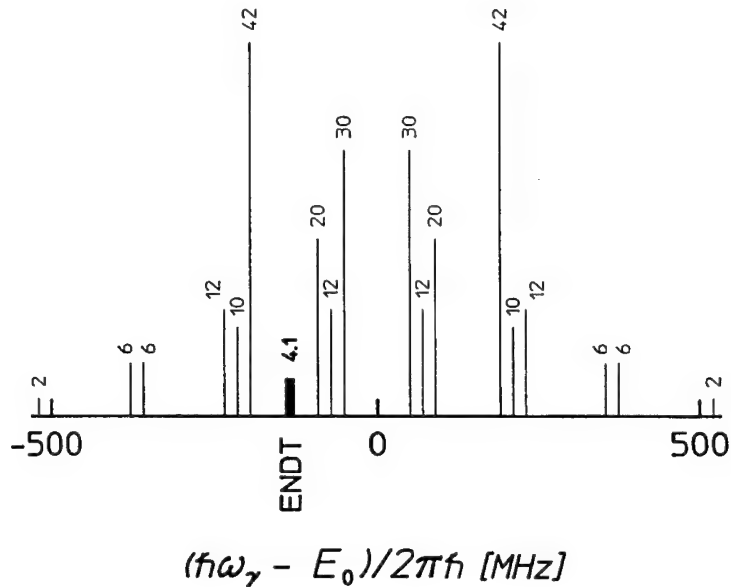


Fig. 2. Gamma-ray lines produced by $^{151}\text{Eu}^{2+}$ in CaF_2 in a static magnetic field $H = 5 \text{ T}$ and a microwave magnetic field of frequency 142 GHz of amplitude $H_{\text{mw}} = 10^{-4} \text{ T}$.

alongside with the regular, single-photon Mössbauer spectrum. The heights of the bars and the accompanying numbers give the relative intensities of the gamma-ray lines. The relative intensity of the ENDT line is $R = 0.098$.

The electron–nuclear double transition $M = -\frac{7}{2}, m_u = \frac{7}{2} \rightarrow M = -\frac{5}{2}, m_l = \frac{5}{2}$ considered in the previous section provides an interesting possibility for amplification of gamma rays without the need for achieving an inversion of nuclear populations employing upper-state microwave resonance. In that direct ENDT, the $^{151}\text{Eu}^{2+}$ system is initially in the $M = -\frac{7}{2}, m_u = \frac{7}{2}$ state which absorbed a microwave photon up to the $M = -\frac{5}{2}, m_u = \frac{7}{2}$ intermediate state before emitting a gamma-ray photon to reach the final, $M = -\frac{5}{2}, m_l = \frac{5}{2}$ state. This is shown in fig. 1 labeled as “Direct ENDT”. The cross section for the stimulated emission of the gamma-ray photon via this electron–nuclear double transition is denoted by σ_{ENDT} . The inverse electron–nuclear double transition occurs when the $^{151}\text{Eu}^{2+}$ system, initially in the $M = -\frac{5}{2}, m_l = \frac{5}{2}$ state, absorbs a gamma-ray photon up to the intermediate $M = -\frac{5}{2}, m_u = \frac{7}{2}$ state and then emits a microwave photon to reach the final $M = -\frac{7}{2}, m_u = \frac{7}{2}$ state. This process is also displayed in fig. 1 as “Inverse ENDT” and its cross section for the absorption of a gamma-ray photon will have the same value σ_{ENDT} as the direct electron–nuclear double transition. The concentrations of excited and ground state ^{151}Eu nuclei in the CaF_2 lattice are denoted by n_u and n_l , respectively. Similarly, the concentrations of Eu^{2+} ions in the $M = -\frac{5}{2}$ and $M = -\frac{7}{2}$ states are given by $N_{-5/2}$ and $N_{-7/2}$, respectively. In order for stimulated emission of gamma-ray photons via direct ENDT to prevail over the absor-

tion of gamma-ray photons via inverse ENDT, there must be a population inversion between the states $M = -\frac{7}{2}$, $m_u = \frac{7}{2}$ and $M = -\frac{5}{2}$, $m_l = \frac{5}{2}$. This may be written as

$$n_u N_{-7/2} > n_l N_{-5/2}, \quad (8)$$

or

$$\frac{n_u}{n_l} > \frac{N_{-5/2}}{N_{-7/2}}. \quad (9)$$

Since it can be arranged as discussed before for $N_{-5/2}/N_{-7/2} \ll 1$ at low temperatures, it is possible for $n_u/n_l < 1$ while still satisfying the overall inversion condition of eq. (8). This provides amplification of gamma rays by electron–nuclear double transitions when $n_u/n_l < 1$, that is even without inversion of the nuclear populations. The asymmetry between the emission and absorption of gamma rays in ENDTs is explained by the fact that in the emission process the initial state of the Eu^{2+} ion is the populated $M = -\frac{7}{2}$ electronic state, while in the absorption process the initial state of the ion is the relatively unpopulated $M = -\frac{5}{2}$ level. The principle is that the lack of inversion of the nuclear populations can be compensated by a sufficiently low population of Eu^{2+} ions in the $M = -\frac{5}{2}$ state. This ultimately generates an inversion of population for the entire electron–nuclear system of $^{151}\text{Eu}^{2+}$.

Another view is that the asymmetry is accomplished by using the microwave photon to shift the energy of the emitted gamma ray away from available absorption resonances. In the direct ENDT, the emitted gamma-ray energy is shifted by 38 MHz from nearest single-photon resonance, while the natural width of the gamma-ray transition is only 11.7 MHz. The practical limitations of the concept of amplification of gamma rays without nuclear inversion by ENDTs will be discussed further.

The use of ENDTs makes it possible to consider low-lying resonant Mössbauer gamma-ray transitions in the context of induced gamma emission. The fact that the pumping intensities are much higher at the relatively low energies of these resonant transitions is overshadowed to a certain extent by the fact that the relative concentration of the active nuclei in the sample cannot exceed a limit of about 10^{-3} .

Another interesting possibility would be to use isomeric nuclear states as the initial states of ENDTs to the ground nuclear state. The microwave power would act in this case as a switch of the process of amplification in the sample. The difficulties would now be associated with the linewidth of isomeric states having a halflife greater than about 1 μs .

The influence of an applied microwave magnetic field on gamma-ray emission of a nucleus has been analyzed for electron–nuclear double transitions of $^{151}\text{Eu}^{2+}$ in CaF_2 . These are two photon processes involving the emission of a gamma-ray photon and the simultaneous absorption of a microwave photon by the electrons and are rendered possible by the hyperfine interaction between the nucleus and the electrons. It has been shown that the intensities of these transitions become comparable to those of the single-photon gamma-ray lines for certain resonance fre-

quencies of the microwave field. At microwave resonance frequencies on the order of tens of GHz, it is in principle possible to achieve amplification of gamma rays without inversion of nuclear populations using electron–nuclear double transitions at liquid helium temperatures. This relaxes the stringent restrictions of cooling to the millikelvin range required by other amplification schemes. Detailed further work is needed to assess the practicality of using electron–nuclear double transitions for the problem of gamma-ray amplification, and in particular for a gamma-ray laser.

References

- [1] S. Olariu, report to contract 611B-B11-1994 of the Romanian Ministry of Research and Technology, unpublished.
- [2] S.E. Harris, Phys. Rev. Lett. 62 (1989) 1033.
- [3] S.E. Harris and J.J. Macklin, Phys. Rev. A 40 (1989) 4135.
- [4] A. Imamoglu, Phys. Rev. A 40 (1989) 2835.
- [5] O. Kocharovskaya, P. Mandel and Y.V. Radeonychev, Phys. Rev. A 45 (1992) 1997.
- [6] M.O. Scully, Phys. Rev. Lett. 67 (1991) 1855.
- [7] J.E. Field, K.H. Hahn and S.E. Harris, Phys. Rev. Lett. 67 (1991) 3062.
- [8] S.E. Harris, Phys. Rev. Lett. 70 (1993) 552.
- [9] R. Coussement, M. Van den Bergh, G. S'heeren, G. Neyens, R. Nouwen and P. Boolchand, Phys. Rev. Lett. 71 (1993) 1824.
- [10] E.K. Sadykov, Phys. Stat. Sol. B 123 (1984) 703.

Lasing without inversion due to cooling subsystem

R.N. Shakhmuratov

*Kazan Physical-Technical Institute of Russian Academy of Sciences, 10/7 Sibirsky trakt st., Kazan
420029, Russia*
E-mail: shakhmuratov@ksc.iasnet.com

The new possibility of inversionless lasing is discussed. We have considered the resonant interaction of a two-level system (TLS) with photons and the adiabatic interaction with an ensemble of Bose particles. It is found out that a TLS with equally populated energy levels amplifies the coherent light with Stokes-shifted frequency. This becomes possible as photon emission is accompanied by Bose particles excitation. The energy flow from the TLS to the photon subsystem is realized due to the Bose subsystem being at finite temperature and playing the cooler role. The advantage of this new lasing principle is discussed. It is shown that lasing conditions strongly differ from conventional ones.

1. Introduction

There is no stimulated amplification of coherent light by two-level systems (TLS) with equally populated energy levels. This is forbidden by thermodynamics because the energy flow between two systems with infinite temperature is impossible (coherent light is supposed to be infinitely hot). Meanwhile, one can introduce a third system as a cooler and thus make the energy flow between TLS and coherent light possible. This third system should absorb a fraction of TLS energy by stimulated light emission and emit the same fraction by stimulated absorption. As energy absorption is higher than emission (for a system of finite temperature), the coherent light stimulated emission exceeds the absorption. Due to the imposed condition, the light frequency is lower than the TLS resonant frequency. In this paper we will discuss an example of a “cooling machine” realized in solids, due to phonon–impurity interaction. We show that coherent light renders this interaction inelastic [1]. As the third system, phonons give the possibility of lasing without inversion.

2. Field influence on TLS relaxation

Description of TLS interaction with both the coherent light and the reservoir responsible for adiabatic relaxation (dephasing) is rather complicated. Therefore, these interactions are usually treated separately, step by step. In the first step, the equations describing TLS interaction with the reservoir are derived by means of

perturbation theory. Then, averaging on the reservoir states is performed and one can obtain the master equation. In the last step, interaction with coherent light is simply included into the master equation. This approach neglects some coherent effects. Recent experiments on hole burning and related transient phenomena in solids [2] prompted to revise this approach. A more accurate description is achieved by the derivation of master equations for a compound TLS + photons system. One can exactly calculate the TLS spectrum and states driven by coherent light. Then, it is possible to derive (using the perturbation theory) the master equation for this compound system interacting with the reservoir. This approach takes into account that TLS is in a coherent superposition state when interacting with light, whereas the traditional approach neglects this fact. The modified master equation, which is derived, for example, in paper [3], in order to describe anomalous saturation reported in ref. [2], takes into account the fast oscillations induced by the intense driving field. These oscillations average out the reservoir influence on the TLS polarization and dephasing suppression takes place. Phase relaxation quenching by intense coherent relaxation explained the anomalous saturation observed in experiment [2].

In this paper, we propose to consider the coherent effects at very low field intensity. This corresponds to TLS linear response calculation, when TLS (being in the superposition state) interacts with the reservoir. It is possible to extend this consideration to the high intensity field limit, with the only restriction that the Rabi frequency does not exceed the reservoir excitation bandwidth. Comparison of our approach with both the conventional one and the new one, described in paper [3], shows that the last one takes into account the Rabi frequency value which exceeds the reservoir bandwidth, compared to the conventional description which omit it. As for our approach, it takes into account the finite reservoir temperature, whereas both previous descriptions neglect this reservoir feature.

The modified master equations were derived in paper [1]. We considered both TLS interaction with the resonant field and adiabatic reservoir randomly shifting the TLS resonant frequency. We described the impurity ion interaction with photons playing the reservoir role. This description could be generalized for any other type of reservoir regarding an ensemble of Bose particles. Within this article, we discuss the physics of amplification without inversion, revealed in paper [1]. As well, we consider lasing conditions which strongly differ from conventional ones.

We will briefly list below the main stages of the derivation of the modified master equation. We will consider TLS interaction with a classical field. Then, by means of a U unitary transformation, we transform the Hamiltonian into the representation where TLS-field interaction does not depend on time and TLS frequency is modified. The U transformation does not change the TLS-reservoir interaction, as this is adiabatic. Then, by means of the V transformation, we diagonalize the Hamiltonian of the TLS interaction with the field. The new TLS states are called quasi-energy states. The resonant frequency of the new TLS depends on resonant detuning and Rabi frequency. The TLS interaction with the reservoir is modified.

Due to the \mathbf{V} transformation it becomes nonadiabatic. Thus, the reservoir induces transitions between the quasi-energy levels. As the reservoir temperature is finite, the quasi-energy TLS (Q-TLS) tends to equilibrium with a population difference determined by the Q-TLS energy gap and reservoir temperature. As Q-TLS population difference is proportional to the TLS polarization component (which is in phase with the driving field), the relaxation modification gives additional alignment of polarization along the driving field. The TLS master equation, known as the optical Bloch equation (OBE), is modified in the following mode. The two equations describing the v and w components of the Bloch vector keep the previous form. The modification is performed due to the appearance of an additional term in the equation of the u -component, i.e.

$$\frac{\partial u}{\partial t} = -\Delta v - \Gamma(u - u_0), \quad (1)$$

where $w = \rho_{22} - \rho_{11}$; $u + iv = 2\rho_{12}e^{-i\omega t}$, ρ_{ij} is the matrix element of the TLS density matrix; $\Delta = \omega_{21} - \omega$ is the resonant detuning; ω_{21} is the resonant frequency; ω is the driving field frequency, Γ is the rate of the phase relaxation induced by the reservoir, $u_0 = \hbar\chi/2kT$, χ is the Rabi frequency and T is the reservoir temperature. This additional term present in the equation modifies the absorption (amplification) coefficient as follows:

$$\begin{aligned} \gamma(\omega) &= \gamma_c(\omega) + (\hbar\Gamma/2kTw_0)\gamma_{S-A}(\omega), \\ \gamma_c(\omega) &= A \frac{\Gamma}{\Gamma^2 + \Delta^2}, \\ \gamma_{S-A}(\omega) &= AS \frac{\Delta}{\Gamma^2 + \Delta^2}, \end{aligned} \quad (2)$$

where $A = w_0|d_{12}|^2NK/\hbar n^2$; γ_c is the unmodified part of the coefficient; γ_{S-A} is the modified part of the coefficient; w_0 is the unperturbed population difference; d_{12} is the matrix element of the TLS dipolar moment; N is the concentration of TLS particles in the medium; n is the refractive index; K is the wave number; $S = \rho_{11} + \rho_{22}$. The unmodified coefficient part is a usually bell-shaped absorption or emission coefficient, depending on the w_0 sign. The modified part has two components. The Stokes component is an amplifying one while the anti-Stokes component is an absorbing one. Their maxima are shifted from the resonant frequency towards the Γ value. When the w_0 population difference equals zero we obtain the largest Stokes component amplification. When only the ground state is populated, OBE modification leads to a very small absorption line distortion. By adjusting the Δ , T and w_0 parameters (the last one can be driven by incoherent pumping via other energy levels), one can achieve amplification without inversion ($w_0 < 0$ or $\rho_{22} < \rho_{11}$). A question rises – where does the energy come from and which are the processes involved? To answer these questions we consider the TLS with equally

populated states. If relaxation is caused only by spontaneous emission, then the driving field is not able to induce TLS polarization, as this is proportional to the population difference. The adiabatic reservoir changes TLS interaction with the field. We have three interacting subsystems, i.e. a) TLS with infinite temperature, b) coherent infinitely hot field, and c) the equilibrium state reservoir with finite temperature and infinite thermal capacity. Let us consider two types of transitions. The first one (when $\omega > \omega_{21}$) is shown in fig. 1. The transition with TLS energy loss (the transition from the upper state to the ground state) is depicted by the bold arrow. The $\hbar\Omega$ reservoir energy quantum (denoted by wavy arrow) is added to the first quantum. The total $\hbar\omega$ energy quantum, which is the sum of $\hbar\omega_{21}$ and $\hbar\Omega$ is emitted as a field quantum. The W_e probability for this process is equal to the product of the TLS transition probability from state 2 to 1 (W_{\downarrow}) and w_{\downarrow} is the probability that the reservoir loses the $\hbar\Omega$ energy quantum. The reverse process shown on the right-hand side of fig. 1 takes place by absorption of an $\omega = \omega_{21} + \Omega$ frequency photon. Its W_a probability is equal to the product between the W_{\uparrow} probability of $\hbar\omega_{21}$ quantum absorption by TLS and the w_{\uparrow} probability of $\hbar\Omega$ quantum absorption by reservoir. As TLS has an infinite temperature, the W_{\uparrow} and W_{\downarrow} probabilities are equal. As for the reservoir, the w_{\downarrow} emission probability is less than w_{\uparrow} absorption probability, as its temperature is finite. As a result, we have $W_a > W_e$, i.e. the field absorption probability is higher than the emission probability. Therefore the TLS+reservoir compound system absorbs the light with a $\omega > \omega_{21}$ frequency (anti-Stokes component). The second type of transitions is shown in fig. 2. This is the case when the ω field frequency is lower than the TLS ω_{21} resonant frequency. The $\hbar\omega$ quantum emission takes place by TLS $\hbar\omega_{21}$ quantum emission and by reservoir $\hbar\Omega$ energy quantum absorption. The reverse process is shown on the right-hand side of fig. 2. The $\hbar\omega$ photon emission probability is equal to the $W_{\downarrow}w_{\uparrow}$ product, whereas the

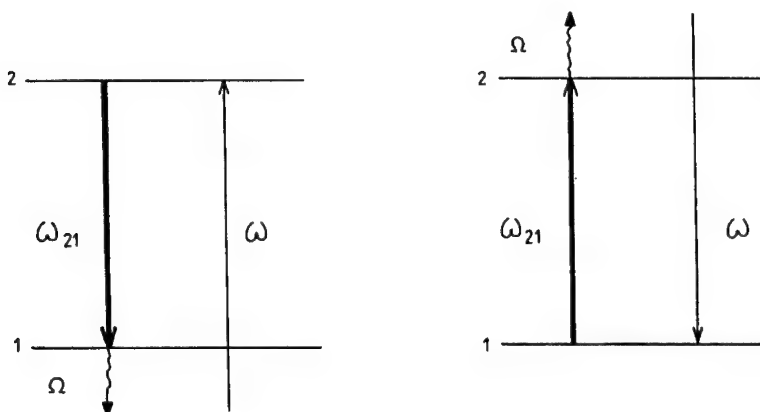


Fig. 1.

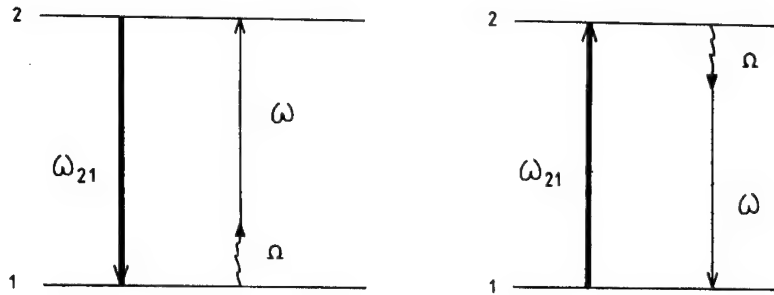


Fig. 2.

absorption probability is equal to $W_\uparrow w_\downarrow$. Using the same speculations one can obtain the $W_e > W_a$ inequality. Therefore, the compound TLS+ reservoir system amplifies the field of $\omega < \omega_{21}$ frequency. The absorption-amplification line of this compound system can be explained by the following. The W_e emission and W_a absorption probabilities depend on the w_\uparrow, w_\downarrow probabilities for transitions within the reservoir. The last ones depend on the reservoir quasi-particles number for an Ω frequency. At exact resonance ($\omega = \omega_{21}$) this frequency is zero and, for example, in a phonon system reservoir, there are no quasi-particles. Therefore, TLS does not interact with a field ($W_e = W_a$). On resonant detuning $|\omega - \omega_{21}| = \Omega$ increase, the phonon number increases and, consequently the w_\uparrow, w_\downarrow probabilities increase. The maximum phonon contribution to dephasing occurs at the $\Omega = \Gamma$ frequency. Together with the next Ω frequency increase, the probabilities will decrease. As a result, the two-component line (presenting Stokes amplifying and anti-Stokes absorbing components) appear. The energy balance analysis performed using the modified master equations solutions shows that, when $\omega < \omega_{21}$, TLS gives the $\hbar\omega w/2$ energy to the field at $1/T_1$ rate, where T_1 is the TLS excited state lifetime. The $\hbar(\omega_{21} - \omega)w/2$ rest of TLS energy is given to the phonons. Then, the TLS population difference decreases and TLS cools. When $\omega > \omega_{21}$, TLS absorbs the $\hbar\omega_{21}w/2$ field energy at a rate of $1/T_1$. The remainder $\hbar(\omega - \omega_{21})w/2$ is given to the reservoir. As a result, the TLS excited state population increases and TLS acquires population inversion. Thus, we obtain some kind of a cooling machine. Two subsystems, i.e. TLS and coherent field, being at infinite temperature, can exchange energy one with the other, due to the lower temperature reservoir. The reservoir works as a cooler. If its temperature decreases, the energy transfer efficiency increases. The maximal value of the amplification coefficient by the TLS particles medium is

$$\gamma_{\max}(\omega_{21} - \Gamma) = \frac{KN|d_{12}|^2}{4n^2kT_r} . \quad (3)$$

Thus, for lower T_r reservoir temperature and higher d_{12} dipolar transition matrix

element the amplification coefficient value increases. The amplification threshold condition (i.e. the condition when coefficient γ is positive) is expressed as

$$\frac{\hbar\Gamma}{2kT_r} + w_0 > 0. \quad (4)$$

Thus, one can achieve the inversionless gain if the population satisfies this inequality. As the Γ rate dephasing is temperature dependent, one can achieve the threshold condition (4) by adjusting the temperature, when the $w_0 = \rho_{22} - \rho_{11}$ population difference is higher than -1 . As an example, for impurity-ion-phonon interaction in a crystal, the Γ dephasing rate is proportional to $T^7 J_3(\theta/T)$, where T is the phonon system temperature, θ is the Debye temperature and $J_3(x)$ is the 3rd-order Bessel function. Thus for higher phonon temperature, the Γ/T ratio increases.

Let us compare the conditions of conventional lasing due to population inversion with the conditions of our inversionless lasing. The first demands the possibility of obtaining population inversion. Therefore, it is necessary to use very weak transitions with small transition matrix elements. As the amplification depends on the inverse value of the Γ dephasing rate, it is preferable to use very sharp lines.

The considered inversionless gain demands very strong transitions (with large d_{12}) and very broad lines. This means that we have proposed an alternative lasing principle. As the $|d_{12}|^2$ value for an allowed transition is 10^4 times higher than for a forbidden one, very high gain can be obtained at small excitation of the upper lasing level. This high gain can produce a giant pulse which is usually very short (about 10^{-8} – 10^{-9} s). Therefore, if it is possible to somehow equalize (for example, by cascade pumping) the population of two levels for a time longer than 10^{-8} – 10^{-9} s, lasing by giant pulses will be achieved.

3. Discussions

Using the described method, one can get lasing in visible, ultraviolet or X-ray bands. It is not necessary to use the reservoir with Bose statistics. Therefore, particle collisions in a gas or ionization processes in solids can serve as a supplementary process in lasing. It is hard to expect this principle to be applied in the gamma band. However, if any broadening process of gamma emission spectrum exists (apart from life time broadening), then this lasing principle can be applied. In our opinion, it may be that nuclear spins excitation by strong radio frequency field could serve as one of these broadening mechanisms.

Acknowledgement

The author expresses his thanks to ISF for support (Grant no. RKC 300).

References

- [1] R.N. Schakhmuratov, *Kvantovaya Elektron. Mosk. (USSR)* 13 (1986) 271.
- [2] R.G. DeVoe and R.G. Brewer, *Phys. Rev. Lett.* 50 (1983) 1269.
- [3] A. Schenzle et al., *Phys. Rev. A* 30 (1984) 325.

Sub-threshold inversionless quasi-stationary gamma amplification on the basis of Mössbauer ^{57}Fe nuclei and spin-crossover systems in non-conductive complex compounds with ^{57}Co

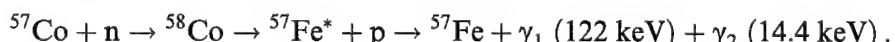
V.I. Vysotskii^a, V.V. Vysotskii^a, R.N. Kuz'min^b and V.P. Bugrov^b

^aKiev Shevchenko University, Radiophysical Dept., 252017, Kiev, Ukraine

^bMoscow State University, Physical Faculty, 119899, Moscow, Russia

It is shown that, using non-conductive ^{57}Co compounds with large electron relaxation time $\tau_1 \approx 40$ ns, it is possible to create a sub-threshold inversionless quasi-stationary gamma laser for the system of ^{57}Fe nuclear resonant levels.

Refs. [1,2] have considered the possibility of gamma-laser creation (with $E_\gamma = 14.4$ keV quanta energy) on the basis of gamma-transitions in ^{57}Fe nuclei. The $^{57}\text{Fe}^*$ excited states of these nuclei can be obtained using the $^{57}\text{Co}(n,p)^{57}\text{Fe}^*$ nuclear reaction. According to the models [1,2], the complete transitions scheme for the analyzed system is



Here, the last quantum of the nuclear cascade, γ_2 , has the $E_{\gamma_2} = 14.4$ keV energy which remains unmodified for emission and absorption (with Mössbauer effect present).

Under the general classification given in ref. [3], this is the typical threshold scheme of gamma-laser, requiring the inversion $n_2 > n_1$ for the operating $2 \rightarrow 1$ transition. Like all other threshold schemes, this one also requires an incredible high-intensity neutron pumping, $I_n > 10^{26} \text{ cm}^{-2}\text{s}^{-1}$.

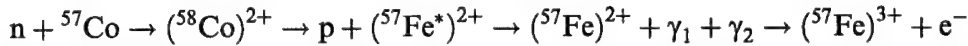
The utilization of pulse pumping with $\Delta t < \tau_{21} = \tau$ duration, partially takes away the problem of inversion but leads to a number of other very important problems: sharp reduction of resonant amplification cross-section (far from the $\sigma \approx \lambda^2 f / 2\pi(1 + \alpha)$ asymptotic value which can be achieved only at $\Delta t \gg \tau$ [4]) and the impossibility to re-use the active medium due to ^{57}Fe nuclei accumulation in the main state.

Indeed, the real transition scheme for the $^{57}\text{Co} \rightarrow ^{58}\text{Co} \rightarrow ^{57}\text{Fe}$ reaction, significantly differs from the one analyzed in refs. [1,2]. Immediately after transition of $^{58}\text{Co} \rightarrow ^{57}\text{Fe}^*$ nuclei (i.e. after proton emission) the electron cover of the $^{57}\text{Fe}^*$ nucleus still retains the ^{58}Co structure. Consideration of chemical shift leads to

energy level displacement, compared to the case when both nucleus and electron cover correspond to ^{57}Fe . Only after some time (τ_1), the electron subsystem relaxes to the ^{57}Fe atom equilibrium state. This circumstance can be used to optimize the gamma-laser system.

We have proposed earlier [3,5] the sub-threshold gamma-laser model using the transitions between the high-spin (H) and low-spin (L) states of the Fe electron cover.

Within the framework of general sub-threshold gamma amplification idea [1] we consider the possibility of inversion-free gamma-laser featuring the pump reaction



in non-conductive complex compounds, containing ^{57}Co with long HS \rightarrow LS relaxation in spin-crossover system (like $[^{57}\text{Co}(\text{phen})_3](\text{ClO}_4)_2$, $^{57}\text{Co}[\text{Fe}(\text{CN})_6]$, etc.). The traditional experiment scheme (e.g. refs. [1,2]) and the one we proposed, are shown in fig. 1a and b.

The splitting of the resonance levels $E_\gamma = 136$ keV, (3a,3); $E_\gamma = 14.4$ keV, (2a,2); (1a,1), is caused by a chemical shift and exceeds the width of level 2. In case a, the Co \rightarrow Fe the electron cover relaxaton process has a short duration, $\tau_r \equiv \tau_{\text{Co},\text{Fe}} \equiv \tau_{3a,3} \leq 10^{-14}$ s, which results in a 3a \rightarrow 3 \rightarrow 2 \rightarrow 1 traditional decay scheme.

As a result, the ω_{12} resonant absorption and ω_{21} amplification frequencies are equal, which causes the $n_2 > n_1$ inversion and high pumping intensity requirements.

In case b, we have an electron cover with long duration τ_r . For example, the $[^{57}\text{Co}(\text{phen})_3](\text{ClO}_4)_2$ compound forms a low-spin LS final condition $(^{57}\text{Fe})^{3+}$ from a high-spin HL, $(^{57}\text{Co})^{2+}$, with $\tau_r \approx 200$ ns at $T = 47$ K and $\tau_r \approx 100$ ns at $T = 100$ K [3], with $\tau_s \gg \tau_3 = 8.6$ ns, $\tau_r > \tau_3 = 98.6$ ns corresponding condition and 3a \rightarrow 2a \rightarrow 1a \rightarrow 1 primary decay scheme.

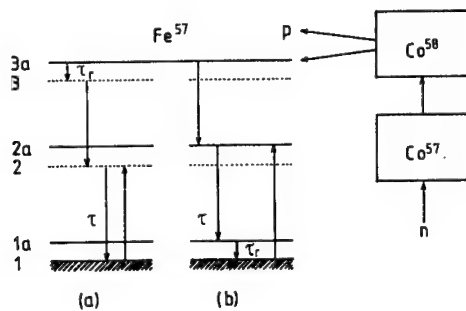


Fig 1.

Here, the $\omega_{2a,1a}$ amplification and $\omega_{21,2a}$ absorption frequencies do not coincide, fact which excludes the need of inversion and allows the use of long pumping realizing an asymptotically large (stationary) $\sigma_{2a,1a}(1 \gg 1/\Gamma_{2a,1a})$ amplification cross-section.

This case qualitatively corresponds to the situation occurring at very deep cooling of Zeeman sublevels of the nucleus ground state and cannot be achieved for $T \leq 10^{-3}$ K [3] but for $T \geq 100$ K.

In such a system, it is possible to decrease the required pumping intensity by 1–2 orders of magnitude.

It is interesting to consider the question of the optimal τ_r relaxation time. At quasi-stationary pumping, the $n_{1a} = n_{2a}\tau_r/\tau$ population of 1a lower level for the operating transition is determined from:

$$\frac{dn_{1a}}{dt} = n_{2a}/\tau - n_{1a}/\tau_r = 0.$$

The broadening parameter of the operating transition is:

$$\Gamma\tau = (\tau^{-1} + \tau_r^{-1})\tau = 1 + \tau/\tau_r.$$

The amplification coefficient of the $2a \rightarrow 1a$ transition is expressed as:

$$G = \frac{\lambda^2}{2\pi(1+\alpha)(1+\tau/\tau_r)} f n_{2a}(1 - \tau_r/\tau),$$

where f is the recoil free parameter and α is the conversion coefficient. The G maximal value corresponds to the $\tau_r = \tau(\sqrt{2} - 1)$ condition, which is satisfied at $T = 150$ K in the above regarded compound.

References

- [1] C.D. Bowman, *6th Int. Symp. on Capture Gamma-Ray Spectroscopy* (1987).
- [2] G. Baldwin and J. Solem, *Kinetics of neutron-burst pumping gamma-ray lasers*, preprint Los Alamos National Laboratory LAUR 94-1403 (1994).
- [3] V.I. Vysotskii and R.N. Kuz'min, *Gamma-lasers* (Moscow, 1989).
- [4] V.I. Vysotskii and V.I. Vorontsov, Sov. Phys. JETP 39 (1974) 748.
- [5] P. Gütlich and A. Hauser, Spiering Int. Ed. Engl. 33 (1994) 2024.

Section 4

Mössbauer Effects

Gamma-ray tuning by stimulated emission of recoil phonons

A.A. Zadernovsky

*Moscow Institute of Radio Engineering, Electronics and Automation,
78 Vernadsky Ave., Moscow 117454, Russia*

Tuning of gamma radiation by exciting the ultrasonic vibrations of different coherence degree in crystals is discussed. The quantum approach based on the formalism of coherent quantum states is used to take into account statistical properties of the stimulating ultrasonic wave. Multi-quantum transitions with emission of gamma quanta and simultaneous stimulated emission of recoil phonons or absorption of one or several phonons from an external ultrasonic wave are considered as an example of multi-quantum transitions with quanta coupled to different degrees of freedom of the radiating nuclei. The spectrum of gamma radiation is determined for a partially coherent stimulating ultrasonic wave with fixed amplitude and uncertain phase, and completely incoherent casual acoustic oscillations. A comparison is made with some known results obtained by both classical and quantum methods.

1. Introduction

Stimulated multi-quantum transitions involving quanta of different nature recently attracted increasing attention, due to the possibility of using one type of quanta in order to influence emission or absorption of another type of quanta. In this paper, we consider the possibility of tuning gamma radiation from nuclei in solids by stimulating the recoil phonon emission using an external source of ultrasonic vibration. It is well known [1,2] that ultrasonic waves excited in crystals result in a drastic transformation of the gamma radiation spectrum. The ultrasonic modulation phenomena involving Mössbauer radiation, have been intensively investigated both theoretically and experimentally [2,3]. Within the framework of the quantum approach, we summarize a wealth of data on the possibility of controlling the gamma radiation line spectrum shape.

It is well known that the gamma radiation spectrum of nuclei in solids contains, under certain conditions, a narrow line with the natural width corresponding to single-quantum nuclear radiative transitions that are not accompanied by emission of recoil phonons (the Mössbauer effect). Broad wings of this spectrum are due to multi-quantum transitions with gamma-quanta emission and simultaneous emission or absorption of one or several phonons.

A specific feature of the multi-quantum transition under consideration should

be outlined: the quanta involved in these transitions belong not only to oscillations of different nature but in addition these quanta are coupled to different degrees of freedom of the radiating nuclei. Indeed, the emission of a gamma quantum by the nucleus is accompanied by a change of the internal energy of the nucleus, i.e., of the energy of the relative motion of nucleons which compose the nucleus. Emission or absorption of phonons is associated with vibronic motion of the nucleus as a whole within a crystal lattice. Redistribution of energy between various degrees of freedom of the same radiating nucleus is governed by the energy and momentum conservation laws. No interaction mechanism is required in order to couple the radiation field to the phonon field of a crystal. Therefore, stimulation of the considered multi-quantum transition phononic component can not enhance the total gamma quanta spontaneous emission rate (in contrast, for example, to the photon-phonon interband electron transitions in indirect-gap semiconductors [4], where photons and phonons turn out to be coupled to the same electronic degree of freedom). In other words, the area under the spectral curve of the gamma radiation intensity for nuclei in solids remains constant. However, we can modify the spectral curve shape by changing the stimulating ultrasonic wave parameters.

Stimulation of the phononic component of the considered multi-quantum transitions increases the rate of the processes so that, in addition to gamma quanta emission, it implies emission of phonons which carry away the recoil energy or absorption of phonons excited in the crystal using an external source. As a result, the wings amplitude in the gamma radiation intensity spectrum increases. At the same time, the non-shifted Mössbauer spectral line amplitude decreases, so that the area under the spectral intensity curve remains unchanged. Thus, intensity modulation of stimulating ultrasonic vibrations gives rise to amplitude modulation of the Mössbauer line in the gamma emission spectrum.

If the intensity of stimulating ultrasonic vibrations exceeds (for a given frequency range) the intensity of background thermal oscillations of nuclei, the emission of recoil phonons will mainly occur within the frequency band width of the stimulating ultrasonic wave. In this case, the gamma radiation spectrum features a set of equidistant sidebands (satellites), shifted in comparison with the Mössbauer line by frequencies that are multiples of the stimulating ultrasonic vibrations frequency. These satellites are due to the multi-quantum transitions with a gamma quantum emission and simultaneous stimulated emission or absorption of one, two, etc. phonons. As the degree of monochromaticity of the ultrasonic wave increases these satellites frequency width decreases and approaches the natural width. By varying the ultrasonic wave frequency, we can vary the satellite frequencies.

The relative amplitudes of the Mössbauer and the satellite lines are determined by the excitation conditions of the stimulating acoustic vibrations and depend on the intensity, polarization, propagation direction and degree of coherence of the ultrasonic wave.

The above specified method for gamma radiation frequency tuning, has been ori-

ginally considered in refs. [1–3,5] and it is widely used in gamma-resonance spectroscopy of solids (see the review in ref. [6]).

Below, we provide a detailed analysis of gamma radiation tuning by excitation of different coherency degree ultrasonic vibrations in crystals. The quantum approach based on the coherent quantum states formalism is used with the aim to take into account the ultrasonic wave statistical properties. The shapes of the gamma radiation spectral curves are determined for partially coherent and completely incoherent accidental acoustic oscillations.

2. Spectral line shape

The probability that a nucleus with radiative transition energy E_0 emits a gamma quantum of energy E in the interval dE , is given by $P(E) dE$, where $P(E)$, for observation times much longer than the $\tau = 1/\Gamma$ nuclear radiative decay time, can be expressed as [3]

$$P(E) = \frac{1}{2\pi\hbar} \int_{-\infty}^{+\infty} \langle Q(t) \rangle \exp(-\frac{1}{2}\Gamma|t|) \exp\left\{-\frac{i}{\hbar}(E - E_0)t\right\} dt, \quad (1)$$

where $\langle Q(t) \rangle$ is the correlation function of the crystal acoustic field described by the operator

$$Q(t) = e^{i\kappa x(t)} e^{-i\kappa x(0)}, \quad (2)$$

averaged using the density matrix ρ of the crystal lattice, i.e. $\langle Q(t) \rangle = \text{Sp}(\rho Q(t))$ and $\kappa = E_0/\hbar c$, while $x(t)$ is the radiating nucleus displacement from the equilibrium position at the moment of time t . The $x(t)$ operator can be expressed as a sum of normal oscillations

$$x(t) = \sum_s \left(\frac{\hbar}{2MN\Omega_s} \right)^{1/2} e_s (a_s e^{-i\Omega_s t} + a_s^+ e^{i\Omega_s t}), \quad (3)$$

for a crystal with N nuclei of mass M , whilst a^+ and a represent the operators for creation and annihilation of phonons in the s th acoustic field mode.

Employing the diagonal representation of the density matrix ρ , in the basis of coherent quantum states [7]

$$\rho = \int w(z) |z\rangle \langle z| d^2z, \quad (4)$$

where $z = z' + iz''$ and $d^2z = dz'dz''$. We can express $\langle Q(t) \rangle$ as a product [8],

$$\langle Q(t) \rangle = \langle Q(t) \rangle_T \cdot \langle Q_0(t) \rangle, \quad (5)$$

between the correlation function of the crystal thermal acoustic field, $\langle Q(t) \rangle_T$, and the one of the stimulating acoustic field excited in the crystal, $\langle Q_0(t) \rangle$. Here,

$\langle Q(t) \rangle_T$ is the result of the $Q(t)$ operator (eq. (2)) averaging using the density matrix of the equilibrium thermal acoustic field for the crystal lattice at the temperature T ,

$$\langle Q(t) \rangle_T = \exp \left[- \sum_s |\alpha_s|^2 (2n_s + 1) \right] \cdot \exp \left\{ \sum_s |\alpha_s|^2 [(n_s + 1)e^{-i\Omega_s t} + n_s e^{i\Omega_s t}] \right\}, \quad (6)$$

where

$$\alpha_s(t) = i \left(\frac{\hbar}{2MN\Omega_s} \right)^{1/2} (\kappa e_s) e^{i\Omega_s t}, \quad (7)$$

and $n_s = [\exp(\hbar\Omega_s/kT) - 1]^{-1}$ is the mean number of phonons in the s th mode. The correlation function of the stimulating acoustic field, $\langle Q_0(t) \rangle$, can be expressed as

$$\langle Q_0(t) \rangle = \int w_0(z) e^{\Delta\alpha_0 z^* - \Delta\alpha_0^* z} d^2z, \quad (8)$$

where $\Delta\alpha_0 = \alpha_0(t) - \alpha_0(0)$, and $\alpha_0(t)$ denotes α_s (eq. (7)) for $\Omega_s = \Omega_0$ ultrasonic waves frequency.

3. Thermal acoustic field

Let us consider the $\langle Q(t) \rangle_T$ correlation function (eq. (6)) of the crystal thermal acoustic field. Using the well known expression for the phonon modes spectral density, we can easily verify that sums over s in eq. (6) are proportional to the ratio of the $E_R = E_0^2/(2Mc^2)$ recoil energy to the $\hbar\Omega_D$ Debye energy of the crystal. Therefore, with a view to provide a more detailed investigation of $\langle Q(t) \rangle_T$, we will consider two limiting cases: the low recoil energy case, $E_R \ll \hbar\Omega_D$ and the high recoil energy case, $E_R \gg \hbar\Omega_D$.

In both limiting cases we can use eqs. (3) and (7) to rewrite the first exponential in eq. (6) as $\exp(-x_T^2/\lambda^2)$, where x_T is the thermal root-mean-square displacement of nuclei in the lattice, in the emission direction of gamma quanta with $\lambda = \lambda/2\pi$ reduced wavelength. This is the well known Debye–Waller factor.

For $E_R \ll \hbar\Omega_D$ the second exponential in eq. (6) can be expanded in a series. Restricting our consideration to the first two terms of the resulting expansion, we obtain

$$\langle Q(t) \rangle_T = e^{-x_T^2/\lambda^2} + e^{-x_T^2/\lambda^2} \sum_s |\alpha_s|^2 [(n_s + 1)e^{-i\Omega_s t} + n_s e^{i\Omega_s t}]. \quad (9)$$

Substituting eq. (9) into $P(E)$ (eq. (1)) and performing integration over t , we can see that the gamma emission spectrum for a nucleus in a crystal lattice in the

thermal equilibrium state features a non-shifted line at the $E = E_0$ energy with amplitude equal to $\exp(-x_T^2/\lambda^2)$ and natural line width Γ . Each mode of the thermal oscillation gives birth to gamma emission with $E = E_0 \pm \hbar\Omega_s$ energy. This result can be interpreted as a multi-quantum transition with emission of a gamma quantum and absorption or emission of a single recoil phonon. Taking into account higher-order terms in the expansion of eq. (9), we can find other emission spectrum components for the $E = E_0 \pm \hbar\Omega_s \pm \hbar\Omega_s$ energies, which correspond to the transitions with simultaneous emission or absorption of two phonons, etc. It should be observed that emission of a recoil phonon in the s th mode of the acoustic field, is described by a term proportional with $(n_s + 1)$. In other words, the emission of recoil phonons may be either spontaneous or stimulated [9].

From this point of view, a broad-band thermal acoustic field of a crystal stimulates the emission of recoil phonons within the entire frequency range starting from 0 up to the Debye frequency Ω_D , which results in a broadening of the wings in the gamma radiation spectrum, from the Γ natural width up to the Debye width Ω_D . Exciting ultrasonic vibrations in the crystal, in order to modify the spectrum of phonons which form the stimulating field, we can radically change the gamma radiation spectrum. In particular, the sidebands of the spectrum can be narrowed down to the natural linewidth.

In the opposite case, when $E_R \gg \hbar\Omega_D$, the second exponential in eq. (9) varies so rapidly that we can replace the $e^{\pm i\Omega_s t}$ exponential by a few elementary terms of the corresponding expansions. Restricting ourselves to the quadratic terms of these expansions, we obtain:

$$\langle Q(t) \rangle_T = \exp\left(-\frac{iE_R t}{\hbar} - \frac{2\epsilon E_R t^2}{\hbar^2}\right). \quad (10)$$

Substituting eq. (10) into (1) we can see that the first term in the argument of the exponential of eq. (10) produces a shift of the gamma radiation spectral line centre with the E_R recoil energy. The second term of the exponential argument, proportional to the ϵ mean kinetic energy of the thermal vibrations of the radiating nucleus along the gamma quantum emission direction is responsible for Doppler broadening of the spectral line up to a magnitude of $\sim \sqrt{\epsilon E_R}$. Thus, in the considered limiting case, the line shape of the gamma radiation from nuclei in solids, in presence of the thermal acoustic field, is similar to the corresponding line shape in rarefied gases.

4. Stimulating acoustic field

The character of acoustic vibrations within a gamma emission source sample, excited by means of a piezocconverter, is determined by the propagation conditions of ultrasonic waves in a composite acoustic resonator which includes the piezocconverter and the sample. Specific features of standing ultrasonic waves excitation in

composite resonators were studied in refs. [5,10]. It was shown that the excited ultrasonic vibration intensity strongly depends on the coincidence between its frequency and the mechanical resonance frequency. Varying the frequency of electric oscillations applied to the piezoconverter, we can ensure excitation of a definite mode of the composite resonator. The line width of the $\Delta\Omega_0$ mode is determined by the decay of the ultrasonic waves in the sample and piezoconverter materials. It is usually about an order of magnitude less than the separation between the modes, $\Delta\Omega = 10^6\text{--}10^7 \text{ s}^{-1}$. Therefore, the stimulating acoustic field is assumed to be a standing ultrasonic wave with a definite Ω_0 frequency. Obviously, this approximation is valid only when $\Delta\Omega_0 \ll \Gamma$. This inequality is usually satisfied because, for typical conditions, $\Gamma = 10^7\text{--}10^8 \text{ s}^{-1}$.

The degree of coherence of the excited ultrasonic wave depends on the relation between the $T_0 = 2\pi/\Omega_0$ oscillation period, the amplitude relaxation time τ_1 and the relaxation time τ_2 of the oscillations phase. The character of acoustic vibrations excited within the mode is determined by anharmonic scattering of ultrasonic phonons on the lattice thermal phonons, ultrasonic phonons scattering on defects and impurities in the crystal and reflection condition of the ultrasonic wave on the faces of the crystal which forms an acoustic resonator. On the whole, all these processes determine the statistical properties of the amplitude and phase of the generated ultrasonic vibrations. Due to these effects, an ultrasonic wave with fixed amplitude and phase is first transformed (within a time τ_2) into random chaotic phase wave and after a time τ_1 into a random amplitude wave.

If there are no considerable phase and amplitude jumps of the ultrasonic wave during the oscillation period, i.e. if $T_0 \ll \tau_1, \tau_2$, the excited ultrasonic wave can be described by the coherent state of a quantum oscillator with the distribution function

$$w_0(z) = \delta(z' - z'_0)\delta(z'' - z''_0). \quad (11)$$

For $\tau_2 \ll T_0 \ll \tau_1$ we deal with fixed amplitude and uncertain phase vibrations, described by the distribution function

$$w_0(z) = \frac{\delta(|z| - |z_0|)}{2\pi|z_0|}. \quad (12)$$

Finally, for $T_0 \gg \tau_1, \tau_2$ the statistical properties of the excited ultrasonic vibrations are similar to the statistical properties of the thermal vibrations and can be described by the Gaussian distribution function

$$W_0(z) = \frac{e^{-|z|^2/n_0}}{\pi n_0}, \quad (13)$$

where n_0 is the mean number of phonons in the ultrasonic wave.

Acoustic vibrations of frequency $\Omega_0 = 10^8\text{--}10^9 \text{ s}^{-1}$, excited within the crystal at room temperature, for $\tau_1 \sim 10^{-10}\text{--}10^{-11} \text{ s}$ and $\tau_2 \sim 10^{-11}\text{--}10^{-12} \text{ s}$, are completely incoherent. Using the distribution function of eq. (13), we can obtain the expression

for the correlation function (eq. (8)) of incoherent stimulating ultrasonic vibrations as [3,5]

$$\langle Q_0(t) \rangle = e^{-x_0^2/\lambda^2} \sum_{m=-\infty}^{+\infty} I_m(x_0^2/\lambda^2) e^{im\Omega_0 t}, \quad (14)$$

where I_m is the m th order modified Bessel function and x_0 is the root-mean-square displacement of a nucleus in the lattice, in the gamma quanta emission direction, under the ultrasonic wave action.

If the crystal surfaces forming the phonon resonator are sufficiently perfect, the lowering of the crystal temperature may result in a τ_1 and τ_2 increase up to values of 10^{-6} – 10^{-7} s and 10^{-9} – 10^{-10} s, respectively. In this case, the ultrasonic wave is considered to be a fixed amplitude wave. Using the distribution function of eq. (12), we can obtain the following expression for $\langle Q_0(t) \rangle$ [3,5]

$$\langle Q_0(t) \rangle = \sum_{m=-\infty}^{+\infty} J_m^2(x'_0/\lambda) e^{im\Omega_0 t}, \quad (15)$$

where J_m is the m th order Bessel function and x'_0 is the mean amplitude of nuclear vibrations along the gamma quanta emission direction for the considered ultrasonic wave.

In practice, it is difficult to satisfy the $T_0 \ll \tau_1, \tau_2$ conditions. Therefore, within this paper, we do not consider the excitation of ultrasonic vibration with a purely coherent state.

5. Gamma radiation spectrum

If the correlation function of the crystal thermal acoustic field has a form similar to eq. (9) and the $\exp(-x_T^2/\lambda^2)$ Mössbauer term is larger than the thermal background term (i.e., we can observe the Mössbauer effect for the considered crystal) then the resulting $\langle Q(t) \rangle$ (eq. (5)) correlation function can be expressed as

$$\langle Q(t) \rangle = e^{-x_T^2/\lambda^2} \sum_{m=-\infty}^{+\infty} Q_m e^{im\Omega_0 t}, \quad (16)$$

where $Q_m = e^{-x_0^2/\lambda^2} I_m(x_0^2/\lambda^2)$ for completely incoherent stimulating ultrasonic wave and $Q_m = J_m^2(x'_0/\lambda)$ for a partially coherent ultrasonic wave with fixed amplitude and uncertain phase. Substituting eq. (16) into (1) and performing integration over t we obtain the gamma radiation spectral line as the sum

$$P(E) = \exp(-x_T^2/\lambda^2) \sum_{m=-\infty}^{+\infty} Q_m P_m(E), \quad (17)$$

consisting of Lorentzian-shaped equidistant lines

$$P_m(E) = \frac{1}{\pi} \frac{\hbar\Gamma/2}{(E - E_0 - m\hbar\Omega_0)^2 + (\hbar\Gamma/2)^2}, \quad (18)$$

each of relative intensity Q_m and centered on the energy $E = E_0 + m\hbar\Omega_0$. The sidebands are distinctly separated (resolved) one from another only if $\Omega_0 \gg \Gamma$. This condition determines the lower limit of the Ω_0 modulation frequency. Typically, $\Gamma = 10^7\text{--}10^8 \text{ s}^{-1}$ and, consequently, $\Omega_0 = 10^8\text{--}10^9 \text{ s}^{-1}$. To obtain satellites with natural linewidth Γ , the ultrasonic wave spectral band width $\Delta\Omega_0$ should be narrower than Γ . Therefore, the required ultrasonic wave monochromaticity degree is $\Delta\Omega_0/\Omega_0 = 10^{-2}\text{--}10^{-3}$.

The ultrasonic wave intensity I is related to the mean square displacement x_0^2 of a nucleus along the gamma emission observation direction through the expression:

$$x_0^2 = I \cos^2 \varphi / (\rho_0 u \Omega_0^2), \quad (19)$$

where ρ_0 is the crystal density, u is the ultrasonic wave velocity and φ is the angle between the ultrasonic wave polarization direction and the gamma radiation observation direction.

An estimation for the I_0 ultrasonic vibrations threshold intensity can be obtained from the condition that the x_0^2 mean square displacement of a nucleus (eq. (19)), caused by the ultrasonic wave, should be greater than the thermal mean square displacement of the nucleus

$$x^2 = \frac{3n_T \hbar \Omega_0}{M \Omega_D^3} \cdot \frac{\Delta\Omega_0 \Delta\Phi}{4\pi}, \quad (20)$$

caused by thermal acoustic oscillation which falls within the frequency band $\Delta\Omega_0$ and body angle $\Delta\Phi$ around the ultrasonic wave propagation direction.

Taking into account that n_T represents the mean number of thermal phonons in the Ω_0 frequency mode we obtain the following expression for the I_0 threshold intensity

$$I_0 = 3u\hbar\Omega_0(N/V)(\Delta\Omega_0/\Omega_0)(T/\theta)^3(\Delta\Phi/4\pi), \quad (21)$$

where N/V is the concentration of the nuclei within the crystal and θ is the Debye temperature. Assuming that $N/V = 10^{23} \text{ cm}^{-3}$, $u = 10^5 \text{ cm/s}$, $\Omega_0 = 10^8\text{--}10^9 \text{ s}^{-1}$, $(\Delta\Omega_0/\Omega_0) = 10^{-2}$, $T/\theta = 10^{-1}$, $\Delta\Phi/4\pi = 10^{-2}$, we obtain $I_0 = 10^{-4}\text{--}10^{-5} \text{ W/cm}^2$.

As can be seen from eq. (16), in the case of incoherent vibrations an increase of the ultrasonic wave intensity I leads to a monotonic decrease of the $m = 0$ Mössbauer line intensity. For partially coherent ultrasonic waves, a decrease of the Mössbauer line intensity is accompanied by intensity oscillations around zero.

Concurrently, with the intensity increase I of the stimulating ultrasonic wave, the sidebands intensity first increases as I^m and then either falls monotonically (in

case of incoherent ultrasonic vibrations) or features a decrease with the oscillations intensity around the zero level (in case of partially coherent ultrasonic vibrations). In all cases, as the I intensity increases, the sidebands intensity maximum is shifted towards larger $|m|$ values.

If the correlation function of the crystal thermal acoustic field is described by expression (10) (i.e., we cannot observe the Mössbauer effect for this crystal) then the resulting correlation function will be:

$$\langle Q(t) \rangle = \exp\left(-\frac{iE_R t}{\hbar} - \frac{2\epsilon E_R t^2}{\hbar^2}\right) \sum_{m=-\infty}^{+\infty} Q_m e^{im\Omega_0 t}, \quad (22)$$

and the stimulating ultrasonic wave action converts the gamma radiation spectrum into the sum:

$$P(E) = \sum_{m=-\infty}^{+\infty} Q_m P'_m(E), \quad (23)$$

consisting of Gaussian-shaped equidistant lines (if $\hbar\Gamma \ll \sqrt{\epsilon E_R}$)

$$P'_m(E) = (8\pi\epsilon E_R)^{-1/2} \exp\left[-\frac{(E - E_0 + E_R - m\hbar\Omega_0)^2}{8\epsilon E_R}\right], \quad (24)$$

centered on the $E = E_0 - E_R + m\hbar\Omega_0$ energies, each one of $\Delta E = 4(2\epsilon E_R \ln 2)^{1/2}$ spectral width, which is typical for Doppler broadening.

The ϵ mean kinetic energy of the thermal vibrations of a nucleus along the gamma emission direction varies within a broad range. However, even for sufficiently low temperatures, $kT \approx 10^{-2}\hbar\Omega_D$ when $\epsilon = 10^{-4}-10^{-5}$ eV, the width of each line is estimated to be $\Delta E = 10^{-3}-10^{-4}$ eV, for a typical recoil energy value $E_R = 10^{-2}-10^{-3}$ eV. Under these conditions, all the lines forming sum (23) merge into a single broad line, centered on the energy $E = E_0 - E_R$. Thus, in the case under consideration, the stimulating ultrasonic vibrations action gives birth only to additional broadening of the spectral line, which already was rather broad before excitation via the ultrasonic wave.

6. Conclusions

In this paper, we have considered the tuning of gamma radiation from nuclei in solids by means of recoil phonons stimulated emission. The quantum approach based on the coherent quantum states formalism, has been used in order to take into account the stimulating ultrasonic wave statistical properties. By utilization of the diagonal representation for the acoustic field density matrix, in a basis of coherent quantum states, the spectral line shapes have been determined for completely incoherent stimulating ultrasonic waves and partially coherent waves with fixed amplitude and uncertain phase.

Specific features of the multi-quantum transitions with emission of gamma quantum and simultaneous emission or absorption of one or several phonons have been discussed. The quanta involved in these transitions are coupled to different degrees of freedom of the radiating nucleus. For this reason, phonons component stimulation for the considered transitions cannot enhance the radiative decay rates of the nucleus. Thus, gamma emission tuning is reduced to spectral line shape reformation but the area under the intensity spectral curve remains unchanged.

Another example of multi-quantum transitions with quanta coupled to different degrees of freedom, is represented by nuclear radiative transitions in an external alternating magnetic field. As well known [11–14], the Mössbauer spectrum of nuclei interacting with an external radio-frequency magnetic field is similar to the Mössbauer spectrum of gamma emission in the presence of ultrasonic vibrations. In particular, there are a set of sidebands displaced from the Mössbauer line by integral multiples of the magnetic field frequency. The origin of these sidebands can be attributed to multi-quantum transitions with emission of a quantum and simultaneous emission or absorption of one or several photons of the radio-frequency electromagnetic field. These photons are associated with direct interaction of an alternating magnetic field with the nuclear magnetic moments.

The similarity between these two phenomena originates in nuclear energy periodical perturbation associated, in both cases, with external degrees of freedom of the radiating nucleus. From the classical point of view, either an ultrasonic modulation of the kinetic energy associated with the translation motion of the nucleus occurs or a radio-frequency modulation of the nuclear potential energy in an external magnetic field.

The classical approach to ultrasonic modulation phenomena in a gamma radiation spectrum is based on the first-order Doppler effect [6]. The influence of the second-order Doppler effect was discussed in refs. [5,6]. We estimate here the ΔE variation in the emitted gamma quanta energy, in the acoustic field of an ultrasonic wave with intensity I . Using eq. (19) and the well-known relationship $\Delta E/E = -\langle u^2 \rangle/(2c^2)$, where $\langle u^2 \rangle$ is the mean square nuclear velocity for ultrasonic vibrations, we obtain:

$$\frac{\Delta E}{E} = -\frac{1}{2} \frac{I}{\rho_0 u c^2}. \quad (25)$$

In order to be detectable, the ΔE energy shift must be larger than the $\hbar\Gamma$ natural linewidth. Even in the most favourable case of the ^{67}Zn nucleus with $\hbar\Gamma/E = 5 \times 10^{-16}$, estimation (25) brings us to a rather rigid requirement for the ultrasonic wave intensity, $I \approx 2 \times 10^5 \text{ W/cm}^2$.

Acknowledgement

I would like to express my gratitude to Prof. L.A. Rivlin for proposing the sub-

ject of this investigation and for stimulating discussions. The research described in this paper has partly been made possible by Grant no. JF1100 of the International Science Foundation.

References

- [1] S.L. Ruby and D.I. Bolef, Phys. Rev. Lett. 5 (1960) 5.
- [2] A. Abragam, Compt. Rend. 250 (1960) 4334.
- [3] A. Abragam, in: *Low Temperature Physics* (Gordon and Breach, New York, 1962).
- [4] L.A. Rivlin and A.A. Zadernovsky, Opt. Commun. 100 (1993) 322.
- [5] J. Mishory and D.I. Bolef, in: *Mössbauer Effect Methodology*, vol. 4 (Plenum Press, New York, 1968) p. 13.
- [6] E.F. Makarov and A.V. Mitin, Usp. Fiz. Nauk. 120 (1976) 55 (in Russian).
- [7] J.R. Klauder and E.C.G. Sudarshan, *Fundaments of Quantum Optics* (Benjamin, New York, 1968).
- [8] A.A. Zadernovsky, Laser Phys. 5 (1995) 362.
- [9] H.J. Lipkin, Ann. Phys. 9 (1960) 332.
- [10] J. Mishory and D.I. Bolef, Ultrasonics 7 (1969) 121.
- [11] Yu.A. Ilyinsky and R.V. Khokhlov, Zh. Eksp. Teor. Fiz. 65 (1973) 1619.
- [12] C.B. Collins, P.W. Rettinger and T.W. Sinor, Phys. Rev. B39 (1989) 9655.
- [13] C.B. Collins, P.W. Rettinger and T.W. Sinor, Phys. Rev. Lett. 62 (1989) 2547.
- [14] C.B. Collins and B.D. De Paola, Opt. Lett. 10 (1985) 25.

Experiments on the gravity effect on the ^{109}Ag gamma resonance

V.G. Alpatov, Yu.D. Bayukov, A.V. Davydov, Yu.N. Isaev, G.R. Kartashov,
M.M. Korotkov, V.E. Rad'ko, A.A. Sadovsky and V.M. Samoylov

*Institute for Theoretical and Experimental Physics, B. Cheremushkinskaya 25,
Moscow 117259, Russia*

The temperature dependence of the ^{109}Ag γ -ray self-absorption was investigated for the horizontal and vertical directions of emission. The source was a single-crystal silver plate containing atoms of parent radionuclide ^{109}Cd . Gamma-radiation of this γ -source and that of the monitoring γ -source, ^{57}Co , were registered by a pair of Ge(Li)-detectors. As a result of cooling the source from 77 K to \sim 12 K a relative decrease was observed of the intensity of the horizontally emitted γ -rays equal to $0.000\,64 \pm 0.000\,44$. For the vertical direction the corresponding intensity change turned out to be $-0.000\,47 \pm 0.000\,51$. Although these data, as one would see, give some evidence for the possible effect of the gravitation on the resonant γ -ray absorption, future measurements must show if these results aren't a consequence of any apparatus effect. The ways for developments in this study are discussed and some hindrances are considered.

Keywords: gamma quantum; Mössbauer effect; isomer; silver; resonant absorption; gravitation; red shift

1. Preface

The problem of gamma resonant excitation of long-living isomeric nuclear states is one of the most interesting but also most difficult tasks to be resolved by the investigators of the Mössbauer effect. The nuclear levels of interest have a mean life time of about one minute or more, such as the excited states of ^{107}Ag (93.1 keV, $\tau = 63$ s), ^{109}Ag (88 keV, $\tau = 57$ s), ^{103}Rh (39.75 keV, $\tau = 81$ min). During more than 30 years repeated attempts were undertaken to excite the isomeric levels of both silver isotopes by the Mössbauer effect [1–8], but so far nobody could achieve a reliably reproducible effect on a scale that would permit to use the long-living isomers in the Mössbauer experiments.

The ultimately small natural widths of isomeric states of these nuclei ($\sim 10^{-17}$ eV for both silver isomers) lead to a situation where the emission and absorption spectra are subject to relatively large, even enormous, effects of broadening, splitting and shift by the action of such small fields, which do not play any visible role in the ordinary Mössbauer experiments. For example, the Earth's magnetic field with an intensity less than 1 Oe splits the γ -lines of silver isomers through

the Zeeman effect into 14 components. The spacing between these components exceeds the natural line width about 10^6 times. There are some mechanisms of gamma resonance broadening. The most important are the broadening through the interaction of nuclear magnetic moments of neighbouring atoms (dipole-dipole broadening), through interaction of magnetic moments of nuclei and conduction electrons, and the temperature broadening. The latter is proportional to the seventh power of the temperature [9,10] and may be suppressed by sufficient cooling. The conduction-electron-nucleus magnetic interaction must also fall off with decreasing temperature T because the number of effectively interacting electrons is proportional to kT/E_F (k is the Boltzmann constant, E_F the Fermi energy). At 4.2 K in silver the corresponding width is about 5×10^{-12} eV. The first cause of broadening, however, cannot be removed by simple methods and would manifest itself in all the experiments which were performed so far with silver isomers. The maximum value of the magnetic dipole-dipole interaction energy which determines the broadening scale of the resonant line, is expressed by the formula

$$U = \frac{2d_1 d_2}{R^3},$$

where d_1 and d_2 are the magnetic moments of two neighbouring silver nuclei, one of which is in the excited state, and R is the distance between these nuclei.

For both silver isomers, which are similar in almost all respects, $U \sim 10^{-12}$ eV. Thus the resonant γ -lines of silver isomers must be broadened according to the theoretical estimates about 10^5 times in comparison with their natural widths.

Many years ago our group has performed experiments on the γ -excitation of the $^{107,109}\text{Ag}$ isomeric states [1–5]. A method was used that consisted of the activation of an initially inactive polycrystal silver sample by γ -rays of a strong source ($\sim 1\text{--}2$ Ci) at the liquid helium temperature. In the experiments with ^{109}Ag we used a diamagnetic silver palladium alloy. The arising absorber activity was measured after the removal of the source beyond a sufficient layer of lead shielding. It was possible to reserve time for it, thanks to the large life time of the excited activity. The observed effect was however small – it did not exceed several counts per minute over the background. Moreover, the effect sometimes was not reproduced in experiments which were performed in, as one would think, just the same conditions as the successful measurements. These experiments have shown that the scale of the activation effect agreed with the above-mentioned theoretical estimate of the γ -resonance broadening.

In recent years works appeared [6–8] in which an alternative method was used to observe the γ -resonant excitation of the ^{109}Ag isomeric state. The samples to be investigated were single-crystal silver plates containing radioactive ^{109}Cd atoms which were imbedded by thermodiffusion. The decay of ^{109}Cd leads to the production of the ^{109}Ag nucleus in the excited state which de-excites by highly converted emission of an 88 keV γ -ray. The dependence on the temperature of the emitted γ -ray intensity was observed (in refs. [7,8] the X-rays were also detected). The authors

expected the appearance of additional photon absorption through the Mössbauer effect at a sufficiently low temperature. When silver is cooled from room temperature to 77 K the γ self-absorption increases perceptibly (about 1% for a sample of 1 mm thickness) due to the temperature compression of matter and corresponding rise of density. However, in the transition from 77 to 4.2 K the analogous compression of the matter is much smaller and permits in principle to notice the effects of an anomalous increase of photon absorption.

In ref. [6] such additional absorption was observed of the order of $\sim 0.1\%$. This is connected, by the author's opinion, with Mössbauer absorption of 88 keV γ -rays corresponding to the cross section for only 30-fold broadening of the γ -line. The authors of ref. [6] (just as the authors of the following works [7,8]) do not touch the possible causes of small broadening and avoid the problem of relating their results to previous experimental data and to theoretical estimates. The data of ref. [6] naturally caused some doubts, all the more because there was no mention in this paper about any checking measurements, without which the observed effect could be ascribed to other causes, for example, to cryostat deformations in the cooling process and corresponding change of the distance between the source and the detector. Another possible origin of this effect may be the silver compacting during the cooling process as a result of a so far unknown phase transition. To check the latter assumption we performed an experiment [11] with a polycrystal sample of very pure silver in which there was some activity of ^{109}Cd . This sample was used previously as a strong γ -source in the experiment with ^{107}Ag and was therefore irradiated during several hours by protons at the cyclotron. Both nuclides, ^{107}Cd and ^{109}Cd , were produced in the (p,n)-reactions, but short-living ^{107}Cd had decayed practically completely at the start time of the new measurement. One cannot consider this experiment as a test of ref. [6] because it was performed with polycrystal and ^{109}Cd was introduced in silver by the other technology which was moreover accompanied by the formation of many structural defects. Moreover, the design of the cryostat used in this experiment permitted to detect photons in the vertical direction only. Therefore the effective absorption length for these photons in the case of 30-fold line broadening couldn't exceed 30 μm in consequence of the gravitational red shift. This would lead in any case to an additional resonant absorption much less than 0.1%. Besides the ^{109}Ag γ -rays ^{155}Eu γ -quanta with an energy of 86.5 keV were used in this experiment. The study of temperature dependencies of the absorption of both γ -rays did not show any anomalous effect. We believe that this fact proves the impossibility of ascribing the effect observed in ref. [6] to the phase transition in silver.

Some time after ref. [6] the papers of another group were published [7,8]. The authors of these works have improved the method of ref. [6] by detecting the characteristic X-rays of silver atoms besides the 88 keV γ -rays. This leads to two results. Firstly, if Mössbauer absorption takes place, the γ -ray yield must decrease but that of X-rays must increase because the de-excitation of a nuclear state goes in most of the cases through the inner conversion process after which the X-ray cascade fol-

lows. Therefore one may hope measuring the ratio of gammas to X-photons to see stronger weakening of this value with temperature decrease than for the detected γ -quantum number alone. Secondly, the simultaneous detection of both radiations permits to exclude the effect of geometry changing. In refs. [7,8] the confirmation was obtained of the [6] data and, as was estimated, even with lesser broadening (16–20-fold). However there are again some doubts on the reliability of these data. In particular the authors point out that they successfully observed the wanted effect for the vertical direction of the photon emission (where it must be very small) but couldn't reach a good reproducibility of the results for the horizontal direction (where the effect as one would think must be large). Note that none of the quoted works considers the influence of the Earth's magnetic field. However this field is able to change the resonant absorption effect markedly if a suitable protection is absent. This means that if the authors of refs. [6–8] did not take into account the line splitting by the Earth's magnetic field then the estimated broadenings must be changed from 16–30-fold to a lesser value. Nevertheless the collection of all these works is of great interest. If the authors of refs. [6–8] are right then a serious contradiction takes place between the generally accepted theoretical ideas, which moreover were confirmed by the experiments with the polycrystalline samples, and the experimental data for the single crystals. Undoubtedly if such a situation exists it will demand essential changes in the insights about the forming mechanism of the particularly narrow γ -resonances. Moreover, the possibility of Mössbauer experiments with supernarrow lines which are broadened only 16–30 times (or maybe even less?) must permit to improve the resolving power of Mössbauer spectroscopy by several orders of magnitude and to approach closely the solution of the γ -laser problem at last. Taking into consideration the importance of this situation we have undertaken experiments, which, as we believe, may give the correct evidence of presence (or absence) of a small γ -resonance broadening in the ^{109}Ag case.

2. The experimental part

The experiment consists of the detection of the 88 keV γ -quanta emitted in horizontal and vertical directions from a silver single crystal. The coaxial Ge(Li)-spectrometers were used as detectors. The temperature dependencies were measured of the photon intensities detected by both detectors. If the γ -line is 30-fold broadened then the effect of additional (resonant) absorption must be much more visible for the horizontally emitted photons. In the vertical direction the resonant absorption is suppressed by the action of the gravitation on the photon energy.

We have fabricated the gamma-source as a nearly round plate, 1.08 mm in thickness and ~ 26 mm in diameter. The plate was cut off by means of an electro-erosion tool from a single crystal of especially pure silver. ^{109}Cd was imbedded into the plate by thermodiffusion, the initial source activity being about 5 mCi. The procedures for the source fabrication and the determination of the cadmium mean penetration

depth into silver are presented in our papers [12]. Besides this sample a monitoring γ -source was used. That was a thin copper foil disk containing ^{57}Co activity. Both sources were mounted together in close contact (the ^{57}Co source was placed at the side directed to the detectors) in the cryostat at a 45° angle to the horizon. The cryostat might be cooled by the weak stream of liquid helium or nitrogen. The rate of the helium flow was about 1 l/h. A sketch of the experimental device is shown in fig. 1. The Ge(Li)-detectors were connected through the corresponding spectrometric circuits with a common amplitude analyzer, a Nokia LP 4900B, which registered the pulse spectra from both detectors simultaneously. A preliminary theoretical estimate of the expected effect was made for the 30-fold γ -line broadening taking into account the Zeeman splitting of the γ -line by the Earth's magnetic field. The corresponding relative decrease of the horizontally emitted photon intensity was expected to be about 5×10^{-4} when the silver sample was being cooled

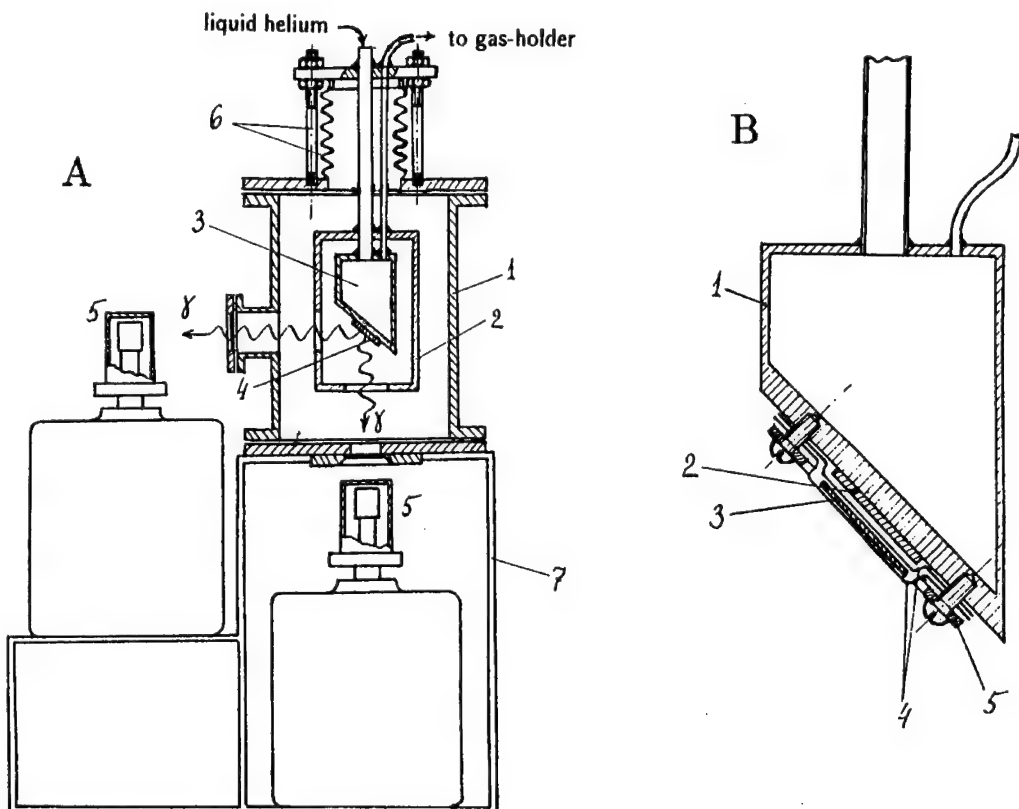


Fig. 1. (A) Sketch of the experimental device. (1) The cryostat body; (2) the heat shield cooling by the outgoing helium vapors; (3) the liquid helium volume; (4) the γ -sources; (5) the Ge(Li)-detectors; (6) the unit of the helium volume anchoring, consisting of three studs and the bellows; (7) the stand. (B) Scheme of the γ -source mounting. (1) Body of the liquid helium volume; (2) the silver γ -source; (3) the copper foil containing the ^{57}Co activity; (4) aluminium foils; (5) the mounting ring.

from 77 to ~ 12 K (the latter is a working temperature of the γ -sources in the given cryostat). One must expect practically the same value if the source would be cooled to the lower temperature because the Mössbauer factor varies weakly in this temperature range. Therefore such an experiment requires a stable operationed device which would permit to measure the photon intensity with a relative precision of at least $\sim 10^{-4}$. It was found convenient to measure by each detector the ratio of the intensities of γ -lines with energies of 88 keV (^{109}Ag) and 122 keV (^{57}Fe), which were detected simultaneously. We have satisfied ourselves that this ratio remained stable within the limits of the corresponding statistical struggling if the measurement was being continued several days. To reach it, one must determine the intensity of both γ -lines as a sum of the counts in the range of the channel number which exceeds the gamma peak width by several times. The computing program of the Nokia analyzer took into account the half-life difference of two γ -sources. Moreover, the correction was introduced for the low-energy tail of the 122 and 136 keV γ -lines of (^{57}Fe), which hitted in the common sum with the counts of the ^{109}Ag 88 keV γ -line. This part of the pedestal under the 88 keV γ -line falls down in time with a different rate than the line itself. There is no sence to detect the X-rays of silver in our case because this radiation is emitted by atoms almost isotropically and its registration would only make difficult to reveal the desired effect.

In fig. 2 a typical γ -spectrum is shown from one of the detectors. One may choose the different intervals of channel numbers to obtain the sums of counts for both γ -lines and the corresponding ratios of these sums. The totality of the spectra measured at a given temperature permits to determine the real straggling of these ratios, that is the root-mean-square error. On the other hand the measured sums of counts make it possible to calculate the expected statistical errors of the ratios. The criterion of a satisfactory choice for the minimum summing interval is the approximate equality of the errors determined through the real straggling of the ratios and as the estimated statistical standard devitions. In table 1 the data are shown for four versions of the summing interval choice. These data are determined from the 118 spectra measured at room temperature. The corresponding intervals of summing are shown by the brackets on fig. 2. One may see from the table that the acceptable correlation between the real and estimated root-mean-square errors is conserved in the wide range of summing intervals. Moreover this means that there are no visible errors which would not be connected with count statistics. Note that it is useful to shorten only the summing interval for the low-energy peak (88 keV) to reduce the above-mentioned correction connected with the contribution of the tail of the ^{57}Fe γ -lines. Similar results for the errors were obtained at other temperatures. So in two sets of 89 spectra measured by two detectors at the liquid helium temperature only 28 and 24 values of the line area ratios fall outside the limits of one standard deviation from the mean value. This corresponds quite well to the expected statistical straggling. Thus the stability of the experimental device permits to reach the required accuracy of the measurements.

In the first preliminary experiments we have obtained the following data. When

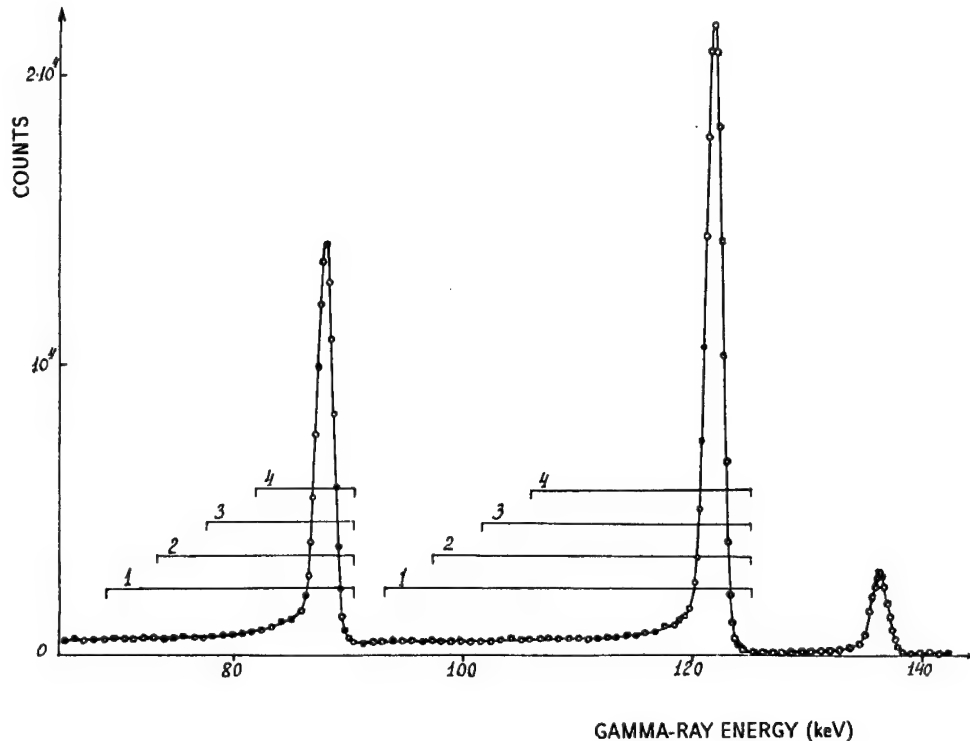


Fig. 2. Typical γ -spectrum from one of the detectors. The brackets with numbers from 1 to 4 show the various intervals of count summing.

the γ -sources were cooled from 77 to ~ 12 K, the intensity ratios of γ -lines 88 and 122 keV have changed by the following mode:

For the horizontal direction:

$$\frac{R_{77\text{ K}} - R_{12\text{ K}}}{R_{77\text{ K}}} = 0.000\,64 \pm 0.000\,44.$$

For the vertical direction:

$$\frac{R_{77\text{ K}} - R_{12\text{ K}}}{R_{77\text{ K}}} = -0.000\,47 \pm 0.000\,51.$$

Here R_T is the intensity ratio of γ -lines 88 and 122 keV at the temperature T . The errors are determined from the real straggling (which agree with the statistical one) and correspond to the 68% level of likelihood.

The result for the horizontal direction does not contradict the data of ref. [6] where excess self-absorption was observed at the 0.1% level. However one must come to be beyond three standard deviations from our measured value in order to approach the 0.1% level for the vertical direction. Therefore these data, as one

Table 1

Number of summing interval	Number of channels in the summing interval for ^{109}Ag peak	Analogous number for ^{57}Fe peak	Area ratios of the ^{109}Ag and ^{57}Co peaks		Root-mean-square errors of these ratios, σ_{rms}		Expected statistical errors of the ratios σ_{st}		$\frac{\sigma_{\text{rms}}}{\sigma_{\text{st}}}$
			detector N1	detector N2	detector N1	detector N2	detector N1	detector N2	
1	102	151	0.68695	0.36762	0.00017	0.00013	0.00020	0.00012	0.85
2	82	131	0.66727	0.36109	0.00017	0.00013	0.00020	0.00012	0.85
3	62	111	0.64505	0.35286	0.00018	0.00013	0.00019	0.00012	0.95
4	42	91	0.61373	0.33742	0.00017	0.00013	0.00019	0.00012	0.89

might think, give evidence for the small γ -resonance broadening. However one ought to consider these data as especially preliminary and not only in consequence of the still insufficient count statistics. There were some peculiarities in the cryostat design and arrangement which could lead in principle to the distortion of the results. In particular, the aperture of the lower window through which the vertical γ -ray beam passed was rather small. If large deformations of the inner cryostat parts took place during the process of cooling (the deformations were not controlled in this experiment) it could lead to the formation of a semi-shadow in the γ -beam elucidation of the lower detector. The presence of such a semi-shadow could distort the value of the γ -line intensity ratio because the two γ -sources were of different geometries: the silver disk radiated uniformly over the whole area but the activity of the ^{57}Co was concentrated in the small spot in its centre. The second circumstance that may simulate the effect of the self-absorption difference for two directions is connected with the action of the Earth's magnetic field. The intensity of each of the 14 components in the Zeeman hyperfine structure of the emission (and absorption) spectrum depends differently on the angle ϑ between the direction of the magnetic field vector and the direction of the photon propagation. Owing to this the absorption cross section in the case of the splitted γ -line depends also on ϑ (see the Appendix). For γ -rays which are detected in the vertical direction the angle ϑ is fixed and cannot be changed without considerable change of the geography of an experiment. In a correct experiment performed without suppression or compensation of the Earth's magnetic field, the cryostat must be arranged so that the angle ϑ would be the same for both directions of γ -ray detection (or ϑ for one direction must be equal to $180^\circ - \vartheta$ for the other one). In the experiment described here this condition was not fulfilled judging by the direction of the unperturbed magnetic field of the Earth, but we did not make a direct measurement of the field direction inside the cryostat. The possible difference of the angle ϑ in our case most probably increase the probability of the resonant absorption for the vertical direction as compared with the horizontal one.

We'll try to remove these shortcomings before repeating the experiment. Besides the enlargement of the lower window aperture and the fabrication of a new ^{57}Co monitoring source, we shall check and measure optically the possible deformations of the cooled parts of the cryostat. The use of a theodolite for this purpose permits to reach a precision of $\pm 20\text{ }\mu\text{m}$ in the measurement of linear displacement. We'll try also to measure the magnetic field direction inside the cryostat and to arrange the latter corresponding to it.

3. Conclusion

It is necessary for further successive development of Mössbauer experiment with ^{109}Ag to take measures for the improvement of the method. First of all, one must get rid of the influence of the Earth's magnetic field and, at the same time, of the

other parasitic magnetic fields. It is not an easy task because the magnetic field needed to produce Zeeman splitting of the ^{109}Ag γ -line corresponding to its natural width is exclusively small – $\sim 0.8 \times 10^{-6}$ Oe. The magnetic field compensation does not effect on the γ -resonant absorption until the hyperfine structure components of the Mössbauer emission and absorption spectra do not cover sufficiently each other. The field decrease by 10^3 , 10^4 times will not lead to the desirable effect. A decreasing factor of the Earth's magnetic field intensity is required that exceeds 10^6 times. If the outer fields are compensated, one may use a weak artificial magnetic field and try to measure the γ -resonance width by altering its value.

The second improvement of the methodology concerns the deliverance from the possible inhomogenous isomeric shifts of the γ -resonant line inside the bulk of the γ -source. These shifts may appear in connection with the irregular distribution of the ^{109}Cd atoms over a silver volume. So far as ^{109}Cd is being imbedded into silver by thermodiffusion its concentration depends strongly on the depth of bedding, x . In the case of one-fold imbedding procedure this dependence is described by a function of the form Ae^{-bx^2} . In our group a method was suggested of a source fabrication which permits to make the conditions when the emitted in the direction to the detector γ -quanta propagates inside the source in the directions along which the cadmium concentrations are constant. The sequence of the production procedures is shown in fig. 3. At first the ^{109}Cd atoms are being imbedded into a flat silver plate by the usual thermodiffusion. Then the plate is being cut into a set of the parallel strips. After this, each strip is rotated around the axis parallel to its long side by an angle of 90° . The rotated strips are being fixed in the common plate so that they form again a plate-like structure. If now one will detect γ -quanta in the direction perpendicular to the plane of such a new structure, then the quanta to be detected will pass the corresponding silver strip parallel to the diffusion front of the cadmium. Thus each γ -quantum will propagate along the direction corresponding to the constant cadmium concentration in spite of the various cadmium concentrations in the different silver layers parallel to the diffusion front. That the various photons pass in these conditions the layers with different cadmium concentrations is obviously of no importance.

Although our experiment, as the other attempts to observe the Mössbauer self-absorption of the ^{109}Ag γ -rays, is performed with a single crystal of silver, it seems to us that the effect of a small broadening, if it exists, must be manifested in the same degree for the polycrystal samples. These samples must be naturally of very high purity. So one has to plan similar experiments with polycrystals. The question may arise why such a small effect of γ -resonant absorption was observed in our previous works [1–5] with $^{107,109}\text{Ag}$ in the polycrystal silver. The scale of this effect agreed with the theoretical estimates of a broadening factor as 10^5 – 10^6 . The explanation may be connected with the quite different treatment performed with the sources and the absorbers in these experiments. The irradiation of a silver target in the cyclotron by protons of 22 MeV energy with an intensity of more than $100 \mu\text{A}$ created an enormous amount of radiative damage and, moreover, saturated the silver

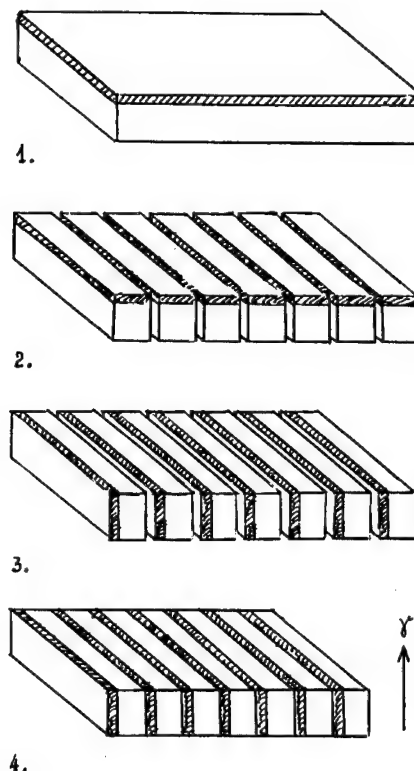


Fig. 3. The successive operations for the fabrication of the γ -source free from the inhomogenous isomeric shift. (1) The initial silver plate with imbedded ^{109}Cd in the layer which is shown cross-hatched; (2) the plate is cut into strips; (3) each strip is rotated by an angle of 90° around the axis parallel to its long side; (4) the rotated strips are fixed in the common plane as a new plate-like structure.

with hydrogen. The annealing of the source, which continued during five hours, couldn't remove completely both these factors. The absorbers however were not damaged and kept their initial state. Therefore, it is possible that some isomeric shift presented between the γ -resonant lines of the source and the absorber. The partial loss of the data reproducibility in the identical experiments may have as a cause the difference in the isomeric shift value caused by the peculiarities of the concrete cyclotron irradiation.

It is tempting to perform analogous experiments at a superlow temperature using, for example, refrigerators based on the continuous dissolving of ^3He in ^4He . At temperatures of about 20–30 mK the line broadening factor must decrease essentially which has to be connected with magnetic moment interaction of the nuclei and the conduction electrons. It is possible however to meet here unexpected effects which may be conditioned by the still unknown depressing mechanism of the γ -line broadening. In addition to the latter remark note that if the effects indicating

the small broadening of the ^{109}Ag γ -resonance will be convincingly confirmed, it will be necessary to explain the absence of the expected broadening theoretically. Maybe the possible lack of the broadening is connected with physical averaging to the almost zero value of the fast altering hyperfine interaction factors during the long life time of the excited nuclear state. It will require to reconcile such a mechanism with existing ideas about γ -quantum emission process. If the mechanisms of an averaging act, then the broadening, but not the narrowing, of the γ -line may show itself in the experiment at a superlow temperature as compared with the 4.2 K case because the spin relaxation must be slowed down.

Appendix

THE EFFECT OF THE EARTH'S MAGNETIC FIELD ON THE RESULTS OF THE MÖSSBAUER EXPERIMENTS WITH ^{109}Ag

Magnetic moments of the ^{109}Ag nucleus are equal to 4.4 nuclear magnetons for the isomeric state (88 keV, $7/2^+$), and 0.130 690 5 n.m. for the ground state [13]. The magnetic field splits the isomeric state into eight sublevels and the ground state into two sublevels. The radiative transitions between the sublevels of isomeric and ground states provide the hyperfine structure (HFS) of the γ -spectrum consisting of 14 components (see fig. 4). The energy of the sublevel with magnetic number m is defined by the known expression:

$$E_m = E_0 - \frac{\mu H m}{I} . \quad (\text{A.1})$$

Here E_0 is the energy of an unsplitted level, H is the intensity of a magnetic field, I is the spin of a level, μ is the nuclear magnetic moment.

It follows from eq. (A.1) that the energy spacing ΔE between the neighbouring m -sublevels equals in magnitude to $\Delta E = \mu H / I$. The estimate of the magnetic field intensity for the case when ΔE equals to the natural width Γ of the ^{109}Ag isomeric level is given as:

$$H = \frac{\Gamma I}{\mu} = \frac{1.844 \times 10^{-29} \times 3.5}{5 \times 10^{-24} \times 4.4} = 2.93 \times 10^{-6} \text{ Oe} .$$

The Earth's magnetic field intensity varies from 0.42 to 0.70 Oe depending on the coordinates on the Earth's surface. One may accept the value of this intensity for the middle latitude equal to 0.56 Oe. In such a field the value of ΔE is 3.52×10^{-24} erg. This value exceeds Γ by $\sim 2 \times 10^5$ times. Therefore, in order to exclude the Zeemann splitting of the ^{109}Ag levels and to obtain the entire mutual overlap of the HFS components it needs to diminish H at least by 10^6 times.

The intensity of each HFS component depends definitely on the angle ϑ between

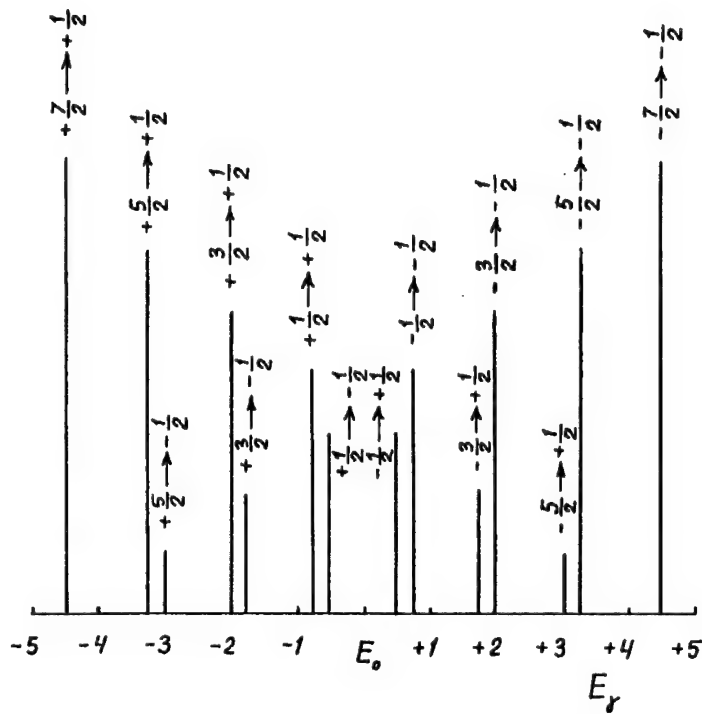


Fig. 4. The hyperfine structure of the magnetically splitted γ -line of ^{109}Ag . The vertical segments are proportional to the squares of the corresponding Clebsch-Gordan coefficients. E_γ is the photon energy counted off the unsplitted γ -line energy E_0 in arbitrary units.

the magnetic field vector and the γ -quantum momentum. This may be expressed as follows:

$$I(m_i, m_f) = \left| C_{I_i m_i L M}^{I_f m_f} \right|^2 \times F(\vartheta, \Delta m). \quad (\text{A.2})$$

The first factor on the right-hand side of eq. (A.2) is the squared Clebsch-Gordan coefficient corresponding to the transition from the sublevel with spin I_i and magnetic quantum number m_i to the sublevel with spin I_f and magnetic quantum number m_f . In this transition the photon is emitted with angular momentum L and its projection on the quantization axis M .

The expressions of $F(\vartheta, \Delta m)$ for each HFS component of the ^{109}Ag γ -spectrum are shown in table 2 together with the values of the Clebsch-Gordan coefficients.

If the emitting and the absorbing nuclei undergo the action of the same fields then the energies of the corresponding HFS components of the emission and the absorption spectra are also the same. So far as the spacings between the components are much larger than their widths, the photons of each component of the emission spectrum may be absorbed only in the bounds of the width of the corresponding absorption spectrum component. These twin components are

Table 2

HFS component	Square of the Clebsch–Gordan coefficient	Function $F(\vartheta, m_i, m_f)$ which describes the angular dependence of the emission probability of the HFS component
$+7/2 \rightarrow +1/2$ and $-7/2 \rightarrow -1/2$	1	$F(\vartheta, \Delta m = 3) \sim \frac{315}{16} \sin^4 \vartheta (\cos^2 \vartheta + 1)$
$+5/2 \rightarrow +1/2$ and $-5/2 \rightarrow -1/2$	6/7	$F(\vartheta, \Delta m = 2) \sim \frac{105}{16} \sin^2 \vartheta \times (8 \sin^2 \vartheta \cos^2 \vartheta + \sin^4 \vartheta + (5 \cos^2 \vartheta - 1)^2)$
$+3/2 \rightarrow +1/2$ and $-3/2 \rightarrow -1/2$	5/7	$F(\vartheta, \Delta m = 1) \sim \frac{21}{16} ((5 \cos^2 \vartheta - 1)^2 \sin^2 \vartheta + 50 \sin^4 \vartheta \cos^2 \vartheta + 8(5 \cos^2 \vartheta - 3)^2 \cos^2 \vartheta)$
$+1/2 \rightarrow +1/2$ and $-1/2 \rightarrow -1/2$	4/7	$F(\vartheta, \Delta m = 0) \sim \frac{252}{16} (5 \cos^2 \vartheta - 1)^2 \sin^2 \vartheta$
$-1/2 \rightarrow +1/2$ and $+1/2 \rightarrow -1/2$	3/7	$F(\vartheta, \Delta m = -1) = F(\vartheta, \Delta m = +1)$
$-3/2 \rightarrow +1/2$ and $+3/2 \rightarrow -1/2$	2/7	$F(\vartheta, \Delta m = -2) = F(\vartheta, \Delta m = +2)$
$-5/2 \rightarrow +1/2$ and $+5/2 \rightarrow -1/2$	1/7	$F(\vartheta, \Delta m = -3) = F(\vartheta, \Delta m = +3)$

mutually overlapping and have the same polarization characteristics. Our detectors do not distinguish between the separate HFS components and register all the γ -spectrum with the same common efficiency. In this condition the measured number P_a of resonantly absorbed photons is proportional to the sum of the products of the intensities of the HFS components for the emission and absorption spectra which are equal by a magnitude and coincide in energy:

$$P_a \approx \sum_{n=1}^{14} I_n^2. \quad (\text{A.3})$$

Up to a constant factor:

$$\begin{aligned}
 P_a \approx & 5625(1 + \cos^2 \vartheta)^2 \sin^8 \vartheta \\
 & + 500(8 \sin^2 \vartheta \cos^2 \vartheta + \sin^4 \vartheta + (5 \cos^2 \vartheta - 1)^2)^2 \sin^4 \vartheta \\
 & + 17((5 \cos^2 \vartheta - 1)^2 \sin^2 \vartheta + 50 \sin^4 \vartheta \cos^2 \vartheta + 8(5 \cos^2 \vartheta - 3)^2 \cos^2 \vartheta)^2 \\
 & + 1152(5 \cos^2 \vartheta - 1)^4 \sin^4 \vartheta.
 \end{aligned}$$

The plot of this function is shown in fig. 5. One may see that the intensity of the resonant absorption depends strongly on the angle ϑ . So one may obtain an incorrect result if one does not take into account this fact when arranging the detectors for a gravitational experiment. In the correctly organized experiment the angles ϑ must be equal for the detectors which register the γ -quanta emitted in the horizontal and vertical directions (or one of these angles must be additional to 180° for the other one).

If a γ -line is not splitted (the magnetic field is absent), then the intensity of the resonant absorption in a thin absorber is spatially isotropic and proportional to the square of the intensity sum of all the spectrum components (which are degenerated).

Very substantial is the problem of the magnetic field gradient in the area where the γ -source is placed. If the energies of corresponding HFS lines in the emission and absorption spectra differ at least on the width of these lines (that is on 10^{-5} – 10^{-6} of the spacing between the HFS lines), then the resonant absorption becomes impossible. If the effective thickness of the silver γ -source-absorber equals ~ 0.5 mm, then the limiting gradient value is $\sim 2 \times 10^{-5}$ Oe/cm for the unbroa-

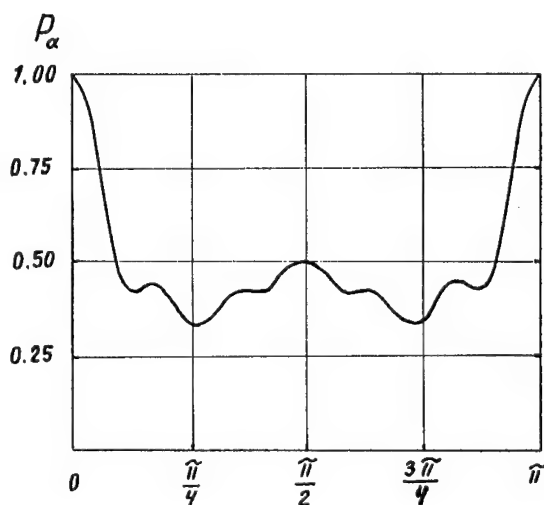


Fig. 5. The curve showing the dependence of the resonant absorption intensity P_a on the angle between the magnetic field vector and the propagation direction of the γ -quantum.

dened ^{109}Ag γ -line and $\sim 6 \times 10^{-4}$ Oe/cm in the case of the broadening factor of 30. The measurement of the weak magnetic field with such accuracy is a very uneasy problem. In the free space and in the absence of any ferromagnetic objects the Earth's magnetic field may be considered as uniform. However the presence of ferromagnetic parts near the experimental device, such as pumps, gas cylinders and so on, may distort the situation strongly. So the best way (however quite uneasy) is to perform a full protection of the experimental device from all external magnetic fields with an accuracy of about 10^{-6} Oe.

Acknowledgement

The authors thank G.E. Bizina for her great contribution in the assimilation of the fabrication technology of the γ -sources on the base of ^{109}Cd imbedded into silver single crystals.

References

- [1] G.E. Bizina, A.G. Beda, N.A. Burgov and A.V. Davydov, Sov. JETP 45, no. 5(11) (1963) 1408.
- [2] A.G. Beda, G.E. Bizina and A.V. Davydov, in: *Problemy Jadernoy Fiziki i Fiziki Elementarnykh Chastits (Problems of Nuclear Physics and Physics of Elementary Particles)* (Moscow, Nauka, 1975) p. 209.
- [3] V.G. Alpatov, A.G. Beda, G.E. Bizina, A.V. Davydov and M.M. Korotkov, *Proc. 5th Int. Conf. on Mössbauer Spectroscopy, 1973*, part 3 (Bratislava, Czechoslovakia, Praha, 1975) p. 499.
- [4] V.G. Alpatov, A.G. Beda, G.E. Bizina, A.V. Davydov and M.M. Korotkov, Collection of papers *Prikladnaya Jadernaya Spectroscopiya (Applied Nuclear Spectroscopy)*, no. 7 (Atomizdat, Moscow, 1977) 232.
- [5] V.G. Alpatov, A.G. Beda, G.E. Bizina, A.V. Davydov and M.M. Korotkov, *Proc. Int. Conf. on Mössbauer Spectroscopy*, vol. 1 (Bucharest, Romania, 1977) p. 43.
- [6] W. Wildner and U. Gonzer, *J. de Phys. Coll. Suppl.* 40(3) (1979) C2-47.
- [7] R.D. Taylor and G.R. Hoy, *SPIE* 875 (1988) 126.
- [8] G.R. Hoy and R.D. Taylor, *J. Quant. Spectrosc. Radiat. Transfer* 40(6) (1988) 763.
- [9] Yu.M. Kagan, Sov. JETP 47 (1964) 367.
- [10] H.H.F. Wegener, *Z. Phys.* A281 (1977) 183.
- [11] V.G. Alpatov, G.E. Bizina, A.V. Davydov, M.M. Korotkov and G.V. Kostina, Preprint ITEP 130 (Moscow, 1984); see also the paper of the same authors in: *Voprosy Tochnosti v Jadernoy Spectroscopii (The Topics of Precision in Nuclear Spectroscopy)* (Phys. Inst. Academy of Sciences of Lithuanian Soc. Rep., Vilnius, 1984).
- [12] G.E. Bizina, A.V. Davydov, G.R. Kartashov and A.A. Sadovsky, Preprint ITEP 15-90 (Moscow, 1990);
G.E. Bizina, A.V. Davydov, G.R. Kartashov, A.A. Sadovskythe and V.G. Alpatov, *Izmer. Tekh.* no. 1 (1994) 58.
- [13] A.I. Levon and O.F. Nemez, *Electro-Magnitnye Momenty Vozbujdennyh i Radioaktivnyh Jader (Electro-Magnetic Moments of the Excited and Radioactive Nuclei)* (Naukova Dumka, Kiev, Ukraine, 1989) p. 407.

Recoil-free resonant gamma-ray absorption in ^{57}Fe nuclei in the presence of a strong microwave field

M. Petrascu, D. Barb, I. Bibicu and D. Tarina

Institute of Atomic Physics, MG-6 Bucharest, Romania

A calculation of the cross-section of resonant gamma-ray absorption in the presence of strong microwave fields has been performed. This calculation is based on papers published earlier [1–3], in which the possibility of nuclear recoil compensation at the absorption of gamma-rays, by means of optical photons, was considered. Preliminary experimental results concerning the recoil-free gamma absorption in the presence of a 3 GHz strong microwave field are presented.

1. Introduction

The problem of compensation of the energy lost by a gamma-ray in the recoils of emitters and absorbers is highly interesting, since the achievement of resonant gamma-ray absorption at energies beyond those attained currently by the Mössbauer technique depends on this compensation. An approach to this problem based on two-photon absorption, for gamma-rays with an energy of the order of 1 MeV has been considered in refs. [1–3]. A formalism based on dipole interaction has been developed [2] and by taking into account the leading term in the matrix element, a formula for the absorption cross-section was obtained. This formalism will be presented in section 2. It is emphasized in this contribution, that the most convenient testing of the two-photon absorption mechanism would be within the framework of Mössbauer spectroscopy, due to the fact that the absorption cross-sections in this case are the highest and, on the other hand, the energy conservation relation does not contain the recoil and Doppler terms. In section 3, estimates of the cross-sections for different gamma-ray energies in the presence of a microwave field will be presented. In section 4, the experiment performed on resonant gamma-ray absorption in ^{57}Fe in the presence of a strong microwave field will be described. Finally, in section 5, the conclusions will be presented.

2. A formalism for two-photon absorption

In principle, the transition probability for a two-photon process involving photons of different energy can be treated [2] in the same manner as in the better

understood computations for the absorption of two optical photons [4–6]. However, the problem of the gauge of the electromagnetic field is extremely critical in this case, because of the large difference in the energies of the two photons. Although it has been shown [7] that the transition probabilities are gauge invariant, when summed over all intermediate states, in the case of resonant two-photon absorption the leading terms in the sums for the two commonly used gauges, the dipole interaction $\mathbf{E} \cdot \mathbf{r}$, and the Coulomb-gauge interaction $\mathbf{A} \cdot \mathbf{p}$, differ by five orders of magnitude. Since only the leading term will be retained, differences of 10^{10} in the calculated transition probabilities can result from a change of gauge. Since it has been shown that the dipole interaction term, $\mathbf{E} \cdot \mathbf{r}$, leads to the most rapid convergence [6], that representation, which also gives the smaller transition probability, has been used [2]. If it is assumed that the Hamiltonian of the perturbation is of the form $\mathbf{E} \cdot \mathbf{r}$, the time-dependent second-order perturbation theory yields the cross-section σ for the absorption of gamma photons in the field of optical photons:

$$\sigma = 2\pi^3 K \left(\frac{e^2}{hc} \right)^2 R^4 \frac{\omega_1 \omega_2}{\omega_{nn_0}} |Q_{nn_0}|^2 \frac{N_2}{\text{Max}(\Gamma_1, \Gamma_2)}, \quad (1)$$

where ω_1 and ω_2 are the frequencies of the γ and optical photons, respectively, ω_{nn_0} is the transition frequency, N_2 is the optical photon flux, $\text{Max}(\Gamma_1, \Gamma_2)$ is the larger of the frequency band-width of the two photons, R is the nuclear radius, K is the integral over line-shape functions and is of the order of unity, and Q_{nn_0} is a dimensionless matrix element given by:

$$Q_{nn_0} = \frac{\omega_{nn_0}}{R^2} \sum_{n'} \left(\frac{(\mathbf{e}_1 \cdot \mathbf{r}_{nn'}) (\mathbf{e}_2 \cdot \mathbf{r}_{n'n_0})}{\omega_{n'n_0} - \omega_2} + \frac{(\mathbf{e}_2 \cdot \mathbf{r}_{nn'}) (\mathbf{e}_1 \cdot \mathbf{r}_{n'n_0})}{\omega_{n'n_0} - \omega_1} \right), \quad (2)$$

where \mathbf{e}_1 and \mathbf{e}_2 are the dimensionless polarization vectors of the electromagnetic radiations and r_{ij} are matrix elements of the radius vector between initial n_0 , intermediate n' and final n states. When n' is energetically near to either the initial or the final state and when $\omega_1 \gg \omega_2$ the leading term in the sum is $Q \approx \omega_{nn_0}/\Delta\omega$, where $\Delta\omega$ is the smaller of $\omega_{n'n_0} - \omega_1$ and $\omega_{n'n_0} - \omega_2$, the frequency corresponding to the energy defect which the gamma photon misses for being resonant with a transition from either the initial or the final state to the intermediate state. Substituting this value into eq. (1) and converting the units gives

$$\sigma = 4.3 \times 10^{-36} \frac{E_\gamma \Phi_2 A^{4/3}}{(\Delta E)^2 \text{Max}(\Gamma_1, \Gamma_2)}, \quad (3)$$

in which σ is in cm^2 , E_γ is the γ energy in MeV, ΔE is in keV, Φ_2 is the photon flux in W/cm^2 and Γ_1, Γ_2 are the spectral widths in W/cm^2 .

Table 1

Isotopes for which recoil-free γ absorption has been observed and source speeds corresponding to the resonances

Isotope	^{57}Fe	^{119}Sn	^{127}I	^{125}Te	^{195}Pt
γ energy (keV)	14.41	29.83	57.6	35.5	98.8
Velocity (mm/s)	0.194	0.647	2.513	5.177	17.084

3. Estimates of cross-sections for recoil-free gamma resonant absorption in the presence of a microwave field

The above formula (eq. (3)) was used to estimate the cross-section for recoil-free resonant gamma-ray absorption in the presence of a microwave field. The calculations were performed for the Mössbauer transitions specified in table 1[8].

The results of the cross-section calculations are presented in fig. 1. In each case the flux of the microwave field has been taken to be 1 W/cm^2 . The results in fig. 1 are to be interpreted as the cross-sections by which, for a given microwave field frequency, the resonance absorption should take place, in the absence of any movement of the source with regard to the target. In this way it is inferred that the sampling of the resonant absorption line can be obtained by small variations of the microwave frequency, instead of a variation of the source speed. In fig. 1 it can be

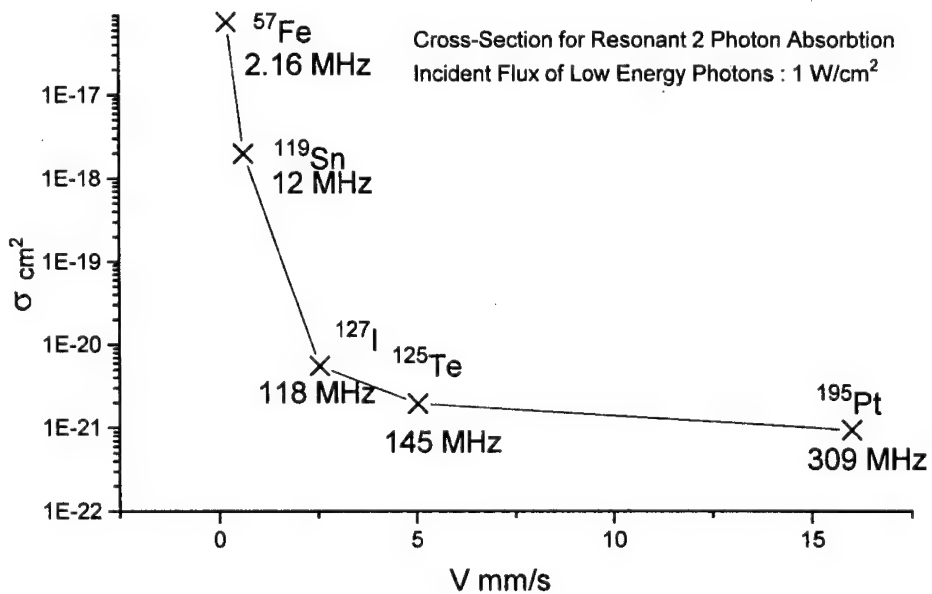


Fig. 1. Calculated cross-section values for recoil-free γ absorption in the presence of microwave fields.

seen that the cross-section for resonant absorption reaches quite high values even at low microwave fluxes of 1 W/cm^2 , in the case of ^{57}Fe .

The experiment to be presented in the following, has been performed in the presence of a 3 GHz microwave field, the flux being 1 MW/pulse. By using eq. (3), it can be easily seen that the cross-section for resonant absorption is of the order of 10^{-16} cm , thus being comparable with the highest cross-sections provided in fig. 1.

4. Experiment

An experiment of recoil-free 14.4 keV resonant gamma-ray absorption on polycrystalline $\text{K}_3[\text{Fe}(\text{C}_2\text{O}_4)_3]\text{3H}_2\text{O}$ sample exposed to a strong microwave field was carried out using a conventional constant acceleration Mössbauer transmission spectrometer. The schematic view of the experimental arrangement is shown in fig. 2. The gamma-beam was provided by a ^{57}Co Mössbauer source in a Cu matrix (MS), mounted on a linear velocity transducer (LVT) able to operate with both a sawtooth or a triangular velocity waveform. The pulsed microwave field was generated by a magnetron (M) with the following characteristics: the power $P = 1 \text{ MW}$, the frequency $\nu = 3 \text{ GHz}$, the frequency stability $\Delta\nu = 50 \text{ kHz}/^\circ\text{C}$, the pulse width $\tau = 1 \mu\text{s}$ and the pulse train frequency $\nu_t = 222 \text{ Hz}$. The sample (S), originated from a single crystal as a finely ground powder, was uniformly pasted by silicon grease

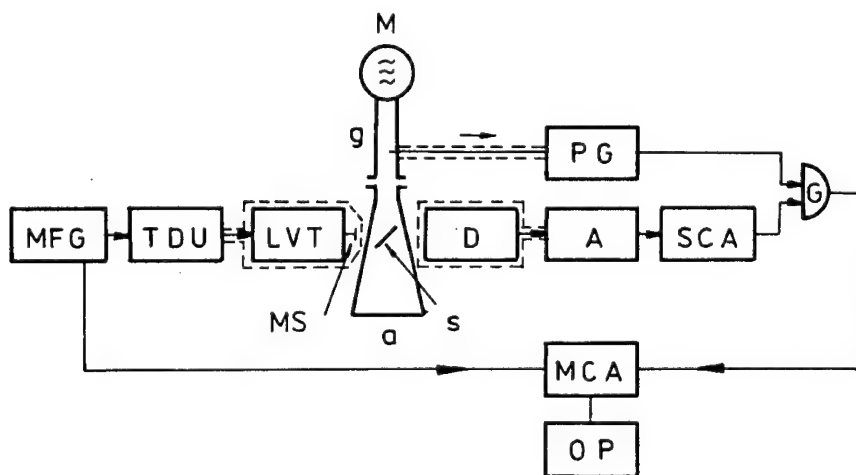


Fig. 2. Schematic drawing of the experimental arrangement for the microwave-Mössbauer resonant absorption (S: sample; MS: Mössbauer γ source; M: magnetron; MFG: Mössbauer function generator; TDU: transducer driving unit; LVT: linear velocity transducer; D: detector; A: spectroscopy amplifier; SCA: single channel analyzer; MCA: programmable data acquisition and processing system; PG: pulse generator; G: wave guide; a: balanced resistive load; OP: data output/input device).

on a Teflon support making a 45° angle toward the reciprocally perpendicular directions of the gamma-beam and the guided field propagation. The sample is a single-line thin absorber (≈ 0.1 mg $^{57}\text{Fe}/\text{cm}^2$) with very large half linewidth ($\Gamma \approx 3$ mm/s) and low isomer shift ($\delta \cong 0.1$ mm/s relative to copper) (fig. 4a). Two reasons prevailed in the choice of the absorber: a) large enough linewidth to be detectable on the large Doppler velocity scale demanded by the frequency ν ; b) absence of the internal electric or magnetic collective phenomena to avoid any acoustic or other undesirable RF effects. The signal from the NaI(Tl) scintillation detector (D) was routed to the multichannel analyser (MCA) by the $1\ \mu\text{s}$ linear gate (G), allowing data acquisition during the action of the microwaves on the sample. The electronics was carefully protected from the influence of the microwave field.

A Doppler velocity scale of $30\ \text{cm/s}$ with a triangular waveform extended over 800 channels was used to look for the first-order microwave sideband which was expected to appear at $-25.8\ \text{cm/s}$. The $30\ \text{cm/s}$ microwave Mössbauer spectrum is presented in fig. 3 together with the reference spectrum recorded in the same conditions but with no microwave field applied. As one can see in the reference spectrum (fig. 3a), the absorption line of the potassium trioxalatoferate absorber is clearly observed at the channels 211 and 619, while in the spectrum recorded in the presence of microwaves (fig. 3b), this parent line does not seem to be detectable within the statistical error. However, the shifted resonances corresponding to the frequency ν are slightly revealed at about $-25.8\ \text{cm/s}$ on both slopes of the triangular velocity waveform (channels 45 and 777 indicated by arrows).

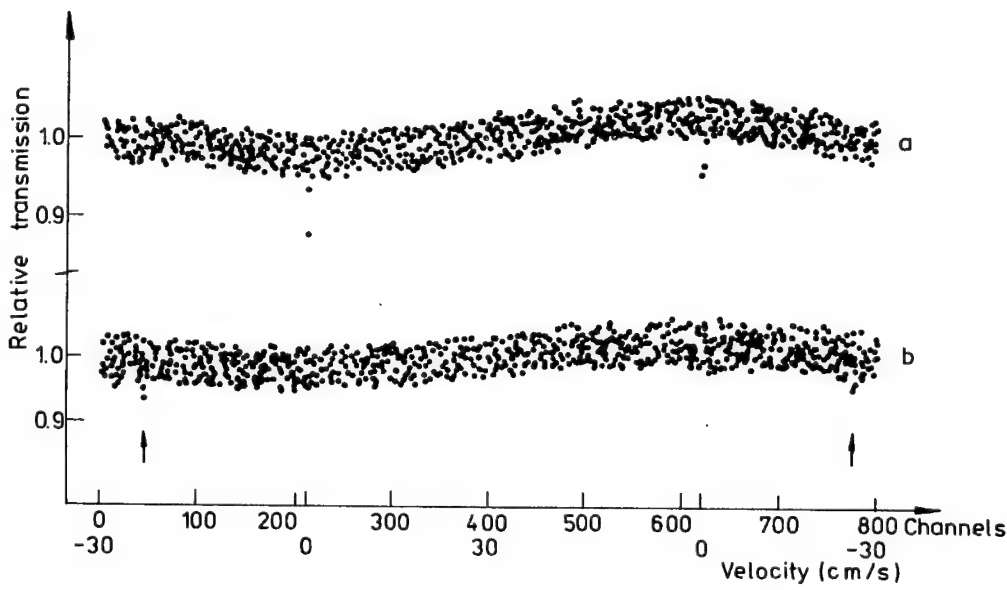


Fig. 3. Mössbauer spectra of $\text{K}_3[\text{Fe}(\text{C}_2\text{O}_4)_3]\text{3H}_2\text{O}$ recorded on a $30\ \text{cm/s}$ scale: (a) with no microwave field applied (reference spectrum); (b) with a microwave field of $3\ \text{GHz}$, $1\ \text{MW}$ and $1\ \mu\text{s}$ pulse width.

In order to search the influence of the applied microwave field on the parent line, the spectra were measured as well on a narrower velocity scale (10 mm/s sawtooth velocity waveform extended over 400 channels) where the Mössbauer resonance lies on about 50 channels and thus can be better observed. The 10 mm/s reference spectrum 1 and the 10 mm/s microwave Mössbauer spectrum 2 both recorded by the 1 μ s gate circuit, are plotted in fig. 4b and c, respectively. As one can see in fig. 4c, the applied microwave power did not destroy entirely the parent resonance. It appears doubtless at the unshifted usual position with $\delta \cong 0.1$ mm/s. A careful computer fitting analysis of the spectra 1 and 2 was performed and the resulting spectral parameters (i.e. line position E_0 , half linewidth Γ , effect ϵ , and area ratio a) are given in table 2. Comparing the two series of data, one remarks a clear decrease

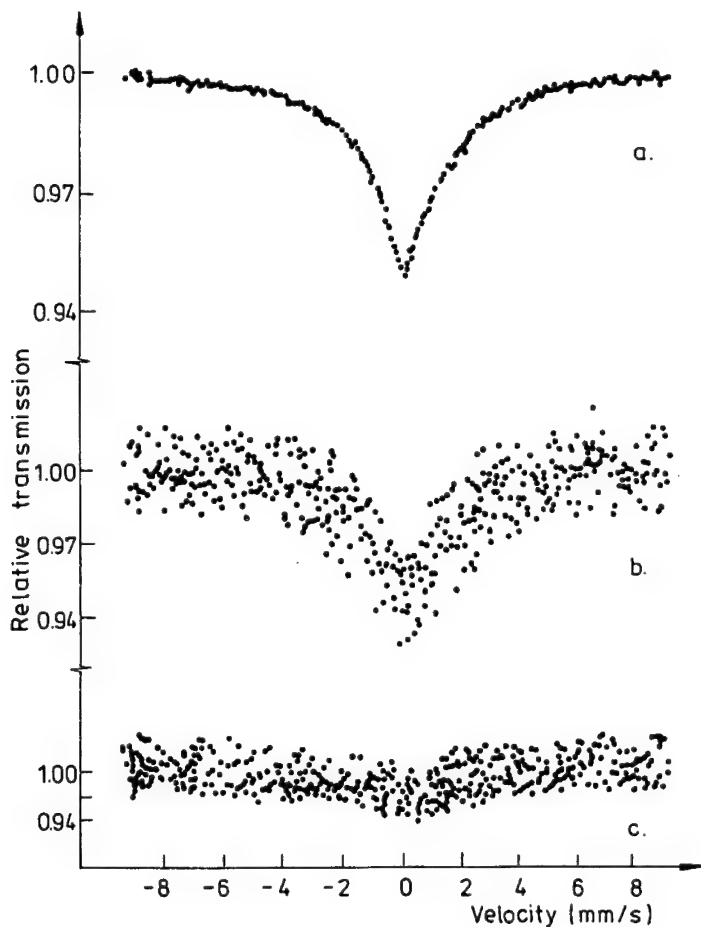


Fig. 4. Mössbauer spectra of $K_3[Fe(C_2O_4)_3]3H_2O$ recorded on a 10 mm/s scale: (a) reference spectrum, usual recording; (b) reference spectrum recorded by 1 μ s gate, (1); (c) with applied microwave field of 3 GHz, 1 MW and 1 μ s pulse width, (2).

Table 2

Computer-fitting spectral parameters (line position E_0 , half linewidth Γ , effect ϵ , area ratio a) for 10 mm/s reference spectrum (1) and microwave Mössbauer spectrum (2) of the $K_3[Fe(C_2O_4)_3]3H_2O$ absorber. The standard errors in parentheses

Spectrum	E_0 (mm/s)	Γ (mm/s)	ϵ (%)	a	a_2/a_1
1	0.15(9)	3.3(3)	5.0(3)	1.24(8)	0.67(17)
2	0.1(2)	3.2(7)	3.3(5)	0.8(2)	

of the area parameter (a) for the spectrum 2 without a sensitive change of the Γ linewidth. The ratio $r = a_2/a_1$ shows a value of 0.67 and therefore an area decreasing effect of 33%, two times greater than the relative error ($e_r = 0.17$) found for r .

In order to eliminate the doubt of a heating effect caused by the microwave action, additional temperature dependence measurements were carried out, searching the change of the Mössbauer spectra on the whole range from room temperature (T_0) to the degradation temperature ($\approx 100^\circ C$) of the sample. In fig. 5 the measured spectral parameters $\Gamma(T)/\Gamma_0$ and $a(T)/a_0$ are displayed as well as the recoil-free fraction ratio $f(T)/f_0$ obtained by using the well-known relation [9]

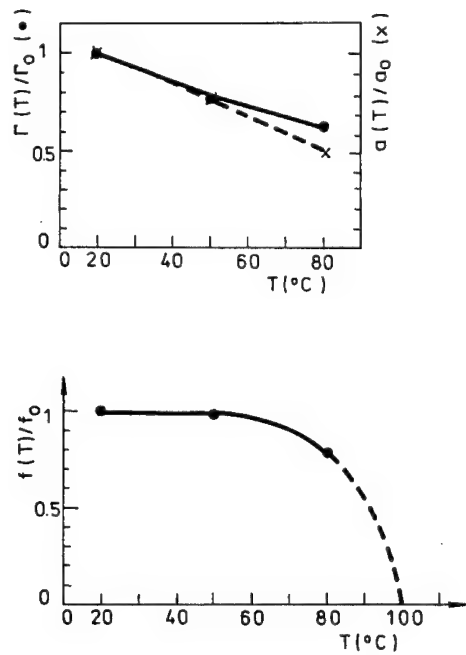


Fig. 5. Relative Mössbauer linewidth Γ (●), area ratio a (x), and recoil-free fraction f versus temperature T for $K_3[Fe(C_2O_4)_3]3H_2O$.

$$a = \frac{1}{2}\pi\sigma_0 f_s f n \Gamma. \quad (4)$$

Here a is the normalized area of the resonance, σ_0 is Mössbauer absorption cross-section, f_s and f are the recoil-free fractions for the source and the absorber, respectively, n is the number of resonant nuclei on the surface unit of the absorber and Γ is the half linewidth for the absorber. From the data given in fig. 5 it results that the decrease of the resonance area for the temperature range 20–50°C is almost exclusively determined by the decrease of the Γ value, while the decrease of the f -factor becomes important only above 50°C. As no significant change of the Γ linewidth was observed in the presence of microwaves, (table 2), one can assert that the decrease of the area of the parent line in spectrum 2 is not a secondary, thermal effect, but a direct action of the applied microwave field on the ^{57}Fe nuclei. This evident diminishing of the parent resonance as an effect of the microwave power is consistent with the appearance of the shifted resonances observed in the 30 cm/s spectrum in fig. 3b. Thus, a two-photon nature can be attributed to the microwave perturbation observed in this experiment.

5. Conclusions

A cross-section calculation for recoil-free gamma-ray absorption in the presence of a microwave field, based on a mechanism developed earlier [1–3], has been performed. Quite large values of the gamma-ray absorption cross-section, depending on the microwave field frequency have been obtained, indicating that the recoil-free gamma-ray absorption could be a test bench for the two-photon processes, when a large difference between the photon frequencies does exist.

An experiment indicating a notable effect of a microwave field on the ^{57}Fe recoil-free 14.4 keV γ absorption has been performed.

Due to the importance of the two-photon processes, either from the theoretical point of view or in relation to the problem of a gamma-ray laser, a systematic experimental investigation of this problem would be desirable.

Acknowledgement

The authors express their thanks to Dr. Doina Tarabasanu-Mihaila for the preparation of the single crystal enriched in ^{57}Fe .

References

- [1] M. Petrascu, RSCNE-Report no. 56 (1975).
- [2] C.B. Collins, S. Olariu, M. Petrascu and I. Popescu, Phys. Rev. Lett. 42 (1979) 1397.

- [3] C.B. Collins, S. Olariu, M. Petrascu and I. Popescu, Phys. Rev. C20 (1979) 1942.
- [4] P. Lambropoulos, Phys. Rev. A9 (1974) 1992.
- [5] H.B. Bebb and A. Gold, Phys. Rev. 143 (1966) 1.
- [6] H.B. Bebb, Phys. Rev. 149 (1966) 25.
- [7] D.H. Kobe, Phys. Rev. Lett. 40 (1978) 538.
- [8] D. Barb, *Grundlagen und Anwendungen der Mössbauer-Spektroskopie*, ed. W. Meisel (Akademie-Verlag, Berlin, 1980) p. 404.
- [9] R.M. Housley, N.E. Erickson and J.G. Dash, Nucl. Instrum. Meth. 27 (1964) 29.

Mössbauer transition dynamics in conditions of strong excitation of nuclear spins

E.K. Sadykov, A.G. Isavnin and A.I. Skvortsov

Kazan State University, Kazan, 420008, Russia

The state of the art Mössbauer spectroscopy has made unquestionable advance possible in the solid microstructure study. Apart from that application of the Mössbauer effect, another domain of investigations has been outlined since the outset, in the sixties, wherein the properties of gamma-radiation interaction with resonant nuclei in a recoilless mode are stressed. There were these recoilless processes that enabled to distinguish the gamma-radiation of natural width, and greatly encouraged the arising of traditional optics problems in the gamma range. The subject of interest in this article deals as well with the Mössbauer gamma optics. Essentially it is a gamma-ray (Mössbauer) susceptibility of the excited, non-equilibrium state of the nuclear spin system. We analyze the Mössbauer transitions in the strong coherent excitation of nuclear spins regime and the possibilities to deliberately vary the polarization, spectral and/or temporal properties of gamma-radiation propagating through a time-modulated medium.

1. Preliminary remarks

The non-equilibrium state behaviour of the solids has been investigated for a long time by means of Mössbauer spectroscopy. Pioneer works of Ruby and Bolef [1] and Hack and Hamermesh [2] have founded the modulation Mössbauer spectroscopy using high-frequency external fields. Remarkable effects were revealed within this field. First of all, this is an acoustic modulation of the gamma radiation – an appearance of satellite structure in the absorption (emission) Mössbauer spectra (MS), influenced by piezo-quartz ultrasonic excitation [1,3,4]. Another effect – MS lines splitting in the nuclear spin excitation regime by means of an alternating magnetic field on the NMR frequency [2,4,6] (which is an analogy of the Autler-Towns effect [7]) – could not be directly observed in experiment for a long time. The investigations on this phenomenon have eventually grown up to a very interesting and tedious problem.

Mössbauer spectroscopy followed radio- and optical spectroscopy where double resonance methods together with modulation and transition phenomena are widely used. Besides this stimulating similarity, there are specific problems for double R.F. + gamma resonance (DGR) phenomena. Thus, for the RF field amplitudes applied on a nucleus to exceed the gamma-radiation natural line width (strong field condition), the effects described in ref. [2] should be sought in magnetic materials (compounds with the Mössbauer isotope ^{57}Fe), wherein an external field is ampli-

fied on the nucleus by means of hyperfine interaction. Hence, the fields on a nucleus appear to be in a tight dependence of the sample temporal magnetization behaviour (more exactly, of a single magnetic ion). This fact has a great applied significance but it has also become a source of complications in the experimental realization of the effect. A substantial hindrance in magnetically ordered materials is a dynamic magnetostriction in the RF fields that results in MS transformation [8,9] due to an acoustic modulation of Mössbauer radiation. The reasons of unsuccessful DGR experiments also associate with magnetic anisotropy fields leading to inhomogeneity in the physical conditions. A more complicating factor is the collapse of magnetic spectra hyperfine structure, a phenomenon caused by complete micro-scale magnetic reversal [10,11] and, as follows from the experimental results, magnetization jumps have a rather chaotic character [12,13].

DGR was investigated in paramagnetic (Fe^{3+}) samples as well as where the magnetorestriction phenomenon is absent, but relaxation of electron spin and the quite cumbersome scheme of electron-nuclear levels make the experimental conditions very difficult [14,15]. Notice also the proposal on DGR realization in diamagnetic substances based on the quadrupole interaction of a nucleus [16,17]. Developments of research performed in this field are enlightened in reviews [18,19].

The physics of the DGR phenomenon continually attracts the explorers attention, since we deal with quantum spin dynamics in the coherent nuclear fields [20–26]. The magnetodynamical RF effects influence on Mössbauer samples is also interesting as an indispensable component of more precise physical experiments, and up to now there is a certain progress achieved in this field.

The controllable modification of the hyperfine field direction was used as a magnetic shutter [27]. Quite interesting experiments have been performed testifying about the introduction of large-scale fields into stainless steel foils [28]. Various large-amplitude theoretical models for a nucleus [26] have been proposed and some model calculations have been fulfilled [20]. Ultimately, using enriched thin iron films [29] and $^{57}\text{Fe}_{18}\text{Ni}_{82}$ films [30], the spectral structure predicted in ref. [2] was experimentally confirmed. All this makes investigations in the field of Mössbauer spectroscopy of non-equilibrium spin systems more actual. It is essential that, unlike the previous problem setting, magnetodynamical effects in the Mössbauer spectra prove not to be restricted by DGR conditions. Nuclear spins in magnetic materials often turn out in the large-scale amplitude regime, under conditions which have no analogy in optics. The “large-scale amplitude” regime term should be distinguished from the “strong field” one in optics. In the first case, the alternating field amplitude is not only larger than the probing field natural width but, comparable or even much larger than the constant field component on a nucleus and that is frequently a reason of collapse.

The theory of Mössbauer response under RF influence was also generalized to the sphere of temporal and time-frequency measurements [31–34]. Results similar to those of temporal Mössbauer spectroscopy based on Doppler modulation of a source have been obtained. Since temporal effects in spectra are a consequence of

amplitude interference, it is easy to understand that time dependence in the two above-mentioned cases is due to different degrees of freedom. Theoretical, as well as experimental investigations of magnetodynamical effects in Mössbauer spectra were performed in recent years [35–38]; the theory has been developed and a set of peculiarities [35] has been revealed waiting for experimental confirmation. They could prove themselves interesting for the gamma-optics purposes. This article also focuses on modulation effects of the spin system, caused by non-resonant large-amplitude fields. Methods of MS calculation using a quasi-energy concept have been developed. The most interesting new results are displayed at the Rabi frequencies for the ground and excited nuclear states. At low frequencies collapse does not occur. This adiabatic regime corresponds to RF field frequencies much smaller than the Larmor frequency, associated with the instant value of a nuclear field.

In the following, the theory of modulation effects in nuclear gamma-resonance is outlined within the limits of the magnetodynamical mechanism. The expression for the amplitude of Mössbauer scattering is obtained starting from first principles (section 2). The total information about the hyperfine interaction of the Mössbauer nucleus is contained in the evolution superoperator, which determines time-gated as well as traditionally recorded (time-averaged) Mössbauer absorption spectra. We have made an attempt to build the theory of gamma radiation propagation in the medium with temporal modulated magnetic hyperfine interaction, generalizing the refraction index formalism to the time-dependent case (section 3). The equations of motion for the evolution superoperator and the methods to solve them for arbitrary periodical fields on a nucleus are discussed (section 4). Interesting effects are expected for large-scale fields, especially in the low-frequency region (section 5). In conclusion, some experimental problems specific for magnetic materials are discussed.

2. Theoretical background

First of all, we have to derive the amplitude of the gamma radiation resonant scattering on the nucleus, in the case of Mössbauer transition assumption. The Hamiltonian for this problem is [39,40]:

$$H = H_R + H_N + H_\gamma + H_{hf}(t), \quad (1)$$

where H_R and H_N represent the Hamiltonians of the γ -radiation field and of the nucleus, H_γ describes the nuclear interaction with gamma-radiation, $H_{hf}(t)$ is the Hamiltonian of nuclear interaction with classical (hyperfine) fields; it may be generalized to the case of nuclear interaction with another quantum system. We have the following commutation rules:

$$[H_R, H_N] = [H_R, H_{hf}(t)] = [H_N, H_{hf}(t)] = 0.$$

We are interested in the nuclear excitation process due to a $k1$ quantum absorption,

followed by a $k2$ quantum emission by this nucleus. Let us use the equation of motion in the interaction representation:

$$i \frac{d\tilde{\varphi}}{dt} = \tilde{H}_\gamma \tilde{\varphi},$$

$$\tilde{\varphi} = V^+(t)\varphi, \quad \tilde{H}_\gamma = V^+(t)H_\gamma V(t),$$

$$V(t) = V_0(t) \times V_1(t).$$

$$V_0(t) \equiv V_0(t, t_0) = \exp[-i(H_N + H_R)(t - t_0)],$$

$$V_1(t) \equiv V_1(t, t_0) = T \exp \left[-i \int_{t_0}^t H_{hf}(t') dt' \right]. \quad (2)$$

Here $H_{hf} = H^{e,g}$ and $V_1 = V^{e,g}$ stand for the excited (E_0 energy) and, respectively, ground level of the Mössbauer nucleus. We represent the φ wave function in the basis of eigenstates of H_N , with certain projections of the $|I_e, M\rangle$, $|I_g, m\rangle$ nuclear spins and eigenstates of H_R , $|0\rangle$ and $|k2\rangle$, without quantum and with $k2$ quantum, respectively:

$$\tilde{\varphi} = V^+(t)\varphi = \sum_M b_M |M, 0\rangle + \sum_{m, k2} b_{mk2} |m, k2\rangle,$$

$$|I_e, M\rangle |0\rangle \equiv |M, 0\rangle, \quad |I_g, m\rangle |k2\rangle \equiv |m, k2\rangle. \quad (3)$$

The equations system for the b_i coefficients is given as

$$ib_M = \sum_{m, k2} \langle M, 0 | \tilde{H}_\gamma(t) | m, k2 \rangle b_{mk2} + \langle M, 0 | \tilde{H}_\gamma(t) | m_i, k1 \rangle b_{m_i k1}, \quad (4.1)$$

$$ib_{mk2} = \sum_M \langle m, k2 | \tilde{H}_\gamma(t) | M, 0 \rangle b_M, \quad mk2 \neq m_i k1, \quad (4.2)$$

$$ib_{m_i k1} = \sum_M \langle m_i, k1 | \tilde{H}_\gamma(t) | M, 0 \rangle b_M. \quad (4.3)$$

The $|m_i, k1\rangle$ initial state is singled out according to the initial conditions

$$b_{mk2}(t_0) = \delta_{mm_i} \delta_{k1 k2}, \quad b_M(t_0) = 0.$$

In the natural line width approximation (γ -line width of excited nuclear state)

$$b_M(t) = (-i) \int_{t_0}^t dt' \exp(-\gamma(t - t')/2) \langle M, 0 | \tilde{H}_\gamma(t') | m_i, k1 \rangle b_{m_i k1}(t'). \quad (5)$$

Let us substitute eq. (5) into (4.2) and integrate it with the assumption that $b_{m_i k1}(t') \approx 1$ and $t_0 \rightarrow -\infty$:

$$b_{mk2}(t) = (-i)^2 \int_{-\infty}^t dt' \sum_{M,M',m'} \langle m, k2 | \tilde{H}_\gamma(t') | M, 0 \rangle U_{Mm_iM'm'}^{(t)}(p) \\ \times \langle M', 0 | \tilde{H}_\gamma(t') | m', k1 \rangle, \quad (6)$$

where the evolution superoperator is introduced as follows:

$$U(t + \tau, t)A(t) = U^{(t)}(\tau)A(t) = V_1^+(t + \tau, t)A(t)V_1(t + \tau, t), \quad (7)$$

$$U(p, t) = U^{(t)}(p) = \int_{-\infty}^0 d\tau \exp(p\tau) U^{(t)}(\tau), \quad p = -i(E_{k1} - E_0) + \gamma/2. \quad (8)$$

The supermatrix $U_{MmM'm'}^{(t)}(p)$ in eq. (6) is defined on time-shifted states $V(t)|m\rangle$ and $V(t)|M\rangle$. Let us clear up the meaning of the upper (t) index, the external time mark. Since we deal with the gamma-quantum absorption (emission) process, we shall express the integral of eq. (8) in the gamma transition process time scale. The $t = 0$ instant of this scale corresponds to the t instant in the laboratory time reference system. Therefore the external periodical perturbation phase at the moment t is $\phi(t) = 2\pi t/T = \omega t$, where T is the modulation period.

Expression (6) enables us to define the resonant scattering amplitude of the $k1 \rightarrow k2$ gamma quantum. One can further derive the resonant absorption cross-section for the gamma quanta using the optical theorem

$$\sigma(E_{k1}, t) = \frac{2}{(2\pi)^3 k} \left(\frac{kv}{2\pi c} \right) \text{Re} \sum_{m_i m' MM'} \langle m_i, k1 | \tilde{H}_\gamma(t) | M, 0 \rangle U_{Mm_iM'm'}^{(t)}(p) \\ \times \langle M', 0 | \tilde{H}_\gamma(t) | m', k1 \rangle, \quad (9)$$

where v represents the normalization volume.

This expression has been obtained assuming an arbitrary time dependence $H_{hf}(t)$, and it describes the MS temporal variations in the external time mark regime. Note that the $\Delta t \ll T$ condition should be satisfied, where Δt is the time per temporal channel. We see that the information about the hyperfine interaction is contained in the $U_{Mm_iM'm'}^{(t)}(p)$ superoperator. In case of the H_{hf} stationary Hamiltonian the $U(p)$ temporal dependence disappears and for the diagonal magnetic quantum numbers Hamiltonian the result is

$$U_{Mm_iM'm'}(p) = U_{Mm_iM'm'}(p) \delta_{MM'} \delta_{m_i m'}.$$

3. Gamma-wave propagation through time-modulated medium

In this section we present the expressions which describe the gamma-radiation propagation process in a time-modulated medium. Let us use the (\hat{n}) refraction

index formalism which has also been used in the case of the stationary interaction medium [41]:

$$\frac{\partial\psi(z, \omega)}{\partial z} = ik\hat{n}\psi(z, \omega), \quad (10)$$

where $\psi(z, \omega)$ is the gamma-wave Fourier component

$$n_{\nu\nu'} = E + (2\pi/k^2)Ndf_{\nu\nu}, \quad d = \left(-\frac{kv}{2\pi c}\right)R,$$

where R stands for the recoilless factor and $f_{\nu\nu'}$ is the forward scattering amplitude. ν is the polarization index and N represents the concentration of Mössbauer centers. In the case of a time-modulated medium, the equation describing the Fourier component evolution in space and time looks like [35]

$$\begin{aligned} \frac{\partial\psi_\nu(z, \omega, t)}{\partial z} &= ik[E + 2\pi Nd/k^2 f_{\nu\nu}^{(t)}]\psi_\nu(z, \omega, t) - ik(2\pi Nd/k^2) \\ &\times \int_{-\infty}^t dt' f_{\nu\nu'}^{(t')} \frac{\partial\psi_{\nu'}(z, \omega, t')}{\partial t'}. \end{aligned} \quad (11)$$

After some simulations we write eq. (11) using the \hat{n}_I integral refraction index, according to

$$\begin{aligned} \frac{\partial\psi(z, \omega', t)}{\partial z} &= ik\hat{n}_I\psi(z, \omega', t) \\ &= ik\psi(z, \omega', t) - 2\pi Nd/k \int_{-\infty}^t dt' \exp(p(t' - t)) \\ &\times \sum_{MM'M''mm'm''} H_{mM}^+ \left[U_{MmM'm'}^{\phi(t)}(t' - t) \left\{ \frac{d}{dt'} U_{M'm'M''m''}^{\phi(t')}(p) + p U_{M'm'M''m''}^{\phi(t')}(p) \right\} \right. \\ &\left. + \frac{d}{dt'} U_{MmM'm'}^{\phi(t)}(t' - t) U_{M'm'M''m''}^{\phi(t')}(p) \right] \cdot H_{M''m''} \psi(z, \omega', t'). \end{aligned} \quad (12)$$

In eq. (12) we have supposed that U does not depend on the sample thickness z . This dependence has to exist due to the finite propagation velocity of the modulating fields. One may neglect such effects if the condition $l/c \ll T$ is valid (l is the linear dimension of the sample). After finding the solution of this equation, we can easily derive the probability of the gamma-quantum detection after its passage through the z thickness modulated medium, in the time differential (with external or internal time mark) or in the time integral recording regimes. Solving of eq. (12) implies the calculation of $U^{\phi(t)}(t)$ and $U^{\phi(t)}(p)$. However, in the thin-absorber limit, the equation may be solved with $U(p)$ of non-evident form. In order to do so, we use an iteration procedure. The zero-order solution of (12) (in absence of the absorber) for the Fourier component, reads as:

$$\psi^{(0)}(z, \omega) = \psi(0, \omega) \exp(ikz). \quad (13)$$

In a first-order approximation for the interaction, $\psi(z, \omega, t)$ is described by the equation:

$$\frac{\partial\psi^{(1)}(z, \omega, t)}{\partial z} = ik\psi^{(1)}(z, \omega, t) - \frac{2\pi N d}{k} \sum_{mm' MM'} H_{mM}^+ U_{MmM'm'}^{\phi(t)}(p) H_{M'm'} \psi^{(0)}(z, \omega). \quad (14)$$

The solution of eq. (14) is

$$\psi^{(1)}(z, \omega, t) = \left(E - \frac{2\pi z N d}{k} \sum_{mm' MM'} H_{mM}^+ U_{MmM'm'}^{\phi(t)}(p) H_{M'm'} \right) \psi(0, \omega) \exp(ikz). \quad (15)$$

In this approximation the transmitted gamma wave is

$$\psi(z, t, t_0) = \int_{-\infty}^{+\infty} d\omega \psi^{(1)}(z, \omega, t) \exp(-i\omega(t - t_0)),$$

where t_0 corresponds to the beginning of nuclear decay within the source. The probability of gamma quanta detection in the time differential regime is:

$$\begin{aligned} \langle |\psi(z, t, t_0)|^2 \rangle_{t_0, \rho} &= \int_{\infty}^{+\infty} d\omega' \langle |\psi(z, \omega', t)|^2 \rangle_{\rho} \\ &= \int_{-\infty}^{+\infty} d\omega' \frac{\gamma_s/2\pi}{(\omega' - \omega_s)^2 + (\gamma_s/2)^2} \\ &\quad \times \left\langle \left\{ E - \frac{2\pi z N d}{k} \times \sum_{mm' MM'} \text{Re}[H_{mM}^+ U_{MmM'm'}^{\phi(t)}(p) H_{M'm'}] \right\} \right\rangle_{\rho} \\ &= 1 - Nz\sigma_{\rho}(\omega_{\gamma}, t), \end{aligned} \quad (16)$$

$$p = -i(\omega' - \omega_a) + \gamma_a/2,$$

where the time-dependent cross-section is

$$\sigma_{\rho}(\omega_{\gamma}^s, t) = \frac{4\pi d}{k} \sum_{\nu\nu'} \rho_{\nu\nu'} \sum_{mm' MM'} \text{Re}[H_{mM}^+(\nu') U_{MmM'm'}^{\phi(t)}(p') H_{M'm'}(\nu)], \quad (17)$$

$$p' = -i\omega_{\gamma}^s + \gamma/2, \quad \gamma = \gamma_s + \gamma_a,$$

where $\langle \dots \rangle_{\rho}$ is an average on the gamma radiation polarization state, $\omega_{\gamma}^s = (\omega_s - \omega_a)$. ω_a , ω_s and γ_a , γ_s correspond to the absorber (modulated) and to the source, respectively.

The absorption cross-section expression in the time-averaged recording regime assumption, may be written as:

$$\sigma_{\rho}(\omega_{\gamma}^s) = \frac{4\pi d}{k} \sum_{\nu\nu'} \rho_{\nu\nu'} \sum_{mm' MM'} \text{Re}[H_{mM}^+(\nu') \langle U_{MmM'm'}(p') \rangle_t H_{M'm'}(\nu)], \quad (18)$$

$$\langle U^{\phi(t)}(p') \rangle_t = (1/T) \int_0^T dt' U^{\phi(t')}(p') .$$

4. Calculation methods. Arbitrary periodical hyperfine fields

We consider the most realistic situation, when $H_{hf}(t)$ is an arbitrary periodic temporal function. The basic assumption is the validity of the effective hyperfine field model. The magnetic field on the nucleus is defined as proportional to the magnetization ($\bar{H}_{hf} = \alpha \bar{M}$). Under such conditions, the effective field on the nucleus displays the micromagnetization temporal evolution, which may be in the total magnetization reversal regime for soft magnetic materials. Proceeding from definition (7), the equation of motion for the evolution superoperator may be written as

$$\frac{d}{dt} U(t) = iU(t)L(t),$$

$$U(t) = \hat{A} \exp\left\{ i \int_{t_0}^t dt' L(t') \right\}, \quad (19)$$

where \hat{A} is the time anti-ordering operator.

Here, the Liouville superoperator has been introduced as:

$$\{L(t)\}_{\lambda i \lambda' i'} = H_{\lambda \lambda'}^e(t) \delta_{ii'} - H_{i i'}^g(t) \delta_{\lambda \lambda'}$$

The time periodical operators

$$H^{g,e}(t) = \sum_n H_n^{g,e} \exp(in(\omega t + \varphi)),$$

with n integer numbers, result in:

$$L(t) = \sum_n L_n \exp(in(\omega t + \varphi)). \quad (20)$$

In the simplest case of $n = 0 \pm 1$ oscillating field, we have the following recurrence relation [24] for $U(p)$:

$$(p\mathbf{1} - iL_0)U^\varphi(p) = \mathbf{1} + i \sum_{n=\pm 1} L_n U^\varphi(p - in\omega) e^{in\varphi}. \quad (21)$$

A recurrence relation similar to eq. (21) was used in ref. [36] in order to calculate the density matrix for a nucleus. Eq. (21) may be solved with the continued fraction technique [36,39]. This method becomes cumbersome if the number of terms in summation (20) is large. There is an opportunity to calculate the MS by means of a numerical solution for eq. (19). In case of an arbitrary periodic perturbation, the condition $L(t+T) = L(t)$ leads to the following two relations for the $U(t)$ evolution operator [13]:

$$\begin{aligned} U(T(n+1), Tn) &= \hat{T} \exp \left[i \int_{Tn}^{T(n+1)} L(t') dt' \right] \\ &= \hat{T} \exp \left[i \int_0^T dt' L(t' + nT) \right] = U(T, 0), \end{aligned}$$

and

$$\int_{Tn}^{T(n+1)} dt' \exp(-pt') U(t', 0) = \exp(-pTn) \int_0^T dt' \exp(-pt') U(t', 0) U(nT, 0).$$

Using the above relations, the Laplace-transform $U(p, t)$ may be expressed as

$$\begin{aligned} U(p, t) &= \int_t^T U(t', t) \exp(-p(t' - t)) dt' + \int_0^T U(t', 0) \exp(-pt') dt' \\ &\quad \times [E - \exp(-pt) U(T, 0)]^{-1} U(T, t) \exp(-p(T - t)), \end{aligned}$$

$$U(p) = (1/T) \int_0^T dt U(p, t),$$

where E is a unit matrix in the U superoperator space.

The $U(p)$ and $U(p, t)$ supermatrices can be calculated at any desired accuracy performing a numerical integration within the T interval following the method described in ref. [42]. The last is based on the continued fractions approximation for $U(t_k, t_i)$,

$$U(t_k, t_i) = U^{-1}(t_i, t_k) = \frac{E}{E + \int_{t_k}^{t_i} ds_1 L(s_1) U(s_1, t_k)} = \frac{E}{E + \int_{t_k}^{t_i} \frac{ds_1 L(s_1)}{E + \int_{s_1}^{t_k} \frac{ds_2 L(s_2)}{E + \dots}}},$$

with a finite (truncated) fraction, which can be written as:

$$\begin{aligned} U(t_{i+1}, t_i) &= [E - (h_i/2)L(t_{i+1}) - (h_i^2/12)(L^2(t_{i+1}) + L'(t_{i+1}))]^{-1} \\ &\quad \times [E - (h_i/2)L(t_i) + (h_i^2/12)(L^2(t_i) + L'(t_i))] + O(h_i^5), \end{aligned}$$

where $h_i = t_{i+1} - t_i$, $L'(t_i) = (dL(t)/dt)|_{t_i}$.

For an arbitrary finite time interval, the $u(t_m, t_0)$ superoperator can be represented as

$$U(t_m, t_0) = \prod_{i=1}^m U(t_i, t_{i-1}),$$

with a $\{h_i\}$ set, providing the required accuracy.

As an application of this method, we have calculated the MS for the case when the magnetization vector moves along a semicircle (fig. 1).

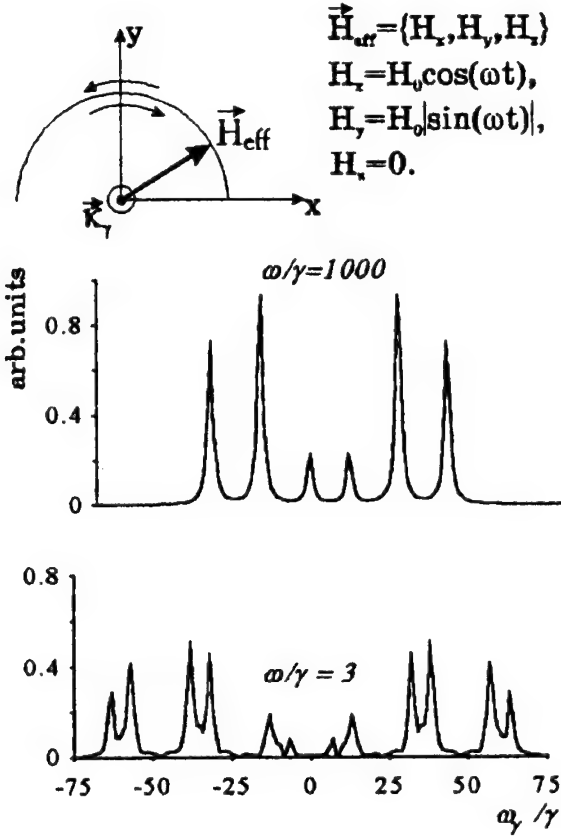


Fig. 1. MS absorption of unpolarized gamma-radiation in a geometry indicated above the spectra. At low frequencies, the satellite structure appears. Opposed to the rotating field case, satellites of superior orders (> 1) appear. At high frequencies collapse of the hyperfine structure take place. The sextet corresponds to $H = (2/\pi)H_0$.

5. Large-scale amplitudes: the rotation field model. Quasi-energy concept

In this section, some effects of the nonresonant RF field in the large-scale amplitude regime are treated. We mean the soft magnetically ordered compounds containing ^{57}Fe . We have especially considered the case of a rotating field model [39]

$$\begin{aligned}
 L(t) &= L_0 + L_+ \exp(-i(\omega t + \varphi)) + L_- \exp(i(\omega t + \varphi)), \\
 \{L_{\pm}\}_{mMm'M'} &= (1/2)\{\omega_1^g (\hat{I}_\pm^g)_{mm'} \delta_{MM'} - \omega_1^e (\hat{I}_\pm^e)_{M'M} \delta_{mm'}\}, \\
 \{L_0\}_{mMm'M'} &= \{\omega_0^g (\hat{I}_z^g)_{mm'} \delta_{MM'} - \omega_0^e (\hat{I}_z^e)_{M'M} \delta_{mm'}\},
 \end{aligned} \tag{22}$$

One should bear in mind that, within the framework of the effective field model, the total field (constant + alternating) on the nucleus has to be constant in magnitude:

$$(\omega_{\text{eff}}^{\text{e,g}})^2 = (\omega_0^{\text{e,g}})^2 + (\omega_1^{\text{e,g}})^2 = \text{const.}$$

$$\omega_1^{\text{e,g}}/\omega_0^{\text{e,g}} = \eta.$$

A large-scale amplitude area corresponds to $\eta \geq 1$. It is known that the adopted model allows an exact solution of the problem [35]:

$$\begin{aligned} U_{mMm'M'}^{(t)}(p) &= M_{mMm'M'}^{-1}(p + i\omega F(m, M), t) \\ &= M_{mMm'M'}^{-1}(p + i\omega F(m, M), 0) \exp(i\omega t(m - M - m' + M')), \end{aligned}$$

$$M_{mMm'M'}(p) = p\delta_{mm'}\delta_{MM'} - i\{L(t)\}_{mMm'M'},$$

where $F(m, M)$ is some combinatorial function of the m, M, I^g, I^e quantum numbers.

A remarkable result occurs for $\eta \rightarrow \infty$ and low frequencies ($\omega \sim \gamma$). For example, fig. 2a depicts the absorption spectrum for $\omega = 2\gamma$ and for the propagation direction of the unpolarized gamma radiation perpendicular to the RF field rotation plane. As shown, each component of the absorption spectrum is split $\Delta = 2\omega$. The splitting mechanism may be easily understood. The absorption cross-section would oscillate periodically, becoming zero when linearly polarized gamma radiation is used (the hyperfine field rotates slowly relative to the polarization direction). As known, such periodic dependence leads to frequency splitting due to the amplitude modulation effect. The same splitting will be conserved in the case of unpolarized radiation consisting of two linearly polarized components. All these are also confirmed by the absorption cross-section form, under identical conditions for circularly polarized gamma radiation (see fig. 2b) where splitting is absent but the sextet lines positions are identical with the left component ones of the 2a spectrum. Besides purely physical interest, such a phenomenon can be used for the realization of the polarizing effect using gamma radiation propagation within a modulated resonant medium in the above-described geometry.

This result can be otherwise obtained introducing the $\psi_{M'}(t)$ spin quasi-energetic states in a rotating field [39] (see diagram 1):

$$\psi_{M'}(t) = \exp(iE_{M'}t) \sum_M d_{M'M}^I |I_i, M\rangle \exp(i(M - M')\omega t + iM\varphi),$$

for nuclear excited and ground states, where $d_{M'M}^I$ are the rotating matrices and E_M are the quasi-energies

$$E_{M'} = -M'\omega - M'((\omega_0^i - \omega)^2 + (\omega_1)^2)^{1/2}, \quad i = g, e.$$

Knowing these state, one can find the gamma-radiation absorption spectrum,

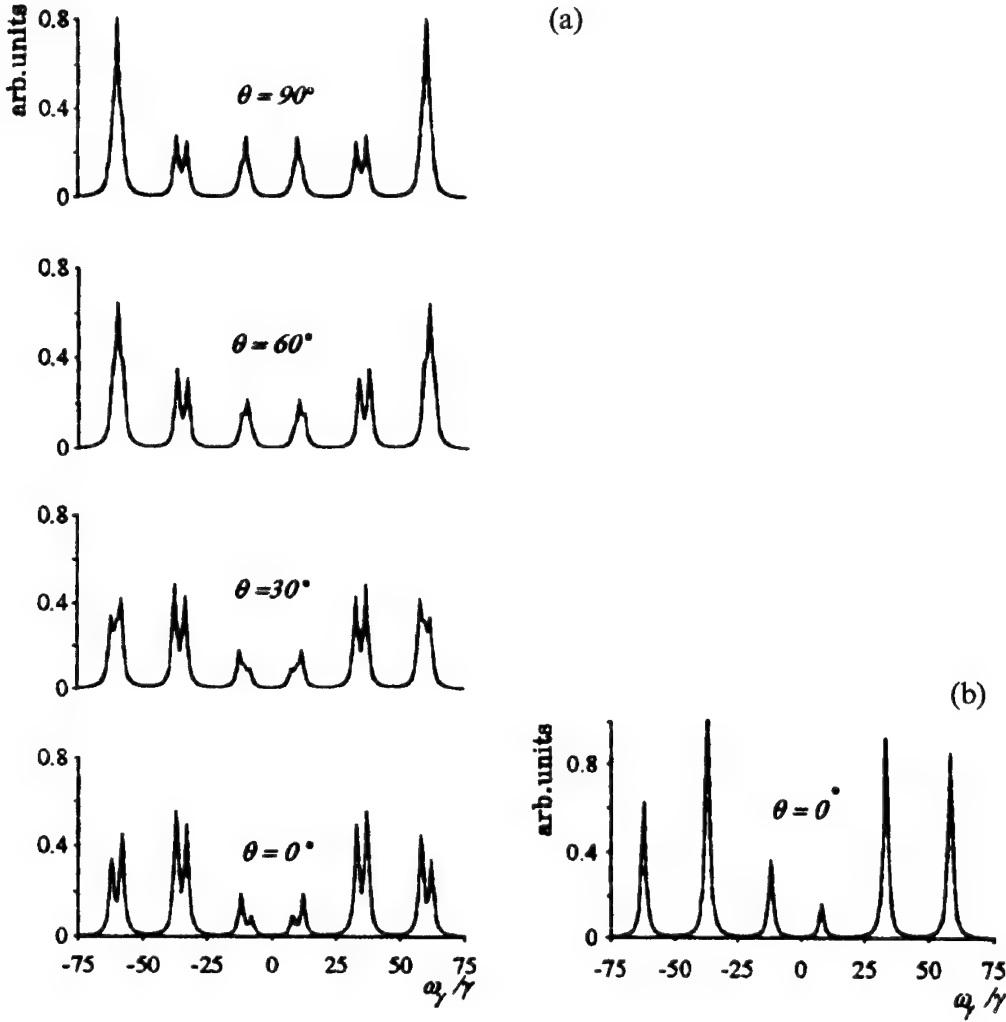


Fig. 2. (a) MS absorption of unpolarized gamma radiation $\eta \rightarrow \infty$, $\omega/\gamma = 2$. θ is the angle between the propagation direction and the normal to the field rotation plane. (b) MS absorption of circularly polarized gamma radiation $\eta \rightarrow \infty$, $\omega/\gamma = 2$, $\theta = 0^\circ$.

generalizing the familiar quantum mechanics formula for the transition between stationary states under alternating perturbation, to the quasi-energetic states case.

$$P_{M'm'} = \frac{2\pi}{\hbar} \sum_{M-m} \left| \sum_{M-m=\text{const}} \langle I^e M | H_\gamma | I^g m \rangle d_{M'M}^{I*} d_{m'm}^I \right|^2 \times \delta(E_{M'} - E_{m'} - \hbar\omega_\gamma - (M-m)\omega + (M'-m')\omega). \quad (23)$$

QUASIEnergIES IN ROTATING FIELD.

Fe^{57} , Mossbauer transition $I = 3/2 \rightarrow I = 1/2$.

$E'_{M'} = E_{M'} + \Delta n\omega$, $E_{M'}$ - basic zone quasienergies (solid lines).

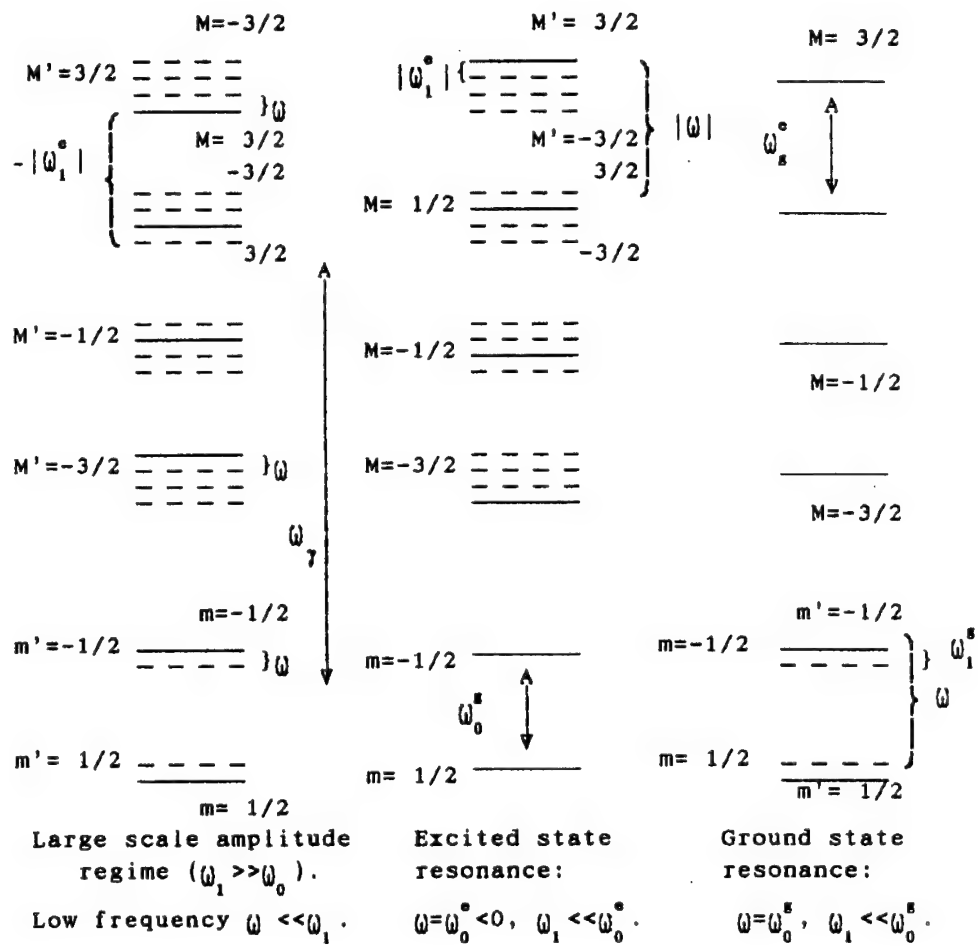


Diagram 1.

We have another phenomenon present in the large-scale amplitude case at high RF field frequencies $\omega > \omega_{\text{eff}}^{\text{eg}}$. The magnetic hyperfine structure collapse begins when the ω frequency in this region increases. The spectrum collapse process has peculiarities at Rabi frequencies and at sufficiently large values of η ($\eta \geq 3$). In fig. 3 we display the time-gated spectrum for $\phi(t) = 0$. So, the structure of the spectrum is

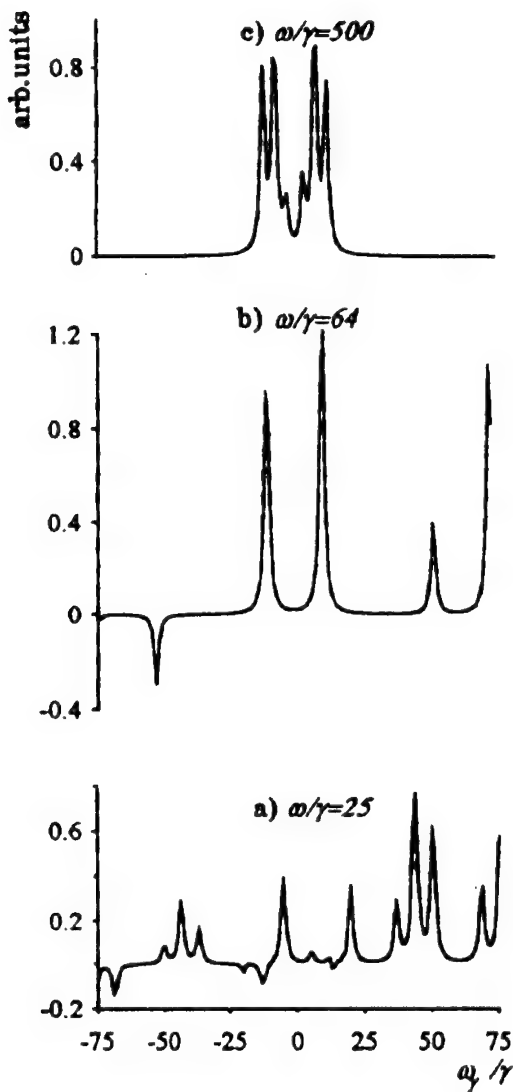


Fig. 3. Time-gated MS absorption ($\phi = 0^\circ$), for circularly polarized radiation $\eta = 5$, $\theta = 90^\circ$. The Rabi "resonance" $\omega = \omega_R^g = 64\gamma$ is singled out.

simplified taking a doublet form at the Rabi frequency (say for an excited state) (fig. 3b).

$$\omega^2 = (\omega_R^e)^2 = (\omega_0^e - \omega)^2 + (\omega_1^e)^2, \quad (24)$$

or taking into account the η and ω_{eff}^e ,

$$\omega = (1/2)\omega_{\text{eff}}^e(1 + \eta^2)^{1/2}.$$

As known, the Zeeman splitting in the rotation reference system is determined

by the ω_R^e value. Therefore, the $U(p)$ superoperator poles caused by Rabi frequencies for the nuclear excited state coincide with satellite lines. The central part of the spectrum is now determined only by the ground-state Rabi frequencies. Then, the doublet splitting of the spectrum central part in fig. 3b, is (^{57}Fe):

$$\Delta_1 = (1/2)\omega_{\text{eff}}^e(1 + \eta^2)^{1/2} - \{(\omega_{\text{eff}}^g + \omega_{\text{eff}}^e/2) + \eta^2(\omega_{\text{eff}}^e)^2/4\}^{1/2}. \quad (25)$$

When equality (24) fails, we have again the sextet form spectrum (see fig. 3c). A similar spectrum transformation takes place if $\omega = \omega_R^g$. The spectrum has a quadruplet form for this frequency (fig. 4). Thus, the spectra transformations shown in

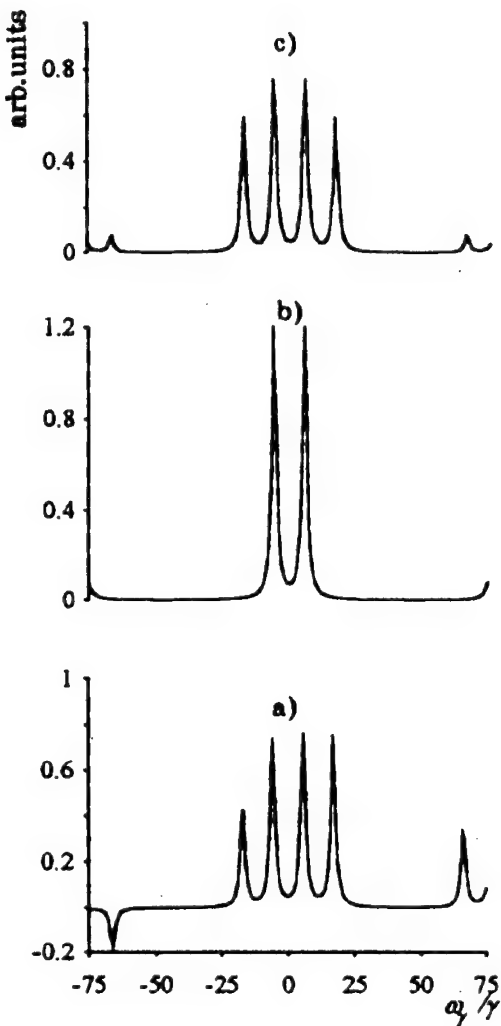


Fig. 4. Time-gated MS absorption ($\phi = 0^\circ$) of circular (a), linear (b) and unpolarized (c) gamma radiation at the Rabi "resonance" $\omega = \omega_R^g = -72\gamma$, $\eta = 3$, $\theta = 90^\circ$.

figs. 3 and 4 occur when the field frequency coincides with the Rabi frequency of the nuclear ground or excited states. In this sense we have the "resonant" effect again.

The magnetodynamic effects in the Mössbauer absorption spectra become apparent due to the collapse of the hyperfine structure and the appearance of satellites. The extent of the collapse process depends on the frequency and amplitude of the alternating field component on a nucleus. The complete collapse occurs at high frequencies where there is no constant field component. As regarding the satellites, their number and intensity is determined by the modulating field type as well as by the propagation direction and polarization of the gamma radiation. The simplest analysis is achieved for the rotating field model. It is natural to associate the main spectrum and satellite lines with the basic zone $E_{M'}$, $E_{m'}$ quasi-energies and the $\omega(M' - M)$ terms express photon dressing in the $\psi_{M'}(t)$. Speaking about the magnetodynamic origin satellites, we should point out how they relate with the possible magnetostriction origin satellites. The appearance mechanism for the latter ones is caused by the phonon mechanism [19]. In the presence of both satellite formation mechanisms, the Mössbauer cross-section resulting spectrum can be submitted as a superposition of the initial magnetodynamic spectrum (with all satellites included) together with its satellites appearing due to the phonon way.

A remarkable specificity of the temporal spectra is the emergence of negative areas (fig. 5). It is the temporal diffraction effect, an analogy to the familiar effect occurring at Doppler modulation of the source radiation [4]. It means that radiation propagating through an absorber will be amplified only in certain phases of the external modulation. This is the constructive interference effect of propagating and re-emitted quanta captured by a nucleus at an earlier time. At the same time, it is a consequence of the angular dependence of gamma transitions matrix elements.

6. Conclusions

Hyperfine interactions of Mössbauer nuclei, viewed from the gamma optical point of view, are tools used in order to single out the desired frequency and polarization radiation. Similarly, the spectral lines behaviour in alternating hyperfine fields is very interesting. Under these conditions, a coherent mixing of the hyperfine levels is assumed to control also the gamma transitions intensities [44].

We have studied the alternating hyperfine fields influence on the MS structure (including temporal ones), especially stressing the large-scale amplitudes case. The expressions for the Mössbauer absorption cross-section with an arbitrary time dependence of hyperfine fields were obtained by means of evolution superoperators for the gamma transitions. Using the periodicity properties of the nuclear fields, recurrence relations for the superoperators have been written. The method for MS calculation in the case of a periodical perturbation of arbitrary form has been proposed based on numerical integration over the perturbation period.

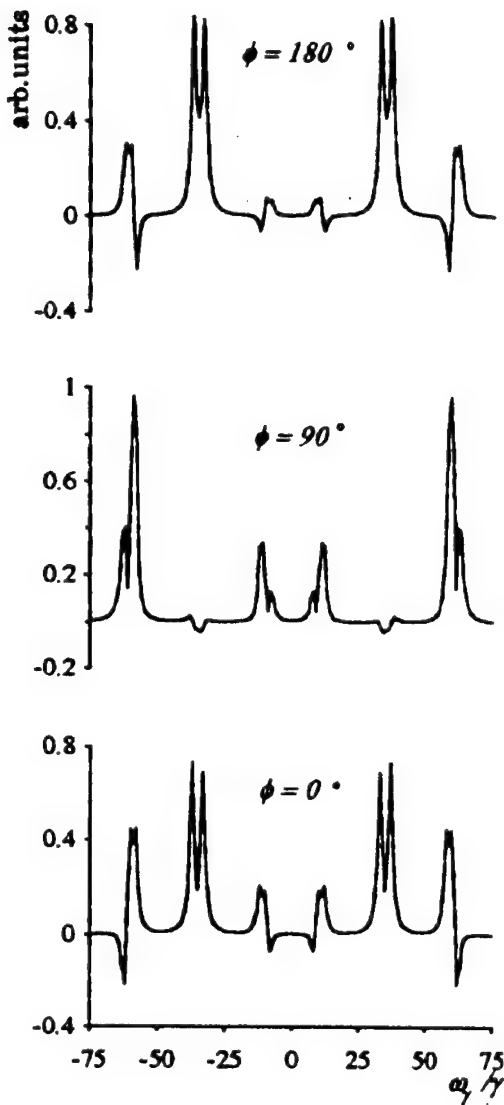


Fig. 5. Time-gated MS absorption of linearly polarized radiation $\eta \rightarrow \infty$, $\omega/\gamma = 2$, $\theta = 30^\circ$.

Special consideration is given to the rotation field model. It is obvious that the remarkable nonresonant transformation of the MS absorption shape is peculiar to the arbitrary large-amplitude periodic fields. At the same time, the rotating field case has been considered not only for the calculations but also due to its interest as a special experimental study subject. Realization of these fields in magnetic materials seems to be more probable than the achievement of nuclear oscillating fields. In this case, quasi-energy effects in MS display most sharply within a wide frequency range. It is for the rotating field that we have theoretically revealed a "resonance"

in the Rabi frequencies domain. A case of special interest is that of low-frequency fields, where spectra transformation is not complicated by the phenomenon of hyperfine structure collapse. Here, the MS hyperfine structure line splitting into certain polarization components takes place.

In the time-frequency spectra, one can observe regions of source negative absorption at certain external perturbation phase values. This is a consequence of the “temporal diffraction”, an analogy of such an effect under source radiation Doppler modulation [4].

An experimental confirmation of the discussed effects would be very useful. There are not too many options in materials with easily controlled magnetization. Above all, the samples should have small magnetic anisotropy fields. FeBO_3 , which has an easy plane, fits especially for these purposes. Precise experiments on the controllable magnetization variations have been performed using FeBO_3 [45]. The magnetization dynamics must be taken into account using the Landau–Gilbert equations for each concrete sample, as has been done in ref. [26].

Stochastic effects in the magnetization reversal are to be taken into consideration. One can analyze this case on the basis of eq. (19) [13]. The stochasticization mechanism of the hyperfine field on the magnetic material nuclei caused by anisotropic fields is also discussed in ref. [13]. We should like to draw attention over the modulation effects in Mössbauer spectra of superparamagnetic systems [43], where stochastic motion is inevitable. It has been shown [46], that a new type of amplification mechanism for alternating hyperfine field exists in this case.

The MS theory (including temporal spectra) we have presented assumes a steady regime of RF perturbation and it does not hold for transition processes.

Acknowledgement

We are grateful to G.V. Smirnov for stimulating discussions and to A.Ya. Dzyublik for the preprints of his work. Research work was partly supported by the ISF Grant no. NNT000.

References

- [1] S.L. Ruby and D.I. Bolef, Phys. Rev. Lett. 50 (1960) 5.
- [2] M.N. Hack and M. Hamermesh, Nuovo Cimento 19 (1961) 546.
- [3] G.J. Perlow, Phys. Rev. Lett. 40 (1978) 896.
- [4] J.E. Monahan and G.J. Perlow, Phys. Rev. A20 (1979) 1499.
- [5] A.V. Mitin, JETP 52 (1967) 1596.
- [6] H. Gabriel, Phys. Rev. 184 (1969) 359.
- [7] S. Autler and C. Towns, Phys. Rev. 100 (1965) 703.
- [8] J. Perlow, Phys. Rev. 172 (1968) 319.
- [9] L. Pfeiffer, N.D. Heiman and J.C. Walker, Phys. Rev. B6 (1972) 74.

- [10] L. Pfeiffer, J. Appl. Phys. 42 (1971) 1725.
- [11] M. Kopcewicz and A. Kotlicki, J. Phys. Chem. Solids 91 (1980) 631.
- [12] S.R. Julian and J.M. Daniels, Phys. Rev. B38 (1988) 4394.
- [13] E.K. Sadykov and A.I. Skvortsov, Phys. Stat. Solidi (b) 158 (1990) 685.
- [14] A.V. Mitin and G.P. Chugunova, Phys. Lett. A49 (1974) 111.
- [15] A.M. Afanasev, P.A. Alexandrov and S.S. Jakimov, Preprint of Inst. Atom. Energy, N3337/9 (1980) p. 25.
- [16] Sh.Sh. Bashkirov and E.K. Sadykov, Fiz. Tverd. Tela 17 (1975) 1864.
- [17] S. Olariu, M. Sorescu, I.I. Popescu and C.B. Collins, Europhys. Lett. 2 (1986) 725.
- [18] J.K. Srivastava, in: *Adv. Mössbauer Spectroscopy Appl. Phys. Chem. Biol.* (Amsterdam, 1983) p. 761.
- [19] M.A. Andreeva and R.N. Kuz'min, *Mössbauer gamma optics* (Moscow University, 1982) p. 226.
- [20] Yu.V. Baldochin, S.A. Borsch, L.M. Klinger and V.A. Povitsky, JETF 63 (1972) 708.
- [21] Sh.Sh. Bashkirov, A.L. Beljanin and E.K. Sadykov, Phys. Stat. Solidi (b) 93 (1979) 437.
- [22] Sh.Sh. Bashkirov and E.K. Sadykov, Izv. Vyssh. Uchebn. Zaved. Fiz. 9 (1981) 111.
- [23] A.Ja. Dzyublik, Phys. Stat. Solidi (b) 104 (1981) 81.
- [24] E.K. Sadykov, Phys. Stat. Solidi (b) 123 (1984) 703.
- [25] B.K. Voitovetsk and S.B. Sazonov, Preprint of Inst. Atom. Energy, N3952/2 (1984) p. 52.
- [26] S. Olariu, Phys. Rev. B37 (1988) 7698.
- [27] G.V. Smirnov, Yu.V. Shvydko, O.S. Kolotov, V.A. Pogozhev, M. Kotrbova, S. Kadechkova and I. Novak, JETF 86 (1984) 1495.
- [28] T.W. Sinor, P.W. Reitinger and C.B. Collins, Phys. Rev. Lett. 62 (1989) 2547.
- [29] F.G. Vagizov, Hyp. Int. 61 (1990) 1359.
- [30] I. Tittonen, M. Lippmaa, E. Ikonen, J. Linden and T. Katila, Phys. Rev. Lett. 69 (1992) 2815.
- [31] A.V. Mitin, Phys. Lett. A84 (1981) 278.
- [32] E.K. Sadykov and A.I. Skvortsov, Fiz. Tverd. Tela 29 (1987) 3162.
- [33] E. Ikonen, P. Helisto, J. Hietaniemi and T. Katila, Phys. Rev. Lett. 60 (1988) 643.
- [34] E. Ikonen, J. Hietaniemi and T. Katila, Phys. Rev. B38 (1988) 6380.
- [35] E.K. Sadykov and A.I. Skvortsov, Phys. Stat. Solidi (b) 156 (1989) 605.
- [36] M. Salkova and S. Stenholm, Phys. Rev. A41 (1990) 3838.
- [37] S. Olariu, C.B. Collins and T.W. Sinor, Phys. Rev. B50 (1994) 43, 616.
- [38] A.Ja. Dzyublik, Phys. Stat. Solidi (b) 194 (1996) 699.
- [39] E.K. Sadykov, Doctoral dissertation (Kazan, 1993);
I. Tittonen, J. Javanainen, M. Lippman and T. Katila, Hyp. Int. 78 (1993) 397.
- [40] F. Hartmann-Boutron and D. Spanjard, J. de Physique 33 (1972) 285.
- [41] M. Blume and O.C. Kistner, Phys. Rev. 171 (1968) 417.
- [42] M.S. Sjavavko, Dokl. Akad. Nauk. SSSR 292 (1986) 1065.
- [43] E.K. Sadykov and A.I. Skvortsov, Fiz. Tverd. Tela 33 (1991) 2725.
- [44] R. Coussement, M. Van den Bergh, G. S'heeren, G. Neyens, R. Nouwen and R. Bolchand, Phys. Rev. Lett. 71 (1993) 1824.
- [45] G.V. Smirnov, Hyp. Int. 27 (1986) 203.
- [46] E.K. Sadykov and A.G. Isavnn, Fiz. Tverd. Tela 36 (1994) 3473.

The problem of gamma-laser and controlling of Mössbauer nuclei decay (theory and practice)

V.I. Vysotskii^a, V.P. Bugrov^b, A.A. Kornilova^b, R.N. Kuz'min^b and S.I. Reiman^b

^aKiev Shevchenko University, Radiophysical Dept., 252017, Kiev, Ukraine

^bMoscow State University, 119899, Moscow, Russia

This paper discusses the control process of the radioactive Mössbauer nuclei spontaneous decay probability. The possibility of using this effect in order to produce an optimized gamma-laser is considered. For the first time, the experiment has shown radioactive lifetime doubling for ^{57}Fe nuclei and a general lifetime increase (including conversion and non-Mössbauer decay channels) by 2%.

The famous dilemma of gamma-laser (that is, it requires nuclei exhibiting short-lived transitions with $\tau < 10^{-6}$ s, $\Gamma\tau = 1$, maximal amplification coefficient $G = \lambda^2\Delta nf/2\pi(1 + \alpha)$ and very intensive pumping, or long-lived nuclei with $\tau > 1$ s, $\Gamma\tau \gg 1$, small amplification coefficient $G = \lambda^2\Delta nf/2\pi(1 + \alpha)\Gamma\tau$ and slight pumping) can be successfully solved in case of controlled nuclear decay, when τ equals τ_{\max} during pumping and τ_{\min} during gamma-generation.

In ref. [1] we have considered the possibility to control the A_{ij} decay probability for excited Mössbauer nuclei by means of electromagnetic vacuum controlled mode restriction. The main idea of spontaneous decay velocity control consists in the strong influence of averaged modes density in a unit frequency interval

$$\langle \rho(\nu_{ij}) \rangle = \int \int \rho(\nu_n) f(\nu_n, \nu_{ij}, \Omega) d\nu_n d\Omega, \quad \rho(\nu_n) = 8\pi\nu_n^2/c^3,$$

upon the final possible decay

$$A_{ij} = 8\pi^3 \nu_{ij} |d_{ij}|^2 \langle \rho(\nu_{ij}) \rangle / 3h = 1/\tau,$$

where $f(\nu_n, \nu_{ij}, \Omega)$ is the spectral-angular mode density which has a ν_n central frequency and spreads in the Ω spatial angle direction. Generally,

$$f(\nu_n, \nu_{ij}, \Omega) = \gamma_n / 8\pi^2 [(\nu_n - \nu_{ij})^2 + \gamma_n^2/4], \quad \gamma_n = \gamma_n(\nu_n, \Omega)$$

The spectral width of the γ_n mode is defined by the lifetime of the photon $\Delta t = Q_n/\nu_n$ in this mode. Q_n is the quality factor of mode ν_n .

In the case of free space (fig. 1a): $\gamma_n = \nu_n/Q \rightarrow 0$, $f(\nu_n, \nu_{ij}, \Omega) \rightarrow \delta(\nu_n - \nu_{ij})$ (δ is the Dirac function) and $\langle \rho(\nu_{ij}) \rangle = \rho(\nu_{ij})$, $\tau = A_{ij}^{-1} = 3hc^3/32\pi^3\nu_{ij}^3|d_{ij}|^2$.

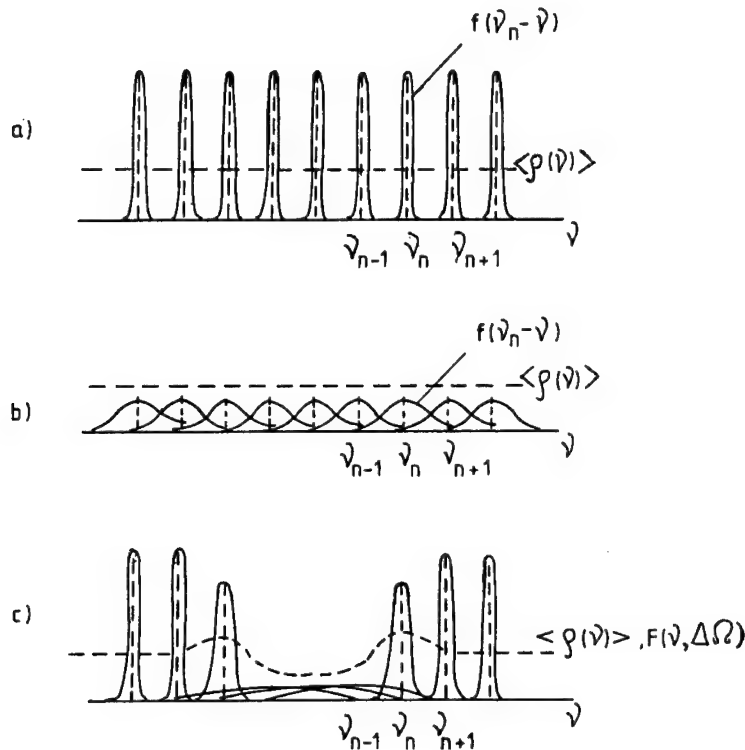


Fig. 1. Frequency structure of electromagnetic field modes in the case of: (a) free space; (b) non-resonant absorber; (c) frequency-selective absorber.

In case of frequency non-selective absorption, within the $V \gg \lambda^3$ volume, $\gamma_n = \text{const} \neq \gamma_n(\nu_n)$ and (see fig. 1b) we obtain the same result

$$\langle \rho(\nu_{ij}) \rangle = \rho(\nu_{ij}), \quad \tau = A_{ij}^{-1} = 3hc^3/32\pi^3\nu_{ij}^3|d_{ij}|^2.$$

Another situation appears in the presence of a frequency-selective absorber acting as a “black” screen (for instance a sphere of radius R) in a $\Delta\nu \leq \Gamma = 1/\tau$ narrow frequency band, near ν_0 (near resonant frequency of Mössbauer transition in source – fig. 1c). In this case, the lifetime of the resonant photons is defined by their run $\Delta t \approx 2R/c$ between the frequency-selective absorber walls and $\gamma_n \approx c/2R$. On the other hand, the nonresonant photons pass through the absorber freely and for them $\gamma_n \approx 1/\Delta t \approx 0$. The $Q_n = \nu_n/\gamma_n \approx 2\pi\nu_0 R/c$ quality factor decrease for modes laying within a small $\Delta\nu = c/2R$ interval of ν frequencies, causes an essential variation of the mean modes density

$$\langle \rho(\nu_{ij}) \rangle = \rho(\nu_{ij})F(\nu_{ij}, \Delta\Omega), \quad F(\nu_{ij}, \Delta\Omega) = \int \int f(\nu_n, \nu_{ij}, \Omega) d\nu_n d\Omega,$$

$$\tau^* = 3hc^3/32\pi^3\nu_{ij}|d_{ij}|^2F(\nu_{ij}, \Delta\Omega).$$

As a result, it leads to a decrease (at $\nu = \nu_0$) and an increase (at $\nu \approx \nu_0 + \Gamma/2$) of the spontaneous decay probability intensity.

The equation for the $n_2 \equiv n_e$ excited nuclei population is expressed as

$$\frac{dn_2}{dt} = \sum_{i>2} n_i/\tau_{i2} - n_2 \Delta\Omega f / 4\pi\tau^* - n_2(1-f)/\tau - n_2 f(1 - \Delta\Omega/4\pi)/\tau - n_2 \alpha/\tau,$$

where α is the electron conversion coefficient, f is the recoil-free radiation parameter and $\Delta\Omega$ is the spatial angle blocked by the absorber.

In the equilibrium state, the relation between the n_2^* excited nuclei population for $\Delta\Omega \neq 0$ (with selective absorption) and the n_2 excited nuclei population for $\Delta\Omega = 0$ (without selective absorption) shows as:

$$n_2^*/n_2 = 1/\{1 - f\Delta\Omega(1 - \tau_2/\tau_2^*)/4\pi(1 + \alpha)\}.$$

The total J_γ^* intensity of Mössbauer radiation in the non-blocked direction ($4\pi - \Omega$) also modifies and $J_\gamma^* = J_\gamma(n_2^*/n_2)$.

Let us describe this variation as $J_\gamma^* = J_\gamma/(1 - g)$, $g = f\Delta\Omega(1 - \tau_2/\tau_2^*)/4\pi(1 + \alpha)$. In this case:

$$\tau_2^* = \tau_2/\{1 - 4\pi g(1 + \alpha)/\Delta\Omega f\}.$$

The experiment of nuclei decay control was performed based on our theory. The experimental layout is presented in fig. 2. A ^{57}Co isotope (1), with a 10 mCi activity lying in a chromium matrix, was used as a Mössbauer radiation source. This source has a natural width single line spectrum. The source is fixed in the Plexiglas disc located in the center ($l = 2.5$ cm) or near the edge ($l = 1$ cm) of the resonant absorber 2 having a cylindrical shape with diameter $D = 2$ cm and length $L = 5$ cm. It is made of ^{57}Fe isotope (200 mg) in stainless steel (100 mg). The 7 mg/cm² absorber thickness obeys the requirement of resonant radiation total absorption (for $|\nu - \nu_0| < \Gamma/2$) and almost full transparency for non-resonant radiation (for $|\nu - \nu_0| > \Gamma$).

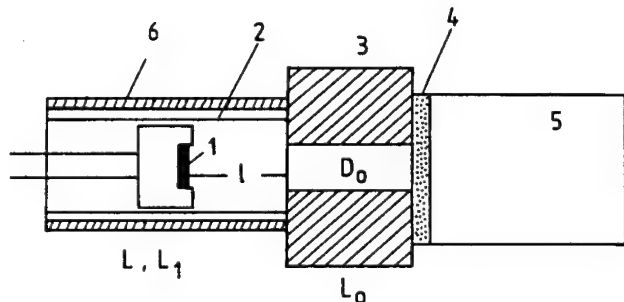


Fig. 2. Experimental layout for detecting the effect of controlling the radiational nuclear decay time.

The lead diaphragm (3) has a $D_0 = 1$ cm diameter and $L_0 = 2.5$ cm length hole. Behind the diaphragm are located the NaJ(Tl) crystal amplitude detector (4) (with a 10^{-2} cm width) and the photo-electronic multiplier (5).

The signal-processing system picked out the part of the amplitude spectrum which is close to the $E_\gamma = 14.4$ keV gamma line. The measurements with a direct gamma-beam were performed in two regimes. In the first case, the quanta wave counted $N^* = J_\gamma^* \Delta t$ in the presence of only the resonant absorber. In the second case, another lead cylinder (6) of $D_1 = 2.2$ cm diameter, $L_1 = 4$ cm length and $S_1 = 0.2$ cm thickness was placed around the resonant absorber cylinder. It totally absorbs both resonant and non-resonant radiation in the range of energies close to $E_\gamma = 14.4$ keV. This corresponds to a completely non-selective absorber and leads to the J_γ intensity of the recorded gamma-quanta flux and $N = J_\gamma \Delta t$.

Such a method excludes uncontrolled influence of resonant gamma-quanta reverse scattering after modifying resonant absorption into non-resonant (which would occur when resonant absorber cylinder is simply taken off the source).

Each measurement lasted a time $\Delta t = 100$ s. The results of the measurement are presented in fig. 3. It can be seen that the presence of additional non-selective absorber in side direction reduced the intensity of radiation coming from the source

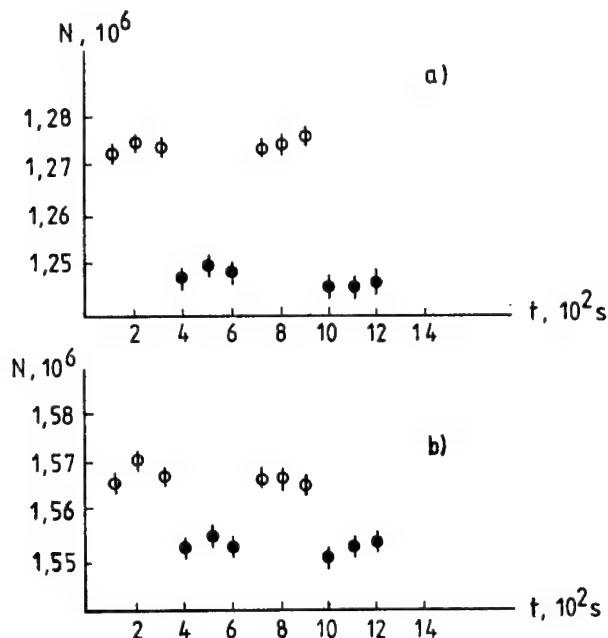


Fig. 3. The influence of the spatial position of the non-resonant totally absorbing screen (6 in fig. 2) upon the intensity of the gamma-quanta direct beam: filled circles – screen is placed around the resonant absorber; empty circles – screen is taken off. Case (a) corresponds to the source (1 in fig. 2) situated in the resonant absorber center ($l = 2.5$ cm), and case (b) to the source located at $l = 1$ cm.

in the detector direction. It fully agrees with the theory described in ref. [1] and above.

The count rate variation is defined by $g = 0.022 \pm 0.002$ for $l = 2.5$ cm, and $g = 0.008 \pm 0.002$ for $l = 1$ cm, with corresponding modifications (increases) of ^{57}Fe ($E_\gamma = 14.4$ keV) nuclear decay radiation time for Mössbauer component $\tau^* = 2\tau$ for $l = 2.5$ cm and $\tau^* = 1.4\tau$ for $l = 1$ cm.

In fact, considering the scattering of non-resonant gamma-quanta (in the $E_\gamma = 14.4$ keV region) from lead absorber, which increases J_γ , the τ^* lifetime increase will be even greater.

The total ^{57}Fe lifetime (defined by partial probabilities of Mössbauer radiation in $\Delta\Omega f/4\pi\tau^*$ blocked angle, Mössbauer radiation in $(1 - \Delta\Omega/4\pi)f\tau$ non-blocked angle, non-Mössbauer radiation $(1 - f)/\tau$ and electron conversion α/τ) equals

$$\tau_{\text{tot}}^* = \tau_{\text{tot}}/(1 - g),$$

where $\tau_{\text{tot}} = \tau/(1 + \alpha)$ is the standard ^{57}Fe total lifetime.

When the experiment is performed in vacuum (which increases the Q quality factor of non-resonant modes compared to the experiments described in this paper, which were performed in air) only with resonant absorber, $\Delta\Omega = 4\pi$ and gamma transitions with $f \approx 1$ and $\alpha \approx 0$ are employed, it is possible to increase $\tau_{\text{tot}}^* \gg \tau_{\text{tot}}$ (in the gamma-generation regime). This allows to solve many gamma-laser realization problems [2].

References

- [1] V.I. Vysotskii, V.I. Vorontsov and R.N. Kuz'min, Pis'ma Zh. Teor. Fiz. (Sov. Phys. JTP Lett.) 10 (1984) 300
- [2] V.I. Vysotskii and R.N. Kuz'min, *Gamma-lasers* (monograph) (Moscow State University Publishing House, Moscow, 1989).

Inhomogeneous and homogeneous broadening effects on nuclear resonance experiments

B. Balko, I.W. Kay, J. Nicoll, J.D. Silk

Institute for Defense Analyses, Alexandria, VA 22311-1772, USA

and

G. Herling

*University of New Mexico, Center for Advanced Studies, Albuquerque,
NM 87131-1156, USA*

Inhomogeneous broadening of resonance lines causes a reduction of absorption in nuclear resonance experiments. This is particularly devastating to the observation of the Mössbauer effect in isomers like ^{107}Ag with a half-life of 44 s. It has been suggested in the literature that homogeneous broadening can provide overlap of resonance lines and thus the Mössbauer effect can be recovered. The analysis presented in this paper shows that this is not the case for Mössbauer experiments, unless the radiative width Γ_γ also increases. Although overlap occurs when the lines are homogeneously broadened to a total width Γ_H which exceeds the natural width Γ , and the inhomogeneous width Δ , the Mössbauer absorption remains low because it is proportional to the factor of Γ_γ/Γ_H .

1. Introduction

The recent work in gamma-ray lasers has concentrated on two approaches for obtaining nuclear inversion [1]. In one approach the nucleus is prepared in an isomeric level and then pumped up to a nearby short-lived upper lasing level by an optical laser. The difference in energy between the “upconversion” photon and the γ photon emitted in the lasing processes could be four to five orders of magnitude as shown in fig. 1a. The major issues in this concept are (1) identification of the nucleus with a short-lived level near an isomeric level [2], and (2) the power requirements on the pumping laser [3]. No real nucleus that could satisfy these requirements has been located yet. Recent calculations show that even under the most ideal conditions (using good Mössbauer nuclei) pumping requirements are prohibitive because of competing internal conversion [4]. The second approach involves fast preparation of a nucleus in an isomeric level which then also serves as the upper lasing level as shown in fig. 1b. The main concern in this concept is the inhomogeneous broadening that would prevent nuclei in the inverted population from being on resonance. The size of the inhomogeneous broadening and the effectiveness of ways

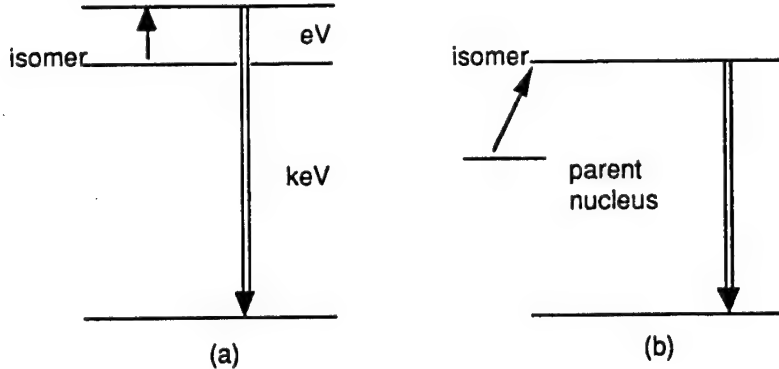


Fig. 1. Schematics showing two possible gamma-ray laser pumping schemes. In (a) a long-wavelength photon pumps a nucleus from an isomeric to a short-lived nearby level which acts as the upper lasing level. In (b) a thermal neutron reaction converts a parent nucleus into the lasing nucleus in the isomeric level, which acts as the upper lasing level.

to reduce it are issues to be resolved. We have shown [4] that for one real nucleus pumping with a flux of 10^{18} neutrons/(cm 2 s) may produce superfluorescent emission even with a modest amount of inhomogeneous broadening present (less than 20 times natural linewidth).

The second approach was actually introduced by Vali and Vali [5] in 1959 and abandoned in favor of the first, because inhomogeneous broadening, thought to be on the order of 10^5 times the natural linewidth or higher, was considered too difficult to overcome. However, later experiments by two groups [6,7] measured significantly smaller broadening, and an explanation for the smaller broadening based on dynamic or relaxation effects was proposed [8,9].

We agree with refs. [8,9] that dynamic effects could wipe out inhomogeneous broadening, but only in the limit of "motional narrowing" #¹ when the relaxation time is much greater than the inverse of the inhomogeneous broadening #². The authors in refs. [8,9], however, claim that inhomogeneous broadening could be overcome in the intermediate region of relaxation when the homogeneous line broadening due to relaxation is as large as the inhomogeneous broadening, i.e. the individual lines are homogeneously broadened until there is complete overlap between all the lines. We disagree with this in general #³ and show in the present paper that the overlap of lines that are homogeneously broadened by relaxation doesn't lead to a strong resonance effect (absorption or scattering). Only if the line broadening is due to an increase in the radiation rate rather than to relaxation do

#¹ Term used to describe line-shape modification due to dynamics of spins. See, e.g., ref. [10].

#² Balko and Kay [11] show the interplay between inhomogeneous broadening, relaxation, and their combined effect on superfluorescence phenomena.

#³ A discussion of the specific problems leading to the erroneous conclusions of ref. [9] is presented in ref. [12].

we get a strong effect. Such a condition is not relevant to Mössbauer experiments wherein the radiation rate is unaffected and the emission is between levels orders of magnitude (on the order of 10^{12}) higher than the difference in energy between the relaxation levels.

2. Inhomogeneous broadening and the resonance effect

Nuclei imbedded in a solid host interact with the neighboring atoms, which produces inhomogeneous broadening. The effect of impurities, crystal dislocations, and crystal boundaries is to introduce slightly different fields at nuclei located in different positions in the lattice and thereby shift the nuclear resonant energies.

Even if the crystal were perfect and we considered only those nuclei well within the regular structure, so that boundary effects were negligible, there would still be a slightly different resonance energy at different lattice sites. The nuclear spin–spin or magnetic dipole–dipole interaction between the emitting or absorbing nuclei and their nearest neighbors would be different due to random orientations of the magnetic moments of nearest neighbors. This is an inherently nuclear effect, and if it were possible to eliminate all of the solid state and geometrical factors this interaction would still remain.

The spin–spin interaction energy is given by [13]

$$E_{\text{d-d}} = \frac{2\mu_1 \cdot \mu_2}{r^3}, \quad (1)$$

where μ_1, μ_2 , are the magnetic moments of the respective nuclei and r is the distance separating their centers. For ^{107}Ag , this energy has been estimated to be about 10^{-12} eV (ref. [13]). Such a weak interaction is not important in experiments with good Mössbauer nuclei, such as ^{57}Fe , which has a natural linewidth of 10^{-9} eV. This interaction, could essentially destroy resonance between long-lived or isomeric nuclei such as ^{107}Ag or ^{109}Ag because the effective lineshape for the absorber and source would then be smeared out over an energy band much larger than the natural linewidth, which is on the order of 10^{-17} eV.

Inhomogeneous broadening of resonance levels is depicted in fig. 2, where the resonance condition for a good Mössbauer isotope ^{57}Fe is compared to the resonance condition for a poor Mössbauer isotope, ^{107}Ag ^{#4}. In fig. 2a, the resonances of the emitting and absorbing nuclei are separated by an energy, $\Delta\varepsilon$, which arises because of the slight difference in the local environment of the two nuclei. The natural linewidth, Γ_n of ^{57}Fe , is large enough that the overlap region provides a good resonance effect. On the other hand, as shown in fig. 2b, for the long-lived isotope with the very narrow natural line the environmental difference between the nuclear

^{#4} For the moment, the difference in the recoilless fraction, f , between the two isotopes is ignored.

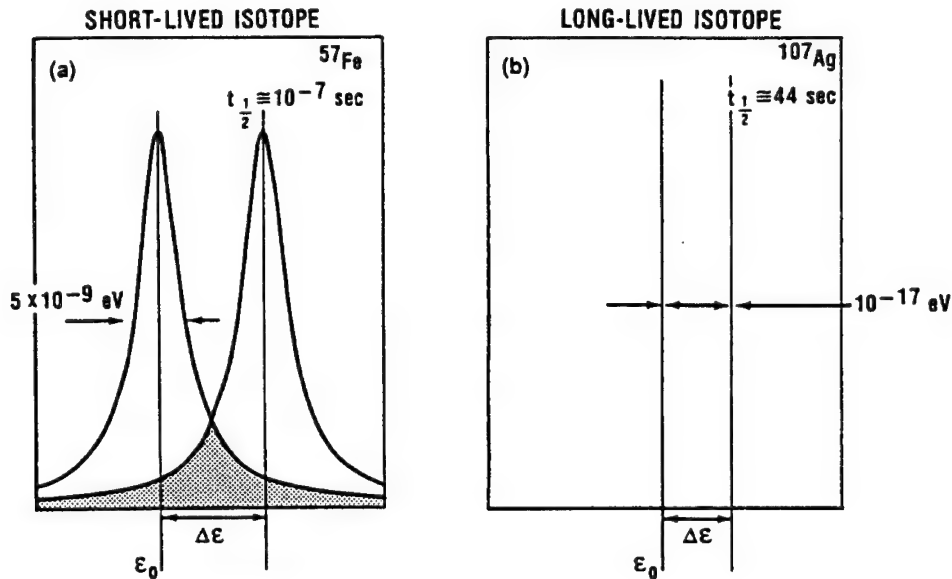


Fig. 2. Resonance conditions for short- and long-lived isotopes. For comparison we show in (a) ^{57}Fe , a good Mössbauer isotope but difficult to invert because of the short lifetime, and in (b) ^{107}Ag , relatively easier to invert because of the long lifetime but not a good Mössbauer isotope because of the narrow lines which result in a reduction of resonance overlap.

sites, which induces the energy shift $\Delta\epsilon$, destroys the resonance condition between emitter and absorber.

Fig. 3a shows the composition of the inhomogeneously broadened line of width $\Gamma_{\text{eff}} = (1 + a)\Gamma$ as consisting of the individual resonances displaced from the non-perturbed resonance energy E_0 . Fig. 3b picks out two of those resonances and shows the effect of homogeneous broadening of the lines in producing overlap as indicated by the shaded regions in fig. 3b. Although overlap is increased by homogeneous broadening, the resonance absorption is actually decreased as the lines are homogeneously broadened. In the appendix this is shown explicitly for two lines.

In a recent publication we derived an expression for the inhomogeneously broadened lineshape expected in a Mössbauer absorption experiment [14]. Assuming that the nuclei interacted incoherently, the expression for absorption was given as a product of the incoming beam intensity and the single nucleus absorption cross section. We summarize the results here and then derive an expression assuming coherent processes for scattering of emissions from a multi-nuclear source by a multi-nuclear absorber. The calculation presented here was done to check the claims often made [8,9,15] that homogeneous broadening in both source and absorber lines could produce an enhanced Mössbauer effect.

The experimental condition assumed for both calculations is shown in fig. 4a,

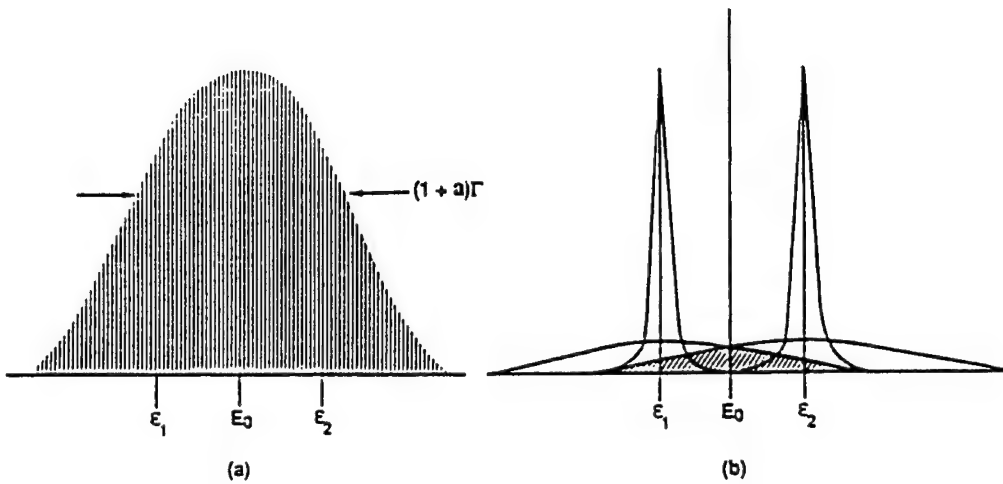


Fig. 3. An inhomogeneously broadened Mössbauer line shown in (a) as composed of many narrow individual lines displaced from the central resonance energy E_0 . In (b) two individual lines at energies ε_1 and ε_2 are shown homogeneously broadened by the same amount, for two different linewidths.

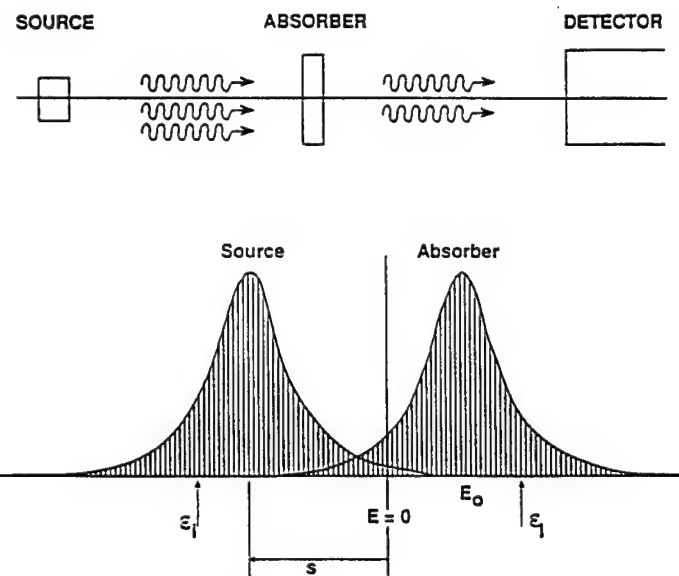


Fig. 4. (a) A schematic showing the Mössbauer transmission experimental geometry. (b) A graphic representation of the source and absorber lineshapes. The vertical lines represent some of the natural lines of the different nuclei in the source and absorber whose envelopes are the inhomogeneously broadened lines. S represents the Doppler shift of the source and ε_i and ε_j the resonance energies of nuclei i and j in the source and absorber, respectively.

and the lineshapes for both the inhomogeneously broadened source and absorber are depicted in fig. 4b.

3. Incoherent approach

The detected loss in the total photon count, I_D , because of the presence of the absorber is given by

$$I_D = \int_{t_1}^{t_2} dt \int_{-\infty}^{+\infty} I(E, \Gamma, S) n \sigma(E, \Gamma) dE. \quad (2)$$

where n is the number of resonant nuclei in the beam per cm², and the measurement is performed during the time interval $t_2 - t_1$. $I(E, \Gamma, S)$ is the source radiation line-shape and $\sigma(E, \Gamma)$ is the resonant cross section of the nuclei in the absorber.

The source lineshape is given by

$$I(E, \Gamma, S) = \sum_i^N P_i(\varepsilon_i) \frac{I_0(\Gamma/2\pi)f_s}{[E - (E_0 - \varepsilon_i) - S]^2 + (\Gamma/2)^2}, \quad (3)$$

where I_0 is the flux of photons from the source in cm⁻²s⁻¹ in the direction of the detector, E_0 is the resonant energy of an unperturbed nucleus, ε_i is the perturbation of the energy of nucleus i due to the environment, S is the Doppler shift due to the relative motion of the source and absorber nuclei and is given by $S = v/cE$, with velocity v where c is the speed of light, Γ is the natural linewidth^{#5} and f_s is the recoil-free fraction in the source. It is assumed in eq. (2) that the integration time is short enough that I_0 can be taken as constant.

The distribution of nuclear environments is assumed to be normal with width Δ so that the probability of finding a nucleus with energy ε_i displaced from the resonance energy E_0 in a width $\Delta\varepsilon_i$ is given by

$$P_i(\varepsilon_i) = \frac{1}{\sqrt{\pi}\Delta} e^{-\varepsilon_i^2/\Delta^2} \Delta\varepsilon_i. \quad (4)$$

Similarly, for the effective cross section of the absorber we have

$$\sigma(E, \Gamma) = \sum_i^N P_i(\varepsilon_i) \frac{\sigma_0 \Gamma_\gamma \Gamma f_a}{[E - (E_0 - \varepsilon_i)]^2 + (\Gamma/2)^2}, \quad (5)$$

where σ_0 is the cross section on resonance and is given by

$$\sigma_0 = \frac{\lambda^2}{2\pi} \frac{2I_e + 1}{2I_g + 1} \frac{1}{1 + \alpha}.$$

^{#5} Γ is the total level width, which is a sum of the level widths of all the processes contributing to the level decay.

I_e and I_g are the nuclear spin quantum numbers of the excited and ground states, respectively, α is the internal conversion coefficient of the transition, λ is the nominal wavelength of the gamma-ray, Γ_γ is the photon absorption partial width.

Assuming the source lineshape, absorber cross section, and distribution of nuclear environments as given by eqs. (3)–(5), respectively, the intensity of the beam, I' , absorbed by a thin absorber^{#6} ($E_0 = 0$ without loss of generality) is given by

$$I'(\Gamma, \Delta, S) = \frac{I_0 \sigma_0}{4\pi \Delta_1 \Delta_2} n_a \sum_i^{N_s} \sum_j^{N_a} e^{-\varepsilon_i^2/\Delta_1^2} e^{-\varepsilon_j^2/\Delta_2^2} \Delta \varepsilon_i \Delta \varepsilon_j \\ \times \int_{-\infty}^{+\infty} dE \frac{(\Gamma/2\pi)}{(E - \varepsilon_i - S)^2 + (\Gamma/2)^2} \frac{\Gamma_\gamma \Gamma}{(E - \varepsilon_j)^2 + (\Gamma/2)^2}, \quad (6)$$

where N_s , N_a are the total number of sites with energy shifts ε_i and ε_j in the source and absorber, respectively, and where n_a is the number of nuclei per cm^2 in the absorber. Converting the sum to an integral one has

$$I'(\Gamma, \Delta, S) = \frac{\sqrt{2\pi}}{4} I_0 \sigma_0 (\Gamma_\gamma / \Delta) n_a \operatorname{Re}(e^{Z^2}) \operatorname{erfc}(Z), \quad (7)$$

where

$$\Delta^2 \equiv (\Delta_1^2 + \Delta_2^2)/2, \quad \text{and} \quad Z \equiv (\Gamma + iS)/\sqrt{2}\Delta.$$

The maximum normalized resonant absorption ($S = 0$) is given by

$$I''(\Gamma, \Delta) = I'(\Gamma, \Delta, S = 0) / (\frac{1}{2} I_0 n_a \sigma_0) \\ = \frac{\sqrt{\pi}}{2} \left(\frac{\Gamma_\gamma}{\Gamma} \right) [x e^{x^2} \operatorname{erfc}(x)], \quad (8)$$

where

$$x = \frac{\Gamma}{\sqrt{2}\Delta}.$$

Fig. 5 shows the normalized plot of eq. (8). Note that there is a dependence on $x = \Gamma/\sqrt{2}\Delta$ through the exponential and error function terms and a dependence on Γ alone through the factor Γ_γ/Γ . When the inhomogeneous broadening is

^{#6} A thin Mössbauer absorber is one for which the lineshape of the beam passing through the absorber is not sufficiently modified to show saturation effects. This is discussed in ref. [16], where it is shown that for the Mössbauer thickness $\beta < 10$ the ratios of the intensities of the lines in the spectrum are close to their theoretical values and saturation effects are small. Under such conditions, it is appropriate to use eq. (2) for the absorption calculations. Mössbauer thickness is defined as $\beta = n\sigma_0 f T$ where n is the number of nuclei per cm^3 in the beam, σ_0 is the maximum resonant cross section, f is the recoilless fraction and T is the thickness of the sample.

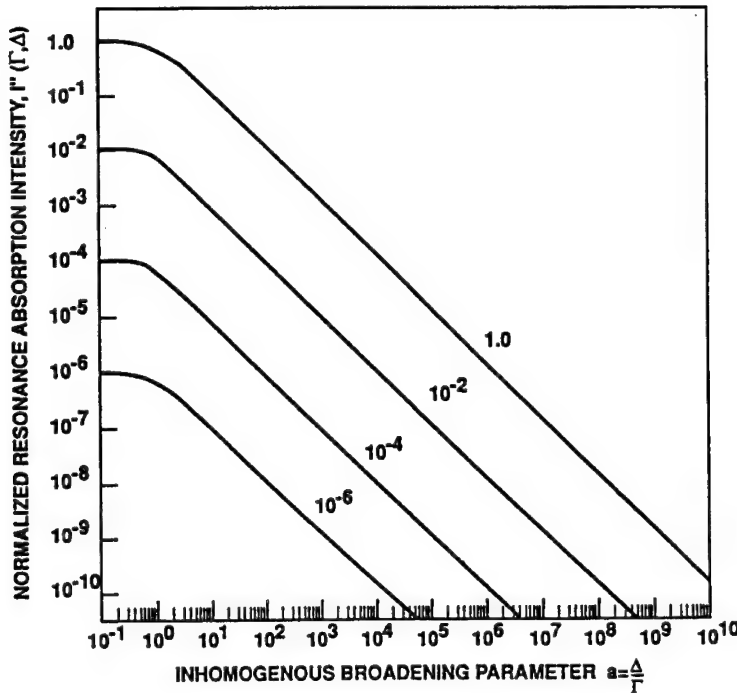


Fig. 5. Plots of the maximum normalized resonance absorption curves, $I''(\Gamma, \Delta)$, calculated from eq. (8) and plotted as a function of Δ/Γ . The numbers labeling the curves give the different values of Γ_γ/Γ .

reduced by some means $\Delta \rightarrow 0$, $x \rightarrow \infty$ and I'' approaches a maximum $\frac{1}{2}I_0\sigma_0n_a$ (Γ_γ/Γ). When the lines are homogeneously broadened to obtain overlap $\Gamma \rightarrow \Gamma_H \rightarrow \Delta$, or in the limit $\Gamma \rightarrow \infty$, $x \rightarrow \infty$ and the second term becomes maximum, but then $(\Gamma_\gamma/\Gamma) \rightarrow 0$. Thus, although total overlap is achieved the resonant effect disappears because the maximum radiative cross section on resonance is reduced to keep the total integrated cross section constant.

This does not happen when $\Gamma_H = \Gamma = \Gamma_\gamma$, a highly unlikely condition in nuclear systems. Generally, the total width Γ is a sum of several parts including the radiative width Γ_γ the internal conversion Γ_a and other transitions Γ_i so that

$$\Gamma = \Gamma_\gamma + \Gamma_a + \sum_i \Gamma_i. \quad (9)$$

Under these more realistic conditions homogeneous broadening alone will not increase the resonant effect even though complete overlap of lines is achieved, unless we go to the "motonally" narrowed limit and all the inhomogeneous effects are wiped out.

4. Coherent approach

To treat the problem coherently, since we do not know which nucleus emitted and which is going to be excited, we must sum over the amplitudes for all nuclear processes. The amplitudes must be calculated for a scattering process since we also must include the de-excitations coherently.

Consider the emission of a photon of energy E by the i th nucleus in the source which has a resonance energy $E_0 + \varepsilon_i$ where ε_i is the energy shift due to the environment at the i th site. This shift is responsible for the inhomogeneous broadening of the source system linewidth. The photon, γ' , scattered by the j th nucleus in the absorber has energy E' . The j th nucleus has resonance energy $E_0 + \varepsilon_j$. The process is depicted in fig. 6.

Heitler [17] has shown how to calculate the differential scattering cross section for a single resonator (nucleus or atom) using second-order perturbation theory. Boyle and Hall [18] (see also ref. [15]) have generalized these results to a system of many nuclei.

Our discussion follows these two developments. Following Heitler and Boyle and Hall, the amplitude of absorption by nucleus j of a photon of energy E emitted by nucleus i and emission of a photon of energy E' is given by

$$A_{ij} = S_0 P_i \frac{1}{[(E' - E) - i\gamma/2]} \frac{1}{[(E' - \varepsilon_j - E_0) - i\Gamma/2]}, \quad (10)$$

where P_i is the probability nucleus i emits at energy E .

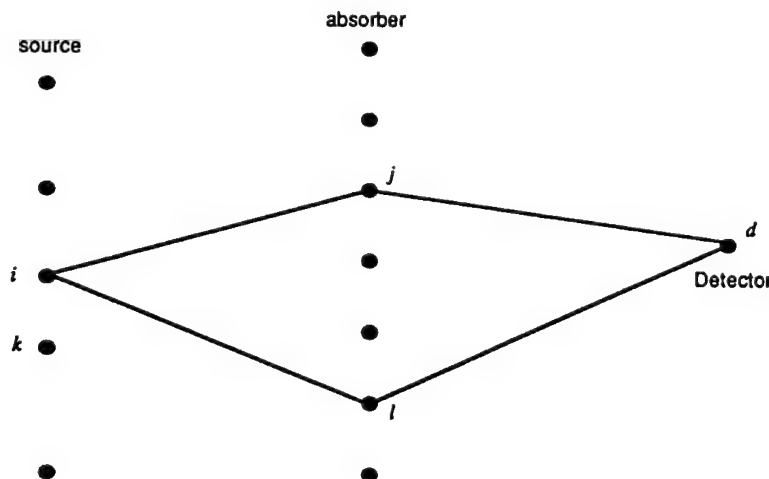


Fig. 6. A graphic representation of the scattering process. Nuclei in the source emit photons that are scattered by the absorber and eventually detected. As an example, processes $i \rightarrow j$ and $i \rightarrow l \rightarrow d$ are possible to contribute but not $k \rightarrow l \rightarrow d$.

From Boyle and Hall's result we find that

$$S_0^2 = \frac{\gamma}{2\pi} \left(\frac{\Gamma^2}{4} \right) \sigma_0 f_s \left(\frac{\Gamma_\gamma}{\Gamma} \right) F(\theta), \quad (11)$$

where γ is the width of the ground state due to the presence of radiation, Γ is the natural width of the transition and the angular term can be written in terms of Clebsch–Gordan coefficients and vector spherical harmonics [19,20].

For a system of N source nuclei and M absorber nuclei we get for the total scattered intensity

$$I_{\text{total}} = \sum_i^N \left| \sum_j^M A_{ij} \right|^2, \quad (12)$$

of which the incoherent part is given by

$$I_{\text{incoh}} = \sum_{i,j}^{N,M} |A_{ij}|^2, \quad (13)$$

and the interference term by

$$I_{\text{int}} = \sum_i^N \sum_{\substack{j,k \\ j \neq k}}^M A_{ij} A_{ik}^*. \quad (14)$$

Assuming a normal distribution of nuclear environment as given by eq. (4) and converting the sums to integrals we get:

$$\begin{aligned} I_{\text{total}}(E) &= \int_{-\infty}^{+\infty} d\varepsilon \int_{-\infty}^{+\infty} d\varepsilon_1 \int_{-\infty}^{+\infty} d\varepsilon_2 I_{\text{beam}}(E, \varepsilon) A(E, E', \varepsilon_1) A^*(E, E', \varepsilon_2) \\ &\times P(\varepsilon) P(\varepsilon_1) P(\varepsilon_2) n_s n_a^2 \frac{d\Omega}{4\pi} dA, \end{aligned} \quad (15)$$

with the incoming beam profile given by

$$\begin{aligned} I_{\text{beam}}(E, \varepsilon) &= \frac{(\Gamma/2\pi)f_s}{(E - E_0 - \varepsilon)^2 + (\Gamma/2)^2}, \\ A(E, E', \varepsilon') &= S_0 \frac{1}{[(E' - E) - i\gamma/2]} \frac{1}{[(E' - \varepsilon' - E_0) - i\Gamma/2]}, \end{aligned} \quad (16)$$

$$P(\varepsilon) = \frac{1}{\sqrt{\pi}\Delta} e^{-\varepsilon^2/\Delta^2}, \quad (17)$$

and n_s, n_a the number density of nuclei in source and absorber, respectively, $d\Omega$ is

the solid angle intercepting the absorber area dA . The factor $\frac{d\Omega}{4\pi}n_s$ picks out the nuclei emitting in the direction of the absorber and intercepting the absorber area dA .

For maximum effect, assuming $S = E_0 = 0$ and replacing S_0^2 by its definition we get

$$\begin{aligned} I_{\text{tot}}(E) &= \frac{\gamma}{2\pi} \left(\frac{\Gamma^2}{4} \right) \left(\frac{\Gamma}{2\pi} \right) \sigma_0 \frac{\Gamma_\gamma}{\Gamma} \frac{n_a^2 n_s}{\sqrt{\pi}\Delta} \\ &\times \int_{-\infty}^{+\infty} \int dE' \frac{1}{(E - \varepsilon)^2 + (\Gamma/2)^2} \frac{e^{-\varepsilon^2/\Delta^2} d\varepsilon}{[(E' - E)^2 + (\gamma/2)^2]} \\ &\times \frac{1}{\sqrt{\pi}\Delta} \int_{-\infty}^{+\infty} \frac{e^{-\varepsilon_1^2/\Delta^2} d\varepsilon_1}{[(E' - \varepsilon_1) - i\Gamma/2]} \frac{1}{\sqrt{\pi}\Delta} \int_{-\infty}^{+\infty} \frac{e^{-\varepsilon_2^2/\Delta^2} d\varepsilon_2}{[(E' - \varepsilon_2) + i\Gamma/2]}. \end{aligned} \quad (18)$$

If we look at eq. (18) and group $\sigma_0\Gamma^2/4$, $\gamma/2\pi$, and $\Gamma/2\pi$ with the resonant denominators containing Γ and γ , respectively, then these terms will be normalized like an absorption cross section with maximum σ_0 in units of area and a beam with integrated intensity of one photon/area [compare eqs. (3) and (5)]. The maximum intensity will occur at energies such that all terms are on resonance. The factor multiplying the overall expression will be Γ_γ/Γ . In general, when the total cross section Γ is increased to $\Gamma_H \approx \Delta$ to obtain overlap of resonance lines, the factor Γ_γ/Γ_H will reduce the overall effect.

We first perform the integral over E in eq. (18) to get

$$\begin{aligned} I_{\text{tot}}(E') &= \frac{\gamma}{2\pi} \left(\frac{\Gamma^2}{4} \right) \sigma_0 \frac{\Gamma_\gamma}{\Gamma} \frac{n_a^2 n_s}{\sqrt{\pi}\Delta} \left(1 + \frac{\Gamma}{\gamma} \right) \\ &\times \int_{-\infty}^{+\infty} \frac{e^{-\varepsilon^2/\Delta^2} d\varepsilon}{\{(E' - \varepsilon)^2 + [(\Gamma + \gamma)/2]^2\}} \frac{1}{\sqrt{\pi}\Delta} \int_{-\infty}^{+\infty} \frac{e^{-\varepsilon_1^2/\Delta^2} d\varepsilon_1}{[(E' - \varepsilon_1) - i\Gamma/2]} \\ &\times \frac{1}{\sqrt{\pi}\Delta} \int_{-\infty}^{+\infty} \frac{e^{-\varepsilon_2^2/\Delta^2} d\varepsilon_2}{[(E' - \varepsilon_2) + i\Gamma/2]}. \end{aligned} \quad (19)$$

The right-hand side of eq. (19) can be evaluated further by noting that the expression breaks up into a product of three integrals of form

$$B_1(z, \Delta, \Gamma) = \int_{-\infty}^{+\infty} \frac{e^{-x^2/\Delta^2} dx}{(E' - x)^2 + (\Gamma/2)^2} = \frac{\pi}{\Gamma} e^{z^2} \operatorname{erfc} z, \quad (20)$$

$$B_2(z_1, \Delta, \Gamma) = \int_{-\infty}^{+\infty} \frac{e^{-x^2/\Delta^2} dx}{(E' - x) - i\Gamma/2} = i \frac{\pi}{2} e^{z_1^2} \operatorname{erfc} z_1, \quad (21)$$

$$B_3(z_2, \Delta, \Gamma) = i\pi e^{z_2^2} \operatorname{erfc} z_2 - 2\pi i e^{-z_2^2}, \quad (22)$$

where

$$z = \frac{\Gamma + iE'}{2\Delta}, \quad z_1 = \frac{iE' - \Gamma/2}{\Delta}, \text{ and} \quad z_2 = \frac{-(iE' + \Gamma/2)}{\Delta}.$$

Using expressions (20), (21), and (22) we can rewrite (18) as

$$\begin{aligned} I_{\text{tot}}(E') &= S_0^2 n_s n_a^2 \frac{1}{\frac{3}{2}\pi\Delta^3} \\ &\times B_1(z, \Delta, \Gamma) B_2(z_1, \Delta, \Gamma) B_3(z_2, \Delta, \Gamma). \end{aligned}$$

The total number of events at the detector is obtained by integrating over the scattered energy E' to get

$$\begin{aligned} I &= \int_{-\infty}^{+\infty} I_{\text{tot}}(E') dE' \\ &= \sigma_0 \left(\frac{\Gamma_\gamma}{\Gamma} \right) \frac{n_s n_a^2}{\pi^{5/2}} \left(\frac{\Gamma}{2\Delta} \right)^3 \\ &\times \int_{-\infty}^{+\infty} dE' B_1(z, \Delta, \Gamma) B_2(z_1, \Delta, \Gamma) B_3(z_2, \Delta, \Gamma). \end{aligned}$$

The integration must be done numerically for arbitrary parameters, but in the limit $\Gamma/2\Delta \rightarrow \infty$ we get an explicit result, $I \rightarrow \sigma_0(\Gamma_\gamma/\Gamma) n_s n_a^2 / 3\pi^2$, which can be interpreted as follows. For $\Delta \rightarrow 0$ and Γ finite, i.e., the natural linewidth, the maximum effect is observed. For $\Delta = \text{finite}$ and $\Gamma \rightarrow \Gamma_H \rightarrow \infty$, i.e., large homogeneous broadening, the effect goes to zero because of the factor Γ_γ/Γ_H , in agreement with the incoherent calculation.

5. Conclusions

We have examined the effect of inhomogeneous broadening on nuclear resonance absorption in a Mössbauer experiment. As the inhomogeneous broadening increases, the resonance effect between source and absorber decreases. In contradiction to statements made in a recent publication [8,9], increasing the homogeneous broadening, i.e., the broadening of each resonance line in a system by the same amount in the source and absorber, increases the overlap of lines but *decreases* the overall Mössbauer effect, and remains true for both incoherent and coherent treatments. Thus, homogeneous broadening alone – in both the inhomogeneously broadened source and absorber – will not improve the resonance effect in general.

Appendix – Overlap of lines and resonance effect

For the two Lorentzian lines pictured in fig. 7 the overlap area is given by

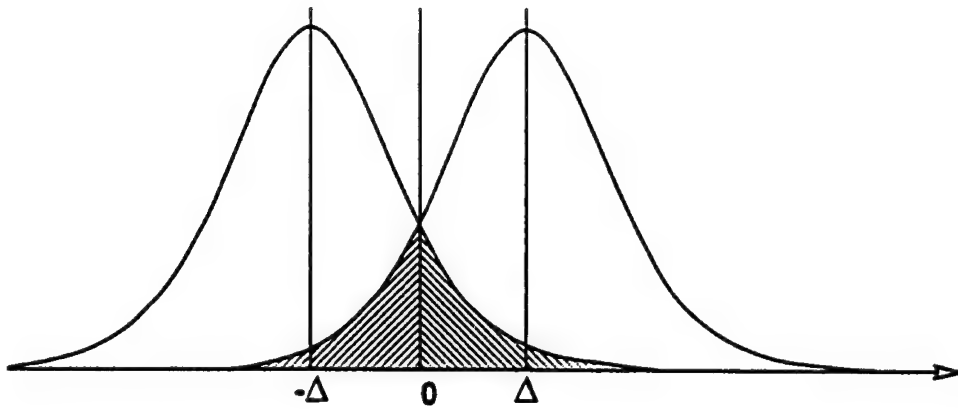


Fig. 7. Overlap of two Lorentzian lines with resonance energies displaced by 2Δ .

$$A = \int_{-\infty}^0 I_2(E) dE + \int_0^{+\infty} I_1(E) dE, \quad (\text{A.1})$$

where

$$I_1(E) = \frac{\Gamma/2\pi}{(E - E_0 + \Delta)^2 + (\Gamma/2)^2}, \quad (\text{A.2})$$

and

$$I_2(E) = \frac{\Gamma/2\pi}{(E - E_0 - \Delta)^2 + (\Gamma/2)^2}. \quad (\text{A.3})$$

Note that $I_1(E)$ and $I_2(E)$ are normalized so that the area under each curve is 1. The result of the integration is

$$A = \frac{2}{\pi} \tan^{-1} \left[\frac{2(E - E_0)}{\Gamma} \right] \Big|_0^\infty = \frac{2}{\pi} \left(\frac{\pi}{2} - \tan^{-1} \left(\frac{2E_0}{\Gamma} \right) \right). \quad (\text{A.4})$$

In the limit of large homogeneous broadening $\Gamma \rightarrow \infty$, $\tan^{-1}(2E_0/\Gamma) \rightarrow 2E_0/\Gamma \rightarrow 0$, and so $A \rightarrow 1$ and complete overlap is achieved.

On the other hand the resonance effect for a nuclear absorption process is given by

$$R = \int_{-\infty}^{+\infty} \frac{I_0(\Gamma/2\pi) dE}{(E - E_0 + \Delta)^2 + (\Gamma/2)^2 (E - E_0 - \Delta)^2 + (\Gamma/2)^2},$$

where the first Lorentzian represents the beam profile and is normalized to unity so that the beam intensity is given by I_0 . The second Lorentzian represents the scattering or absorption of a photon with a partial width for the process Γ_γ and a total width Γ composed of several parts in general,

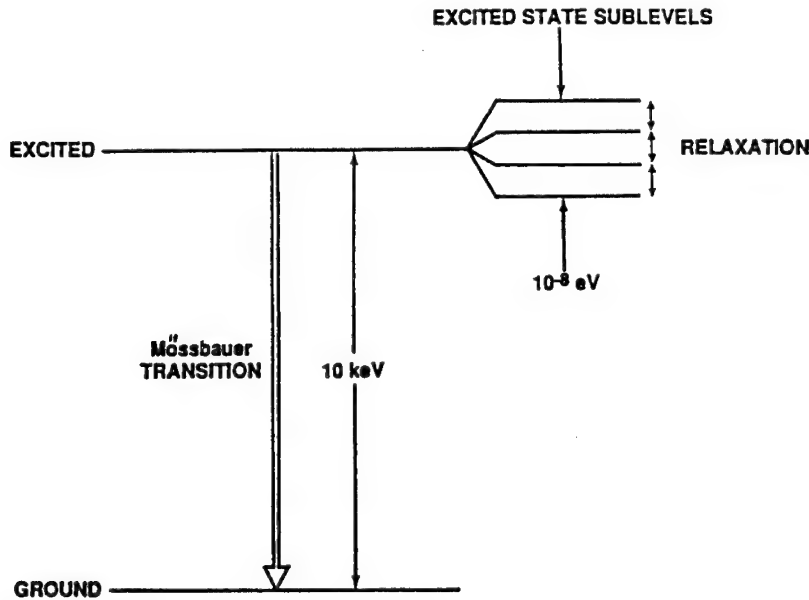


Fig. 8. Typical energy splittings affecting the Mössbauer transition and lineshape. Relaxation between the sublevels affect the lineshape and the total linewidth Γ but not the radiative width Γ_γ corresponding to the Mössbauer transition.

$$\Gamma = \Gamma_\gamma + \Gamma_a + \sum_i^n \Gamma_i,$$

where Γ_γ is the radiative width, Γ_a the internal conversion width and Γ_i are widths corresponding to the other n transitions, for example relaxation processes between sublevels as pictured in fig. 8. Whereas the radiative transition can involve energies of tens of keV or more, the sublevels taking part in the relaxation process could be separated by the hyperfine interaction energies on the order of 10^{-8} eV.

Carrying out the integration one finds that

$$R = I_0 \frac{\sigma_0}{2\pi} \left(\frac{\Gamma_\gamma}{\Gamma} \right) \left(\frac{1}{\Delta^2 + 1} \right).$$

Increasing the inhomogeneous broadening decreases the resonance effect except when $\Gamma_\gamma = \Gamma$ or the transition of interest (measured absorption) is responsible for the total width. This is not possible for the case of interest shown in fig. 8, which depicts energy levels and transitions in a Mössbauer or nuclear resonance experiment. Increase in the total width Γ is not caused by the increase in the radiative rate Γ_γ but instead by the relaxation between the spin sublevels.

References

- [1] B. Balko, J. Quant. Spectrosc. Radiat. Transfer 40(6) (1988).
- [2] A. Artna-Cohen, J. Quant. Spectrosc. Radiat. Transfer 40(6) (1988) 663.
- [3] D.A. Sparrow, B. Balko and S. Dixit, J. Quant. Spectrosc. Radiat. Transfer 40(6) (1988) 741.
- [4] B. Balko, I.W. Kay, J.D. Silk and D.A. Sparrow, Laser Phys. 5(2) (1995).
- [5] V. Vali and W. Vali, Proc. IEEE 51 (1963) 182.
- [6] W. Wildner and U. Gonser, J. de Physique Coll. 40(2 suppl. au no. 3) (1979).
- [7] R.D. Taylor and G.R. Hoy, *Short and Ultrashort Wavelength Lasers*, SPIE Vol. 875 (1988).
- [8] R. Coussemant, G. Shevoneels, F. Harderman and P. Boolchand, Hyp. Int. 42 (1988) 1169.
- [9] R. Coussemant, G. S'heeren, M. Van Den Berg and P. Boolchand, Phys. Rev. B 45 (1992) 9755.
- [10] A. Abragam, *The Principles of Nuclear Magnetic* (Oxford University Press) p. 447.
- [11] B. Balko and I.W. Kay, Phys. Rev. B, submitted.
- [12] B. Balko, I.W. Kay, J. Nicoll, G. Herling, J. Silk and D.P. Sparrow, *Comment on "Nuclear resonant absorption in long-lived isomeric transitions"*, Phys. Rev. B, submitted.
- [13] G.E. Bizina, A.G. Beda, N.A. Burgov and A.V. Davidov, Sov. Phys. JETP 18 (1973) 1964.
- [14] B. Balko, L. Cohen and J. Nicoll, *IDA Gamma-Ray Laser Summary Report (1987), Investigation of the Feasibility of Developing a Laser Using Nuclear Transitions*, IDA Paper P-2083 (Institute for Defense Analyses, 1985).
- [15] G. S'heeren, M. Van Den Bergh, R. Coussemant, R.N. Enzweiler, R. Harris, Y. Wu, P. Boolchand, R.D. Taylor, M. Cyamukungu, J. Lehmann and L. Grenacs, in: *Proc. Int. Conf. on Lasers '90*, eds. D.G. Harris and T.M. Shay (STS Press, McLean VA, 1991) pp. 17–23.
- [16] B. Balko and G.R. Hoy, Phys. Rev. B 10 (1973) 4523.
- [17] W. Heitler, *Quantum Theory of Radiation* (Clarendon, Oxford, 1954) pp. 196–204.
- [18] A.J.F. Boyle and H.E. Hall, Rep. Prog. Phys. 25 (1962) 441.
- [19] G.R. Hoy and S. Chandra, J. Chem. Phys. 47 (1967) 961.
- [20] B. Balko and G.R. Hoy, Phys. Rev. B 10 (1974) 36.

Models for homogeneous line broadening in long-lived nuclear states

J. Odeurs and R. Coussement

*University of Leuven, Instituut voor Kern- en Stralingsphysica,
Celestijnenlaan 200D, B-3001 Leuven, Belgium*

Nuclei embedded in a lattice are submitted to interactions with their surroundings. This produces a randomly fluctuating microfield at the nuclei, perturbing their energy levels. These perturbations can be considered as stochastic processes. Many of the fluctuating phenomena represent the result of a very large number of very small changes. The standard description of such fluctuations is a Gaussian process, defined as a process for which only the first and second moments are different from zero. If a radiating nucleus is constantly perturbed the radiated field can be regarded as undergoing phase fluctuations around the unperturbed nuclear Bohr frequency ω_0 . The instant frequency can then be written as $\omega(t) = \omega_0 - x(t)$, where $x(t)$ is the value of a stochastic variable X with zero mean. The first-order correlation function, whose Fourier transform gives the radiated frequency spectrum, depends on the probability function governing X . For a Gaussian, stationary, delta-correlated process, it is shown that the frequency spectrum is Lorentzian. For an arbitrary perturbation having a broad spectrum, it is shown that the frequency spectrum is again Lorentzian. For a narrow perturbation spectrum, the corresponding frequency spectrum is Gaussian.

1. Introduction

Recently [1], we have presented a relatively simple model describing homogeneous line broadening in long-lived states of nuclei incorporated in a solid-state lattice. This study has been inspired by a model proposed by Coussement et al. [2], developed among others to explain why a Mössbauer effect could be observed using the 88 keV γ -transition in ^{109}Ag , as has been claimed by several groups [3–5]. Without this homogeneous line broadening, it is rather hopeless to try to observe a Mössbauer effect using this isotope, since its isomeric state has a natural width of about 10^{-17} eV.

The model represented in ref. [1] considers the phase shifts of the wave-train emitted by the nuclei due to their interactions with the lattice.

The first-order correlation function defined in ref. [1] has been calculated using a relatively simple model for the perturbations, based on a Markov process. The frequency spectrum derived from it is Lorentzian with width equal to the sum of the width due to a pure nuclear radiative decay γ and a width γ_b due to the interactions of the nuclei with the lattice. If $\gamma_b \gg \gamma$ then the line broadening is essentially due to

the interactions of the nuclei with the lattice. It has been shown in ref. [1] that the line broadening is homogeneous for long-lived nuclear states such as the isomeric state of ^{109}Ag .

In the present article we will sketch other models leading also to homogeneous line broadening.

2. Frequency spectrum

As in ref. [1], the frequency spectrum of electromagnetic classical radiation is given by the Fourier transform of the first-order correlation function $g^{(1)}(\tau)$:

$$F(\omega) = \frac{1}{\pi} \operatorname{Re} \int_0^\infty g^{(1)}(\tau) e^{i\omega\tau} d\tau, \quad (1)$$

with $g^{(1)}(\tau)$ defined by the statistical average [6,7] over all possible field values of a component $E(t)$ of a classical electric or magnetic field:

$$g^{(1)}(\tau) = \frac{\langle E^*(t)E(t+\tau) \rangle}{\langle E^*(t)E(t) \rangle}. \quad (2)$$

The first-order correlation function contains thus a two-time average $\langle E^*(t)E(t+\tau) \rangle$. The denominator normalizes $g^{(1)}(0)$.

In the following we will suppose that the properties of the emitting source are stationary, which means that the influence governing the statistical fluctuations does not depend on the starting time of the observations. This means, among others, that the observation period must be long compared to the time scale of the fluctuations. For long-lived nuclei this condition is always met.

3. Generalities on stochastic processes

When nuclei are incorporated in a crystalline lattice, their interactions with the atoms surrounding them perturb (continuously or not) the nuclear energy levels. So the nuclear Bohr frequencies are shifted from their unperturbed value ω_0 . The instantaneous Bohr frequency can be written as

$$\omega(t) = \omega_0 - x(t), \quad (3)$$

where $x(t)$ is the value at time t of a stochastic variable X . The mean value of X can be taken as zero. The first-order correlation function corresponding to the field radiated by the nucleus can then be written [1] as

$$g^{(1)}(\tau) = e^{-i\omega_0\tau} \left\langle \exp \left(i \int_0^\tau x(t) dt \right) \right\rangle. \quad (4)$$

In eq. (4) the radioactive nuclear decay has been omitted temporarily. The stochas-

tic average $\langle \dots \rangle$ depends on the probability density function governing the stochastic variable X , thus on the nature of the interactions between the radiating nuclei and their surroundings in the lattice. We will dwell further on the stochastic variable X . The perturbers – the neighboring atoms – produce at the nucleus a randomly fluctuating microfield. So we have a stochastic process, i.e. a randomly fluctuating function of time $X(t)$, defined by the possible values that the stochastic variable X may take at any instant. These values constitute the sample space of the stochastic variable X [8]. The possible values x that may take the variable X are determined by the probability with which the value x occurs. For a continuous variable one has the probability density function $f(x)$, such that $f(x) dx$ is the probability to have a value of X in the interval $[x, x + dx]$.

The stochastic variable X (which is in our case simply related to the energy of the nucleus in the lattice) is subject to uncontrollable actions that render precise predictions impossible. A process is stationary if all statistical properties are unchanged when all time arguments are shifted by the same amount. In particular $g^{(1)}(t + \tau) = g^{(1)}(\tau)$.

A stationary process is ergodic if all statistical properties can be deduced from a single realization of infinite duration. Then the ensemble average $\langle \dots \rangle$ is equal to a time average. For long-lived nuclei interacting with their neighboring atoms in a lattice in which they are embedded, the fluctuations on the nuclei should be described as an ergodic process.

The stochastic average of a variable X is defined as

$$\langle X(t) \rangle = \int x f(x, t) dx, \quad (5)$$

with $f(x, t)$ the probability density function, describing the probability that X takes the value x at time t .

The stochastic moments $\mu_n(t_n, \dots, t_1)$ are defined as

$$\mu_n(t_n, \dots, t_1) = \langle X(t_n) \dots X(t_1) \rangle. \quad (6)$$

The first moment is thus the mean. The second moment is defined as

$$\mu_2(t_2, t_1) = \langle X(t_2) X(t_1) \rangle = \int \int dx_1 dx_2 x_1 x_2 g(x_2, t_2; x_1, t_1), \quad (7)$$

with $g(x_2, t_2; x_1, t_1)$ the probability density function describing that the stochastic variable X has value x_1 at time t_1 and value x_2 at time t_2 . Higher moments are defined in a similar way.

The auto-correlation function $G(t_2, t_1)$ is defined as

$$G(t_2, t_1) = \mu_2(t_2, t_1) - \mu_1(t_2)\mu_1(t_1). \quad (8)$$

For a stochastic variable X with mean zero one has

$$G(t_2, t_1) = \mu_2(t_2, t_1). \quad (9)$$

Higher correlation functions can be defined in a similar way. However these functions will not play any role in the processes we will consider.

A process with mean zero is Gaussian if the only non-zero correlation function is $G(t_2, t_1)$. It can be shown [8] that for a Gaussian process with mean zero, one has:

$$\left\langle \exp\left(i \int_0^\tau dt x(t)\right) \right\rangle = \exp\left(-\frac{1}{2} \int_0^\tau dt_1 \int_0^\tau dt_2 \langle x(t_1)x(t_2) \rangle\right). \quad (10)$$

Many of the fluctuating phenomena represent the result of a very large number of very small changes in some parameter, in our case the result of independent encounters between radiating nuclei and perturbing atoms in their neighborhood. If the nuclear states are long-lived, numerous encounters occur during their life-time. The standard description of the fluctuations is as a Gaussian process [8,9].

4. Models for the stochastic variable X . Calculation of the spectrum

4.1. INTRODUCTION

In order to calculate $g^{(1)}(\tau)$ (eq. (4)) and the frequency spectrum derived from it (eq. (1)), one has to calculate

$$f(\tau) = \left\langle \exp\left(i \int_0^\tau x(t) dt\right) \right\rangle. \quad (11)$$

In ref. [1] the stochastic average has been calculated supposing that the random interactions of the nuclei with the lattice are very brief uncorrelated events, which should be a plausible hypothesis for long-lived nuclei. The perturbation on the nuclei due to the lattice has been approximated then by a Dirac-delta correlation, which is known as the Markov approximation [8] (somewhat loosely termed as the “no-memory” approximation). Based on an analysis borrowed from quantum optics [10], we have shown that:

$$f(\tau) = e^{-(\gamma_b/2)\tau}. \quad (12)$$

The frequency spectrum derived from eq. (12), with eq. (4) and with the radiative damping included (damping coefficient γ) is:

$$F(\omega) = \frac{1}{2\pi} \frac{\gamma + \gamma_b}{(\omega - \omega_0)^2 + (\gamma + \gamma_b/2)^2}. \quad (13)$$

$F(\omega)$ represents a Lorentzian with full width at half maximum $\gamma + \gamma_b$.

Due to the interaction between the nuclei and the lattice there has been a line broadening which for long-lived nuclei is a homogeneous one, since all nuclei go through the same processes during their long life-time.

As already mentioned in ref. [1], the derivation of eq. (12) from eq. (11) can be

done immediately if one supposes a Gaussian process defined in the previous section. (Note that a Gaussian process does not have necessarily a Gaussian spectrum.) For a Gaussian process one has eq. (10). If the Gaussian process is a Markovian one has

$$\langle x(t_1)x(t_2) \rangle = \gamma_b \delta(t_2 - t_1). \quad (14)$$

Eq. (14) in eq. (10) leads immediately to eq. (12) and hence to eq. (13).

In the next section we will present other models leading also to line broadening. We will again suppose stationary Gaussian processes, but which are not necessarily Markovian so that eq. (14) does not necessarily hold.

4.2. ARBITRARY PERTURBATION

As already has been mentioned the key element for the first-order correlation function, from which the frequency spectrum is derived, is the stochastic average (eq. (11)), which for a Gaussian process is

$$f(\tau) = \left\langle \exp\left(i \int_0^\tau x(t) dt\right) \right\rangle = \exp\left(-\frac{1}{2} \int_0^\tau dt_1 \int_0^\tau dt_2 \langle x(t_1)x(t_2) \rangle\right). \quad (15)$$

$f(\tau)$ is thus completely determined by $\langle x(t_1)x(t_2) \rangle$ and thus by the probability (density) function describing the stochastic variable X . It can be shown [11] that for a stationary process

$$\exp\left(-\frac{1}{2} \int_0^\tau dt_1 \int_0^\tau dt_2 \langle x(t_2)x(t_1) \rangle\right) = \exp\left(- \int_0^\tau dt (\tau - t) \langle x(t)x(0) \rangle\right). \quad (16)$$

Let us express $\langle x(t)x(0) \rangle$ with the help of its Fourier cosine transform:

$$\langle x(t)x(0) \rangle = \int_0^\infty d\omega \cos \omega t S(\omega). \quad (17)$$

It is supposed that $\langle x(t)x(0) \rangle$ is an even function.

One has the inverse formula

$$S(\omega) = \frac{2}{\pi} \int_0^\infty dt \cos \omega t \langle x(t)x(0) \rangle. \quad (18)$$

Let us define $k(\tau)$ by

$$k(\tau) = \int_0^\tau dt (\tau - t) \langle x(t)x(0) \rangle. \quad (19)$$

Using eq. (17):

$$k(\tau) = \int_0^\tau dt (\tau - t) \int_0^\infty d\omega \cos \omega t S(\omega). \quad (20)$$

Performing the t -integration:

$$k(\tau) = 2 \int_0^\infty \frac{\sin^2 \omega \tau / 2}{\omega^2} S(\omega) d\omega. \quad (21)$$

This general form has two particular limits:

(i) Let us consider first the case where the spectrum $S(\omega)$ is broad compared to $2\pi/\tau$, which can be considered as the "width" of $(\sin^2 \omega \tau / 2)/\omega^2$.

In order to evaluate the integral in eq. (21), one has to remember that $(\sin^2 \omega \tau / 2)/\omega^2$ is a rapidly oscillating damped function presenting a maximum at $\omega = 0$. Since $S(\omega)$ is supposed to be a much slower varying function, $S(\omega)$ can be replaced in the integral by $S(0)$:

$$\int_0^\infty \frac{\sin^2 \omega \tau / 2}{\omega^2} S(\omega) d\omega \approx S(0) \int_0^\infty \frac{\sin^2 \omega \tau / 2}{\omega^2} d\omega. \quad (22)$$

The remaining standard integral is $(\tau/4)\pi$. So $k(\tau)$ depends linearly upon τ :

$$k(\tau) = \pi S(0) \tau / 2. \quad (23)$$

With eqs. (23), (15), (16) and (11) and also including radioactive damping (coefficient γ), the first-order correlation function becomes then:

$$g^{(1)}(\tau) = e^{-i\omega_0\tau} e^{-(\gamma/2)\tau} e^{-\pi S(0)\tau/2}. \quad (24)$$

The frequency spectrum derived from it is

$$F(\omega) = \frac{1}{2\pi} \frac{\gamma + \gamma_b}{(\omega - \omega_0)^2 + ((\gamma + \gamma_b)/2)^2}, \quad (25)$$

with γ_b defined by

$$\gamma_b = \pi S(0). \quad (26)$$

The spectrum is Lorentzian with width $\gamma + \gamma_b$.

(ii) If the spectrum $S(\omega)$ is narrow (width ΔS) compared to $2\pi/\tau$ and centered about its average zero, then $(\sin^2 \omega \tau / 2)/\omega^2$ does practically not change over the interval ΔS , so we can replace $(\sin^2 \omega \tau / 2)/\omega^2$ by its value at $\omega = 0$, i.e. $\tau^2/4$, and

$$k(\tau) = \frac{\tau^2}{2} \int S(\omega) d\omega. \quad (27)$$

The first-order correlation function is then, including radioactive damping,

$$g^{(1)}(\tau) = e^{-i\omega_0\tau} e^{-(\gamma/2)\tau} \exp\left(-\tau^2 \frac{1}{2} \int S(\omega) d\omega\right). \quad (28)$$

The frequency spectrum derived from it is

$$F(\omega) = \frac{1}{\pi} \operatorname{Re} \int_0^\infty e^{-i\omega_0\tau} e^{-(\gamma/2)\tau} \exp\left(-\tau^2 \frac{1}{2} \int S(\omega) d\omega\right) e^{i\omega\tau} d\tau. \quad (29)$$

It can then be shown that $F(\omega)$ is given by

$$F(\omega) = \frac{1}{\sqrt{\pi}} \frac{1}{2\delta} \exp\left(\frac{-(\omega - \omega_0)^2}{4\delta^2} + \frac{\gamma^2}{16\delta^2}\right) \cos \frac{\gamma(\omega - \omega_0)}{4\delta^2}, \quad (30)$$

with

$$\delta^2 = \frac{1}{2} \int S(\omega) d\omega. \quad (31)$$

If the natural linewidth γ is small compared to the “width” of the exponential function, which can be taken approximately as 2δ , $F(\omega)$ is then approximately equal to

$$F(\omega) = \frac{1}{\sqrt{\pi}} \frac{1}{2\delta} e^{-(\omega - \omega_0)^2/4\delta^2}, \quad (32)$$

which is a Gaussian.

5. Conclusions

The wave-trains emitted by long-lived nuclei incorporated in a solid-state lattice, are continuously modified due to the interactions of the nuclei with their surroundings.

The perturbation of the nuclear Bohr frequency can be considered as a stochastic process. The stochastic variable X associated to this process is the difference between the unperturbed nuclear frequency ω_0 and the instantaneous frequency $\omega(t)$.

The first-order correlation function, whose Fourier transform gives the frequency spectrum of the photons emitted by the nuclei, depends among others on $\langle \exp(i \int_0^T x(t) dt) \rangle$ with $\langle \dots \rangle$ the ensemble average, $x(t)$ being the value of X at time t .

Several models have been considered:

1. For a Gaussian, stationary delta-correlated process, it is shown that the frequency spectrum is Lorentzian with width equal to the sum of the natural linewidth γ and a lattice-induced linewidth γ_b . The composite line broadening is homogeneous.
2. For an arbitrary perturbation it is shown that for a broad perturbation spectrum, the frequency spectrum is again Lorentzian with width $\gamma + \gamma_b$. For a narrow perturbation spectrum one has a complicated frequency spectrum which for small natural linewidths becomes a Gaussian.

All models give a lattice-induced homogeneous line broadening which adds to the natural linewidth.

References

- [1] J. Odeurs, Phys. Rev. B52 (1995) 6166.
- [2] R. Coussement, G. S'heeren, M. Van Den Bergh and P. Boolchand, Phys. Rev. B 45 (1992) 9755.
- [3] W. Wildner and U. Gonser, J. de Phys. (Paris) 40 (1979) C2-47.
- [4] G.R. Hoy and R.D. Taylor, J. Quant. Spectrosc. Radiat. Transfer 40 (1988) 763.
- [5] G.R. Hoy, S. Rezaie-Serej and R.D. Taylor, Hyp. Int. 58 (1990) 2513.
- [6] J.D. Cresser, Phys. Rep. 94 (1983) 47.
- [7] R. Loudon, *The Quantum Theory of Light* (Clarendon Press, Oxford, 1986).
- [8] N.G. Van Kampen, *Stochastic Processes in Physics and Chemistry* (North-Holland, Amsterdam, 1981).
- [9] B.W. Shore, *The Theory of Coherent Atomic Excitation*, Vol. 2 (Wiley, New York, 1990).
- [10] P. Meystre and M. Sargent III, *Elements of Quantum Optics* (Springer, New York, 1992).
- [11] D.S. Elliot, R. Roy and S.J. Smith, Phys. Rev. A26 (1982) 12.

Quantum interferences at nuclear level crossing

R. Coussement and G. Neyens¹

*University of Leuven, Instituut voor Kern- en Stralingsphysica,
Celestijnlaan 200 D, B-3001 Leuven, Belgium*

Two nuclear hyperfine levels can cross when a quadrupole and magnetic interaction are combined. When the levels come close enough, interferences between two transitions can occur if coherence conditions are fulfilled. In this paper we discuss the possibility that coherence and interferences could occur if the zero fluctuations of an electromagnetic field in a crystal lattice would be anisotropic.

1. Introduction

In quantum optics the use of lasers has allowed the study of coherence effects in atomic transitions. For nuclear transitions we do not have any coherent beam of gamma radiation and therefore the study of coherence has been focused on the observation of quantum beats in what is called *perturbed angular correlation*, a technique which is routinely used to study the hyperfine interaction of the nuclear moments with their environment. However, in quantum optics many other effects appear. Lasing without population inversion is one example, another one is the reduction of the zero fluctuations when the atoms are constrained in a cavity of the dimensions of the optical wavelength.

We will discuss in this paper the possibility of observing quantum interferences in nuclear transitions. As coherent bichromatic gamma-ray fields are not available, we use two closely spaced levels which we can easily obtain with level crossing. An important difference between optical transitions and gamma radiation is that the wavelength of the gamma radiation is of the same order of magnitude as the interatomic distances in a lattice. Therefore, the isotropy of the vacuum fluctuations could be broken in a lattice. The breaking of the spherical symmetry of the vacuum fluctuation field can then result in mixing of the crossing levels (anticrossing) and in interferences between transitions in a Mössbauer spectrum.

2. Nuclear level crossing

Let us first explain how we bring two nuclear levels to cross or to anticross.

¹ Supported by the National Fund for Scientific Research (N.F.W.O.).

Later on we will consider its effect on the resonant emission and absorption of gamma radiation.

Consider a nucleus submitted to the combined interaction of an electric field gradient (EFG) and a magnetic field. We will assume that the EFG has axial symmetry and we will choose the symmetry axis as the z-axis. The Hamiltonian can be written in three terms: the first one expresses the quadrupole interaction, the second the interaction of the nuclear magnetic moment with the component of the magnetic field parallel to the EFG-axis and the third one the interaction with the perpendicular component:

$$H = \frac{\omega_Q}{\hbar} (3I_z^2 - I^2) - \omega_B \cos \beta I_z + \frac{\omega_B}{2} \sin \beta (I_+ + I_-). \quad (1)$$

In this paper the misalignment angle β between the EFG-axis and the magnetic field will be considered small but adjustable. As a first case we consider the EFG-axis being oriented parallel to the magnetic field and we investigate the hyperfine splitting as a function of an increasing magnetic field. In this case axial symmetry is conserved, m is a good quantum number, and at well defined fields some of the nuclear hyperfine levels $|m\rangle$ and $|m'\rangle$ are crossing (fig. 1). However we must keep in mind that as soon as there is somewhere a small interaction that breaks the axial symmetry, the levels will anticross and the wave functions of the two hyperfine m -states will mix so that indeed m is no more a good quantum number. When the misalignment of the magnetic field with respect to the EFG-axis is small, the small perpendicular component in the hamiltonian slightly breaks the axial symmetry. In the m -representation, the Hamiltonian matrix has a small non-diagonal matrix element which can be neglected against the much larger diagonal ones. But near a level crossing the situation is different because two levels come so close in energy that their energy difference becomes smaller than the non-diagonal matrix element ($E_m - E_{m'} < W_{mm'}$), such that the latter can no longer be neglected. We can then use

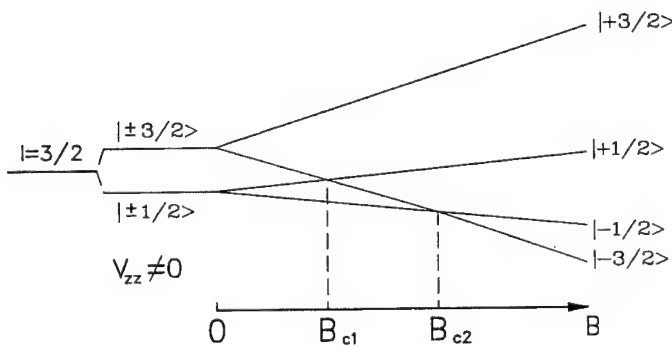


Fig. 1. When a nucleus is submitted to a static magnetic field and an electric field gradient, the degeneracy of the nuclear hyperfine levels of a state with spin I is lifted and level crossings occur as a function of the magnetic field strength.

a two-level approximation in which we solve the Hamiltonian for this two levels. The two-by-two Hamiltonian can be solved analytically and gives the following results for the energy and the two wave functions:

$$E_{1,2} = \frac{E_m + E_{m'}}{2} + \frac{1}{2} \sqrt{(E_m - E_{m'})^2 + 4W_{mm'}} . \quad (2)$$

$$\begin{aligned} |1\rangle &= \frac{1}{\sqrt{1+R^2}} (R|m\rangle + |m'\rangle) , \\ |2\rangle &= \frac{1}{\sqrt{1+R^2}} (|m\rangle - R|m'\rangle) , \end{aligned} \quad (3)$$

with

$$R = \frac{E_m - E_{m'}}{2W_{mm'}} \sqrt{\left(\frac{E_m - E_{m'}}{2W_{mm'}}\right)^2 + 1} . \quad (4)$$

From this equation we can easily derive that the minimum repelling distance between the two states is twice the non-diagonal matrix element $W_{mm'} = \langle m | H^\perp | m' \rangle \approx B \sin \beta$. As this one is proportional to $\sin \beta$ we can adjust the misalignment according to the desired minimum distance, a fact of importance later on. At the crossing field where $E_m = E_{m'}$, the wave functions become rather simple:

$$\begin{aligned} |1\rangle &= \frac{1}{\sqrt{2}} (|m\rangle + |m'\rangle) , \\ |2\rangle &= \frac{1}{\sqrt{2}} (|m\rangle - |m'\rangle) . \end{aligned} \quad (5)$$

They are similar to the wave functions of a pair of coupled oscillators, one is the symmetric, the other is the anti-symmetric wave function. In earlier work we have shown that the effect of the anticrossing on the angular distribution of nuclear radiation is to produce resonances similar to NMR resonances [1,2].

In this paper we study the effect of the crossing and anticrossing on a Mössbauer spectrum. The most trivial effect is the overlapping of two Mössbauer lines. However the most interesting effect is that the two lines can interfere as soon as the two levels come close enough in energy:

$$E_1 - E_2 \approx \hbar\gamma , \quad (6)$$

with $\hbar\gamma$ the natural linewidth. In order to obtain interference there are two more conditions to be fulfilled. A single gamma photon must be able to ring the two transitions not only from the point of view of energy conservation, but also angular momentum conservation. Secondly, there may be a phase problem (random phases or phase locking). These two points deserve our attention in the following section.

3. Angular momentum conservation

We assume that the photon propagates in a direction given by the angle θ with respect to the EFG-axis (photon momentum $\hat{k} = (0, \theta, 0)$). A photon with circular polarization σ can be written in terms of the Δm partial wave functions by using the rotation matrix elements [3]:

$$|\sigma\rangle = \sum_{\Delta m=-1,0,1} D^1_{\Delta m, \sigma}(0, \theta, 0) |\Delta m\rangle = \sum_{\Delta m=-1,0,1} d^1_{\Delta m, \sigma}(\theta) |\Delta m\rangle. \quad (7)$$

For an arbitrary angle θ a photon can induce transitions with $\Delta m = +1, 0$ and -1 . Therefore, at an angle $\theta = 90^\circ$ only the $\Delta m = +1$ and $\Delta m = -1$ transitions can occur simultaneously with one single photon. For gamma rays entering at $\theta = 0^\circ$ a photon with $\sigma = +1$ can only induce $\Delta m = +1$ transitions and, similarly, for a $\Delta m = -1$ one needs a photon with circular polarization $\sigma = -1$. As the circular polarization of a photon takes either the values $+1$ or -1 , interferences between $\Delta m = +1$ and $\Delta m = -1$ cannot occur at $\theta = 0^\circ$, while at $\theta = 90^\circ$ these interferences can occur if other conditions concerning phases are fulfilled (see later).

In the case of axial symmetry and thus pure level crossing, the nuclear hyperfine states are pure m -states, and the transitions are characterized by a single Δm . Then there cannot be any interferences for photons entering the absorber along the EFG-axis. However, interferences will be possible when the axial symmetry is broken because then the levels are mixed according to eq. (2).

4. Phase locking or coherence

We consider a transition from a single ground state to a level crossing or level mixing doublet. The magnetic field is tuned to such a value that the distance between the levels of the upper doublet is smaller than (or of the same order as) the natural linewidth, so that by energy conservation the two levels can be excited by the same photon. The amplitudes have a random phase difference because of the random phase of the final doublet states.

$$A_1 = \langle 1 | H_{\text{int}} | g \rangle e^{i(\varphi_1 - \varphi_g)} |1\rangle, \quad \text{and} \quad A_2 = \langle 2 | H_{\text{int}} | g \rangle e^{i(\varphi_2 - \varphi_g)} |2\rangle. \quad (8)$$

In the total transition probability the random phase difference remains in the product of the two amplitudes:

$$|A|^2 = |A_1 + A_2|^2 = |A_1|^2 + |A_2|^2 + \langle 1 | H_{\text{int}} | g \rangle \langle g | H_{\text{int}} | 2 \rangle e^{i(\varphi_1 - \varphi_2)} \langle 2 | 1 \rangle + \text{c.c.} \quad (9)$$

The interference term cancels because of the orthogonality of $|1\rangle$ and $|2\rangle$ and because of random phase integration when the transition probability over a large number of events is observed:

$$\int_0^{2\pi} d(\varphi_1 - \varphi_2) e^{i(\varphi_1 - \varphi_2)} \equiv 0. \quad (10)$$

In that case the only effect of the crossing or anticrossing is the superposition of the two Mössbauer lines.

However, when a four-level system is created, the two phases in the doublet can be locked and the interferences will not cancel by random phase differences. Such a four-level scheme is discussed in the paper presented by Neyens in which the coherence is achieved by a NMR-transition to the doublet [4]. There are however many possible schemes available, one of them being given in fig. 2, in which the transition from $|g\rangle$ to the doublet is followed by a transition to one or more lower levels. Consider first a four-level-scheme, for which we calculate the total probability of a two-step transition from the ground state to one lower state $|f\rangle$:

$$P_{g \rightarrow f} = |A_1 B_1^* + A_2 B_2^*|^2, \quad (11)$$

in which A_1 is the amplitude for the $|g\rangle \rightarrow |1\rangle$ transition and B_1 for the $|f\rangle \rightarrow |1\rangle$ transition. In the product $A_1 B_1^*$ the random phase of level $|1\rangle$ disappears:

$$\begin{aligned} A_1 B_1^* &= \langle 1 | H_{\text{int}} | g \rangle e^{i(\varphi_1 - \varphi_g)} \langle f | H_{\text{int}}^* | 1 \rangle e^{i(\varphi_f - \varphi_1)} \langle 1 | 1 \rangle \\ &= \langle f | H_{\text{int}}^* | 1 \rangle \langle 1 | H_{\text{int}} | g \rangle e^{i(\varphi_f - \varphi_g)}. \end{aligned} \quad (12)$$

The same happens to $A_2 B_2^*$ and thus the interference term $A_1 B_1^* A_2^* B_2 + \text{c.c.}$ is no longer canceled by random phase differences between the intermediate doublet levels.

5. Interference in resonant absorption and scattering

The scheme as given in fig. 2, where decay to all lower levels is considered, has a particular significance for resonant absorption and scattering. In resonant scattering the photon is re-emitted in a well defined direction. In absorption one has re-

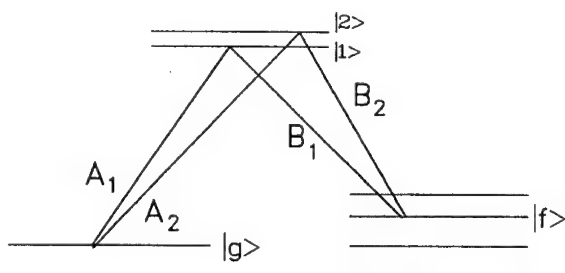


Fig. 2. A four-level system in which we consider transitions between a ground-state hyperfine level and a doublet in the excited state and the spontaneous decay of the doublet to one or more ground-state levels.

emission in all channels that are possible from the point of view of direction, polarization and final state $|f\rangle$, including electronic conversion. We can show that in the scattering in a well defined direction, one will indeed have interferences. In the case of absorption there will be no interferences, as is normally expected in a Mössbauer absorption experiment. We will show that the interferences disappear because of the random symmetry of the spontaneous emission in the second step of the total process. In order to demonstrate this, we specify the transition amplitudes B_1 and B_2 with H_{int} the interaction with the vacuum fluctuations:

$$\begin{aligned} B_{f \rightarrow 1} &= \langle 1 | H_{\text{int}} | f \rangle e^{i(\varphi_1 - \varphi_f)} | 1 \rangle \\ &= \sum_{m_1} \sum_{m_f} \langle 1 | m_1 \rangle \langle m_1 | \mathbf{j} \cdot \mathbf{A}_{\text{vac}} | m_f \rangle \langle m_f | f \rangle e^{i(\varphi_1 - \varphi_f)} | 1 \rangle, \end{aligned} \quad (13)$$

and

$$B_{f \rightarrow 2} = \sum_{m_2} \sum_{m_{f'}} \langle 2 | m_2 \rangle \langle m_2 | \mathbf{j} \cdot \mathbf{A}_{\text{vac}} | m_{f'} \rangle \langle m_{f'} | f \rangle e^{i(\varphi_2 - \varphi_f)} | 2 \rangle. \quad (14)$$

The interference term in the total transition probability is then proportional to

$$\begin{aligned} \sum_f B_{f \rightarrow 1}^* B_{f \rightarrow 2} &\approx \\ &e^{i(\varphi_1 - \varphi_2)} \langle 1 | 2 \rangle \sum_{m_1 m_f} \langle 1 | m_1 \rangle^* \langle m_1 | \mathbf{j} \cdot \mathbf{A}_{\text{vac}} | m_f \rangle^* \\ &\times \sum_{m_2 m_{f'}} \langle 2 | m_2 \rangle \langle m_2 | \mathbf{j} \cdot \mathbf{A}_{\text{vac}} | m_{f'} \rangle \sum_f \langle m_{f'} | f \rangle \langle f | m_f \rangle, \end{aligned} \quad (15)$$

in which the last factor equals $\delta_{m_f m_{f'}}$. When we consider the spontaneous re-emission of a photon with wave vector \mathbf{k} and polarization σ , the corresponding mode of the vacuum fluctuation field is

$$\mathbf{A}_{\text{vac}} \rightarrow A_{\mathbf{k}, \sigma}(\mathbf{r}, t).$$

In order to obtain the directional dependence of such a mode, we use the multipole expansion of the radiation field [3]:

$$\begin{aligned} A_{\mathbf{k}, \sigma}(\mathbf{r}, t) &= \sum_{1, \lambda} a_{1\lambda}(\sigma) Y_\lambda^1(\hat{\mathbf{r}}) d_{\Delta m, \sigma}^\lambda(\theta) e^{-i\omega t} \\ &= \sum_{1, \lambda} A_{1\lambda}(\hat{\mathbf{r}}) d_{\Delta m, \sigma}^\lambda(\theta) e^{-i\omega t}. \end{aligned} \quad (16)$$

Using the Wigner–Eckart theorem, expression (15) becomes proportional to

$$\sum_{1, \lambda} \sum_{m_f} \left[\frac{\sum_{m_1} \langle 1 | m_1 \rangle^* \langle I | \mathbf{j} \cdot \mathbf{A}_1 | I_f \rangle^* \sum_{\Delta m_1} \langle I m_1 \lambda \Delta m_1 | I_f m_f \rangle^* d_{\sigma \Delta m_1}^\lambda(\theta)^*}{\sum_{m_2} \langle 2 | m_2 \rangle \langle I | \mathbf{j} \cdot \mathbf{A}_1 | I_f \rangle \sum_{\Delta m_2} \langle I m_2 \lambda \Delta m_2 | I_f m_f \rangle d_{\sigma \Delta m_2}^\lambda(\theta)} \right], \quad (17)$$

and the interference term does not cancel if we observe the re-emitted gamma-

ray in a well defined direction θ ($\hat{k} = (0, \theta, 0)$). If however, we do not observe the re-emitted gamma-radiation, or the electron conversion, then we must integrate over all emission directions which provides us with the constraining equation

$$\int_{\theta=0}^{\pi} d_{\sigma, \Delta m_1}^{\lambda}(\theta)^* d_{\sigma, \Delta m_2}^{\lambda}(\theta) \sin \theta d\theta \approx \delta_{\Delta m_1, \Delta m_2}. \quad (18)$$

The interference term in the total transition probability is proportional to eq. (17) which in case of re-emission in all directions reduces to:

$$\begin{aligned} & |\langle I | \mathbf{j} \cdot \mathbf{A}_1 | I_f \rangle|^2 \sum_{m_1, m_2} \langle 2 | m_2 \rangle \langle m_1 | 1 \rangle \sum_{m_f, \Delta m} \langle I m_2 \lambda \Delta m | I_f m_f \rangle \langle I_f m_f | I m_1 \lambda \Delta m \rangle \\ & = |\langle I | \mathbf{j} \cdot \mathbf{A}_1 | I_f \rangle|^2 \sum_{m_1, m_2} \langle 2 | m_2 \rangle \langle m_1 | 1 \rangle \delta_{m_1, m_2}. \end{aligned} \quad (19)$$

If $|1\rangle$ and $|2\rangle$ are crossing levels, they are orthogonal and the interference term vanishes. For mixed levels (eq. (3)), the interference term cancels too. This calculation proves what we normally expect: in a normal Mössbauer absorption measurement, it is not possible to see any interferences.

We have however to be very cautious because we have assumed here that the re-emission is due to vacuum fluctuations, for which we assumed that they are broad-banded and randomly oriented. This is certainly correct in a real vacuum. However, it is also well known that the vacuum approximation fails when the cavity, in which the electromagnetic waves are enclosed, is of the order of magnitude of the wavelength. Therefore we can raise the question if we can use the random vacuum fluctuations as zero fluctuations of an electromagnetic field bound to a lattice where the nuclei are positioned periodically at distances of the same order of magnitude as the wavelength. If we assume that in such a matrix the zero fluctuations of the electromagnetic field are no more spherically symmetric, then the integration in eq. (18) has to be replaced by

$$\int_{\theta=0}^{\pi} d_{\sigma, \Delta m_1}^{\lambda}(\theta) d_{\sigma, \Delta m_2}^{\lambda}(\theta)^* |f(\theta)|^2 \sin \theta d\theta, \quad (20)$$

in which $f(\theta)$ is some kind of a form factor related to the fact that the nuclei are imbedded in a lattice. As eq. (20) is no longer an orthogonality relation, it does not give us a delta-function and the interference term (eq. (19)) does not cancel.

Remark that we can use eq. (19) to describe the possibility for interferences when the re-emitted gamma radiation is detected under a finite solid angle θ . It is also well known that when the primary gamma radiation enters the crystal under a Bragg angle, the re-emission in the Bragg-reflection direction is strongly enhanced by cooperative effects. In that case interferences between two Mössbauer transitions will occur.

6. Symmetry breaking in a single crystal

We address the question if two levels that are crossing can be coupled and mixed by their interaction with the zero-fluctuations (fig. 3). Mixing a level $|m_1\rangle$ with a level $|m_2\rangle$ would require a breaking of the axial symmetry. As vacuum fluctuations are assumed to be randomly oriented, that interaction will not cause any mixing. However, let us assume again that the zero fluctuations are not random but that some directions for the transitions B_1 and B_2 are favored. If those directions are not pointing along the z -axis we can understand that the axial symmetry can be broken.

According to the scheme in fig. 3 we must calculate the coupling due to resonant or near-resonant emission from state $|m_1\rangle$ and reabsorption to state $|m_2\rangle$. Due to conservation of energy and momentum, levels $|1\rangle$ and $|2\rangle$ must be close enough in energy (within a distance of the order of the natural linewidth) and the first emission with impuls vector \mathbf{k} must be followed by the reabsorption with the inverse impuls $-\mathbf{k}$. The process just described can be seen as an inverse resonant scattering process. The matrix element responsible for mixing between level $|1\rangle$ and level $|2\rangle$ is then

$$W_{m_1 m_2}(\mathbf{k}) = \sum_{m_f} \frac{\langle m_1 | B_1(\mathbf{k}) | m_f \rangle \langle m_f | B_2(-\mathbf{k}) | m_2 \rangle}{E_{m_1} - E_{m_f} - \omega_k + i\Gamma/2}. \quad (21)$$

Using the multipole expansion of the radiation field (eq. (16)) we obtain for the coupling matrix element (the scattering amplitude):

$$W_{m_1 m_2}(\mathbf{k}) = \sum_{\lambda, 1} \langle I \| A_{1,\lambda} \| I_f \rangle^2 d_{\Delta m_1, \sigma}^\lambda(\mathbf{k}) d_{\Delta m_2, \sigma}^\lambda(\mathbf{k})^* \frac{1}{E_{m_1} E_{m_f} - \omega_k + i\Gamma/2} \times \sum_{m_f} \langle I m_1 \lambda \Delta m_1 | I_f m_f \rangle \langle I_f m_f | I m_2 \lambda \Delta m_2 \rangle, \quad (22)$$

with $\langle I \| A_{1,\lambda} \| I_f \rangle$ the reduced nuclear matrix element. As $B_1 B_2$ is a virtual

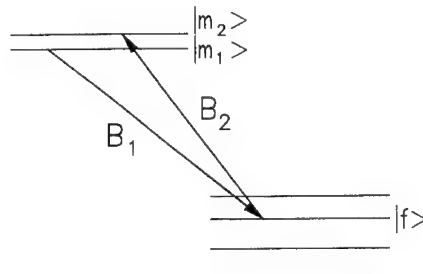


Fig. 3. Two crossing hyperfine levels $|m\rangle$ and $|m'\rangle$ can be coupled and thus mixed if a transition to the same final state $|f\rangle$ is possible.

transition, induced by vacuum fluctuations, we must integrate over all directions \hat{k} ,

$$\int_{\hat{k}} d_{\Delta m_1, \sigma}^{\lambda}(\hat{k}) d_{\Delta m_2, \sigma}^{\lambda}(\hat{k})^* d\hat{k} = \delta_{\Delta m_1 \Delta m_2}, \quad (23)$$

and the coupling disappears. If however, we assume that the zero fluctuations deviate from vacuum fluctuations, then we have again that some modes are favored, and the integration becomes

$$\int_{\hat{k}} d_{\Delta m_1, \sigma}^{\lambda}(\hat{k}) d_{\Delta m_2, \sigma}^{\lambda}(\hat{k})^* |f(\hat{k})|^2 d\hat{k} \neq \delta_{\Delta m_1 \Delta m_2}. \quad (24)$$

Consequently the coupling is not zero and the levels m_1 and m_2 will be mixed and will anticross. In order to observe such a mixing and anticrossing in a Mössbauer spectrum the distance between the mixed levels has to be of the order of the natural linewidth. We can thus conclude that anisotropy of the zero fluctuations can first of all be observed in the mixing of nuclear hyperfine levels and secondly as interferences in the absorption.

7. Experimental test

We consider a nuclear level crossing scheme for the excited state of ^{57}Fe with spin $I = \frac{3}{2}$ (fig. 1). We make sure that the EFG is axially symmetric and that the magnetic field is applied strictly along the EFG-axis, in order to maintain axial symmetry. We consider two levels $m = \frac{1}{2}$ and $m = -\frac{3}{2}$ that cross at the first crossing field B_{c1} . By applying the field B_{c1} , two Mössbauer lines will overlap in a Mössbauer absorption measurement, namely line 4 ($-\frac{1}{2} \rightarrow -\frac{3}{2}$) and line 5 ($-\frac{1}{2} \rightarrow +\frac{1}{2}$) (fig. 4). The first line is a $\Delta m = -1$ transition while the other is a $\Delta m = +1$ transition. We choose the direction of the gamma radiation \hat{k} parallel to the z-axis so that for the first line a $\sigma_1 = \Delta m_1 = -1$ gamma photon and for the second line a $\sigma_2 = \Delta m_2 = -1$ photon can be absorbed. This geometry has the advantage that both transitions occur with different photons and thus the effective thickness does not change when the two lines come together in energy. Therefore, if no mixing and no interferences occur, the total intensity of the overlapping lines in the Mössbauer spectrum should be the sum of the intensities of their non-overlapping partner lines, line 1 ($+\frac{1}{2} \rightarrow +\frac{3}{2}$) and line 3 ($+\frac{1}{2} \rightarrow -\frac{1}{2}$).

Experiments are being done in Leuven and Cincinnati [6] using single crystals of FeCO_3 and the preliminary results suggest an intensity change of 10% with respect to what is expected according to the previous discussion. However, more statistics and careful analysis are necessary before we can conclude that the difference in intensity is due to mixing of the doublet levels and interferences in the absorption.

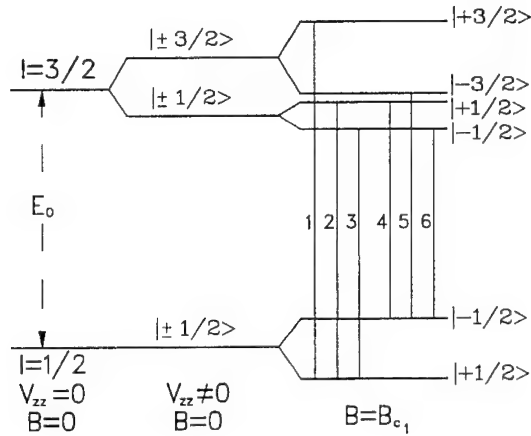


Fig. 4. In the Mössbauer spectrum of ^{57}Fe submitted to a combined magnetic dipole and electric quadrupole interaction, six lines can be distinguished. Near the first level crossing field B_{c1} (see fig. 1) two of these lines will come together in energy.

8. Summary

We can conclude that with level crossing and anticrossing, one can explore some fascinating aspects of nuclear quantum optics. Experimental tests can be performed using Mössbauer spectroscopy on ^{57}Fe .

References

- [1] R. Coussement, P. Put, G. Schevemeels and F. Hardeman, Hyp. Int. 23 (1985) 273.
- [2] G. Schevemeels, F. Hardeman, G. Neyens and R. Coussement, Hyp. Int. (1990).
- [3] D.M. Brink and G.R. Satchler in: *Angular Momentum* (Oxford University Press, London, 1968).
- [4] G. Neyens, R. Coussement and J. Odeurs, these proceedings (1st Int. Gamma-Ray Laser Worksh., 1995), Hyp. Int. 107 (1997) 319.
- [5] G. Neyens, R. Coussement, P. Boolchand and W. Bresser, Proc. Int. Conf. on LASERS '94, Quebec, Canada.
- [6] P. Boolchand, private communication.

Section 5

Collective Phenomena

Quantum optics with nuclear gamma radiation

G. Neyens¹, R. Coussement and J. Odeurs

*Instituut voor Kern- en Stralingsphysica, University of Leuven, Celestijnenlaan 200D,
B-3001 Leuven, Belgium*

Some features of quantum optics related to inversionless amplification are translated to nuclear systems. Nuclei and nuclear transitions differ in several ways from atomic systems: gamma radiation has a much shorter wavelength (of the order of lattice-distances), nuclear transitions are many orders of magnitude weaker than atomic ones (making nuclear pumping extremely hard), no coherent gamma-ray sources are available to produce bichromatic gamma radiation. All this makes it very hard to merely translate quantum optical results to nuclear systems. We show that under very specific conditions destructive quantum interferences can occur in the nuclear absorption probability, while the stimulated emission probability is not affected. Nuclear level mixing plays a crucial role in this.

1. Introduction

During the past few years, in the field of quantum optics, a lot of work has been dedicated to the study of amplification of radiation without the need for population inversion [1–3]. Several schemes have been presented which may allow for amplification without inversion. In all these mechanisms some hidden inversion can be found: atoms in the excited state interact with the radiation field (leading to stimulated emission), while the lower-level atoms do not (or only partially) absorb the radiation.

In this paper we will present a way in which such hidden inversion can be obtained in a nuclear system. Because nuclear transition probabilities are so small that no efficient pumping mechanisms exist, inversionless amplification is a first step in the long way to achieve gamma-ray lasing. If nuclei from the ground state can be prohibited from interacting with the radiation field, while the field keeps its possibility to stimulate nuclei in the excited state to emit photons, then population inversion is no longer needed to obtain amplification. No matter how small the amount of nuclei in the excited state is, it forms a completely inverted system with respect to the non-interacting ground state. First we will repeat briefly the requirements which have to be fulfilled to obtain destructive interference in the absorption. Then we will show how these strict conditions can be met in a nuclear system, using

¹ This work is supported by the Belgian National Science Foundation (N.F.W.O.).

the principle of mixing of hyperfine levels by applying a combined static electromagnetic interaction.

2. Quantum interferences in nuclear transitions

As nuclear transitions involve high-frequency radiation, we do not have the possibility to use bichromatic radiation as is often proposed in quantum optics [4]. In this sense a real Λ or double- Λ scheme (fig. 1a) is excluded. On the other hand, it is very easy to bring two nuclear hyperfine levels so close in energy, that they can both be resonantly excited by the same photon frequency (fig. 1b). In a simple three-level scheme with a closely spaced doublet in the ground state, the resonant absorption probability to level $|3\rangle$ is given by:

$$\begin{aligned} P_{\text{abs}} &= \left| A_{13} e^{i(\varphi_{13} + \delta_1 t)} + A_{23} e^{i(\varphi_{23} + \delta_2 t)} \right|^2 p_y \\ &= |A_{13}|^2 + |A_{23}|^2 + A_{13} A_{23}^* e^{i(\varphi_{13} - \varphi_{23}) + i\omega_{12} t} + \text{c.c.} \end{aligned} \quad (1)$$

in which φ_{13} and φ_{23} are the relative phases of the initial and final stationary states and $\delta_{1(2)} = \omega - \omega_{31(2)}$ is the detuning of the probe frequency from the $|3\rangle$ to $|1\rangle$ (respectively $|2\rangle$) transition frequency. The interference term is non-zero if both transitions A_{13} and A_{23} fulfill the same selection rules and if the ensemble average does not cancel due to random phase integration. Indeed, if the initial doublet is not prepared in a coherent way, levels $|1\rangle$ and $|2\rangle$ are not phase-locked and the interference term cancels when the ensemble average over random relative phases (with $\varphi_{13} - \varphi_{23} = \varphi_{12}$) is taken:

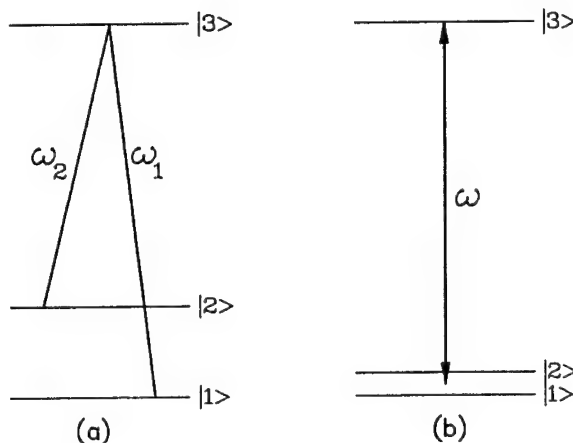


Fig. 1. (a) A Λ -scheme. (b) A closely spaced doublet interacting with a third level via the same photon frequency ω .

$$\int_0^{2\pi} d\varphi_{12} e^{i\varphi_{12}} = 0. \quad (2)$$

Only if the doublet levels are phase-locked, the interference term persists and interference in the nuclear absorption will be possible. Phase locking of the doublet levels can be achieved, for example, by connecting them to a fourth level [3]. If this level is another member of the hyperfine multiplet of the ground state, a low-frequency transition such as an NMR field can be used. The transition probability from level $|i\rangle$ to level $|3\rangle$ is then given by (fig. 2)

$$P_{i3} = |B_{i1}A_{13}e^{i(\varphi_{i1}+\varphi_{13})+i(\Delta_1+\delta_1)t} + B_{i2}A_{23}e^{i(\varphi_{i2}+\varphi_{23})+i(\Delta_2+\delta_2)t}|^2. \quad (3)$$

The only phases left in the interference term will be the detunings of the gamma radiation ($\delta_1 = \omega - \omega_{31}$) and of the low-frequency radiation ($\Delta_1 = \Omega - \omega_{1i}$). However, if we demand that $\Omega + \omega = \omega_{3i}$ then the detunings also drop out and the interference term always exists:

$$P_{i3} = |B_{i1}A_{13}|^2 + |B_{i2}A_{23}|^2 + 2 \operatorname{Re}(B_{i1}A_{13}B_{i2}^*A_{23}^*). \quad (4)$$

In general, we can say that quantum interferences will survive the ensemble averaging only if a closed system is considered: two quantum paths starting from one initial state and ending at the same final state via an intermediate doublet. Complete destructive interference is possible if the interference term cancels the transition probabilities of path 1 and path 2, which is, for example, the case for: $B_{i1} = \pm B_{i2}$ and $A_{13} = \mp A_{23}$ (see eq. (4)). We will show in the next section how these conditions can be fulfilled.

We have now obtained our first goal: the nuclei in the doublet state cannot interact with the gamma radiation field. However, reversibility requires that the inverse transition from $|3\rangle$ to $|i\rangle$ is forbidden too. This is indeed so, but it does not mean that

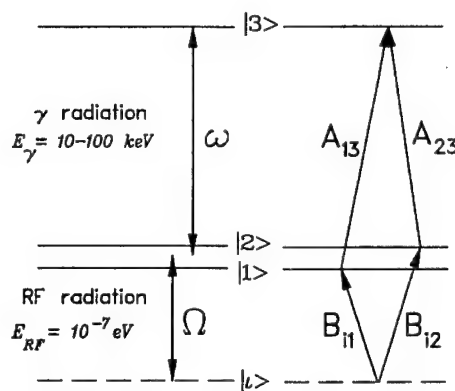


Fig. 2. A four-level scheme in which the first three levels are hyperfine levels of the same nuclear state with spin $I > \frac{1}{2}$ and the upper state is a hyperfine level of an excited state in that nucleus.

stimulated emission from the excited state $|3\rangle$ to the doublet levels is cancelled. What happens is that in both directions, emission and absorption, the first step always occurs and prepares the doublet in a “coherent state” which allows the second step to be cancelled by interference.

The whole process of emission from and absorption to level $|3\rangle$ can be described in a more formal way with the density matrix formalism. Consider a four-level scheme (fig. 2) in which a continuous RF field acts on the three ground-state hyperfine levels $|i\rangle$, $|1\rangle$ and $|2\rangle$ and a gamma radiation field connects the doublet with the excited level $|3\rangle$. The transition matrix elements can be written in the rotating wave approximation as [5]

$$\begin{aligned} H_{1i}^{\text{RF}} &= \frac{\mathcal{R}}{2} B_{1i} (e^{-i\Omega t} + e^{i\Omega t}) \approx \frac{\mathcal{R}}{2} B_{1i} e^{-i\Omega t} & (B_{1i} = B_{i1}), \\ H_{31}^\gamma &= \epsilon_0 A_{31} (e^{-i\omega t} + e^{i\omega t}) \approx \epsilon_0 A_{31} e^{-i\omega t} & (A_{31} = A_{13}). \end{aligned} \quad (5)$$

The evolution of the four-level system can be described by the Liouville operator,

$$-i\hbar \frac{\partial \rho}{\partial t} = [\rho, H], \quad (6)$$

which gives rise to a set of nine coupled differential equations:

$$-i\hbar \frac{\partial \rho_{ii}}{\partial t} = \rho_{i1} H_{1i}^{\text{RF}} - H_{i1}^{\text{RF}} \rho_{i1} + \rho_{12} H_{2i}^{\text{RF}} - H_{i2}^{\text{RF}} \rho_{2i} + i\hbar\gamma\rho_{ii}, \quad (7)$$

$$-i\hbar \frac{\partial \rho_{11}}{\partial t} = \rho_{1i} H_{1i}^{\text{RF}} - H_{1i}^{\text{RF}} \rho_{1i} + \rho_{13} H_{31}^\gamma - H_{13}^\gamma \rho_{31}, \quad (8)$$

$$-i\hbar \frac{\partial \rho_{22}}{\partial t} = \rho_{2i} H_{i2}^{\text{RF}} - H_{i2}^{\text{RF}} \rho_{2i} + \rho_{23} H_{31}^\gamma - H_{23}^\gamma \rho_{32}, \quad (9)$$

$$-i\hbar \frac{\partial \rho_{i1}}{\partial t} = (\rho_{ii} - \rho_{11}) H_{1i}^{\text{RF}} - H_{i1}^{\text{RF}} \rho_{21} + i\hbar(\frac{1}{2}\gamma - i\omega_{1i})\rho_{i1}, \quad (10)$$

$$-i\hbar \frac{\partial \rho_{i2}}{\partial t} = (\rho_{ii} - \rho_{22}) H_{i2}^{\text{RF}} - H_{i2}^{\text{RF}} \rho_{12} + i\hbar(\frac{1}{2}\gamma - i\omega_{2i})\rho_{i2}, \quad (11)$$

$$-i\hbar \frac{\partial \rho_{12}}{\partial t} = \rho_{1i} H_{i2}^{\text{RF}} - H_{i1}^{\text{RF}} \rho_{i2} + \rho_{13} H_{32}^\gamma - H_{13}^\gamma \rho_{32} + \hbar\omega_{21}\rho_{12}, \quad (12)$$

$$-i\hbar \frac{\partial \rho_{33}}{\partial t} = \rho_{31} H_{13}^\gamma - H_{31}^\gamma \rho_{13} + \rho_{32} H_{23}^\gamma - H_{32}^\gamma \rho_{23} + i\hbar\Gamma\rho_{33}, \quad (13)$$

$$-i\hbar \frac{\partial \rho_{13}}{\partial t} = (\rho_{11} - \rho_{33}) H_{13}^\gamma + \rho_{12} H_{23}^\gamma + i\hbar(\frac{1}{2}\Gamma - i\omega_{31})\rho_{13}, \quad (14)$$

$$-\mathrm{i}\hbar \frac{\partial \rho_{23}}{\partial t} = (\rho_{22} - \rho_{33})H'_{23} + \rho_{21}H'_{13} + \mathrm{i}\hbar(\frac{1}{2}\Gamma - \mathrm{i}\omega_{32})\rho_{23}. \quad (15)$$

The natural linewidth of the upper level is Γ and the RF-field has a width γ . The absorption and emission rates are related to the evolution of the upper-level population $\partial\rho_{33}/\partial t$. To solve the four-level problem we will use an approximation: we solve the problem in two consecutive steps, assuming that the level populations in the ground state (levels $|i\rangle$, $|1\rangle$ and $|2\rangle$) are mainly determined by the interaction with the strong RF field. If we neglect the interaction with the gamma radiation in the first step, we can use eqs. (7)–(12) to calculate the absorption rate to the doublet levels and the coherence between them due to the interaction with the RF field. We assume that the level population of the doublet levels is proportional to the absorption rate from level $|i\rangle$ to these levels. Using as initial conditions $\rho_{11}^{t=0} = 0$, $\rho_{22}^{t=0} = 0$, $\rho_{12}^{t=0} = 0$, we find the following results:

$$\begin{aligned} \frac{\partial \rho_{11}}{\partial t} &= \frac{\mathcal{R}^2}{4\hbar^2} \left[\rho_{ii}|B_{1i}|^2 \frac{\gamma}{(\frac{1}{2}\gamma)^2 + \Delta_1^2} \right] \sim \rho_{11}^0 \quad (\text{step 2}), \\ \frac{\partial \rho_{22}}{\partial t} &= \frac{\mathcal{R}^2}{4\hbar^2} \left[\rho_{ii}|B_{2i}|^2 \frac{\gamma}{(\frac{1}{2}\gamma)^2 + \Delta_2^2} \right] \sim \rho_{22}^0 \quad (\text{step 2}), \\ \frac{\partial \rho_{12}}{\partial t} &= \frac{\mathcal{R}^2}{4\hbar^2} \left[\rho_{ii} \frac{B_{1i}B_{i2}}{\frac{1}{2}\gamma - \mathrm{i}\Delta_1} + \rho_{ii} \frac{B_{1i}B_{i2}}{\frac{1}{2}\gamma + \mathrm{i}\Delta_2} \right] \sim \rho_{12}^0 \quad (\text{step 2}). \end{aligned} \quad (16)$$

This result is used as the initial condition for the solution of the second step: the absorption of a gamma-ray by the doublet levels (eqs. (13)–(15)). The absorption rate to level $|3\rangle$ is then given by

$$\begin{aligned} \left(\frac{\partial \rho_{33}}{\partial t} \right)_{\text{abs}} &= \frac{\epsilon_0^2 A_{13}^2}{\hbar^2} \frac{\Gamma}{\frac{1}{4}\Gamma^2 + \delta_1^2} \rho_{11}^0 + \frac{\epsilon_0^2 A_{23}^2}{\hbar^2} \frac{\Gamma}{\frac{1}{4}\Gamma^2 + \delta_2^2} \rho_{22}^0 \\ &\quad + \frac{\epsilon_0^2 A_{13}A_{23}}{\hbar^2} \left[\frac{\Gamma - \mathrm{i}\omega_{12}}{(\frac{1}{2}\Gamma - \mathrm{i}\delta_1)(\frac{1}{2}\Gamma + \mathrm{i}\delta_2)} \rho_{12}^0 + \text{c.c.} \right]. \end{aligned} \quad (17)$$

To calculate the emission from level $|3\rangle$, we use as initial conditions $\rho_{11} = \rho_{22} = \rho_{12} = 0$ and $\rho_{33} = 1$. The emission rate from level $|3\rangle$ is then

$$\left(\frac{\partial \rho_{33}}{\partial t} \right)_{\text{em}} = -\frac{\epsilon_0^2 A_{13}^2}{\hbar^2} \frac{\Gamma}{\frac{1}{4}\Gamma^2 + \delta_1^2} - \frac{\epsilon_0^2 A_{23}^2}{\hbar^2} \frac{\Gamma}{\frac{1}{4}\Gamma^2 + \delta_2^2}. \quad (18)$$

In the emission we don't have any interference while we do have interference in the absorption due to the coherence ρ_{12}^0 of the doublet levels. We can conclude that indeed there is a non-reciprocity between absorption and emission. The interference in the gamma-ray absorption can be constructive or destructive, depending on

the relative phase of the transition matrix elements. In case of destructive interference, the detuning and the level splitting $\hbar\omega_{12}$ of the doublet can be adjusted such that the interference term cancels the total absorption probability. How to create a nuclear system which fulfills the above conditions is explained in the following.

3. Nuclear quantum interference due to level mixing

When a nuclear ensemble is submitted to a static magnetic field B , the hyperfine levels of a nuclear state with spin I are split due to the Zeeman interaction: $H_B = -\mu \cdot B$. A similar thing happens when the nuclei interact with the electric field gradient of a host material. If the host has an axially symmetric electric field gradient (EFG), the quadrupole interaction Hamiltonian can be written as

$$H_Q = \frac{\omega_Q}{\hbar} (3I_z^2 - I^2), \quad (19)$$

in the principal axis system of the electric field gradient. If both interactions are present, we will distinguish two situations [6]: the magnetic field parallel to the axial symmetry axis of the EFG or misaligned by a small angle β .

In the collinear case the Hamiltonian,

$$H_{\parallel} = \frac{\omega_Q}{\hbar} (3I_z^2 - I^2) - \omega_B I_z, \quad (20)$$

is fully axially symmetric and the eigenstates of the combined interaction are the angular momentum eigenstates $|Im\rangle$. As a function of B the energy levels of the system are crossing at well defined values (fig. 3). At (or near) such a level crossing two hyperfine levels are completely (or nearly) degenerate. They can thus be excited by the same photon frequency ω . However, to obtain interferences in the absorption from such a degenerate doublet, it has first to be prepared coherently by a transition from another hyperfine level. This transition has to be with the same photon, so with the same helicity $|\sigma\rangle$. When the photons enter the ensemble in a direction which is non-collinear with the EFG axis, then $\Delta m = +1, 0, -1$ transitions are all possible with the same photon [7]. In some cases, for example when starting from the $|m = -\frac{1}{2}\rangle$ level, both the $|m = +\frac{1}{2}\rangle$ and the $|m = -\frac{3}{2}\rangle$ in the first crossing can be excited resonantly with the same photon helicity $|\sigma\rangle$. Interference can then occur in a subsequent gamma-transition to a hyperfine level in the excited state. However, as the transition amplitudes from both hyperfine levels are proportional to the Clebsch–Gordan coefficients, they are always different, and complete destructive interference is excluded.

In case the EFG axis is non-collinear with the magnetic field direction, the axial symmetry of the stationary system is broken and if β is small, the symmetry-breaking part $\omega_B(I^+ + I^-)/2$ can be regarded as a small perturbation of H_{\parallel} . The perturbation will only change the eigenstates of the Hamiltonian near a level crossing field value B_c (fig. 3, inset). At these crossing fields the eigenstates of the total

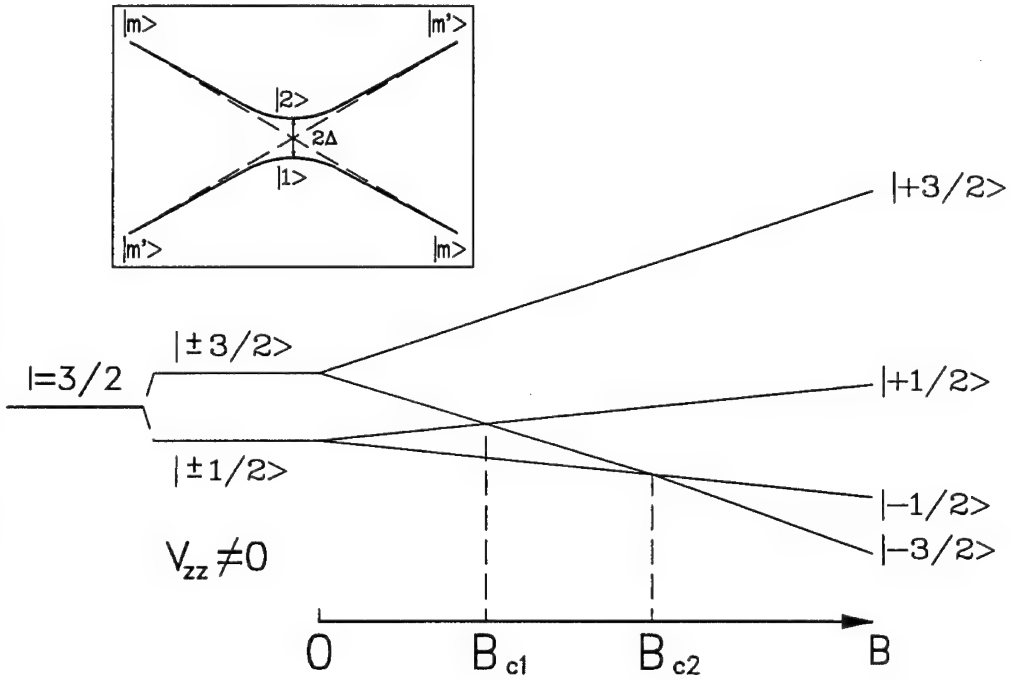


Fig. 3. The hyperfine levels of a nuclear state submitted to a combined static electric and magnetic field are crossing at well defined magnetic field values if both interactions are collinear. If the interactions are slightly misaligned, the pure levels are mixed near a level crossing point (inset).

Hamiltonian are no longer pure, but an in-phase and out-of-phase mixture of the pure crossing levels $|m\rangle$ and $|m'\rangle$:

$$\begin{aligned} |1\rangle &= \frac{1}{\sqrt{2}}(|m\rangle + |m'\rangle) \\ |2\rangle &= \frac{1}{\sqrt{2}}(|m\rangle - |m'\rangle). \end{aligned} \quad (21)$$

The mixed levels $|1\rangle$ and $|2\rangle$ are nearly degenerate and their level splitting Δ can be tuned by changing the misalignment angle: Δ is proportional to $(\sin \beta)^{\Delta m}$, with $\Delta m = |m - m'|$ the order of the mixing [6]. We can show that this doublet of mixed levels fulfills all the conditions to obtain complete destructive interference in the absorption (or the emission) from these levels. Their splitting can be adjusted by tuning the angle β , such that they are within the natural linewidth of the gamma radiation. The selection rules can always be fulfilled for both levels as they contain the same pure m -states. Moreover, if we choose the direction of the gamma radiation such that the transition from $|m'\rangle$ to $|3\rangle$ is allowed and from $|m\rangle$ to $|3\rangle$ forbidden and at the same time make the low-energy transition allowed for $|i\rangle \rightarrow |m\rangle$ and for-

bidden for the $|i\rangle \rightarrow |m'\rangle$ transition, then the conditions in eq. (4) for complete destructive interference in the absorption of the gamma-radiation are fulfilled [8]. In fig. 4 an example of such a situation is given for the second crossing field of fig. 3 (mixing of the $m = -\frac{1}{2}$ and $m' = -\frac{3}{2}$ levels). If $m_i = +\frac{1}{2}$, then with a $|\sigma = \pm 1\rangle$ photon entering non-collinear to the EFG axis, the low-energy transition to $m = -\frac{1}{2}$ is allowed, while the other transition is forbidden. Consequently, we find $B_{i1} = B_{i2}$. Furthermore, if we look to the absorption of a gamma-ray photon in the direction of the EFG axis (for example in a transmission Mössbauer experiment), absorption to a hyperfine level with $m_3 = -\frac{1}{2}$ is forbidden from $m = -\frac{1}{2}$ ($\Delta m = 0$) and allowed from the $m' = -\frac{3}{2}$ level with a $|\sigma = +1\rangle$ photon. In that case $A_{13} = -A_{23}$ and all conditions for complete destructive interference are fulfilled.

4. Co-operative effects in stimulated emission

Now that we have shown that cancellation of the absorption is possible in particular cases, it means that population inversion is no longer needed to obtain amplification of gamma radiation by stimulated emission. A system with a certain percentage of nuclei in the excited state is already enough to obtain more stimulated emission than nuclear absorption. However, the electronic absorption has to be taken into account. Very often the interaction of the gamma radiation with the nuclear ensemble is much weaker than the electronic interactions. If we use, for example, a long-lived isomer both as storage and lasing level [9], the stimulated emission cross section is very small because of the very weak coupling between the gamma radiation and the nuclei. If, however, co-operative effects could play a role, amplification and hence the gain could be enhanced substantially.

Consider an incoming gamma radiation with a resonant (or near-resonant) fre-

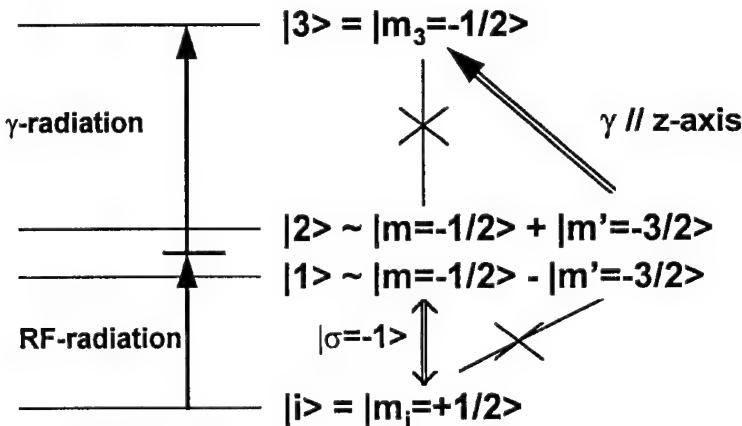


Fig. 4. An example of RF- and gamma-ray transitions in which total destructive interference can be obtained in the gamma-ray absorption probability.

quency interacting with nuclei embedded in a lattice. This radiation interacts with all the nuclei in the ensemble and can stimulate those nuclei that are in the excited state to emit a photon. The initial state of the system, consisting of $n_{k,\sigma}$ incoming photons having wave vector \mathbf{k} and helicity σ and an ensemble of N nuclei in the excited state, can be written as

$$|\psi_i\rangle = |n_{k,\sigma}\rangle \otimes |\psi_e\rangle \equiv |n_{k,\sigma}, \psi_e\rangle, \quad (22)$$

where $|\psi_e\rangle$ is the nuclear state of the ensemble of N excited nuclei. If a photon is produced by stimulated emission, we have the state of the radiation field $|n_{k,\sigma} + 1\rangle$ and the nuclear state $|\psi'_e\rangle$, yet to be specified. The interaction part of the Hamiltonian can be written as [10]

$$H_{\text{int}} = -\frac{1}{c} \int \int \int \mathbf{J} \cdot \mathbf{A} \, d^3r, \quad (23)$$

where \mathbf{J} is the total nuclear current density operator and \mathbf{A} the electromagnetic vector potential. The matrix element describing the transition from $|\psi_i\rangle$ to $|\psi_f\rangle = |n_{k,\sigma} + 1\rangle \otimes |\psi'_e\rangle \equiv |n_{k,\sigma} + 1, \psi'_e\rangle$ is explicitly given by

$$M_{f,i} = -\frac{1}{c} \left\langle n_{k,\sigma} + 1, \psi'_e \left| \int \int \int \mathbf{J} \cdot \mathbf{A} \, d^3r \right| n_{k,\sigma}, \psi_e \right\rangle. \quad (24)$$

The vector potential corresponding to one mode can be written in terms of creation and annihilation operators [11]:

$$\mathbf{A} = \sqrt{\frac{\hbar}{2\epsilon_0\omega_k V}} \epsilon_{k,\sigma} [a_{k,\sigma} e^{-i(\omega_k t - \mathbf{k} \cdot \mathbf{r})} + a_{k,\sigma}^+ e^{i(\omega_k t - \mathbf{k} \cdot \mathbf{r})}]. \quad (25)$$

Because we restrict the discussion to stimulated emission produced by one mode \mathbf{k}, σ of the radiation field, we only have to consider that part of the vector potential containing the creation operator $a_{k,\sigma}^+$. Then

$$M_{f,i} = -\frac{1}{c} \sqrt{\frac{\hbar}{2\epsilon_0\omega_k V}} \times \left\langle n_{k,\sigma} + 1, \psi'_e \left| \int \int \int \mathbf{J} \cdot \epsilon_{k,\sigma} a_{k,\sigma}^+ e^{-i\mathbf{k} \cdot \mathbf{r}} \, d^3r \right| n_{k,\sigma}, \psi_e \right\rangle e^{-i\omega_k t}. \quad (26)$$

This can be simplified to

$$M_{f,i} = -\frac{1}{c} \sqrt{\frac{\hbar}{2\epsilon_0\omega_k V}} \sqrt{n_{k,\sigma} + 1} \int \int \int \mathbf{J}_{e',e}(\mathbf{r}) \cdot \epsilon_{k,\sigma} e^{-i\mathbf{k} \cdot \mathbf{r}} \, d^3r e^{-i\omega_k t}, \quad (27)$$

with $\mathbf{J}_{e',e}(\mathbf{r}) = \langle \psi'_e | \mathbf{J}(\mathbf{r}) | \psi_e \rangle$. This matrix element depends clearly on the form of the initial and final (collective) nuclear state of the ensemble. The total nuclear current operator \mathbf{J} can be written as a sum of currents j_i each belonging to a single nucleus,

$$\mathbf{J} = \sum_{i=1}^N \mathbf{j}_i . \quad (28)$$

The integral in eq. (27) can be written as

$$I = \sum_{i=1}^N \int \int \int \mathbf{j}_{i,\text{e}',\text{e}}(\mathbf{r}) \cdot \boldsymbol{\varepsilon}_{\mathbf{k},\sigma} e^{-i\mathbf{k}\cdot\mathbf{r}} d^3\mathbf{r} . \quad (29)$$

For $|\psi_e\rangle$ one can take the product state,

$$|\psi_e\rangle = \prod_{i=1}^N |\psi_{i,\text{e}}\rangle , \quad (30)$$

where $|\psi_{i,\text{e}}\rangle$ represents the excited state of nucleus i .

If we take for $\psi'_e\rangle$ the state where nucleus m is in the ground state $|\psi_m\rangle$, the other nuclei remaining in the excited state, then

$$|\psi'_e\rangle = |\psi_{1,\text{e}}\rangle \otimes |\psi_{2,\text{e}}\rangle \otimes \dots \otimes |\psi_m\rangle \otimes |\psi_{m+1,\text{e}}\rangle \otimes \dots \otimes |\psi_{N,\text{e}}\rangle . \quad (31)$$

Making use of the fact that $\mathbf{j}_{i,\text{e}',\text{e}}(\mathbf{r}) = 0$ for $i \neq m$, eq. (29) becomes

$$I_m = \int \int \int \mathbf{j}_{m,\text{e}',\text{e}}(\mathbf{r}) \cdot \boldsymbol{\varepsilon}_{\mathbf{k},\sigma} e^{-i\mathbf{k}\cdot\mathbf{r}} d^3\mathbf{r} , \quad (32)$$

where a subscript m has been affected to I .

For the calculation of this integral we can make a translation from the origin to the nuclear mass center \mathbf{r}_m (Fig. 5). Eq. (32) can then be written as

$$I_m = e^{-i\mathbf{k}\cdot\mathbf{r}_m} \int \int \int e^{-i\mathbf{k}\cdot\boldsymbol{\rho}} \mathbf{j}_{m,\text{e}',\text{e}}(\boldsymbol{\rho}) \cdot \boldsymbol{\varepsilon}_{\mathbf{k},\sigma} d^3\boldsymbol{\rho} . \quad (33)$$

We do not know in advance which nucleus m will undergo stimulated emission.

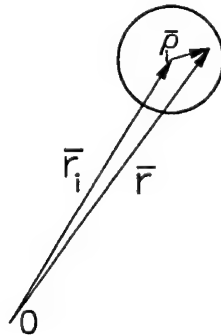


Fig. 5. Definition of the nuclear position and charge distribution vector.

For each nucleus there will be an expression such as the one given by eq. (33). Assuming that the nuclear charge distribution is the same for all initial, respectively final, states, the functions $j_{m,e',e}(\rho)$ are the same for all nuclei. This means that the integral in eq. (33) is the same for all nuclei and the subscript m is not necessary anymore. The only factor that distinguishes the nuclei is $e^{-ik \cdot r_m}$. The final states are all distinguishable, because in principle it is possible to determine which nucleus is in the ground state. This means that, in order to obtain the total probability for stimulated emission, one has to square the absolute value of expressions such as eq. (33) and then add them together:

$$P_{\text{stim em}} \propto N \left| \int \int \int e^{-ik \cdot \rho} j_{e',e}(\rho) \cdot \varepsilon_{k,\sigma} d^3 \rho \right|^2 (n_{k,\sigma} + 1). \quad (34)$$

The probability is just proportional to the number of nuclei involved in the stimulated emission process and to the number of photons present $n_{k,\sigma}$ (the term 1 in the factor $n_{k,\sigma} + 1$ corresponds to spontaneous emission). The electronic absorption rate is also proportional to N , so this case is not favourable as such.

If the final nuclear state would be a delocalized excitation, somewhat analogous to the states introduced recently by Preparata [13], then coherent effects could play an important role as will be sketched below. Suppose the nuclear state is given by

$$\begin{aligned} |\psi'_e\rangle = & \frac{1}{\sqrt{N}} (|\psi_1\rangle \otimes |\psi_{2,e}\rangle \otimes \dots \otimes |\psi_{i,e}\rangle \otimes \dots \otimes |\psi_{N,e}\rangle \\ & + |\psi_{1,e}\rangle \otimes |\psi_2\rangle \otimes \dots \otimes |\psi_{i,e}\rangle \otimes \dots \otimes |\psi_{N,e}\rangle \\ & + \dots + |\psi_{1,e}\rangle \otimes |\psi_{2,e}\rangle \otimes \dots \otimes |\psi_i\rangle \otimes \dots \otimes |\psi_{N,e}\rangle \\ & + \dots + |\psi_{1,e}\rangle \otimes |\psi_{2,e}\rangle \otimes \dots \otimes |\psi_{i,e}\rangle \otimes \dots \otimes |\psi_N\rangle). \end{aligned} \quad (35)$$

The stimulated emission probability (taking into account that this state is weighted by N , as has been done in the incoherent case) is then given by

$$P_{\text{stim em}} \propto \sum_{i,j=1}^N e^{-ik \cdot (r_i - r_j)} \left| \int \int \int e^{-ik \cdot \rho} j_{e',e}(\rho) \cdot \varepsilon_{k,\sigma} d^3 \rho \right|^2 (n_{k,\sigma} + 1). \quad (36)$$

For the large disordered system, only terms with $i = j$ will be retained, all others will give a vanishing contribution due to the randomness of the relative nuclear positions, and one has

$$\sum_{i,j=1}^N e^{-ik \cdot (r_i - r_j)} = N. \quad (37)$$

In a single crystal, terms with $i \neq j$ can contribute to the stimulated emission probability, provided that the gamma rays are coming in under a well defined angle with respect to $r_i - r_j$. If k coincides with a reciprocal lattice vector [14], then

$$\sum_{i,j=1}^N e^{-ik \cdot (r_i - r_j)} = N^2. \quad (38)$$

The stimulated emission probability is then proportional to

$$P_{\text{stim em}} \propto N^2 \left| \int \int \int e^{-ik \cdot p} j_{e', e}(p) \cdot \epsilon_{k, \sigma} d^3 p \right|^2 (n_{k, \sigma} + 1). \quad (39)$$

In this case the co-operative interaction of the N nuclei gives a stimulated emission probability which is proportional to N^2 , so that the stimulated emission can be much stronger than electronic absorption.

Eq. (35) is just one of the possible coherent nuclear states [13]. A complete analysis should take into account the distribution of final states as well as their symmetries. This needs further investigation.

5. Conclusions

We have shown that nuclear level mixing can provide a means to create a nuclear system in which the absorption of gamma radiation of a specific frequency, polarization and direction can be cancelled by destructive interference. Among the many possible applications, inversionless amplification of gamma radiation is the first which crosses our mind. However, other effects such as electronic absorption of gamma rays may still make gain impossible. To cope with these problems, we will have to use the fact that nuclei in a lattice can interact co-operatively with the radiation field. In this way, the emitted radiation could be enhanced considerably.

References

- [1] S.E. Harris, Phys. Rev. Lett. 62 (1989) 1033.
- [2] M.O. Scully, Phys. Rep. 219 (1992) 191.
- [3] O. Kocharovskaya, Phys. Rep. 219 (1992) 175.
- [4] O. Kocharovskaya and P. Mandel, Phys. Rev. A42 (1990) 523.
- [5] P. Meystre and M. Sargent, in: *Elements of Quantum Optics* (Springer, Berlin, Heidelberg, 1990).
- [6] R. Coussement, P. Put, G. Schevemeels and F. Hardeman, Hyp. Int. 23 (1985) 273.
- [7] R. Coussement and G. Neyens, these proceedings (1st Int. Gamma-Ray Laser Worksh., 1995), Hyp. Int. 107 (1997) 307.
- [8] R. Coussement, M. Van Den Bergh, G. S'heeren, G. Neyens, R. Nouwen and P. Boolchand, Phys. Rev. Lett. 71 (1993) 1824.
- [9] R. Coussement, G. S'heeren, M. Van Den Bergh and P. Boolchand, Phys. Rev. B45 (1992) 9755.

-
- [10] A. deShalit and H. Feshbach, in: *Theoretical Nuclear Physics, Volume 1: Nuclear Structure* (Wiley, New York, Chichester, Toronto, 1990).
 - [11] R. Loudon, in: *The Quantum Theory of Light* (Clarendon Press, Oxford, 1986).
 - [12] L. Mandel and E. Wolf, in: *Optical Coherence and Quantum Optics* (Cambridge University Press, Cambridge, New York, Melbourne, 1995).
 - [13] G. Preparata, in: *QED Coherence in Matter* (World Scientific, Singapore, 1995).
 - [14] N.W. Ashcroft and N.D. Mermin, in: *Solid State Physics* (Holt, Rinehart and Winston, New York, 1976).

Two-photon cooperative emission in the presence of a thermal electromagnetic field

N.A. Enaki^a and D. Mihalache^b

^a Institute of Applied Physics, Academy of Sciences of Moldova, 277028 Chisinau, Moldova

^b Institute of Atomic Physics, R-76900, Magurele, Bucharest, Romania

The possibility of cooperative spontaneous two-photon emission of an extended radiators system and the influence of the external thermal electromagnetic field on the spontaneous emission rate, in such a system, are investigated. It is concluded that, in an external electromagnetic field, the two-photon cooperative emission rate increases significantly. The importance of this effect on the emission of gamma rays from inverted long-lived isomers triggered by X-ray thermal fields, is emphasized.

1. Introduction

Superradiant emission is a cooperative process involving collective modes of the inverted radiators system (nuclei, atoms) [1–3]. It is very well known that superradiance is a collective spontaneous decay which occurs as a result of mutual phase influence of separated inverted dipoles of a system during spontaneous emission. In this case, the radiation intensity becomes proportional to the square of the number of inverted radiators. An important mechanism for coherent emission in the gamma spectrum region is the superradiant emission of photons [3–5]. It is interesting to investigate the behaviour of superradiance in the case when the distance between the nuclei (atoms) is greater or equal to the wavelength of the radiation field. In this situation, the diffraction-type function, which represents the exchange integral between the radiators, oscillates as a function of the distance and the geometry of the sample plays an important role [1–3].

The new cooperative emission phenomenon for a dipole forbidden transition of inverted radiators can be observed in the process of two-photon spontaneous emission [6]. In this paper it will be shown that, in the spontaneous emission process, the radiators enter the regime of two-photon superradiance and the collective rate of photon pairs (biphotons) increases proportionally to the square number of radiators. We have studied the conditions under which a concentrated sample of radiators with dimension less than the radiation wavelength goes into the regime of two-photon cooperative emission relative to the forbidden transition $|2\rangle - |1\rangle$, where $|2\rangle$ and $|1\rangle$ are the excited and ground states, respectively (fig. 1). It was demonstrated [6] that, in processes of spontaneous emission of hydrogen-like or helium-

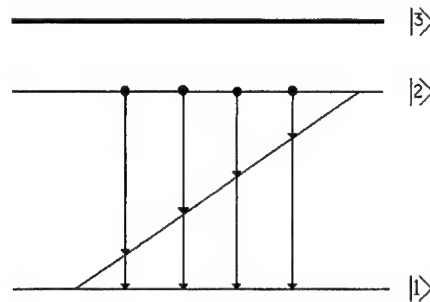


Fig. 1. Possible two-photon spontaneous emission processes for dipole forbidden transitions $|2\rangle - |1\rangle$.

like atoms, the dipole forbidden transitions $2^2S_{1/2} - 1^1S_{1/2}$ or $2^2S_0 - 1^1S_0$ generate pairs of correlated photons (biphotons). The correlation function between the pairs of photons becomes larger than the correlation function between the individual photons from different pairs.

In this paper the behaviour of the two-photon correlations between the radiators (nuclei), either in the presence or in the absence of a thermal electromagnetic field (EMF), is studied. This thermal EMF plays a similar role as the X-ray field in the excitation problems of short lifetime level $|3\rangle$ lying above the isomeric inverted state in nuclei (see figs. 1 and 2). The two-photon transitions are very frequently observed in nuclei [7,8]. The two-photon cooperative phenomenon could play an important role for gamma coherent emission. In the case of excitation of isomeric nuclei with X-ray thermal source a strong correlation between X-ray and gamma-ray photons can occur. The second-order coherence function between the X-ray and gamma-ray photons can become larger than the first-order function. The rate of two-photon transitions between the upper and ground dipole forbidden states

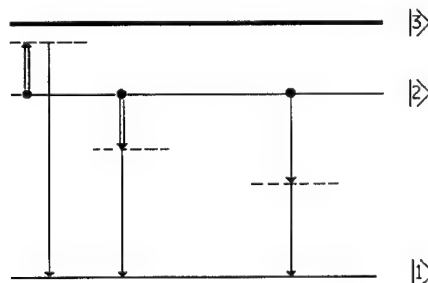


Fig. 2. Possible processes of spontaneous transitions of excited nuclei to the ground state $|1\rangle$. The double lines denote photons of the external thermal EMF, and the single lines correspond to spontaneous created photons.

depends not only on the square of the number of radiators (nuclei) but also on the intensity and frequency of the external X-ray source.

In the second section we derive a master equation for the density matrix of the radiator subsystem for two-photon interaction with an external thermal EMF. In section 3, by using a semiclassical method for the uncoupled chain of equations, a theory of two-photon superradiance stimulated by the thermal EMF in cylindrical samples is proposed. It is demonstrated that the second-order correlation describes the coherence phenomena between the biphotons. In this case the first-order coherent function is very small. In the last section the possibility of experimental observation of collective two-photon emission is suggested.

2. Master equation for the nuclei subsystem density matrix

We consider N inverted radiators relative to the forbidden transition $|2\rangle - |1\rangle$. In this situation the transition between the excited state $|2\rangle$ and the ground state $|1\rangle$ takes place via the intermediate state $|3\rangle$ (see figs. 1 and 2). The Hamiltonian of the extended system of N radiators is:

$$H = H_0 + H_i, \quad (1a)$$

$$H_0 = \sum_{\alpha=1}^3 \sum_{j=1}^N \hbar\omega_\alpha U_{j\alpha}^\alpha + \sum_k \hbar\omega_k a_k^+ a_k, \quad (1b)$$

$$H_i = \sum_{\beta=1}^2 \sum_{j=1}^N (d_{3\beta}, E(r_j)) (U_{j\beta}^\beta + U_{j\beta}^3). \quad (1c)$$

Here $\hbar\omega_\alpha$ is the energy of α radiator level, $d_{3\beta}$ is the dipole moment of the transition between the second excited state $|3\rangle$ and the state $|\beta\rangle$, while $E(r, t) = E^-(r, t) + E^+(r, t)$ is the electric field strength,

$$\begin{aligned} E^+(r_j, t) &= -i \sum_k g_k a_k^+ \exp[-i(k, r_j)], \\ E^-(r_j, t) &= (E^+(r_j, t))^+. \end{aligned} \quad (2)$$

a_k^+ and a_k are the creation and annihilation operators for photons with momentum k , energy ω_k and polarization λ , $g_k = (2\pi\omega_k/V)^{1/2} e_\lambda$ is the photon polarization vector, V is the EMF quantization volume, $U_{j\beta}^3$ is the corresponding matrix of the transition between states $|3\rangle$ and $|\beta\rangle$ of the j -th atom. The operators $U_{j\beta}^\alpha$ satisfy the commutation relations:

$$[U_{l\beta}^\alpha, U_{j\beta'}^{\alpha'}] = \delta_{lj} (\delta_{\beta,\beta'} U_{j\beta'}^\alpha - \delta_{\alpha,\alpha'} U_{j\beta'}^{\alpha'}), \quad (3)$$

The behaviour of the second-order coherence processes between the photon pairs can be studied by the second-order correlation function [9,10]:

$$K_2(\mathbf{r}, t, \tau') = \langle : (\mathbf{E}^-(\mathbf{r}, t), \mathbf{E}^+(\mathbf{r}, t)) (\mathbf{E}^-(\mathbf{r}, t - \tau), \mathbf{E}^+(\mathbf{r}, t - \tau)) : \rangle,$$

which describes the correlation between the EMF densities at the time moments t and $t - \tau$. The time dependence of quantum fluctuations of EMF density can be investigated with the following formula:

$$\Lambda^2(\mathbf{r}, t, \tau) = K_2(\mathbf{r}, t, \tau) - K_1(\mathbf{r}, t)K_1(\mathbf{r}, t - \tau). \quad (4)$$

Here $K_1(\mathbf{r}, t) = \langle (\mathbf{E}^-, \mathbf{E}^+) \rangle$ is the EMF density at the observation point \mathbf{r} .

A chain of equations describing the possibility of the transition of a radiator ensemble into the two-photon superradiance regime was obtained in refs. [6,10] for the nuclei operators $U_{i\beta}^\alpha$ from the correlation functions by the method of excluding the EMF operators a_k^+ and a_k . The elimination of the boson operators from the chain of equations is, however, somewhat difficult, since this procedure must be employed in each new chain of equations for the nuclei-subsystem correlators. It is therefore of interest to obtain a master equation for the density matrix of a radiator subsystem from which the EMF boson operators have already been excluded. We derive below, by the method of projection operators, a master equation for the density matrix of a radiator subsystem in an external thermal field (X-ray field). The equation for the density matrix of a total “atoms + field” system takes in the interaction representation the form:

$$i \frac{\partial \rho(t)}{\partial t} = \frac{1}{\hbar} [H_i(t), \rho(t)], \quad (5)$$

where

$$H_i(t) = \exp \left\{ \frac{i}{\hbar} H_0 t \right\} H_i \exp \left\{ - \frac{i}{\hbar} H_0 t \right\}. \quad (6)$$

Let P be the projection operator for the complete density matrix $\rho(t)$ in the basis of free EMF:

$$\rho_s(t) = P\rho(t), \quad \rho_b(t) = \tilde{P}\rho(t), \quad (7)$$

where ρ_s is the slow part of the density matrix $\rho(t)$, ρ_b is its rapidly oscillating part and $\tilde{P} = 1 - P$. The operator P has the properties $P^2 = P$ and $P\tilde{P} = 0$. The equations for the matrices $\rho_s(t)$ and $\rho_b(t)$ are

$$\frac{\partial}{\partial t} \rho_s(t) = -i\lambda PL_i(t)(\rho_s(t) + \rho_b(t)), \quad (8a)$$

$$\frac{\partial}{\partial t} \rho_b(t) = -i\lambda \tilde{P}L_i(t)(\rho_s(t) + \rho_b(t)), \quad (8b)$$

where

$$\lambda L_i(t) = [H_i(t), \dots] / \hbar.$$

Following the known procedure for eliminating the rapidly oscillating part of a density matrix, we integrate eq. (8b) with respect to $\rho_b(t)$ and substitute the resultant solution in eq. (8a), which becomes:

$$\frac{\partial}{\partial t} \rho_s(t) = -\lambda^2 P \int_0^t d\tau L_i(t) U(t, t-\tau) L_i(t-\tau) \rho_s(t-\tau), \quad (9)$$

where

$$U(t, t-\tau) = T \exp \left\{ -i\lambda \tilde{P} \int_{t-\tau}^t d\tau_1 L_i(\tau_1) \right\}.$$

Recognizing that for $t = 0$ an ensemble of radiators does not interact with the EMF, we define the operator P as:

$$P = \rho_{ph}(0) * Sp_{ph}\{\rho_{ph}(0) \dots\},$$

where $\rho_{ph}(0) = A^{-1} \exp\{-\omega_{k_0} a_{k_0}^\dagger a_{k_0} / k_b T\} \prod_{k \neq k_0} |O_k\rangle \langle O_k|$ is the density matrix of the single-mode external EMF, k_b is the Boltzmann constant, and T is the temperature of photons in the mode k_0 , $|O_k\rangle \langle O_k|$ is the vacuum state of mode k . In this paper we consider that $\omega_0 \ll \omega_{12}$. With allowance for the foregoing, it can be shown that

$$PH_i(t)P = 0, \quad \rho_s(t) = \rho_{ph}(0)W(t),$$

where $W(t)$ is the density matrix of the atomic subsystem.

Restraining ourselves to the second order of the expansion in the small parameter $\lambda(\rho_s(t-\tau) \approx \rho_s(t), U(t, t-\tau) = 1)$, we obtain the zero contribution on two-photon transition processes. The two-photon spontaneous emission processes can be taken into account in the fourth order of the expansion in the small parameter on the right-hand side of eq. (9). To this end, we represent the evolution operator U and the density matrix ρ in the form:

$$U(t, t-\tau) \cong 1 - i\lambda \tilde{P} \int_{t-\tau}^t d\tau_1 L_i(\tau_1) + (i\lambda)^2 \int_{t-\tau}^t d\tau_1 \tilde{P} L_i(\tau_1) \int_{t-\tau}^{\tau_1} d\tau_2 \tilde{P} L_i(\tau_2), \quad (10a)$$

$$\begin{aligned} \rho_s(t-\tau) &= \rho_s(t) + \lambda^2 P \int_0^t d\tau_1 L_i(t-\tau_1) \int_0^{t-\tau_1} d\tau_2 L_i \\ &\times (t-\tau_1-\tau_2) \rho_s(t-\tau_1-\tau_2). \end{aligned} \quad (10b)$$

Upon substitution of eq. (10) in eq. (8) the equation for $\rho_s(t)$ becomes:

$$\frac{\partial}{\partial t} \rho_s(t) = -\lambda^4 \int_0^t d\tau_1 \int_0^{\tau_1} d\tau_2 \int_0^{\tau_2} d\tau_3 P L_i(t) L_i(\tau_1) L_i(\tau_2) L_i(\tau_3) \rho_s(\tau_3). \quad (11)$$

We average next eq. (11) over the EMF states (taking into account the explicit form of the operator P). Neglecting, thus, the retardation in the slow part ρ_s of the density matrix and separating the basic diagrams of the transition, we obtain the following master equation for the radiator-subsystem density matrix:

$$\frac{\partial}{\partial t} W(t) = -\frac{1}{2} \sum_{j=1}^N \sum_{l=1}^N \gamma_{jl} \left\{ [U_{j1}^2, U_{l2}^1 W(t)] + \text{h.c.} \right\}, \quad (12)$$

where

$$\gamma_{jl} = \gamma_{jl}^1 + \gamma_{jl}^2, \quad (13)$$

$$\begin{aligned} \gamma_{jl}^1 &= \frac{\pi}{\hbar^4} \sum_{k_1} \sum_{k_2} \exp[i(\mathbf{k}_1, \mathbf{r}_j - \mathbf{r}_l)] * \exp[-i(\mathbf{k}_1, \mathbf{r}_j - \mathbf{r}_l)] \{2N_{k_0} \cdot \delta_{k_0, k_1} + 1\} \\ &\quad * \delta(\omega_{k_1} + \omega_{k_2} - \omega_{21}) \frac{(\omega_{31} + \omega_{32})^2}{(\omega_{31} - \omega_{k_1})^2 (\omega_{32} + \omega_{k_1})^2} (\mathbf{d}_{31}, \mathbf{g}_{k_2})^2 (\mathbf{d}_{31}, \mathbf{g}_{k_1})^2 + \text{h.c.}, \end{aligned} \quad (14a)$$

$$\begin{aligned} \gamma_{jl}^2 &= \frac{\pi}{\hbar^4} \sum_k \exp[i(\mathbf{k}, \mathbf{r}_j - \mathbf{r}_l)] * \exp[-i(\mathbf{k}_0, \mathbf{r}_j - \mathbf{r}_l)] N_{k_0} \\ &\quad * \delta(\omega_k + \omega_0 - \omega_{21}) \frac{(\omega_{31} + \omega_{32})^2}{(\omega_{31} + \omega_0)^2 (\omega_{32} - \omega_0)^2} (\mathbf{d}_{31}, \mathbf{g}_{k_0})^2 (\mathbf{d}_{31}, \mathbf{g}_k)^2 + \text{h.c.} \end{aligned} \quad (14b)$$

$N_{k_0} = \langle a_{k_0}^\dagger a_{k_0} \rangle = \{\exp(\hbar\omega_0/k_b T) - 1\}^{-1}$ is the number of external thermal photons in the mode k_0 , $\omega_{3\alpha} = \omega_3 - \omega_\alpha$ ($\alpha = 1, 2$). The operators U_{j1}^2 and U_{l2}^1 take into account the cooperative two-photon transitions between the dipole forbidden states of radiators. The function γ_{jl} is the two-photon exchange interference integral between the j and l radiators which describes the cooperative amplification of the spontaneous rate. All possible two-photon processes of spontaneous emission from the upper state $|2\rangle$ to the ground state $|1\rangle$ are presented in fig. 2. In the absence of the external field N_{k_0} the functions $\gamma_{jl}^2 = 0$ and γ_{jl}^1 take into account only the correlations between radiators i and j through the two-photon vacuum of EMF. Two-photon superradiance between the upper and the ground states in this situation is possible (see fig. 1). In the presence of an external EMF the probability of two-photon transition increases significantly. It is not difficult to show that the two-photon scattering of the thermal field increases when the number of photons in the mode k_0 is large and the frequency ω_0 is near resonance with level $|3\rangle$. In this situation the factor $N_{k_0}/(\omega_{32} - \omega_0)^2$ in the expression (14b) approaches a large value.

3. Two-photon superradiance and the correlation functions for an EMF

From the master equation (12) it is not difficult to obtain the following equation for the number of excited radiators:

$$\frac{d\langle U_2^2(t) \rangle}{dt} = - \sum_{j=1}^N \sum_{l=1}^N \gamma_{jl} \langle U_{j1}^2(t) U_{l2}^1(t) \rangle. \quad (15)$$

We consider two cases: A) the external field is absent and two-photon cooperative emission is possible; B) the external thermal field (X-ray field) is very strong so that $k_b T \gg \omega_0 \hbar$.

A. In the absence of an external thermal field ($N_{k_0} = 0$) it is not difficult to obtain, from eq. (14a), the following exchange two-photon interference integral:

$$\begin{aligned} \gamma_{ij}^0 = & \frac{2^3}{\pi \hbar^2 c^6} \int_0^{\omega_{21}} dx_1 x_1^3 \int_0^{\omega_{21}} dx_2 x_2^3 \delta(x_1 + x_2 - \omega_{21}) \\ & \times \frac{d_{31}^2 d_{32}^2 (\omega_{31} + \omega_{32})^2}{(\omega_{31} - x_1)^2 (\omega_{32} + x_1)^2} F_{ij}(x_1) F_{ij}(x_2), \end{aligned} \quad (16)$$

where

$$\begin{aligned} F_{ij}(x) = & [1 - (\mathbf{n}_d, \mathbf{n}_{ij})^2] \frac{\sin(xr_{ij}/c)}{xr_{ij}/c} + [1 - 3(\mathbf{n}_d, \mathbf{n}_{ij})^2] \\ & \times \left\{ \frac{\cos(xr_{ij}/c)}{(xr_{ij}/c)^2} - \frac{\sin(xr_{ij}/c)}{(xr_{ij}/c)^3} \right\}, \end{aligned}$$

$$\mathbf{n}_d = \frac{\mathbf{d}_{3\alpha}}{d_{3\alpha}}, \quad \mathbf{n}_{ij} = \frac{\mathbf{r}_i - \mathbf{r}_j}{|\mathbf{r}_i - \mathbf{r}_j|}.$$

Such a two-photon cooperative generation may be produced by the nuclei which have a short-lived (about 10^{-6} s) excited isomeric state (see fig. 1). Using the method of excluding the EMF boson operators developed in refs. [6,9,10] we obtain the following expression for the second-order correlation function:

$$\begin{aligned} K_2(r, t, \tau) = & \frac{d_{31}^2 d_{32}^2 [1 - (\mathbf{n}_r, \mathbf{n}_d)^2]^2}{4\pi^2 r^4 c^{12}} \left\{ \int_0^{\omega_{21}} x^2 (\omega_{21} - x)^2 dx \frac{(\omega_{31} + \omega_{32}) \exp(-ix\tau)}{(\omega_{31} - x)(\omega_{32} + x)} \right\} \\ & * \left\{ \int_0^{\omega_{21}} y^2 (\omega_{21} - y)^2 dy \frac{(\omega_{31} + \omega_{32}) \exp(+iy\tau)}{(\omega_{31} - y)(\omega_{32} + y)} \right\} \\ & \times \sum_j^N \sum_l^N \cos[\omega_{21}(|\mathbf{r} - \mathbf{r}_j| - |\mathbf{r} - \mathbf{r}_l|)] * \langle U_{j1}^2(t_r) U_{l2}^1(t_r) \rangle, \end{aligned} \quad (17)$$

where $\mathbf{n}_r = \mathbf{r}/n$, $\mathbf{n}_d = \mathbf{d}_{3\alpha}/d_{3\alpha}$, $\alpha = 1, 2$, $t_r = t - r/c$. In eq. (17) it was supposed that $r \gg r_{ij}$.

For simplicity, we will consider a concentrated system of nuclei with dimensions much smaller than the minimum radiation wavelength. In this situation the Bloch vector is conserved:

$$R^2 = R_z^2 + \frac{1}{2} \{ U_1^2 U_2^1 + U_2^1 U_1^2 \}, \quad \text{where } U_\beta^\alpha = \sum_j U_{j\beta}^\alpha, \quad R_z^N = U_2^2 - U_1^1. \quad (18)$$

From eqs. (15) and (18) we therefore obtain the following expression for the population difference of the system

$$\frac{\partial}{\partial t} \langle R_z(t) \rangle = -\frac{1}{\tau_0} \left[\langle R_z(t) \rangle - \frac{N}{2} \right] + \frac{1}{\tau_0} \left[\langle R_z(t) \rangle^2 - \frac{N^2}{4} \right],$$

whose solution is well-known in one-photon superradiance theory [1,2]:

$$\langle R_z(t) \rangle = -\frac{N}{2} \operatorname{th} \left[\frac{t - t_0}{2\tau_r} \right], \quad (19)$$

where $t_0 = \tau_r \ln N$ is the delay of the collective radiation pulse of the photon pair and $\tau_r = \tau_0/N$ is the collectivization time of the ensemble of atoms from two-photon spontaneous decay of the $|2\rangle$ excited state, τ_0 is the two-photon spontaneous decay time of the level $|2\rangle$,

$$\frac{1}{\tau_0} = \frac{1}{\pi \tau_{31} \tau_{31}} \frac{\omega_{32} + \omega_{31}}{\omega_{31}^3 \omega_{32}^3} \int_0^{\omega_{21}} dx \frac{x^3 (\omega_{21} - x)^3}{(\omega_{31} - x)^2 (\omega_{32} + x)};$$

$$\tau_{3\alpha} = 3\hbar c^3 / 4\omega_{3\alpha}^3 d_{3\alpha}^2; \quad \alpha = 1, 2.$$

It follows from eq. (19) that the ensemble of atoms collectively emits photon pairs in the interval $(0, \omega_{12})$ with a total energy $\hbar(\omega_{k1} + \omega_{k2}) = \hbar\omega_{21}$ (see fig. 1). The emission rate of such photon pairs is equal to:

$$V_{21} = -\frac{\partial}{\partial t} R_z(t) = \frac{N}{4\tau_r} \operatorname{sech}^2 \left[\frac{t - t_0}{2\tau_r} \right]. \quad (20)$$

Using the method of excluding the EMF operators a_k^+ and a_k [6], we obtain for the quantum fluctuation of the EMF the following expression:

$$\Lambda^2(r, t, 0) = \frac{7\hbar^2 \omega_{21}^3 N^2}{15 \times 2^7 \pi c^2 r^4 \tau_0} \operatorname{sech}^2 \left[\frac{t_r - t_0}{2\tau_r} \right] \left\{ 1 - \frac{9N^2}{7\omega_{21}\tau_0} \operatorname{sech}^2 \left[\frac{t_r - t_0}{2\tau_r} \right] \right\}. \quad (21)$$

The second term in eq. (21) describes the behaviour of the square of the EMF density in the point r . As follows from eq. (21) the second-order density correlation function $K_2(r, t, \tau = 0)$ is greater than $K_1^2 (K_2 \approx \Lambda^2)$ and this function describes the density of biphotons in the observation point r . The density of photon pairs in the point r decreases inversely proportional to r^4 .

B. In the presence of an external thermal field two-photon cooperative scattering

processes are possible in which thermal photons are created or annihilated (see fig. 2). In this situation the lifetime of the isomeric state $|3\rangle$ may be larger than the similar one in case A. For the concentrated system of atoms we obtain similar solutions to eqs. (19) and (20). The cooperative time of two-photon emission is $\tau_c = \tau_r \tau_d / (\tau_r + \tau_d)$, where the cooperative scattering time is defined as:

$$\frac{1}{\tau_d} = 2N_{k0}(\mathbf{g}_{k_0}, \mathbf{d}_{32})(\mathbf{g}_{k_0}, \mathbf{d}_{31}) \frac{4\pi d_{31}d_{32}N}{3\hbar^3 c^3} \\ \times \left[\frac{(\omega_{31} + \omega_{32})^2(\omega_{21} + \omega_0)^3}{(\omega_{31} + \omega_0)^2(\omega_{32} - \omega_0)^2} + \frac{(\omega_{31} + \omega_{32})^2(\omega_{21} - \omega_0)^3}{(\omega_{31} - \omega_0)^2(\omega_{32} + \omega_0)^2} \right]. \quad (22)$$

If the external EMF is strong ($k_b T \gg \hbar\omega_0$) and the frequency ω_0 is near resonance, $\omega_0 \sim \omega_{32}$, the cooperative time τ_c is equal to τ_d . In this case, two-photon spontaneous decay can be neglected (see fig. 1) and the more simple exchange two-photon interference integral γ_{jl}^c can be obtained from eqs. (14a) and (14b):

$$\gamma_{jl}^c = \gamma_{jl}^s + \gamma_{jl}^a; \\ \gamma_{jl}^s = 2 \frac{d_{31}^2 d_{32}^2 g_{k0}^2}{\hbar^3 c^3} \cos(\omega_0 r_{ij}/c) \frac{(\omega_{21} - \omega_0)^3 (\omega_{31} + \omega_{32})^2}{(\omega_{31} - \omega_0)^2 (\omega_{32} + \omega_0)^2} F_{lj}(\omega_s); \quad (23a)$$

$$\gamma_{jl}^a = 2 \frac{d_{31}^2 d_{32}^2 g_{k0}^2}{\hbar^3 c^3} \cos(\omega_0 r_{ij}/c) \frac{(\omega_{21} + \omega_0)^3 (\omega_{31} + \omega_{32})^2}{(\omega_{31} + \omega_0)^2 (\omega_{32} - \omega_0)^2} F_{lj}(\omega_a); \quad (23b)$$

where $\omega_s = \omega_{21} - \omega_0$, $\omega_a = \omega_{21} + \omega_0$. This exchange integral is similar to the one-photon exchange integral and in this situation we can find the behaviour of the inverted system of radiators for cylindrical samples with sizes greater than the radiation wavelength λ . Using the master equation (12) one obtains the following equation for the correlator $\langle U_{l1}^2(t) U_{j2}^1(t) \rangle$:

$$\frac{\partial}{\partial t} \sum_{l=1}^N \sum_{j=2}^N \gamma_{lj}^c \langle U_{l1}^2(t) U_{j2}^1(t) \rangle = \sum_{l=1}^N \sum_{j=2}^N \sum_{m=1}^N \{ \gamma_{lj}^c \gamma_{lm}^c \langle U_{m1}^2(t) R_{lz}(t) U_{j2}^1(t) \rangle \\ + \gamma_{lj}^c \gamma_{jm}^c \langle U_{l1}^2(t) R_{jz}(t) U_{m2}^1(t) \rangle \}. \quad (24)$$

Neglecting the fluctuations of the population difference operator, R_{lz} we decouple the chain of eqs. (15) and (24) as follows:

$$\langle U_{m1}^2(t) R_{lz}(t) U_{j2}^1(t) \rangle|_{l \neq j} = \langle U_{m1}^2(t) U_{j2}^1(t) \rangle \langle R_{lz}(t) \rangle. \quad (25)$$

The main suppositions consist of the following: (a) the mean distance between the radiators of the system is less than $\lambda_{s(a)} = 2\pi/k_{s(a)}$; (b) the population difference of the radiators of the system $R_{iz} = U_{iz}^2 - U_{il}^1$ is independent of their location in the system; (c) the sample size is larger than $\lambda_{s(a)}$. In this situation we can represent the summation over j in eq. (24) in the following approximation [12]:

$$\Phi_{lm} = \sum_{j=1}^N \gamma_{lj}^c \gamma_{jm}^c \langle R_{lz}(t) \rangle \cong \left\{ \frac{1}{\tau_{0s}} \gamma_{lm}^s D_s + \frac{1}{\tau_{0a}} \gamma_{lm}^a D_a \right\} \langle R_z(t) \rangle, \quad (26)$$

where

$$\frac{1}{\tau_s} = 2N_{k_0}(\mathbf{g}_{k_0}, \mathbf{d}_{32})(\mathbf{g}_{k_0}, \mathbf{d}_{31}) \frac{4\pi d_{31} d_{32}}{3\hbar^3 c^3} \frac{(\omega_{31} + \omega_{32})^2 (\omega_{21} - \omega_0)^3}{(\omega_{31} - \omega_0)^2 (\omega_{32} + \omega_0)^2}, \quad (27)$$

$$D_\beta = \begin{cases} \frac{\lambda_\beta^2}{2\pi^2 S^2}, & \text{for } F \sim 1, \\ \frac{1}{R_\beta L}, & \text{for } F \ll 1, \end{cases} \quad \beta = s, a, \quad (28)$$

$F = \pi S/(L\lambda)$ is the Fresnel number, and L and S are the length and the cross section, respectively, of the cylinder.

When the frequency of the external thermal field (X-ray field) lies near the resonance with level $|3\rangle$ ($\omega_{21}/(\omega_{32} - \omega_0) \gg 1$), the first term in eq. (26) becomes smaller than the second one ($\tau_a \ll \tau_s$). In this situation the generation of gamma photons with frequency $\omega_a = \omega_{21} + \omega_0$ is more probable. From eqs. (15) and (24) we obtain the following equation for the inversion $\langle R_z(t) \rangle = J_z(t)$:

$$\frac{\partial^2}{\partial t^2} J_z(t) = -\frac{1}{\tau_a} \frac{\partial}{\partial t} J_z(t) + \frac{2N}{\tau_a} D_a J_z(t) \frac{\partial}{\partial t} J_z(t) + \frac{2N}{\tau_a^2} D_a J_z(t) [J_z(t) + \frac{1}{2}]. \quad (29)$$

The solution of eq. (28), near the maximum of two-photon superradiance, can be represented as:

$$J_z(t) = -\frac{N}{2} \text{th} \left[\frac{t - t_0}{\tau_r^e} \right], \quad \tau_r^e = \tau_a / (D_a N). \quad (30)$$

We neglected in eq. (25) the quantum fluctuations of the operator R_z . It can be shown, in analogy with the procedure used for one-photon transitions, that for $N \gg 1$ the fluctuations of the operator R_z are smaller than the mean values of the same operators. In one-photon collective processes the approximation (25) is equivalent to neglecting the quantum fluctuations of EMF density. In our problem, neglecting the quantum fluctuations of the above operators is equivalent to neglecting the squared EMF density operator fluctuations at the observation point r . In other words, the separated correlators (25) describe with good accuracy the time behaviour of the EMF density fluctuations $\Lambda(\mathbf{r}, t, \tau)$. This function is proportional to the decay rate $V_{21} = -\partial \langle R(t) \rangle / \partial t$.

4. Conclusions

We proposed the two-photon gamma cooperative generation by isomers excited

with X-ray thermal emission from an appropriate source, such as a pseudospark-like discharge described in more detail in refs. [13–16]. We assumed that the short lifetime level $|3\rangle$ lying above the quasi-isomeric state $|2\rangle$ can be excited from the metastable state $|2\rangle$ by thermal X-ray emission. In this case, a superradiant pulse, stimulated by thermal EMF can be generated. The second-order coherence between gamma-ray and X-ray photons plays an important role in cooperative radiation. A two-photon detector can be used in order to observe experimentally the two-photon cooperative emission. Thus, let us suppose that such a detector consists of a system of two-level nuclei which can be excited by two-photon absorption from the investigated beam. In this case the probability of two-photon absorption is proportional to the second-order correlation function [6]:

$$|\langle 1' | W | 2' \rangle|^2 = \frac{1}{2} \sum_{k_i} (i=1, \dots, 4) w_{k_1 k_3}^* w_{k_2 k_4} \langle a_{k_3}^+ a_{k_1}^+ a_{k_2} a_{k_4} \rangle.$$

Because the second-order correlation function of the EMF is proportional to the correlation function,

$$K_2(r, t, \tau) \sim V_{21} = \sum_{i,l} \gamma_{il} \langle U_{l1}^2(t) U_{i2}^1(t) \rangle,$$

between the radiators, the collective interaction of nuclei located at a distance $\delta \leq c\tau_r^e$ in extended media can become the primary agent for stimulated scattering of gamma-photons at the frequency $\omega_a = \omega_{21} + \omega_0$. The second-order coherence between the pairs of photons can be observed, for instance, with a two-photon detector, as well as with a Hanbury–Brown–Twiss heterodyne detector [17].

Acknowledgement

Thanks are due to professor Ioan-Iovitz Popescu, member of the Romanian Academy, for suggesting us the present cooperative multiphoton process approach of the induced gamma emission problem and for his permanent encouragement and help.

References

- [1] R.H. Dicke, Phys. Rev. 93 (1954) 99.
- [2] M. Gross and S. Haroche, Phys. Rep. 93 (1982) 303.
- [3] A.V. Andreev, V.I. Emelyanov and Yu.A. Iliinsky, Usp. Fiz. Nauk 131 (1980) 653.
- [4] A.V. Andreev, Zh. Eksp. Teor. Fiz. 72 (1977) 1397.
- [5] A.V. Andreev, Yu.A. Iliinsky and R.V. Khokhlov, Zh. Eksp. Teor. Fiz. 73 (1977) 1296.
- [6] N.A. Enaki, Sov. Phys. JETP 67 (1988) 2033.
- [7] C.B. Collins, C.D. Eberhard, J.W. Glesener and J.A. Anderson, Phys. Rev. C37 (1988) 2267.

- [8] J.J. Carroll, M.J. Byrd, K.N. Taylor, D.G. Richmond, T.W. Sinor, W.L. Hodge, Y. Paiss, C.D. Eberhard, J.A. Anderson, C.B. Collins, E.C. Scarbrough, P.P. Antich, F.J. Agee, D. Davis, G.A. Huttlin, K.G. Kerris, M.S. Litz and D.A. Wittaker, Phys. Rev. C43 (1991) 1238.
- [9] N.A. Enaki, Sov. Phys. JETP 71 (1990) 435.
- [10] N.A. Enaki and O.B. Prepelitsa, Opt. Spektrosk. 69 (1990) 617.
- [11] N.A. Enaki and O.B. Prepelitsa, Teor. Mat. Fiz. 88 (1991) 416.
- [12] P.I. Bardetski and N.A. Enaki, Sov. Phys. Opt. Spectrosc. 72 (1990) 829.
- [13] F. Hoffmann, M. Konijnenberg, C. Schultheiss, M. Schwall, K. Mittag and G. Mueller, KFK Nachr. 24 (1992) 254.
- [14] M. Ganciu, G. Modreanu, A.M. Pointu and I.-Iovitz Popescu, J. Phys. D27 (1994) 1370.
- [15] M. Ganciu, E. Dewald, N. Nistor, D. Penache, I.-Iovitz Popescu and V. Zoran, Rom. J. Phys. 39 (1994) 787.
- [16] V.I. Zoran, M. Ganciu, A.M. Pointu, C.B. Collins and I.-Iovitz Popescu, these proceedings (1st Int. Gamma-Ray Laser Worksh., 1995), Hyp. Int. 107 (1997) 415.
- [17] H. Carmichael, in: *An Open Systems Approach to Quantum Optics* (Springer, Berlin, 1993).

Theory of single-photon echo (SP-echo) and the possibility of its experimental study in the gamma-region

S.A. Moiseev

Kazan Physical-Technical Institute, Russian Academy of Science, Kazan, 420029, Russia

The single-photon echo (SP-echo) effect is predicted to appear in the case of three-level medium excitation by means of a single photon propagating to the medium along two optical paths with a mutual time delay surpassing the temporal duration of the photon wave packet. The quantum electrodynamical theory describing this interaction is presented and the S -matrix of the field is shown for infinite time ($t = \infty$). Using the S -matrix approach, physical properties of the scattering field are studied. Hence, it is shown that the field has an echo signal at the ω_{32}^0 carrier frequency. It has been shown that the echo signal exists only in the field amplitude while being absent in its intensity behaviour. Thus, SP-echo is an interference effect and is not influenced by the energy irradiation. The problems of SP-echo detection in the gamma-region (where special generation difficulties appear) are discussed. The influence of the additional detection of the ω_{21}^0 frequency field on the echo signal has been shown. A special case is the EPR-paradox which can appear within the echo phenomenon.

1. Introduction

Single-photon time-delayed self-interference (TDSI) was studied using photon resonant interaction with two-level atom systems [1–3]. It has been shown that TDSI can exist although different photon wave packets along the paths of two optical interferometers do not interfere within the medium. That is, TDSI exists if the delay time between packets is greater than the temporal length of the packet t_{ph} , but smaller than the medium phase memory time T_2 ($t_{ph} \ll \tau \ll T_2$).

An accurate study of TDSI leads to new problems connected with overcoming the experimental difficulties due to the very low amplitude of TDSI. As shown in refs. [1,2], one method of TDSI recording can be found by using an additional intensive readout laser pulse. However, intensive pulses lead to large incoherent noise due to spontaneous luminiscence. The problem of TDSI detection is intensified in the absence of the primary echo signal when the two excited pulses are connected with a single-photon field. The absence has a fundamental nature, connected with the nonlinear nature of the echo phenomenon on the one hand (Hahn echo [4] and its achievement in the optical region [5,6]) and with the single-photon quantum nature on the other hand. Related to this it is topical to note the possibility of the gamma-echo effect [7]. This effect appears only if two pulses excite the resonant me-

dium and propagate along the same direction as the gamma echo signal, solely for special phase modulation of the two pulses. The gamma echo is the result of the interference of the two pulses after propagation through the thick resonant medium. It is important to stress that this result will also be valid when the two pulses propagate through the medium at any moment of time. In what concerns the results for transmitted pulses, the delay time must be taken sufficiently short by using, for example, an optical delay line. So, in this situation, the gamma echo effect could obtain another title.

Returning to the formal echo effect we must expect unusual quantum properties of echo fields caused by the nonlinear nature of the echo phenomenon and the quantum nature of the photon. That is, the stimulated echo signal from the TDSI exists only in the echo amplitude but not in its intensity! Such unusual field properties are impossible in the classical field theory. For the following detailed study of this quantum field it is desirable to find its wave function. Inasmuch as this field is weak, its experimental study demands the exception of the influence or existence of incoherent spontaneous irradiation caused by the action of the intensive laser pulse on the medium. Thus, the examined problems are interesting for the study of the quantum properties of a single photon, the new quantum field states theory and also for the coherence of the photon echo.

In the case of real motion, in order to find a solution for these problems, it is important to answer the following question: is single-photon echo possible without an additional intensive laser pulse? Thus, on the one side, single-photon echo detection eliminates the problems connected with incoherent noise suppression, and on the other side it was the confirmation of the TDSI existence in experiment, without using the concept of the wave function as a coherent many-particles quantum ensemble. By state of the art solutions to these problems the search for methods for the study of nonlocal properties of a single quantum particle and the detection of its wave function continues [8]. In our case this problem is connected to the study of the quantum properties of a single photon. In ref. [9] the author has shown the possibility of a single-photon echo while the present paper is devoted to the solution of the above-mentioned tasks.

2. The photon resonant scattering theory for the three-level atom system

Let us consider the three-level atom system interacting at resonance with an electromagnetic field, which is well proved for processes with real field absorption [10]. We will solve the Schrödinger equation

$$i\hbar \frac{d}{dt} |\psi(t)\rangle = \hat{\mathcal{H}} |\psi(t)\rangle, \quad (1)$$

where the Hamiltonian is chosen in the approximation of small-sized medium with

respect to the wavelength ($L < \lambda_{\min}$). This simple supposition is the first necessary step towards finding a solution for the $L > \lambda_{\min}$ case,

$$\begin{aligned} \hat{\mathcal{H}} &= \hat{\mathcal{H}}_a + \hat{\mathcal{H}}_{ph} + \hat{V}, \\ \hat{\mathcal{H}}_a &= \sum_j^N \sum_{n=1}^3 E_n^j \hat{P}_{nn'}^j, \quad \hat{\mathcal{H}}_{ph} = \int_{-\infty}^{\infty} d^3k \hbar \omega_k \hat{a}_k^+ \hat{a}_k, \\ \hat{V} &= \hbar \sum_{j=1}^N \sum_{n>n'}^3 \int_{-\infty}^{\infty} d^3k [g_{nn'}(k) \hat{a}_k \hat{P}_{nn'}^j + g_{nn'}^*(k) \hat{a}_k^+ \hat{P}_{n'n}^j], \end{aligned} \quad (2)$$

where \mathcal{H}_{ph} , \mathcal{H}_a and \hat{V} represent the Hamiltonians of the field, atoms and their interaction, respectively, $[\hat{a}_k, \hat{a}_k^+] = \delta(k - k')$, $\omega_k = ck$, $\hat{P}_{nn'}^j = |n_j\rangle \langle n'_j|$, $g_{nn'}(k) = i(e_{\omega k} d_{nn'}) (2\pi\omega_{nn'}^2/\omega_k \hbar)^{1/2}$, $e_{\omega k}$ is the polarization vector for the (ω, k) -mode, $d_{nn'}$ is the dipole moment of the $|n\rangle \Rightarrow |n'\rangle$ transition, E_n^j stands for the j -atomic energy in the $|n_j\rangle$ state. Let $E_3^j > E_2^j > E_1^j$; where E_3^0 , E_2^0 , E_1^0 represent the central level positions. Let the atomic spectrum be non-equidistant and we have the following correlated inhomogeneous broadening character: $\omega_{nn'}^j = (E_n^j - E_{n'}^j)/\hbar = \omega_{nn'}^0(1 + \alpha^j)$. Generally, the α^j parameter is fixed for any j -atom. The total distribution of the α^j parameters is described by the function $G(\alpha)$

$$G(\alpha) = \sum_{j=1}^N \delta_{\alpha, \alpha^j}. \quad (3)$$

For a better understanding of single-photon echo generation, we will consider the model experiment, shown in fig. 1. The S photon source intensity is considered low, so that the mean time between nearest photons, τ_0 , is large enough, $\tau_0 \gg t_{ph} + \tau_{AB} + \tau_S$, where τ_{AB} is the delay time for photon propagation along two separated optical paths: directly through beam splitter A and after reflection on mirrors A and B, τ_S stands for the photon irradiation time of the M medium after its excitation. So, at any moment there can be no more than one photon in the experimental apparatus. Thus, it is possible to assume that for $t = -\infty$ (before the interaction) the physical system is described by the wave function.

$$|\psi_{in}(-\infty)\rangle = \int_{-\infty}^{\infty} d^3k \mathcal{F}(-\infty; k) \hat{a}_k^+ |0B\rangle, \quad (4a)$$

where $|0B\rangle = |0\rangle \otimes |B\rangle$; $|B\rangle$ is the field vacuum state, while $\hat{a}_k |B\rangle = 0$, and $|0\rangle = \prod_j^N |1_j\rangle$ represent the atomic ground state. $\mathcal{F}(-\infty, k) = \mathcal{F}_0(-\infty; k - k_1)$ is a complex normalized function which has a sharp peak at $k = k_1$. The $|\psi_{in}(-\infty)\rangle$ function corresponds to single-photon propagation along the $k = k_1$ direction [11] incident to the first mirror A (fig. 1).

We will presume that the second mirror B moves with the velocity v . After field

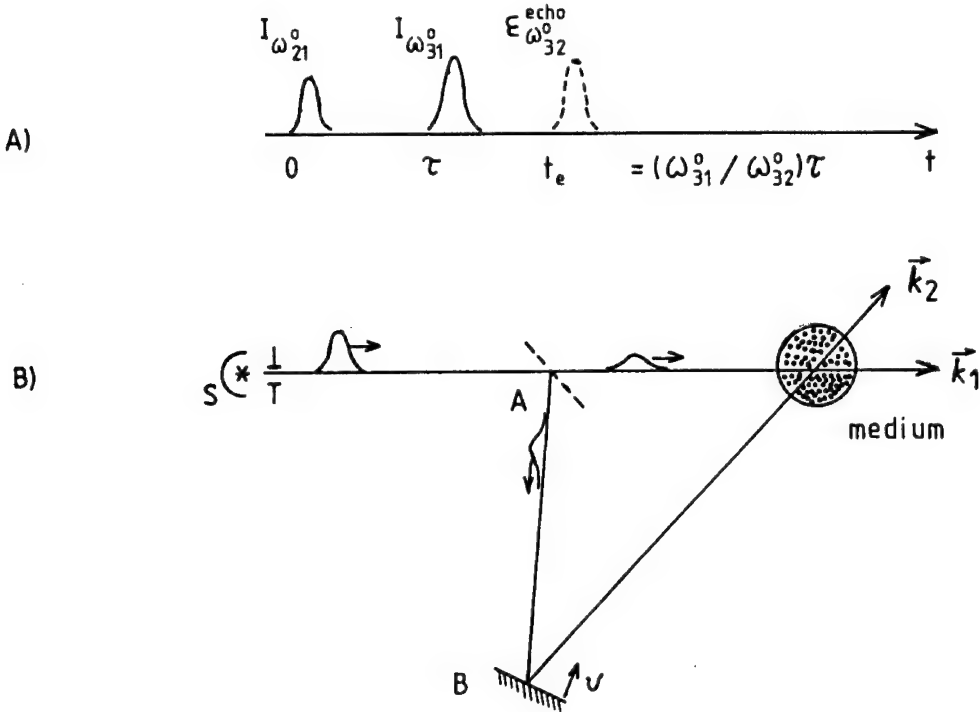


Fig. 1. Main diagram for SP-echo generation in a three-level medium. (a) The first two pulses are the single-photon excited pulses, while the third pulse represents the echo pulse at the moment $t_e = (\omega_{31}^0 / \omega_{32}^0)\tau$. (b) Spatial diagram of photon propagation to a three-level medium.

reflection on the mirror, its two wave packets will arrive at the medium at different time instants, while presenting different carrier frequencies. Let the velocity v have such a value, that the Doppler shift coincides with the ω_{32}^0 frequency. In this case, two photon field pulses will be in resonance with two transitions of ω_{21}^0 and ω_{32}^0 frequencies in a three-level medium. This is obvious only from the experimental method which can only serve for the physical possibility of a similar quantum state preparation ("two-colour" photon). In a real experiment, this method is hardly possible, but the author will not discuss below other preparation methods for these two-colour photon states.

Thus, in accordance with the superposition principle [12], the field wave function after interaction with the two mirrors is

$$\mathcal{F}_{\text{in}}(-\infty; k|k_1, k_2) = \frac{1}{\sqrt{2}} \{ \mathcal{F}_0(-\infty; k - k_1) e^{-i(kL_1)} + \mathcal{F}_0(-\infty; k - k_2) \}, \quad (4b)$$

where $|k_1| = \omega_{21}^0/c$; $|k_2| = \omega_{31}^0/c$; $(k_1 L_1)/kc = \tau$; $L_2 = 0$.

State (4) is the initial state (for $t = -\infty$) in the case of the photon interacting with

three-level atoms. This problem can be solved using the interaction representation, as shown in the following:

$$i \frac{d}{dt} |\psi_v(t)\rangle = \hat{V}(t) |\psi_v(t)\rangle, \quad (5)$$

where the Hamiltonians are expressed below

$$\hat{V}(t) = \sum_{l=1}^3 \hat{V}_l(t),$$

$$\hat{V}_l(t) = \sum_{j=1}^N \int_{-\infty}^{\infty} d^3k [g_l(k) \hat{a}_k \hat{\mathcal{P}}_l^j \exp\{i[(\omega_l^j - \omega_k)t]\} + \text{h.c.}],$$

with $\hat{\mathcal{P}}_1^j = \hat{P}_{31}^j$; $\hat{\mathcal{P}}_2^j = \hat{P}_{32}^j$; $\hat{\mathcal{P}}_3^j = \hat{P}_{21}^j$. Analogue relations are valid for $g_l(k)$ and ω_l^j . In the rotating-wave approximation, the $|\psi(t)\rangle$ wave function (index v is taken off) is a superposition of the six following terms:

$$|\psi(t)\rangle = \sum_{n=1}^6 |\psi_n(t)\rangle, \quad (6a)$$

where

$$|\psi_{1,2}(t)\rangle = |\psi_{\text{ph},1,2}(t)\rangle = \int_{-\infty}^{\infty} d^3k \mathcal{F}_{1,2}(t; k) \hat{a}_k^+ |0B\rangle, \quad (6b)$$

$$|\psi_3(t)\rangle = \sum_{j=1}^N b_j(t) \hat{P}_{21}^j |0B\rangle, \quad (6c)$$

$$|\psi_4(t)\rangle = \sum_{j=1}^N a_j(t) \hat{P}_{31}^j |0B\rangle, \quad (6d)$$

$$|\psi_5(t)\rangle = \sum_{j=1}^N \int_{-\infty}^{\infty} d^3k c_j(k; t) \hat{a}_k^+ \hat{P}_{21}^j |0B\rangle, \quad (6e)$$

$$|\psi_6(t)\rangle = \int_{-\infty}^{\infty} \int_{-\infty}^{\infty} d^3k d^3k' \mathcal{F}(t; k; k') \hat{a}_k^+ \hat{a}_{k'}^+ |0B\rangle. \quad (6f)$$

In our initial state ($t = -\infty$), only two terms are not equal to zero, where $\lim_{t \rightarrow -\infty} \mathcal{F}_{1,2}(t; k) \Rightarrow \mathcal{F}_0(-\infty; k - k_{1,2})/\sqrt{2}$. The solutions for these functions are separated. As other functions can be found starting from $\mathcal{F}_{1,2}(t; k)$, the total equation system is divided into two blocks. The first block includes the $|\psi_1(t)\rangle$ and $|\psi_3(t)\rangle$ functions. The second block consists of the $|\psi_2(t)\rangle$, $|\psi_4(t)\rangle$, $|\psi_5(t)\rangle$ and $|\psi_6(t)\rangle$ functions.

$$|\psi_1(t)\rangle = |\psi_1(-\infty)\rangle - i \int_{-\infty}^t dt' \hat{V}_3(t') |\psi_3(t')\rangle, \quad (7a)$$

$$|\psi_3(t)\rangle = -i \int_{-\infty}^t dt' \hat{V}_3(t') |\psi_1(t')\rangle, \quad (7b)$$

$$|\psi_2(t)\rangle = |\psi_2(-\infty)\rangle - i \int_{-\infty}^t dt' \hat{V}_1(t') |\psi_4(t')\rangle, \quad (7c)$$

$$|\psi_4(t)\rangle = -i \int_{-\infty}^t dt' \hat{V}_1(t') |\psi_2(t')\rangle - i \int_{-\infty}^t dt' \hat{V}_2(t') |\psi_5(t')\rangle, \quad (7d)$$

$$|\psi_5(t)\rangle = -i \int_{-\infty}^t dt' \left\{ \hat{V}_2(t') |\psi_4(t')\rangle - i \int_{-\infty}^t dt' \hat{V}_3(t') |\psi_6(t')\rangle \right\}, \quad (7e)$$

$$|\psi_6(t)\rangle = -i \int_{-\infty}^t dt' \hat{V}_3(t') |\psi_5(t')\rangle. \quad (7f)$$

In order to find a solution to these equations, we have taken into account the fact, that the electromagnetic field spectrum is very spread out and continuous in the vacuum. We also remind [13], that integration over the vacuum modes interacting with two- or three-level atoms is difficult to estimate in the high-frequencies region. Thus, this integration is made using the regularization function model. Regularization is usually made under the condition that single-atom interaction with the vacuum is determined by the value of the dipole moments and the density of vacuum modes for atomic frequencies, and gives the values of the γ_{31} , γ_{21} , γ_{32} decay constants. This formal mathematic procedure can be effectuated using the following rule. We will introduce the frequency distribution function for the $d^3k g_m(k)$ term for any of the three transitions with ω_1^0 , ω_2^0 , ω_3^0 frequencies under the condition

$$\int_{-\infty}^{\infty} d^3k |g_m(k)|^2 \exp\{i[\omega_m^j - \omega_k](t' - t'')\} \cong 2\pi N_m g_m^2 \exp\{-\Omega_m(t' - t'')\}, \quad (8a)$$

where $\rho_m(\omega_m^j) \cong \rho_m(\omega_m^0) = N_m/\Omega_m$ represents the density of the vacuum modes and Ω_m is the effective spectral width of the distribution of the modes.

The second step requires the realization of the condition

$$2\pi N_m g_m^2 \int_{-\infty}^t dt'' b_j(t'') \exp\{-\Omega_m(t' - t'')\} \cong \gamma_m b_j(t'), \quad (8b)$$

which is achieved if $\Omega_m \gg \omega_m^j - \omega_m$ and $db_j(t'')/dt'' \ll \Omega_m b_j(t'')$. For the conditions in eqs. (8a) and (8b) we will obtain the excited atom exponential decay with the constants $\gamma_m = 4\pi N_m g_m^2/\Omega_m$, which is realized in the experiments of refs. [10,13]. The

second result of the atomic interaction with the vacuum is the appearance of atomic level Lamb shifts [10], which we can include in the ω_{mn}^j frequencies. Using eq. (8) we will analytically find the solution of eqs. (7a) and (7b) for $|\psi_1(t)\rangle$ and $|\psi_3(t)\rangle$ without any additional approximations. We are interested only in the state of the total field + atoms system for $t \Rightarrow \infty$, when the interaction has ended. We have:

$$\mathcal{F}_1(\infty; k) = \lim_{t \rightarrow \infty} \mathcal{F}_1(t; k) = \mathcal{F}_1(-\infty; k) + \mathcal{F}_{1R}(+\infty; k), \quad (9)$$

where the scattering part $\mathcal{F}_{1R}(-\infty; k)$ is:

$$\mathcal{F}_{1R}(+\infty; k) = -Ng(k) \lim_{\epsilon \Rightarrow 0} \frac{F_1(\omega_k - \omega_{21}^0) G_{\epsilon;21}(\omega_k - \omega_{21}^0) e^{-i\omega_k \tau}}{1 + N\gamma_{21} G_{\epsilon;21}(\omega_k - \omega_{21}^0)}, \quad (10)$$

$$F_{1,2}(\omega_k - \omega_{21,31}^0) = 2\pi \int_{-\infty}^{\infty} d^3k g_3(k) \mathcal{F}_{1,2}(-\infty; k) \delta(\omega_k - \omega_{21,31}^0), \quad (11)$$

$$G_{\epsilon;mn}(\Delta) = \frac{1}{N} \sum_j^N [\epsilon - i(\Delta - \alpha^j \omega_{mn}^0)]^{-1}. \quad (12)$$

In the single-atom (nucleus, molecule) case solution (9) coincides with the well known one obtained by means of a different method [14]. Let us write the result for $|\psi_3(\infty)\rangle = \lim_{\epsilon \Rightarrow 0} |\psi_3(\epsilon, \infty)\rangle$ expressing the atomic state at $t = -\infty$:

$$|\psi_3(\infty)\rangle = \lim_{\epsilon \Rightarrow 0} |\psi_3(\epsilon, \infty)\rangle \equiv 0, \quad (13a)$$

where

$$|\psi_3(\epsilon, \infty)\rangle = (-i) \sum_j^N \frac{F_1(\alpha^j \omega_{21}^0) e^{-i\omega_{21}^j \tau}}{1 + N\gamma_{21} G_{\epsilon;21}(\alpha^j \omega_{21}^0)} \hat{P}_{21}^j |0B\rangle. \quad (13b)$$

Using eqs. (8a) and (8b), we find the solutions of the $|\psi_2(t)\rangle$, $|\psi_4(t)\rangle$, $|\psi_5(t)\rangle$ and $|\psi_6(t)\rangle$ functions by means of the same method and the exact results are:

$$|\psi_4(\infty)\rangle = |\psi_5(\infty)\rangle \equiv 0. \quad (14)$$

Expressions (13) and (14) indicate that the atomic system will be in the ground state for $t \Rightarrow \infty$ and the field leaves the medium. It differs from the result of ref. [15]. In ref. [15], it has been obtained that for $t \Rightarrow \infty$ there is a non-zero probability to find atoms in the excited level, where Lorentz inhomogeneous resonant line broadening is present. These differences in the atomic behaviour are caused by the continuous form of the broadening, which is correct only for an infinite large number of atoms. Using eq. (13b) it is possible to demonstrate that before imposing the $\epsilon \Rightarrow 0$ limit, we can perform an integration over the continuous frequency distribution of Lorentzian shape, instead of a \sum_j summation. We will obtain:

$$G_{\epsilon;21}^L(\alpha^j \omega_{21}) = [\epsilon + \Delta_n^{21} - i\alpha^j \omega_{21}^0]^{-1} \Rightarrow [\Delta_n^{21} - i\alpha^j \omega_{21}^0]^{-1}, \quad (15)$$

$$b_j^L(\infty) = (-i) \frac{\Delta_n^{21} - i\alpha^j \omega_{21}^0}{\Delta_n^{21} + N\gamma_{21} - i\alpha^j \omega_{21}^0} F_1(\alpha^j \omega_{21}^0) e^{-i\omega_{21}^j \tau} \neq 0, \quad (16)$$

which show that the probability to find any j -atom in the excited level is non-zero, a result which is opposed to eq. (13a). The same situation stands for $\langle \psi_5^L(\infty) | \psi_5^L(\infty) \rangle \neq 0$.

Returning to the discrete frequency distribution (for a finite number of N atoms) we will obtain two non-zero terms: $|\psi_2(\infty)\rangle$ and $|\psi_6(\infty)\rangle$. The latter is interesting for the following consideration:

$$\mathcal{F}(\infty; k, ; k') = iN g(k) g(k') \frac{F_2(\omega_k + \omega_{k'} - \omega_{31}^0) \mathcal{L}(\omega_k; \omega_{k'})}{1 + N\gamma_{31}(1 - \kappa) G_{\gamma_{31}, 32}(\omega_k + \omega_{k'} - \omega_{31}^0)}$$

where $\mathcal{L}(\omega_k; \omega_{k'})$ gives the main part of the correlation between the ω_k and $\omega_{k'}$ frequencies:

$$\mathcal{L}(\omega_k; \omega_{k'}) = \lim_{\epsilon \Rightarrow 0} \frac{\frac{1}{N} \sum_j^N [\epsilon - i(\omega_k - \omega_{21}^j)]^{-1} [\gamma_{32} - i(\omega_k + \omega_{k'} - \omega_{31}^j)]^{-1}}{1 + N\gamma_{21} G_{\epsilon, 21}(\alpha^j \omega_{21}^0)}, \quad (18)$$

where the κ parameter is very small for large numbers of N atoms in the $\Omega_{32} \approx 0$ (within the resonator) case,

$$\kappa \cong \frac{\gamma_{21} \gamma_{32}}{\gamma_{31} (\Omega_{32} + N\gamma_{21})} \ll 1. \quad (19)$$

It determines the reabsorption value for the $|3\rangle \Rightarrow |2\rangle$ transition, and reabsorption decreases as the $|2\rangle \Rightarrow |1\rangle$ transition collective decay increases.

A calculus of the $|\psi_{\text{out}}(\infty)\rangle = |\psi_1(\infty)\rangle + |\psi_2(\infty)\rangle + |\psi_6(\infty)\rangle$ wave function reduces in fact to the $S(\infty; -\infty)$ matrix calculation, connecting the initial and final field states $|\psi_{\text{out}}(\infty)\rangle = S(\infty; -\infty) |\psi_{\text{in}}(\infty)\rangle$. We will use these results in order to study the echo-field radiated by the medium.

3. Single-photon echo (SP-echo)

The study of the echo field is achieved by calculating the expectation values for the $\hat{E}^+(t, r)$ and $\hat{E}^-(t, r)$ field operators: $\langle \hat{E}^+(t, r) \rangle^* = \langle \hat{E}^-(t, r) \rangle$ represents the field amplitude and the radiation intensity operator is $\hat{I}(t, r) = \langle \hat{E}^+(t, r) \hat{E}^-(t, r) \rangle c/4\pi$. Calculus shows that the echo signal exists only in the field amplitude for the ω_{32}^0 carrier frequency. Thus, the intensity for the same ω_{32}^0 frequency has no echo behaviour, which is seen analysing the expression:

$$\mathcal{E}_e(t, r) = \langle \hat{E}_{\omega_{32}^0}^-(t, r) \rangle = \langle \psi_1(t) | \hat{E}_{\omega_{32}^0}^-(t, r) | \psi_6(t) \rangle, \quad (20)$$

$$I_e(t, r) = \langle \hat{E}_{\omega_{32}^0}^+(t, r) \hat{E}_{\omega_{32}^0}^-(t, r) \rangle = \langle \psi_6(t) | \hat{E}_{\omega_{32}^0}^+(t, r) \hat{E}_{\omega_{32}^0}^-(t, r) | \psi_6(t) \rangle, \quad (21)$$

where we must consider $\lim_{t \rightarrow \infty} |\psi_{1,6}(t)\rangle = |\psi_{1,6}(\infty)\rangle$.

The $|\psi_1(\infty)\rangle$ wave function contains all necessary information about the photon-atoms interaction for the first wave packet while the $|\psi_6(\infty)\rangle$ function gives information about the second wave packet interaction. Thus, only expression (20) has the information about these two packets. In the eq. (21) intensity expression, this complete information is absent and the appearance of the echo signal does not influence the temporal behaviour of the intensity for the ω_{32}^0 frequency. Consequently, we will study only the field amplitude. The corresponding expression for the electric field amplitude is [10,1]:

$$\mathcal{E}_e(t, r) = \left\langle \int d^3k \mathcal{E}(k) e^{-i(\omega_k t - kr)} \hat{a}_k \right\rangle = \int d^3k \mathcal{E}(k) e^{-i(\omega_k t - kr)} \mathcal{R}(k), \quad (22)$$

where

$$\mathcal{E}(k) = i \frac{(\hbar c k)^{1/2}}{2\pi} e_{\omega k},$$

$$\mathcal{R}(k) = \int d^3k' \mathcal{F}_1^*(\infty; k') \mathcal{F}(\infty; k'; k). \quad (23)$$

The $\mathcal{R}_R(k)$ scattering part presents a particular interest with the interaction between photon and medium:

$$\mathcal{R}_R(k) = \int d^3k' \mathcal{F}_{1R}^*(\infty; k') \mathcal{F}(\infty; k'; k). \quad (24)$$

After calculating $\mathcal{R}_R(k)$, we introduce the inhomogeneous broadening supposition, i.e., homogeneously distributed atomic frequencies whose number is sufficiently large in the γ_{32} frequency interval, so that the inequality $N\gamma_{32}/\Delta_n^{32} \gg 1$ is valid. Let us consider the function $\mathcal{R}(k)$ in the $\omega_k \cong \omega_{21}^j$, frequency region where $|\omega_k - \omega_{21}^j| < |\omega_{21}^{j+1} - \omega_{21}^j| = \Delta_{\min}^{21} \cong \Delta_n^{21}/N \ll \gamma_{32}$. If the ϵ parameter satisfies the condition $\epsilon \ll \Delta_{\min}^{21}$, we will obtain for the main part of the sum

$$\sum_1^N [\epsilon - i(\omega_k - \omega_{21}^1)]^{-1} \cong [\epsilon - i(\omega_k - \omega_{21}^j)]^{-1} \cong \epsilon^{-1}. \quad (25)$$

Applying this procedure to eq. (18) we find for $\mathcal{F}_{1R}^*(\infty; k')$ and $\mathcal{F}(\infty; k'; k)$:

$$\mathcal{F}_{1R}^*(\infty; k') \xrightarrow[\omega_k \rightarrow \omega_{21}^j]{} -\frac{g^*(k')}{\gamma_{21}} F_1^*(\omega_k - \omega_{21}^0) e^{i\omega_k \tau}, \quad (26)$$

$$\mathcal{F}(\infty; k'; k) \xrightarrow[\omega_k \rightarrow \omega_{21}^j]{} \frac{i g(k) g(k') F_2(\omega_k + \omega_{21}^j - \omega_{31}^0)}{\gamma_{21} \{\gamma_{32} - i(\omega_k - \omega_{32}^0)\} [1 + N\gamma_{31}(1 - \kappa) G_{\gamma_{32}; 31}(\omega_k + \omega_{21}^j - \omega_{31}^0)]}. \quad (27)$$

Expressions (26) and (27) are exact for $\omega_k = \omega_{21}^j$. It is obvious that, in the frequency interval near ω_{21}^j , these expressions are approximately identical. Let us introduce the $\Delta_m \cong \beta \Delta_{\min}^{2j}$ interval, where $\beta < 1$. Under this condition, effectuating the $d^3 k'$ to $\rho(\omega_{21}^j) \Delta_m$, substitution, we will obtain

$$\begin{aligned} \mathcal{R}_R(k) = & -i\Delta_m \frac{g(k)}{2\pi\gamma_{21}} \\ & \times \sum_j \frac{F_1^*(\omega_{21}^j - \omega_{21}^0) F_2(\omega_k + \omega_{21}^j - \omega_{31}^0) e^{i\omega_{21}^j \tau}}{\{\gamma_{32} - i(\omega_k - \omega_{32}^j)\}[1 + N\gamma_{31}(1 - \kappa)G_{\gamma_{32};31}(\omega_k + \omega_{21}^j - \omega_{31}^0)]}. \end{aligned} \quad (28)$$

If $\Delta_m \ll \gamma_{32}$, the $G_{\gamma_{32};31}(\omega_k + \omega_{21}^j - \omega_{31}^0)$ function can be calculated under the homogeneous broadening continuous approximation

$$G_{\gamma_{32};31}(\omega_k + \omega_{21}^j - \omega_{31}^0) = \frac{1}{\Delta_n^{31} + \gamma_{32} - i(\omega_k + \omega_{21}^j - \omega_{31}^0)} \cong \frac{1}{\Delta_n^{31} + \gamma_{32}}. \quad (29)$$

We will integrate then eq. (22) with $d^3 k$, using the substitution

$$\int d^3 k g(k) \dots = (4\pi)^{-1} \int d\omega_k \rho(\omega_k) \int_{\Omega_r} d\theta_r d\varphi_r \sin \theta_r g(\omega_k, \Omega_r), \quad (30)$$

where $d\Omega_r = \sin \theta_r d\varphi_r$, with the z-axis parallel to r .

As in the echo theory we will consider that the $F^2(\omega_k + \omega_{21}^j - \omega_{31}^0)$ spectral width is larger than γ_{32} , which is equivalent to the $\tau_{ph} \ll \gamma_{32}^{-1}$ condition. Thus, from eq. (22) we obtain

$$\begin{aligned} \mathcal{E}_e(t, r) = & \frac{\Delta_m (\Delta_n^{31} + \gamma_{32}) \rho(\omega_{32}^0)}{2\pi\gamma_{21} (\Delta_n^{31} + \gamma_{32} + N\gamma_{31})} \int \frac{d\Omega_r}{4\pi} g(\omega_k, \Omega_r) \mathcal{E}(\omega_k, \Omega_r) \eta(t - n_\Omega r/c) \\ & \times \exp(-\gamma_{32}(t - n_\Omega r/c)) \Phi_{\text{echo}}(t - n_\Omega r/c - t_e) e^{-i\omega_{32}^0(t - n_\Omega r/c - t_e)}, \end{aligned} \quad (31)$$

where $\eta(x)$ is the Heavyside function, $t_e = (\omega_{31}^0/\omega_{32}^0)\tau$ and $\Phi_{\text{echo}}(t - n_\Omega r/c - t_e)$ is a well known function in the echo theory. In this case, it is expressed as depending on the single-photon state and inhomogeneous broadening parameters (see eqs. (3) and (11)):

$$\Phi_{\text{echo}}(\xi_e) = \int_{-\infty}^{+\infty} d\alpha G(\alpha) F_1^*(\alpha\omega_{21}^0) F_2(\alpha\omega_{31}^0) e^{-i\alpha^j \omega_{21}^0 \xi_e}. \quad (32)$$

The $\Phi_{\text{echo}}(\xi_e)$ function is maximal for $\xi_e = t - n_\Omega r/c - t_e = 0$, which corresponds to the echo signal appearance after the second pulse (second wave packet) (in fig. 1a, $t_e = (\omega_{31}^0/\omega_{32}^0)\tau$ is the temporal localization of the echo signal appearance). The $n_\Omega r/c = \cos \theta r/c$ term is the time delay within a distance r from the medium. Using the $n_\Omega r/c \cong (1 - \theta^2/2)r/c$ and $\sin \theta d\theta \cong \theta d\theta$ approximations, corrected for large r values, it is easy to integrate eq. (31) with θ , by the constant phase method [17]

$$\begin{aligned} \mathcal{E}_e(t, r) \cong & \frac{i\Delta_m(\Delta_n^{31} + \gamma_{32})\rho(\omega_{32}^0)}{2^3\pi^2\gamma_{21}(\Delta_n^{31} + \gamma_{32} + N\gamma_{31})} \frac{c/\omega_{32}^0}{r} g(\omega_k, 0)\mathcal{E}(\omega_k, 0) \exp(-\gamma_{32}(t - r/c)) \\ & \times \Phi_{\text{echo}}(t - r/c - t_e) e^{-i\omega_{32}^0(t - r/c - t_e)}. \end{aligned} \quad (33)$$

This expression for the radiated field coincides with that of the echo field radiated by the classical phasing polarization in ordinary echo theory. The obtained solution gives the condition for good echo generation

$$\Delta_n^{31} + \gamma_{32} \geq N\gamma_{31}, \quad (34)$$

which approximately coincides with $\Delta_n^{31} \geq N\gamma_{31}$.

4. The main tasks of SP-echo generation in the gamma-region

The investigated single-photon echo is possible in any three-level medium with correlated inhomogeneous broadening for all the three transitions. The main condition in order to obtain this effect is not connected with the use of intensive coherent electromagnetic fields, so that the single photon is sufficiently for the echo phenomena appearance. This situation is especially important for the gamma region, where there are not enough intensive coherent sources for the ordinary Hahn echo [4–6] generation. However in the gamma region, single-photon field detection is possible so that the SP-echo can be also detected in the gamma-region, where special problems occur.

(A) Task one. It is necessary to find “three-level” nuclei, where all three transitions are not forbidden. In the optical region, this condition is realized in non-symmetrical molecules, so that the nuclear states must probably be non-symmetrical.

(B) Second task. The experimental preparation of the “two-colour” photon state. This task can be solved without using a Doppler mirror if the first task is satisfied.

(C) Third task. Experimental realization of the phase detection method in the gamma-region. As it is interesting to prove that SP-echo is absent in the intensity behaviour this experiment can be made without the phase detection method.

The solution of all these problems demands additional papers.

5. Conclusion

Thus, it is possible to conclude that single-photon echo is possible. In the present paper, it was proved that SP-echo can be generated in three-level mediums without additional intensive coherent pulses. This phenomenon can be achieved in the combined echo regime (see ref. [18]). Moreover, expressions (31) and (33) can be used in quantitative estimates and subsequent calculations in a real experimental case.

However, it is necessary to remember that the field energy flow is described by expression (21), which has not the echo pulse form! This very interesting phenomenon is impossible in the classical field theory. Thus, detection of the echo signal demands the technique of phase detection. I can also add that, in order to prove such quantum field properties, it is necessary to detect the absence of an echo signal in the intensity behaviour during the experiment, which can be made by ordinary experimental techniques. Other possible modes can be found in order to experimentally prove the existence of such new quantum field states. Maybe, the described method will be replaced by indirect methods.

The described theory corresponds to the measuring process of only the ω_{32} frequency field (signal frequency according to terminology [19]). A new interesting situation appears if, together with this field, the ω_{21} frequency field will also be detected. In a correlated measurement the detection of one field frequency will modify the additional field parameters. Thus, if we will have a sufficiently narrow filter in the ω_{21} frequency region, the frequency measurement will extend the duration of the echo signal time. The effect can be described using the quantum correlator which includes both fields (with the ω_{32} and ω_{21} frequencies) [20]. This will be the first known demonstration of the Einstein–Podolsky–Rozen effect in the echo phenomenon. This circumstance warns about the possible difficulties to be encountered in the experimental SP-echo study.

As our approach is valid for a general three-level system interacting with quantum electromagnetic fields, the obtained results will also exhibit a general character. This result can be especially interesting for the gamma-region where sufficiently intensive coherent sources are not available, but single-photon fields are well detected since a long time. SP-echo study in the gamma-region rises new special problems for future investigations.

Acknowledgement

This paper was supported by the Russian Fund of Fundamental Investigation (93-02-2595).

References

- [1] A.R. Kessel and S.A. Moiseev, Pis'ma Zh. Eksp. Teor. Fiz. 58 (1993).
- [2] A.R. Kessel and S.A. Moiseev, Izv. AN, ser. Fiz. 58 (1994) 135, in Russian.
- [3] A.R. Kessel and S.A. Moiseev, Congress Ampere, Kazan, August 21–28 (1994) 360.
- [4] E.L. Hahn, Phys. Rev. 80 (1950) 580.
- [5] U.Kh. Kopvillem and V.R. Nagibarov, Fiz. Met. Metall. 15 (1963) 313.
- [6] N.A. Kurnit, I.D. Abella and S.R. Hartmann, Phys. Rev. Lett. 6 (1964) 567.
- [7] P. Helisto, I. Tittonen, M. Lippmaa and T. Katila, Phys. Rev. Lett. 66 (1995) 2037.
- [8] Y. Ahoronov and L. Vaidman, Phys. Lett. A178 (1993) 38.

- [9] S.A. Moiseev, *Congress Ampere, Kazan, August 21–28 (1994)* 369.
- [10] G.S. Agarwal, in: *Quantum Optics* (Springer Verlag, 1974) 70 (1974) 135.
- [11] D.I. Blokhintsev, in: *Space and Time in the Microworld* (Nauka, Moscow, 1982).
- [12] P. Feynman, B. Leighton and M. Sands, in: *The Feynman Lectures on Physics*, vol.3 (Massachusetts, Palo Alto, London, 1963).
- [13] A.I. Oraevsky, Usp. Fiz. Nauk 164 (1994) 415, in Russian.
- [14] F.A. Novak, J.M. Freidman and R.M. Hochstrasser, in: *Laser and Coherence Spectroscopy*, ed. J.I. Steinfeld (Plenum Press, New York and London, 1978).
- [15] N.N. Bogoliubov (jr.), F.L. Kien and A.S. Shumovsky, Physica 128 (1984) 82.
- [16] R.J. Glauber, in: *Quantum Optics and Electronics* eds. C. de Witt, A. Blondin and C.C. Cohen-Tannoudji (Gordon and Breach, New York, 1964).
- [17] U.V. Sidorov, M.V. Fedoruk and M.I. Shabunin, in: *Lectures about the Theory of Complex Variable Functions*, 2nd ed. (Moscow, Nauka, 1982) in Russian.
- [18] S.M. Sakharov and E.A. Manykin, Sov. Phys. JETP 4 (1986) 1289.
- [19] D.N. Klyshko, Usp. Fiz. Nauk 154 (1988) 133, in Russian.
- [20] D.N. Klyshko, Usp. Fiz. Nauk 164 (1994) 1187, in Russian.

Dicke superradiance in a biphenyl crystal doped with pyrene molecules and the possibility of this phenomenon in the gamma range

V.V. Samartsev

*Kazan Physical-Technical Institute, Russian Academy of Sciences, 10/7,
Sibirsky Trakt, Kazan, 420029, Russia*

Dicke superradiance (DSR) is observed in a molecular mixed crystal, biphenyl with pyrene (wavelength: 373.9 nm; $T = 1.5\text{--}4.2$ K). Characteristics of DSR under broad-band and narrow-band excitations are studied. The influence of phonons on the DSR appearance is investigated and the pseudo-localized phonon parameters are established. Two-frequencies DSR and superradiance within a cavity are also observed. The possibility of DSR observation in the gamma range is analyzed.

1. Introduction

The program for gamma-laser creation requires a solution to many problems [1]. Let us name only one of these problems: the gamma-laser cavity creation. This problem can be automatically solved in the DSR regime, since DSR is the coherent, spontaneous radiation in single propagation across the inverted resonant medium [2]. The solutions to other problems (such as line narrowing) connects with the fact that line narrowing in the $N\lambda^2$ times (where N is the active particle number and λ is the wavelength) occurs in the DSR process. The homogeneous width of the nuclear sublevels can be narrowed by means of the many-pulsed Waugh–Haeberlen technique [3]. The gamma DSR realization can be possible using long-lived isomers of needle-like form [4].

The history of the gamma-laser creation process, beginning with the Rivlin paper [5], is described in ref. [1]. The theoretical papers [6,7] are closely connected to the thematic of this article. When these papers appeared, Dicke superradiance (DSR) was observed only in gaseous systems [8]. The first DSR experiments in solids were carried out by the authors of papers [9,10] (see ref. [11]). Our DSR experiments [10–15] are performed within a biphenyl crystal mixed with pyrene molecules [16]. The experimental results are discussed within this paper. The problems of achieving such experiments in the gamma range are also analyzed.

Optical superradiance is a spontaneous, narrow-directional, coherent emission of light energy quanta with intensity proportional to the radiators ($\sim N^2$). DSR

was theoretically predicted by Robert Dicke in 1954, before the laser generation discovery and can be considered itself as an alternative coherent radiation source.

It is essential that spontaneous emission of radiation from a system with some pre-inverted particles is not independent for various particles under certain conditions, because the particle behavior is made collective by their common radiation field. The information about the radiation onset by one or more particles in the pre-inverted atomic system with L linear direction, will be transferred to the other particles via the radiation field within a time $\tau = Lc$, where c is the light velocity. If the magnitude τ is less than the duration of the first light quantum emission $\tau_c = \tau_1/N$, where τ_1 is the radiation life-time of an isolated particle, then all the particles will collectively radiate as one macroatom. This is the type of coherent radiation process which we call superradiance.

So, the main condition for superradiance observation is:

$$\tau < \tau_c < T_2, \quad (1)$$

where T_2 is the transverse dipole lifetime defined by the dephasing processes which limit the superradiance. The right-hand part of inequality (1) shows the mode to develop a new coherent spectroscopy method – the superradiant spectroscopy – yielding much more powerful signals than the traditional methods, such as the photon echo spectroscopy. Various relaxation processes diminish the superradiance signal intensity, so that the superradiance pulses analysis can provide information about the relaxation processes. In this paper, superradiance investigation will be presented for the left-hand part breakdown case in condition (1). It is important for the gamma-superradiance problem because of small τ_c within the gamma diapason.

2. DSR experiment in the biphenyl crystal doped with pyrene molecules

The biphenyl crystal has C_{2h}^5 space group symmetry with two molecules inside each cell. The pyrene molecule ($C_{16}H_{10}$) has D_{2h} point group symmetry. The polarization spectra of biphenyl and pyrene crystal absorption and luminescence are studied within the paper. The biphenyl with pyrene crystal is a mixed molecular crystal with a weak electron–phonon interaction.

The DSR experiment geometry and the operating level scheme for pyrene molecules in biphenyl are depicted in fig. 1. DSR is observed on the ${}^1B_{2u}-{}^1A_g$ pyrene transition at a 373.9 nm wavelength for $T = 1.5\text{--}4.2$ K. We can use the four-level model in order to consider the superradiance of a pyrene molecules ensemble. Levels 1 and 2 (1A_g and ${}^1B_{2u}$, respectively, are singlet ones, while 3 and 4 are vibronic ones, the nearest of them laying at 1408 cm^{-1} from the corresponding singlet level). Pumping to one of the vibronic levels (3), whose lifetimes are in the picosecond range, was achieved using various lasers: by means of a nitrogen laser on the 337 nm wavelength, by the third Nd^{3+} glass laser harmonic on 359.2 nm wavelength

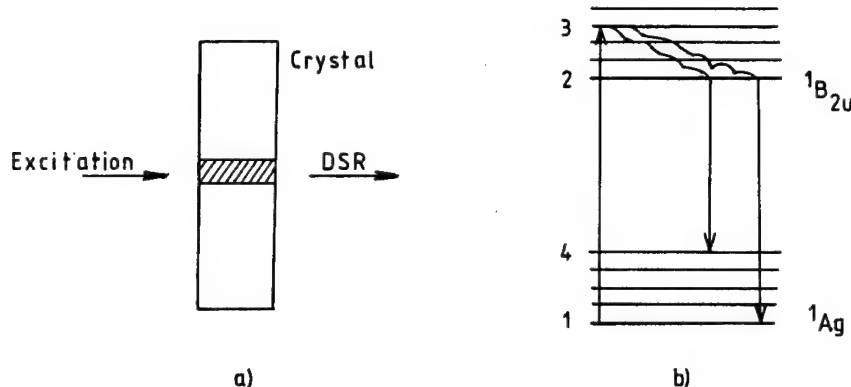


Fig. 1. Experimental geometry (a) and operating level scheme of pyrene molecules in biphenyl; DSR was observed for the transition between them (b).

and by the third YAG : Nd³⁺ laser harmonic on the 354.7 nm wavelength. As a result of radiationless transitions, electrons from pyrene appear instantly on the 2 singlet level, out of which they can be transferred either to the 1 singlet level (0-0 transition) or to the 4 vibronic level, characterized by a short lifetime in the picosecond range. Radiation from the 2-1 transition is a Dicke superradiance.

The DSR intensity dependence on the pyrene molecules concentration was first obtained and its quadratic character has been estimated (fig. 2a). Secondly, this radiation was defined to be narrow directional in space (fig. 2b). The superradiance peak intensity was about a thousand times larger than the noncoherent spontaneous background. The superradiance is highly polarized (the polarization degree is equal to 0.95). This could be observed, if the pumping power was larger than 0.5 MW/cm². A sharp decrease in the emission time was observed for the "2-1"-transition (0-0 transition), from 110 ns down to 5-6 ns. In the high guest concentration sample, the DSR pulse shape changed from a single peak to a double peak with an excitation intensity increase. As the sample temperature increase, the DSR intensity drops due to electron-phonon interaction (fig. 3).

Thus, the main features typical for DSR were observed. But, there is another phenomenon exhibiting the same features, including the quadratic concentration dependence in some cases. It is a superfluorescence – the amplified spontaneous emission (ASE). ASE is achieved when inequality (1) is totally inverted. When only the left-hand side of condition (1) is broken, both phenomena manifest themselves. The last case will be considered in the final section of this paper. ASE differs from DSR by the temporal form of its signal. The ASE pulse retardation time is smaller than its width, while the DSR pulses delay is larger than the pulse width. In our experiment, the delay was 10 ns which is larger than the 5-6 ns pulse duration.

Moreover, one can directly check the validity of condition (1) by calculating τ_c . In the DSR phenomenon theory, it is shown that the DSR pulse intensity is equal to:

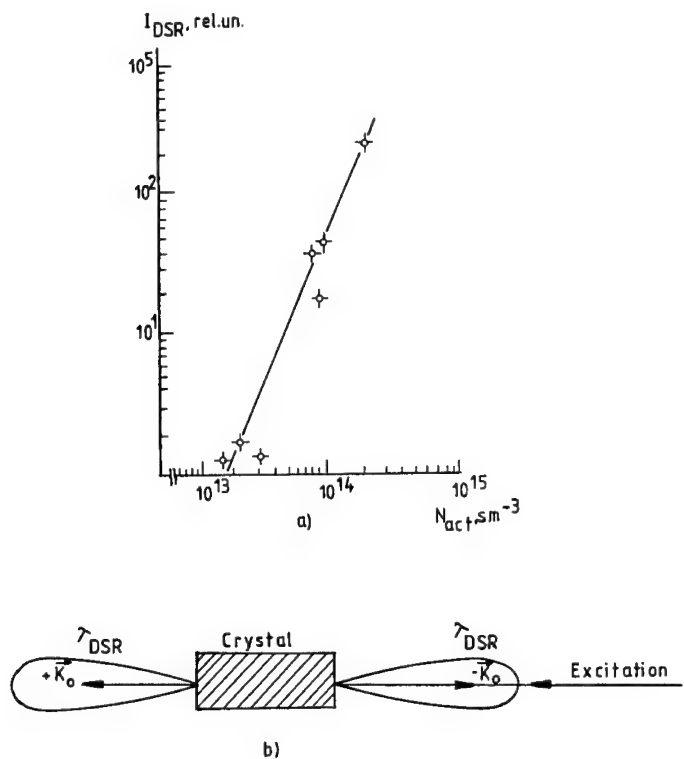


Fig. 2. (a) Concentration dependence of the emission intensity for the "2-1" transition in pyrene molecules in biphenyl at 4.2 K; N_{act} is the number of active centers. (b) Directorial diagram of DSR intensity in a pyrene-doped biphenyl crystal.

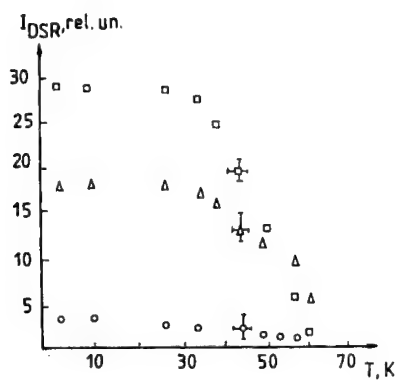


Fig. 3. Temperature dependence of peak DSR intensity in a pyrene-doped biphenyl crystal under different excitations: ■ - 100 kW; △ - 60 kW; ○ - 20 kW.

$$I(\mathbf{k}, t) = I_0(\mathbf{k}) \frac{N^2 \lambda^2}{4S} \operatorname{sech}^2 \frac{t - t_0}{\tau_c}, \quad (2)$$

where $I_0(\mathbf{k}) = \hbar\omega_0/T_1$ is the spontaneous emission intensity for a single particle in the \mathbf{k} direction, τ_c is a self-induced correlation time equal to the DSR pulse duration, t_0 is the DSR pulse delay time. However, MacGillivray and Feld [17] reached another formula for the maximal DSR intensity, when the medium reaction is taken into account.

$$I_{\max} \approx 4N \cdot \hbar\omega_0 \frac{1}{\tau_c \Phi^2}, \quad (3)$$

where $\Phi \approx \frac{1}{2} \ln N$, $\tau_c = T_1 8\pi S/(N\lambda^2)$, S is the cross-sectional area and λ is the wavelength,

$$\Delta t_c = \tau_R \cdot \Phi$$

is the duration of the superradiant pulse. For our crystal, we have $N = 10^{13}-10^{14} \text{ cm}^{-3}$, for the impurity concentration, $\lambda = 3.47 \times 10^{-5} \text{ cm}$, $L = 0.4 \text{ cm}$, $T_2 = 10^{-8} \text{ s}$ and $T_1 = 10^{-7} \text{ s}$. Hence, $\tau_c = (2-8) \times (10^{-10}-10^{-11}) \text{ s}$, $\tau = L/C \approx 10^{-11} \text{ s}$ and inequality (1) is verified. Taking into account the above-mentioned formulas, we can also obtain the values for DSR pulse duration.

If the excitation spectrum totally overlaps the inhomogeneously broadened line, inequality (1) is more rigid. We must include the T_2^* transverse reversible relaxation time on the right-hand side of it. But we had the selective excitation. As is well known, T_2^* is connected with τ_c by the Friedberg–Hartmann equation,

$$\alpha L = 2T_2^*/\tau_c. \quad (4)$$

So, when $\alpha L > 1$, $2T_2^* > \tau_c$. But one should keep in mind that the Friedberg–Hartmann equation is deduced by association of T_2^* with $\pi g(0)$. This is not the case if selective excitation is used. In case of selective excitation, we must assume that:

$$\pi g(0) = (\Delta\omega_p)^{-1},$$

where $\Delta\omega_p$ is the excitation pulse spectral width. Thus, taking into account that:

$$\tau_c = (\Delta\omega_s)^{-1},$$

where $\Delta\omega_s$ is the superradiance pulse spectral width, we can rewrite eq. (4) as:

$$\alpha L = 2\Delta\omega_p/\Delta\omega_s \geq 1. \quad (5)$$

In the experiment, we had $\Delta\omega_p = 0.1 \text{ cm}^{-1}$, $\Delta\omega_s = 0.08 \text{ cm}^{-1}$, $\alpha = 6 \text{ cm}^{-1}$ and $L = 0.4 \text{ cm}$. This way, the condition (5) is also fulfilled.

3. Results of the DSR theory in solids

Using the non-equilibrium statistic operator (NSO) method, we reached the following equation for DSR intensity in solids [18]:

(a) for the initial stage

$$I = \frac{D^2 \hbar \omega_0}{2(1 + 2\tau_1/\tau_{1k_0})} \operatorname{sech}^2 \left[\frac{D}{2} (t - t_0) \right], \quad (6)$$

where ω_0 is the resonant frequency of the operative transition; t_0 is the DSR delay time;

$$t_0 = \frac{\tau_1}{D} \ln \left\| \frac{\left(1 + 2\frac{\tau_1}{\tau_{1k_0}}\right)N - \left(1 + 2n_0 + \frac{\tau_1}{\tau_{1k_0}}N\right) + D}{\left(1 + 2\frac{\tau_1}{\tau_{1k_0}}\right)N - \left(1 + 2n_0 + \frac{\tau_1}{\tau_{1k_0}}N\right) - D} \right\|; \quad (7)$$

n_0 is the photon initial value in the k_0 coherent mode; N is the initial number of active particles;

$$\frac{1}{\tau_1} = \frac{1}{\tau_1(0)} \left[1 + \alpha \operatorname{cth} \frac{\hbar \Omega_0}{2k_B T} \right]; \quad (8)$$

$$\alpha = (2\hbar\omega_0)^{-1} \sum_q \varphi_q; \quad (9)$$

φ_q is the constant of interaction between the active particles and the phonon mode q ; q is the phonon wave vector; k_B is the Boltzmann factor; T is the solid temperature; Ω_0 is the pseudo-localized phonon frequency and τ_{1k_0} is the τ_1 value, which corresponds to the k_0 mode.

(b) the radiation intensity in the stationary regime is described by the following equation:

$$I = \frac{\hbar \omega_0}{\tau_{\text{phot}}} \langle n_{k_0} \rangle, \quad (10)$$

where $\langle n_{k_0} \rangle = n_0 + \frac{\tau_1}{2\tau_{1k_0}} (N - \langle R_z \rangle)$,

$$\langle R_z \rangle = -\frac{1}{1 + 2\tau_1/\tau_{1k_0}} \left\{ D \cdot \operatorname{th} \left[\frac{D}{2} (t - t_0) \right] + \left(1 + 2n_0 + \frac{\tau_1}{\tau_{1k_0}} N \right) \right\}.$$

4. Connection of DSR with other transient phenomena

Thus, we observed and investigated the Dicke optical superradiance in the biphenyl and pyrene crystal and we have theoretically described some of the solid-state

DSR features. DSR can be used as an optical coherent spectroscopy method. It can open perspectives for practical applications.

DSR is closely related to other coherent optical phenomena. Spano and Warren [19] have shown (by double application of eq. (3)) that the $\pi/2-\pi$ pulse sequence yields the echo superradiative signal at the moment of time equal to the interpulse duration for homogeneous systems, just as in the conventional echo with inhomogeneous dephasing. The difference is that the superradiant echo is a much more powerful signal. Moreover, the pulse area variation does not alter the signal power which varies only in the moment of its regaining. One interesting example is a triggered DSR, where a small triggering pulse is applied after the first π -pulse. It was observed by Carlson et al. [20]. In what regards the conventional echo, its observation time is limited by τ_1 in the stimulated echo case. It is known that, in paramagnetic crystals, such as $\text{LaF}_3 : \text{Pr}^{3+}$, $\text{Y}_2\text{O}_3 : \text{Eu}^{3+}$ and $\text{YAlO}_3 : \text{Eu}^{3+}$ the long-lived stimulated echo is observed due to the long τ_1 lifetimes of their superfine levels. We believe that, in such crystals, long-lived triggered DSR is possible. Another possibility to obtain long-lived superradiative signals is to employ the subradiance effect, which allows superradiant echo observation, for times which are up to $\tau_1 \cdot N$ in some cases.

5. Possibility of observation of gamma DSR

One of the main peculiarities of the gamma-range is the low wavelength ($\lambda = 1-10 \text{ \AA}$), which is close to the molecular size or to the distance between them [11]. In this case, the mechanism of DSR formation by means of the radiation field cannot be singular. Other superradiant mechanisms, such as the exciton superradiance [21] and the annihilation superradiance in the positron-atoms system [22], can be effective.

The following condition [23]:

$$\mathbf{K}_\gamma = 2\pi\mathbf{b},$$

(where \mathbf{K}_γ is the gamma-radiation wave vector, and \mathbf{b} is the vector of the reverse lattice) is important for the gamma-generation achievement.

Another peculiarity of the gamma-range is the difficulty of obtaining total population inversion. However, total inversion is not obligatory for DSR. This coherent phenomenon can show up in states with a low value of the R cooperation number. Under these conditions, the various modes of coherent state attainment, such as in ref. [24], can prove to be useful.

The small section of forced gamma-quanta radiation is not important for gamma DSR, since it represents spontaneous emission. At present, the gamma-echo experiment is carried out [25], where a collective phase of the ^{57}Fe Mössbauer gamma-radiators is achieved. In a previous issue of this paper, we have already discussed the connection between DSR, gamma echo and other transient phenomena. It is

known that the echo-signal has a lower intensity compared to the superradiant signal. A certain observation of gamma-echo in ref. [25] permits to believe in gamma-DSR observation. Modern development of the gamma-ray detectors, described by Alberto Tebo [26] increases this hope. The experiment [25] corresponds to the regime of gamma-ray propagation across a long resonant medium [27]. As already known [28], under these conditions, the equations describing the superradiance evolution and phenomena, such as self-induced transparency, are similar. The different solutions of these equations, corresponding to various transient phenomena, are defined by the initial and boundary conditions. In ref. [7] the condition for the existence of the coherent component of the gamma radiation is found as:

$$\mu L > 1 + 1/\Gamma T_1, \quad (11)$$

where μ is the resonant coefficient of the strengthening; L is the sample length; $\Gamma = 1/T_2$; T_1 and T_2 are the longitudinal and transverse nonreversible relaxation times, respectively. This condition of many long-lived isomers can be satisfied if the many-pulses technique [3] of line narrowing is applied.

Acknowledgement

This paper is supported by the International Scientific Fund of Soros (grant no. NNW300). Thanks to T.G. Mitrofanova for help.

References

- [1] V.I. Goldansky, R.N. Kuzmin and V.A. Nameot, *Mössbauer spectroscopy* (Mir, Moscow, 1983) p. 65.
- [2] R.H. Dicke, Phys. Rev. 93 (1954) 99.
- [3] U. Haeberlen and M. Mering, *High Resolution NMR in Solids* (Mir, Moscow, 1980).
- [4] A.V. Andreev, V.I. Emelianov and Ya.A. Iliinsky, Usp. Fiz. Nauk. 131 (1980) 653.
- [5] L.A. Rivlin, Vopr. Radioelektron. 6 (1963) 42.
- [6] A.V. Andreev, JETP 72 (1977) 1397.
- [7] A.V. Andreev, Ya.A. Iliinsky and R.V. Khokhlov, JETP 73 (1977) 1296.
- [8] N. Skribanowitz, I.P. Herman, J.C. MacGillivray and M.S. Feld, Phys. Rev. Lett. 30 (1973) 309.
- [9] R. Florian, L.Q. Schwan and D. Schwan, Solid. State Commun. 42 (1982) 55.
- [10] P.V. Zinoviev, S.V. Lopina, Yu.V. Naboikin, N.B. Silaeva, V.V. Samartsev and Yu.E. Sheibut, JETP 85 (1983) 1945.
- [11] P.V. Zinoviev, V.V. Samartsev and N.B. Silaeva, Laser Phys. 1 (1981) 1.
- [12] Yu.V. Naboikin et al., JETP 89 (1985) 1146.
- [13] S.V. Andrianov et al., JETP 91 (1986) 1990.
- [14] S.V. Andrianov et al., Usp. Fiz. Nauk. 150 (1986) 457.
- [15] V.A. Golenischev-Kutuzov, V.V. Samartsev and B.M. Khabibullin, *Pulsed optical and acoustical coherent spectroscopy* (Nauka, Moscow, 1988).

-
- [16] Yu.V. Naboikin, V.V. Samartsev, P.V. Zinoviev and N.B. Silaeva, *Coherent spectroscopy of molecular crystals* (Naukova Dumka, Kiev, 1986).
 - [17] J.C. MacGillivray and M.S. Feld, *Contemp. Phys.* 22 (1986) 299.
 - [18] V.V. Samartsev et al., *Laser Phys.* 5 (1995) 1.
 - [19] F.C. Spano and W.C. Warren, *J. Chem. Phys.* 90 (1989) 6034.
 - [20] N.W. Carlson et al, *Opt. Commun.* 32 (1980) 350.
 - [21] S.V. Andrianov, V.V. Samartsev and Yu.E. Sheibut, *Theor. Math. Phys.* 72 (1987) 286.
 - [22] R.A. Vlasov, O.N. Gandomsky and V.V. Samartsev, *Theor. Math. Phys.* 79 (1989) 423.
 - [23] I.H. Terhune and G.S. Baldwin, *Phys. Rev. Lett.* 14 (1965) 589.
 - [24] O.A. Kocharovskaya and Ya.I. Khanin, *JETP Lett.* 48 (1988) 581.
 - [25] P. Helisto, I. Tittonen, M. Lippmaa and T. Katila, *Phys. Rev. Lett.* 66 (1991) 2037.
 - [26] A. Tebo, *OE Reports*, Oct.-Nov. (1994) 1.
 - [27] M.D. Crisp, *Phys. Rev. Lett.* 22 (1969) 826.
 - [28] V.V. Samartsev and Yu.E. Sheibut, *Laser Phys.* 1 (1991) 482.

Superfluorescence in the presence of inhomogeneous broadening and relaxation

B. Balko, I.W. Kay, J.D. Silk

Institute for Defense Analyses, Alexandria, VA 22311, USA

R. Vuduc

Cornell University, Ithaca, NY 14850, USA

and

J.W. Neuberger

University of North Texas, Denton, TX 76203, USA

In this paper we show how inhomogeneous broadening produces dephasing, inhibits cooperative emission and thus reduces the intensity of the SF pulse. We also show how electronic relaxation or time-dependent hyperfine interactions can mollify the effect of inhomogeneous broadening so that SF can be recovered.

1. Introduction

One of the early concepts introduced for developing a γ -ray laser [1] was based on the idea of direct emission from isomeric nuclear levels. Such levels, because of their long lifetime, permitted long pumping times and were considered to be good storage levels. Unfortunately, because of the narrow natural linewidths associated with the long lifetimes, and the relatively large environmental effects which cause inhomogeneous broadening, resonance conditions for transitions involving such levels are difficult to achieve. Several approaches to alleviate the problem have been put forth. One of the approaches proposes to reduce the line broadening by means of external fields [2,3].

Inhomogeneous broadening effects can also be overcome by internal fluctuating fields. Such dynamic effects produce characteristic lineshape modifications in nuclear resonance spectra. The process is commonly referred to as relaxation [4,5]. The purpose of this paper is to present a model of SF in the presence of inhomogeneous broadening and relaxation and to examine the proposition that time-dependent hyperfine interactions can be used to recover SF in inhomogeneously broadened systems. SF emission is interesting because when a γ -ray laser is finally

developed it will probably operate in the SF mode. We show how the Maxwell–Bloch equation used to model SF can be modified to account for inhomogeneous broadening and determine to what extent relaxation in an inhomogeneously broadened environment can modify the effect of broadening and how it can influence the recovery of SF emission.

2. Superfluorescence

SF can be viewed as a spontaneous emission by N coupled, cooperating radiators which produces the experimentally interesting effect depicted in fig. 1; a short pulse with intensity proportional to N^2 , occurring at a fraction of the natural lifetime ($\sim (1/N)\tau_n$). For a sample shaped like a needle the pulse is emitted along the axis.

The SF process is initiated by quantum fluctuations of the vacuum electromagnetic field which gives rise to a phasing or buildup of correlations between the radiators in the inverted region. SF is governed by the dynamics of the evolving system of Maxwell–Bloch equations with random noise sources [6]. No simple threshold condition connecting the pertinent parameters exists as in the case of lasing^{#1}. Conditions for the occurrence of SF are described in terms of characteristic times representing the speed of competing processes: namely, the single nucleus lifetime τ_n , the radiative lifetime τ_r , the cooperation time τ_c , the time of emission of the SF pulse τ_{SF} , the delay time of the pulse τ_D , the dephasing time^{#2} τ_φ and the pumping time τ_γ . The cooperation time^{#3} τ_c sets the absolute upper limit on the SF time τ_{SF} and consequently on the delay time τ_D . Intuitively one expects that for SF to occur the following conditions should hold:

$$\tau_\gamma < \tau_D < \tau_\varphi, \tau_n, \tau_c .$$

More rigorous analysis [9] shows that

$$\sqrt{\tau_D \tau_{SF}} < \tau_\varphi$$

^{#1} For the steady-state nuclear laser the Schawlow–Townes gain condition given by Trammell and Hannon [7] is $k = (\lambda^2/2\pi)(f\Delta n^*/(1+\alpha)(1+a)) - \mu > 0$, where k is the gain coefficient, λ is the wavelength of the emitted radiation, f is the recoilless fraction of the transmission, α the internal conversion coefficient, a the inhomogeneous broadening parameters and μ the linear attenuation coefficient. This condition is modified for the pulsed laser to account for the reduction of the inversion during the emission process, but a sharp cutoff is still present. As we show in ref. [10] this is not the case for SF emission.

^{#2} This commonly is due to collisions or inhomogeneous broadening.

^{#3} The cooperation time is obtained from the Dicke formula for the emission rate [8], $\gamma_c = \frac{1}{4} N_c (1/t_r) \lambda^2 / A$, where N_c is the number of emitters, λ the linewidth of the radiation and A the cross section of the rod forming the inverted region, and a self-consistent argument determining how many atoms can be covered by the emission of a single atom during the Dicke emission time, $1/\gamma_c$. With $N_c = (c/\gamma_c)A\rho$ we get $\tau_c = 2/\sqrt{c\rho\Gamma\lambda^2}$.

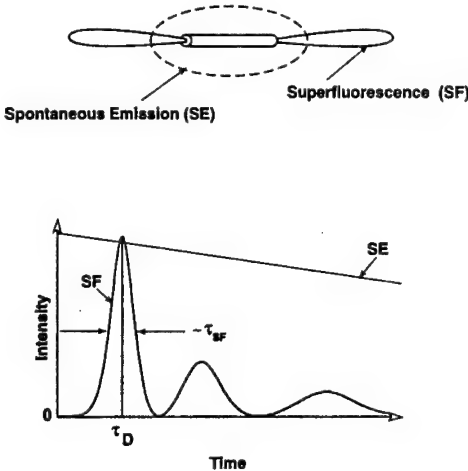


Fig. 1. Superfluorescent pulse emission. The top figure shows the angular distribution of the radiation and the bottom figure the temporal variation of the pulse. In both cases a comparison with normal non-cooperative spontaneous emission with each nucleus emitting independently is made.

is actually the appropriate condition between the delay time, SF time, and the dephasing time.

The basis for our theoretical model of nuclear SF is described in detail in ref. [10] and is the set of Maxwell–Bloch equations in dimensionless units in the form introduced by Haake and Reibold [6]

$$\frac{\partial}{\partial t} N_3 = \gamma N_3, \quad (1a)$$

$$\frac{\partial}{\partial t} N_2 = -(E^+ R^+ + E^- R^-) - \Gamma N_2 + \gamma N_3, \quad (1b)$$

$$\frac{\partial}{\partial t} N_1 = -(E^+ R^+ + E^- R^-) - \Gamma N_2, \quad (1c)$$

$$\frac{\partial}{\partial t} R^\pm = (N_2 - N_1) E^\pm - \frac{1}{2} [\Gamma + \Gamma_\phi] R^\pm + \xi^\pm, \quad (1d)$$

$$\frac{\partial}{\partial x} E^\pm = g_0 R^\pm - \frac{1}{2} \mu E^\pm. \quad (1e)$$

In the above equations distance is normalized to the length of the active region l and retarded time is used normalized to the superfluorescence time given by

$$\tau_{SF} = \frac{8\pi\tau_0}{3\lambda^2\rho l}$$

where τ_0 is the natural lifetime, ρ is the inversion density of nuclei, and λ is the photon wavelength.

The quantities N_1 , N_2 , N_3 in eq. (1) are the population density operators of the lowest, middle, and upper levels of a three-level atomic or nuclear structure. The quantities R^\pm are the positive and negative frequency components of the polarization operator, and the quantities E^\pm are the positive and negative frequency components of the electric field operator. The quantities ξ^\pm similarly represent noise operators due to quantum electrodynamic fluctuations of the vacuum state. These quantities and their effect on the SF emission are discussed in detail in ref. [10].

Three decay constants that are associated with emission linewidths occur explicitly in eqs. (1a)–(1e). One of the constants is the pumping rate γ which is identified with the natural linewidth of the pumping level, another is Γ , the inverse of the lifetime (τ_0^{-1}), which is identified with the natural linewidth of the SF level, and the third is Γ_ϕ , which is a dephasing parameter associated with the homogeneously broadened line.

In addition, we can associate a fourth decay constant, Γ_θ , with the inhomogeneously broadened SF linewidth. An inspection reveals that it does not appear explicitly in any of the eqs. (1a)–(1e). Its physical effect must therefore be different from that of Γ_ϕ , which, as indicated on the right side of eq. (1d), is simply to increment the natural linewidth.

3. Time-dependent coupling parameter

Eq. (1e) has to be modified before the model can be applied to SF emission in inhomogeneously broadened systems. The original equations apply to identical nuclei which see precisely the same environment. Inhomogeneous broadening introduces decorrelation between different nuclei because of their slightly different resonant energies. It turns out that the required modification is simply to change the coupling constant g to a time-dependent parameter.

A number of authors [11–13] have derived the effect of inhomogeneous broadening in earlier models of SF. Although the derivations are essentially equivalent, the one given by Bonifacio and Lugiato in ref. [11] is particularly convenient for adaptation to our model.

Those authors observe that the rotating wave approximation of the interaction Hamiltonian ^{#4} leading to the Maxwell–Bloch equations for their case has the form

^{#4} Ref. [11] uses a special representation that removes the Schrödinger picture time dependence of the free field photon and atomic operators. The resulting interaction Hamiltonian is therefore time dependent.

$$H_1(t) = -\frac{i\hbar}{\sqrt{V}} \sum_{\mathbf{a}}^N \sum_{\mathbf{k}} g_{\mathbf{k}} [a_{\mathbf{k}}^+ R^-(\mathbf{a}) f^*(\mathbf{k} - \mathbf{a}, t) - \text{H.C.}], \quad (2)$$

where \mathbf{a} represents the reciprocal lattice modes and the coefficients $g_{\mathbf{k}}$ outside the brackets in the double sum on the right side are coupling constants relating the photon and polarization operators, and the c number function appearing inside the brackets is given by

$$f(\eta, t) = \frac{1}{N} \sum_{j=1}^N e^{i\eta \cdot \mathbf{x}} e^{(w_j - w_0)t}. \quad (3)$$

The outer sum in eq. (2) is over the individual atomic positions at the lattice points in a crystal lattice, and the polarization operators R^{\pm} in each term of the sum characterize the state of the corresponding atom.

The time-dependent factor in each term in the sum on the right side of eq. (3) introduces a phase shift due to a shift w_j about the resonant frequency w_0 . Arriving photons emitted by atoms at other locations, because of phenomena such as Doppler shifts caused by differing relative motion of the remote atoms or different hyperfine fields at different sites, contribute to the different w_j . The resulting phase shifts, which are random, are responsible for the inhomogeneous line-broadening effect.

Eq. (3) is clearly an average of a large sample of random phase factors from some statistical distribution and should, therefore, reduce to the ensemble average of the random variable representing a single phase factor, i.e.,

$$f(\eta, t) = \langle e^{i\eta \cdot \mathbf{x}} e^{i(w - w_0)t} \rangle = \langle e^{i\eta \cdot \mathbf{x}} \rangle \langle e^{i(w - w_0)t} \rangle = F(\eta) g_1(t). \quad (4)$$

Note that this equation includes the case in which the atomic locations may also be random – as long as they are statistically independent of the random phase shifts.

As indicated by the notation in eq. (4), the function $g_1(t)$ is the average value of a time-dependent random variable $\exp[i(w - w_0)t]$ with some probability distribution of frequencies. That is,

$$g_1(t) = \int_{-\infty}^{\infty} \hat{g}(\xi) e^{i\xi t} d\xi, \quad (5)$$

where the function $\hat{g}(w - w_0)$ is a normalized frequency distribution, which is usually assumed to be either Gaussian or Lorentzian.

The effect of inhomogeneous line broadening then is to replace the coupling constant $g_{\mathbf{k}}$ by a function of time obtained by multiplying $g_{\mathbf{k}}$ by the function $g_1(t)$ that the relations (4) and (5) define. The same argument applied to the corresponding Hamiltonian in ref. [14], which, according to ref. [15], motivated the derivation of the Maxwell–Bloch equations for the Haake–Reibold model, leads to a similar

result. An analysis similar to that of ref. [6] shows that the result carries over into eq. (1e).

If the normalized frequency distribution that determines $g_1(t)$ is Lorentzian the result is an exponentially decaying function of time. Thus, assuming a Lorentzian frequency distribution, the introduction of inhomogeneous broadening into the Haake–Reibold model is accomplished by replacing the coupling constant g_0 on the right-hand side of eq. (1e) by the function^{#5}

$$g(t) = g_0 e^{-(\Gamma_\theta/2)t}. \quad (6)$$

4. Effect of relaxation on $g_1(t)$

Using the time-dependent coupling function $g_1(t)$ instead of the constant g in eq. (1e) we can model the effect of inhomogeneous broadening on the SF pulse shape. Fig. 2a gives some calculated results showing the modification of the SF pulse shape due to inhomogeneous and homogeneous broadening for comparison. Homogeneous broadening is accounted for by the decay rate Γ_φ in eq. (1c) and thus plays a different role in the emission processes. For the same effective amount of broadening (when $\Gamma_\varphi = \Gamma_\theta$), inhomogeneous broadening has a more drastic effect on the pulse shapes as shown in fig. 2b.

An inhomogeneously broadened line is formed by a collection of resonances each displaced from the center frequency by an amount determined by some distribution as depicted graphically in fig. 3a. In the figure only a small number of lines is shown, each centered at a frequency ω_i , displaced from the center frequency ω_0 , and each representing a sum of resonances corresponding to the number of nuclei with that particular resonance energy. The intensity of each line is determined by the prescribed distribution. Shifting the resonances closer together provides an increase in overlap of lines as shown in figs. 3b and c. Homogeneous broadening of the lines also provides an increase in overlap as shown in figs. 3d and e but since the maximum is also reduced, as discussed in ref. [17], the resonant effect between a source and absorber remains small. In general both effects can contribute, as shown in figs. 3f and g.

Relaxation between the lines $(\omega_0 + \omega_i, \omega_0 - \omega_i)$ on opposite sides of the average resonance, ω_0 has the combined effect of broadening the lines and shifting them toward the center until a total collapse at the outer frequency occurs at high relaxation rates, i.e., in the “motionally narrowed region”. This effect has been observed

^{#5} This is equivalent to a special case of the result that was obtained elsewhere [16]: $(\partial/\partial x + (1/v)\partial/\partial t)E^\pm(x, t) = \int p(v)R^\pm(x, t, v)dv$, taking into account the fact that the Haake–Reibold independent variables involve the retarded time while Haake et al. [16] use the true time and that $p(v)$ replaces $g(\omega - \omega_0)$ as the frequency distribution associated with detuning contributions from all atoms.

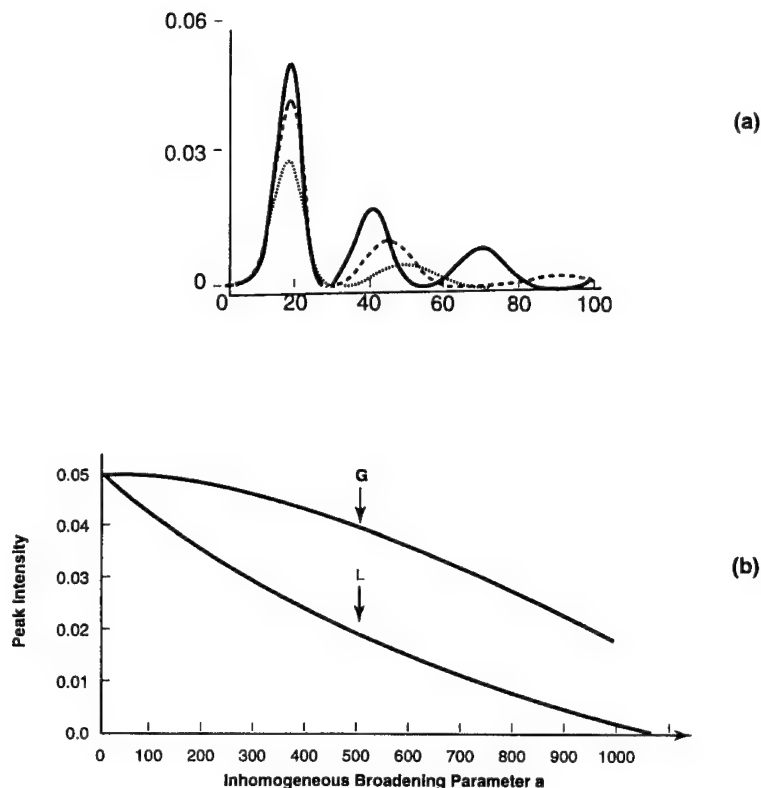


Fig. 2. Effect of inhomogeneous and homogeneous broadening on SF emission. In (a) the solid line shows the pulse without broadening and the dashed and dotted lines show the pulses emitted from homogeneously broadened and inhomogeneously broadened systems each with broadening of 200 times the natural linewidth. In (b) we show the effect of increasing broadening on the pulse intensity with curve L obtained using a Lorentzian distribution and curve G using a Gaussian distribution.

in Mössbauer experiments in many compounds. In fig. 4 we show some typical spectra of a classical paramagnet in a temperature range where at the low relaxation rate (low temperature) a typical Zeeman splitting occurs. As the relaxation rate increases the lines broaden until at very high rates there is a collapse to a single central line^{#6}. There are some special compounds which exhibit this simple classical

^{#6} This behavior can be easily understood if one assumes a classical field flipping model for the relaxation [4]. The parameter that determines the lineshape is the ratio of the relaxation rate to the Larmor precession frequency of the levels. The lifetime of the excited state only determines the minimum linewidth [5]. At low relaxation rates the full Zeeman-split spectrum is observed because the nucleus responds to a particular field at its site. At very high relaxation rates with respect to the Larmor precession frequency the nuclear spins cannot respond to the changing field and so the average effect of zero field is observed. At intermediate relaxation rates the lines broaden and collapse in a complicated fashion and a complete theory has to be used to describe the detailed line-shapes.

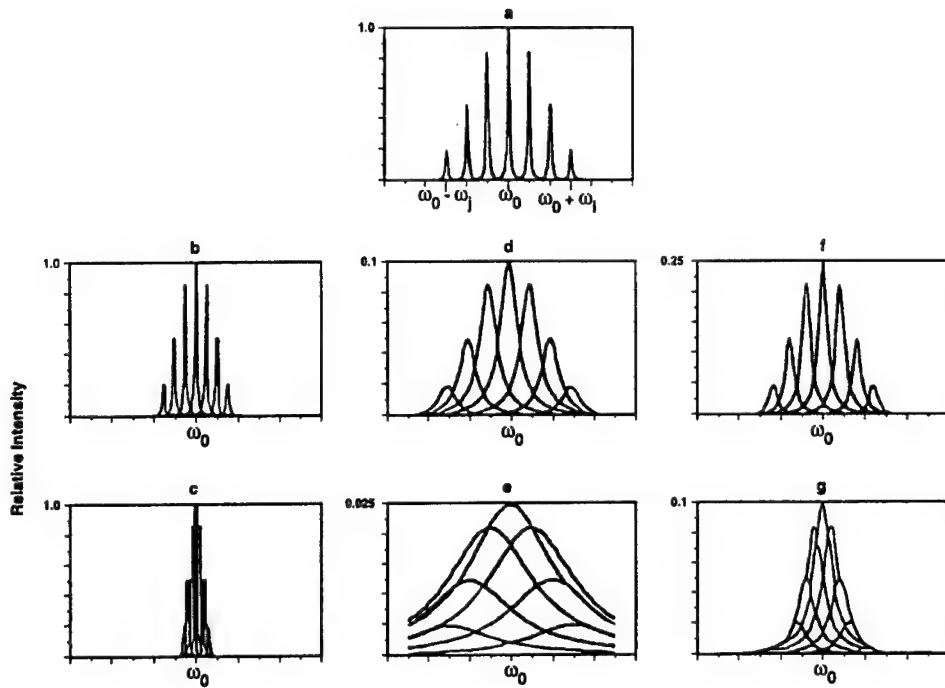


Fig. 3. A graphic representation of inhomogeneous broadening (a) and the increase in overlap produced by shifting lines (b,c), homogeneously broadening the lines (d,e), and the combined effect of both (f,g).

paramagnetic behavior, but, in general, more complex and not easily predictable behavior can occur as described in ref. [18]. Also, transmission spectra can hide some complex dynamic behavior, because completely different phenomena can give deceptively similar transmission spectra. To uncover the true relaxation mechanisms more discriminating experiments have to be performed [19]. Nevertheless one thing is clear. However complex the relaxation mechanisms, the effect is to produce a simpler, higher-intensity peak in the transmission spectrum in the high relaxation or "motionally narrowed" limit. It seems reasonable to expect that in this limit one would also obtain an increase in the peak intensity in SF emission.

As can be seen from the previous section, the inhomogeneous broadening produces a temporal variation of the coupling factor $g_1(t)$ (eqs. (3) and (5)), even though the resonance frequencies at different sites ω_j may be time independent. If the hyperfine fields cause the energies ω_j in eq. (3) to jump between different values, then the correlation function in eq. (5) is modified and can be calculated using the approach introduced in the literature [5] for dealing with time-varying fields. For example, according to Blume, if the hyperfine energy jumps between two values ω_j and $-\omega_j$, then the correlation function required in eq. (4),

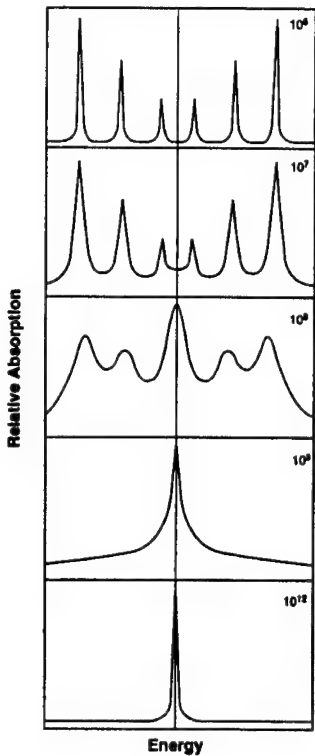


Fig. 4. Effect of relaxation on lineshape in a classic paramagnet. The numbers in the figure give the relaxation rate or the flipping rate of the magnetic field (550 kG) producing the Zeeman splitting in s^{-1} .

$$g_1(t) = \langle e^{i(\omega - \omega_j)t} \rangle,$$

becomes

$$g_1(t) - \langle e^{i\alpha \int_0^t f(t') dt'} \rangle_{av} = \left(\cos x\Omega t + \frac{1}{x} \sin x\Omega t \right) e^{-\Omega t} = G(\Omega, \alpha, t), \quad (7)$$

where $\alpha = 2\omega_j$, Ω is the relaxation rate and $x = [(\alpha^2/\Omega^2) - 1]^{1/2}$.

To model inhomogeneous broadening α should take on values from $-\infty$ to $+\infty$ subject to some probability distribution $\gamma(\alpha, \sigma)$ that describes the broadening. The effective inhomogeneously broadened coupling factor then is given by $G(\Omega, \sigma, T) = \int_{-\infty}^{\infty} \gamma(\alpha, \sigma) G(\Omega, \alpha, t) d\alpha$ and replaces g_0 in eq. (1e). These approaches, when applied to SF pulse emission, provide a reduction of the effect of inhomogeneous broadening.

Consider fig. 5a where we show two SF pulses calculated assuming the same amount of inhomogeneous broadening in the system but different relaxation rates.

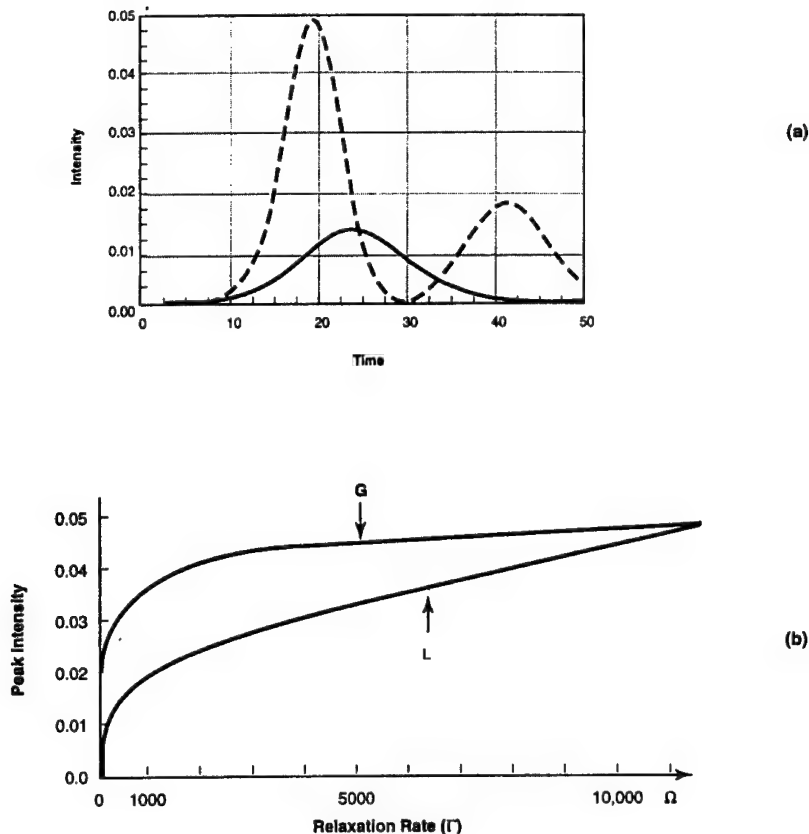


Fig. 5. Effect of relaxation on SF emission in an inhomogeneously broadened system. In (a) the solid line shows the pulse suppressed due to inhomogeneous broadening modeled by a Gaussian distribution with $\sigma = 10^6$ times the natural linewidth and the dashed line shows the pulse recovered with relaxation ($\Omega = 10^3 \Gamma$). In (b) we show the effect of relaxation on SF in inhomogeneously broadened systems with a Gaussian distribution (solid line) and Lorentzian distribution (dashed line). The relaxation rate is given in units of Γ .

The increased relaxation rate produces a sharper, more intense, main peak and also a smaller secondary peak which is characteristic of a strong SF emission. Fig. 5b shows the effect of relaxation on SF intensity for inhomogeneously broadened systems when the broadening is modeled by Gaussian and Lorentzian distributions. The Lorentzian distribution is more effective in depressing the SF peak but at high relaxation rates both broadening effects can be overcome.

5. Conclusion

Our results show that while SF emission is suppressed due to inhomogeneous

broadening it can also be recovered through fast relaxation between levels producing the broadening. For full recovery the relaxation has to be fast enough to produce a collapse in an absorption spectrum to a single narrow line. However, partial recovery of the SF may also provide a large enough signal to be observed.

References

- [1] V. Vali and W. Vali, Proc. IEEE 51 (1963) 1822.
- [2] A.V. Andreev, Y.A. Il'inskii and R.V. Khokhlov, Sov. Phys. JETP 40 (1975) 816.
- [3] Y.A. Il'inskii and R.V. Khokhlov, Sov. Phys. JETP 38 (1974) 809.
- [4] H.H. Wickman, in: *Hyperfine Structure and Nuclear Radiations*, eds. E. Mathias and D.A. Shirley (North Holland, Amsterdam, 1968) p. 928–947.
- [5] M. Blume, in: *Hyperfine Structure and Nuclear Radiations*, eds. E. Mathias and D.A. Shirley (North Holland, Amsterdam, 1968) pp. 911–927.
- [6] F. Haake and R. Reibold, Phys. Rev. A29 (1984) 3208.
- [7] Trammell and Hannon, Opt. Commun. 15 (1975) 325.
- [8] F.T. Arrechi and E. Courtens, Phys. Rev. A2 (1970) 1730;
R.M. Dicke, Phys. Rev. 93 (1954) 68.
- [9] M.F.H. Schuurmans and D. Polder, Phys. Lett. 72A (1979) 306.
- [10] B. Balko, I.W. Kay and J.W. Neuberger, Phys. Rev. B 52 (1995) 858.
- [11] R. Bonifacio and L.A. Lugiato, Phys. Rev. A11 (1975) 1507.
- [12] F. Haake et al., Phys. Rev. A23 (1981) 1322.
- [13] R.H. Eberly, Acta Phys. Pol. A39 (1971) 633.
- [14] D. Polder, Phys. Rev. A19 (1979) 1192.
- [15] F. Haake and R. Reibold, Phys. Rev. A29 (1984) 3208.
- [16] F. Haake, J.W. House, M. King, G. Schroder and R. Glauber, Phys. Rev. A23 (1981) 1322.
- [17] B. Balko, I.W. Kay, J. Nicoll, J.D. Silk and G. Herling, these proceedings (1st Int. Gamma-Ray Laser Worksh., 1995), Hyp. Int. 107 (1997) 283.
- [18] G.R. Hoy, M.R. Corson and B. Balko, Phys. Rev. B27 (1983) 2652.
- [19] B. Balko, Phys. Rev. B33 (1986) 7421.

Time-domain, nuclear-resonant, forward scattering: the classical approach

Gilbert R. Hoy

Physics Department, Old Dominion University, Norfolk, Va 23529-0458, USA

This paper deals with the interaction of electromagnetic radiation with matter assuming the matter to have nuclear transitions in resonance with incident electromagnetic radiation. The source of the radiation is taken to be of two types; natural radioactive gamma decay and synchrotron radiation. Numerical examples using ^{57}Fe are given for the two types of source radiation. Calculated results are contrasted for the two cases. Electromagnetic radiation produced by recoil-free gamma-ray emission has essentially the natural linewidth. Electromagnetic radiation from a synchrotron, even with the best monochromators available, has a relatively broad-band spectrum, essentially constant for these considerations. Polarization effects are considered. In general, the nuclear-resonant medium changes the polarization of the input radiation on traversing the medium. Calculations are presented to illustrate that synchrotron radiation studies using nuclear-resonant forward scattering have the potential for making high-precision measurements of hyperfine fields and recoilless fractions. An interesting aspect of nuclear-resonant forward scattering, relative to possible gamma-ray laser development, is the so-called “speed-up” effect.

1. Introduction

The Mössbauer effect [1,2] is a consequence of the recoil-free emission and/or recoil-free absorption of gamma radiation that can happen in solids. In the standard method of doing Mössbauer spectroscopy (MS) the source radiation is Doppler-shifted through the resonance levels of an absorber and a spectrum is obtained which shows the absorption of the radiation as a function of energy of the source photons. Very soon after researchers developed this method of doing MS, it became clear that interesting results could be obtained using time-differential Mössbauer spectroscopy (TDMS) [3–11]. Hamermesh [4] solved the problem analytically for the case in which the nuclear-resonant medium has only one absorptive transition. The approach taken here uses numerical solutions based on fast Fourier-transform techniques.

The availability of synchrotron radiation to investigate nuclear-resonant processes has provided an additional stimulus to the field of nuclear-resonant gamma-ray spectroscopy. Because of the “time-bunch” structure of most synchrotrons, time-domain measurements of nuclear-resonant absorption and emission pro-

cesses can be done conveniently. Considerable research [12] has already been done in this field. The first experiments using synchrotron radiation (SR) interacting with nuclear-resonant matter [13] were performed using a single crystal of yttrium iron garnet enriched in ^{57}Fe and observing the subsequent nuclear Bragg scattering.

Over the years, a number of laboratories have developed codes for analyzing TDMS results, but interest in this area has diminished in recent years. On the other hand, interest in time-domain synchrotron-radiation spectroscopy (TDSR) has increased greatly due, at least in part, to the existence of third-generation synchrotron radiation facilities. As a consequence, a complete computational program package has been developed [15] named CONUSS.

The purpose of this paper is to describe some of the physics needed for analyzing and interpreting TDMS and TDSR data, and to present some numerical simulations for the purpose of discussion. A classical approach is taken here to analyze such experiments. The source radiation is designated as an "input" signal. This input signal traverses the nuclear-resonant medium and is finally recorded in a gamma-ray detector as a function of time after the occurrence of the input signal. In essence the input signal is resonantly absorbed by the medium and radiation is subsequently re-emitted from the medium. Thus, the nuclear-resonant medium "operates" on the input signal to produce an output signal.

The initial part of the analysis is carried out in the frequency domain. When the medium operates on the input signal, it can change the phase and amplitude of each Fourier component. Furthermore, the polarization of the output signal is, in general, different from that of the input signal. The Fourier transform of the frequency-dependent output amplitude brings one back into the time domain. The absolute value squared of the time-domain amplitude gives the measured intensity distribution of the output signal as a function of time.

2. Outline of the analysis

Using the classical approach, one can write,

$$\mathbf{a}_{\text{output}}(\omega) = e^{i\kappa(\omega)d} \mathbf{a}_{\text{input}}(\omega). \quad (1)$$

It is known that when the medium's scattering centers are distributed at random [16,17] the effective wave number can be written as

$$\kappa(\omega) = kn(\omega). \quad (2)$$

Since $\kappa(\omega)$ is complex, it is clear that each Fourier component of the input amplitude can suffer a phase change and absorption on traversing the medium.

2.1. INDEX OF REFRACTION DYADIC

In eq. (2), k is the wave number in the absence of the medium and $\mathbf{n}(\omega)$ is the index of refraction of the medium taken as an operator when considering polarization effects. Neglecting polarization effects and confining our attention to nuclear forward scattering, $\mathbf{n}(\omega)$ is given by

$$\mathbf{n}(\omega) = 1 + \frac{2\pi}{k^2} N_0 F(\omega), \quad (3)$$

where N_0 is the number density of resonant-nuclear scattering centers, and $F(\omega)$ is the *total* elastic scattering amplitude in the forward direction. $F(\omega)$ is a sum over all possible nuclear transitions in the medium corresponding to the elastic-scattering amplitudes in the forward direction.

In order to consider polarization effects the elastic-scattering amplitude must be expressed more generally. The elastic-scattering dyadic for the i th transition (\tilde{F}_i) assuming dipole radiation [18] is

$$\tilde{F}_i = C \sum_{M,M'} \frac{\mathbf{X}_{1,M}^* \langle g_i | \mathbf{O}^\dagger | e_i \rangle \langle e_i | \mathbf{O} | g_i \rangle \mathbf{X}_{1,M'}}{(\omega - \omega_i - i\gamma/2)}, \quad (4)$$

where C is a constant including a number of factors mentioned later; the $\mathbf{X}_{1,M}$'s are the vector spherical harmonics for dipole radiation, which is the case considered, that carry the directional and polarization information of the incident and scattered photons; g_i and e_i are the ground and excited state nuclear levels that correspond to a particular transition at frequency ω_i ; and \mathbf{O} is the dipole operator responsible for the transition. Forward scattering is obtained by proper evaluation of the angular parameters of the vector spherical harmonics. (It is convenient to choose the quantization z-axis in the direction of propagation of the input signal, see below.) It should be emphasized that all possible pairs of vector spherical harmonics must be considered, as indicated by the summations, because the nuclear levels cannot in general be labeled as pure " m " states. The dyadic form is used because the index of refraction operator must be represented in some two-dimensional basis system to account for possible polarization effects. A convenient basis system is in terms of left (\mathbf{e}_L) and right-circular (\mathbf{e}_R) polarization states. Of course, an orthogonal set of linear polarization states would work as well. The index of refraction dyadic is given by

$$\tilde{\mathbf{n}} = \overleftrightarrow{\mathbb{I}} + \frac{2\pi}{k^2} \sum_i \tilde{F}_i, \quad (5)$$

where the first term on the right side is the unit dyadic. A representation of the index of refraction in the circular-polarization basis system, expressed as a 2×2 matrix, is obtained by evaluating the matrix elements such as,

$$n_{LL} = \mathbf{e}_L^\dagger \cdot \vec{n} \cdot \mathbf{e}_L . \quad (6)$$

2.2. NUCLEAR-RESONANT MEDIUM OPERATOR

The situation can be described in terms of a nuclear-resonant medium matrix, $\mathbf{M}_{rm}(\omega)$, such that,

$$\mathbf{a}_{\text{output}}(\omega) = \mathbf{M}_{rm}(\omega) \cdot \mathbf{a}_{\text{input}}(\omega) , \quad (7)$$

where $\mathbf{a}(\omega)$ can be represented as a two-component vector, and the matrix $\mathbf{M}_{rm}(\omega)$ takes the form

$$\mathbf{M}_{rm} = \exp(i k n d) . \quad (8)$$

Since the unit matrix, \mathbb{I} , and the Pauli matrices, σ , can describe the most general 2×2 matrix, one can write

$$e^{iknd} = e^{i(a\mathbb{I} + b \cdot \sigma)} . \quad (9)$$

Because of the properties of the Pauli matrices,

$$e^{ib \cdot \sigma} = \cos(b)\mathbb{I} + i \sin(b)(\mathbf{b}_n \cdot \sigma) , \quad (10)$$

where $\mathbf{b}_n = \mathbf{b}/b$. The parameters a and b are given [19] by

$$a = \frac{1}{2}kd(n_{LL} + n_{RR}) , \quad (11)$$

$$b_x = \frac{1}{2}kd(n_{LR} + n_{RL}) , \quad (12)$$

$$b_y = i\frac{1}{2}kd(n_{LR}n_{RL}) , \quad (13)$$

$$b_z = \frac{1}{2}kd(n_{LL} - n_{RR}) , \quad (14)$$

and one must use eqs. (4)–(10) to explicitly evaluate the nuclear-resonant medium matrix.

2.3. EVALUATION OF THE NUCLEAR-RESONANT MEDIUM MATRIX

In order to calculate the required nuclear-elastic scattering amplitudes one needs to specify the nuclear energy levels and select a quantization z -axis. (Recall the choice here is the z -axis to be in the direction of the incident radiation.) With this choice, the vector spherical harmonics that appear in the elastic-scattering dyadic (eq. (4)) are evaluated for their angular arguments at $\theta = 0$ and $\phi = 0$. In order not to complicate the appearance of the expressions, assume that the eigenstates of the nuclear system can be labeled by the magnetic quantum numbers m_e and m_g of the excited and ground states, respectively. If this is not the case, the hyperfine

Hamiltonian must be diagonalized and the resulting eigenvectors must be used. In general the quantization axis for the nuclear Hamiltonian does not correspond to our selected z -axis. However, the nuclear states can be expressed in the selected z -axis system by rotating the coordinate axes. Such a rotation is accomplished by using the familiar "D" matrices. The excited nuclear levels expressed in the selected z -axis system are given by

$$|m'_e\rangle = \sum_{m_e} |m_e\rangle D_{m_e, m'_e}^e(\phi_q, \theta_q, \chi_q), \quad (15)$$

and the ground nuclear levels by,

$$|m'_g\rangle = \sum_{m_g} |m_g\rangle D_{m_g, m'_g}(\phi_q, \theta_q, \chi_q), \quad (16)$$

where ϕ_q , θ_q , and χ_q are the Euler angles needed to rotate the hyperfine axis system into the selected z -axis system. These nuclear states are then substituted into eq. (4) corresponding to a particular nuclear transition labeled by the subscript i . For each transition i all possible combinations of dipole vector spherical harmonics must be considered. The transition matrix elements in eq. (4) will consist of all the appropriate Clebsch-Gordan coefficients after using the Wigner-Eckart theorem. The index of refraction involves a sum over all possible transitions as indicated by eq. (5). Finally the index of refraction matrix is formed according to eq. (6), and the result is incorporated into the nuclear-resonant medium operator given in eq. (8).

2.4. THE INPUT SIGNAL

The input signal $a_{\text{input}}(\omega)$ for the radioactive-source case in which there is only one decay transition is simply the Fourier transform of the damped harmonic oscillator semi-classical temporal function, i.e., the familiar Lorentzian amplitude,

$$a_{\text{input}}(\omega) = \sqrt{\frac{\gamma}{2\pi}} \frac{1}{(\omega - \omega_0 - i\gamma/2)}. \quad (17)$$

In such cases, the source radiation is usually unpolarized so the formalism is simplified. When there is more than one source emission "line", each line must be treated incoherently, assuming no overlap of the lines. The resonance denominator in eq. (17) is associated with the lifetime of the source excited state level through the time-energy uncertainty principle. Thus the "photons" coming from such a source are spread-out in time, i.e., they have a coherence length, $l_c \approx c\tau$, where c is the speed of light and τ is the lifetime of the excited state. (For the case of ^{57}Fe , $l_c \approx 42 \text{ m}$.)

For source radiation from a synchrotron the situation is quite different. The bandwidth using the best monochromators is about 5 meV which is about six orders

of magnitude larger than the recoil-free nuclear-resonant bandwidth. (Thus the coherence length for synchrotron radiation photons is about 40 μm .) Synchrotron radiation is highly polarized, so polarization effects must, in general, be included in the analysis. In the numerical results that follow, the polarization of the synchrotron radiation will be taken to be along the x -axis and assumed to be 100%. Including effects due to incomplete polarization can also be treated using these methods.

2.5. CONSTANT FACTORS

Perhaps the easiest way to see the values of the needed constants in the total elastic forward scattering amplitudes is to consider the form of the dispersive index of refraction, $n(\omega)$, in the non-operator form for the case when the medium consists of nuclei that have only one nuclear-resonant transition,

$$n(\omega) = 1 + \frac{N_0 f \sigma_0}{2k} \frac{\gamma/2}{(\omega - \omega_0 - i\gamma/2)}. \quad (18)$$

In eq. (18) f is the recoil-free fraction, σ_0 is the resonant-absorption cross section evaluated on resonance including the excited and ground state multiplicity factors, as well as the internal conversion coefficient, γ is the total width of the excited-state energy level in frequency units, and ω_0 is the resonant frequency. We can check this by using the optical theorem which says that the absorption cross section is equal to $4\pi/k$ times the imaginary part of the forward scattering amplitude. Thus, the general form of the index of refraction, as indicated by eqs. (4) and (5) in the case of a medium having a number of nuclear transitions, must reduce to the form given by eq. (18) when the nuclear level splittings in the excited and ground states go to zero.

3. Numerical results

The numerical results presented below will assume the nuclear-resonant medium is iron metal and the nuclear levels involved in the transitions are those between the ground and first-excited nuclear levels in ^{57}Fe . The nuclear spin of the excited state I_e is $\frac{3}{2}$ and the ground state I_g is $\frac{1}{2}$. The transition is of the magnetic dipole (M1) type. For M1 radiation, the vector spherical harmonic gives the polarization [20] of the radiation. The Clebsch-Gordan coefficients $C(1, M; \frac{1}{2}, m_g | \frac{3}{2}, m_e)$ for this case are well known to be the square root of 1, $\frac{2}{3}$, and $\frac{1}{3}$ for the appropriate transitions. The nuclear-resonant cross section (σ_0) is $2.459 \times 10^{-18} \text{ cm}^2$. The isotopic abundance of ^{57}Fe in natural iron is 2.19%. The nuclear-resonant medium thickness parameter is given by $\beta = N_0 f \sigma_0 d$, where the recoil-free fraction $f = 0.77$, the number of resonant nuclei per cm^3 $N_0 = 1.85 \times 10^{21}$, and d is the thickness of the medium in centimeters.

3.1. SAMPLE MEDIUM HAVING ONLY ONE RESONANT TRANSITION

First consider the situation in which the sample medium has only one resonant transition. Using a radioactive source as the input signal, assume that the source has one transition also, and this to occur at the same frequency as in the sample medium, i.e., the absorber. Next consider the case when synchrotron radiation provides the input signal. It is of interest to observe the consequences in time-domain spectroscopy for the two cases as the nuclear-resonant medium becomes thicker.

The resonant medium will produce a phase shift in each of the Fourier components of the input signal. These phase shifts depend on frequency and the thickness of the sample medium. Such phase shifts for three medium thicknesses are shown in fig. 1. What is depicted in fig. 1 is the real part of $kn(\omega)d$ which occurs in exponent of the medium function. Such shapes may be somewhat confusing when one recalls that there is a π phase shift in the scattered wave after a single scattering event. However to recover that result one must simply expand the exponential medium function in the thin absorber limit.

Similarly, the medium will absorb each Fourier component of the input signal differently. The absorption will also depend on the frequency of the input component and the thickness of the sample medium. Figs. 2 shows the absorption effect on each Fourier component of an input signal by evaluating the imaginary part of $kn(\omega)d$ for three values of the medium thickness parameter β for this single-transi-

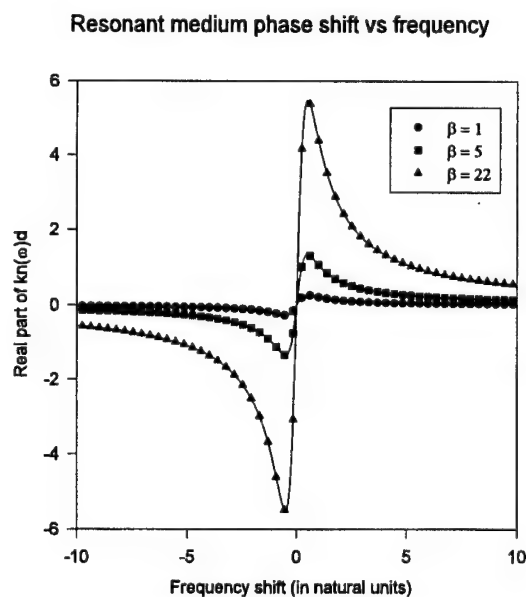


Fig. 1. The phase shift produced by the medium, as a function of frequency, for three different thicknesses of the resonant medium.

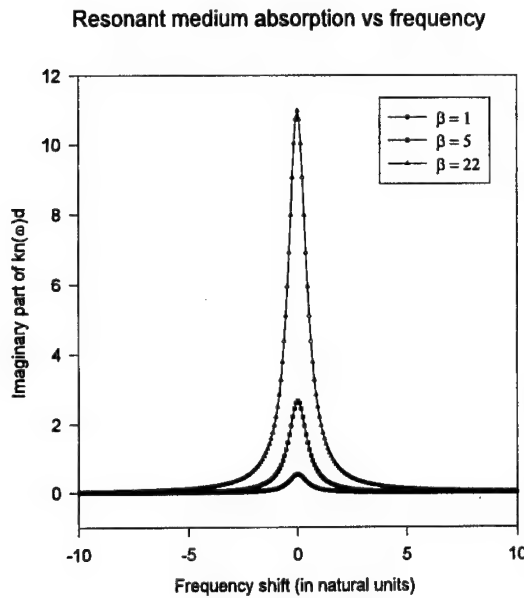


Fig. 2. The absorption produced by the medium, as a function of frequency, for three different thicknesses of the resonant medium.

tion case. Fig. 3 shows the output intensity as a function of frequency for the radioactive-source case. Notice the "hole burning" or "self-inversion" effect [21] as the medium becomes thicker. At the two larger values of β , the re-emitted radiation shows a "pseudo two-line emission" spectrum.

Calculated results for TDMS are presented in fig. 4. In general, one observes that the decay rate does not correspond to the normal lifetime ($\tau = 141$ ns): there is a "speed-up" effect. In addition to the speed-up, the TDMS spectrum develops an oscillatory or beat aspect when the thickness of the medium becomes greater than a critical value associated with the self-inversion effect.

When the input signal is due to synchrotron radiation, the source spectrum is broad-band; essentially "white". Consequently, the medium absorbs radiation in the neighborhood of the resonance and then, due to its resonant character, delivers radiation for times greater than or equal to zero. The results in the time domain (TDSR) for three different thicknesses of the medium are shown in fig. 5. In fig. 5 the result for each medium thickness has been normalized to have the value 1 at time $t = 0$. In reality, the intensity at time $t = 0$ goes like the thickness parameter squared, i. e., like β^2 . (The integrated area in the time spectrum goes like β , but tends to saturate for large β values.) Once again the speed-up effect is clear. Although an oscillatory aspect is not seen in these results, it does arise also in TDSR spectroscopy as the thickness of the medium increases, and, mathematically speaking, is associated with the zeroes of the J_1 Bessel function in the analytical solution.

Output intensity vs energy shift

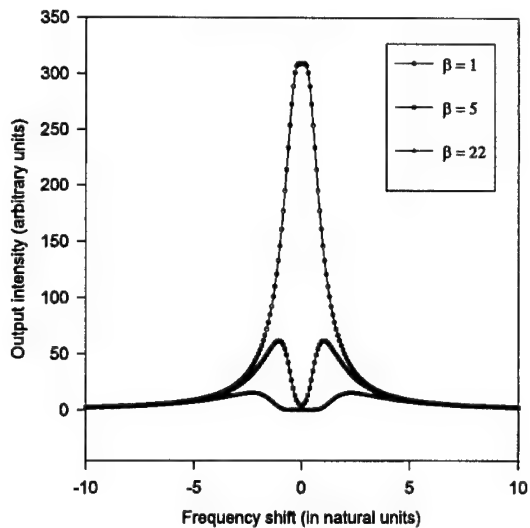


Fig. 3. The output intensity, as a function of frequency, for a "single-line" radioactive source input signal in resonance with a "single-line" nuclear-resonant medium. Evaluations are made for three different thicknesses of the medium.

Intensity (radioactive source) vs time

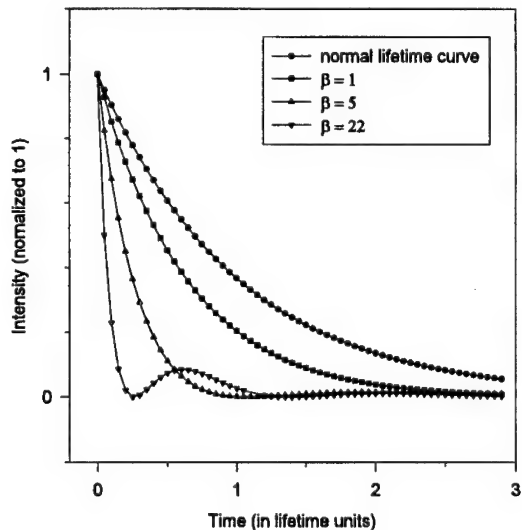


Fig. 4. Time-domain spectral (TDMS) results using a single-line radioactive source in resonance with a single-line medium for three different values of the nuclear-resonant thickness parameter β . Notice the pseudo-two-line beating due to the self-inversion effect, as seen most clearly, in the $\beta = 22$ case.

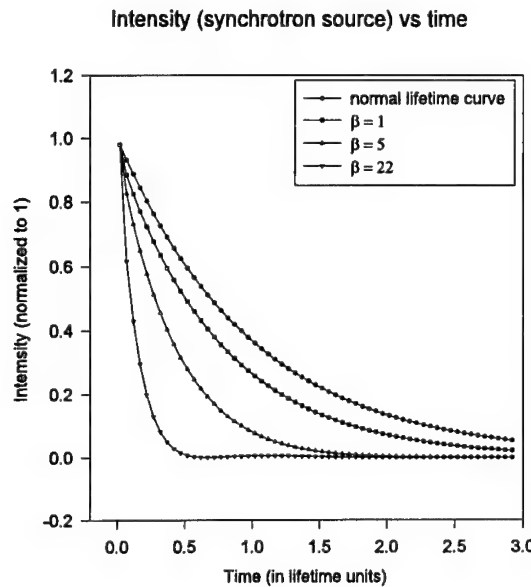


Fig. 5. Time-domain spectral (TDSR) results using synchrotron radiation as the source and a single-line absorber medium for three different values of the nuclear-resonant thickness parameter β . Notice the difference between figs. 4 and 5.

Overall one can observe that deviation from the normal lifetime curve is more dramatic using TDMS than TDSR spectroscopy for a given medium thickness. If one uses rather thick absorbers, it is possible to determine the recoil-free fraction (f) accurately. This is because the TDSR spectrum [22] is quite sensitive to the value of the thickness parameter β . Fig. 6 gives some idea of this sensitivity. Notice that in fig. 6 the TDSR spectra have not been normalized to one at time $t = 0$. Thus, in order to show all three results, a logarithmic scale has been used. For $\beta = 16$ there is one minimum in the plotted time range, for $\beta = 22$ there is still only one minimum but it has moved closer to $t = 0$, and for $\beta = 80$ there are three minima. If one makes such measurements using several thicknesses of the same resonant material, it should be possible to determine the value of the recoil-free fraction (f) with high precision by observing the time positions of the minima.

3.2. MAGNETIC FIELD APPLIED ALONG THE DIRECTION OF THE INCIDENT BEAM USING SYNCHROTRON RADIATION

Consider the case using synchrotron radiation as the input signal, and natural iron metal as the nuclear-resonant medium. Assume that a magnetic field is applied to the medium along the direction of the incident beam, i.e., the z -axis. For this case, using a circular-polarization basis system, the resonant-medium function is diagonal, i.e., the matrix evaluated according to eq. (10) is diagonal. Since the incident

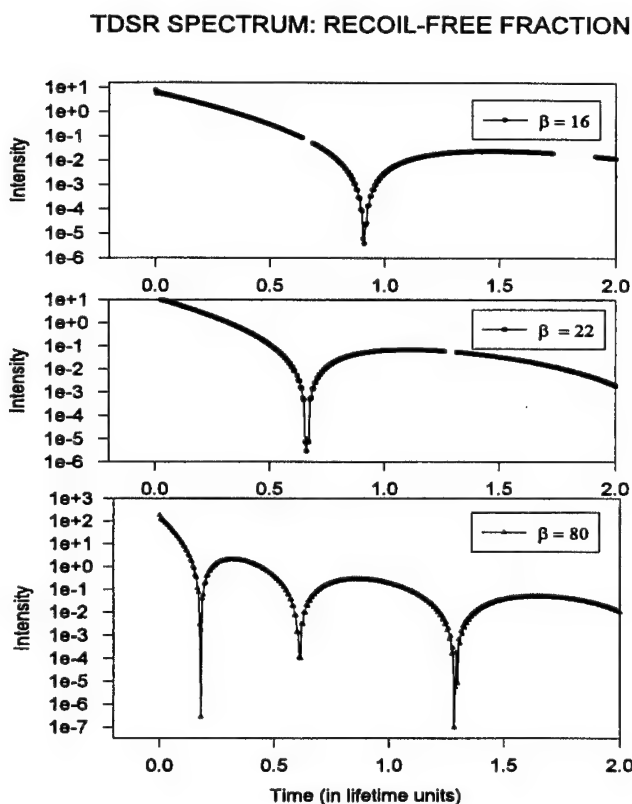


Fig. 6. Time-domain spectral (TDSR) results using synchrotron radiation as the source and a single-line absorber medium for three relatively large values of the nuclear-resonant thickness parameter β . These results show the sensitivity of the method for determining the value of the recoil-free fraction.

synchrotron radiation is taken to be polarized in the x -direction, the incident synchrotron radiation can be represented as a coherent superposition of left and right circular polarizations. Absorption by the medium of the left-circularly and right-circularly polarized incident radiation will occur. These results correspond to absorptions in which $\Delta m = \pm 1$. The "delayed" re-emitted radiation will, of course, also be emitted in the $\Delta m = \pm 1$ transitions, corresponding to left and right circularly polarized photons. Even though the resonant-medium is diagonal one could still ask how the medium treats the left- and right-circularly polarized photons since these photons correspond to different frequencies. The phase shifts and absorptions of the two frequency components in each of the left- and right-circularly polarized emitted photons, as a consequence of traversing the medium, are the same. Thus, the polarization of the transmitted radiation is unchanged at time $t = 0$ on traversing the medium.

The intensity of the emitted radiation as a function of time is found by taking the Fourier transform and adding the absolute value squared of each circular com-

ponent. The results for three different thicknesses of the medium are shown in fig. 7. From the upper figure in fig. 7 one observes that there is only one "beat" period corresponding to about 14 ns. This beat period arises from the difference in frequencies between the two left-circularly polarized components, which is identical to that of the two right-circularly polarized components. For calculations where the nuclear-resonant medium thickness parameter β ranges from 1 to 10, the spectra show the simple beat pattern, as in the top portion of fig. 7, modulated by a decaying exponential function due to the speed-up effect. As the nuclear-resonant medium becomes thicker, the resulting spectra take on a more complicated structure as seen in the two lower figures in fig. 7.

If a polarization crystal is used on the transmitted radiation such that the intensity is recorded, for radiation polarized in the x -direction, as a function of time, the result is shown in fig. 8. Notice that at $t = 0$ the intensity is a maximum for each value of the thickness parameter, as mentioned above. It is also interesting to note

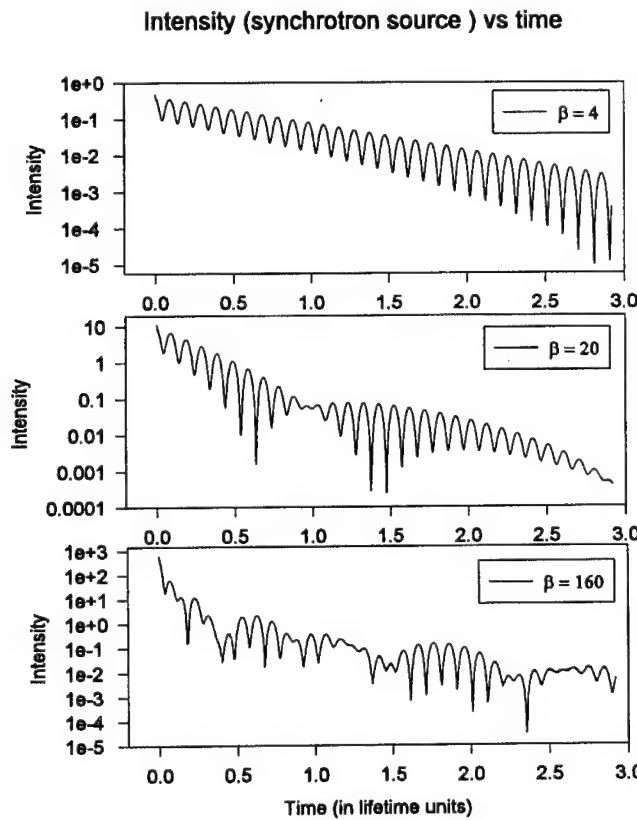


Fig. 7. Calculated TDSR spectra assuming 100% linear polarization of the input signal in the x -direction. The medium is iron metal. An applied magnetic field is in the same direction as the incident beam, i.e., the z -direction. Such a case will excite the $\Delta m = \pm 1$ transitions in the medium corresponding to left and right circular polarized photons.

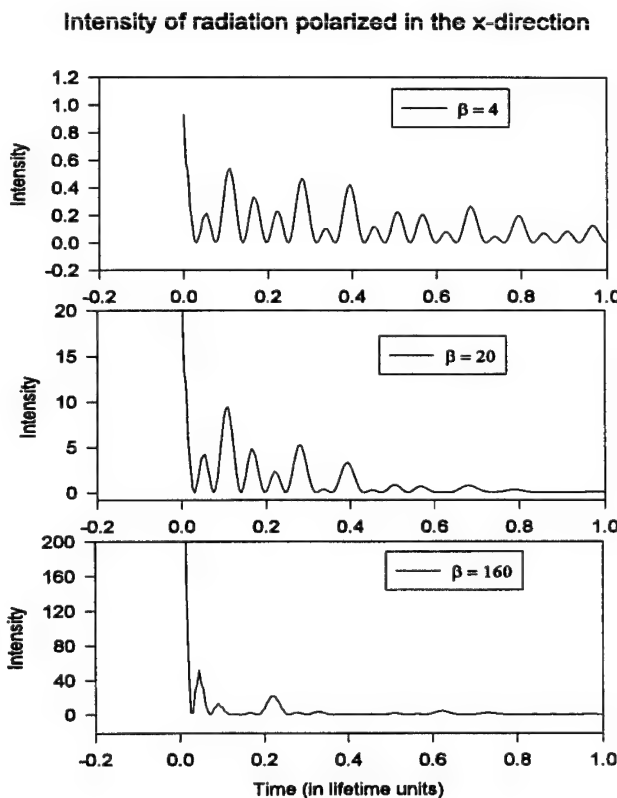


Fig. 8. Intensity of radiation versus time if one counts only radiation polarized in the x-direction after traversing the medium. The situation corresponds to that depicted in fig. 7 except for the polarization aspect and time range.

that the spacings between local maxima are not constant. Thus there is no sense in which there is a "rotation" of the plane of polarization, since the polarization direction is changing in a rather irregular fashion.

3.3. MAGNETIC FIELD APPLIED PERPENDICULAR TO THE DIRECTION OF THE INCIDENT BEAM

Consider again the case using synchrotron radiation as the input signal and natural iron metal as the nuclear-resonant medium. For this case assume that a magnetic field is applied perpendicular to the direction of the beam, i.e., along the y -axis in the selected coordinate system. Now the resonant-medium function is non-diagonal, i.e., left and right circularly polarized photons are changed into each other on traversing the medium. For the left- and right-circularly polarized components absorption occurs corresponding to the $\Delta m = 0$ transitions with respect to the z -axis system taken along the applied magnetic field. (Recall the z -axis is chosen

along the direction of the incident and emitted photons.) The required rotation matrices causes the excited and ground states to become a linear combination of the "m" values. The absorption is the same for both left- and right-circular polarized photons. This result follows from the fact that each circular component can be written as a superposition of two orthogonal linear polarizations. The final calculated results are shown in fig. 9. Again, for modest values of the nuclear-resonant medium thickness parameter, the spectra show a single beat pattern modulated by the speed-up envelope. The beat period is still about 14 ns even though it arises from the difference between two frequencies which are different from those in the case when the applied magnetic field is along the beam direction. A series of similar calculations [22] have already been done. Furthermore, experimental results [23] have been obtained which can be interpreted according to this classical optical model.

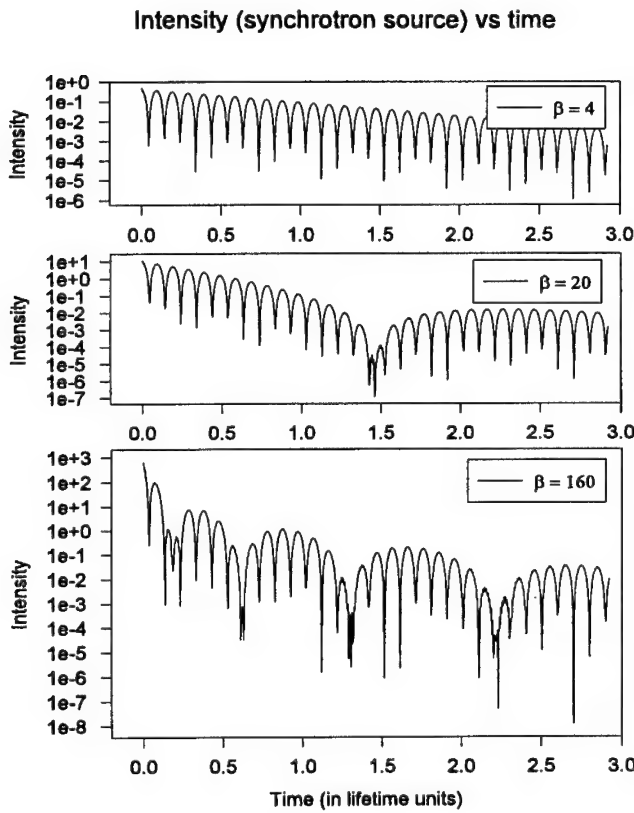


Fig. 9. Calculated TDSR spectra assuming 100% linear polarization of the input signal in the x-direction. The medium is iron metal. An applied magnetic field is taken to be in the y-direction. Such a case will excite the $\Delta m = 0$ transitions (with respect to the magnetic field axis) in the medium.

3.4. SYNCHROTRON RADIATION STUDIES OF HYPERFINE FIELDS

It appears that TDSR nuclear-resonant forward scattering has the potential for providing accurate measurements of hyperfine structure. Fig. 10 shows calculations for the case where the applied magnetic field is along the incident beam direction, i.e., the selected z-axis. The two curves in the figure show the effect when the hyperfine magnetic fields differ by 10%. In order to keep the figure from becoming too crowded, the time axis only goes to 0.4 of the lifetime. Notice, however, that the difference, between the local maxima corresponding to each field value, becomes greater as one moves out in time. Quite clearly one can determine the value of the hyperfine field more precisely if one can "see" many oscillations in the spectrum. When the third generation synchrotron radiation facilities come on line, it may be possible to follow the oscillations in the beat pattern out to a lifetime or two. One can speculate about whether or not such experiments may have value with respect to the measurements of such things as critical fluctuations as one approaches the critical temperature in magnetic materials.

As a final example of the use of TDSR nuclear-resonant forward scattering, as applied to the study of hyperfine interactions, consider the following situation. Assume there is an axially symmetric electric-field gradient whose major principal

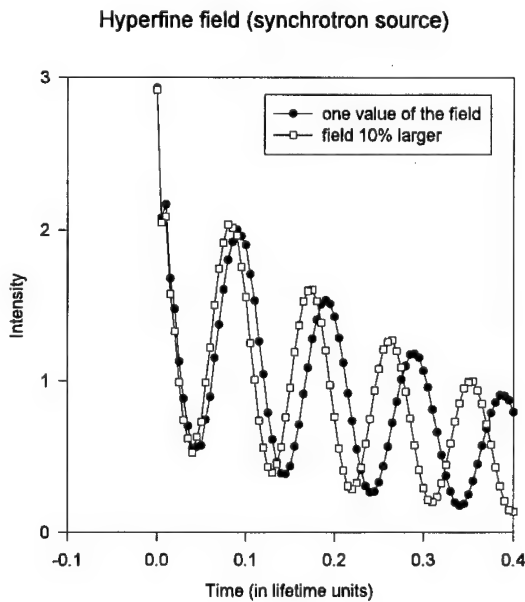


Fig. 10. Calculated TDSR spectra assuming 100% linear polarization of the input synchrotron radiation signal in the x-direction. The medium is iron metal. An applied magnetic field is the same direction as the incident beam, and the value is such that the ground state splitting is 3.92 mm/s. The second curve shows the result when the field is increased by 10%. (The value of $\beta = 10$ was used in the calculation.)

axis is in the direction of the applied magnetic field. This direction is taken to be along the incident beam direction. The medium is taken to be unenriched iron foils, for numerical purposes, and the value of the electric-field gradient (EFG) parameter ($e^2 q Q/2$) was chosen to be +1.7 mm/s. The results are shown in fig. 11. In this case the introduction of the EFG produces two beat frequencies at about 12 and 16 ns. The two curves in fig. 11 show the effect of including the EFG. In order for the field of hyperfine structure measurements using TDSR nuclear-resonant forward scattering to advance, it would appear that a number of calculations need to be made in order to establish a "catalogue" of expected results under various conditions.

4. Discussion

One can discuss the nuclear-resonant medium function in a "hand-waving" fashion. Imagine that the medium is very thin so that we can expand the exponential. We clearly see that the resulting Lorentzian function will contribute some "delayed" or "spread-out" photons. So the resonant-medium function already has built-in the fact that radiation appears after time $t = 0$, when the medium is excited. Furthermore, if we express the exponential, according to its definition, as the limit

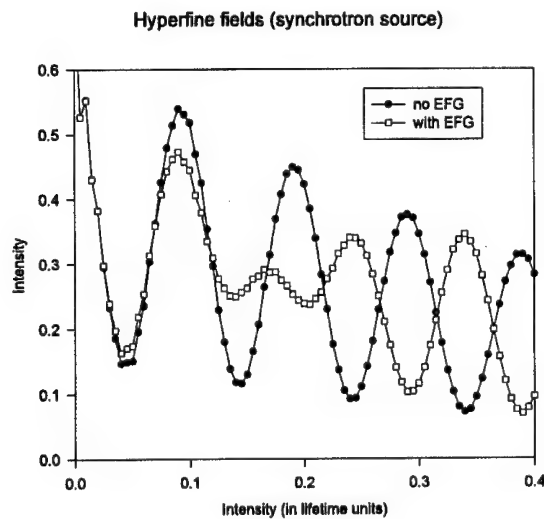


Fig. 11. Calculated TDSR spectra assuming 100% linear polarization of the input synchrotron radiation signal in the x -direction. The medium is iron metal. An applied magnetic field is in the same direction as the incident beam, and the value is such that the ground state splitting is 3.92 mm/s. In one curve there is no electric field gradient (EFG), while for the other curve the EFG ($e^2 q Q/2$) was set at +1.7 mm/s. The assumed axially symmetric EFG was taken to have its principal axis along the field direction. (The value of $\beta = 5$ was used in the calculation.)

of a sum, we see that each infinitesimal slab of the medium "operates" on *its* input signal to produce the correct *input signal* for the *next* infinitesimal slab.

As seen in figs. 4 and 5, for a given thickness, the time-domain single-line spectra are modified more when using a radioactive source as the input signal compared to using synchrotron radiation as the input. This is because of the narrow bandwidth of the input signal in the radioactive-source case. Both cases result in a "speed-up" in the decay rate: the effective lifetime simply gets shorter as the medium becomes thicker. This "speed-up" is more dramatic in the radioactive-source case in which the narrow input-signal line shape is more drastically effected by the medium.

The input signal, due to a radioactive "single-line" source in which the ME is occurring, has a narrow "natural" bandwidth. When a radioactive-source "line" is exactly on resonance with an absorber "line", the absorber medium "eats" away the center portion of the peak preferentially. Thus, heuristically speaking, the spectral line becomes broadened and, from the time-energy uncertainty principle, one expects a speed-up in the decay of the excited-state nuclear level as viewed through the resonant medium. As the medium gets thicker, a type of "hole burning" or "self-inversion" of the resonance line can occur. This manifests itself in TDMS as a "pseudo two-line" beating pattern.

The radioactive source may, however, possess several transitions, and if the energy differences between these transitions are greater than the natural linewidth each transition must be treated incoherently in the final result, i.e., each radioactive-source line is incoherent with any other source line. Each such contribution, after passing through the resonant medium, will show a modification from the normal lifetime curve.

In the case of synchrotron radiation, the bandwidth of the radiation is extremely broad relative to the natural linewidth and hence the input signal is a constant, independent of frequency, but polarized. Because of this very broad bandwidth one can consider the photons to have a very short longitudinal correlation length, and when the synchrotron photon pulse hits the medium the nuclear "oscillators" are excited coherently at the same time. Because of the broad bandwidth of the incident radiation, all of the nuclear hyperfine levels can be excited. Since these "oscillators" in the medium are excited coherently at the same time, the resulting time spectrum shows a beating between all of the coherent frequency components emitted by the resonant medium. Additionally, the time spectrum shows thickness speed-up effects.

Multilined-resonant media do not present a real problem when using this numerical analysis of either TDMS or TDSR results. Furthermore in TDMS, even if source lines overlap within the natural linewidth, the analysis can be made by treating the appropriate fraction of each individual line coherently with the other line.

The TDMS technique has its main application to problems in which there is a time-dependent effect in the source associated with the $t = 0$ event, e.g., a time-dependent recoil-free fraction. One can also apply the coincidence procedure to

eliminate most of the background in an ordinary Mössbauer effect experiment in an effort to determine the value of the recoil-free fraction more precisely. On the other hand, it would appear that the TDSR technique using radiation emitted in the forward direction is a powerful tool for studying hyperfine interactions in solids. Since the technique does not rely on having a convenient radioactive source parent, the scope of possibilities is increased. The potential exists for making high precision measurements of the hyperfine parameters.

The “speed-up” effect in nuclear-resonant scattering in the forward direction is quite interesting. Notice that the location of the resonant nuclei in the scattering medium is irrelevant, and furthermore the effect does not depend on the wavelength of the radiation. (Of course the wavelength must be such that the resonance condition is satisfied.) Thus, conditions normally considered for coherent processes, such as in superradiance [24], do not obtain. Considerations of this sort lead one to speculate about the result of an experiment where synchrotron radiation is incident on a nuclear-resonant medium containing, not only nuclei in the ground state, but also nuclei in the excited state, i.e., essentially a radioactive source. Of course, in such a case, there is no population inversion in the medium. In the conventional way of thinking, unless there is population inversion there is no gain because there is more absorption than stimulated emission. Now, however, with thick samples there is the speed-up effect which causes even the absorbed radiation to be emitted rapidly. Perhaps, in some sense, we already have a type of gamma-ray laser.

References

- [1] R.L. Mössbauer, Z. Phys. 151 (1958) 124.
- [2] See, e.g., G.R. Hoy, in: *Encyclopedia of Physical Science and Technology*, vol. 10 (Academic Press, 1992) pp. 469-483.
- [3] R.E. Holland, F.J. Lynch, G.J. Perlow and S.S. Hanna, Phys. Rev. Lett. 4 (1960) 181.
- [4] F.J. Lynch, R.E. Holland and M. Hamermesh, Phys. Rev. 120 (1960) 513.
- [5] C.S. Wu, Y.K. Lee, N. Benczer-Koller and P. Simms, Phys. Rev. Lett. 5 (1960) 432.
- [6] S.M. Harris, Phys. Rev. 124 (1961) 1178.
- [7] W. Neuwirth, Z. Phys. 197 (1966) 473.
- [8] W. Triftshäuser and P.P. Craig, Phys. Rev. Lett. 16 (1966) 1161.
- [9] W. Triftshäuser and P.P. Craig, Phys. Rev. 162 (1967) 274.
- [10] D.W. Hamill and G.R. Hoy, Phys. Rev. Lett. 21 (1968) 724.
- [11] G.R. Hoy and P.P. Wintersteiner, Phys. Rev. Lett. 28 (1972) 877.
- [12] See, e.g., U. van Bürck and G.V. Smirnov, Hyp. Int. 19 (1994) 313.
- [13] E. Gerdau, R. Rüffer, H. Winkler, W. Tolksdorf, C.P. Klages and J.P. Hannon, Phys. Rev. Lett. 54 (1985) 835.
- [14] E. Gerdau, R. Rüffer, R. Hollatz and J.P. Hannon, Phys. Rev. Lett. 57 (1986) 1141.
- [15] W. Sturhahn and E. Gerdau, Phys. Rev. B 49 (1994) 9285.
- [16] L.L. Foldy, Phys. Rev. 67 (1945) 107.
- [17] M. Lax, Rev. Mod. Phys. 23 (1951) 287.
- [18] J.P. Hannon and G.T. Trammell, Phys. Rev. 186 (1969) 306.
- [19] M. Blume and O.C. Kistner, Phys. Rev. 171 (1968) 417.

-
- [20] See, e.g., J.M. Blatt and V.F. Weisskopf, *Theoretical Nuclear Physics* (Wiley, New York, 1952).
 - [21] R.L. Mössbauer, H.E. Seelbach, B. Persson, M. Bent and G. Longworth, Phys. Lett. A 28 (1968) 94.
 - [22] U. Bergman, *Resonant Nuclear Scattering Using Synchrotron Radiation*, Ph.D. dissertation (State University of New York, Stony Brook, 1994) p. 33.
 - [23] U. van Bürck, D.P. Siddons, J.B. Hastings, U. Bergmann and R. Hollatz, Phys. Rev B 46 (1992) 6207.
 - [24] R.H. Dicke, Phys. Rev. 93 (1954) 99.

Collective polynuclear superradiance rather than stimulated emission of Mössbauer radiation from $^{125m^2}\text{Te}$ and $^{123m^2}\text{Te}$

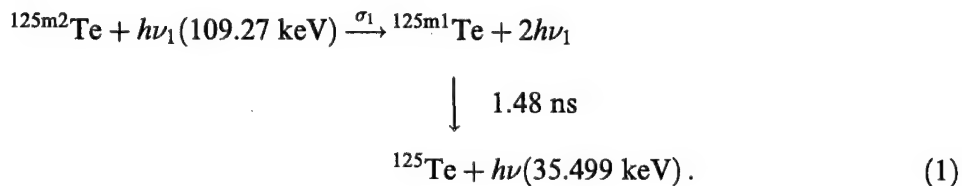
G.A. Skorobogatov and B.E. Dzevitskii

*Department of Chemistry, St. Petersburg State University, Universitetskii prosp.,
2, Petrodvorets, St. Petersburg 198904, Russia*

Acts attributed to single-particle stimulated emission, $^{125\text{m}2}\text{Te}(\gamma, 2\gamma)^{125\text{m}1}\text{Te}$, had been observed previously in a $\text{Be}^{125\text{m}2}\text{Te}$ sample as a variation of the line intensity at $E_\gamma = 109.27$ keV and by the appearance of a line of double energy at $E_{2\gamma} = 218.54$ keV. This effect occurred when the sample temperature, T was lowered from 300 to 4 K. In the present work, the first observation is reported of stimulated emission events in the reaction $^{123\text{m}2}\text{Te}(\gamma, 2\gamma)^{123\text{m}1}\text{Te}$ which were registered from a $\text{Mg}_3^{123\text{m}2}\text{TeO}_6$ sample when cooled in a similar fashion. It is shown here that the mechanism of these experimentally observed events is polynuclear superradiance rather than a single-particle stimulated emission of Mössbauer radiation as earlier suggested.

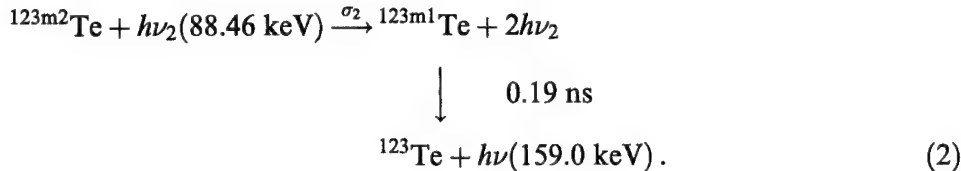
1. Introduction

The papers of refs. [1–4] presented observations of events attributed to single-particle stimulated emission of γ radiation in the transition



Investigations [3,4] performed in an independent laboratory verified the existence of this process and provided a measured cross section of $\sigma_1 = (5 \pm 3) \times 10^{-19} \text{ cm}^2$, compared with the value of $\sigma_1 = (2 \pm 1) \times 10^{-19} \text{ cm}^2$ obtained in refs. [1,2]. Despite this good agreement, some researchers still expressed concern over the interpretation of the experiments.

This work presents a wider study of processes like that of eq. (1) in order to obtain more convincing experimental data. Experiments were conducted to re-investigate that reaction and the similar one



Again, the reaction was experimentally observed. However, the value of the cross section obtained in this study forced a reconsideration of the single-particle theoretical model previously considered in refs. [1–4].

The collective model considered here presents two important advantages. First, within error limits this model agrees with all experimental observations for the processes of eqs. (1) and (2), while the single-particle model only applies to eq. (1). Second, unlike the earlier approach [1–7], no revision of either the second Einstein relation nor any other points of standard radiation theory is necessary.

A gamma-ray laser would be based on stimulated emission of γ radiation from a nuclear transition. It was felt that stimulated emission of gamma radiation had been observed [1,2] in 1983 for the process of eq. (1). Refs. [1,2] deal with an experiment in which an enhancement of about 1.2% was observed for the intensity of the 109.27 keV line emitted by ${}^{125m^2}\text{Te}$ from a $\text{Be}{}^{125m^2}\text{Te}$ polycrystal. This effect was observed when the crystal was cooled from 300 to 78 K. Ref. [1] is a brief note that discusses this result. The second paper [2] contains more details, particularly on the preliminary single-particle concept (according to the number of interacting elementary radiators). A relative increase, ϵ , of the intensity of the 109.27 keV gamma line was used to register the occurrence of that transition from ${}^{125m^2}\text{Te}$ within the $\text{Be}{}^{125m^2}\text{Te}$ sample when cooled. A value of $\epsilon = 1.2\%$ was measured [2] which led to a cross section for the process of $\sigma_1 = (2 \pm 1) \times 10^{-19} \text{ cm}^2$. Remarkably, this value corresponded to the wave cross section

$$\sigma_{\text{wave}} = \frac{\Lambda_1^2}{4\pi} = 1.026 \times 10^{-19} \text{ cm}^2, \quad (3)$$

where $\Lambda_1 = 0.1136 \text{ \AA}$ is the wavelength of the 109.27 keV photons participating in the transition of eq. (1).

Russian physicists criticized the work of refs. [1,2] on the basis that the activation cross section [8] used for the reaction ${}^{124}\text{Te}(n,\gamma){}^{125m^2}\text{Te}$ was taken to be $\sigma_a = 5\text{--}7 \text{ b}$. Those values are now considered to be obsolete and modern experiments [9] gave $\sigma_a = 0.04 \text{ b}$. In response to this criticism [10] the concentration of ${}^{125m^2}\text{Te}$ nuclei within the sample was calculated not from σ_a and the thermal neutron flux, but directly from the absolute gamma-ray activity of the sample measured from the 109.27 keV line. The resulting concentration, N_{Te} was found to be

$$N_{\text{Te}} = (1.2 \pm 0.5) \times 10^{19} \text{ cm}^{-3}, \quad (4)$$

a value which did not depend on any uncertainties in either activation cross section σ_a or thermal neutron flux. According to the single-particle view of eq. (1) and using

the concentration of eq. (4), a value of $\sigma_1 = (1.0 \pm 0.4) \times 10^{-19} \text{ cm}^2$ was found [10], again coinciding with the wave cross section of eq. (3). Furthermore, the value of the $^{125\text{m}2}\text{Te}$ concentration enabled the calculation of activation cross section which was found to be $\sigma_a = (2.0 \pm 0.5) \text{ b}$. Despite this confirmation, some skepticism remained due to high regard for the work conducted at Brookhaven National Laboratory (BNL) which gave a much lower value for the activation cross section [9]. This polemic came to an end in 1995 with new experiments which measured [11] activation cross sections for the production of tellurium isomers for mass numbers 123, 125, 127 and 129. The value obtained [11] for the reaction $^{124}\text{Te}(n,\gamma)^{125\text{m}2}\text{Te}$ was $\sigma_a = (1.12 \pm 0.07) \text{ b}$, in agreement with that found in ref. [10]. The value of activation cross section is not central to the observations of refs. [1,2,10], but attention is drawn to this issue due to the possible tendency to incorrectly judge those works on the basis of their disagreement with the original BNL measurement [9].

A more persistent cause of concern was that the value found for the stimulated emission cross section, $\sigma_1 = (2 \pm 1) \times 10^{-19} \text{ cm}^2$, exceeded that predicted by the second Einstein relation by 19 orders of magnitude. Joint experiments were conducted to test the data of refs. [1,2] by a group of the most skeptical scientists at ITEPh (Moscow), resulting in the papers of refs. [3,4]. The latter two works also described a previously unnoticed phenomenon, the appearance at low temperature of a double-energy line at $E_{2\gamma} = 218.54 \text{ keV}$. The ITEPh group joined in acknowledging the presence of that spectral feature, and a stimulated emission cross section of $\sigma_1 = (4.9 \pm 3.0) \times 10^{-19} \text{ cm}^2$ was determined. This value was again 19 orders of magnitude larger than that predicted by the Einstein relation.

The works of refs. [1–4] proved the correctness of the measured values of the cross section and that the observed 1.2% excess of 109.27 keV gamma quanta was a real effect. This meant that in 1987 stimulated emission of gamma radiation had been realized, with an extremely large cross section [1,2]. Therefore, refs. [5–7] considered the compatibility of a generalized second Einstein equation with other physical laws.

The publication of ref. [7] marked the general acceptance of the concept of a revision to the Einstein relation. However, at the moment we became uncertain as to the validity of the single-particle stimulated emission interpretation of the experimental observations of the process of eq. (1). Importantly, the measurements for the reaction of eq. (2) provided a cross section σ_2 which was by a factor of 100 smaller than the corresponding wave cross section. These experimental results forced a search for an alternative explanation. The present work discusses a suitable theory, a collective model of a running wave within the framework of nonstationary optics [13]. The new concept will be detailed following a review of the experimental results.

2. Experimental results for $^{125\text{m}2}\text{Te}$

Beryllium telluride was prepared from tellurium containing 93% ^{124}Te and beryl-

lum in a 13.5 : 1 ratio. This fine-grained mixture of reactants was placed in a quartz capillary tube with a graphitized inner surface. The tube was then evacuated, sealed hermetically and heated from 300 to 1400 K at a rate of 2 K per minute [14]. The Be¹²⁴Te resulting sample had a length of 3.5 mm, a diameter of 1.3 mm, a mass of 16 mg and a density of 3.4 g cm⁻³. This sample was placed into an evacuated sealed quartz ampoule and exposed to activation by thermal neutrons at a flux of $\varphi_n = 1.8 \times 10^{13} \text{ cm}^{-2}\text{s}^{-1}$ for a period of 4 months until the integrated dose reached $2 \times 10^{20} \text{ cm}^{-2}$. After neutron activation the quartz ampoule was opened in an argon atmosphere and the resulting Be^{125m²}Te sample was placed into a brass container. The latter was closed hermetically and then placed within a helium cryostat.

Gamma rays from the Be^{125m²}Te sample reached a Ge(Li) semiconductor detector via the thin end of the cylindrical container and the thin window of the cryostat. The geometric efficiency of the measuring unit was $\eta_{\text{geom}} = (1.32 \pm 0.08) \times 10^{-3}$. The overall efficiency for detection of 109.27 keV photons was $\eta_{\text{det}} = (0.83 \pm 0.06)$. The detector was connected with a Nokia-LP-4900 multichannel analyzer which registered gamma quanta from 10 to 300 keV with a resolution of 0.6 keV. The measurement of gamma activity was made at sample temperatures of 300 and 10 K when liquid helium vapor was supplied into the cryostat. A representative example of an amplitude spectra is given in fig. 1. The latter demonstrates that when the temperature of the Be^{125m²}Te sample was reduced from 300 to 10 K, the detector (operating under a steady state) registered a noticeable peak at (218.5 ± 1.0) keV. That energy exactly corresponds to double the energy of the $11/2^- \rightarrow 3/2^+$ transition in ¹²⁵Te. The magnitude of the signal at 218.5 keV was 20 times larger than the standard experimental error.

In the above experiment, the probability of simultaneous counting of two independent gamma quanta did not exceed 10^{-7} under the experimental conditions (number of counts of about 3800 pulses s⁻¹ in the 109 keV channel, etc.). This means the level of counts at 218.5 keV is 10^5 higher than the level of background by chance coincident detection of independent photons within the instrumental resolving time. Thus there can be no doubt about the presence of the stimulated emission effect of eq. (1) when a Be^{125m²}Te sample is cooled to 4–10 K. The measurements gave a ratio of

$$\epsilon_{\text{exp}} = \frac{N_{2\gamma}(10 \text{ K})}{N_\gamma(300 \text{ K})} = 0.0030 \pm 0.0005, \quad (5)$$

where N_γ and $N_{2\gamma}$ are the numbers of counts at 109.3 and 218.5 keV, respectively.

As the temperature is decreased, the number of counts observed at 109.3 keV also decreases by

$$\frac{-\Delta N_\gamma}{N_\gamma(300 \text{ K})} = \frac{N_\gamma(300 \text{ K}) - N_\gamma(10 \text{ K})}{N_\gamma(300 \text{ K})} = 0.0060 \pm 0.0005. \quad (6)$$

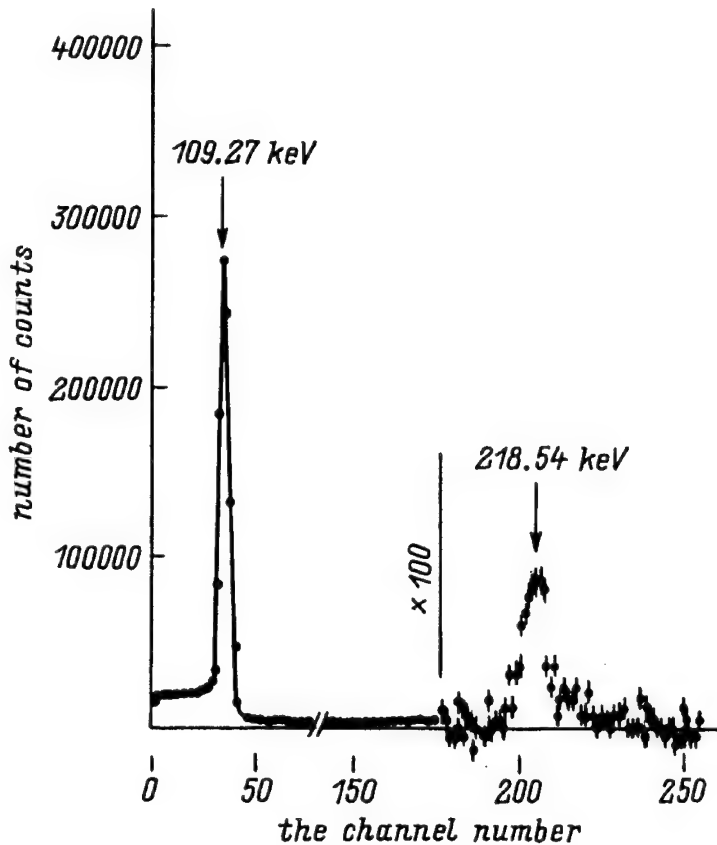


Fig. 1. Measured gamma spectrum of the $\text{Be}^{125\text{m}^2}\text{Te}$ sample at a temperature of 4–10 K.

Taking into account thermal contraction [10], the decrease of the number of counts due entirely to the process of eq. (1) is not that of eq. (6), but instead becomes

$$-N_\gamma = (0.0030 \pm 0.0020)N_\gamma(300 \text{ K}). \quad (7)$$

In the experimental arrangement, the number of counted 109.27 keV photons emitted by the cylindrical sample of $\text{Be}^{125\text{m}^2}\text{Te}$ is given by

$$\begin{aligned} N_\gamma(300 \text{ K}) &= \eta_{\text{cor}} \eta_{\text{geom}} \eta_{\text{det}} \frac{\lambda_2}{1 + \alpha_2} N_{\text{Te}} \pi \left(\frac{d}{2}\right)^2 \frac{1 - \exp(-\mu_0 L)}{\mu_0} \\ &= \eta_{\text{cor}} \eta_{\text{geom}} \eta_{\text{det}} \Phi_\gamma(300 \text{ K}), \end{aligned} \quad (8)$$

where $\lambda_2 = 1.383 \times 10^{-7} \text{ s}^{-1}$ is the decay constant of ${}^{125\text{m}^2}\text{Te}$ [15], $\alpha_2 = 352$ is the conversion coefficient for the transition of eq. (1) [16], N_{Te} is the concentration of ${}^{125\text{m}^2}\text{Te}$ nuclei in the sample, $\mu_0 = (4.85 \pm 0.05) \text{ cm}^{-1}$ [17] is a linear absorption coefficient, $\eta_{\text{cor}} = (0.8 \pm 0.1)$ is the permeability of the “corridor” for 109.3 keV

quanta, and $\eta_{\text{cor}}\eta_{\text{geom}}\eta_{\text{det}} = (8.8 \pm 2.2) \times 10^{-4}$. At 300 K, the number of counts was $N_c = 3800 \text{ pulses s}^{-1}$, which from eq. (8) immediately yields

$$N_{\text{Te}} = (4.9 \pm 1.5) \times 10^{18} \text{ cm}^{-3}. \quad (9)$$

In all calculations below, the experimentally obtained concentration of $^{125m^2}\text{Te}$ nuclei from eq. (9) is used and thus they do not depend on any error in measurement of φ_n or on uncertainty in values of σ_a in the literature. The presently measured value for that activation cross section for the $^{124}\text{Te}(n,\gamma)^{125m^2}\text{Te}$ process is determined to be

$$\sigma_a = (2.5 \pm 1.0) \times 10^{-24} \text{ cm}^2. \quad (10)$$

The spontaneously emitted 109.27 keV photons, $\Delta\Phi$ in number, and the additional photons of the same energy generated in the process of eq. (1) are indistinguishable. At 10 K the flux of spontaneously emitted photons can be written as $\Phi_\gamma(300 \text{ K}) - \Delta\Phi$ and that of photons in two-particle states $|2\rangle$ as $2\Delta\Phi$. The number of counts of 109.27 keV photons is proportional to $\Phi_\gamma(300 \text{ K})\eta_{\text{det}}$ at 300 K and to

$$[(\Phi_\gamma(300 \text{ K}) - \Delta\Phi)\eta_{\text{det}} + 2\Delta\Phi\eta_{\text{det}}(1 - \eta_{\text{det}})] \quad (11)$$

at a temperature of 10 K. The number of counts of 218.54 keV pulses at 10 K is proportional to $\Delta\Phi\eta_{\text{det}}^2$. Thus the relative decrease of the number of counted 109.27 keV photons is given by

$$\frac{\Delta N_\gamma}{N_\gamma(300 \text{ K})} = \frac{\Delta\Phi}{\Phi_\gamma(300 \text{ K})} (1 - 2\eta_{\text{det}}). \quad (12)$$

In the present case, $\eta_{\text{det}} = (0.83 \pm 0.06)$, so that from the measured value of ΔN_γ ,

$$\epsilon_{\text{exp}} = \frac{\Delta\Phi}{\Phi_\gamma(300 \text{ K})} = (0.0045 \pm 0.0030), \quad (13)$$

within experimental error limits which agrees with eq. (5). In the works of refs. [2,10] $\eta_{\text{det}} = (0.010 \pm 0.001)$, so the measured value of ΔN_γ must be positive as discussed previously.

3. Experimental results for $^{123m^2}\text{Te}$

In the present work the realization of the stimulated emission process depicted in eq. (2) was attempted for $^{123m^2}\text{Te}$ ($T_{1/2} = 119.7 \text{ d}$ [15]). Because the energy of the $h\nu_{10} = 159.0 \text{ keV}$ photons is larger than that of the $h\nu_{21} = 88.46 \text{ keV}$ quanta, the Compton “tail” from the $h\nu_{10}$ photons creates an intense background in the region of the lower-energy emission. Also, the conversion coefficient is large, $\alpha_2 = 1152$ [18], so bremsstrahlung from conversion 88.46 keV and 159.0 keV electrons creates a background in the same region. As a result, neither the 88.46 keV nor the two-photon 176.9 keV line can be separated from the background.

To alleviate these difficulties, an attempt was made to observe the process of eq. (2) by registering coincident lines at $2(88.46 \text{ keV}) + 159.0 \text{ keV}$ at low temperatures. Since $\alpha_1 = 0.2$ [18], 80% of stimulated emission events (eq. (2)) are accompanied by emission of $h\nu_{10} = 159.0 \text{ keV}$ photons. The dead time of the detector is more than 1 ns and the intensity of counts did not exceed $10^5 \text{ pulses s}^{-1}$. So with a detector efficiency of more than 0.5, coherent $2(88.46 \text{ keV})$ pairs were registered with a $h\nu_{10} = 159.0 \text{ keV}$ photons as a single 335.9 keV pulse.

A sample of ^{122}Te at 91.2% concentration was activated for two months by thermal neutrons having a flux of $10^{15} \text{ cm}^{-2}\text{s}^{-1}$. According to the literature [19], the value of the activation cross section for $^{122}\text{Te}(n,\gamma)^{123\text{m}^2}\text{Te}$ is 1.1 b, which yielded at the end of the irradiation a calculated activity of $(40 \pm 8) \text{ Ci g}^{-1}$. One month after the end of the activation, the radioactive tellurium was converted to magnesium tellurate, from which a cylindrical sample of ceramic Mg_3TeO_6 was made. The sample was 5 mm in length and 1.3 mm in diameter. The total activity of the sample was $(0.40 \pm 0.08) \text{ Ci}$ which corresponded to a concentration of $^{123\text{m}^2}\text{Te}$ nuclei of

$$N_{\text{Te}} = (3.4 \pm 0.7) \times 10^{19} \text{ cm}^{-3}. \quad (14)$$

The signal from a BDRK detector was input into a Nokia-LP-4900 amplitude analyzer with about 12 channels falling at the 336 keV line. On cooling the $\text{Mg}_3^{123\text{m}^2}\text{TeO}_6$ sample to liquid helium temperatures, the detector under unvarying conditions registered signals on the order of several pulses s^{-1} in each channel in the 336 keV region. Because the signal was 10–15 times larger than the error, there was no doubt in the appearance of this peak when the sample was cooled to 4–10 K. The counting was performed until up to 10^6 pulses were obtained for the entire 336 keV line. The total number of two-photon states $|2\rangle$ produced from the sample was $N_{2\gamma}(10 \text{ K}) = (6 \pm 3) \times 10^3 \text{ s}^{-1}$. On the other hand, from eq. (14) it was possible to obtain the total number of 88.46 keV photons produced in the sample as $N_\gamma(300 \text{ K}) = (1.3 \pm 0.3) \times 10^7 \text{ s}^{-1}$. From these values it was found that

$$\epsilon_{\text{exp}} = \frac{N_{2\gamma}(10 \text{ K})}{N_\gamma(300 \text{ K})} = (5 \pm 3) \times 10^{-4}. \quad (15)$$

4. Discussion

The concentration in eq. (14) is higher than that in eq. (9) and the wave cross section for 88.46 keV photons, $\sigma_{\text{wave}} = 1.565 \times 10^{-19} \text{ cm}^2$, is larger than that of eq. (3). However, the ratio of eq. (15) for $^{123\text{m}^2}\text{Te}$ is less than that measured for $^{125\text{m}^2}\text{Te}$ (cf. eqs. (5) and (13)). This experimental fact cannot be understood in the framework of a non-collective model.

Superradiance in the processes of eqs. (1) and (2) should not be expected because the wavelength Λ_{21} is less than both the intrinsic dimensions of the radiating system (on the order of $1/\mu_0$) and the average distance between elementary radiators,

$$\Lambda_{21} \ll \text{Min}(\mu_0^{-1}, N_{\text{Te}}^{-1/3}), \quad (16)$$

where N_{Te} is again the concentration of tellurium isomers. However, the condition of eq. (16) does not need to be satisfied if spatial synchronism occurs by the moving-wave mechanism under superradiation of an extended system [13]. Upon first examination, the conditions of spatial synchronism in the polycrystalline Be^*Te and $\text{Mg}_3^*\text{TeO}_6$ samples appear to be violated at any emission angle for quanta of $h\nu_{12}$. This condition would hold only for stimulated emission in the optical or IR regions. However, for γ radiation a new effect appears when the temperature of the polycrystal is lowered. Unfortunately, no theory is available in the literature to explain this behavior based on known models of superradiation [20] because all approaches employ the “long-wave approximation” when the radiation wavelength Λ exceeds the dimensions of the region Δa where the wavefunctions of the elementary radiators is not negligible. This occurs for

$$|\mathbf{k}| |\Delta a| = \frac{2\pi}{\Lambda} |\Delta a| \ll 1. \quad (17)$$

Here \mathbf{k} is the wave vector for the emitted radiation and Δa is the region of integration [21] of matrix elements giving the probability of transition between levels of an elementary radiator,

$$\Delta a = \text{Max}(a, \Delta z), \quad (18)$$

where a is the spatial dimension of the elementary radiator and Δz is the Heisenberg uncertainty of its spatial coordinates. In the following a semiclassical approximation is used [13].

A spatial system is considered in which superradiation is modeled by a sinusoidal plane wave. This superradiation has a direction according to field modes which effectively collect energy from elementary radiators that satisfy the condition of spatial synchronism [13]

$$\varphi_j = \mathbf{k}z_j, \quad (19)$$

where φ_j is a coherent state phase of the j th elementary radiator and z_j is its coordinate. In the strict sense, for any crystal with finite dimensions the probability of precise fulfillment of eq. (19) vanishes. Thus one should consider the spatial region Δa which contains most of the wave function of the j th elementary radiator [21]. The condition of spatial synchronism is then fulfilled for those angles $\Delta\Omega$ which correspond to the condition

$$kz_j \leq \varphi_j \leq k(z_j + \Delta a_j). \quad (20)$$

Thus for the power of superradiation of n elementary radiators which are prepared in coherent states [13],

$$\rho_{\text{coh}} = \frac{\Delta\Omega}{4\pi} \hbar\omega_{21} \frac{A_{21}n(n+1)}{4}, \quad (21)$$

while the power of spontaneous radiation of n independent elementary radiators is equal to

$$\varphi_{\text{non-coh}} = \frac{1}{2} \hbar \omega_{21} A_{21} n. \quad (22)$$

Eq. (21) is obtained for a non-broadened lower level. If the lower level is broadened then the value of power is reduced by the factor Γ_{21}/Γ_r where Γ_r is the partial radiation width and Γ_{21} is the broadened width. Thus it follows from eq. (21) that

$$\varphi_{\text{coh}} = \hbar \omega_{21} \frac{A_{21} n (n+1) \Gamma_r \Delta \Omega}{16 \pi \Gamma_{21}} = \varphi_{\text{non-coh}} \frac{\Delta \Omega (n+1) \Gamma_r}{8 \pi \Gamma_{21}}. \quad (23)$$

Now an essential step in the present theoretical treatment is introduced which is not possible in the long-wave limit. As the temperature of the matrix containing the elementary radiators is lowered, eventually a temperature T_a is reached at which the Heisenberg uncertainty of each atom becomes larger than the value of $|\alpha|$, for example at $T_a = 4.2$ K for ${}^4\text{He}$. At $T < T_a$ eq. (18) gives $\Delta \alpha_j = \Delta z_j$. A temperature can be reached at which

$$T \leq T_A = \frac{(\hbar/\Lambda)^2}{2km}, \quad (24)$$

when the following condition is fulfilled:

$$|\Delta \alpha_j| = |\Delta z_j| > \Lambda. \quad (25)$$

Here m is the mass of an elementary radiator and k is the Boltzmann constant. For optical and IR wavelengths and atoms in the middle of the periodic chart, $T_A \leq 10^{-4}$ K. No optical experiments have been carried out at such a low temperature and it is difficult to reach a temperature lower than 100 μK . However, in the gamma region it is possible to reach an inequality of $T_a < T_A$. For the processes of eqs. (1) and (2), eq. (24) gives $T_A = 15$ K and $T_A = 10$ K, respectively.

Therefore, the processes of eqs. (1) and (2) fulfill the condition of eq. (25) at temperatures higher than that of liquid helium. This means that even in an irregular polycrystal matrix all elementary radiators satisfy the wave synchronism condition of eq. (20). Consequently, at $T \leq T_A$ the angle $\Delta \Omega = 4\pi$ at all times. Eq. (23) then gives

$$\epsilon_{\text{theory}} = \frac{\varphi_{\text{coh}}}{\varphi_{\text{non-coh}}} = \frac{(n+1) \Gamma_r}{2 \Gamma_{21}}. \quad (26)$$

At $T \leq T_A$ the number of radiators which are in coherent states, denoted by 2X , is given by

$$n_2 X = \frac{4}{3} \pi N_{\text{Te}} (l_{\text{col}})^3, \quad (27)$$

where the collective interaction length has been introduced,

$$l_{\text{col}} = \text{Min}(l_{\text{coh}}, \mu_0^{-1}, V^{1/3}). \quad (28)$$

Eq. (28) includes the volume, V of the polycrystalline sample containing the 2X nuclei and l_{coh} is the photon coherence length. Using eq. (27), the relation of eq. (26) becomes for $T \leq T_A$

$$\epsilon_{\text{theory}} = \frac{P_{\text{coh}}}{P_{\text{non-coh}}} = \frac{1}{2} \left(1 + \frac{4}{3} \pi N_{\text{Te}} (l_{\text{col}})^3 \right) \frac{f_M \beta \tau_1}{(1 + \alpha_2)(\tau_2 + \tau_1)}, \quad (29)$$

where f_M is the Mössbauer recoil-free fraction, β is the branching ratio, α_2 is the conversion coefficient, τ_2 is the lifetime of the upper level (the 2X nuclei) and τ_1 is the lifetime of the nuclei in the lower level, denoted by 1X . The present experiment fulfills the conditions $l_{\text{col}} = \mu_0^{-1}$, ${}^2X = {}^{\text{*}}\text{Te}$ and $\mu_0^{-3} \cdot N_{\text{Te}} \gg 1$. Thus eq. (29) gives

$$\epsilon_{\text{theory}} = \frac{P_{\text{coh}}}{P_{\text{non-coh}}} = \frac{2\pi N_{\text{Te}} f_M \beta \tau_1}{3\mu_0^3 (1 + \alpha_2)(\tau_2 + \tau_1)}, \quad (30)$$

where N_{Te} is used to represent the concentration of ${}^{\text{*}}\text{Te}$ nuclei (either ${}^{125\text{m}2}\text{Te}$ or ${}^{123\text{m}2}\text{Te}$).

Table 1 compares theoretically calculated, ϵ_{theory} and experimentally measured, ϵ_{exp} values for the excess numbers of gamma quanta of energy $h\nu_{21}$ produced by superradiation as the $\text{Be}{}^{125\text{m}2}\text{Te}$ and $\text{Mg}_3{}^{123\text{m}2}\text{TeO}_6$ samples were cooled from 300 to 10 K. A similar comparison is also shown for $\text{Be}{}^{125\text{m}2}\text{Te}$ [2,10] and ${}^{119\text{m}2}\text{SnO}$ [22] samples. The values shown in the table clearly demonstrate that the collective running-wave mechanism discussed above quantitatively explains the experimentally observed data within error limits. Importantly, it is not necessary to introduce any

Table 1

Comparison of theoretically calculated (eq. (30)) and experimentally measured enhancement ratios, $\epsilon = \Delta\Phi_\gamma/\Phi_\gamma$, where $\Delta\Phi_\gamma$ is the number of gamma quanta emitted by stimulation at a matrix temperature of T_{exp} . The number of gamma quanta emitted spontaneously for a matrix temperature of 300 K is Φ_γ .

Nuclide (*X)	${}^{125\text{m}2}\text{Te}$	${}^{123\text{m}2}\text{Te}$	${}^{119\text{m}2}\text{Sn}$
Polycrystal	BeTe	Mg_3TeO_6	SnO
T_A (K)	15.2	10.1	5.7
Debye Temp. (K)	390	350	154
$N \cdot X$ (10^{18} cm^{-3})	12 ± 5	4.9 ± 1.5	34 ± 7
T_{exp} (K)	78	10	10
Mössbauer factor $f_M(T_{\text{exp}})$	0.10 ± 0.02	0.108	0.18 ± 0.01
μ_0^{-1} (cm)	0.2062	0.2062	0.1639
$\frac{4}{3} \pi \mu_0^{-3} (N \cdot X) (10^{16} \text{ atoms})$	44 ± 18	18 ± 6	63 ± 13
$\frac{f_M \tau_1}{2(1 + \alpha_2)(\tau_2 + \tau_1)} (10^{20})$	4.03	4.35	0.148
ϵ_{theory} (%)	1.8 ± 0.7	0.8 ± 0.3	0.09 ± 0.02
ϵ_{exp} [%]	1.2 ± 0.6	0.35 ± 0.15	0.05 ± 0.03
Ref. for ϵ_{exp}	[2,10]	This work, eqs. (5), (13)	This work, eq. (15)

revisions to the second Einstein relation nor to any other points of standard radiation theory.

References

- [1] G.A. Skorobogatov and B.E. Dzevitskii, in: *Proc. Conf. Prospects for Radiochemistry at the Ural, 1983*, Perm (Acad. Press, Perm, 1983) p. 106–107.
- [2] G.A. Skorobogatov and B.E. Dzevitskii, Izv. Acad. Sci. USSR, Ser. Phys. 48 (1984) 1934.
- [3] V.G. Alpatov, G.E. Bisina, A.V. Davydov, B.E. Dzevitskii, G.R. Kartashov, M.M. Korotkov, G.V. Kostina, A.A. Sadovskii and G.A. Skorobogatov, Izv. Acad. Sci. USSR, Ser. Phys. 50 (1986) 2013.
- [4] V.G. Alpatov, G.E. Bisina, S.K. Godovikov, A.V. Davydov, B.E. Dzevitskii, G.R. Kartashov, M.M. Korotkov, V.V. Metlushko, A.A. Sadovskii and G.A. Skorobogatov, in: *Proc. 37th Conf. Nucl. Spectr. Nucl. Struct.*, 1987, Yurmala (Nauka, Leningrad, 1987) p. 224.
- [5] G.A. Skorobogatov, Bull. Leningrad Univ., Phys. Chem., no. 18 (1987) 43.
- [6] G.A. Skorobogatov, Nuovo Cimento (D) 12 (1990) 793.
- [7] G.A. Skorobogatov and B.E. Dzevitskii, Sov. J. Chem. Phys. 12 (1994) 666.
- [8] O.R. Frish (ed.), *The Nuclear Handbook*, ch. 10 (George Newnes Ltd., London, 1958).
- [9] S.F. Mughabghab, M. Divadeenam and N.E. Holden, *Neutron Cross Sections*, vol. 1, part A (Acad. Press, New York–London, 1981).
- [10] G.A. Skorobogatov, Bull. Leningrad Univ., Phys. Chem. no. 18 (1988) 39.
- [11] V.G. Alpatov, A.V. Davydov, G.R. Kartashov, M.M. Korotkov, G.V. Kostina, P.A. Polozov and A.A. Sadovskii, Nucl. Phys. (Russ.) 58 (1995) 15.
- [12] G.A. Skorobogatov and B.E. Dzevitskii, Laser Phys. 5 (1995) 258.
- [13] D.N. Klyshko, *Physical Grounds for Quantum Electronics* (Nauka, Moscow, 1986).
- [14] D.M. Chizhikov and V.P. Schastlivyi, *Tellurium and Tellurides* (Nauka, Moscow, 1966).
- [15] V. McLane, C.L. Dunford and P.F. Rose, *Neutron Cross Sections*, vol. 2 (Acad. Press, New York) p. 451.
- [16] T. Tamura, Z. Matumoto and M. Ohshima, Nucl. Data Sheets 32 (1981) 497.
- [17] E. Storm and H.I. Israel, Nucl. Data Tables A7 (1970) 565.
- [18] T. Tamura, Z. Matumoto, K. Miyano and S. Ohya, Nucl. Data Sheets 29 (1980) 453.
- [19] T.S. Belanova, A.V. Ignatjuk, A.B. Paschenko and V.I. Pljaskin, *Radiational Neutron Capture* (Energoatomizdat, Moscow, 1986).
- [20] N.N. Bogoljubov Jr. and A.S. Shumovskii *Superradiation* (JINR, Dubna, 1987).
- [21] W. Heitler, *The Quantum Theory of Radiation* (Clarendon Press, Oxford, 1954).
- [22] V.G. Alpatov, A.A. Antipov, G.E. Bisina, S.K. Godovikov, A.V. Davydov, G.R. Kartashov, M.M. Korotkov, P.A. Polozov, B.I. Rogosev, A.A. Sadovskii, I.A. Suvorov and A.N. Cheltsov, Izv. Acad. Sci. USSR, Ser. Phys. 53 (1989) 2052.

Section 6

Pump Sources

X-ray generation in inverse capillary discharges for pumping

V.I. Zoran^a, M. Ganciu^a, A.M. Pointu^b, C.B. Collins^c and I.-Iovitz Popescu^a

^a*Institute of Atomic Physics, P.O. Box MG-6, Bucharest, Romania*

^b*Laboratoire de Physique des Gaz et des Plasmas, Université Paris-Sud, 91405 Orsay, France*

^c*Center for Quantum Electronics, University of Texas at Dallas, P.O. Box 830688,
Richardson, TX, USA*

An inexpensive, tunable, filamentary X-ray generator, based on the bremsstrahlung of a pulsed, high-power-density electron beam cruising along a dielectric fiber is presented. At small scale, it encodes some of the features of an X-ray machine for triggering the energy stored in the long-lived $^{178}\text{Hf}^m$ nuclear isomer, in particular an optimum coupling to the active medium.

1. Introduction

Energy can be stored at very large densities in long-lived nuclear isomers. Its release as incoherent or coherent flashes of gamma-rays would open the avenue towards new scientific and technological endeavours, without the restrictions imposed by handling radioactive or fissile materials. One possible way to achieve this release is to pump the isomeric state into fluorescing levels by using intense electromagnetic radiation.

In an encyclopaedic review [1] it was generally concluded that a gamma-ray laser based upon all techniques for pumping known in 1980 was impossible. Shortly after, the renaissance in gamma-ray laser research was driven by the interdisciplinary concept of upconversion [2], based on the identification and exploitation of a nuclear “bandwidth funnel”, analogous to the broad absorption band linked through efficient cascading down to the narrow lasing level in the ruby laser. Following this approach, in 1988 it was first demonstrated [3] that intense X-ray flashes could dump the energy stored in the (fully inverted) naturally occurring $^{280}\text{Ta}^m$ isomer. The populations of the $^{280}\text{Ta}^m$ are pumped down through two isolated resonances of extraordinary strength, with integrated cross sections about 10^6 times larger than those typically measured for excitation of nuclei by X-rays. Surveying the pumping of isomers in 19 isotopes [4] allowed to find more such “giant pumping resonances” in nuclides near $A = 180$.

Presently, the best candidate material from the perspective of X-ray pumping a gamma-ray laser seems to be the 31-year isomer of ^{178}Hf . Such a long lifetime of the ^{178}Hf isomeric state against spontaneous decay is due to the selection rules on the quantum number K , which is the projection of the nuclear spin I on the axis of this

oblate nucleus. According to the systematics, a “K-mixing” giant pumping resonance is expected at less than 300 keV above the isomeric level [5]. If this expectation will be met, one can eventually obtain the release of the 2.45 MeV stored in the 31-year, $K = 16$ isomer of ^{178}Hf by relatively soft photons, within the capability of the existing X-ray machines [6]. Moreover, one can conceive new, more flexible, dedicated triggering devices. Such machines should deliver X-rays in the range 0–500 keV with tunable endpoint, pulsed in the nanosecond range (as determined by the lifetime of the lasing level relative to the nuclear M1 transitions) with a repetition rate of about 100 Hz. The radiation should be efficiently coupled to the active medium, preferably in a cylindrical geometry. If possible, they should be light-weight, inexpensive, and allowing easy screening.

In this work we explore a new way of producing intense flashes of X-rays for pumping by coupling to a narrow cylindrical dielectric active medium [7] of a high-density pulsed electron beam obtained in a superposition of two discharges [8,9]. The experimental device proposed encodes many of the above-mentioned requirements.

Our approach is based on recent developments of spark discharges which lead to new solutions of obtaining “directional” particle and radiation energy with the help of rather small and inexpensive devices [8–19]. These are low-pressure spark-like discharges in tubes with various special geometries, such as transient hollow cathode discharges, pseudosparks and capillary discharges or channel sparks, having the remarkable advantage of working at high repetition rates, up to several kHz, at a pulse power density of the order of a GW/cm². Focusing the electron beams of such discharges onto appropriate targets, a significant fraction of the pulsed electrical energy is transformed into intense bremsstrahlung X-ray flashes.

Why is, in contrast to the common vacuum chamber of the electron beam accelerators, a low-pressure gas filling actually necessary to produce a high-density pulsed electron beam? The answer is that the electron beam, with an energy of up to several tens of keV, carrying a current density of up to several MA/cm², would undergo such a strong electrostatic space-charge repulsion among the electrons in the vacuum, that the beam would actually blow up. The presence of the gas allows a strong gas ionization and the formation of a plasma medium by the electron beam itself, which compensates the beam space charge, and an exponential build-up of the beam current up to very high values. Flashing of the gas fill, accompanying the dense plasma formation during the passage of the electron beam, reminds the spark of the ordinary high-pressure spark, thereof the terminology preserved even for low gas pressure conditions.

In addition to the beam focusing caused by space-charge compensation, the azimuthal magnetic field around the beam, reaching values of the order of a tesla for a typical beam radius of 0.2 mm, offers an additional confining effect, which compensates any residual electrostatic space-charge repulsion of the fast electrons in the beam.

In order to illustrate the state-of-the-art of the low-pressure spark-like alterna-

tive, we shall first emphasize the performances of the Erlangen research team of professor Jens Christiansen [10,11], the founder of pseudospark systems, who obtained intense electron beams of 20 keV energy, power density of a GW/cm² and 20 ns pulse duration. An important application has been substantiated concerning high-quality coating with high-temperature superconducting thin films by electron beam ablation of high- T_c materials [20]. Thus, such electron beams turn out to be good tools for materials processing, comparable in many respects with the corresponding application spectrum of pulsed high-power lasers.

Recently, the Karlsruhe group of F. Hoffmann and his colleagues [16] confirmed this new capability with a channel spark as a source of magnetically self-focused pulsed electron beams having current intensities up to 1.5 kA/cm², current densities of the order of 10⁵ A/cm², electron energy of 10 keV and a pulse duration of 100 ns. In addition, they showed that the channel spark in hydrogen ends in a stable magnetically compressed Z-pinch plasma column with a temperature of three million degrees for a period of one microsecond. By introduction into the pinch of specific atoms having higher atomic numbers, the plasma energy is converted into soft X-radiation.

Very recently, Jorge Rocca and his co-workers at Colorado State University have reported [21] the first soft-X-ray laser at 46.9 nm ($J = 0\text{--}1$ line of Ne-like Ar) in a 12 cm length capillary discharge in argon.

Finally, we mention the recent studies of pseudospark-like discharges carried out at the Institute of Atomic Physics at Bucharest, in cooperation with the Laboratoire de Physique des Gaz et des Plasmas at Orsay. These studies have been performed using a very handy, non-expensive device. It allows us to obtain pulsed, intense electron beams having 280 A peak current, 20 keV energy, about 10 ns pulse duration, and up to 50 μm diameter [8]. An exceptional radial stability over a few centimeters length has been achieved without any collimating device or external magnetic field, by taking advantage of the plasma lens effect of an auxiliary discharge, as well as of the partial space-charge compensation by the positive ions created and trapped by the beam [9]. The lack of inner electrodes opens the possibility to work with high-purity fill gases. This new type of discharge has been used to investigate the behavior of intense electron beams in the proximity of dielectric surfaces (the “cruise” effect [7]), which will be exploited to achieve an optimum coupling of the bremsstrahlung to the active media.

In the next section we describe the pulsed electron beam. Section 3 presents the “cruise” effect, its qualitative explanation, as well as our preliminary results concerning X-ray generation in inverse capillary discharges associated with this effect. The last section is devoted to a few conclusions.

2. Pulsed electron beams by superposition of two discharges

Besides thermionic diodes or field emission diodes, pseudosparks [10–15] have

been found promising in producing high-current-density electron beams for several applications such as producing intense X-ray flashes. In the present chapter we describe a source configuration producing pulsed electron beams whose diameter, peak current and pulse duration are quite similar to those of pseudosparks under the same voltage and pressure conditions. Its originality consists of the fact that beam collimation requires neither internal diaphragms nor any peculiar anode geometry but only uses the synergy of two discharges. The analogies and differences relative to the classical pseudosparks are revealed by investigating the influence of both cathode geometry and preionization upon the electron beam generation and collimation. The fact that the collimated beam can be obtained by using entirely external electrodes extends the field of potential applications to those requiring high gas purity.

2.1. EXPERIMENTAL SET-UPS

The experimental set-up used first [8] is shown in fig. 1a. It is mainly composed of a quartz tube (2.8–3 cm diameter, 100 cm length) containing gas at a pressure of 0.1–1 mbar, along which two discharges are produced. The first one, the “main discharge”, uses two identical external cylindrical electrodes, having 8 or 16 cm length, l , adjacent to and surrounding the tube (anode A_1 , cathode K_1), biased with high-voltage pulses. The second one, the “auxiliary” discharge, is a DC negative glow-type discharge (a few mA, a few hundred V) created by internal electrodes consisting of an axial disc-shaped cathode, K_2 , and a lateral grounded anode, A_2 , which are decoupled by means of two inductances. The typical distance, d , between K_1 and K_2 is 5–10 cm and the inter-electrode gap of the pulsed discharge, $K_1 A_1$ is 2–4 cm.

High-voltage pulses are generated by a rotary spark gap (RSG) through a delay line, partially wound around ferrite cores. These pulses are characterized by a voltage U in the range 4–20 kV and a rise time of about 10 ns, with a repetition rate of a few tens of hertz. They are measured, with the help of a calibrated capacitive divider consisting of a differentiating circuit, followed by an integrating circuit having a 4 μ s constant time. The corresponding currents are measured with a Rogowski coil. Plasma light emission is investigated by means of an optical fiber coupled to a common spectrometer–photomultiplier system, and the signals are sent to a microcomputer interfaced oscilloscope.

The second experimental set-up [22], shown in fig. 1b, is dedicated to the comparison with classical pseudospark discharges and to the investigation of the role of the cathode geometry. Thus, the cylindrical discharge tube, made of glass, contains a cylindrical hollow cathode (K), a flat anode (A) and an auxiliary cylindrical electrode (P) for preionization. The possibility of introducing internal diaphragms is provided. In addition to the first experimental set-up, also a system of pulsed voltage doubling has been used, based on the following principle: The oscillating discharge of the capacitor C_1 through a coaxial cable (15 m long and 50 Ω impedance)

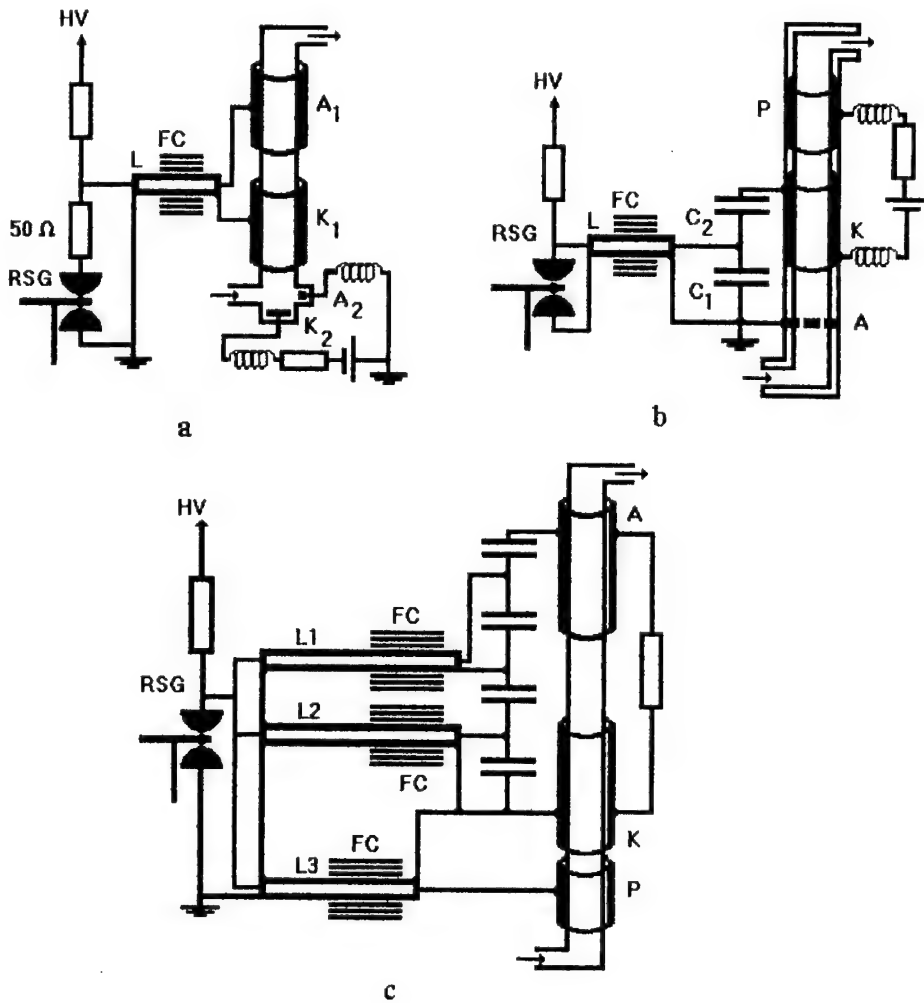


Fig. 1. Experimental set-ups for pulsed electron beam generation by superposition of two discharges.

and a rotary spark gap generates a negative high-voltage pulse on the cathode K of the main discharge. This pulse has a peak value two times the charging voltage of the capacitors C_1 and C_2 , a rise time of about 50 ns, and a duration of about 150 ns. The maximum repetition rate (100 Hz) was limited only by the performance characteristics of the rotary spark gap used. For higher repetition rates (up to a few kHz) the rotary spark gap can be replaced by a classical pseudospark switch.

The third experimental set-up [9] is schematically shown in fig. 1c. It consists of a quartz tube (30–100 mm diameter) without inner electrodes, containing gas or gaseous mixtures at pressures of 0.1–3 mbar, capacitively coupled to a pulse generator. Two discharges are produced along the tube. The first one takes place

between the cathode K and the electrode P which creates a convenient plasma inside the tube just before the proper moment when the second discharge starts between the cathode K and the anode A. Both discharges are produced by high-voltage pulses generated by a rotary spark-gap and transmitted through delay lines partially wound around ferrite cores. This permits to choose an appropriate delay between the preionization discharge and the main discharge. The applied voltage pulse for the main discharge ranges from 10 to 50 kV with a voltage multiplication factor of 3.8 relative to the RSG voltage generator and having a rise time of about 50 ns and a repetition rate which can be chosen between 1 and 100 Hz. The peculiarity of this set-up resides in the fact that both a pulsed preionization discharge and entirely external electrodes are used.

2.2. THE ROLE OF THE PREIONIZATION AND THE ELECTRON BEAM CHARACTERISTICS

Referring to fig. 1a, for given values of pressure, p , pulse voltage, U , and position of electrodes A_1 K_1 relative to K_2 A_2 (distance d), the DC discharge current, I_2 , is slowly increased from its lowest value. Initially, the pulsed discharge merely creates a diffuse plasma glow between and inside the electrodes K_1 and A_1 . Further increase in I_2 only extends the DC negative glow from A_2 towards K_1 but, when I_2 reaches a critical value, I_{2c} (a few mA), the pulsed discharge changes into a bright and narrow axial plasma channel with a constant diameter over the whole length between K_1 and A_1 (fig. 2). In this case, the aluminum electrodes were replaced with transparent electrodes, as we shall describe in a next paper. Further increase in I_2 leads to progressive enlargement, and finally to the disappearance of this channel. The critical value I_{2c} depends on the set of p , U and d values and corresponds approximately to the same position between K_1 and A_1 of the DC diffuse negative glow tip. While inserting on the tube axis small targets of various materials (metals or insulator) between K_1 and A_1 , the bright channel develops in the gap between K_1

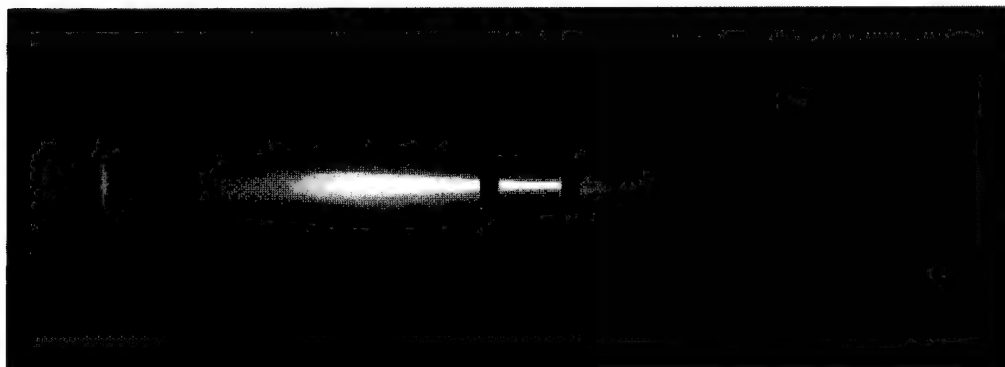


Fig. 2. The bright and narrow axial plasma channel obtained in argon for the configuration given in fig. 1a, using transparent electrodes.

and the targets, and a small adjustment of I_{2c} is necessary in order to maintain its narrowness.

The deflection of the bright channel under the action of a transverse magnetic field proves that the channel plasma is produced by a fast electron beam. Monitoring this deflection by the fluorescence produced in a NE 102 scintillator, used as a target, allows the comparison with the deflection of a probing collimated continuous electron beam of known energy, produced in the same discharge tube configuration.

By varying p , U or d , it is always possible to find a convenient I_{2c} current. It is worthwhile to notice that interchanging the polarities of A_1 and K_1 prohibits beam formation, even if the new cathode is placed at the same position as the previous one. Under the conditions of a well-collimated electron beam, one can replace the quartz effective internal faces of A_1 and K_1 by metal (simply by introducing two aluminum cylinders into the discharge tube) without any noticeable change of the beam characteristics. By replacing the cylindrical anode A_1 with an internal transverse and planar one, no change occurs in the electron beam characteristics. As fill gases air, O_2 , CH_4 and Ar have been used in the pressure range of 0.1–3 mbar. A hole of about 50 μm diameter has been drilled in a 50 μm thick copper target, submitted to 1200 shots, thus demonstrating a beam diameter of less than 50 μm and good spatial stability of the beam.

In the second experimental set-up (fig. 1b), an initial plasma having a density decreasing from the cathode towards the anode has been achieved by means of a DC glow discharge between the cathode (K) and the auxiliary electrode (P), the latter playing the role of either cathode or anode for this discharge. Each polarity implies, however, a different optimum preionization current. The optimization of the preionization current allowed to extend significantly the working pressure range for well-collimated beams. At a given pressure, the delay time between the moments of high-voltage application and electron beam generation can be controlled by the current of the preionization discharge in the range of tens of ns [22].

The extraction of the electron beam for energy and current measurements has been performed through a small circular hole (100 μm diameter) bored in the center of the anode (A), which may possibly be drilled by the beam itself. A Faraday cup has been used to measure the charge carried by the electron beam and the intensity of the beam. The energy spectrum of the energetic electrons was measured with a magnetic analyzer. For this purpose, the electrons were deflected in a magnetic field produced between two soft iron pieces by a solenoid mounted on one arm of the magnetic circuit. The deviation of the electron beam was detected on a scintillator covered with a thin aluminum layer in order to prevent the plasma light to reach the scintillator. The light from the fluorescent spot produced by the energetic electrons was collected with an optical fiber coupled to a fast photomultiplier. The temporal dependence of the intensity of the electron beam for a selected electron energy is recorded on the oscilloscope by using a narrow exit slit of the analyzer system. Some information concerning the electron beam effective diameter and its internal

structure has been obtained from target-damage analysis of a 50 μm thick aluminum foil placed on the anode front surface [22]. Typical parameters of the electron beam obtained in our experiments are: a mean kinetic energy of 0.5–0.7 of the maximum applied voltage to the main electrodes, a peak electron current of 0.1–0.3 of the maximum discharge current, an average charge in the beam of 1–2 μC and a temporal width measured at half maximum of peak intensity of less than 15 ns [23].

In fig. 3, typical oscillograms of the applied voltage and discharge current are given, corresponding to the experiments with inner electrodes, which allow to measure the effective voltage drop during the main discharge. One observes a simultaneous instability of both current and voltage characteristics, associated with a sharp variation of the plasma channel inductivity at the moment of the narrow beam formation. The position of the instability in the voltage oscillogram is consistent with the measured beam energy.

To avoid inner electrodes, in the third experimental set-up the auxiliary DC discharge has been replaced by a pulsed discharge between a cylindrical external anode P and the same cathode K of the main discharge (fig. 1c). The HV device was used to generate a first HV pulse between K and P and a second one between K and A, with a delay time determined by the difference $L_1 - L_3$ in the cable lengths ($L_1 = L_2$). For a given delay, an electron beam similar to the one described previously was obtained between K and A, for a given critical value, p_c , of the gas pressure. A decrease in delay (from 200 to 50 ns) increases the value of the critical pressure from 0.3 to 1 mbar.

It has been verified that beam formation can also be obtained for various gases

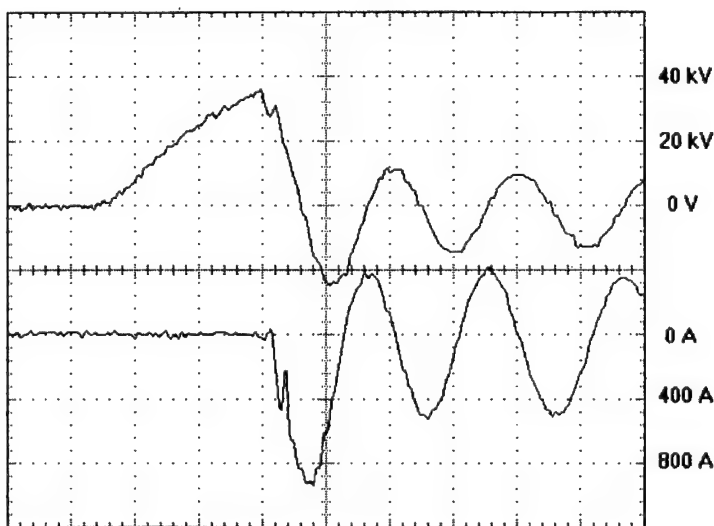


Fig. 3. Typical oscilloscope trace of the applied voltage and discharge current.

and larger tube diameters, up to 10 cm. Finally, within the same range of pressure, we have also obtained a collimated electron beam with a third type of auxiliary discharge, consisting of a RF (13.56 MHz) driven surface wave discharge launched by two external cylinders, similar to the discharge studied in ref. [24].

The best results have been obtained with the experimental set-up shown in fig. 1c. For a given gas and for fixed values of pressure p and main voltage pulse U , there always exists a set of values of the preionization voltage pulse and of the delay time such that an electron beam can be produced along the tube axis between K and A. For a 30 mm diameter, 16 cm length cathode and anode, and with an equivalent external capacity between them of 125 pF, the beam can reach current pulses of 10 to 50 ns duration, with peak values of about 280 A for $U = 50$ kV, producing along more than 40 mm length a 0.5 mm diameter bright plasma channel. Moreover, while in previous experiments done with peak voltage of about 15 kV the electron velocity increased along the axis [8], in the present configuration a constant brightness along the axis has been observed at a peak pulse voltage of 50 kV, thus indicating an approximately constant electron velocity along the beam. Moreover, in a hybrid configuration (a + c, with a dielectric cathode and a floating diaphragm coupled to a mesh around the discharge tube) the length of the electron beam has been increased up to more than 10 cm (fig. 4)

2.3. THE ROLE OF CATHODE GEOMETRY

Pulsed electron beams of similar intensity, energy and diameter have been obtained also in pseudospark discharges, however by using inner diaphragms which may impurify the working gas. Furthermore, the beam characteristics vary along the axis [11].

In order to compare our discharge configuration with the classical pseudospark

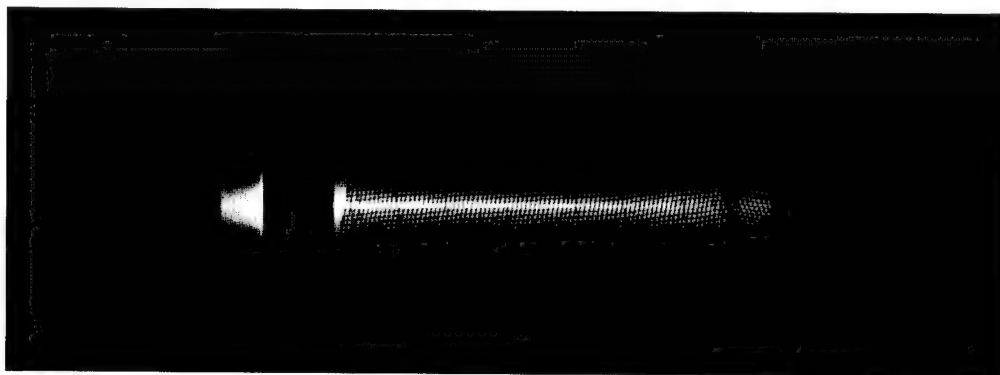


Fig. 4. Photography of the axial plasma channel associated with the pulsed electron beam in argon, in a hybrid discharge configuration optimized for maximum length (the bright cathode region on the left has a length of 15 mm).

geometry used for electron beam generation, we partially closed the anodic end of the cylindrical hollow cathode by introducing various shapes of exit slits, as shown in fig. 5a–e.

Thus, rectangular slits, fig. 5a and b or circular apertures of different sizes, placed symmetrically on the cathode axis, do not affect the electron beam parameters. It is interesting to note that the electron beam can be generated also through an off-axis aperture, fig. 5c, the beam converging towards the axis after leaving the aperture. Moreover, two or more beams can be simultaneously generated through symmetrically placed off-axis apertures, fig. 5d, which eventually also converge towards the axis. A similar effect was observed by placing a metallic rod inside the cathode, fig. 5e, the beam exit from the cathode taking place through the “central point” of the free surface of this half-moon-like hollow cathode geometry. An important conclusion of these experiments is that the electron beam can be generated in different cathode configurations. Moreover, the cylindrical symmetry of the cathode is not compulsory. On the other hand, the position at which the beam leaves the cathode can be controlled by the aperture place and more than a single beam can simultaneously be generated through off-axis symmetrically placed apertures. After leaving the exit slits, all these beams converge towards the axis due to strong negative charging of the inner surface of the glass tube.

This flexibility in using different cathode configurations, in particular large apertures or fully open hollow cathodes, allows to avoid plasma–wall interaction and heating of the aperture edges which usually occur in the high-current-discharge phase [12]. Moreover, the high-density region of the plasma between the cathode and the anode is concentrated along the axis, which determines a low level of impurification from wall materials. Relatively high-current filamentary discharges (~ 400 A) were produced in this configuration with the cathode and the anode inside the glass tube.

Optical microscope observations of the electron beam markings on aluminum foils [22] revealed similar structures to those produced by electron-beam filaments reported by Nardi et al. [25]. It is worthwhile to note that, while the last authors investigated very high-power electron pulses (of TW/cm^2) which are split into

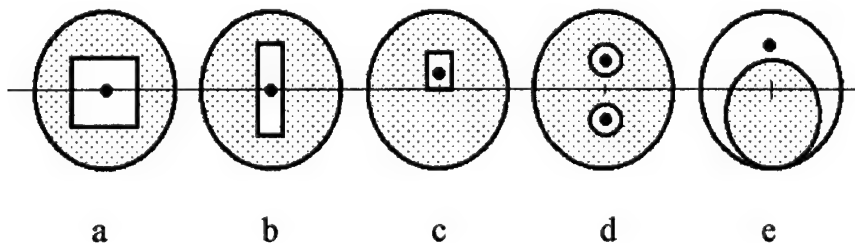


Fig. 5. Different apertures used at the anodic end of the cylindrical cathode. The dot indicates the spot where the electron beam leaves the cathode exit slit.

many ($\sim 10^3$) filaments, our device allows the investigation and optimization of single such electron-beam filaments under various and well controlled boundary conditions. Moreover, the position of the electron beam spot on the anode can be controlled by deflection in magnetic or electric fields, thus providing a movable point-like X-ray source.

We conclude this section by a qualitative explanation of the mechanism involved in the formation and self-collimation of the electron beam, based on the synergy of two discharges. Thus, we may tentatively consider the main discharge as a pulsed hollow cathode discharge, similar to pseudospark discharges, producing intense electron beams, the propagation of which being explained by both space-charge neutralization due to ionized gas atoms and by the self-focusing of the beam due to its own azimuthal magnetic field [26]. However unlike pseudosparks, our experiment does not require internal bore holes to collimate and stabilize the electron beam. We simply replaced them by an appropriate, but highly versatile, auxiliary preionization. We assume that a narrow electron propagation channel develops at the start of the main discharge, due to compensation of beam space charge by the auxiliary plasma [26]. This initial plasma has a decreasing density from cathode to anode, matching the decrease of the beam electron density because the increase of electron velocities. Once the channel has been developed, the beam advances along the same channel, even up to very high current intensities, by creating the appropriate strong ionization necessary for its own space-charge neutralization.

3. A filamentary X-ray generator using the “cruise” effect

3.1. THE “CRUISE” EFFECT

In a set-up similar to that described in fig. 1b, an optical fiber has been inserted along the discharge tube axis in the region between the cathode and anode [7]. The fiber had a diameter of $100\text{ }\mu\text{m}$ and a length of 10 cm. The discharge takes place in air in the pressure range $0.1\text{--}1\text{ mbar}$. By optimizing the preionization discharge, an electron beam of the type described in this paper (200 A , $10\text{--}20\text{ ns}$) has been generated by the main discharge. For distances less than about 1 mm of the optical fiber relative to the beam, the latter gets captured by the fiber and continues to propagate along it. This effect occurs both with inner and outer metallic electrodes of the discharge tube.

The collimation of the beam along the fiber is stronger at higher pressures, when the fiber becomes fluorescent. The fluorescence can be locally enhanced with the aid of an external magnetic field. An inspection of the fibers exposed to higher pressure discharges shows significant sputtering of their surfaces. When the dielectric fiber is replaced by a metallic wire at floating potential, instead of being captured, the electron beam is repelled.

Along with the explanation given for the self-focusing electron beam, in the present experiment we suppose that the “cruising” of the electron beam along the dielectric fiber surface is due to the positive charging of the surface by secondary electron emission following its photon, fast electron and ion bombardment. The phenomenon is favored by the relatively high secondary electron emission rate for dielectrics and by the fact that the positive charge remains localized while, for currents less than the Alfvén limit [26], the emitted electrons are rapidly expelled by the excess negative charge in the beam.

The “cruise” effect can be described qualitatively by extending the ion trap model [9] of the pulsed electron beam. Thus, when dielectric fiber is absent, the exceptional radial stability along many centimeters of the electron beam described in the previous section (fig. 4) is the result of counterbalancing of the Lorentz and electrostatic forces. Under steady-state conditions this implies the well-known equilibrium condition [26]:

$$n_i(x, t) = n_e(x, t)[1 - v_e^2(x, t)/c^2].$$

Here n_e and v_e stand for the electron density and velocity, respectively, at a distance x along the beam axis and at the moment t of the discharge. This relationship has been deduced by assuming a homogeneous current tube and n_i denotes an effective ion density accounting for the existence of multiply charged ions.

Since our beam currents are below the Alfvén limit [26], for the slow electrons the magnetic force is small and these electrons are expelled from the axial region. Consequently, the electron beam becomes surrounded by a thin layer of positive charge which ensures the vanishing of the electric field at the limit of the neutral plasma. The fast electrons which lose energy by collisions are still kept along the beam by the radial potential pockets of this double layer and eventually regain energy from the axial electric field, while the secondary electrons are rapidly removed. On the other hand, the potential seen by the ions looks rather like a simple potential well, whose characteristics were inferred in ref. [9] under the assumption of a uniform initial radial in density and a constant electron density. For the typical conditions of our experiment, $v_e \approx 10^8$ m/s and $n_e \approx 10^{16}$ cm⁻³. In spite of the high electron space charge in which the ions are embedded during the discharge, the recombination is prohibited due to the velocity mismatch between the electron and the ions.

The presence of the dielectric fiber can be modelled by a layer of positive charge along its surface. The corresponding change of the radial electric field and of the potential seen by the ions within the beam is shown comparatively in fig. 6. The electric film in the proximity of the fiber is attracting the electrons of the beam. As a result, the beam is captured by the fiber and is “dressing” it. The ions in the beam, although repelled by the fiber, have enough kinetic energy in the potential well to be able to deposit on the fiber, in a dynamic equilibrium with the electrons which tend to neutralize it.

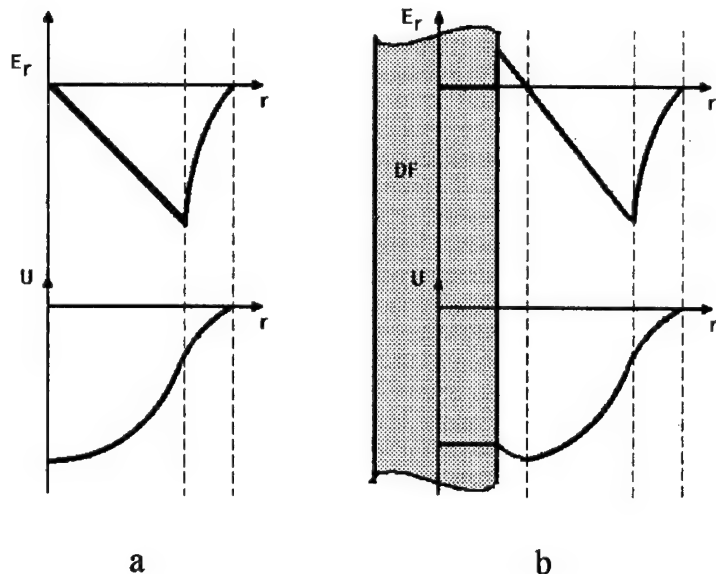


Fig. 6. A model of the radial component of the electric field and of the electric potential within the axial electron beam, as seen by the positive ions, versus the distance to the axis, without (a) and with (b) dielectric fiber, respectively.

3.2. X-RAY FROM INVERSE CAPILLARY DISCHARGES

The main source of hard X-ray production in wall-assisted discharge is the bremsstrahlung following the fast electron interaction with the walls. When the diameter of the discharge tube shrinks, one speaks about capillary discharges. When the channel plasma collapses on the axis, it becomes a source of soft X-rays and possibly an active medium for soft X-ray lasers [21].

While for capillaries the discharge is assisted by the capillary dielectric walls, in the case of the "cruise" effect the discharge is mainly assisted by an axial dielectric fiber. Consequently, we may call this system an "inverse capillary discharge".

The enhanced fluorescence observed when the dielectric fiber is "dressed" by the electron beam suggests the possibility of X-ray emission following the interaction of the fast electrons with the fiber surface under conditions of minimum self-absorption.

In order to check this hypothesis, we used an experimental set-up similar to that shown in fig. 1c, at a repetition rate of 100 Hz. A quartz fiber having a diameter of 100 μm has been inserted in the region between the cathode and the anode along the discharge tube axis. The gas fill was air at a pressure between 0.4 and 1 mbar. In order to avoid X-ray emission by the discharge tube walls under fast electron impact in the vicinity of the cathode [27], an insulating diaphragm was collimating the discharge at the cathode exit (fig. 7). For X-ray detection a 2 mm thick NE 102

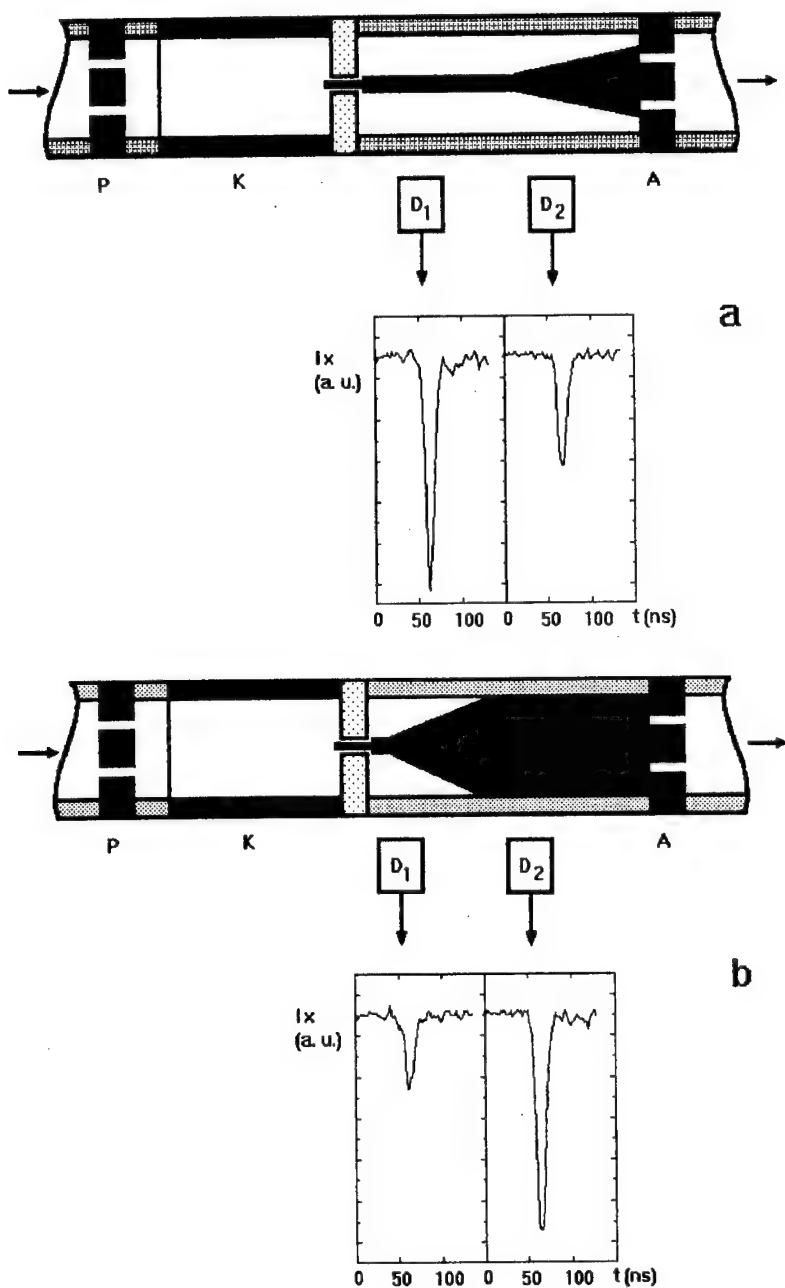


Fig. 7 A schematic representation of the discharge conditions during X-ray measurements and the corresponding X-ray oscillosograms: (a) the electron beam dressing the dielectric fiber; (b) a defocused electron beam.

scintillator pellet shielded for visible light has been used and coupled via an optical fiber to a RCA 7265 photomultiplier. The signal has been registered by a Tektronix digital oscilloscope connected to a microcomputer. The measurements have been done with the scintillator in two positions marked by D₁ and D₂ in fig. 7, for two regimes of the discharge: With the beam dressing the fiber (fig. 7a) and with the beam being defocused (fig. 7b), respectively.

The signal of X-rays penetrating through the 2 mm thick quartz wall of the discharge tube started to emerge from noise when the applied discharge voltage pulse became larger than 20 keV. The phototube signals registered at 30 kV are shown in fig. 7. The results shown in fig. 7a clearly demonstrate that the main source of X-rays under conditions of a "cruising" beam is the bremsstrahlung generated by the fast electron interaction with the dielectric fiber. By contrast, fig. 7b demonstrates an X-ray emission following the interaction of the defocused beam with the tube walls, similar to that observed in ref. [27].

4. Conclusions and outlook

In the present work we described a table-top, inexpensive, tunable filamentary X-ray generator. The X-ray emission is essentially the bremsstrahlung of a fast electron beam dressing a dielectric fiber. The pulsed, high-power-density electron beam has been generated in a pseudospark-like discharge and optimized by a preionization discharge.

The radiation flux increases with increasing beam intensity. Unfortunately, the parameters of a single discharge filament cannot be controlled when the current exceeds the Alfvén limit. This difficulty, however, can be circumvented by splitting the main discharge into a few controlled filaments, as in fig. 5d. Guiding each of these filaments along a dielectric fiber may eventually lead to a stacked X-ray generator with a higher intensity.

In contrast to the beam intensity, no limits are expected in principle concerning the discharge voltage (and thus the electron energy) up to several hundreds of kV, as well as concerning the repetition rate up to a few kHz. Accordingly, our current research is devoted to the development of fast high-voltage pulse generators to investigate the inverse capillary discharges at higher voltages and higher repetition rates.

Under certain conditions, a dielectric fiber containing nuclear isomers such as ¹⁷⁸Hf^{m2} may become an active medium for induced gamma-ray emission. An X-ray pumping generator based on the scheme proposed in this work may provide an optimum coupling of the radiation to the active medium. More specifically, assuming that the nuclear isomers are concentrated along the axis of the fiber and the X-rays are generated around the fiber, the radiation power density at the isomer is inversely proportional to the radius of the (cylindrical) emitting surface. Referring to the experiment described in this work, if the X-ray power emitted by the walls (fig. 7b) is comparable to that emitted by the fiber (fig. 7a), as the results seem to suggest,

the power density in the center of the fiber is enhanced several hundred times more when the discharge is “cruising” along the dielectric fiber surface.

References

- [1] G.C. Baldwin, J.C. Solem and V.I. Goldanskii, Rev. Mod. Phys. 53 (1981) 687.
- [2] C.B. Collins, F.W. Lee, D.M. Shemwell, B.D. DePaola, S. Olariu and I.-Iovitz Popescu, J. Appl. Phys. 53 (1982) 4645.
- [3] C.B. Collins, C.D. Eberhard, J.W. Glesener and J.A. Anderson, Phys. Rev. C37 (1988) 2267.
- [4] J.J. Carroll et al., Phys. Rev. C43 (1991) 1238.
- [5] C.B. Collins and J.J. Carroll, these proceedings (1st Int. Gamma-Ray Laser Worksh., 1995), Hyp. Int. 107 (1997) 3.
- [6] F.J. Agee, these proceedings (1st Int. Gamma-Ray Laser Worksh., 1995), Hyp. Int. 107 (1997) 69.
- [7] M. Ganciu, E. Dewald, M. Nistor, D. Penache, I.-Iovitz Popescu and V. Zoran, Rom. J. Phys. 39 (1994) 787.
- [8] M. Ganciu, G. Modreanu, A.M. Pointu and I.-Iovitz Popescu, J. Phys. D27 (1994) 1370.
- [9] M. Ganciu, I.-Iovitz Popescu, V. Zoran and A.M. Pointu, Nucl. Instr. and Meth. B98 (1995) 541.
- [10] J. Christiansen and Ch. Schultheiss, Z. Physik A290 (1979) 35.
- [11] W. Benker, J. Christiansen, K. Frank, H. Gundel, W. Hartmann, T. Redel and M. Stetter, IEEE Trans. Plasma Sci. 17 (1989) 754.
- [12] M.A. Gundersen and G. Schaefer (editors), *Physics and Applications of Pseudosparks* (Plenum Press, New York, 1990).
- [13] P. Choi, H.H. Chuaqui, M. Favre and E.S. Wyndham, IEEE Trans. Plasma Sci. 15 (1987) 428.
- [14] K.K. Jain, E. Boggash, M. Reiser and M.J. Rhee, Phys. Fluids B2 (1990) 2487.
- [15] W.W. Destler, Z. Segalov, J. Rodgers, K. Ramaswamy and M. Reiser, Appl. Phys. Lett. 62 (1993) 1739.
- [16] F. Hoffmann, M. Konijnenberg, C. Schultheiss, M. Schwall, K. Mittag and G. Mueller, KfK-Nachr. 24 (1992) 254.
- [17] M. Ganciu, G. Modreanu and A.M. Pointu, *Proc. 46th GEC* (Moisan Ed., Montreal, Quebec, 1993) 29.
- [18] J.J. Rocca, D.C. Beethe and M.C. Marconi, Opt. Lett. 13 (1988) 565.
- [19] C. Steden and H.-J. Kunze, Phys. Lett. A151 (1990) 534.
- [20] H.P. Schölch, P. Fickenscher, T. Redel, M. Stetter, G. Saemann-Ischenko, W. Benker, W. Hartmann, K. Frank and J. Christiansen, Appl. Phys. A48 (1989) 397.
- [21] J.J. Roca, V. Shlyaptsev, F.G. Tomasel, O.D. Cortázar, D. Hartshorn and J.L.A. Chilla, Phys. Rev. Lett. 73 (1994) 2192.
- [22] M. Ganciu, A.M. Pointu, N. Mandache and I.-Iovitz Popescu, *Proc. 4th Conf. in Optics ROMOPTO '94, Bucharest, Romania*, SPIE 2461 (1995) 40.
- [23] N.B. Mandache, A.M. Pointu, D.G. Dumitriu, M. Ganciu, G. Musa, I.-Iovitz Popescu, E. Dewald and M. Nistor, Le Vide 275 (Suppl.) (1995) 337.
- [24] O. Guymont, E. Leduc, D. Pagnon, A.M. Pointu, M. Touzeau, M. Vialle, B. Mercey and H. Murray, Plasma Sources Sci. Technol. 1 (1992) 175.
- [25] V. Nardi, W.H. Bostick, J. Feugeas and W. Prior, Phys. Rev. A22 (1980) 2211.
- [26] R.B. Miller, *An Introduction to the Physics of Intense Charged Particle Beams* (Plenum Press, New York, 1982).
- [27] W.H. Bloss, S. Metz and W.F. Fagen, *Proc. 9th Int. Conf. on Phenomena in Ionized Gases, September 1-6, 1969, Bucharest, Romania* (Romanian Academy, Bucharest, 1969) 642.

Stimulation of beta-decay by laser radiation

V.M. Buimistrov

Moscow Institute of Physics and Technology, Russia

This paper deals with the study of new beta-decay acceleration mechanisms. Estimations have proved that there is a real possibility for stimulated beta-decay detection. The required laser intensity has been achieved by now. The mechanism under discussion may be characterized as the opposite process of K-electron capture. This paper makes an essential distinction between the above-mentioned mechanism and other beta-decay acceleration mechanisms.

The additional beta-decay channel is investigated in this paper. We begin with the most simple example, which is neutron beta-decay: $n \Rightarrow p + e^- + \bar{\nu}_e$ (fig. 1). After the beta-decay, the beta-electron interacts with the Coulomb field of the pro-

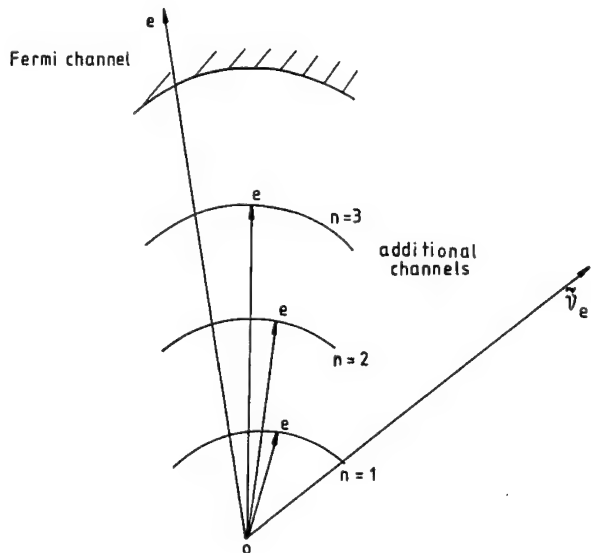


Fig. 1. β -decay of the neutron: $n \Rightarrow p + e^- + \bar{\nu}_e$. After β -decay, the β -electron effectuates a transition on a continuum energy level (Fermi channel) or on a discrete energy level of the new-born hydrogen atom (additional channel). The total probability of the β -decay is the sum of probabilities over all channels.

tons. The energy spectrum for the beta-electron within the proton field, consists of discrete energy levels and a continuum part. According to the general principles of the quantum theory, the beta-decay total probability is expressed as the sum of the probabilities over all electronic transitions:

$$W_{\text{tot}} = \sum_n W_n + W, \quad (1)$$

where W_n is the probability per second for the capture of a beta-electron in the n th state, W_{tot} is the probability of all transitions in states of the continuum energy spectrum. Generally, any unoccupied energy level can capture the beta-electron. W is described as follows:

$$W = A \int_1^{\Delta E} \epsilon \sqrt{\epsilon^2 - 1} (\Delta E - \epsilon)^2 d\epsilon = Af_0(\epsilon),$$

$$A = \frac{m^5 c^4}{2\pi^3 \hbar^7} |\langle f | H_w | i \rangle|^2, \quad (2)$$

where: $f_0(\epsilon)$ is the Fermi function without Coulomb correction, ϵ is the continuous energy spectrum of the beta-electron, ΔE is the nuclear transition energy (ΔE and ϵ are measured in mc^2 units), $\langle f | H_w | i \rangle$ is the matrix element for the nuclear transition from the $|i\rangle$ nuclear state on the $|f\rangle$ state, and H_w is the weak interaction Hamiltonian.

Fermi considered in his famous theory only electronic transitions in the continuum spectrum [1,2]. A question arises: how to detect the capture of a beta-electron on a discrete energy level?

We will consider now the beta-decay of the nucleus ${}^A_Z R$: ${}^A_Z R \Rightarrow {}^A_Z R + e^- + \tilde{\nu}_e$ (fig. 2). If the beta-electron has been captured on the 3s-level of the new-born atom, the $3s \Rightarrow 3p$ radiative transition appears, i.e., the beta-electron radiates a photon. *The atom sends out an optical signal about the new beta-decay channel!*

One can modify the Fermi theory for beta-electron capture on a discrete energy level. The result for a single-electron ion is:

$$W_n = 1.69 \times 10^{-6} \frac{(\Delta E_0 + I_n)^2}{f(\Delta E) \times T_{1/2}} Z^3 \pi |\Psi_n(0)|^2 a_1^3,$$

$$N_n = n_0 \times W_n,$$

$$\Delta E_0 \equiv \Delta E - 1, \quad (3)$$

where $T_{1/2}$ is the beta-decay half-time, Z is the atomic number of the new-born nucleus, I_n is the energy of the $|n\rangle$ state, $\Psi_n(0)$ is the wave-function, a_1 is the hydrogen atom radius, and 0 is the location point of the nucleus (fig. 3). This is the formula for beta-electron capture in the $|n\rangle$ state or *inverse K-capture* (for the K-shell).

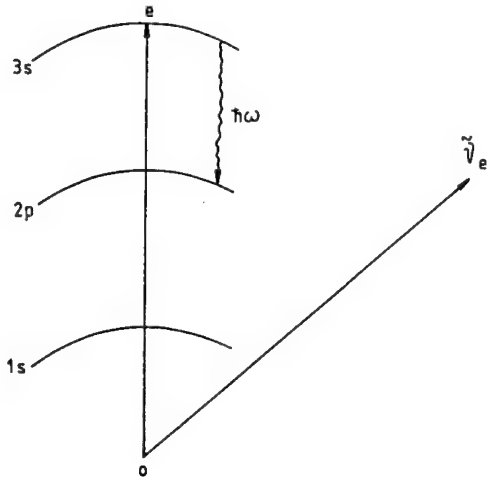


Fig. 2. β -decay of a “bare” nucleus ${}_Z^A R$: ${}_Z^A R \Rightarrow {}_Z^A R + e^- + \tilde{\nu}_e$ with capture of an electron on the 3s-level of the new-born ion, as a hydrogen atom, but with different Z (in the general case). The atom sends out an optical signal describing the decay of the atomic nucleus!

The K-capture formula is very well known [3]. The N_n value stands for the number of beta-electrons captured on the discrete energy level in the unit volume per second, while n_0 represents the number of radioactive atoms in the unit volume. What is the value of the N_{ph} photon number for the $3s \Rightarrow 3p$ radiative transitions, e.g., in the unit volume per second? The N_{ph} value is equal to N_n because the considered optical transition probability per second is very large compared to the probability

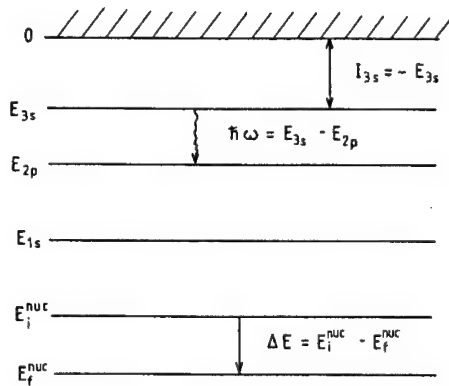


Fig. 3. The energy diagram of β -decay, with the capture of a β -electron on the 3s-level. The energy of the nuclear transition spent on the aperture of the β -electron (captured on the 1s-level) and on the antineutrino appearance is $\Delta E = mc^2 - I_{3s} + \epsilon_\nu$. The $3s \rightarrow 2p$ optical transition probability per second is very large compared to the probability of β -electron capture on the 3s-level. The atoms radiate a number of $h\omega$ photons equal to the number of electrons captured on the 3s-level.

per second of beta-electron capture on the 3s-level. Thus, the atom radiates a number of $\hbar\omega$ photons per second, which equals the number of beta-electrons captured on the 3s-level.

Three examples will be treated in the following:

1. The beta-decay of the tritium nucleus: ${}^3\text{H} \Rightarrow {}^3_2\text{He} + e^- + \tilde{\nu}_e$ (figs. 4 and 5). The beta-decay parameters are: $Z = 2$, $f(\Delta E)T_{1/2} = 1132$ s, $\Delta E_0 = 18.65$ keV, $T_{1/2} = 3.87 \times 10^8$ s [4]. The calculated results are: $W_{1s} = 1.55 \times 10^{-11}$ s $^{-1}$, $W_{2s} = 1.9 \times 10^{-12}$ s $^{-1}$, $W_{3s} = 3.4 \times 10^{-13}$ s $^{-1}$ for the “bare” tritium nucleus (fig. 4). The number of photons in the unit volume per second is $N_{ph}^{ion} = N_{3s}^{ion} = 3.4 \times 10^4$ cm $^{-3}$ s $^{-1}$ and the tritium ion concentration is $n_0 = 10^{17}$ cm $^{-3}$. For the tritium atom, the number of photons is $N_{ph}^{at} = (Z^*/Z)^3 N_{ph}^{ion} = 0.6N_{ph}^{ion}$ (Z^* is the effective charge of the atom [5]), because $Z^* = 1.69$ for the 1s-electron of the new-born helium atom [6]. The increase of the n_0 concentration lightly compensates for the difference between N_{ph}^{at} and N_{ph}^{ion} . The situation for the tritium molecule is similar. Our calculations show that 80, 10 and 2 elementary beta-decay acts happen corresponding to the beta-electron capture on the 1s, 2s and 3s-levels, respectively, if 10^4 elementary beta-decay acts show up with beta-electron capture in the continuum energy spectrum (Fermi channel).
2. The beta-decay of the “bare” sulfur atom nucleus: ${}^{35}_{16}\text{S} \Rightarrow {}^{35}_{17}\text{Cl} + e^- + \tilde{\nu}_e$ (figs. 6 and 7). The beta-decay parameters are: $Z = 17$, $f(\Delta E)T_{1/2} = 10^5$ s, $\Delta E_0 = 167$ keV, $T_{1/2} = 7.52 \times 10^6$ s [7]. The “bare” nucleus or the positive multiply charged ion can capture beta-electrons on the deep level which has been occupied before the ionization process. The ratio between the probability of beta-electron capture on the 1s-level of the new-born chlorine atom and the cap-

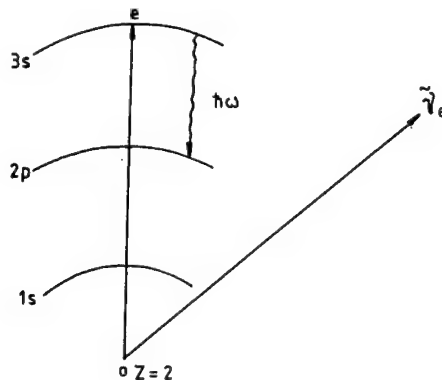


Fig. 4. β -decay of the “bare” tritium nucleus: ${}^3\text{H} \Rightarrow {}^3_2\text{He} + e^- + \tilde{\nu}_e$. The 3s-level of the new-born hydrogen-like helium ion captures the β -electron. The captured β -electron radiates when it descends to the lower 2p-level.

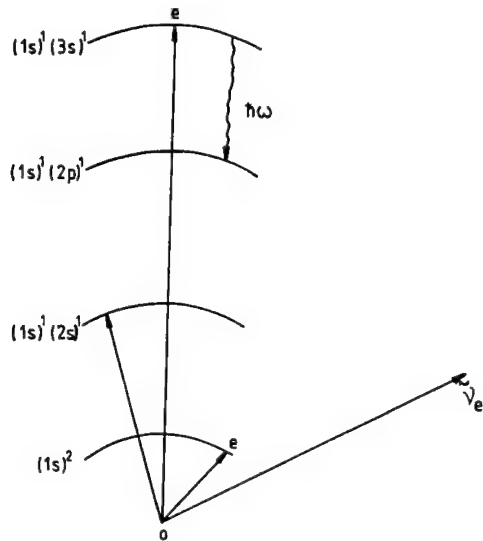


Fig. 5. β -decay of the tritium atom nucleus. The additional β -decay channels arise due to the capture of a β -electron on the new-born helium atom $(1s)^2$; $(1s)^1(2s)^1$; $(1s)^1(3s)^1$ -shells. The electron captured on the $(1s)^1(3s)^1$ shell, descends to the $(1s)^1(2p)^1$ shell and radiates a photon.

ture probability on the lowest level of the sulfur atom is equal to: $(Z/Z^*)^3 = 4.9 \times 10^3$. Higher ionization degrees open new beta-decay channels. The results are as follows: $W_{1s}/W = 110$, $W_{2s}/W = 14$, $W_{3s}/W = 2$.

3. The beta-decay of the "bare" phosphorus nucleus $^{34}_{15}\text{P} \Rightarrow ^{34}_{16}\text{Cl} + e^- + \tilde{\nu}_e$ (figs. 6 and 7). The beta-decay parameters are: $Z = 16$, $\Delta E_0 = 5.4$ MeV, $T_{1/2} = 12.4$ s

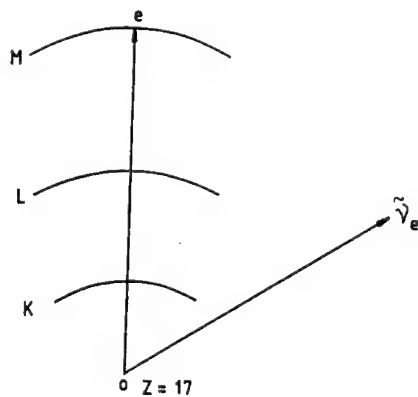


Fig. 6. β -decay of the sulfur atom nucleus: $^{35}_{16}\text{S} \Rightarrow ^{35}_{17}\text{Cl} + e^- + \tilde{\nu}_e$. The M-shell of the new-born chlorine atom captures the β -electron. The closed K-shell and L-shell cannot capture the β -electron.

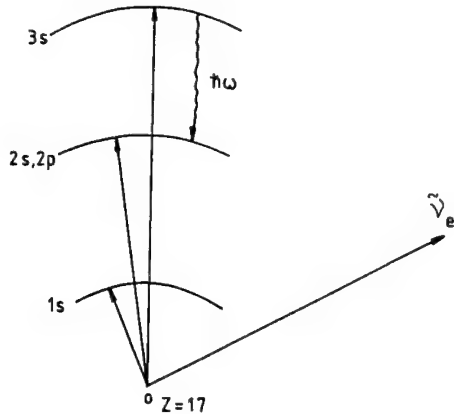


Fig. 7. β -decay of the “bare” sulfur atom nucleus. The electron shells are fully stripped now. The empty $1s$ -, $2s$ - and $3s$ -levels can capture the β -electron. The β -electron captured on the $3s$ -level radiates a $\hbar\omega = 0.546$ eV photon. The probability of β -electron capture increases several times, proportional to Z^3 ; from $Z \sim 1$ for the β -electron in the new-born chlorine atom field to $Z = 17$ in the chlorine nucleus field. β -decay of the “bare” nucleus or of an ion accelerated in the ion trap after atom ionization with high-power laser radiation.

[8], with the theoretical value of the Fermi function (calculated without Coulomb correction) given by: $f_0(\Delta E) = \Delta E^5/30$ for $\Delta E \gg 1$, and is equal to: $f_0(\Delta E) = 6911$; the $f_0(\Delta E)T_{1/2}$ product is equal to 8.57×10^4 s. The results of the calculations are: $W_{1s} = 0.9 \times 10^{-5}$ s $^{-1}$, $W_{3s} = 2 \times 10^{-7}$ s $^{-1}$. Thus, if the ion trap [9] captures 10^7 ions and holds them for one second, one can detect two photons of $\hbar\omega \sim 0.5$ keV (483 eV) energy. For 10^4 ions in the trap, it is necessary to perform 10^3 experiments.

We may conclude that, in addition to the Fermi channel, where the beta-electron appears in the continuum energy spectrum, an extra beta-decay channel exists, namely, the beta-decay with the capture of an electron on the discrete energy level. After capture, this electron may descend to the lower energy level by photon radiation. Observation of the radiation from the tritium ions, atoms and molecules is possible. The number of photons per second in the unit volume is calculated.

After partial or full ionization of an atom, new empty energy levels and new channels for beta-electron capture arise. Thus, the total probability for beta-decay increases. It is necessary to locate the ions inside the ion trap for conservation of these new beta-decay channels. In this case, the captured beta-electrons radiate photons with an energy of about 0.5 keV. Calculations performed for beta-decay of the “bare” phosphorus nucleus prove that a discussion on this experimental problem is needed. The laser intensity required for the suggested mechanism, is needed only for the production of multiply charged ions. The necessary laser intensity has been achieved by now, using very short laser pulses [10]. This article makes an

essential distinction between this mechanism and other beta-decay acceleration mechanisms.

At last, but not less important, we should mention the first article [11] devoted to beta-decay in a laser field and ref. [12] together with the astrophysical applications of beta-electron capture on discrete levels. We also want to call attention to the ion trap problem in the beta-decay acceleration context [9].

References

- [1] E. Fermi, *Zeit. Phys.* 88 (1934) 161.
- [2] H. Frauenfelder and E.M. Henley, in: *Subatomic Physics* (Prentice-Hall, New Jersey, 1974).
- [3] M. Born, in: *Atomic Physics* (Blackie & Son, London, Glasgow, 1963).
- [4] Fizicheskaya Enziclopediya, in: *Sovetskaya Enziclopediya* (Moscow, 1988) in Russian.
- [5] J.C. Slater, *Phys. Rev.* 36 (1930) 57.
- [6] H. Bethe and E. Soltner, in: *The Quantum Theory of Atoms with One and Two Electrons* (Moscow, Fizmatgiz, 1960) in Russian.
- [7] Fizicheskii Enziclopedicheskii Slovar, in: *Sovetskaya enziclopediya* (Moscow, 1960) in Russian.
- [8] Fizicheskie Velichiny. Spravochnik, Energoatomizdat (Moscow, 1991) in Russian.
- [9] V.S. Letokhov and V.P. Chebotaev, in: *Superhigh Resolution Spectroscopy* (Nauka, Moscow, 1990) in Russian.
- [10] S.A. Ahmanov, V.A. Vislouh and A.S. Chirkin, in: *Optics of Femtosecond Pulses* (Nauka, Moscow, 1988) in Russian.
- [11] V.I. Ritus, *JETP* 41 (1961) 1285, in Russian.
- [12] Z. Chen and Z. Spruch, *AIP Conf. Proc.* 189 (1989) 460.

Section 7

Innovative Approaches

Possibilities for gamma-ray stimulated emission experiments

P. Kamenov and A. Petrakiev

Sofia University, Faculty of Physics, Sofia 11-26, Bulgaria

We show that gamma-ray stimulated emission experiments are comparatively easy and inexpensive. The registration of a double- ($N_{2\gamma}/N_\gamma$) and a triple-energy peak ($N_{3\gamma}/N_\gamma$) is possible and the relation between their intensities permits the calculation of the recoilless factor f_s (stimulated) and making a conclusion about constructing a working gamma-ray laser.

The main point of stimulated emission between two excited nuclear levels (upper m and lower n levels with the $\tau_m \gg 1$ s and, respectively, $\tau_n < 10^{-6}$ s corresponding lifetimes leads to the following major advantages: a) A large population inversion which initially (before amplification) is $N_m/N_n = \tau_m/\tau_n$. This population inversion does not modify in time until the recoilless emission conditions ($f \neq 0$) are obtained; b) A very large cross section for stimulated emission $\sigma_{\gamma\gamma} = (g_n/g_m)(\lambda^2/2\pi)$. In some cases, this cross section is larger than the cross sections for Mössbauer effect, because it is not influenced by the upper level conversion coefficient (α_m) and by the f recoilless factor for a second gamma quantum emitted by stimulation (primary gamma quantum must be emitted recoilless); c) No essential cross-section time dependence exists; the delay time depends only on the line natural width, which is large enough because the lower level life-time is short; d) The Mössbauer effect conditions cannot be influenced during pumping, because pumping can take a very long time. Even if these conditions are violated they can be restored later; e) Some isomers (suitable for stimulated emission, as for instance ^{125m}Te) present a Mössbauer transition which can be used for preliminary experiments, especially for f_M recoilless factor study, for different substances and different preparation technologies.

It is the most surprising that, after the new stimulated emission cross section has been obtained by Kamenov [1,2] and Alpatov [3,4] in experiments which confirm them, this domain is still quiet. The explanation lies probably in the long-time illusion in the Einstein coefficient relations [5]. These experiments are easy because: 1) Suitable isomers which allow verification do exist (^{125m}Te and others which exhibit Mössbauer transitions); 2) The required concentration for recording of transition double and triple energy, can be reached in thermal neutron flux $\Phi > 10^{14} \text{ cm}^{-2}\text{s}^{-1}$ (such reactors exist in many places); 3) Natural elements can be

used (tellurium) for the experimental f_M recoilless factor study; 4) Helium temperatures are accessible; 5) High-energy resolution detectors are accessible; 6) The most expensive is enriched $> 94\%$ ^{124}Te (but only about 30–40 mg, if all preliminary experiments are performed with the necessary accuracy). Then, recording of the double-energy ($N_{2\gamma}/N_\gamma$) [3,4] and triple-energy peak ($N_{3\gamma}/N_\gamma$) is possible (N_γ is the number of gamma-quanta with 109.3 keV energy, $N_{2\gamma}$ is the number of 2×109.3 keV quanta and $N_{3\gamma}$ is the number of 3×109.3 keV quanta for ^{125m}Te). The double- and multiple-energy peaks cannot be observed for visible energy stimulated emission because of the lack of suitable detectors.

The f_M (Mössbauer) and f_s (stimulated) recoilless factors depend on the substances in which nuclei are embedded and on the preparation technology. Therefore, preliminary Mössbauer experiments can show which substance and technology are the most adequate (larger f_M). For ^{125m}Te (35 keV Mössbauer transition) the experiments are possible at room temperature. When better technology and substance are used (larger f_M), stimulated gamma-ray experiments must be performed. In fig. 1, a scheme is shown, describing the two possible stimulated emission ways for double-energy peak recording. The source is supposed to be a needle (length $l \gg$ diameter d).

From the dx region, a primary gamma quantum must always be emitted without recoil ($f_s \neq 0$). Stimulated emission interaction (in the dy region) can occur in two ways: a) without recoil (straight arrow), and b) with recoil (curly arrow). In a) the two gamma-quanta are coherent and in b) they are not coherent but they have the same direction and are simultaneous. In both cases, the detector D records $N_{2\gamma}$ double peak energy with ϵ^2 efficiency. In these cases, the probabilities of $dN_{2\gamma}$ recording (for unit time) are:

$$\begin{aligned} a) dN'_{2\gamma} &= \frac{f_s a_0 \Delta\omega \Delta s dx}{(1 + \alpha_m)} e^{-\mu(l-x)} \sigma_{\gamma\gamma} f_s a_0 \tau_m dy \times e^{-\mu(l-y)} \epsilon^2, \\ b) dN''_{2\gamma} &= \frac{f_s a_0 \Delta\omega \Delta s dx}{(1 + \alpha_m)} e^{-\mu(l-x)} \sigma_{\gamma\gamma} (1 - f_s) a_0 \tau_m dy \times e^{-\mu(l-y)} \epsilon^2. \end{aligned} \quad (1)$$

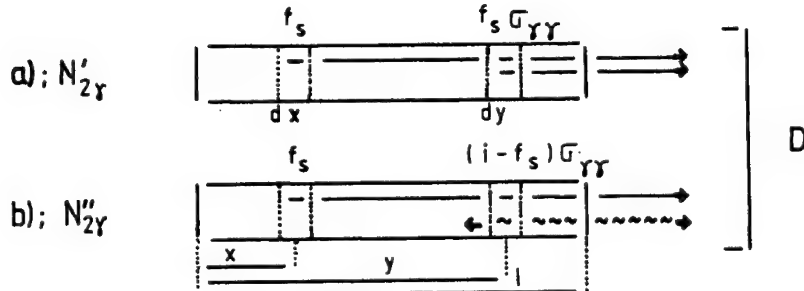


Fig. 1.

Properly made integrations for $N_{2\gamma}$ are obtained:

$$\begin{aligned} \text{a) } N'_{2\gamma} &= \frac{f_s^2 a_0^2 \Delta\omega \Delta s \tau_m \epsilon^2}{(1 + \alpha_m) 2\mu^2} \sigma_{\gamma\gamma} (1 - e^{-\mu l})^2, \\ \text{b) } N''_{2\gamma} &= \frac{f_s a_0^2 \Delta\omega \Delta s (1 - f_s) \tau_m \epsilon^2}{(1 + \alpha_m) 2\mu^2} \sigma_{\gamma\gamma} (1 - e^{-\mu l})^2. \end{aligned}$$

Here a_0 is the activity volume, $\Delta\omega$ is the solid angle, $\Delta s = \pi d^2/4$, μ is the linear absorption coefficient and α_m is the internal conversion coefficient. Summing a) and b) we obtain:

$$N'_{2\gamma} + N''_{2\gamma} = N_{2\gamma} = \frac{f_s a_0^2 \Delta\omega \Delta s \tau_m \epsilon^2}{(1 + \alpha_m) 2\mu^2} \sigma_{\gamma\gamma} (1 - e^{-\mu l})^2. \quad (2)$$

For the single gamma quanta, when $N_\gamma \gg N_{2\gamma}$ we get:

$$N_\gamma = \frac{a_0 \Delta\omega \Delta s \epsilon}{(1 + \alpha_m) \mu} (1 - e^{-\mu l}). \quad (3)$$

Therefore,

$$\frac{N_{2\gamma}}{N_\gamma} = \frac{f_s}{2} a_0 \tau_m \sigma_{\gamma\gamma} \frac{\epsilon}{\mu} (1 - e^{-\mu l}). \quad (4)$$

In fig. 2, the $N_{3\gamma}$ recording probability scheme is shown. There are four possible ways to record $N_{3\gamma}$: a) all gamma quanta are emitted without recoil, b) first and second quanta are recoillessly emitted, c) only the first quantum is recoilless, and d) the first and third quanta are recoilless. When two recoilless quanta travel through the dz third region, they stimulate emission with a $2\sigma_{\gamma\gamma}$ probability. Taking into account these four different probabilities and summing (as in eq. 4), we obtain:

$$\frac{N_{3\gamma}}{N_\gamma} = \frac{(f_s^2 + f_s)}{6} a_0^2 \tau_m^2 \sigma_{\gamma\gamma}^2 \frac{\epsilon^2}{\mu^2} (1 - e^{-\mu l})^2. \quad (5)$$

Comparing eqs. (4) and (5), we can calculate:

$$\frac{N_{3\gamma}}{N_\gamma} = \frac{2(1 + f_s)}{3f_s} \left(\frac{N_{2\gamma}}{N_\gamma} \right)^2. \quad (6)$$

Alpatov et al. [3,4] have experimentally determined the $N_{2\gamma}/N_\gamma \approx 2.7 \times 10^{-3}$ quantity and calculated the experimental cross section for stimulated emission: $\sigma_{\text{exp}} \approx (8.4 \pm 1.7) \times 10^{-19} \text{ cm}^2$ (for $Be^{125m}Te$). The experimental cross-section value compared to the $\sigma_{\gamma\gamma}$ theoretical one is: $\sigma_{\text{exp}} \approx 8.4\sigma_{\gamma\gamma}$, which caused trouble in the [3,4] papers. The authors of refs. [3,4] do not believe that experimental errors are so big and the results could not be explained. True, the error in these experiments is less than 20%. When they calculated σ_{exp} , they did not take into account

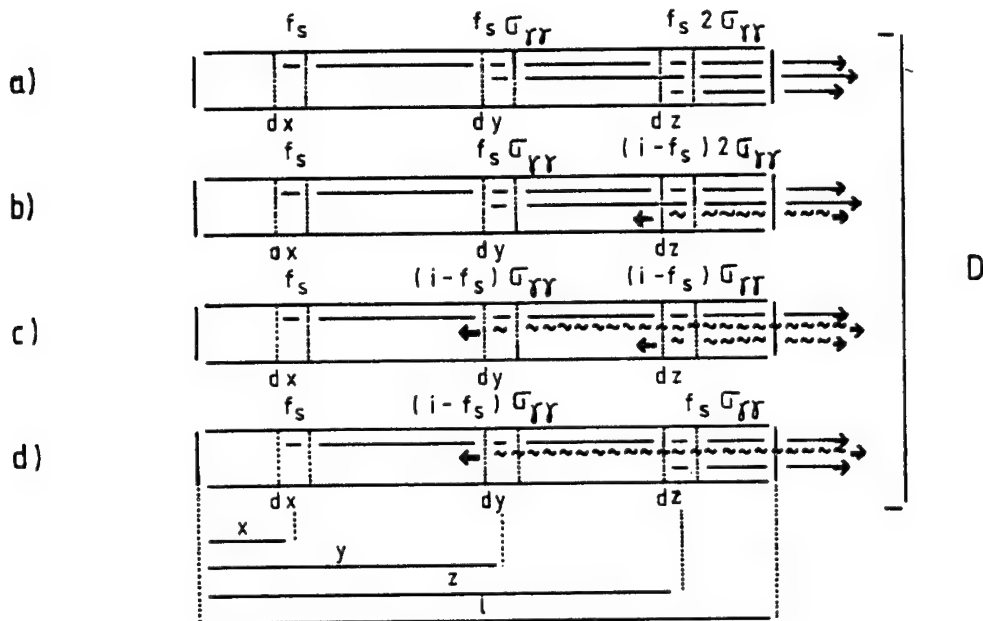


Fig. 2. The four possible ways of $N_{3\gamma}$ simultaneous recording. When two recoilless gamma quanta pass through the dz region the stimulated interaction probability is $2\sigma_{\gamma\gamma}$.

the two modes of stimulated emission (fig. 1) and eq. (4). Indeed $\sigma_{\gamma\gamma} = f_s \sigma_{\text{exp}}$ and the error is less than 20% ($f_s \approx 0.12$).

Conclusions

The relation in eq. (6) enables to calculate the f_s recoilless factor starting from the $(N_{2\gamma}/N_\gamma)$ and $(N_{3\gamma}/N_\gamma)$ experimental values and to draw conclusions about the operating gamma-ray laser possibilities. It is clear from eq. (4) that $N_{2\gamma}/N_\gamma$ is proportional to the concentration of excited nuclei ($k = a_0 \tau_m$) and for equal other conditions, is proportional to the thermal neutron flux (Φ) by which the source is irradiated. We have estimated (from eq. (6)) that, for $\Phi \geq 10^{14} \text{ cm}^{-2}\text{s}^{-1}$, $(N_{3\gamma}/N_\gamma)$ can be experimentally observed (for Russian source see refs. [3,4]). It is high time to perform the stimulated emission experiments. As our friend (Vapirev) said: "They are the only ones who can answer all our questions".

References

- [1] P. Kamenov and T. Bonchev, C.R. Acad. Bulg. Sci. 18 (1965) 1103.

- [2] P. Kamenov, Nuovo Cimento 13D (1991) 1369.
- [3] V. Alpatov et al., Izv. Acad. Nauk. USSR, Fiz. 50 (1986) 2013 (in Russian).
- [4] V. Alpatov et al., *Proc. Conf. on Nucl. Spectroscopy and Structure of Atomic Nucl., Jurmala* (Leningrad, 1987).
- [5] P. Kamenov, A. Petrakiev and A. Apostolov, Int. J. Laser Phys. (special issue) 5(2) (1995) 307.

Section 8

The Gamma-Ray Solid Laser

Gamma-ray solid laser: the heat problem and means of solution

S.V. Karyagin

*Semenov Institute of Chemical Physics, Russian Academy of Sciences,
Kosygin Str. 4, 117334, Moscow, Russia*

The release of heat (10^5 – 10^9 J cm $^{-3}$) during lasing within an Active Medium (AM) is the crucial obstacle to the creation of a Gamma-ray Solid Laser (GSL), especially in the case of short-lived isomers. A concept for the Suppression of the Heat Release and InterRelated Effects (SHRIRE) in an AM is qualitatively considered here. The SHRIRE is based on progress in both pumping of nuclei and knowledge of the migration, transformation and degradation of energy at high-energy release. The SHRIRE was shown to be realizable by using both the AM and a Passive Medium Cooler (PMC) formed together in one single crystal without any physical inner boundaries between them and, hence, without inner temperature discontinuities. This crystal contacts with an outer cooler. The AM dimensions must be less than the mean path length for phonons in the PMC. In this case the “temperature” of the AM can be kept below 10 K during the GSL-lasing.

Introduction

There are two main critical obstacles to creating a Gamma-ray Solid Laser (GSL). First, the important nuclear transitions typically experience relatively large line broadening. Second, there is a high heat release in the range of 10^5 – 10^9 J cm $^{-3}$ during the pumping and the GSL-lasing in the Active Media (AM). The GSL problem can be simply solved in the case of Long-Lived Isomers (LLI), provided the first obstacle is overcome [1,16]. However, in the case of LLI the problem of suppressing line broadening is very difficult and seems to be unresolvable within the near future [1,10,16,18].

For Short-Lived Isomers (SLI), the GSL-problem can be solved on the basis of existing technology [6] if the heat problem can be overcome. Thus, the heating of the AM is the last and the only crucial hindrance in the creation of a GSL that utilizes SLI. Heat release in the AM can lead to the following interrelated effects which disrupt GSL lasing:

- (i) Destruction or microexplosion of the AM material;
- (ii) Suppression of the Mössbauer and the Borrmann effects;

- (iii) Doppler line broadening caused by heat extension of the AM (lengthwise extension or contraction);
- (iv) Depolarization of the nuclei; and
- (v) Thermal acceleration of nuclear spin relaxation.

As a result, these effects give rise to a decrease of the resonance cross section of the working (lasing) transition, increasing the threshold density of Excited Lasing-Active Nuclei (ELAN) [1,4–6,20]. The latter effect amplifies the heat release within the AM and intensifies the destruction of GSL lasing.

In the series of works of refs. [4–6], a concept for the Suppression of the Heat Release and InterRelated Effects (SHRIRE) in the AM which would disrupt GSL lasing was developed. The SHRIRE is based on a series of engineering solutions [4–6,19] described below in sections 1, 3 and 5. The scientific and technological aspects of the SHRIRE are based on a consideration of elementary processes for the migration, transformation and degradation at high-energy primary release in the AM [4–6,13,14]. A broad qualitative sketch which outlines the SHRIRE concept and some its results are presented in the following.

Section 1

Topics

Heat release in the AM for different types of pumping. One-Stage Pumping (OSP). Two-Stage Selective Pumping (TSSP). Two-Phase Selective Pumping (TPSP). Splitting (division) of TPSP into phases of activation and fast creation of inversion (or the phase of “amplification without inversion”). Phase of cooling in TPSP. Fluorescent variant of TSSP. “Non-threshold” pumping. Three-level pumping. Two-step activation. Realistic joint threshold and heat conditions.

The solution of the SHRIRE problem depends crucially on the choice of the GSL pumping scheme. So called “One-Stage Pumping” (OSP) schemes were the most popular in the 1970’s [1,2,10]. In such schemes both the activation of nuclei and the initial gamma lasing processes take place simultaneously and at the same place within an AM. In this case, the heat release in the AM, Q_{AM} is the sum of three components:

- (i) The heat, Q_{act} resulting from direct interaction of the primary activation beams (neutrons, γ -rays, charged particles, etc.) with nuclei and atoms in the AM;
- (ii) Self-heating of the AM, Q_{dec} by internal conversion of Excited Lasing-Active Nuclei (ELAN); and
- (iii) The heat, Q_{las} produced by the effect of GSL lasing.

Thus, $Q_{AM} = Q_{act} + Q_{dec} + Q_{las}$ with the condition $Q_{act} \gg Q_{dec} \gg Q_{las}$ for OSP in the case of weak or moderate lasing power.

In order to significantly decrease the heat, $Q_{AM} \sim Q_{act}$, it is necessary to exclude or soften the direct action of the primary activation beams of neutrons, γ -rays, etc. [1,2]. For this purpose the following schemes of pumping were originally suggested:

- (i) Excited Laser-Active Nuclei (ELAN) are produced in the activation volume, which is located far from the position of the AM. Then ELAN are separated and extracted from the lower-level nuclei by chemical or laser methods. After that the refined ELAN are transferred to the position of the AM [7,8]. Ultimately, both separation methods [7,8] are too slow and thus are not practicable in the case of SLI.
- (ii) The work nuclei originally located at the site of the AM are selectively activated by relatively soft resonance γ radiation. The more selective and soft the radiation is, the narrower the spectral width becomes. For example, soft resonant γ quanta can be emitted by a special intermediate target (converter) placed outside the AM. The converter takes by itself the whole crashing strike of the primary non-resonance activating radiation of neutrons, particles, non-resonance γ -quanta, etc. Such schemes are said to employ "Two-Stage Selective Pumping" (TSSP) [3-5]. In this case, the heat release in the AM, Q_{act} can be one to two orders of magnitude less [3-5] than the heat release from OSP. Hence, with TSSP it is possible to obtain $Q_{act} \sim Q_{dec}$.

A number of other schemes are based on selective pumping [1,10,15,20]. These schemes are distinguished from those of refs. [3,4] only by the method by which the selective radiation is created. Thus, the set of schemes may be said to employ the Two-Stage Selective Pumping method (TSSP).

All the GSL schemes of the 1970's, including those of refs. [3,7,8], have one great overall drawback: Too high a threshold for ELAN densities (10^{22} – 10^{23} cm $^{-3}$), as large as the host atomic densities in solids [1]. At such densities, the self-heating in the AM, $Q_{dec} \sim 10^7$ – 10^9 J/cm 3 , is the insurmountable obstacle for all SHRIRE methods. There are two essential reasons why such enormous ELAN threshold densities arise in the schemes of the 70's:

- (1) The lasing is almost entirely suppressed by the self-absorption; and
- (2) The lasing stage is not partitioned by an apparent temporal boundary from the pumping stage.

It follows from (1) that the great value for the ratio of the threshold of ELAN density to the inverse density, is given by about 100–1000. The consequence of (2) is the large loss (leakage) of inverse population in the pre-generation stage [4]. In addition, because of point (2) the real threshold of ELAN density increases by a factor of 10–1000. Both these factors lead to an enormous increase in the heat release in the AM [4,5].

The next significant step in solving of the SHRIRE problem is the elimination

of both obstacles (1) and (2) by the use of the following three methods, which are called "Two-Phase Selective Pumping" (TPSP) [4–6,19]:

- (a) TPSP based on the action of rf pulses on the nuclear spins [4,5], resulting in the sudden production of an empty lower-lasing level;
- (b) TPSP based on the action of an optical laser on the atoms [4,5], resulting in the sudden appearance of a frequency shift between the resonance emission peak and the resonance self-absorption peak; and
- (c) TPSP based both on fast separation and on rapid transfer of the short-lived ELAN from the site of activation to the position of the AM [5,6]. The rate of action in the methods [5,6] is several orders of magnitude greater than those in early methods [7,8].

Selective Activation (SA) is explicitly used in (a) and (b). However, the process of SA in (c) is substituted by the fast selective laser ionization, which is generally treated as a special form of the basic concept. It is important to note that TPSP schemes (a) and (b) can be realized both in the OSP and in the TSSP modified versions [4,5], as discussed in section 6. In these versions, the activation beams act on the AM during the pumping phase almost in just the same way as do the beams in the ordinary OSP or TSSP methods. However, for OSP and TSSP modified by the TPSP method, the pumping phase is time-isolated from the phase of lasing. Threshold and pumping conditions in such modified versions are much more realizable than that in the primary OSP or TSSP schemes.

Lasing on the basis of both methods (a) and (b) may be defined as "amplification without inversion". This designation for (a) is not entirely correct, because the inversion is absent only before the action of the rf pulse. The rf pulse switches on the population inversion which remains after the pulse passes. However, for (b) this definition is entirely correct, because the inversion is absent before and during the optical action, and, hence, during the gamma lasing. When using the method of (c), an almost complete lack of unexcited working nuclei can be achieved at the initial moment of the lasing phase. Thus, the most effective softening of threshold conditions and the interrelated heat release could be achieved in the method of (c).

In all three methods the lasing phase is time-isolated from the pumping phase by a sharp leap of lasing conditions which is similar to a sharp temporal boundary. Thus, the heat release in the AM is successively decreased in the sequence of One-Stage Pumping (OSP), Two-Stage Selective Pumping (TSSP), and Two-Phase Selective Pumping (TPSP). Three types of pumping occupy an intermediate position between TSSP and TPSP in this sequence: The fluorescent variance of TSSP [3,4]; The optimal variant of Three-Level Pumping (TLP) [1,10,4]; So-called "non-threshold" pumping [10]. For all these methods, the lower lasing level is populated during the pumping which hinders the achievement of inversion threshold [4,10]. The method of TPSP is free from such a drawback. Note that there are still no suita-

ble nuclear candidates for TLP, since the ratio of the lifetimes τ_{1+}/τ_{1-} for the upper and lower lasing levels, respectively, is too far from the optimal value of $\tau_{1+}/\tau_{1-} = 2$ [4].

In case of TPSP in method (c), the heat release is the lowest in the sequence of OSP-TSSP-TPSP. The well-known "two-step" method [15,17,20] is a relatively new one, but with excellent prospects from the perspective of activation. In this method the highly excited LLI (parents) can be quickly transferred into the form of short-lived ELAN. This Two-Step Activation (TSA) can be used in all types of pumping, OSP, TSSP and TPSP. Among numerous types of GSL the case of TPSP (c) shows the smallest heat release in the AM. Thus an estimation of heat release based on TPSP, method (c) will be considered in more detail.

In all three TPSP-methods, the threshold conditions are reached by the sudden increase of the "relative effective inverse population" (REIP) from a zero value at the activation phase to almost 100% at the lasing phase (fig. 1). The REIP is given

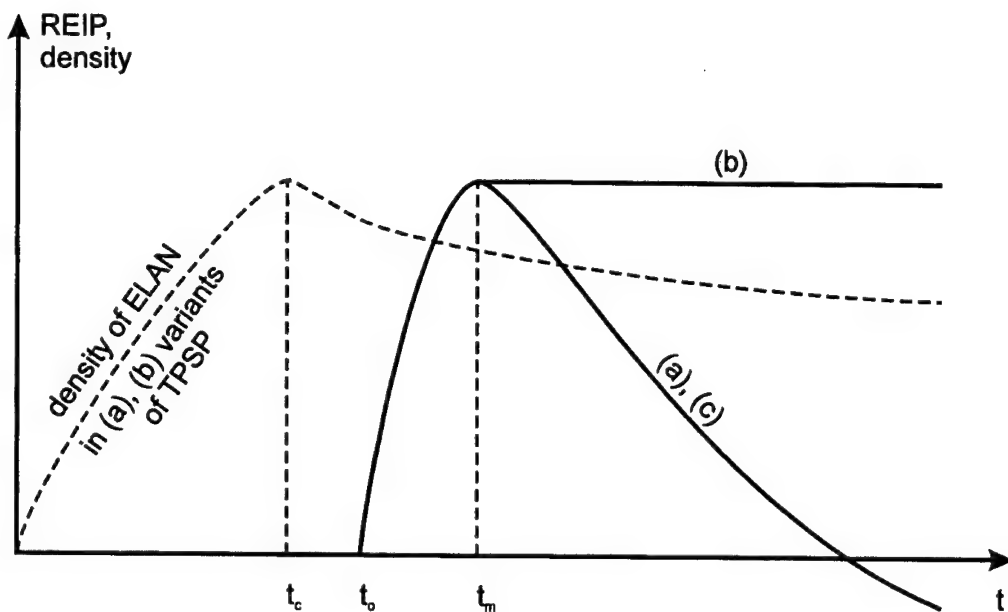


Fig. 1. The sudden increase of the relative effective inverse population (REIP) from zero at the activation phase up to almost 100% at the lasing phase in three methods of two-phase selective pumping (TPSP): (a) TPSP switched on by rf pulse action to the nuclear spins [4,5]; (b) TPSP switched on by selective optical laser action to the atoms [4,5]; (c) TPSP switched on by fast transfer of ELAN into the AM [5,6]. The solid curve represents the REIP developing during TPSP. The REIP development is a special case of (b), since it is a so-called "amplification without inversion". The dashed curve outlines the ELAN density only in cases (a) and (b), since in case (c) the activation phase position is far from the AM. The time intervals of TPSP are: $0-t_c$ is the activation phase in the (a) and (b) cases; t_c-t_0 is the cooling phase in the (a) and (b) cases; t_0-t_m is the switch phase in cases (a), (b) and (c); $t_m-t_c \ll \tau_1$.

by the ratio $(\sigma_{+-}n_+ - \sigma_{-+}n_-)/(\sigma_{+-}n_+ + \sigma_{-+}n_-)$, where n_+ , n_- are the nuclear densities at the top and lower lasing levels, respectively (in other words, n_+ is the ELAN density). The density of work nuclei is $n = n_+ + n_-$ and σ_{+-} , σ_{-+} are the resonant cross sections for the nuclear emission and absorption transitions, respectively. It is important to note that the REIP is a generalization of the usual inversion as commonly used. Indeed, in the case of TPSP (b), the inversion population is zero, but the REIP is about 100%. The heat $Q_{AM} = Q_{act} + Q_{dec}$ at the activation phase. In TPSP methods the activation regime can be chosen so that $Q_{act} < Q_{dec}$. The heat Q_{AM} consists only of Q_{dec} at the initial stage of lasing (fig. 2). Close to the time t_c , the flow of activation needs to be interrupted sharply. After that the AM cools quickly from the T_{act} down to $T_{AM} = T_{dec} < T_{act}$ during the time-interval [5] $\Delta_c = t_0 - t_c \ll \tau_1$. This is very fast as compared to the rate at which the inversion decays. During the time interval Δ_c , the "cooling phase" [4–6], the AM can reach a quite low temperature of $T_{AM} < 10–20$ K, which is necessary for rf or optical laser fields to be effective [4, 5].

The actual threshold conditions [1, 5, 6, 15, 20] are even more strict (even without heating) than the commonly used balance conditions [1, 10, 15, 20]. Thus, estimates of the real threshold ELAN densities and of the related temperatures of an AM are quite high compared to estimates on the basis of the soft balance conditions. Here all estimates of the heat release in an AM are based only on the real threshold condi-

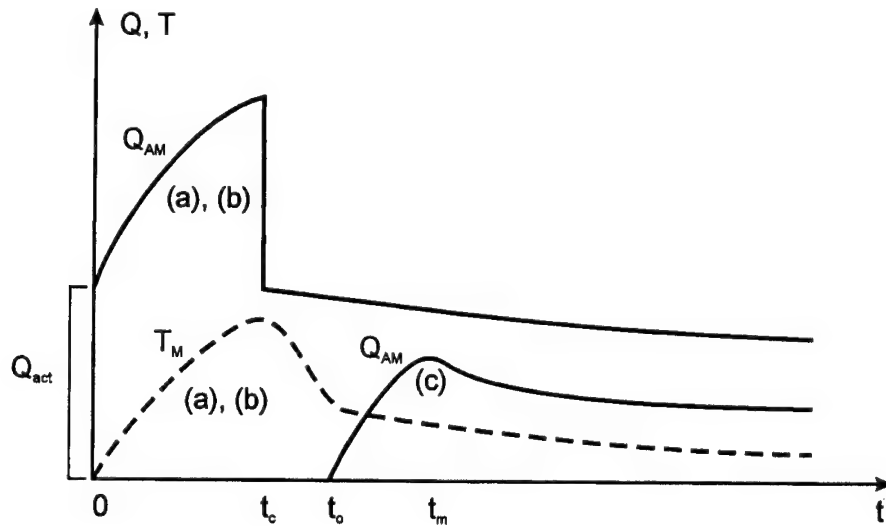


Fig. 2. The time development of the heat release Q_{AM} (solid curve) and the quasi-temperature T_M (dashed curve) of the subsystem of heavy impurity atoms in the AM (Mössbauer quasi-temperature) in the case of TPSP schemes. The heat release in case (c) is less than in the cases (a) and (b). The drops in the (a) and (b) cases are linked with a sudden interruption of the activation phase at the moment t_c . After that time and during the interval $\Delta_c = t_0 - t_c$ ("cooling phase"), the AM is cooling from the "temperature" T_{act} to the Mössbauer "temperature" T_M . A very short time interval $\Delta_c \ll \tau_1$ is quite sufficient [5].

tions which are used throughout this paper. It is assumed that the full linewidth of the SLI transition is reduced to nearly the natural width by an appropriate choice and very careful preparation of both the nuclide candidate and the host-matrix [6]. For a typical example, ^{181}Ta in a beryllium matrix, the heat in the AM is $Q_{\text{dec}} \approx 10^{10} \text{ W/cm}^3$, or $Q_{\text{dec}} \approx 10^5 \text{ J/cm}^3$ for the lasing period $t \sim \tau_1 \sim 10^{-5} \text{ s}$. This creates a temperature of $T_{\text{dec}} \sim 10^5 \text{ K}$ for a realistic threshold dilution of $n_+/n' \sim 10^{-3}$ for ELAN in the light matrix, where $n' = 1.24 \times 10^{23} \text{ cm}^{-3}$ is the density of beryllium atoms. For further decreasing the temperature, the special scheme of GSL-lasing on the basis of the Borrman effect has been suggested [4].

Section 2

Topics

Cooling crisis. Borrman effect. Ineffectiveness of a needle-shaped work-body. Electron–phonon relaxation in a closed system. Needle-shaped AM in liquid helium.

A realistic threshold dilution, $n_+/n' \sim 0.001$ can be enhanced by an additional factor of about 0.01–0.001 in special schemes using the Borrman effect [4]. Thus, a so-called “super dilution” of $n_+/n' \sim 10^{-5}$ can be reached. For such a super dilution a temperature $T_{\text{dec}} < 1000 \text{ K}$ is predicted [4]. However, this is not truly the case, since the Borrman effect in a low-Z host crystal (like Li, Be, B, C, etc.) is strongly damped, if $T_{\text{dec}} > 300 \text{ K}$. Thus, hopes for the saving role of the real Borrman effect may be vain in the case of SLI. Fortunately, prior to 1982 the conditions required for achieving low temperatures both with and without obligatory Borrman enhancement had been analyzed [5].

First, a needle-shaped active body is considered for a GSL. By the mid-1980's the needle (or filament) geometry was overall uniformly adopted. It was also commonly accepted that such a body must be surrounded with a vacuum or placed in contact with liquid helium [1,4,7–10]. However, on the ground of the analysis in ref. [5] it has been proven that the use of such a shape is also ineffective. On the contrary, this construction actually prevents achieving a low temperature in the AM. The major points are:

- (i) Internal conversion electrons can carry off only about $\sim 50\%$ of a transition's decay energy. The rest of this energy is retained in the needle-like shape as the energy of working atoms self-ionized during internal conversion. For example, in the case of ^{181}Ta , more than 30% of the conversion-decay energy remains in the self-ionization of M-shells of Ta atoms [5].
- (ii) It was strictly shown that the threshold energy stored in the electron subsystem of an initially deep-frozen thermally isolated solid is transferred (by self-acceleration) into the phonon subsystem during a time $t \ll \tau_1$ [5]. Therefore, for a thermally isolated AM system using realistic threshold conditions and any

small ELAN life-time τ_1 , there is no hope of obtaining lasing before the lattice overheats [5]. This important result radically contradicts the previously accepted concept [9,10].

- (iii) Suppose the needle-shaped active body is dipped into a liquid-helium bath, as is generally proposed [1,9,10]. In this case the heat transfer from the needle to the liquid helium is impossible if the heat flow exceeds $\sim 0.1 \text{ W/cm}^2$ on the outer surface of the needle. For example, for a commonly accepted needle diameter of $d \sim 10^{-5}\text{--}10^{-4} \text{ cm}$, the heat flow is about $Q_{dec}d \sim 10^5\text{--}10^6 \text{ W/cm}^2 \gg 0.1 \text{ W/cm}^2$ for the threshold conditions. For such a great heat flow, the needle becomes surrounded by a gas bubble and is heated as being a thermally isolated (quasi-closed) body (see point (ii)).

Section 3

Topics

A new type of work body: AM-PMC construction.

A temperature of $T_{dec} < 10\text{--}20 \text{ K}$ is achievable for another GSL work-body construction in which the AM and a Passive Medium Cooler (PMC) form one single crystal [5,6] without any physical inner boundaries, joints, contacts and, hence, without inner temperature discontinuities. The PMC differs from the AM only in its size and the absence of the active lasing nuclei. The heat output of the PMC is in good contact with an exterior cooler such as a liquid helium mixture or a low-temperature massive solid, e.g., a copper pig. Such a work body needs to be moderately prestretched or prestressed by thermostated fixtures along the axis of lasing (see section 5) and precooled below 1–4 K. There are many ways for realizing such an AM-PMC construction as discussed in ref. [5]. The simplest AM-PMC construction has been called the “stripe” configuration for an AM with areal cross section a_1a_2 and length $L \gg a_1, a_2$ (fig. 3). When the Borrman effect is not employed $a_1 = a_2$ [5,6].

Section 4

Topics

Semi-phenomenological estimation of temperature T_{AM} during the GSL lasing phase. Quasi-temperature T_{qu} . Phonon average path. Phonon fission (decay). Phonon wind. Hot spot. Phonon path conditions for the cooling.

The evidence for a low temperature, $T_{AM} \approx T_{dec} < 10 \text{ K}$, during the GSL lasing phase is based on a semi-phenomenological estimate of the so-called “quasi-temperature” in the AM. Two approaches are used to analyze the energy transfer pro-

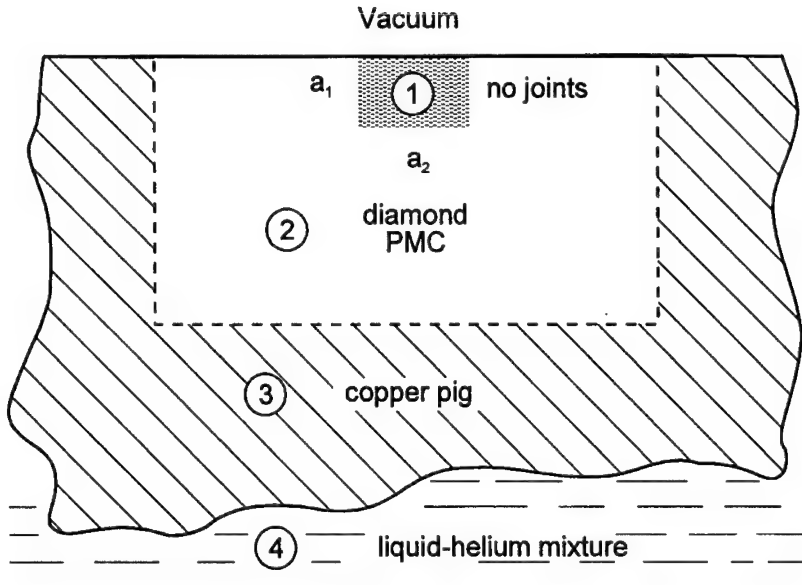


Fig. 3. GSL work-body construction where an AM and a Passive Medium Cooler (PMC) form a single solid construction [5,6] without any inner physical boundaries, joints, contacts and, hence, without inner temperature discontinuities. The PMC differs from the AM only by size and absence of work nuclei. The heat output of the PMC is in the contact with the outer cooler (liquid helium, low-temperature massive solid, e.g., copper pig, etc.). Here: 0 – vacuum; 1 – Active Medium (AM); 2 – PMC; 3 – massive solid; 4 – liquid helium mixture.

cesses: the microkinetics method within the nearest vicinity of the AM and the phenomenological classical heat conductivity equations within the PMC, but far from the AM. The classical heat equations are nonlinear since thermal coefficients are strongly dependent on temperature for $T < 90$ K. The temperature dependence of these coefficients are taken from experimentally measured values. For example, in the case of ^{181}Ta in a diamond matrix a realistic heat regime of the GSL lasing is determined by the following parameters: the threshold ELAN density is $n_+ \approx 5 \times 10^{20} \text{ cm}^{-3}$, $n_- \ll n_+$, the heat released in the AM is $Q_{\text{dec}} \approx E_\gamma n_+ / \tau_1 \approx 5 \times 10^{10} \text{ W/cm}^3$, $a_1 = a_2 \approx 2 \times 10^{-5} \text{ cm}$, and $L = 0.02 \text{ cm}$. The $E_\gamma = 6.3 \text{ keV}$ is the γ quantum energy. The average phonon path is $\Lambda \approx 0.1 \text{ cm}$ in diamond crystals of type II A at 2–90 K. Using the geometry defined in fig. 4, the crystal is taken to have $r_6 = r_c \approx 3 \text{ cm}$ and to be in contact with a liquid helium mixture at $T_0 \approx 1 \text{ K}$. The heat flow through this contact is $J_c = Q_{\text{dec}} a_1^2 L / (2\pi r_c^2) \approx 0.01 \text{ W/cm}^2$, which is an order of magnitude lower than the critical value 0.1 W/cm^2 . Hence, the thermal contact with liquid helium is sufficiently efficient and the heat discontinuity on contact is given by $(\Delta T)_c \approx J_c \kappa / (T_c)^3 \leq 0.4 \text{ K}$. The temperature inside the diamond at the contact with the helium is $T_c \approx 1.4 \text{ K}$.

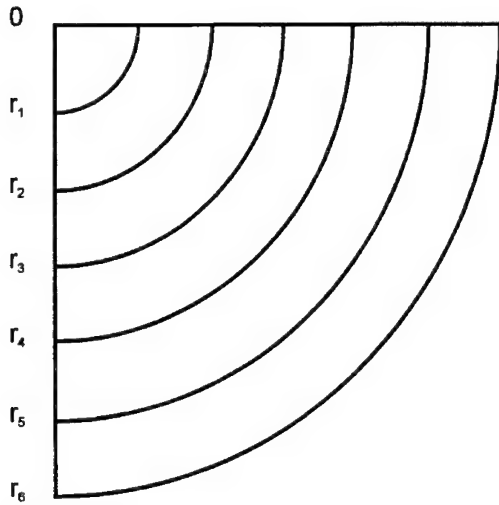


Fig. 4. The zones for energy transfer processes in the AM and the PMC: $0-r_1$ is the zone of primary energy release due to internal conversion; $0-r_2$ is the zone of secondary energy release giving rise to the high-frequency optical or acoustic phonons in electron-hole processes; $r_3 \approx 3\Lambda$ is the approximate boundary beyond which the "phenomenological" equations can be used for a rough estimation of the temperature distribution in the PMC; Λ is the average quasi-ballistic phonon path length (in the quasi-ballistic estimation one considers the phonon to be unscattered after the fission, if the phonon propagation direction is not essentially changed); $0-r_4$ is the zone within which the phonon fission cascade distribution has a frequency peak at about $\omega_D/2$; $0-r_5$ is the zone within which the phonon fission cascade distribution has a frequency peak at about $\omega_M/2$; $r_6 = r_c$ is the outer boundary of the PMC which is in contact with a cooling helium mixture.

In the classical quasilinear heat conductivity equation, in the case of $T < T_D/20 \approx 90$ K, the empirical factors for heat conductivity and heat capacity are $K(T) \approx K_0(T/T_D)^{m_0}$ and $C(T) \approx C_0(T/T_D)^3$, respectively. Such an equation has a simple analytical solution for $r \gg L$:

$$T(r) = T_D \left[(T_c/T_D)^{m_0+1} + \frac{r_c J_c (m_0 + 1)(r_c/r - 1)}{K_0 T_D} \right]^{1/(m_0+1)}. \quad (1)$$

Here $T_D \approx 1860$ K is the Debye temperature for diamond and $m_0 \approx 2.7$, $K_0 \approx 4.1 \times 10^6$ W/cm K, $C_0 \approx 570$ J/(K cm³) and $\kappa \approx 40$ cm² K⁴/W are the empirical parameters. The classical heat equations should be used for $r \gg \Lambda$. The value $r_3 = 3\Lambda$ (fig. 4) is the lower limit for the suitability of the estimation of eq. (1) for the "temperature" distribution in the PMC. In the case of diamond II A, $r_3 = 0.3$ cm and $T(r_3) = 3.0$ K. The AM is surrounded by an electron-hole cloud of an average radius $r_e = r_2 \sim 10^{-4}$ cm (fig. 4) since each internal conversion event creates an avalanche of secondary electrons and holes. The electron-hole energy of each individual avalanche is transferred mainly into the excitation of optical or acoustic phonons of high frequency $\omega \sim 10^{15}$ s⁻¹. This occurs during a very short

time-period of $t \sim 10^{-11}$ s for temperatures of $T \leq 20$ K and $t \sim 10^{-12}-10^{-14}$ s for higher temperatures. The entire electron-hole system (cloud) consists of the manifold of such avalanches and hence this system exists for a time $t \sim \tau_1 \sim 10^{-5}$ s which is longer than that for a single avalanche.

The high-frequency phonons decay with a half-life $\tau_{ph} \approx \tau_0(\omega_0/\omega)^5$ where $\tau_0 \sim 10^{-13}$ s, $\omega_0 \approx 1.5 \times 10^{15}$ s⁻¹. The main channel of phonon fission (decay) is the transfer of one phonon of frequency ω into two phonons with approximately equal frequencies of $\omega/2$. During the time of the GSL lasing, about 10^{-5} s, the phonon system is far from equilibrium. Thus, the temperature at the AM site is not determined in the usual sense. However, in the general case the so-called quasi-temperature T_{qu} can be introduced by means of the formal balance equation [5]

$$\int_0^T C(T') dT' = E_{ph}, \quad (2)$$

where E_{ph} is the energy density in the phonon system. For $T \ll T_D/20$ we have the next estimate both of the quasi-temperature T_{qu} in the non-equilibrium case and of the temperature T_{com} in the usual sense for the equilibrium case:

$$T = T_D(4E_{ph}/(C_0 T_D))^{1/4}. \quad (3)$$

Some readily apparent properties of T_{qu} and T_{com} are as follows [5]:

1. The T_{qu} characterizes the intensity of the atomic vibrations and the phonon energy density. At low T , according to eq. (3), the phonon energy density is proportional to T to the power 4.
2. In the limit of large time the T_{qu} of the closed system becomes equal to the temperature T_{com} in the common sense. That means that T_{com} is the temperature of the closed system after thermal relaxation.
3. For any equilibrium phonon system at $T_{com} = \text{constant}$, the frequency spectrum is constant in time. However, for the non-equilibrium phonon system at $T_{qu} = \text{constant}$ this is not generally true.
4. For real lattices, e.g. diamond, anharmonicity is inherent, which induces phonon fission (decay) and phonon fusion (confluence). So the phonon frequency spectrum may vary until the dynamic equilibrium between phonon fission and the phonon fusion is reached. For a short time period (much shorter than the time of the relaxation to thermal equilibrium) one can neglect phonon fusion. Then the individual phonon cascade arising from the fission of a single initial high-frequency phonon can be considered as a closed subsystem. This means that such subsystems do not interact with each other.
5. As an example, if the initial spectrum of such a subsystem has maximum at $\omega_{max} = \omega_0$, then after a cascade of N phonon fissions the maximum shifts to $\omega_{Nmax} = \omega_0/2^N$ after the time interval $\tau(N) \approx \tau_0 2^{5(N-1)}$.

- 6 The vibrations of the active (Mössbauer) nuclei in the light matrix are effectively characterized by the Debye frequency $\omega_M = \omega_D(M_0/M)^{1/2}$, where M_0 is a mass of the host atom, M is the mass of the heavier Mössbauer impurity, and ω_D is the Debye frequency of the host [12]. For the case of ^{181}Ta in diamond, $\omega_D \approx 2\pi T_D k_B/h \approx 3.0 \times 10^{14} \text{ s}^{-1}$, $\omega_M \approx 7.4 \times 10^{13} \text{ s}^{-1}$, where k_B and h are the Boltzmann and Planck constants, respectively. The Mössbauer factor is sensitive mainly to the frequency region $\omega \leq \omega_M$ with an average $\omega \approx \omega_M/2$. Thus, the Mössbauer factor is influenced by the phonon cascade only after the time-delay period $\tau(N) \approx \tau_0 2^{5(N-1)} \approx 3.0 \times 10^{-7} \text{ s}$, where $N \approx \ln(2\omega_0/\omega_M)/\ln 2 \approx 5.3$. The index M denotes that the value is inherent to the subsystem of heavy impurity (Mössbauer) nuclei.
7. The phonons of the cascade propagate mainly in the direction of the initial phonon. Such cascade phonons are called quasi-ballistic phonons. In the example of figs. 3 and 4, the quasi-ballistic phonons propagate over the hemisphere of radius $r_5 = r(N) \approx V_s \tau(N) \approx 0.45 \text{ cm}$, where $V_s \approx 1.5 \times 10^6 \text{ cm/s}$ is the average velocity of sound in diamond. Thus, the energy density is $E_N \approx Q_{dec} \tau(N) a_1^2 L / (r(N))^3 \pi \approx 2.1 \times 10^{-7} \text{ J/cm}^3$. In this formula the secondary (electron-hole) system is accounted for as a point source, since its maximum size is about $L = 0.02 \text{ cm} \ll r(N)$. Hence, the motion of Mössbauer atoms in the AM is characterized by the quasi-temperature $T_{qu} = T(N) = 1.8 \text{ K}$ (see eq. (3)).

Phonons which are scattered back to the AM from the PMC are not accounted for in this estimation. It is evident that the contribution of these backscattered phonons to the energy density is proportional to the classic temperature $T(r_3)^4$ (eq. (3)). Thus, the full “temperature” at the AM site (for the Mössbauer atoms) during lasing is

$$T_M \approx [(T(r_3))^4 + (T(N))^4]^{1/4} \approx 4.0 \text{ K}. \quad (4)$$

This is a crude estimate because the phonon cascade parameters are strongly dependent on the sample choice. However, the “temperature” of the AM increases only up to $T_M \approx 5.6 \text{ K}$, when the parameter τ_0 decreases to $\tau_0 \approx 10^{-14} \text{ s}$. This can be considered as a guarantee of fulfilling the inequality $T_M \leq 10 \text{ K}$ for any realistic variations of the parameter τ_0 in the case of a diamond (of II A type) PMC.

8. The following two subsystems exist in the AM during the lasing phase: the subsystem of the relatively slow Mössbauer impurities and the subsystem of the light atoms. The dynamics of the host-atom subsystem mainly depends on phonons of high and moderate frequencies $\omega \leq \omega_D$, where $\omega_D \approx 3.0 \times 10^{14} \text{ s}^{-1} \gg \omega_M$. A calculation of the host “temperature,” T_{host} , (analogous to those shown above for T_M) results in $T_{host} \approx 35 \text{ K}$.

The cooling of the AM is enhanced by this so-called “phonon wind” phenomenon [14]: electrons, holes and excitons are removed far from the AM by phonon

streams. So the radius r_2 (fig. 4) can be increased by a factor of about one hundred and the initial high-frequency phonons will be distributed over a larger volume. In this case the AM quasi-temperature may be lowered to $T_M \leq 5$ K.

Thus, the condition

$$a_1 \ll \Lambda, \quad L < \Lambda, \quad (5)$$

is necessary for a deep cooling of the AM. These conditions of eq. (5) are necessary for quasi-ballistic phonon propagation to distances greater than the dimensions of the AM. Changing the conditions of eq. (5) to $a_1 \ll \Lambda$ and $L > \Lambda$ leads to much higher quasi-temperatures $T_M \sim 10\text{--}20$ and $T_{\text{host}} \approx 40\text{--}80$ K. At last, when $a_1 > \Lambda$ and $L \gg \Lambda$, a "hot spot" arises [13]. The hot spot blocks energy flow from the AM and so leads to overheating.

Section 5

Topics

Special questions of the SHRIRE problem. Thermal expansion. Nuclear depolarization. Long-lived isomers. The Fermi amplification. Diamagnetic superdilution. Crystal-chemical narrowing.

There are a few special questions in the SHRIRE problem. The main one is the suppression of Doppler line broadening caused by the thermal changes of the AM dimensions (lengthening or contraction) [10]. Such a problem may be simply solved if the work body is moderately prestretched or prestressed by thermostated fixtures along the axis of lasing [5,6].

The use of a PMC removes the obstacle to lasing connected with the depolarization of the active nuclei [1]. Indeed, at $T < 20$ K the time of nuclear spin-lattice relaxation is $\tau_s \gg \tau_1$ and the fraction of depolarized nuclei is $\sim \tau_1/\tau_s \ll 1$ [4].

The heat problems of a GSL with long-lived isomers are connected with the use of narrowing rf fields [16]. In this case, the problem of suppressing heat release due to the rf field absorption is solved in three ways:

1. Using the contact Fermi interaction for the amplification by more than a thousand-fold of the rf field forces acting on the nuclear moments [16]. This phenomenon we call the "Fermi amplification".
2. Using the Borrman effect for enhancement of a real threshold dilution in a light diamagnetic up to $10^{-5}\text{--}10^{-6}$ ("superdilution" [4]).
3. Using the so-called crystal-chemical narrowing of Mössbauer lines without the action of exterior high-frequency fields: multiparametric effects of the self-compensation of inhomogeneous shifts of the hyperfine interactions, diamagnetic shielding effects, etc. The fundamental possibility of this method was strictly predicted in ref. [16]. Perhaps, this can be partially corroborated by new results on a

self-absorption of Mössbauer gamma-rays in Ag crystals at low temperatures [18].

Section 6

Topics

The practicability of a GSL in case of two-phase selective pumping (TPSP) and the SHRIRE problem.

The solution of the SHRIRE problem facilitates the development of a GSL in a number of ways:

1. The direct experimental demonstration of GSL lasing on the basis of two-phase selective pumping (TPSP) of type (c) as described in section 1. Such experiments are very difficult, but can nevertheless be carried out using existing engineering and technology [6,19].
2. The realization of the two-phase selective pumping on the basis of TPSP (a) and (b) [4,5]. The heat released in the AM is of the same order as in the case (c), since $Q_{act} \sim Q_{dec}$ (section 1). However, for the realization of (a) and (b) cases one needs much longer times than in the case of TPSP (c), because sources of sufficient power for activation in the former cases are unavailable except for such an unacceptable example as a nuclear explosion, which is an undesirable source in the ecological aspect. Moreover, the methods of TPSP (a) and (b) are more complicated than method (c), in both variants OSP and TSSP (section 1).
3. The realization of other schemes listed in section 1 seems to be more problematic than in case of TPSP due to the greater heat releases in the AM.

Conclusion

In conclusion, the concept of the suppression of heat release in an active medium (AM) and the interrelated effects (SHRIRE) important to a gamma-ray laser has been outlined qualitatively. The main feature of this concept is the analysis of engineering proposals in various GSL schemes and the microprocesses of heat release in an AM. The possibility that the temperature of an AM may be kept below 10 K during lasing for the case of short-lived isomers (SLI) is a particular result of this concept in the case of two-phase selective pumping (TPSP) of (c) type. All the remaining aspects of SHRIRE are also applicable in the case of the TPSP method [4–6]. Thus, the last and crucial obstacle to the creation of GSL on the basis of SLI (see introduction) can be overcome and now the GSL problem can be readily solved [6].

Acknowledgement

The author expresses his gratitude to the participants of the theoretical seminar at the Institute of General Physics, Russian Academy of Sciences, headed by A.A. Rukhadze, for valuable discussions of this study and its various aspects from 1991–1992; to G.C. Baldwin and V.I. Gol'danskii for the early discussion of heat problems in messages during 1979–1980; to Vladimir Murzin, Tat'yana Galkina, Andrei Sharkov and Eugenii Fetisov for the discussion of the contemporary state of the heat problem; to L.A. Rivlin, Valeri Zoran, the Organizing Committee of the First International Gamma-Ray Workshop GARALAS'95 and all its participants for the attention to this work; for the preliminary reading of the manuscript by Carl B. Collins and James J. Carroll; to Andrey Marshakov, Yuri Maximov, Victor Shantarovich, Elena Shirany, Artem Sorokin, Ludmila and Sergey Christenco, Nicolay Pimenov, Sergey Vasil'ev and Anna Karyagina for their support and great efforts in preparing this paper.

References

- [1] G.C. Baldwin, J.C. Solem and V.I. Gol'danskii, Rev. Mod. Phys. 53 (1981) 687.
- [2] V.I. Gol'danskii and Yu.M. Kagan, Zh. Eksp. Teor. Fiz. 64 (1973) 90.
- [3] V.I. Gol'danskii, Yu.M. Kagan and V.A. Namiot, Pis'ma Zh. Eksp. Teor. Fiz. 18 (1973) 61.
- [4] S.V. Karyagin, Zh. Eksp. Teor. Fiz. 79 (1980) 730.
- [5] S.V. Karyagin, dep. pap., Vs. Inst. Nauch. Tech. Inf. (VINITI), no. 2797-83 (1983) Dep., 61 pp. (in Russian).
- [6] S.V. Karyagin, Laser Phys. 5(2) (1995) 343.
- [7] L.A. Rivlin, Inventor's Certificate, January 10, 1961.
- [8] V.S. Letokhov, Zh. Eksp. Teor. Fiz. 64 (1973) 1555.
- [9] B.I. Mantsyzov, V.A. Bushuev and R.N. Kuz'min, Zh. Eksp. Teor. Fiz. 80 (1981) 891.
- [10] V.I. Vysotskii and R.N. Kuz'min, in: *Gamma-Ray Lasers* (Mosk. Gos. Univ., Moscow, 1989) (in Russian).
- [11] Electro Optics, Inc. Laser Review, March 1993, vol. 23, no. 105.
- [12] Yu.M. Kagan and Ya.A. Iosilevscii, Zh. Eksp. Teor. Fiz. 44 (1973) 284.
- [13] D.V. Kazakovtcev and I.B. Levinson, Zh. Eksp. Teor. Fiz. 88 (1985) 2228.
- [14] *Electron-Hole Drops in Semiconductors*, eds. K.D. Jeffrys and L.V. Keldysh (Nauka, Moscow, 1988) (in Russian).
- [15] Proc. 1st Int. Laser Science Conf., Dallas, Texas, 1985, Bull. Amer. Phys. Soc. 30 (1985) 1763.
- [16] S.V. Karyagin, invited lect., in: Proc. Int. Conf. on Mössbauer Spectroscopy, Bucharest, eds. D. Barb and D. Jarina, vol. 2 (1977) 1 (in Russian).
- [17] C.B. Collins and J.J. Carroll, Laser Phys. 5(2) (1995) 209.
- [18] S. Rezaie-Serej, G.R. Hoy and R.D. Taylor, Laser Phys. 5(2) (1995) 240.
- [19] S.V. Karyagin, these proceedings (1st Int. Gamma-Ray Laser Worksh., 1995), Hyp. Int. 107 (1997) 465.
- [20] These proceedings (Proc. 1st Int. Gamma-Ray Laser Worksh., GARALAS '95, Predeal, 1995), Hyp. Int. 107 (1997).

Gamma-ray solid laser: realization of pumping

S.V. Karyagin

*Semenov Institute of Chemical Physics, Russian Academy of Sciences, Kosygin str. 4,
117334, Moscow, Russia*

A system of criteria is discussed which is necessary for the realization of a direct gamma-lasing demonstration experiment (DGLDE) as a basis for a specific gamma laser (GL) scheme. The crucial features of the scheme are grounded in experimental techniques and technological advances which have become standard over the past decade. The main characteristics of the DGLDE scheme are estimated for the example of ^{181}Ta nuclei placed on the surface or into the subsurface layers of a diamond host matrix.

1. Introduction

Many schemes have been introduced to pump a gamma-laser (GL) [1–3], but by the end of the 1970s all were faced with a deep crisis. This was due to the following obstacles:

- (i) Complete absence of working, or active, nuclei for the realization of then-existing schemes;
- (ii) Too high threshold intensities for activation beams (neutrons, γ -quanta, charged particles, etc.) required for the realization of then existing schemes, e.g. about $1\text{--}10 \text{ kg/cm}^2$ of neutrons [1].

Attempts to overcome the crisis were made by resorting to so-called “combined” schemes: two-stage selective pumping (TSSP) [17,4–6], two-phase selective pumping (TPSP) [4–6], two-step activation [2,13,18], and many others (GL systematics are outlined in more detail in ref. [15], as well as in section 7 below). For the realization of these schemes a practical question regarding time naturally arises.

It is clear that a direct experimental demonstration of GL generation is very important to accelerate the creation of GLs of all types. The physical foundation for experiments realizable by means of already existing techniques and technologies were given in refs. [5,6]. The experiments are ecologically safe (realizable without using nuclear explosions) and could be performed not only in the nearest future but actually even 10 to 15 years ago. In the following, more general foundations for the choice of schemes of such experiments are presented (as compared to those dis-

cussed in ref. [6]). The main part of these foundations is a system of criteria necessary for the choice of GL schemes appropriate for the realization of a direct gamma-lasing demonstration experiment (DGLDE). For example, the time period necessary for the realization of the DGLDE scheme is one of these crucial criteria.

The source of the many possible variants of the basic DGLDE scheme is the world-wide experience and expertise generated in continuous attempts to study various models for the realization of a GL [1–3, 7, 13]. From this vast storehouse of experience only a few concepts have survived critical analysis from the perspectives (including time) imposed by the necessary criteria. These include: The Mössbauer effect, the Szilard–Chalmers effect, selective multi-photon ionization, two-phase pumping, two-step activation, and a number of well-checked theories and concepts such as the theory of induced emission and the conception of real threshold conditions. It is also important to note the current existence of important research tools such as powerful non-periodic reactors of the Big Kukla type, intense γ -quanta sources of the Aurora type, etc.

The whole multiformity (WMF) of the possible variants of GL creation already suggested is very large [1–3, 7, 13]. However, this WMF becomes essentially infinitely large if an attempt is made to account for every possible hybrid combination from the elements of the WMF. Even worse, the WMF becomes a continuous body when accounting for all useful variations of the characteristic parameters in every variant. In order to simplify the consideration of the WMF of GL it is necessary to introduce:

- (i) The systematics of GL schemes and its elements (section 7);
- (ii) A group (multiformity) consideration of GL schemes and its elements (sections 5 and 6);
- (iii) A system of general and strict criteria for the group search and the group choice of the presently realizable GL experiments (sections 2–4).

2. Basic criteria. Real temperature-threshold conditions “*in situ*” and “*extra situ*”

Only those phenomena, processes, and elements of techniques and technologies, which are well-known (here taken to be proven by experiments, theory and by a time lapse of at least ten years) may be adopted as a basis for a direct gamma-lasing demonstration experiment (DGLDE) [6]. All the rest need be regarded as a reserve in case of unforeseen circumstances. This criterion is particularly important as concerns the choice of threshold conditions. The common (simple) balance threshold conditions (BTC) need to be replaced by real threshold conditions (RTC) [1, 4–8]. A simple BTC has the following form

$$\sigma_{+-}n_+ - \sigma_{-+}n_- \geq \sigma n + \sigma' n', \quad (1)$$

where n_+ and n_- are the work (active) nuclei densities in the upper and lower levels, respectively, and the total population density is $n = n_+ + n_-$. The σ_{+-} and σ_{-+} are the resonant cross sections for the downward and upward nuclear transitions and σ and σ' are the cross sections for nonresonant losses of a narrow pencil beam at the work impurity and host atoms. The n' is the density of the host atoms. In real conditions the parameter "p" for linear amplification at the length of nonresonant losses L_0 should be included

$$p = (\sigma_{+-}n_+ - \sigma_{-+}n_-)/(\sigma n + \sigma' n'), \quad (2)$$

where $L_0 = (\sigma n + \sigma' n')^{-1}$. Then instead of eq. (1) a more realistic and simple form of threshold estimation emerges [4–6]:

$$\sigma_{+-}n_+ - \sigma_{-+}n_- \geq p(\sigma n + \sigma' n'), \quad (3)$$

with $p > 1$ being the critical parameter determined by the nature and kinetics of the gamma-laser process.

In refs. [4,5] $p \geq 3$ was employed since such an estimate of the threshold value of p follows from the approximate theory of nuclear superfluorescence (NSF) [3]. Later on it was determined that there are no existing nuclides for which this estimate can occur in real conditions (cf. ref. [19]). The reason is that due to the natural decay of the upper work level, the inverse population at $p \approx 3$ falls to zero much more quickly than a superfluorescent (SF) flash is achieved. For a SF flash to occur requires much stronger values, $p > 30–100$, which are not really possible.

So realistic NSF conditions are much more difficult to obtain than the threshold conditions for actual induction processes, where $p \gtrsim 10$ [6]. The reason for such a result is the large difference between the time delays (TD) in the processes of NSF and the induced flashes. The TD for NSF is significantly longer than that for induction flash, the latter being called the "lethargy" time [7].

In addition to the condition of eq. (3) for a definite value of p it is necessary to introduce an additional condition on the full length L of the active medium (AM). This condition is related to the number of γ quanta acquired at the γ -laser output. Usually it is necessary to have [6]

$$L \gg pL_0. \quad (4)$$

The cross sectional dimension of an active medium (AM) should be not too small to avoid strong diffraction losses. Hence one obtains the condition

$$a^2 \approx \Lambda L, \quad (5)$$

where Λ is the wavelength and the full length L should be used. Using L_0 instead of L in the general case is incorrect. However, this error is found in almost all papers and monographs [1–3,7,13]. From eq. (5) it is easy to find the volume and total

number N_+ of excited laser-active nuclei (ELAN) [6]. It is clear that the values of n_+ , N_+ , a and L would increase with decreasing σ_{+-} and L_0 . However, without special care for limiting the temperature growth [5,15] the threshold conditions cannot be satisfied. The threshold conditions accounting for the inversion decay, "lethargy", γ diffraction and temperature growth are referred to as the real threshold conditions [1,5–8,15]. The real threshold conditions are much more restrictive than the BTC and they can be fulfilled only for a more seriously reduced set of nuclear candidates. A similar point of view on the gamma-laser problem is being considered by Baldwin and Solem [1,2,7,8] and Balco, Kay, Silk and Sparrow [19].

The progress in the development of gamma-laser (GL) ideas is reflected in the form of the threshold condition (3). The form

$$\sigma_{+-}n_+ - \sigma_{-+}n_- \geq p\sigma n \quad (3a)$$

is based on early ideas that assumed that the heating of a needle-shaped AM is negligible even for 100% concentration of work nuclei. However, in reality this is not so (see refs. [5,15]).

The form

$$k_0(\sigma_{+-}n_+ - \sigma_{-+}n_-) \geq p(k\sigma n + k'\sigma'n') \quad (3b)$$

is based on ideas using the Borrman effect [1–4], e.g., the idea of "superdilution" (SD) of work nuclei in a light host matrix [4]. Here k_0, k, k' are the so-called coupling coefficients. In the case of SD, $k_0 \approx 1, k \approx 1, k' \ll 1$, and $n/n' \lesssim 10^{-5}$. In the absence of the Borrman effect (and hence in the absence of SD) $k_0 \approx k \approx k' \approx 1$ and $n/n' \gtrsim 10^{-3}$ (cf. refs. [4,5,15]). In ref. [4] the scheme of so-called "superdilution", was considered but without taking into account changes in the Borrman effect due to temperature growth. In this scheme (without the special means suggested in ref. [5]) the temperature exceeds 300 K and thus this approach is invalid as was pointed out in ref. [5,15].

Fortunately, the modification of superdilution schemes [4] on the basis of the ideas of refs. [5,15] leads to the necessary low AM temperatures of $T < 300$ K, which are necessary for the Borrman effect to be effective. Note that the realization of a DGLDE program would assist concepts relying on the Borrman effect.

The form

$$\sigma_{+-}n_+ \geq p(\sigma n + \sigma'n') \quad (3c)$$

is based on ideas of "amplification without inversion" (AWI) [2–5,7,8,13,15] with $\sigma_{-+}n_- \ll \sigma_{+-}n_+$ (in refs. [4,5] rf or laser pulses are used, see ref. [15]). Note that realization of a DGLDE program can assist AWI programs for GL creation.

The form

$$\sigma_{+-}n_+ \geq p(\sigma n_+ + \sigma'n') \quad (3d)$$

is based on ideas for creation of an AM having at the initial moment all, or almost all, work nuclei in the upper working level [1–6]. The condition of eq. (3d) is easier to fulfill than that of eq. (3c), since $n_+ < n = n_+ + n_-$.

It should be stressed that the practical realization of any condition consists of two related considerations: Internal (*in situ*), i.e., inside the AM and *extra situ*, i.e., outside the AM [1–6]. The realization of the *in situ* part requires reaching lasing and cooling conditions directly inside an AM. The *extra situ* realization requires organization of the external (with respect to AM) conditions of the experiment, in particular related to necessary activation sources (neutrons, γ quanta, charged particles), intermediate targets/converters, enrichment of nuclear beams by excited nuclei, etc. The transition to the more realizable *in situ* forms of eqs. (3c) and (3d) can be achieved by transferring difficulties from *in situ* to *extra situ* problems, i.e. by making more complicated the “*extra*” part of the experiment. In selecting the GL realization programs it is necessary to consider equally the feasibility of both sides of the experiments: *in situ* and *extra situ*. In this sense at the present moment programs oriented to the realization of the conditions of eq. (3d), such as the DGLDE program [6], are in the best situation (sections 7 and 8). Note that the terms *in situ* and *extra situ* in connection with the gamma-laser problem were introduced in 1979–80 by G.C. Baldwin in communications on the GL problem to V.I. Gol'danskii and the author.

3. The primary criterion: a system of real experimental conditions based on a concrete real unique through-out nuclide candidate (CRUTONC)

In early publications the concentration was on so-called “synthetic” or “hypothetical” candidates. For example, such “synthetic” candidates can have simultaneously very large $\sigma_+ \approx 10^6$ b as for ^{181}Ta , very large cross section for the radiative capture of neutrons by parent nuclei, $\sigma_{n\gamma} \approx 10^6$ b as for ^{135}Xe , very small σ as for the sodium, etc. Such hypothetical candidates are very useful for the first-step checks of any new GL model. However, they are unsatisfactory as a basis of a program pretending to be a practical experimental realization of an idea. There were many ideas in the 1970s based on such “synthetic/hypothetical” candidates. As a result by that decade a crisis in the problem of GL creation arose since it appeared that there were no real candidates that satisfied all real conditions for an experiment simultaneously and which corresponded to any of the models of GL existing at that moment [1, 7].

A similar crisis can arise in attempts in the programs of GL realization proposed in refs. [1–3, 7, 13] whose authors restrict themselves by satisfying the simplified “*in situ*” conditions irrelevant to the conditions of a real experiment, or who take conditions into account which do not correctly pay attention to the heat problem or to *extra situ* restrictions. Any real experiment would only be successful provided that

all real conditions, *in situ* and *extra situ*, are observed without exception for a concrete, unique ("through-out" for all conditions) candidate.

Thus, for the sake of the actual realization (not only in a paper) of a gamma-laser program the primary criterion must be to emphasize *a whole system of real experimental conditions with a concrete real unique, through-out, nuclide candidate (CRUTONC)*.

In ref. [6] only one CRUTONC, ^{181}Ta , was considered. The ^{181}Ta is a real candidate, which has been thoroughly studied experimentally regarding its nuclear, Mössbauer, optical and other physical and chemical properties in solid form. Because of its degree of characterization, ^{181}Ta is chosen as the first example candidate for the DGLDE in spite of the existence of a number of other suitable candidates. In ref. [5] about ten CRUTONCs were considered at first. A more full and careful consideration of a number of other CRUTONCs is now in progress.

4. The time factor. Consideration of possibilities based only on already-existing techniques and technologies in DGLDE-program realization

To avoid obsolescence any program should be periodically reconsidered to incorporate new and progressive elements and ideas. From the 30-year experience of developing the GL problem [1–3, 7, 13, 15, 18] it is natural to expect that during its evolution any concrete program might acquire serious changes over a period of 5–10 years. Thus, it is reasonable to move up a program into experimental form only in the case that the program is worked out on the basis of already existing techniques and technologies without appealing to speculated technical progress in the far future.

5. Main DGLDE-scheme features

The main general features of the basic scheme for the DGLDE are listed below. They were based on experience all over the world in the GL problem selected by the use of the system of criteria outlined above. In this list one can also see the general process employed to reach this selection. Indeed, each following point in the list presents a more concrete realization of all previous points. The selection path, corresponding to the list, is only one branch of the path tree for GL creation. However, this path is the special path of selection:

- (i) This path is selected in the course of consideration of all principal alternative variants (possibilities) at every step of the selection process, in the course of choosing the promising variants and in the course of rejecting all those leading into blind ends;
- (ii) Each such step is indeed a group step, which includes a group of promising con-

cepts with only non-principal (auxiliary) differences between them. Thus, each group step is like a section of the main path-branch with some of its offshoots (little branches).

Because of (i) and (ii) our special path for selection of the basic DGLDE scheme is the unique path-branch with the most promising characteristics and simultaneously this path (as a group or bunch of similar paths) has many so-called non-principal or auxiliary variants. One needs to keep in mind that each group step in the listed path from each upper (previous) point to the lower (next) point is bound to reject a large amount of "unlucky" variants. So, the paths leading to the OSP, TSSP, TPSP-a and TPSP-b types of pumping (see section 7 and ref. [15]) and to many other very interesting and useful gamma-laser schemes were now rejected. In particular, the rejected TPSP-b type, suggested by the author in ref. [4], is the very promising scheme of amplification without inversion (see section 7). Note, that many of the now-rejected GL schemes or their elements could be realized on the basis of more progressive future developments, but not current techniques. Thus, each main general feature of the basic DGLDE scheme covers a unique group of promising experimental methods with this common feature, called here as non-principal or auxiliary variants.

The system of these main common features follows:

1. *The use of a low power of lasing*, although the power must nevertheless be sufficient for definitive detection of the γ -laser pulse in a background of spontaneous γ emission. In this case all conditions of DGLDE creation can be mostly softened.
2. *The use of single-passage lasing only in one diffraction mode* for the economy of excited work nuclei, for efficient cooling, for softening of other real conditions and because there are no sufficiently good mirrors.
3. *The use of a solid Mössbauer active medium*. For over 30 years there has been experimental observation of induced γ -absorption in a solid, now called the Mössbauer effect, which should lead to induced emission in accordance with the Einstein principles. The use of other media (plasma, gaseous, liquid, non-Mössbauer solids, etc.) is presently in the early stages of discussion. Only two essential problems prevent the use of Mössbauer media in a GL: The line broadening and self-heating of the active medium (AM) by α , β and γ radiation from the ELAN. Fortunately, both these problems have real possibilities to be experimentally solved in the case of short-lived isomers [6,15].
4. *The use of schemes for the fast transfer of ELAN from the zone of primary activation to the site of the AM during the time $t \ll \tau_1$ for the creation of inverse population in the site of AM*. Here τ_1 is the lifetime of the ELAN. The alternative variants with the activation of work nuclei in the site of AM are significantly more difficult both *in situ* and *extra situ* (see section 2).

5. *The use of short-lived isomers for the creation of inverse population in the site of AM.* Presently it is possible to use lifetimes of $\tau_1 \sim 10^{-4}-10^{-6}$ s [6]. In the case of progress in the technique of line-narrowing methods it is possible to extend the lifetime range of possible candidates to $\tau_1 > 10^{-4}$ s. In case of progress in activation techniques (sources, converters, moderators etc.), in methods of nuclei transfer and in cooling of active media this range may be extended to shorter life-times $\tau_1 < 10^{-6}$ s.
6. *The use of the Szilard–Chalmers effect (SCE) in obtaining the ELAN in the activation zone.* Research shows that the largest primary relative concentration (PRC) of the ELAN $\sim 0.1\text{--}1\%$ can be rapidly achieved only when using SCE [6]. The other primary activation methods without the SCE provide less PRC of the ELAN and are not so simple [1,3]. The word “primary” here means that we have in mind a second stage for the amplification of primary concentration up to more than 90%.
7. *The use of selective multiphoton ionization (SMI)* [9–11] as the basis for increasing the primary concentration of short-lived work isomers up to more than 90% (see refs. [5,6,14,15]). The other methods (including mass spectral ones, etc.) are not so fast and at the same time are not so selective as SMI.

So, one comes to the conclusion that for the realization of the DGLDE there are no other essentially different groups of competing methods, except the groups outlined by the points 1–7, meeting all common principles outlined in sections 2–4. Hence, the choice of the DGLDE scheme in general features must have also a unique (in a group sense) version of so-called group type, i.e. with the uncertainty of including the group of promising non-principal or auxiliary variants. This group-type version is characterized as a low-power variant of two-phase selective pumping [5,6,15], of (TPSP)-c subtype, the most suitable for DGLDE realization (see section 7).

6. General outline of DGLDE scheme

The general outline of the DGLDE-scheme action could be chosen with the group uncertainty pointed above in section 5. At the first stage, the activating flow (of neutrons, γ quanta, charged particles, etc.) interacts with an intermediate target/converter and knocks off a cloud of recoil atoms enriched with excited nuclei from the near-surface layers of the target (the Szilard–Chalmers effect, SCE). An essential part of this cloud, $\eta \approx 0.1\text{--}10\%$, consists of ELANs. In order to enhance the output of excited nuclei, the converter surface is suggested to be highly developed with an oriented micro-structure. In the following, such a target will be called a converter with an oriented, developed surface (CODS).

At the next stages, atoms with the excited laser-active nuclei (ELAN) are selec-

tively ionized, accelerated by an electric field, and then focused onto a narrow stripe into the active body of the gamma-ray solid laser (GSL). Altogether, these stages constitute an enrichment and focusing system (EFS). In order to amplify the EFS effect the micro-relief of the CODS needs to be oriented with high precision. The overall duration of these two stages of EFS is much less than the ELAN lifetime. So a nearly 100% population inversion can be attained in the AM, and the final stage (consisting of lasing) commences.

The outlined basic pumping scheme for DGLDE [6] coincides with the TPSP-c type of pumping (see Section 6), which is the best possible pumping type. Note, that the use of the SCE was proposed by Gol'danskii and Kagan [12], and the selective laser separation of isomers with intermediate lifetimes $\tau_1 \geq 0.1$ s was suggested by Letokhov [9]. However, these studies did not provide an integrated approach to the use of both methods together. In refs. [5,6] it has been shown that these methods reinforce each other and the selective separation of short-lived isomers with $\tau_1 \approx 10^{-5}$ s appears to be realizable. Such "combined" pumping for the DGLDE can be represented as the following chain: Source of high-power primary activation (neutrons, γ quanta, charged particles, etc.) – CODS – EFS – AM.

A characteristic feature of such "combined" pumping is its variability, which provides a wide choice of auxiliary ways to implement each of its stages: parent nuclei can be activated not only [5,6] by neutrons; short-lived isomers can be separated by a number of laser methods [5,6,10]; the AM can be prepared by a number of different methods [6]. The assortment of appropriate primary candidate nuclei and matrix is also quite rich [4,5]. More careful selection of all elements for DGLDE is in progress. The example of such a selection work is represented in [14] (one of the variants of EFS). Despite this versatility, these "combined" schemes are not moved out of the framework of the TPSP-c type pumping and the general features outlined in section 5 remain. Thus the variations mentioned in this paragraph may be termed auxiliary and non-principal. Thus, in this sense the outlined basic group of the DGLDE schemes is the unique group of different variants united by the general principles of section 5 and by the more concrete features listed in this section. In consideration of these features (common for the outlined basic DGLDE group) the differences between the variants inside this group are non-principal or auxiliary variations.

7. Systematics of GSL pumping

In a series of works [4–6,14,15] the following systematic progression of GSL-pumping schemes was used: one-stage pumping (OSP), two-stage selective pumping (TSSP) and two-phase selective pumping (TPSP). The most perfect type of pumping is TPSP divided into three subtypes: TPSP-a, TPSP-b and TPSP-c. In all three subtypes the inverse population is absent before the switching moment t_0 . The difference between a, b, c is [15]:

- (i) In cases a and b before the moment t_0 the storage of the ELAN is carrying out but inverse population is absent;
- (ii) In case a at moment t_0 the switching rf π pulse creates a population inversion in the nuclear hyperfine structure [4,5];
- (iii) In case b after the moment t_0 the optical selective radiation creates a frequency shift between peak of the Mössbauer emission and the peak of the Mössbauer absorption. However, in this case the inversion population is absent both before and after the moment t_0 . Hence, TPSP-b gives now so-called “amplification without inversion” (AWI). Note that TPSP-b had been suggested in 1980 [4], i.e. long before the appearance of the term AWI in gamma-laser discussions;
- (iv) In case c before the moment t_0 the ELAN are absent, but after the moment t_0 the ELAN are fast introduced into an AM (softly settled on its surface or implanted into its subsurface layers).

The case TPSP-c is the most suitable for the DGLDE-program realization. In accordance with sections 5, 6 and 8 some promising non-principal (auxiliary) variations of the basic “combined” DGLDE-scheme, which do not move the DGLDE program beyond the framework of the TPSP-c pumping type can be regarded. Such variations, as changing of the type of primary radiation from neutrons to γ quanta or changing the working nuclei, called here as “non-principal” or auxiliary, maintain the possibility of DGLDE-program realization on the basis of techniques and technologies existing for more than 10 years.

Thus, the basic “combined” DGLDE-scheme is a unique one with the uncertainty of the choice of the auxiliary or non-principal (in sense outlined above) variations. It should be added that hybrid TPSP-schemes with combined properties of a, b and c types are possible in principle. Hybrid TPSP schemes can have higher qualities than each of the simple types a, b or c used alone. However, hybrid realization is more difficult and, hence, is more removed in time. In ref. [4–6,15] other “extra framework” types of effective pumping similar to TPSP type were mutually compared: three-level pumping, “non-threshold pumping” [3], and fluorescent-type two-stage selective pumping (TSSP) [17,4]. They could be modified in more effective schemes by combining with the TPSP subtypes [6]. But in their initial form they take an intermediate position in the row of effectiveness between the TSSP and TPSP types [6]: one-stage pumping (OSP) – two-stage selective pumping (TSSP) – “extra framework” types – two- phase selective pumping (TPSP). Note that the well-known “two- step” method [1–3,13,18] is a relatively new one. This method is very promising for the primary activation. In this method highly-excited long-lived isomeric nuclei can be rapidly transferred into the form of short-lived ELAN. Such two-step activation (TSA) can be used in all above-mentioned types of pumping. Thus, after surveying all possible types of pumping it can be concluded that TPSP-c is the most suitable type of GL schemes for the DGLDE realization today.

8. Main characteristics for the basic DGLDE scheme: example of ^{181}Ta

The main DGLDE parameters for the example of ^{181}Ta as one of the possible variants of the lasing regime are taken from calculations grounded in the theory of basic processes [6]. A more detailed discussion of DGLDE schemes can be found in ref. [6]. The general characteristics include:

- (i) The main variant of a primary activation radiation source (PARS) is a non-periodic Pulse Research Reactor of the Big Kukla type: flux $F \approx 10^{15} \text{ cm}^{-2}$ during 10^{-5} s over an output area $\sim 10^3 \text{ cm}^2$. This has been realized 10–15 years ago [15].
- (ii) The auxiliary variants of the PARS are:
 - (a) A γ -quanta source of the Aurora type for the direct (or indirect) photo-excitation or photo-burning of ELAN [5,6].
 - (b) A nuclear storage ring for the creation of ELAN in the passing of a bunch of high energy parent nuclei through the CODS [6]. These variants yield emphasis to the main one, since the necessary techniques are not presently standardized.
 - (c) Neutrons or γ radiation from a nuclear explosion are most suitable in technical aspects, but this variant must be rejected as being non-ecological.
- (iii) The coefficient of the CODS surface development: $\eta = (\text{developed surface}) / (\text{visible surface}) = 1000$.
- (iv) The CRUTONC (concrete real unique, through-out, nuclide candidate): ^{181}Ta is the most studied candidates among other CRUTONCs [5,6]. This CRUTONC has the largest values for optical isomeric shifts, which is very suitable for application of EFS [6]. The full width of the working transition of this CRUTONC is taken to be approximately equal to the natural width in the case of sufficiently careful experiments (section 1 in ref. [6]). The other parameters of AM ^{181}Ta in diamond are found in ref. [6].
- (v) Active medium of special comb-like microprofile, periodic along the axis of GSL lasing [5,6]:
 - (a) ^{181}Ta on the surface of diamond;
 - (b) ^{181}Ta in the subsurface layers of diamond.
 - (c) The thickness of comb teeth is $a_0 \approx 10^{-6} \text{ cm}$.
- (vi) Work nuclei (ELAN) density averaged over the teeth volume: $n \approx 7.0 \times 10^{20} \text{ cm}^{-3}$.
- (vii) Effective dilution of work nuclei in diamond host: $n/n' \approx 0.001$. Nuclei of ^{181}Ta must be polarized, with the work transition being from the excited level $m_e = \frac{9}{2}$ to the ground level, $m_g = \frac{7}{2}$. The Ta ions are decelerated down to about 100–1000 eV just before their implantation into the uppermost

layers of the AM [6,14]. Note, that such a low energy of insertion into the upper surface layers is less than that typical for implantation, about 10^5 – 10^7 eV.

- (viii) The optimal value of parameter p (see eq. (3)): $p = 14.2$.
- (ix) Cooling of the AM during GSL lasing: Below 10 K [5,6,15].
- (x) Parameters of enrichment and focusing system (EFS):
 - (a) Enrichment degree more than 90%, coefficient of ELAN transport from converter n-ELAN to AM is ~ 1 –10% (can be improved).
 - (b) Full length of EFS: smaller than 100 cm.
 - (c) Maximum voltage: less than 10^6 V.
 - (d) Energy of ions at EFS output controlled from ~ 100 eV and higher. Ions are accelerated during the first part of the trajectory up to ~ 1 MeV and then are moderated down to the desired energy. Special ion optics allow to compress ion flow by 10^4 – 10^6 times [14].

The relevant parameters of DGLDE at the condition that the number of γ quanta in the GSL-lasing pulse is two times greater than the number of the spontaneous γ quanta in the solid angle of the diffraction mode are:

- (i) The number of γ quanta in the GSL-lasing pulse: 72.
- (ii) The number of spontaneous γ quanta in the solid angle of the diffraction mode: 36.
- (iii) Length of AM: $L = 0.03$ cm.
- (iv) Cross-sectional dimension of the AM is the height of the comb: $a_1 = 2.4 \times 10^{-5}$ cm.
- (v) Full minimal threshold number of work nuclei in the upper state: $N_{+,min} = 1.3 \times 10^{10}$.
- (vi) Variant (I): Nuclear excitation by inelastic collisions:
 - (a) Visible surface of converter of n– γ type for the creation of the minimal threshold amount of ELAN in the upper level by inelastic collisions of fast neutrons with ^{181}Ta : $S_{\min\text{inel}} = 0.6 \text{ cm}^2$.
 - (b) Full visible surface of converter n-ELAN, which can be really achieved: $S_{\text{full vis}} = 10^3 \text{ cm}^2$.
 - (c) The overall margin of reliability of DGLDE for the whole chain of its elements is: $\text{MR}_{\text{full}} = S_{\text{full vis}}/S_{\min\text{inel}} \approx 1.6 \times 10^3$.
- (vii) Variant (II): ELAN burned by neutron capture:
 - (a) Visible surface of converter of n– γ type for the creation of the minimal threshold amount of the ELAN in the upper level burned by neutron cap-

- ture due to real neutron losses for fast-neutron moderation: $S_{\min \text{cap}} = 1.2 \text{ cm}^2$.
- (b) Full visible surface of converter n-ELAN, which can be really achieved: $S_{\text{full vis}} = 10^3 \text{ cm}^2$.
 - (c) The overall margin of reliability of DGLDE for whole chain of its elements: $\text{MR}_{\text{full}} = S_{\text{full vis}}/S_{\min \text{cap}} \approx 8 \times 10^2$.

The relevant parameters of DGLDE at the condition that the number of γ quanta in the GSL-lasing pulse is ten times greater than the number of spontaneous γ quanta in the solid angle of the diffraction mode are:

- (i) The number of γ quanta in the GSL-lasing pulse: 643.
- (ii) The number of spontaneous γ quanta in the solid angle of the diffraction mode: 64.3.
- (iii) Length of the AM: $L = 0.054 \text{ cm}$.
- (iv) Cross-sectional dimension of the AM is the height of the comb: $a_1 = 5.1 \times 10^{-5} \text{ cm}$.
- (v) Full minimal up-threshold number of work nuclei: $N_{+, \min} = 4.1 \times 10^{10}$.
- (vi) Variant (I): Nuclear excitation by inelastic collisions:
 - (a) Visible surface of converter of n- γ type for the creation of the minimal threshold amount of ELAN in the upper level by inelastic collisions of fast neutrons with ^{181}Ta : $S_{\min \text{inel}} = 2.0 \text{ cm}^2$.
 - (b) Full visible surface of converter n-ELAN, which can be really achieved: $S_{\text{full vis}} = 10^3 \text{ cm}^2$.
 - (c) The overall margin of reliability of DGLDE for whole chain of its elements is: $\text{MR}_{\text{full}} = S_{\text{full vis}}/S_{\min \text{inel}} \approx 5.0 \times 10^2$.
- (vii) Variant (II): ELAN burned by neutron capture:
 - (a) Visible surface of converter of n- γ type required for the creation of the minimal threshold amount of ELAN in the upper level burned by neutron capture due to real neutron losses in fast-neutron moderation: $S_{\min \text{cap}} = 3.7 \text{ cm}^2$.
 - (b) Full visible surface of converter n-ELAN, which can be really achieved: $S_{\text{full vis}} = 10^3 \text{ cm}^2$.
 - (c) The overall margin of reliability of DGLDE for whole chain of its elements is: $\text{MR}_{\text{full}} = S_{\text{full vis}}/S_{\min \text{cap}} \approx 2.7 \times 10^2$.

9. Summary

A general system of criteria for the search and choice of a basic scheme and its elements for the realization of a direct demonstration gamma-ray lasing experiment

(DGLDE) is proposed. In particular, the following main concepts were included as the elements of such a criteria system:

- (i) A real threshold conditions system (section 2);
- (ii) The *in situ* and *extra situ* parts of the overall conditions for the real GL experiment (section 2);
- (iii) A concrete, real unique through-out nuclide candidate (CRUTONC) for the whole system of real experimental conditions (section 3);
- (iv) The factor of time leading to the requirement that only the possibilities of already-existing techniques and technologies be considered in the realization of the DGLDE program (section 4);
- (v) The path tree of the gamma-laser realization problem (section 5);
- (vi) The group of basic DGLDE schemes (sections 5, 6 and 7);
- (vii) The margins of reliability of DGLDE and of its elements (for example, section 8).

On the basis of such a criteria system, the main features of the basic DGLDE scheme are introduced (section 5) and the main features of the DGLDE-scheme process are considered (section 6). In its main features the outlined DGLDE scheme is unique, except for some non-principal or auxiliary variations (sections 5–8). In the pumping classification of section 7, the basic DGLDE scheme is two-phase pumping of subtype (c), the most suitable for the DGLDE.

Such a DGLDE scheme fits all main and a number of additional criteria which enhance its experimental suitability:

- (i) All processes on which DGLDE is based are well known and rather easily realized.
- (ii) All elements of the DGLDE chain can be realized on the basis of already existing techniques and technologies.
- (iii) The DGLDE may be realized without a nuclear explosion.
- (iv) The main variant of a primary activation radiation source (PARS) for the DGLDE is a non-periodic Pulse Research Reactor of the Big Kukla type. The auxiliary variants of the PARS are:
 - (a) A γ -quanta source of Aurora type for the direct (or indirect) photo-excitation or photo-burning of ELAN [5,6].
 - (b) A nuclear storage ring for the creation of ELAN in the passing of a bunch of high-energy parent nuclei through the CODS [6]. These variants yield emphasis to the main one, since the necessary techniques is not currently standard.

- (c) Neutrons or γ radiation from a nuclear explosion are the most suitable in technical aspects but this variant is rejected as being non-ecological.
- (v) Action of the DGLDE chain is consistent in all its elements.
- (vi) All main elements and DGLDE as a whole have a high margin of reliability.
- (vii) The basic DGLDE scheme is unique in its main features except for non-principal (auxiliary) variants. Hence, there are many auxiliary (with non-principal differences from the scheme outlined here in sections 5, 6 and 8) variants for all DGLDE elements on the chance of unforeseen circumstances.

All the points listed above create a sufficient guarantee for the completeness of DGLDE at the present time.

Acknowledgements

The author expresses his gratitude to the participants of the theoretical seminar at the Institute of General Physics, Russian Academy of Sciences, headed by A.A. Rukhadze, for valuable discussions of this study and its various aspects from 1991–1992; to G.S. Baldwin, V.I. Gol'danskii, and V.S. Letokhov for the early discussions of pumping problems over a long time; to L.A. Rivlin, Valeriu Zoran, the Organizing Committee of the First International Gamma-Ray Workshop GARALAS'95 and all its participants for the attention to this work; for the discussions at GARALAS'95 and preliminary reading this work to J.J. Carroll and C.B. Collins; to my colleagues and friends Andrey Starostin, Andrey Davydov, Andrey Marshakov, Vitalii Samartcev, Elena Shirany, Artem Sorokin, Ludmila and Sergey Christenco and my daughter Anna Karyagina for the support and large efforts in preparing this paper.

References

- [1] G.C. Baldwin, J.C. Solem, V.I. Gol'danskii, *Rev. Mod. Phys.* 53 (1981) 687.
- [2] *Proc. 1st Int. Laser Science Conf., Dallas, Texas, Nov. 18–22, 1985*, Bull. Amer. Phys. Soc. 30 (1986) 1763.
- [3] V.I. Vysotscii and R.N. Kuz'min, *Gamma-Lasers* (Moscow, 1989) p. 1.
- [4] S.V. Karyagin, *Zh. Eksp. Teor. Fiz.* 79 (1980) 730.
- [5] S.V. Karyagin, deposited paper, Vses. Inst. Nauchn. Techn. Inform. (VINITI), no. 2797-83 (1983) 1.
- [6] S.V. Karyagin, *Int. J. Laser Phys.* 5 (1995) 343.
- [7] G.C. Baldwin and J.C. Solem, *Int. J. Laser Phys.* 5 (1995) 231.
- [8] G.C. Baldwin and J.C. Solem, *Laser Phys.* 5 (1995) 326.
- [9] V.S. Letokhov, *Zh. Eksp. Teor. Fiz.* 64 (1973) 1555.
- [10] V.S. Letokhov, *Nonlinear Selective Photo processes in Atoms and Molecules* (Nauka, Moscow, 1983) (in Russian).

- [11] P. Dyer and G.C. Baldwin, *J. Appl. Phys.* 58 (1985) 2431.
- [12] V.I. Gol'danskii and Yu.M. Kagan, *Zh. Eksp. Teor. Fiz.* 64 (1973) 90.
- [13] These proceedings (Proc. 1st Int. Gamma-Ray Laser Worksh. GARALAS '95, Predeal, 1995), *Hyp. Int.* 107 (1997).
- [14] A.A. Sysoev, I.V. Shchekina and S.V. Karyagin, these proceedings (1st Int. Gamma-Ray Laser Worksh., 1995), *Hyp. Int.* 107 (1997) 481.
- [15] S.V. Karyagin, these proceedings (1st Int. Gamma-Ray Laser Worksh., 1995), *Hyp. Int.* 107 (1997) 449.
- [16] Yu.B. Khariton, A.M. Voinov, V.F. Kiselev et al., in: *Aperiodic Pulse Research Reactors, Problems of Modern Experimental and Theoretical Physics*, ed. A.P. Aleksandrov (Nauka, Leningrad, 1984) (in Russian).
- [17] V.I. Gol'danskii, Yu.M. Kagan and V.A. Namiot, *Pis'ma v Zh. Eksp. Teor. Fiz.* 18 (1973) 61.
- [18] C.B. Collins and J.J. Carroll, *Int. J. Laser Phys.* 5 (1995) 209.
- [19] B. Balko, I.W. Kay, J.D. Silk and D.A. Sparrow, *Int. J. Laser Phys.* 5 (1995) 355.

Gamma-ray solid laser: ion-optical system for fast high-quality focusing of powerful non-paraxial ion beams of large format enriched with excited nuclei

A.A. Sysoev, I.V. Shchekina

*Moscow State Engineering Physics Institute (Technical University), Kashirskoe sh. 31,
Moscow 115409, Russia*

and

S.V. Karyagin

*Semenov Institute of Chemical Physics, Russian Academy of Science, Kosygin Str. 4,
Moscow 117334, Russia*

An ion-optical system (IOS) for fast high-quality focusing of powerful paraxial ion beams of large format is suggested. Such beams could be enriched in excited short-lived (10^{-4} – 10^{-6} s) laser-active nuclei (ELAN). To increase the beam power, ions are collected from the visible surface (10 – 10^4 cm 2) of an intermediate target (converter). The full converter surface is enhanced by a factor of 10^2 – 10^4 by a special micro-relief and achieves 10^3 – 10^7 cm 2 . The atoms containing ELAN are created in the converter by a powerful radiation source using neutrons, γ quanta, charged particles, etc. Those ELAN atoms are emitted from the converter surface and selectively ionized by a dye laser just above the surface. Using a specially chosen emitter (converter) shape, a paraxial ion beam is formed. This is due to the micro-relief structure of the emitter surface, its high-quality orientation, and cylindrical (instead of spherical) ion optics. In the vicinity of an active medium (AM) for a gamma-ray laser, the ions are decelerated so that they can penetrate only into 1–3 outer layers of the host matrix, e.g., diamond. This makes heating of the AM by the ion beam negligible in comparison to self-heating due to internal conversion. Analytical and numerical estimation of the IOS aberrations have shown that the compression of the ion beam exceeds 10^5 – 10^6 , and that a considerable part (10%) of the ELAN reach the AM in a time as short as 10^{-7} s. This ensures the rapid and controllable deposition of ELAN into an AM within a gamma-laser system based on existing techniques without using nuclear explosions.

1. Introduction

Focusing in ion-optical and electron-optical systems is extremely important in a wide variety of applications of ion and electron beams [1]. This is especially true for electron-beam devices [2]. In the majority of cases for either ions or electrons, optics provide paraxial beams [3]. However, in some systems it is necessary to col-

lect and focus ions from a large emitting surface. One such system in which this may be important is in the formation of high-intensity ion beams, with ions separated according to specific physical properties, for the creation of an active medium (AM) in gamma-laser experiments [4,5,8–13]. Such ion-optical systems can be created under concrete conditions [5,10–11].

Some schemes for a gamma-ray solid laser (GSL) are based on a fast transfer of short-lived (10^{-4} – 10^{-6} s) excited laser-active nuclei (ELAN) from the region of their creation to the site of an AM. Those approaches are quite interesting from the perspective of realizing a GSL using existing techniques [4,5,8–13]. In refs. [4,5] a number of fast ELAN transfer schemes have been suggested. In the present paper a so-called “straight-through” ion optical system (IOS) [5] for the fast transfer of short-lived ELAN to the AM is considered. In the straight-through IOS the ELAN are created in a special intermediate target-converter by a powerful radiation pulse using neutrons, γ quanta, charged particles, etc. For example, neutrons might be used with a flux of 10^{15} cm^{-2} during 10^{-5} s and distributed over a large area of 10^3 – 10^4 cm^2 by a non-periodic pulse reactor of the Big Kukla type. The ELAN are extracted from 1–5 surface layers of the converter by the Szilard–Chalmers effect (SCE). The ELAN enrichment of an ion beam due to the SCE is about 0.1–1% [5] and may be regarded only as a preliminary possibility. This degree of enrichment is insufficient to achieve the real threshold conditions [4,5,8–12]. GSL schemes based on ELAN enrichment exclusively by SCE (see ref. 27 in [12]) have been criticized [12]. In our schemes [4,5,9–11] the SCE-enrichment is amplified by pulse optical laser enrichment using multi-photon selective ionization of atoms containing ELAN. This double enrichment can provide 90–99%. The laser pulse enrichment occurs above the visible output surface of the converter during a period of only 10^{-8} – 10^{-7} s. To increase the power of the ELAN beam, the full converter surface is assumed to exhibit a micro-relief pattern so as to provide an enhancement of 10^2 – 10^3 . Hence, the full converter surface provides 10^3 – 10^7 cm^2 although the visible surface is about 10 – 10^4 cm^2 . The micro-relief elements are assumed to be oriented with high precision relative to the visible surface. Because of the initial velocity distribution of ELAN, emission from the converter exhibits a sharp anisotropy with a characteristic angular spread of 0.01–0.001 rad [5]. This behavior is important for the effective action both the IOS and the multi-photon selective ionization of the ELAN atoms. The present paper discusses theoretical and computer simulations of real ELAN transfer for different types of aberrations. The ELAN are transferred from a large-sized converter of 10 – 10^4 cm^2 to an AM of very small size (about 10^{-4} cm^2). For rapid transfer during 10^{-7} s, the ion-beam is accelerated and decelerated several times along its path. In particular, near the AM the ion beam is decelerated in order to prevent strong overheating of the AM. Owing to a special micro-relief of the AM [5] the penetration of ELAN into 1–3 subsurface layers is sufficient for γ lasing without diffraction losses. To achieve this the final kinetic energy of ions must be about 0.1–0.5 keV. Thus, the IOS must simultaneously meet a number of stringent

conditions which are difficult to fulfill self-consistently using ordinary ion optics [1–3]. These conditions are:

- (i) Focusing of an initially large-format (10^1 – 10^4 cm 2) ion beam into an extremely narrow one of about 10 $^{-4}$ cm 2 ;
- (ii) Transferring of ELAN from converter to the AM during a time as short as 10 $^{-7}$ s;
- (iii) Decelerating the ELAN near an AM to kinetic energies less than 0.5 keV.

This paper is devoted to the solution of these technical problems which are very important for the realization of gamma-laser pumping. Analysis was carried out to create an ion-optical system which would fulfill such conflicting demands, including the collection of ions from a large surface and high-quality focusing ion of the beam. It is very necessary to have a large ratio of the initial and final cross sections for the ion beam (up to 10 4 –10 5). The high-quality focusing requires either exclusion or careful correction for aberrations. Therefore, axial-symmetric systems cannot be used in this application where ions are transported along an axis. It is preferable to use focusing systems in which ions move independently along different coordinates. This overcomes restrictions based on the Liouville theorem [6,7].

The solution of this problem is very difficult in general. Therefore, the following assumptions were made: First, an arbitrary choice is made for the emitting surface form. Second, only high-quality focusing for one coordinate is needed. Third, the initial spread of angular and energy distributions of ions is small along the coordinate #¹ in which direction high-quality focusing is required.

2. Description of the ion-optical system

The electrical field in the transported lens (TL) of the ion-optical system (IOS) was designed so that the ions were accelerated only along the direction of their movement (fig. 1). A cylindrical emitting surface provides ion transport to the location of the symmetry axis. The TL is formed by two pairs of coaxial cylindrical electrodes labeled in the figure as 1–4, where electrode 1 acts as the emitter. Between electrodes 1 and 2 a strong accelerating field exists, and between 3 and 4 electrodes a decelerating field of approximately equal strength is arranged. Electrodes 2–4 are two-dimensional grids which are constructed in the form of circles due to the requirement of high-quality focusing in the radial plane (r, φ -plane). These are the filaments indicated parallel to the axis of field symmetry for clarity in fig. 1. In some cases it is sufficient to provide only electrode 4 in this form because it has the largest

^{#1} For example, according to ref. [5] the surface of an emitter is covered by a network of oriented microelements (pores, slits, hairs), which direct the exit of ions with large accuracy. As a result this structure considerably lowers the angular spread of emitted ions.

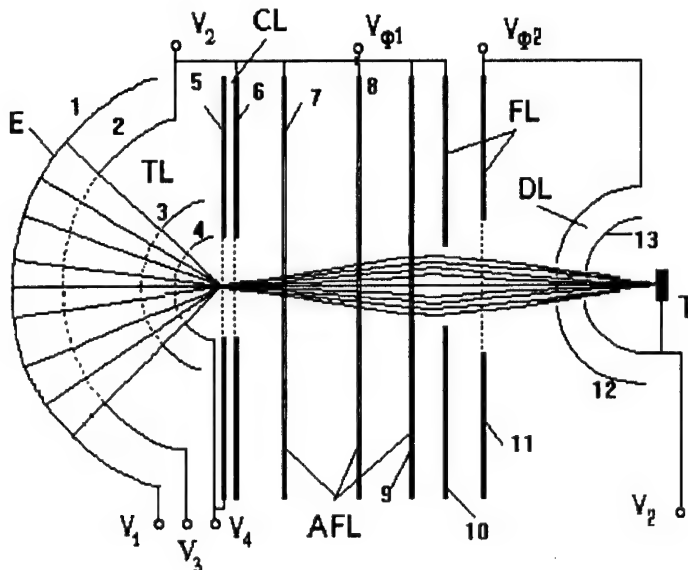


Fig. 1. An ion-optical system for wide-frame beam focusing. The emitting electrode is denoted by E, the transporting lens by TL, the converging lens by CL, the axial focusing lens by AFL, the focusing lens by FL, the decelerating lens by DL and the target by T.

effect on the lens behavior. These effects are appreciable in the radial direction but not axially. The action of these fields is strictly directed along of the primary movement of the ions. In essence, beam focusing on the axis of symmetry is purely a geometrical effect and the electric field only accelerates the ions. Near the symmetry axis the ions are slowed by the action of the opposite field from the slowing-down lens (electrodes 3,4). The transportation lens provides an acceleration in a given direction and transforms the ion beam into a paraxial one and further focusing is produced by the cylindrical focusing lens (FL). The decelerating lens (DL) is placed after the focusing lens such that all trajectories are roughly perpendicular to its external cylindrical surface. The DL decreases the ion energy before impact upon the target without introducing any significant aberration. One of the principal difficulties for the analysis of ion-optical systems by numerical methods is due to the large ratio between the size of the emitting surface and that of the required image. This makes it necessary to simulate the grid area with a large number of cells, which can inhibit calculations performed even with high-power computers. This obstacle is removed by the combined approach used here.

The axial-symmetry problem, connected with the movement of ions in the transporting and slowing-down lenses, was resolved by a pseudo-analytical method. The initial data permit the solution of the problem to be presented in the form of a row of small parameters. The pseudo-analytical solution found in this way was used for numerical simulation of other lenses in the next stage. The ion-optical lens for the

transportation and the focusing of ion beams are simulated by these numerical methods. The boundary conditions for calculation of each following element are chosen on the basis of the solution obtained by considering the previous element.

3. Determination of aberration properties of the transport lens

The calculation of the ion trajectories in axially symmetric electrical fields is most conveniently performed in cylindrical coordinates (fig. 2). The differential equations for ion movement can then be presented in the following form:

$$\begin{aligned}\ddot{r} - r(\dot{\varphi}_*)^2 &= E_r/M, \\ 2\dot{r}\dot{\varphi}_* + r\ddot{\varphi}_* &= E_\varphi/M, \\ \ddot{z} &= E_z/M,\end{aligned}\tag{1}$$

where $M = m/q$, the mass-to-charge ratio. The ion trajectories are determined in $\varphi_*(r), z(r)$ form (see fig. 2, with the z coordinate perpendicular to the planes of the drawing). In order to transform eq. (1) into trajectory equations the following substitutions were used: $\varphi_* = \varphi_0 + \varphi(r)$, $z = z(r)$, where φ_0 is the angular coordinate of the point at which ions exit the emitter. It is also necessary to replace differentiation with respect to time by that with respect to r and to take into account the law of conservation of energy, i.e.

$$(r)^2[1 + r^2(\varphi')^2 + (z')^2] = 2(V - U)/M,\tag{2}$$

where V is the initial energy of ions in volts and U is the current potential. This gives differential equations for the ion trajectory from eq. (1). From the initial conditions it follows that $\varphi'_1 \ll 1$, where φ'_1 is the initial value of the radial derivative of φ , assuming the angular divergence of ions from the emitter is small. As a result the

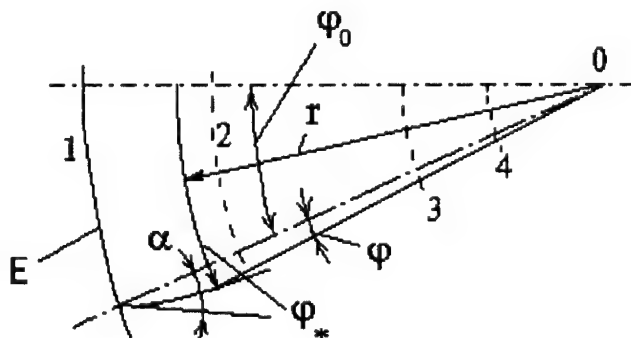


Fig. 2. Coordinate system used to investigate the effect of the transporting lens.

following system of differential equations for ion trajectories can be written (using a linear approximation):

$$\begin{aligned} \varphi'' + \left[\frac{2}{r} + \frac{E_r}{2} \frac{1}{(V-U)} \right] \varphi' &= 0, \\ z'' + \frac{E_r}{2(V-U)} z' - \frac{E_r}{2(V-U)} &= 0. \end{aligned} \quad (3)$$

Substituting the potential and electrical field distributions for a cylindrical condenser into eq. (3) and integrating the first of eq. (3) gives

$$\varphi' = \varphi'_1 (r_1/r)^2 \left[\frac{-a}{\ln X - a} \right]^{1/2}, \quad (4)$$

where $X = r/r_1$, $X_{i1} = r_i/r_1$, and $a = -[(V - V_1)/(V_1 - V_2)] \ln(X_{21})$. The quantity φ'_1 for $X = 1$ is

$$\varphi'_1 \approx \frac{\tan \alpha \cotan \varphi_0 - 1}{r_2(\cotan \varphi_0)}.$$

For example, if $\varphi_0 = 0$, then $\varphi'_1 = (\tan \alpha)/r_2$. By repeated integration the solution for an ion trajectory at a radial plane between electrodes 1 and 2 can be written as

$$\varphi = r_1 \int_1^{X_{21}} \varphi'_1 (1/X)^2 \left[\frac{-a}{\ln X - a} \right]^{1/2} dX + \varphi_0. \quad (5)$$

In the section between electrodes 2 and 3, the electric fields are $E_r = 0$ and $E_z = 0$ and eq. (3) simplifies considerably to

$$\begin{aligned} \varphi'' + \frac{2}{r} \varphi' &= 0, \\ z'' &= 0. \end{aligned} \quad (6)$$

Integration of the first of eq. (6) gives the solution

$$\varphi = r_1 \int_{X_{21}}^{X_{31}} \varphi' dX + \varphi_{02}, \quad (7)$$

where φ_{02} is the value of φ on the cylindrical surface of radius $r = r_2$.

In the space between electrodes 3 and 4 the solution for an ion trajectory in a radial direction is similar to eq. (5) and taking this into account the values become

$$\varphi = r_1 \int_{X_{31}}^{X_{41}} \varphi' dX + \varphi_0, \quad (8)$$

where

$$\varphi' = \varphi'_{03}(X_{31}/X)^2 \left[\frac{-a}{\ln(X/X_{31} - a)} \right]^{1/2},$$

and

$$a = \frac{V - V_2}{V_3 - V_4} \ln(X_{31}/X_{41}).$$

In the section between electrodes 4 and 5 the solution is similar to eq. (7). In the source plane aperture of the transformation lens it is necessary that $\varphi^* = \pm \frac{1}{2}\pi$. Then:

$$\varphi = \frac{-\varphi'_{04}(r_4)^2}{\cos \varphi_{04} + r_4 \varphi'_{04} \sin \varphi_{04}} \frac{1}{\sin \varphi^*}, \quad (9)$$

for both "positive" and "negative" aberration. To calculate the axial coordinate at the aperture of the transformation lens it is more convenient to use the second differential equation of eq. (6). The result is

$$z_p = v_{0z}(t_{12} + t_{23} + t_{34} + t_{45}) + z_0, \quad (10)$$

where v_{0z} is the initial component of the velocity in the axial direction, z_0 is the initial axial coordinate, t_{ij} is the time of flight for ions in the appropriate section and z_t is the total axial coordinate. To calculate the time of flight of an ion in the section between electrodes 1 and 2 and 3 and 4 it is possible to employ the following equation:

$$dt = dr/v = dr/\left[2(V - U)/M\right]^{1/2}.$$

Expressions for t_{12} and t_{34} can be obtained in integral form as

$$t_{12} = r_1(M/2)^{1/2} \int_1^{X_{21}} \frac{dX}{(A_{12} + B_{12} \ln X)^{1/2}}, \quad (11)$$

and

$$t_{34} = r_1(M/2)^{1/2} \int_{X_{31}}^{X_{41}} \frac{dX}{(A_{34} + B_{34} \ln X)^{1/2}}, \quad (12)$$

In the sections between electrodes 2 and 3 and 4 and 5, there are no fields and the ion velocity is constant. Therefore the time of flight in those sections is simply

$$t_{23} = (r_2 - r_3)/v_{23},$$

$$t_{45} = r_4/v_{45}.$$

where V_{ij} is the ion velocity in the appropriate section. The above expressions were used to study the aberration properties of the transport lens for various geometrical

and electrical parameters. In fig. 3 the dependence of aberration in the vicinity of transport lens is shown for an ion emitted from the surface for a specific initial angle in relation to the average trajectory φ_0 . The drawing was constructed using the parameters $V_1 = 0$, $V_2 = V_3 = -1 \times 10^4$ V, $V_4 = -500$ V, $r_2 = 0.9r_1$, $r_3 = 0.2r_1$, $r_4 = 0.1r_1$, and $r_1 = 30$ cm. The ion angular divergence was $\alpha = \pm 10^{-3}$ rad. According to the analysis shown in the drawing, for an angular range of -40° to $+40^\circ$, aberrations are insignificant. A radius of $r_1 = 30$ cm corresponds to an emitting surface with a length of about 40 cm. If the emitting surface height is chosen to be 4 cm, its area will be on the order of 160 cm^2 . The absolute value of aberration at larger angles than $\pm 40^\circ$ depends on the choice of the potentials of electrodes 4 and 5. In fig. 4 the dependence of the aberration on variations in ion energy (in volts) in the section between electrodes 4 and 5 is presented. On the initial site the curves of the aberration decrease sharply, but at energies above 100 V changes are negligible, occurring in the range (1–30) μm . From the curves it follows that it is undesirable to operate the transport lens for ion energies less than 100 V between electrodes 4 and 5.

For comparison a lens of reduced size was considered ($r_1 = 5$ cm, $r_2 = 4$ cm, $r_3 = 2$ cm, $r_4 = 1$ cm). The aberration dependence of the lens for various exit energies is presented in fig. 5. As was to be expected, lens aberration decreased with reduced lens dimensions. A second feature was a greater range of initial angles for which there was no appreciable aberration increase. Within the angular range $-40^\circ < \varphi_0 < 40^\circ$ absolute aberration values were within the 1–2 μm limits. This corresponds to a beam compression of about $(3–7) \times 10^4$.

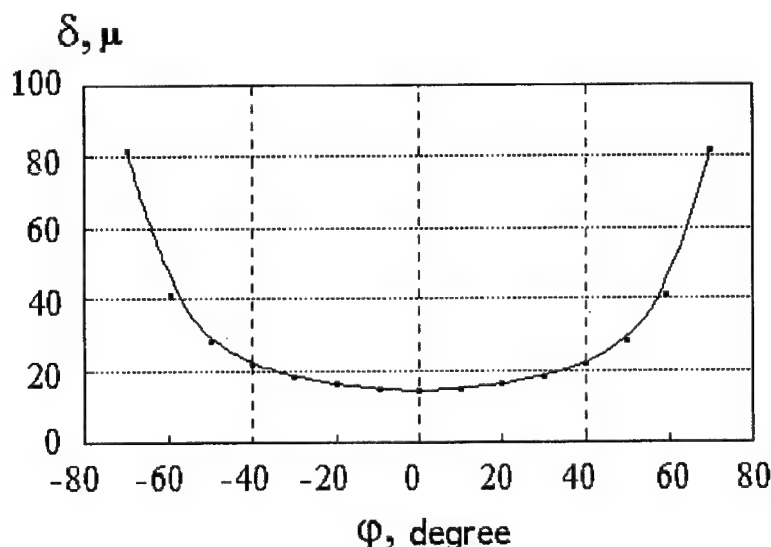


Fig. 3. Dependence of transporting lens aberration on the initial angular coordinate φ_0 with which ions start from the emitting cylindrical surface ($r_1 = 30$ cm).

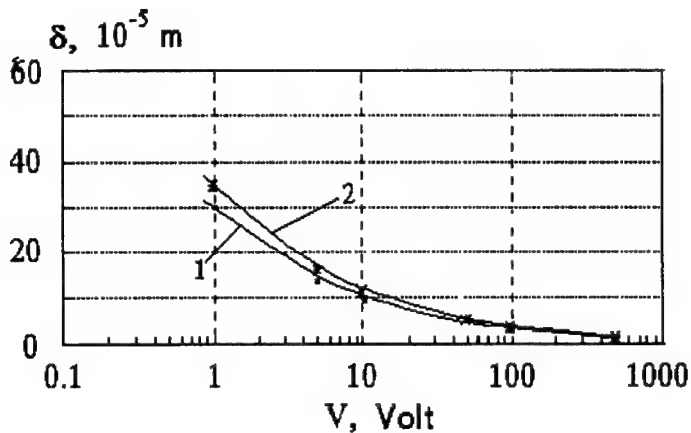


Fig. 4. Dependence of transporting lens aberration on ion energy at its output for 1: $j_0 = 0$; 2: $j_0 = \pm 400$.

A calculation of axial coordinate variations of ion trajectories near the transport lens gives 14 mm for a system with radius $r_1 = 30$ cm. The half-divergence angle at the system exit varies from 1.3° for an ion energy of 500 V to 2.9° for ions of 100 V. Such a large angular divergence at this stage does not play an essential role, because of focusing that occurs later in the system.

4. Transformation of the beam to paraxial and focusing at target

The final transformation of the wide-frame ion beam to a paraxial one is carried

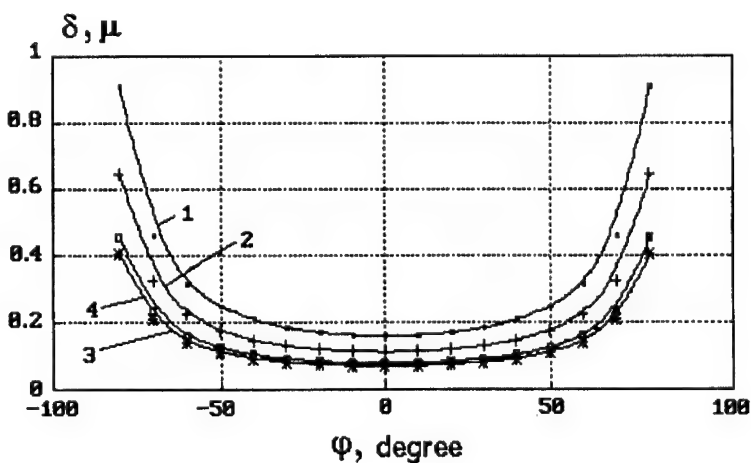


Fig. 5. Dependence of transporting lens aberration (for $r_1 = 5$ cm) on angular coordinate for an ion output for 1: 100 V; 2: 200 V; 3: 400 V; 4: 500 V.

out by the conversion lens. The transformation principle is based on sharp acceleration along the axis of a beam having initially low ion energies. The paraxial ion beam is further compressed with the help of the focusing lens FL. The ion-optical properties of transformation and focusing lenses were studied by numerical methods.

Several variants of the ion-optical systems with different geometrical parameters as well as electrode potentials were considered. For the conversion lens it was convenient to consider a two-size grid in which filaments are set in parallel planes relative to the plane of the drawing (fig. 1 shows filaments perpendicular to the plane of the drawing). The interval between grid planes was chosen to be 4 mm.

In classical examples it is difficult to obtain a low aberration. The main reason is the action of the lens defocusing section on ion trajectories. Therefore, an attempt was made to suppress the defocusing field with the help of the two-size grid (electrode 11 in fig. 1). This decreased the focusing lens aberration. As a result the aberration can in some cases be on the order of 1–10 μm . A specific variant of the lens has the following geometrical parameters: distance from the subject plane up to the first electrode plane (electrode 10 in fig. 1) is $l_1 = 80 \text{ mm}$, distance from the second electrode plane (electrode 11) up to the image (target) plane is $l_2 = 28 \text{ mm}$, distance between electrodes 10 and 11 is 2.5 mm. The slit width in electrode 10 was 1 mm.

The ion trajectory calculation for the decelerating lens (DL) was produced by the same method as between electrodes 3 and 4 (see fig. 1). This role is fulfilled by two coaxial cylindrical electrodes with radii of $r_{12} = 20 \text{ mm}$ and $r_{13} = 10 \text{ mm}$ for the two-size grid apertures. The focusing lens aberration spread at the input of the

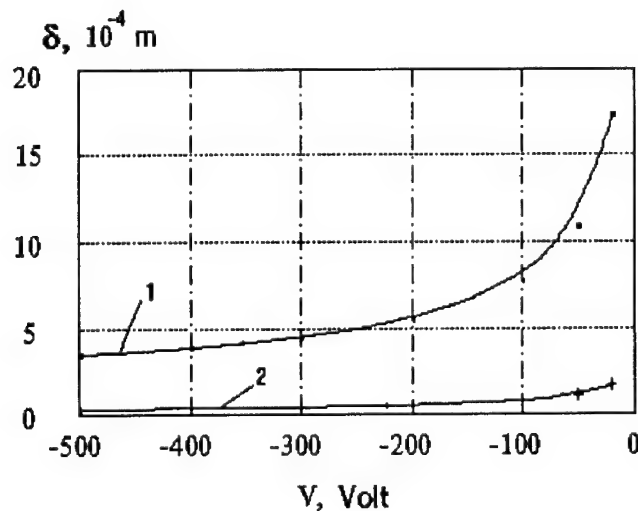


Fig. 6. Aberration dependence in a decelerating lens on ion energy at its output. 1: For aberration of a focusing lens 100 μm ; 2: for aberration of a focusing lens 10 μm .

decelerating lens was used as initial values. Taking into account eq. (9), integration of eq. (8) determines the aberration at the target (T). The magnitude of the aberration depends largely upon the final ion energy and the focusing lens aberration (100 and 10 μ). This is shown in fig. 6. The aberration increases with reduction of ion energy. To achieve the required decrease of image width it is necessary to decrease the image aberration of the focusing lens (curve 2) as far as initial conditions on a decelerating lens, the input to which plays the main role.

Ion focusing in the axial direction is carried out in the traditional way, i.e. with a cylindrical lens consisting of electrodes 7, 8 and 9. In construction of the axial focusing lens, two-size grids are used for edge-field correction. In the calculation of the axial component of the ion coordinates in the lens, the input ion beam assumes parallel trajectories. The simulation of the operation of the lens was carried out for different electrode configurations. One variant provides satisfactory focusing and gives an image on the target of 3–4 mm axial size. The axial lens apertures provides the 4 cm ion beam size.

5. Conclusion

In the traditional approach to ion-optical systems, non-paraxial beam focusing is not generally feasible. However, it has been shown that for some special cases a solution is possible. An original ion-optical system is presented in which the initial focusing of a wide-frame ion beam is realized not by electrical fields, but by “geometrical” means [4,5]. As a result extremely high compression of the ion beam dimensions is provided in a radial direction. It is shown that the above IOS focuses ion beams leaving emitting surfaces with a size up to 160 cm to an image of 90 μm . The cross section of a typical active media (AM) for a GSL is expected to be about 10^{-4} cm as discussed in the introduction. Beam compression in the longitudinal direction of an AM to 1–0.1 cm can be realized using this system. Hence, about 10% of the total initial amount of ELAN can be transferred to an AM. This ensures a large margin of reliability for creation of a GSL based on existing techniques, even without a nuclear explosion [5,10,11].

References

- [1] A.P. Banford, *The Transport of Charged Particle Beams* (E. and F.N. Spon Limited, London, 1966).
- [2] A.A. Jigarev, *Electronic Optics and Electron Beam Devices* (Vyishaya Shkola, Moscow, 1972) (in Russian).
- [3] Yu.A. Berezin (ed.), *Numerical Methods of Optimization of Issuing Electron-optical Systems* (“Science”, Novosibirsk, 1987) (in Russian).
- [4] S.V. Karyagin, Vs. Inst. Nauch. Tech. Inf. (VINITI) 2797 (1983) 1 (in Russian).
- [5] S.V. Karyagin, Laser Physics 5 (1995) 343.

- [6] J.R. Pierce, *Theory and Design of Electron Beams*, 2nd Ed. (Van Nostrand, New York, 1954).
- [7] D.L. Judd, *Annu. Rev. Nucl. Sci.* 8 (1958) 181.
- [8] G.C. Baldwin, J.C. Solem and V.I. Gol'danskii, *Rev. Mod. Phys.* 53 (1981) 687.
- [9] S.V. Karyagin, *Zh. Eksp. Teor. Fiz.* 79 (1980) 730.
- [10] S.V. Karyagin, these proceedings (1st Int. Gamma-Ray Laser Worksh., 1995), *Hyp. Int.* 107 (1997) 449.
- [11] S.V. Karyagin, these proceedings (1st Int. Gamma-Ray Laser Worksh., 1995), *Hyp. Int.* 107 (1997) 465.
- [12] G.C. Baldwin and J.C. Solem, *Laser Physics* 5 (1995) 231.
- [13] These proceedings (Proc. 1st Int. Gamma-Ray Laser Worksh. GARALAS'95, Predeal, 1995), *Hyp. Int.* 107 (1997).

Author index

- Agee, F.J., Radiation machines for gamma-ray laser research 107(1997) 69
 Akaoka, K., see Arisawa, T. 107(1997) 101
 Alpatov, V.G., Yu.D. Bayukov, A.V. Davydov, Yu.N. Isaev,
 G.R. Kartashov, M.M. Korotkov, V.E. Rad'ko, A.A. Sadovsky and
 V.M. Samoylov, Experiments on the gravity effect on the ^{109}Ag gamma
 resonance 107(1997) 231
 Arisawa, T., M. Miyabe, A. Sugiyama, K. Yamazaki, A. Ohzu, Y. Suzuki,
 K. Akaoka, I. Wakaida and Y. Maruyama, Separation of an isotope as a
 precursor of a gamma-ray laser medium 107(1997) 101
 Balko, B., I.W. Kay, J. Nicoll, J.D. Silk and G. Herling, Inhomogeneous and
 homogeneous broadening effects on nuclear resonance experiments 107(1997) 283
 Balko, B., I.W. Kay, J.D. Silk, R. Vuduc and J.W. Neuberger,
 Superfluorescence in the presence of inhomogeneous broadening and
 relaxation 107(1997) 369
 Barb, D., see Petrascu, M. 107(1997) 247
 Bayukov, Yu.D., see Alpatov, V.G. 107(1997) 231
 Belov, A.G., Yu.P. Gangrsky, A.P. Tonchev and P. Zuzaan, Excitation of the
 high-spin ^{180}Hf isomer and de-excitation of the ^{180}Ta isomer in (γ, γ')
 reactions 107(1997) 167
 Bibicu, I., see Petrascu, M. 107(1997) 247
 Briançon, Ch., see Oganessian, Yu.Ts. 107(1997) 129
 Bugrov, V.P., see Vysotskii, V.I. 107(1997) 213
 Bugrov, V.P., see Vysotskii, V.I. 107(1997) 277
 Buimistrov, V.M., Stimulation of beta-decay by laser radiation 107(1997) 431
 Carroll, J.J. and C.B. Collins, Limits on spurious contributions to integrated
 cross sections for photoexcitation and de-excitation of isomers 107(1997) 149
 Carroll, J.J., see Collins, C.B. 107(1997) 3
 Carroll, J.J., see Collins, C.B. 107(1997) 141
 Carroll, J.J., see Olariu, S. 107(1997) 197
 Collins, C.B. and J.J. Carroll, Progress in the pumping of a gamma-ray laser 107(1997) 3
 Collins, C.B., J.J. Carroll, Yu.Ts. Oganessian and S.A. Karamian, Evidence
 for K mixing in ^{178}Hf 107(1997) 141
 Collins, C.B., see Carroll, J.J. 107(1997) 149
 Collins, C.B., see Olariu, S. 107(1997) 197
 Collins, C.B., see Zoran, V.I. 107(1997) 415
 Constantinescu, M., see Oganessian, Yu.Ts. 107(1997) 129
 Constantinescu, O., see Oganessian, Yu.Ts. 107(1997) 129
 Coussement, R. and G. Neyens, Quantum interferences at nuclear level
 crossing 107(1997) 307
 Coussement, R., see Neyens, G. 107(1997) 319

- Coussement, R., see Odeurs, J. 107(1997) 299
- Davydov, A.V., see Alpatov, V.G. 107(1997) 231
- Dzevitskii, B.E., see Skorobogatov, G.A. 107(1997) 401
- Dzjamko, V.S., I.V. Sokolyuk and T.M. Zajac, A mechanism for excitation of metastable levels by (γ, γ') reactions 107(1997) 175
- Enaki, N.A. and D. Mihalache, Two-photon cooperative emission in the presence of a thermal electromagnetic field 107(1997) 333
- Ganciu, M., see Zoran, V.I. 107(1997) 415
- Gangrsky, Yu.P., see Belov, A.G. 107(1997) 167
- Herling, G., see Balko, B. 107(1997) 283
- Hoy, G.R., Time- domain, nuclear-resonant, forward scattering: the classical approach 107(1997) 381
- Hoy, G.R., see McDermott III, W.C. 107(1997) 81
- Hussonnois, M., see Oganessian, Yu.Ts. 107(1997) 129
- Isaev, Yu.N., see Alpatov, V.G. 107(1997) 231
- Isavnin, A.G., see Sadykov, E.K. 107(1997) 257
- Kamenov, P. and A. Petrakiev, Possibilities for gamma-ray stimulated emission experiments 107(1997) 441
- Karamian, S.A., see Collins, C.B. 107(1997) 141
- Karamian, S.A., see Oganessian, Yu.Ts. 107(1997) 43
- Karamian, S.A., see Oganessian, Yu.Ts. 107(1997) 129
- Kartashov, G.R., see Alpatov, V.G. 107(1997) 231
- Karyagin, S.V., Gamma-ray solid laser: the heat problem and means of solution 107(1997) 449
- Karyagin, S.V., Gamma-ray solid laser: realization of pumping 107(1997) 465
- Karyagin, S.V., see Sysoev, A.A. 107(1997) 481
- Kay, I.W., see Balko, B. 107(1997) 283
- Kay, I.W., see Balko, B. 107(1997) 369
- Kim, J.B., see Oganessian, Yu.Ts. 107(1997) 129
- Kocharovskaya, O., Lasing without inversion: problems and prospects 107(1997) 187
- Kornilova, A.A., see Vysotskii, V.I. 107(1997) 277
- Korotkov, M.M., see Alpatov, V.G. 107(1997) 231
- Kuz'min, R.N., see Vysotskii, V.I. 107(1997) 213
- Kuz'min, R.N., see Vysotskii, V.I. 107(1997) 277
- Ledu, D., see Oganessian, Yu.Ts. 107(1997) 129
- Maruyama, Y., see Arisawa, T. 107(1997) 101
- McDermott III, W.C. and G.R. Hoy, The inelastic channel in time-domain Mössbauer spectroscopy 107(1997) 81
- Meunier, R., see Oganessian, Yu.Ts. 107(1997) 129
- Mihalache, D., see Enaki, N.A. 107(1997) 333
- Miyabe, M., see Arisawa, T. 107(1997) 101
- Moiseev, S.A., Theory of single-photon echo (SP-echo) and the possibility of its experimental study in the gamma-region 107(1997) 345

- Neuberger, J.W., see Balko, B. 107(1997) 369
- Neyens, G., R. Coussement and J. Odeurs, Quantum optics with nuclear gamma radiation 107(1997) 319
- Neyens, G., see Coussement, R. 107(1997) 307
- Nicoll, J., see Balko, B. 107(1997) 283
- Odeurs, J. and R. Coussement, Models for homogeneous line broadening in long-lived nuclear states 107(1997) 299
- Odeurs, J., see Neyens, G. 107(1997) 319
- Oganessian, Yu.Ts., M. Hussonnois, Ch. Briançon, S.A. Karamian, Z. Szeglowski, D. Ledu, R. Meunier, M. Constantinescu, J.B. Kim and O. Constantinescu, Production, chemical and isotopic separation of the $^{178m^2}\text{Hf}$ high-spin isomer 107(1997) 129
- Oganessian, Yu.Ts. and S.A. Karamian, K -mixing in nuclear reactions 107(1997) 43
- Oganessian, Yu.Ts., see Collins, C.B. 107(1997) 141
- Ohzu, A., see Arisawa, T. 107(1997) 101
- Olariu, S., J.J. Carroll, C.B. Collins and I.I. Popescu, Emission of gamma rays by electron–nuclear double transitions 107(1997) 197
- Petrakiev, A., see Kamenov, P. 107(1997) 441
- Petrascu, M., D. Barb, I. Bibicu and D. Tarina, Recoil-free resonant gamma-ray absorption in ^{57}Fe nuclei in the presence of a strong microwave field 107(1997) 247
- Pointu, A.M., see Zoran, V.I. 107(1997) 415
- Popescu, I.I., see Olariu, S. 107(1997) 197
- Popescu, I.-I., see Zoran, V.I. 107(1997) 415
- Rad'ko, V.E., see Alpatov, V.G. 107(1997) 231
- Reiman, S.I., see Vysotskii, V.I. 107(1997) 277
- Rivlin, L.A., Gamma-ray lasing by free nuclei and by matter–antimatter beams 107(1997) 57
- Roberts, H., The importance of stimulated gamma release from isomers 107(1997) 91
- Sadovsky, A.A., see Alpatov, V.G. 107(1997) 231
- Sadykov, E.K., A.G. Isavnin and A.I. Skvortsov, Mössbauer transition dynamics in conditions of strong excitation of nuclear spins 107(1997) 257
- Samartsev, V.V., Dicke superradiance in a biphenyl crystal doped with pyrene molecules and the possibility of this phenomenon in the gamma range 107(1997) 359
- Samoylov, V.M., see Alpatov, V.G. 107(1997) 231
- Shakhmuratov, R.N., Lasing without inversion due to cooling subsystem 107(1997) 205
- Shchekina, I.V., see Sysoev, A.A. 107(1997) 481
- Silk, J.D., see Balko, B. 107(1997) 283
- Silk, J.D., see Balko, B. 107(1997) 369
- Skorobogatov, G.A. and B.E. Dzevitskii, Collective polynuclear superradiance rather than stimulated emission of Mössbauer radiation from $^{125m^2}\text{Te}$ and $^{123m^2}\text{Te}$ 107(1997) 401
- Skvortsov, A.I., see Sadykov, E.K. 107(1997) 257
- Sokolyuk, I.V., see Dzjamko, V.S. 107(1997) 175
- Sugiyama, A., see Arisawa, T. 107(1997) 101
- Suzuki, Y., see Arisawa, T. 107(1997) 101

- Sysoev, A.A., I.V. Shchekina and S.V. Karyagin, Gamma-ray solid laser: ion-optical system for fast high-quality focusing of powerful non-paraxial ion beams of large format enriched with excited nuclei 107(1997) 481
- Szeglowski, Z., see Oganessian, Yu.Ts. 107(1997) 129
- Tarina, D., see Petrascu, M. 107(1997) 247
- Tonchev, A.P., see Belov, A.G. 107(1997) 167
- Vuduc, R., see Balko, B. 107(1997) 369
- Vysotskii, V.I., V.V. Vysotskii, R.N. Kuz'min and V.P. Bugrov, Sub-threshold inversionless quasi-stationary gamma amplification on the basis of Mössbauer ^{57}Fe nuclei and spin-crossover systems in non-conductive complex compounds with ^{57}Co 107(1997) 213
- Vysotskii, V.I., V.P. Bugrov, A.A. Kornilova, R.N. Kuz'min and S.I. Reiman, The problem of gamma-laser and controlling of Mössbauer nuclei decay (theory and practice) 107(1997) 277
- Vysotskii, V.V., see Vysotskii, V.I. 107(1997) 213
- Wakaida, I., see Arisawa, T. 107(1997) 101
- Yamazaki, K., see Arisawa, T. 107(1997) 101
- Zadernovsky, A.A., Gamma-ray tuning by stimulated emission of recoil phonons 107(1997) 219
- Zajac, T.M., see Dzjamko, V.S. 107(1997) 175
- Zoran, V.I., M. Ganciu, A.M. Pointu, C.B. Collins and I.-I. Popescu, X-ray generation in inverse capillary discharges for pumping 107(1997) 415
- Zuzaan, P., see Belov, A.G. 107(1997) 167



ICCDU IV



Fourth International Conference on Carbon Dioxide Utilization

DATE: September 7 (Sunday) - 11 (Thursday), 1997

VENUE: Kyoto International Conference Hall (KICH), Kyoto, Japan

CORRESPONDENCE

Secretariat of ICCDU IV
 Department of Energy and Hydrocarbon Chemistry, Graduate School of Engineering, Kyoto University, Sakyo-ku, Kyoto 606-01, Japan
 Phone:+81-75-753-5682 Facsimile:+81-75-771-7285 e-mail:inui@scl.kyoto-u.ac.jp

DEADLINES

Submission of abstract	February 28, 1997	Hotel accommodations	August 1, 1997
Notification of abstract acceptance	April 15, 1997	Distribution of Final Circular	June 1, 1997
Advanced registration and payment	July 15, 1997	Manuscripts for Proceedings	September 7, 8, 1997

ORGANIZED BY: Organizing Committee of Fourth International Conference on Carbon Dioxide Utilization

Chairman: Tomoyuki INUI (Kyoto Univ.)／Vice-Chairman: Tsutomu YAMAGUCHI (RITE)

SPONSORED BY: Research Association of CO₂Chemical Fixation of The Chemical Society of Japan
 Research Institute of Innovative Technology for the Earth (RITE)

SCIENTIFIC COMMITTEE

M. ARESTA (Italy), Permanent Secretary, D. DARENSBOURG (USA), M. M. HALMANN (Israel), S. INOUE (Japan), T. INUI (Japan), A. KAPLAN (Israel), R. KIEFFER (France), L. LJUNGBDAHL (USA), K. NICHOLAS (USA), G. SILVESTRI (Italy), R. THAUER (Germany), Y. YAMADA (Japan)

CONFERENCE TOPICS

- | | |
|--|---|
| (1)General subjects on CO ₂ utilization including roundtable discussion | (5)Biochemical CO ₂ fixation |
| (2)Catalytic CO ₂ fixation | (6)Organometallic CO ₂ fixation |
| (3)Photochemical CO ₂ fixation | (7)Other aspects of CO ₂ utilization |
| (4)Electrochemical CO ₂ fixation | |

INVITED SPEAKERS

Plenary Lecture

- Y. Inagawa (MITI, Japan): Basic Strategy of Japan for Countermeasure to Mitigate Carbon Dioxide
 H. Arakawa (MITI, Japan): Research and Development on New Synthetic Routes for Basic Chemicals by Catalytic Hydrogenation of CO₂
 A. Fujishima (The Univ. of Tokyo, Japan): New Approaches in CO₂ Reduction
 D. DuBois (National Renewable Energy Laboratory, USA):
 Development of Electrocatalysts for Carbon Dioxide Reduction Using Polydentate Ligands to Probe Structure-Activity Relationships
 S. Miyachi (Research Inst. Marine Biotechnology Institute): Carbon Dioxide and Microalgae
 M. Aresta (Univ. of Bari, Italy): title undecided

Keynote Lecture

- K. Yamada (The Univ. of Tokyo, Japan): Scope of Studies on CO₂ Reduction
 R. Kieffer (EHICS, France)
 Hydrogenation of CO₂ toward Alcohols on Rare Earth Oxide Catalysts Influence of the Composition and the Preparation of the Catalyst
 E. Fujita (Brookhaven National Laboratory, USA): Photochemical Carbon Dioxide Reduction by Transition Metal Macrocycles
 J. Augustynski (Univ. of Geneve, Switzerland): Photoelectrochemical Reduction of CO₂ at Semiconductor and Rough Metal Electrodes
 A. Yokota (Nara Inst. of Science & Technology, Japan):
 Photoelectrochemical Reduction of CO₂ at Semiconductor and Rough Metal Electrodes Super-RuBisCO:
 Improvement of Photosynthetic Performances of Plants
 E. Dinjus (Forschungszentrum Karlsruhe, Germany): Organometallic Synthesis of CO₂ Fixation

CALL FOR PAPERS

You are cordially invited to contribute to the scientific program. Those who wish to present at oral and poster sessions are requested to prepare one page abstract.

PROCEEDINGS

Proceedings of the conference will be published by Elsevier Science Publishers.

REGISTRATION FEE

	before July 15, 1997	on or after July 15, 1997
Active Member	¥ 40,000	¥ 50,000
Student	¥ 20,000	¥ 25,000

Above registration fee includes proceeding expense.

If you are interested in the ICCDU IV conference, please let us know !

ORDERFORM HYPERFINE INTERACTIONS

- Please send SUBSCRIPTION 1997, volumes 104 - 110, 1997, ISSN 0304 3834
Subscription price Swiss Francs 2464,00 / US\$ 1823 including postage including postage
- Please send FREE SAMPLE COPY
- Please send SEPARATE VOLUMES:
 institutional price of Swiss Francs 387.- / US\$ 305.- per volume including postage
 personal price of Swiss Francs 123.- / US\$ 97.- per volume including postage

- vol. 103: Proceedings of the International Symposium on Exotic Atoms and Nuclei 1996
- vol.101-102: Muon Catalyzed Fusion: Proceedings of the International Symposium on Muon catalyzed fusion and the Physics of Exotic Atoms and Molecules (muCF-95) 1996
- vol. 100: Special issue. From hyperfine interactions to antimatter: in minute and giant steps; devoted to the memory of Bernie Irwin Deutch. 1996
- vol 99: Regular issue, No. 4, 1996
- vol. 99: No. 1-3, Andreas Wolf, H.-Jürgen Kluge, Herbert Orth: Atomic Physics with Stored Highly Charged Ions
- vol. 97/98: M. Rots, A. Vantomme, J. Dekoster, R. Coussément, G. Langouche: Hyperfine Interactions detected by Nuclear Radiations
- vol 96: Regular Issue. , No. 3-4, 1995
- vol 96 Regular Issue. , No. 1-2, 1995
- vol. 95. Gülich et al. (Eds) Fourth Seeheim Workshop on Mössbauer Spectroscopy. 1995, 1 volume
- vols 90-94: Long et al. (Eds) Applications of the Mössbauer Effect. ICAME '93. 1995. 5 volumes
- vol. 89: McEachran et al. (Eds) Positron Interactions with Atoms, Molecules and Clusters. 1994, 1 volume
- vols 85-87: Brewster et al. (Eds) Muon Spin Rotation, Relaxation and Resonance. 1994. 3 volumes
- vol. 84: Ambe et al. (Eds) Unstable Nuclei and Particles as Probes in Physics and Chemistry. 1994. 1 volume
- vol. 83: Mercader et al. (Eds) Applications of the Mössbauer Effect. 1994. 1 volume
- vol. 82: Froelich (Ed.) Muon Catalyzed Fusion. 1993.
- vol. 81: D'Auria et al. (Eds) Traps for antimatter and radioactive nuclei. 1993. 1 volume
- vols.78-80: Minamisono et al. (Eds) Hyperfine Interactions. Proc. IX. Conf. 1993. 3 volumes
- vol. 76: Eades (Ed.) Antihydrogen. 1993. 1 volume
- vol. 75: Krane (Ed.) On-line Nuclear Orientation. 1992. 1 vol.
- vol. 74: Inamura et al. (Eds) Lasers in Nuclear Physics. 1992. 1 volume
- vol. 81: D'Auria et al. (Eds) Traps for antimatter and radioactive nuclei. 1993. 1 volume
- vols.78-80: Minamisono et al. (Eds) Hyperfine Interactions. Proc. IX. Conf. 1993. 3 volumes
- vol. 76: Eades (Ed.) Antihydrogen. 1993. 1 volume
- vol. 75: Krane (Ed.) On-line Nuclear Orientation. 1992. 1 vol.
- vol. 74: Inamura et al. (Eds) Lasers in Nuclear Physics. 1992. 1 volume
- vol. 73, 1-2: Parcell (Ed.) Positron Interactions with Gases. 1992. 1 volume
- vol. 72, 1-3: Boolchand (Ed.) Nuclear Zeeman Effect and Recent Advances in Mössbauer Spectroscopy. 1992. 1 volume
- vols. 68-71: Hsia (Ed.) Applications of the Mössbauer Effect. ICAME 91. 1991-1992. 4 volumes
- vols. 66-67: Diaz Aquila (Ed.) Applications of the Mössbauer Effect. LACAME '90. 1991. 2 volumes
- vols. 63-65: Cox (Ed.) Muon Spin Rotation. 1991. 3 volumes
- vols. 59-61: Finger (Ed.) Hyperfine Interactions. Proc. VIII. Conf. 1990. 3 volumes
- vols. 53-58: Nagy (Ed.) Applications of the Mössbauer Effect. 1990. 6 volumes
- vols. 49-51: Literst (Ed.) Nuclear Methods in Magnetism. 1989. 3 volumes
- vols. 47-48: Gülich (Ed.) 3rd Seeheim Workshop on Mössbauer Spectroscopy. 1989. 2 volumes
- vols. 45-46: Carbucicchio (Ed.) Industrial Applications of the Mössbauer Effect. 1989. 2 volumes

Please indicate payment method:

- Check enclosed Please send invoice
 Please charge to my credit card Euro/MasterCard VISA

Card no.: Expiry date: Cardholder:

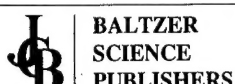
Address:

Postal code: Country:

E-mail address:

Date: Signature:

HOW TO ORDER: In North America please send your order to your usual supplier or to: Baltzer Science Publishers, P.O. Box 8577, Red Bank, NJ 07701-8577. From all other countries please send your order to your usual supplier or to:



P.O. Box 37208, 1030 AE, Amsterdam
The Netherlands, Tel: +31 20 6370061
Fax: +31 20 6323651, E-mail: publish@baltzer.nl